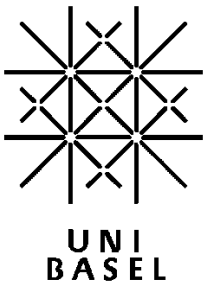

POLYPYRIDYL LIGANDS FOR NANOSTRUCTURED MATERIALS

-

DYE-SENSITIZED SOLAR CELLS

AND

COORDINATION POLYMERS

Inauguraldissertation

Zur

Erlangung der Würde eines Doktors der Philosophie

vorgelegt der

Philosophisch-Naturwissenschaftlichen Fakultät

der Universität Basel

von

Yannick Maximilian Klein

aus Weil am Rhein, Deutschland

Basel, 2018

Genehmigt von der Philosophisch-Naturwissenschaftlichen Fakultät auf Antrag von:

Prof. Dr. Catherine E. Housecroft und Prof. Dr. Konrad Tiefenbacher

Basel, den 27.03.2018

Dekan Prof. Dr. Martin Spiess

ACKNOWLEDGMENTS

I thank Prof. Dr. Catherine E. Housecroft and Prof. Dr. Edwin C. Constable for their outstanding supervision and support during my PhD. I had the freedom to try many different things in the lab, always with the support of Ed and Catherine. I could live out my curiosity and creativity, which made this four years of PhD really enjoyable. I would always choose the Constable/Housecroft group again for doing a PhD. I also thank them for their immense support during the time, when I wrote my thesis and for pressing on with publications. I thank both for proof-reading my thesis.

I thank Prof. Konrad Tiefenbacher for being my co-examiner - I'm very curious about his comments.

I'm grateful, that I was trusted with four great Wahlpraktikum students and that I had the chance to supervise them. Yann Baumgartner, Marco Zutter, Fabian Baca and Sven Freimann are thanked for their work and engagement during their Wahlpraktikum.

I thank Dr. Markus Willgert for measuring Electrochemical Impedance Spectroscopy (EIS). Dr. Sarah Keller, Dr. Collin Morris, Fabian Brunner, Dr. Angelo Lanzilotto and Nathalie Marinakis are thanked for the great collaborations in the group. I thank the crystallographers Dr. Alessandro Prescimone, Dr. Jennifer Zampese and Dr. Markus Neuburger for collecting and solving single crystal structures and for teaching me some crystallography. Dr. Alessandro Prescimone is also thanked for his engagement in high-pressure crystallography of some of my compounds at Diamond Light Source in the UK. Alessandro became a good friend of mine in these four years and I thank him for the many hundreds of kilometres we spent on mountain bike tours together. Dr. Markus Neuburger is also thanked for keeping the powder X-ray diffractometer running and for the fruitful discussions. Beatrice Erismann is thanked for all her administrative support and the small aperos she organized from time to time. I thank Annika Büttner for the self-printed TiO_2 electrodes. Fabian Brunner, Dr. Sven Brauchli and Frederik Malzner are thanked for measuring ESI-MS spectra. I thank Thomas Müntener and Dr. Daniel Häussinger for their support during NMR measurements and especially during low-temperature NMR measurements. I thank Lorenzo Bizzini, Kevin Weiland, Linda Bannwart and Rajesh Mannancherry from the Mayor group for fruitful discussions about organic chemistry and their help with MALDI-TOF and GC-MS measurements. I thank Heinz Nadig and Sylvie Mittelheisser for measuring high-resolution ESI-MS spectra and elemental analysis. I thank

Markus Hauri, Markus Ast, Oliver Ilg and everyone from the technical staff for their support and help. I thank Dr. Thomas Nijs and Prof. Dr. Thomas Jung from the physical department at the University of Basel for their great collaboration in surface physics. Collaborators from the University of Bern - Dr. Karl Krämer, Prof. Dr. Silvio Decurtins and Dr. Shi-Xia Liu are thanked for magnetic measurements. Dr. Mateusz Pitak and Prof. Dr. Simon J. Coles from the University of Southampton are thanked for collecting and solving crystal structures.

I thank all former and current group members of the Constable/Housecroft group for the great and friendly atmosphere inside and outside of the lab. Special thanks go to every one of them.

Last but not least I thank my parents for their financial support during my Bachelor and Master studies and especially for enabling me to study 5 months at the University of Sydney. I thank my beautiful wife and daughter for their support and patience while I was writing this thesis.

For financial support the European Research Council (Advanced grant 267816 LiLo), the Swiss National Science Foundation and the University of Basel are thanked.

This PhD thesis contains two parts, which are presented separately:

Part I – Dye-sensitized solar cells

describes the synthesis of polypyridyl ligands and other compounds and shows their application as dyes in dye-sensitized solar cells.

This part of the thesis can be found on the pages 1-155.

Part II – Coordination polymers

describes the synthesis of polypyridyl ligands and their incorporation as organic linkers into multidimensional coordination polymers.

This part of the thesis can be found on the pages 156 ff.

PART I

DYE-SENSITIZED SOLAR CELLS

TABLE OF CONTENTS

1 ABSTRACT

Burning of fossil fuels in this and the last century lead to global warming and the climate crisis. It is utmost important to prevent further global warming and reverse the increases of the past few decades. A reasonable approach is to replace fossil fuel burning power plants with renewable energy producing technologies. The most promising renewable energy source is the sun. The sun delivers 23 000 TW of sun-light energy every year to the earth, which is a ~1000 times more than the energy consumption of the earth.

One technology to harvest sun light energy and produce electricity is the solar cell. Different solar cell technologies exist, and the approach presented in this thesis is concerning dye-sensitized solar cells. Dye-sensitized solar cells (DSSCs) have the advantage of a relatively easy fabrication and the incorporation of cheap light harvesting materials is possible. In DSSCs a metal oxide (TiO_2) semiconductor is sensitized with an organic or inorganic dye, enabling photon absorption and electron injection into the semiconductor, which generates electric current. The dyes presented in this thesis are based on the relatively cheap and abundant metal copper. Copper in its +1 oxidation state can form heteroleptic complexes with two bisdiimine ligands. One of these ligands (the anchoring ligand) bears anchoring groups, that allow attachment of the complex on TiO_2. The emergence of new anchoring ligands for heteroleptic bisdiimine copper(I) dyes was the aim of my PhD studies and the results are presented in this thesis. In four chapters a systematic investigation of bisdiimine ligands as anchors and capping ligand is described. Various spacers and anchoring groups were incorporated into the anchoring ligand and the performance of these compounds was investigated in solar cell devices. In the last chapter of the main part the synthesis of compound with potential application in p-type DSSCs is presented.

Chapter 3 gives a general introduction about energy problems and solar cell technologies.

Chapter 4 describes the solar cell assembly and characterization of the devices.

Chapter 5 shows the design principle of heteroleptic bisdiimine copper(I) complexes.

Chapter 6 discusses the synthesis of bisdiimine based ancillary ligands and shows their performances in heteroleptic bisdiimine copper(I) complexes for DSSCs.

Chapter 7 describes the synthesis of two anchoring ligands, bearing thiophenediyl groups. It is demonstrated, that the position of the anchoring group on the thiophenediyl influences the device performance.

Chapter 8 introduces four anchoring ligands, bearing cyanoacrylic acid or (1-cyanovinyl)phosphonic acid anchoring groups. Two different ligand cores, 6,6'-dimethyl-2,2'-bipyridine or neocuproine were substituted with the anchoring groups and their performances compared in DSSCs.

Chapter 9 describes the synthesis of a compound bearing three thiophenediyl and a phenylene spacer. The compound is tested on its own and in combination with a bisdiimine copper(I) complex in a DSSC.

Chapter 10 shows the synthesis of an organic dye for p-type DSSCs.

Chapter 11 is the summary and outlook of this thesis.

Chapter 12 gives experimental details of ligand synthesis.

Chapter 13 is the literature reference list.

Part of the work presented in this thesis has been published:

The beneficial effects of trifluoromethyl-substituents on the photoconversion efficiency of copper(I) dyes in dye-sensitized solar cells
F. Brunner, Y. M. Klein, S. Keller, C. D. Morris, A. Prescimone, E. C. Constable, C. E. Housecroft, *RSC Adv.* **2015**, *5*, 58694–58703. DOI: 10.1039/C5RA09590E.

Positional isomerism makes a difference: phosphonic acid anchoring ligands with thienyl spacers in copper(I)-based dye-sensitized solar cells Y. M. Klein, M. Willgert, A. Prescimone, E. C. Constable, C. E. Housecroft, *Dalt. Trans.* **2016**, *45*, 4659–4672. DOI: 10.1039/C6DT00166A.

Cyanoacrylic- and (1-cyanovinyl)phosphonic acid anchoring ligands for application in copper-based dye-sensitized solar cells

Y. Baumgartner, Y. Maximilian Klein, E. C. Constable, C. E. Housecroft, M. Willgert, *RSC Adv.* **2016**, *6*, 86220–86231. DOI: 10.1039/C6RA20375B.

2 ABBREVIATIONS

2D	Two-dimensional
3D	Three-dimensional
Å	Angström
Al_2O_3	Aluminium oxide
AM	Air mass
Bpy	2,2'-Bipyridine
BMII	1-Butyl-3-methylimidazolium iodide
Btu	British thermal unit
CB	Conduction band
CdTe	Cadmium telluride
CIGS	Copper indium gallium selenide
C_μ	Chemical capacitance
COSY	Homonuclear correlation spectroscopy
C_{Pt}	Platinum capacitance
CV	Cyclic voltammetry
δ	Chemical shift
DEPT	Distortionless enhancement by polarization transfer
DFT	Density functional theory
DMF	Dimethylformamide
DMSO	Dimethyl sulfoxide
DSSC	Dye-sensitized solar cell
ε	Extinction coefficient
EIS	Electrochemical impedance spectroscopy
E_{redox}	Redox potential
ERG	Electron releasing group
ESI-MS	Electrospray ionization mass spectrometry
EtOH	Ethanol
eV	Electron volt
EQE	External quantum efficiency
ff	Fill factor
Fc	Ferrocene
Fc^+	Ferrocenium
FIB	Focused ion beam
FT-IR	Fourier-transform infrared spectroscopy
FTO	Fluor-doped tin oxide
GaAs	Gallium arsenide
GNCS	Guanidinium thiocyanate
HMBC	Heteronuclear multiple bond correlation
HMQC	Heteronuclear multiple-quantum correlation
HOMO	Highest occupied molecular orbital
HPLC	High-performance liquid chromatography
InP	Indium phosphide
J/V	Current density/voltage
J_{MP}	Current density at the maximum power point
J_{SC}	Short-circuit current density
λ	Wavelength
LC	Ligand-centered
L_d/L	Length of diffusion/thickness of the porous active layer
LUMO	Lowest unoccupied molecular orbital
m/z	Mass to charge ratio

MALDI-TOF	matrix-assisted laser desorption/ionization – time of flight
MBI	1-Methylbenzimidazole
MC	Metal-centered
Me	Methyl
MeOH	Methanol
MgO	Magnesium oxide
MHz	Megahertz
MLCT	Metal to ligand charge transfer
MO	Molecular orbital
MPN	3-Methoxypropionitrile
MW	Microwave
η	Efficiency
N719	Di-tetrabutylammonium cis-bis(isothiocyanato)bis(2,2'-bipyridyl-4,4'dicarboxylato)ruthenium(II)
NBS	*N*-Bromosuccinimide
NCS	Thiocyanate
NiO	Nickel oxide
NMR	Nuclear magnetic resonance
NOESY	Nuclear Overhauser effect spectroscopy
Ph	Phenyl
Phen	1,10-phenanthroline
P_{in}	Power density of the incident light
P_{MAX}	Maximum power point
Ppm	Parts per million
R_{Pt}	Platinum resistance
R_{rec}	Recombination resistance
R_t	Transport resistance
S	Ground state
S*	Excited state
SEM	Scanning electron microscope
SnO_2	Tin dioxide
τ	Lifetime of the electron
TBP	4-Tert-butylpyridine
THF	Tetrahydrofuran
TiO_2	Titanium dioxide
TMS	Tetramethylsilane
TMS-Br	Bromotrimethylsilane
Tpy	2,2':6′,2"-Terpyridine
TW	Terawatt
U.S.A.	United States of America
UV-VIS	Ultraviolet-visible
VB	Valence band
V_{MP}	Voltage at the maximum power point
V_{OC}	Open circuit voltage
ZnO	Zinc oxide

3 INTRODUCTION

3.1 Energy consumption and the environmental consequences

"How did we end up with the resource and environmental problems we are facing now; how can we decrease the use of fossil fuels and prevent further global warming and reverse the increases of the past few decades?" These are very important questions, if not the most important questions, mankind has to ask and answer this century.

It all started with an important discovery of the industrial revolution in the 18th century - the steam engine by Thomas Newcomen and James Watt. This enabled the development of new machinery for industry, new ways of transportation (steamboats on the Hudson River), electrical motors, and the development of the first diesel engine. It revolutionized everyday live. The improvement of Watt's engine was the use of fossil fuels instead of wood as the energy source, which lead to a second revolution in the late 19th and early 20th centuries. It can be considered a revolution of energy consumption, displayed as an example for the U.S.A. in Fig. 1[1]. The revolution brought forth our modern way of living, but eventually lead to the environmental problems our generation has to face this century.

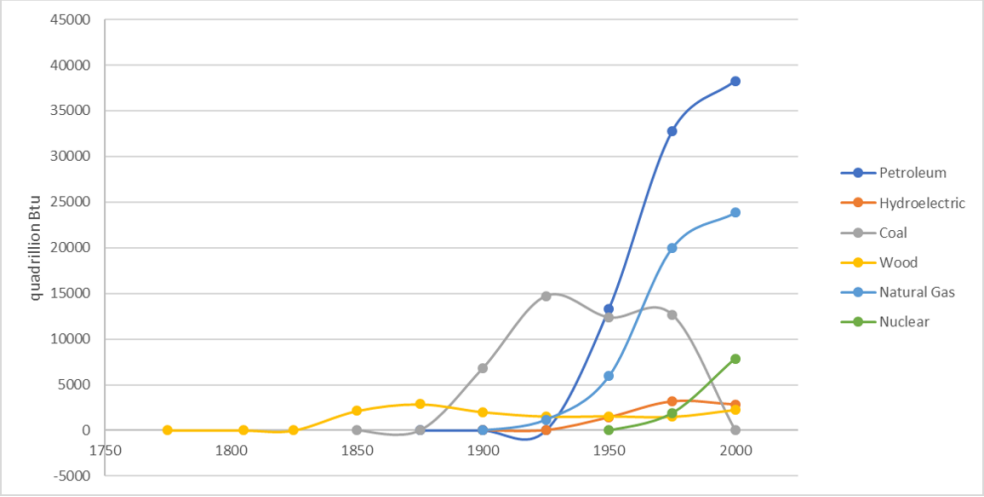

Fig. 1: Energy consumption in the United States, 1775-2000, data from reference[1]. 1Btu (British thermal unit) = 1.055 kJ.

The increasing consumption of the non-renewable resources oil, natural gas and coal since 1900 lead to environmental problems we should be all aware of. New technologies to extract oil from oil sand and the discovery of new oil reserves, especially in Canada[2], delays the event of total resource depletion on our planet to an unknown point in the future. Of greater importance, however, is the increased CO_2 emission, directly correlated to the use of fossil fuels. Burning oil, gas or coal generates heat/energy for example necessary to evaporate water and run steam turbines, which generates electricity. A side product of burning fossil fuels is CO_2. CO_2 emission caused a global rise of temperature by 1.3 °C in the first 6 months of 2016[3], compared to earliest annual data from the late 19th century. The Paris climate change agreement from 2016[4] set a maximum temperature increase of 2°C for our planet (relative to values from the late 19th century), which can only be achieved by reducing CO_2 emissions as soon as possible. At present around 40 gigatons of CO_2 are emitted into the atmosphere per year (36.2 billion tonnes in 2015)[5]. To fulfil the Paris climate change agreement, industry has to improve their manufacturing processes and more sustainable transportation should be promoted, like electric cars and electrified public transportation. This is only useful if the electricity is not produced by burning fossil fuels, thus the question arises where and how this electricity is produced? Most important is the replacement of fossil fuel burning power plants by renewable ones. Since the nuclear disaster in Fukushima in 2011, many countries are turning their backs on nuclear energy. Although some are looking for alternative energies, they still produce most of their electricity by burning fossil fuels. The change to alternative, CO_2 neutral, energy sources is somehow limited. Not every country has appropriate resources available, for example water to use hydroelectric plants, or wind for wind turbines. Other alternative energy sources displayed in Fig. 2 will never be able to produce enough energy to cover the whole energy requirement of our planet[6]. The single renewable, sustainable and near-infinite energy source available is displayed by the big yellow circle, the sun (Fig. 2). The sun delivers the earth 23 000 TW of sun-light energy every year. Less than a thousand times this amount (16 TW in 2009) would be needed to cover the whole energy consumption of the earth. A technology to harvest sun light and convert it into electricity is the solar cell.

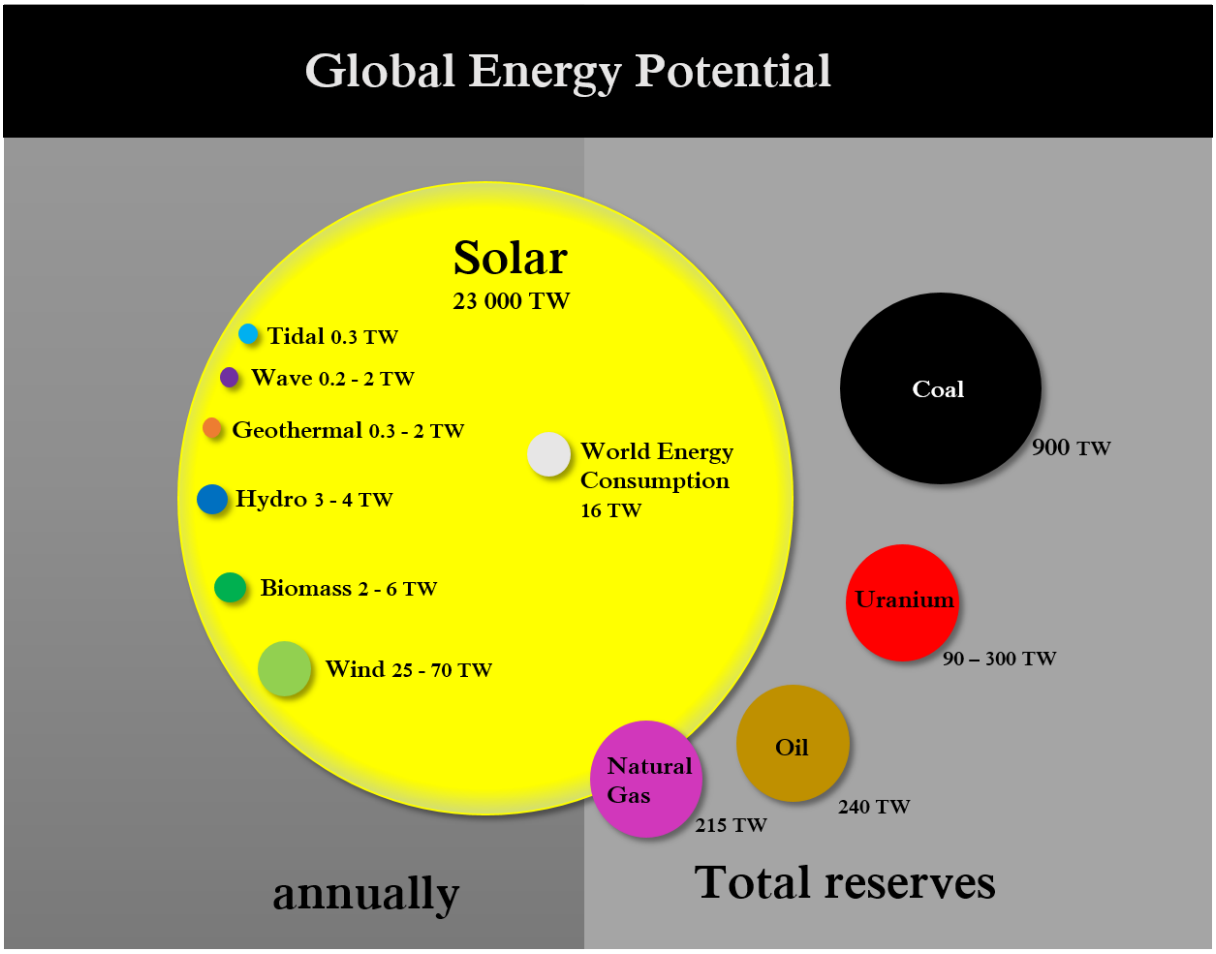

Fig. 2: A fundamental look at energy reserves for the planet by R. Perez & M. Perez 2009, data from ref.[6]

3.2 Solar Cell technologies

A solar cell is a device, that can absorb light (photons) and convert this energy into electricity.

Today's most common solar cells use crystalline silicon as the light harvesting material. These are so-called single junction solar cells with a distinct band gap. Photons with energies below the band gap are not able to generate excitons (excited electron-hole pairs) and photons with higher energies than the band gap lose their excess energy in the form of heat. The theoretical efficiency such a Si-based solar cell can exhibit is limited to 31% (the Shockley-Queisser limit)[7-8]. Single and multicrystalline Si-solar cells are a very robust and reliable technology, can operate for over 30 years with minor loss of efficiency (0.5 – 1%/year)[9] and reach efficiencies of up to 26%[10]. Nevertheless, the production process of these solar cells is difficult, and costs are high compared to burning non-renewable energy sources. To solve the energy problem using solar cells, more innovation and research is necessary to either decrease

production cost and/or increase efficiencies. Apart from mono and polycrystalline silicon other commercial solar cell materials like amorphous silicon, cadmium telluride (CdTe), gallium arsenide (GaAs), indium phosphide (InP) and copper indium gallium selenide (CIGS) exist. These second-generation photovoltaic devices, are based on thin-films of a few micrometres thickness and show efficiencies of 28.8% (GaAs), 22.1% (InP) and 21.0% (CIGS and CdTe)[10]. Production cost, abundancy of elements (In, Ga and Te) and scale-up problems limit the commercialization of these second-generation solar cells. Third generation solar cells are relatively new technologies, with the potential to use multiple junctions within one device, which raises the theoretical efficiency limit to over 40%[11]. Dye-sensitized solar cells (DSSCs) can be divided into two main technologies. On one side, inorganic or organic dyes are used to sensitize a semiconductor and on the other side perovskite materials function as both the dye and hole transporting material. Perovskite solar cells show efficiencies up to 22.1%[12], but suffer from low stability and the use of the toxic metal lead. A combination of 2D/3D perovskite materials proved to be stable over more than 10 000 hours, with a reduced efficiency of 12.9% (compared to 22.1% for the record perovskite solar cell) as the drawback[13]. Efficiencies in this range can also be achieved by organic and inorganic sensitizers, with less effort and fewer drawbacks compared to perovskites.

3.3 Dye-sensitized solar cells

Organic and inorganic DSSCs are single junction solar cells, consisting of a modified semiconductor (TiO_2), which enables absorption and transformation of photons into electrical energy. Compared to other types of solar cells, these DSSCs have the advantage of non-toxic and low-cost materials and show good light harvesting abilities. Dye-sensitized solar cells consist of a dye, which is adsorbed on a nanoporous semiconductor surface. Their ability to absorb photons under irradiation and transform them into separated charges (an electron and a hole) is the main feature these materials possess. The generated electrons can be injected into the TiO_2 semiconductor and used to generate electric power. The hole recombines with electrons from an electrolyte to regenerate the dye in the ground state. The breakthrough DSSC was constructed in 1991 by O'Regan and Grätzel[14]. They used a ruthenium(II)-complex as a dye to modify a nanoporous TiO_2-surface. The huge increase of surface area of the semiconductor enabled increased dye absorption and is the fundamental part of most DSSCs today. Since this report the variety of dyes, electrolytes and electrode-materials has increased tremendously[8, 15-17].

3.3.1 Working principle of a DSSC

A DSSC consists of four main parts (Fig. 3). Conductive glass plates, coated with fluorine-doped tin oxide (FTO) are used as substrates for the working and the counter electrode. The FTO coated working electrode consists of a nanoporous TiO_2 layer in its anatase crystal form. The TiO_2 layer is a semiconductor, which enables electron injection and transport to the FTO. The large band gap of TiO_2 makes this material colourless and only high energy photons in the UV range of the visible light are absorbed.

To enhance the light absorption properties of this material into the visible range of the spectrum (350 – 750 nm) a dye molecule can be anchored to the semiconductor. The dye is the key point of a DSSC and the main research focus. It absorbs photons upon irradiation, transforms them into separate charges (an electron and a hole) and can inject electrons into the TiO_2 semiconductor to generate current.

The electrolyte is the third important part of a DSSC. It is often a liquid, containing a redox couple, which enables transport of charge carriers between both electrodes. Polymer[18] and solid-state electrolytes[19] are another important research field, as leakage of the electrolyte is diminished or prevented in this systems, improving long term stability of these DSSCs. It is one of the key points, that has to be achieved towards a real commercialization and large-scale production of DSSCs. It is necessary to close the electric circuit and make the solar cell work. At the working electrode the electrolyte provides electrons and reduces oxidized dye molecules. During this process it gets oxidized and diffuses to the counter electrode, where it gets reduced. The most common electrolyte is the I^-/I_3^- redox couple, but others like Co^{2+}/Co^{3+}[20] and Cu^+/Cu^{2+}[19, 21] have been successfully incorporated into a DSSC.

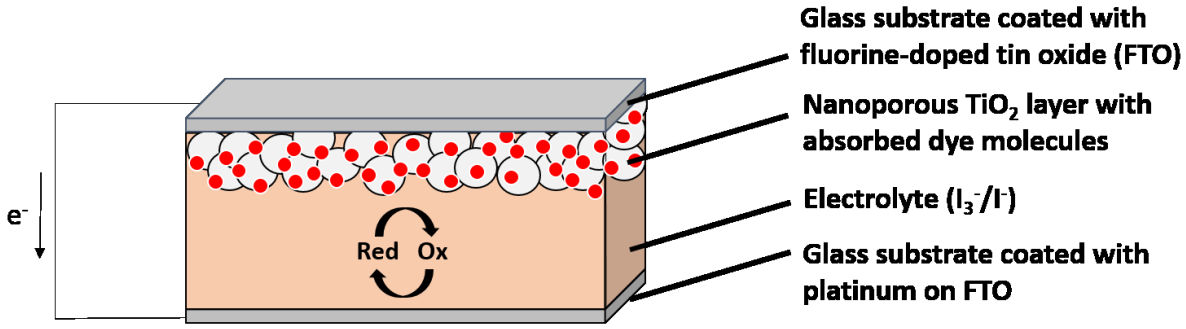

Fig. 3: Schematic structure of a DSSC, showing the four main components.

The last part of the DSSC is the counter electrode. In n-type DSSCs, it is typically a platinum coated FTO glass plate, which provides electrons and enables reduction of the hole carriers in the redox electrolyte. A special case of DSSC exists where the architecture described here is reversed. In a p-type DSSC, the counter electrode is a p-type semiconductor such as NiO, which can be sensitized with a dye and takes over the role of injecting electrons into the electrolyte. p-Type solar cells will be briefly described in the main part of this thesis.

The dying of the TiO_2 surface is a straight forward process. The dye needs to bear an anchoring group, which can bind to the semiconductor, and is dissolved in a solvent. A TiO_2 working electrode is immersed into the dye solution for hours or days, enabling optimal binding to the semiconductor. After soaking, the sensitized TiO_2 electrode is washed, often with the dye bath solvent, to remove non-anchored molecules and dried in a nitrogen stream or using a heat gun (80°C).

To assemble a DSSC, TiO_2 and counter electrode are glued together using hot-melting foil and the electrolyte is added via the vacuum backfilling technique. The solar cell is sealed using hot melting foil and a thin glass plate. Silver paste is added to both electrodes for better contact during measurements (Fig. 4). Detailed dying and assembly procedures, including device measuring and characterization will be discussed in the next chapter.

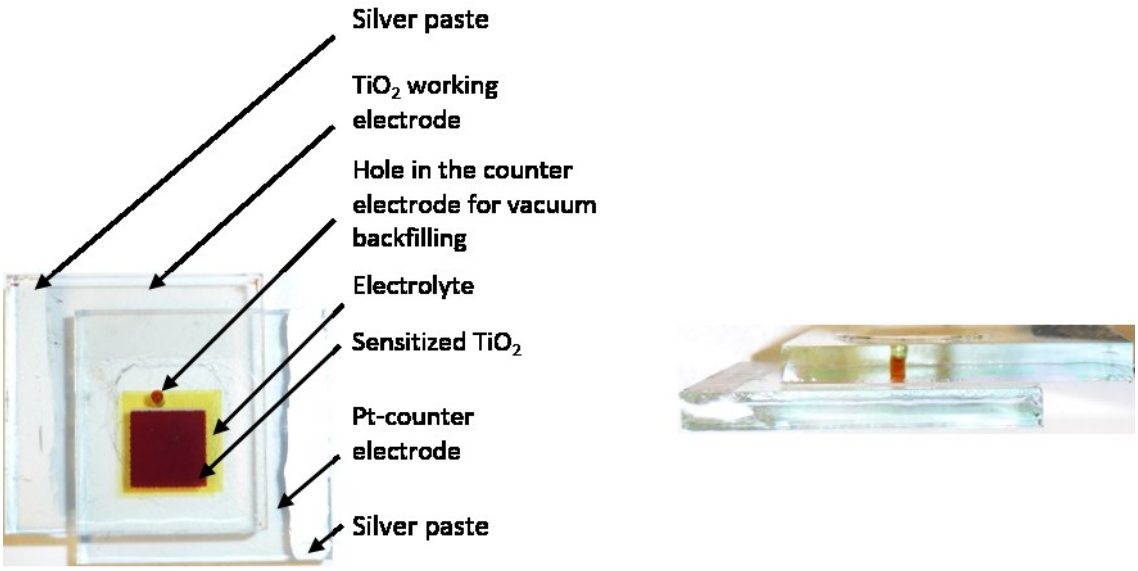

Fig. 4: An assembled DSSC; view through the Pt counter-electrode glass (left) and from the side (right).

The performance of a DSSC greatly depends on the absorbed dye and the redox couple. Energetics of the dye and the electrolyte define the parameters obtained from solar cell measurements and must fulfil properties discussed in this paragraph. Fig. 5 illustrates the processes happening in a working DSSC[16]. Upon irradiation of the dye, photons get absorbed and enable excitation of electrons from the ground state (S) to the excited state (S*). This excited state of the dye has to be higher in energy than the conduction band (CB) of TiO_2 (~ – 0.5 V) to enable electron injection from S*. The injected electron moves through the semiconductor into the FTO and can perform electrical work. Extracting an electron from a dye leaves behind a positive charge, a so-called hole, on the dye molecule. The hole moves through the oxidized dye molecule and combines with electrons provided by the redox electrolyte to regenerate the ground state of the dye. The redox couple has to have a redox potential (E_{redox}) higher in energy than the ground state of the dye to reduce it and lower than the valence band of the counter electrode, to be reduced. Charge carrier mobility, diffusion and recombination are other important properties and will be discussed in section 3.3.3. The oxidized redox couple recombines with electrons injected from the Pt counter-electrode. One important parameter is defined by the energy gap between the redox potential of the electrolyte and the Fermi level of the semiconductor (roughly the CB level), the open-circuit voltage (V_{OC}). The Fermi level is a hypothetical energy level close to the CB, related to the chemical potential of electrons in the semiconductor[22]. The other important parameter is the short-circuit current density (J_{SC}), which mainly depends on the electron injecting properties of the dye molecule. The more electrons that are injected, the higher the J_{SC} of a DSSC is. The described scenario is for the ideal case. In reality other processes can occur in a DSSC. These include recombination reactions of electrons injected in the semiconductor, which can return the oxidized dye to the ground state or interact directly with the redox electrolyte to reduce overall cell performance.

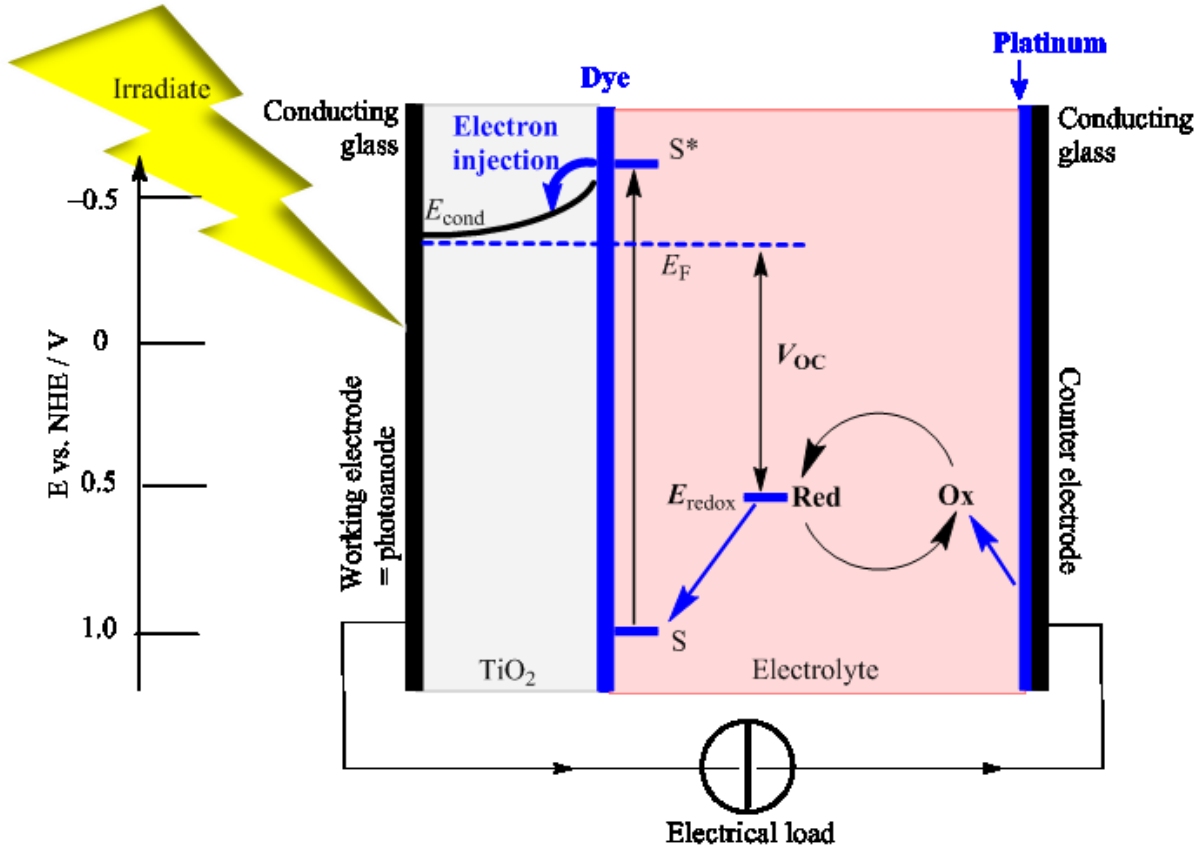

Fig. 5: Electron transfer processes happening in an ideal DSSC (blue arrows)[16].

3.3.2 Components of a DSSC: The semiconductor

TiO_2 is a semiconductor used in DSSCs. TiO_2 exists in different crystalline forms (rutile, anatase and brookite) and has applications as a pigment in paint, sunscreen and toothpaste. In nature it is also found in the mineral ilmenite ($FeTiO_3$).

The most commonly used semiconductor in DSSCs is nanocrystalline TiO_2 in its anatase form. Cells using nanocrystalline material greatly benefit from the increased surface area, which allows increased dye uptake compared to a non-porous material. Anantase has a wide band gap of 3.2 eV[23]. Mesoporous TiO_2 electrodes can be produced by screen-printing TiO_2-paste onto a FTO glass plate (~ 10 µm thickness, ~ 20 nm particle size). This layer has a high surface area and is sensitized by a dye, bearing anchoring groups which enable binding to the surface. The mesoporous layer is covered by a scattering layer (~ 3 µm thickness, ~ 400 nm particle size), to reflect scattered light back onto the dye, for further charge separation. A final treatment with aqueous $TiCl_4$, followed by sintering forms an ultrathin TiO_2 coating (~ 1nm). The ultrathin layer further increases the surface area and leads to enhanced dye uptake[24]. Commercial solar

cells preparation kits, including TiO_2-coated and Pt - electrodes and sealing materials can be purchased from Solaronix SA, Aubonne, Switzerland.

In a previous section it was described how the V_{OC} of a solar cell is defined by the redox potential of the electrolyte and the CB (Fermi level) of the TiO_2 semiconductor (see Fig. 5). To enhance the V_{OC} and, therefore, the overall device performance it is possible to shift the redox potential of the electrolyte to a more positive potential or to shift the CB to a more negative potential. Kakiage *et al*. reported a record V_{OC} of 1.4 V in 2016[25] in a DSSC: this was achieved by changing the electrolyte from the standard I^-/I_3^- to the Br^-/Br_3^- redox couple, which shifted the redox potential to a more positive potential, and increased the V_{OC} tremendously (Fig. 5). Additionally, the TiO_2 semiconductor was doped with Mg to shift the CB to a more negative potential (from –0.5 V to –0.7 V). The introduction of Mg^{2+} ions increases the lattice spacing of the (101) plane of anatase TiO_2 and decreases the TiO_2 particle size, which leads to a blue shift absorption of the doped semiconductor and to a more negative potential[26-27]. These two modifications lead to the highest V_{OC} which shows the great potential of further enhancing the efficiency of DSSCs.

Other semiconductor materials such as ZnO, SnO_2 and modified SnO_2 (coated with a thin shell of MgO and Al_2O_3) have been investigated. In particular, ZnO is known as a good alternative, but lacks the stability of TiO_2. A solar cell using ZnO as the semiconductor sensitized with an **N719** (section 3.3.4.3 Scheme 5) dye yielded efficiencies of 6.6% (no efficiency for a reference cell was given)[28]. The best solar cell fabricated of a pure SnO_2 semiconductor showed an efficiency of 2.8% (relative to 1.2% for an **N719** reference cell), using an organic dye[29].

3.3.3 Components of a DSSC: The electrolyte

The electrolyte in a DSSC is usually a liquid containing a redox couple and dissolved additives. The most common redox couple is I^-/I_3^-. With only minor changes it is today almost the same as the one introduced by Grätzel and O'Regan in 1991[14]. Grätzel and O'Regan used a 0.04 M iodide concentration, compared to 0.05 M used in our group. The iodide source (Grätzel used tetra(n-propyl)ammonium iodide, nowadays LiI is used frequently) and the incorporation of additives, such as 4-tert-butylpyridine) was another change. Grätzel and O'Regan used a mixture of ethylene carbonate and acetonitrile as solvent and acetonitrile remains a frequently used solvent nowadays.

Important features of a liquid electrolyte are its stability under light irradiation and elevated temperature. The electrolyte should not dissolve or destroy cell components, like the Pt counter-electrode, the dye, the semiconductor or the plastic sealings. It should be colourless and not compete with the dye for photon absorption. The solvent plays a very important role and should not be too viscous, to avoid diffusion problems with the charge carriers. The boiling point of the solvent should be high, as volatile solvents lead to pressure increase in sealed cells with temperature increase. Protic solvents, water and alcohols are rarely used, to avoid desorption of dye molecules. The most commonly used solvents are 3-methoxypropionitrile (MPN) and acetonitrile/valeronitrile mixtures, which show good stability and good solubility of the redox couple and additives. One drawback of I^-/I_3^- is observed straight away: the electrolyte is not colourless, but dark orange/brown, and thus absorbs some photons.

At the working electrode I^- provides electrons, reduces the oxidized dye and gets oxidized to I_2.

$$2I^- \rightleftharpoons I_2 + 2\,e^-$$

I_2 reacts with I^- to form the tri-iodide ion I_3^-, which is reduced at the counter-electrode to I^-.

$$I_3^- + 2\,e^- \rightleftharpoons 3I^-$$

Additives in electrolytes can influence both the potential of the redox couple and the conduction band level of the semiconductor and also help to prevent dye aggregation on the TiO_2 surface. 4-tert-Butylpyridine (TBP), a widely applied additive, can coordinate to TiO_2 and shift the conduction band to more negative potentials[30], which increases the V_{OC}[31] but often simultaneously decreases the J_{SC}. Li^+ ions in electrolytes can penetrate the nanoporous TiO_2 and increase electron injection from dye molecules, enhancing the J_{SC}[8, 17]. Li^+ can acts as a dopant, when an electrical potential is applied to a DSSC[32]. Li^+ is able to generate trap states in the TiO_2 semiconductor and lower the Fermi level. The increased energy difference between the LUMO of the dye molecule and the Fermi level promotes enhanced electron injection, thus increasing J_{SC}[26]. These additives are often used together in the same electrolyte to cancel out their negative side effects.

Alternative redox couples for electrolytes have been developed in recent years, of which $[Co(bpy)_3]^{2+/3+}$ (dissolved in acetonitrile) is a good example[33-34]. The redox potential of

$[Co(bpy)_3]^{2+/3+}$ is shifted to a more positive potential than, to I^-/I_3^-, which increases the V_{OC} of the device[20] and therefore its efficiency[33, 35]. These Co complexes are often colourless or slightly yellow, which is another advantage. A Cu^+/Cu^{2+} redox couple also shows a positive shift of its potential[36], relative to I^-/I_3^- and is a feasible alternative electrolyte material[37] and is currently studied intensively. Kakiage *et al.* introduced a Br^-/Br_3^- redox couple[25, 38] into an electrolyte and showed its potential as mentioned in section 3.3.2.

3.3.4 Components of a DSSC: The dye

The heart of a dye-sensitized solar cell is the dye. The dye anchors to the white semiconductor (which absorbs in the UV region) and colours it. A coloured material is able to absorb photons in the visible range of the light spectrum, which is the key process in a solar cell. Ideally, panchromatic absorption is required. Dyes for DSSCs can be divided into three main groups. One group, perovskite materials can be considered a separate technology and will not be discussed in this thesis. The two other groups are inorganic and organic sensitizers.

Dye molecules need an anchoring group to bind to the semiconductor and inject electrons. A wide variety of anchoring groups has been investigated in DSSCs. The most common and promising ones are discussed in the next section.

3.3.4.1 Anchoring groups in DSSCs

The complex published by Grätzel and O'Regan[14] anchored to the TiO_2 surface via carboxylic acid groups.

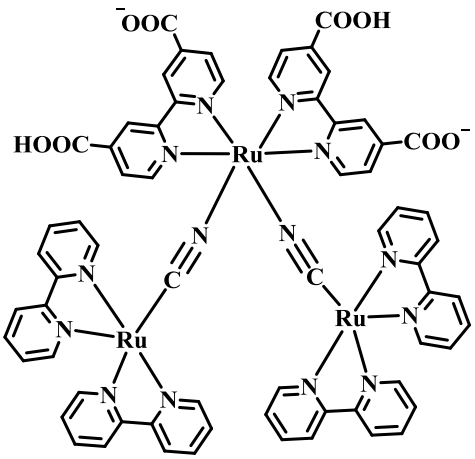

Scheme 1: The CN-bridged trinuclear Ru complex used by Grätzel and O'Regan[14].

Scheme 2 displays possible binding modes of a carboxylic acid group to a metal oxide semiconductor surface[39]. The top row shows binding modes via coordination of O atoms to Ti atoms, in a monotopic, ditopic or ditopic bidentate chelating way. The second row highlights the possibility of binding via H-bonds between COOH----O_2Ti in a mono, or ditopic fashion.

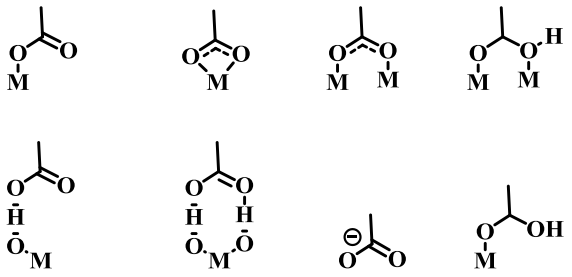

Scheme 2: Some possible binding modes of a carboxylic acid group to a semiconductor surface[39].

Phosphonic acid is a good alternative anchoring group and is regularly used in DSSCs. -$PO(OH)_2$ groups bind more strongly to the semiconductor than carboxylic acids and are less vulnerable to desorption[40]. Mono-, di- and tritopic binding modes, including H-bonds are possible. Despite the stronger binding of phosphonic acid groups to the semiconductor the electron injection is less efficient, shown by a comparative study of carboxylic and phosphonic acids in Ru(II) complexes[41]. Copper(I) based dyes however, show better performance using phosphonic acid anchors[42]. This might be related to desorption of copper-dye molecules bearing carboxylic acid anchors from the DSSC. Considering the growing field of p-type sensitizers, phosphonic acids might experience a revival. In a p-type system a hole hopping mechanism is plausible, which might overcome weak injection properties of phosphonic acids and greatly benefit from the better stability.

A third important anchoring group is a cyanoacrylic acid. It is mainly used in organic "push-pull" dyes and benefits from the electron-withdrawing CN group, pulling electrons towards the anchoring group. Ooyama *et al.* described a system, where the cyano group was spatially separated from the carboxylic anchoring group. Despite this separation, the cyano group was found to be close to the semiconductor surface, inducing strong communication and possible e^- injection. In this study, the role of the carboxylic acid was mainly attributed to its anchoring properties[43]. In summary cyanoacrylic acids benefit from the electron withdrawing properties of the cyano group and anchoring properties of the carboxylic acid group. Based on Ooyamas studies it can be assumed, that electron injection into the semiconductor can happen via both groups[43] of a cyanoacrylic acid. An interesting prospect is the combination of the strong

anchoring abilities of a phosphonic acid group with the electronic properties of a cyano group. A comparison of organic dye molecules bearing a cyanoacrylic acids or a (1-cyanovinyl)phosphonic (Scheme 3) acid revealed similar trends, with carboxylic acids outperforming phosphonic acids[44].

The group of Kakiage *et al.* developed a new silyl anchoring group, by modifying a cyanoacrylic acid with p-aminophenyltrimethoxysilane to form the dye **ADEKA-1** (Scheme 4)[35]. A DSSC co-sensitized with a carboxylic acid dye reached the record efficiency for an organic dye of over 14% (no efficiency for a reference cell was given).

Other less common anchoring groups include pyridines[45], groups with four cyanides[46], perylene dicarboxylic acid anhydrides[47], 2-hydroxybenzonitriles[48] and pyridine-N-oxide[49]. These groups are rarely used and do not show consistent performances.

The structures of anchoring groups discussed above are summarized in Scheme 3.

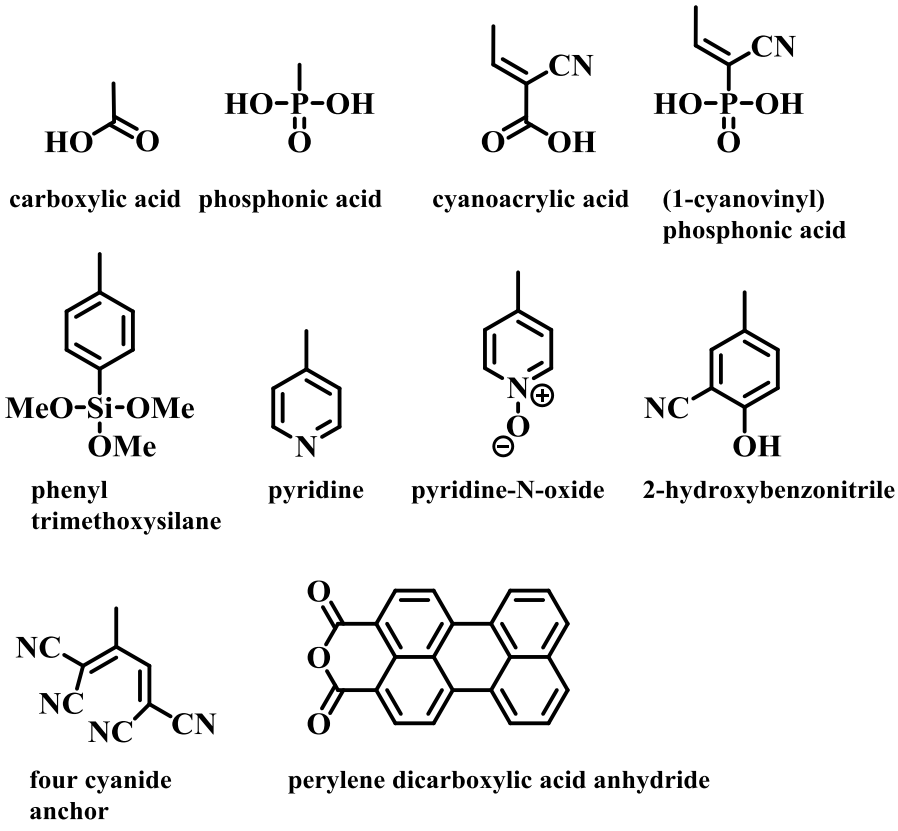

Scheme 3: Common (first three, top row) and less common anchoring groups for semiconductors.

3.3.4.2 Organic dyes

Organic dyes show promising performance with efficiencies of over 14 % (no efficiency for a reference cell was given) using the **ADEKA-1** and **LEG4** dye (Scheme 4) together in one solar cell[35]. Most organic dyes have a donor-π-bridge-acceptor architecture. This architecture enhances electron flux from a donor moiety ("push") to the anchoring group ("pull"), where the electron is injected. Such a design is often referred to as a "push-pull" system. **ADEKA-1** is constructed of the common electron pushing carbazole group and separated from the anchoring group by four 3-hexyl-thiophene spacers. These spacers decrease recombination of injected electrons with the dye and cover the surface with their alkyl chains, preventing recombination of electrons from the semiconductor to the electrolyte. They also prevent larger molecules like **ADEKA-1** from aggregating on the semiconductor surface[50]. The beneficial aspects of cyanoacrylic acids were discussed in the previous section. The newly introduced trimethoxysilane anchoring group shows strong surface binding by forming Si-O-Ti bonds and exhibits an increased V_{OC}[51]. The **TA4** dye reported by Chiu *et al.* (Scheme 4) consists of the second very common donor, a triarylamine group. An azobenzene π-bridge separates donor and the cyano acrylic acid anchor. **TA4** has an efficiency of 4.78% (no efficiency for a reference cell was given)[52]. Recently other π-bridges and donors were explored and the variety of possibilities in this area is extensive. The dye **W24** (Scheme 4) demonstrated the potential of dithieno[3,2-b:2',3'-d]pyrrole groups as donors and the variation of the position of this group relative to the anchoring group showed interesting results. An efficiency of 7.7% (no efficiency for a reference cell was given) for **W24**[53] was obtained, which is higher than for the analogous structure where the donor is separated from the anchor by a spacer. The main drawback of purely organic dyes is their often very complicated and thus expensive and time-consuming synthesis. In contrast, inorganic dyes are more easily synthesized by coordination reactions of metal salts with readily synthesized organic ligands, reducing synthetic steps.

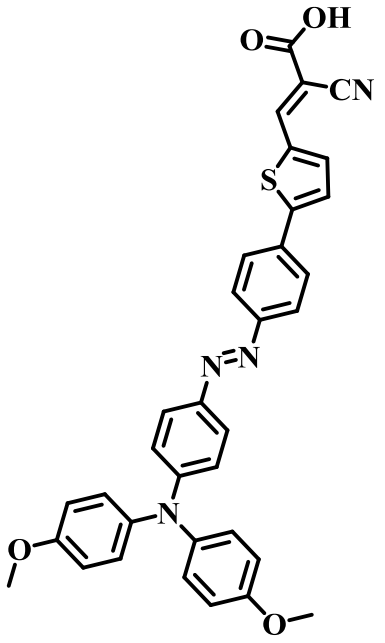

TA4

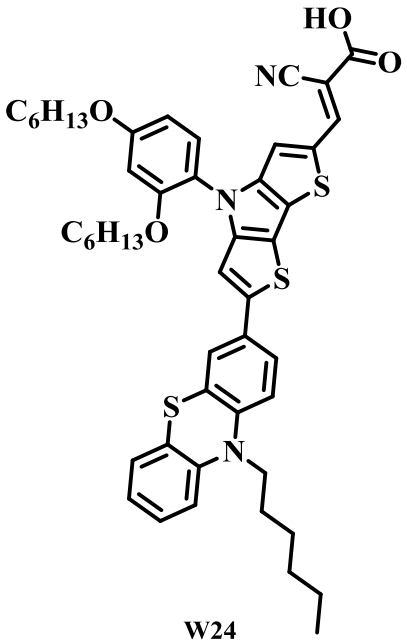

W24

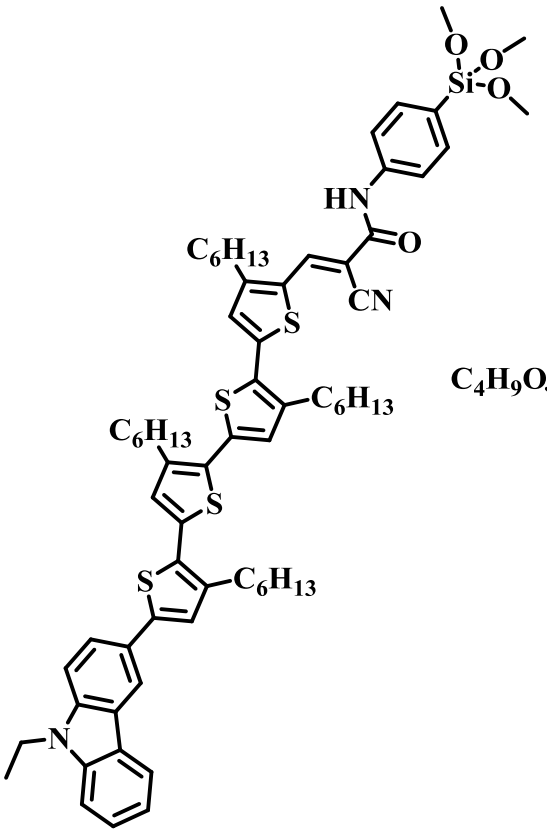

ADEKA-1

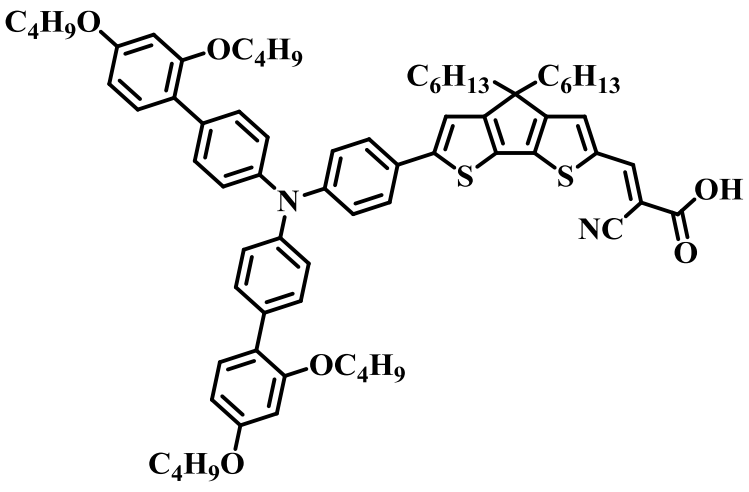

LEG4

Scheme 4: Organic dyes **TA4**, **W24**, **ADEKA-1** and **LEG4** representative for the "push-pull" design. C_6H_{13} represents an *n*hexyl chain and C_4H_9 represents an *n*butyl chain.

3.3.4.3 Inorganic DSSCs

The publication of the first and ground-breaking ruthenium dye in a DSSC, 1991, lead to the development of a wide variety of ruthenium complexes.

The synthesis of Ru(II)-complexes is fast and rather uncomplicated, combining simple ligand design with the outstanding photophysical properties of Ru(II). The organic ligands are often 2,2'-bipyridines (bpy) or 2,2';6',2''-terpyridines (tpy), bearing anchoring groups. Thiocyanato groups (NCS^-) are beneficial for their electron donating properties, which stabilize the excited state of Ru(II)-complexes and red-shifts the absorption[54]. NCS^- groups are incorporated in positions that point away from the semiconductor surface, enabling good contact with the electrolyte and fast dye regeneration[55-57]. Scheme 5 shows the most well-known Ru-dyes **N719**[58], **Z907**[59] and the **black dye** (**N749**)[54].

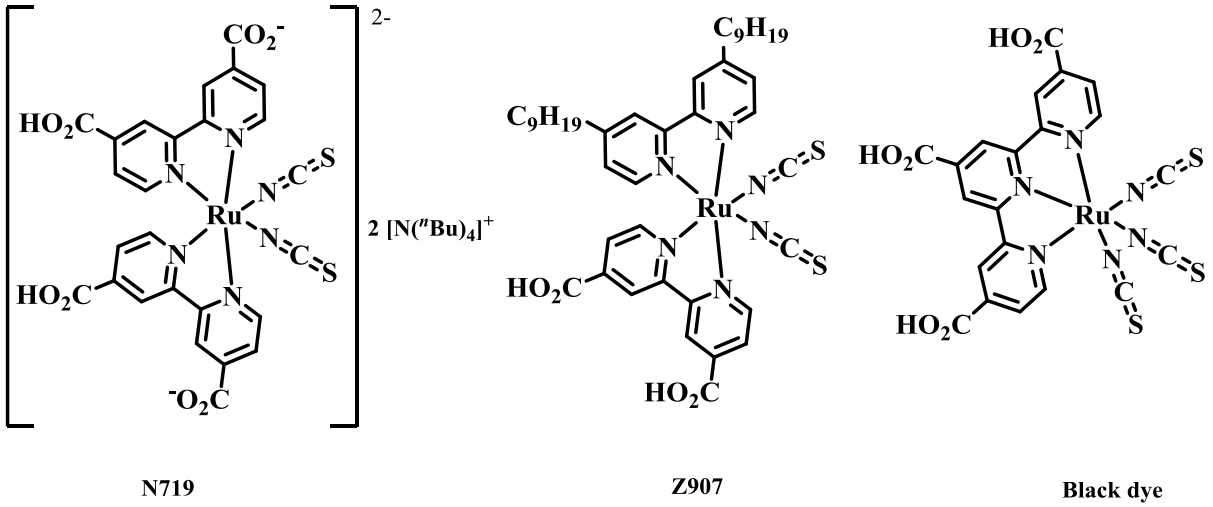

Scheme 5: Ru(II) based dyes **N719**, **Z907** and the **black dye** (**N749**).

The state of the art inorganic Ru(II)-based dye **CYC-B11** (Scheme 6) reaches an efficiency over 11% (no efficiency for a reference cell was given)[60].

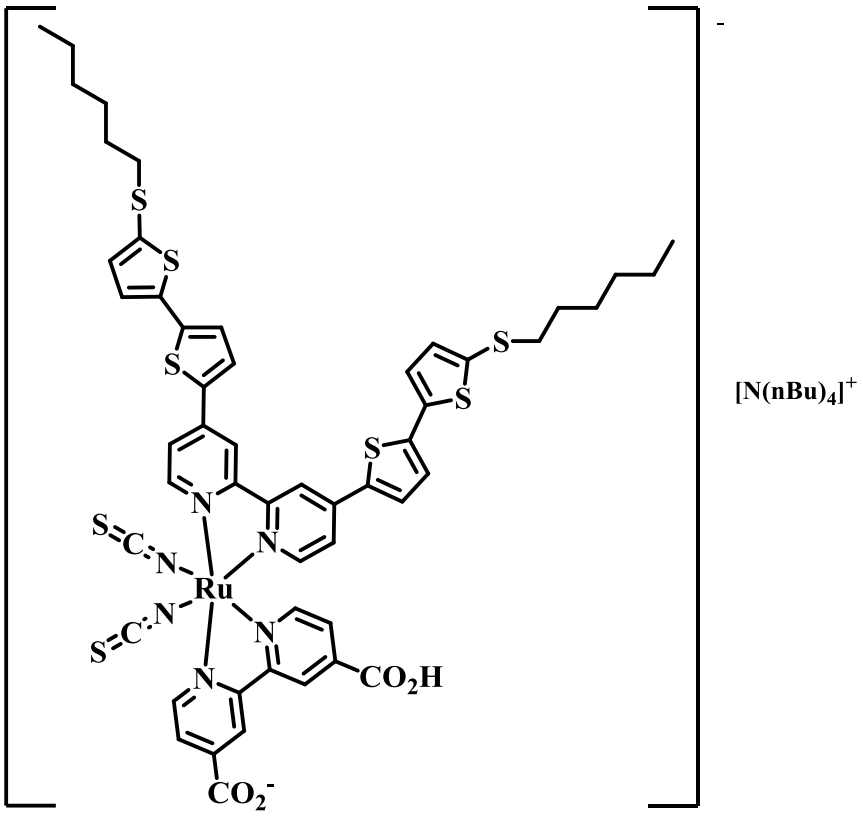

CYC-B11

Scheme 6: State of the art Ru(II)-based dye **CYC-B11**.

The anchoring group of choice in Ru(II) dyes is a carboxylic acid or carboxylate.

Ruthenium (II) complexes are among the best inorganic dyes, but have one major drawback that will hinder commercialization. Ruthenium is a noble metal, very rare (abundancy in the earth crust 0.000037 ppm[16]) and expensive (US$ 6109 per kilogram, 09 January 2018[61]). Incorporating alternative, cheaper and more abundant metals in DSSCs is a major goal in this research topic.

3.4 Cu(I) based dyes - Photophysical properties of transition metal complexes

A cheaper alternative for inorganic DSSCs is copper. Copper is more abundant by a factor of thousand, has two main oxidation states +1 and +2 and especially Cu(I) metal complexes show good photophysical properties. Cu(I) complexes bearing two bisdiimine ligands show strong metal to ligand charge transfer (MLCT) transitions in the visible range of the spectrum. They

are colourful materials with colours ranging from yellow to orange, red and magenta. Cu(I) is a d^{10} metal ion (i.e. has fully filled d-orbitals) and prefers a tetrahedral coordination geometry[62], where 4 donor atoms have least repulsion. A d^{10} metal exhibits no metal centred (MC) d-d transitions and in the case of the Cu(I) complex [Cu(6,6'-dimethyl-2,2'-bipyridine)$_2$](PF_6)[63] its low oxidation potential of +0.17 V (with respect to Fc/Fc^+) favours MLCT to low lying π^*-orbitals of coordinated ligands. The excited MLCT state is relatively long lived, enabling charge separation suitable for application in a DSSC[64]. Upon excitation, Cu(I)-complexes are formally oxidized to Cu(II)-ligand radicals which prefer a square-planar geometry, opening up a 5th coordination site and allowing additional decay pathways via nucleophilic attack by solvent or anion molecules. This problem can be overcome by careful ligand design and will be discussed in the main part of this thesis.

Charge separation, recombination and excited state decay pathways are important aspects that have to be taken into account when a material is to be tested for application in a DSSC. It is somewhat surprising, that the only working inorganic dyes for DSSCs with significant efficiencies (above 2%) are ruthenium, osmium[65], copper and zinc (in porphyrin based complexes[66]) based. To explain this phenomenon, it is important to consider the electronic configurations of transition metals.

Compared to Ru(II), alternative metals of the same column in the periodic table could be Fe(II) and Os(II), that possess the same electronic configuration (d^6). The energetic level of the metal centred (^{3}MC) state in most Fe(II) polypyridine complexes[67] is lower in energy than the ^{3}MLCT state, which enables excited state decay from the ^{3}MLCT to the non-emittive ^{3}MC state (Fig. 6). The metal-to-ligand charge transfer (^{3}MLCT) state in most Os(II) polypyridine complexes[68] is lower in energy than the first excited state (^{3}MLCT) of Ru(II). When charge recombination from the excited state back to the ground state or to other states lower than the CB of TiO_2 is faster than charge injection into the semiconductor, no or only minimal power output is obtained.

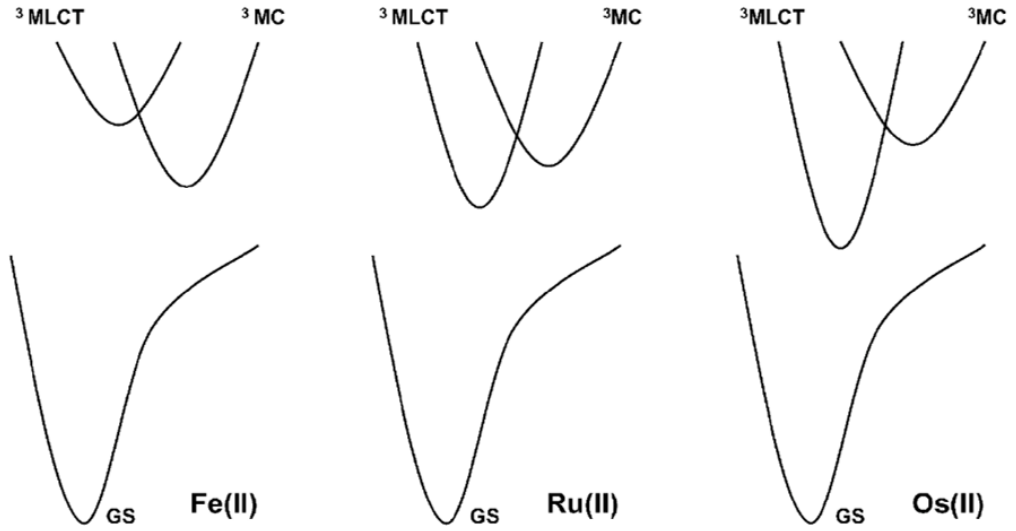

Fig. 6: Potential energy curves for Fe(II), Ru(II) and Os(II) complexes from Barbieri *et al*. Reproduced from ref.[68] with permission of the Royal Society of Chemistry.

In Os(II) complexes this problem was solved by incorporating a 2,6-bis(3-trifluoromethyl-1*H*-1,2,4-triazol-5-yl)pyridine ligand[65], which decreased the electron density on the Os(II) ion and shifts the oxidation potential to a more positive potential, compared to most Os(II) polypyridine complexes. The main advantage is, that the recombination of electrons in the semiconductor to the ground state of the Os(II) complex is slowed down and dye regeneration via the electrolyte becomes faster than the recombination[69-70]. The complexation of this new ligand with an $\{Os(tpy)\}^{2+}$ precursor yielded the complex displayed in Scheme 7, which showed a good solar to power efficiency of 8.85% (relative to 8.21% for a **N749** reference cell, displayed in Scheme 5).

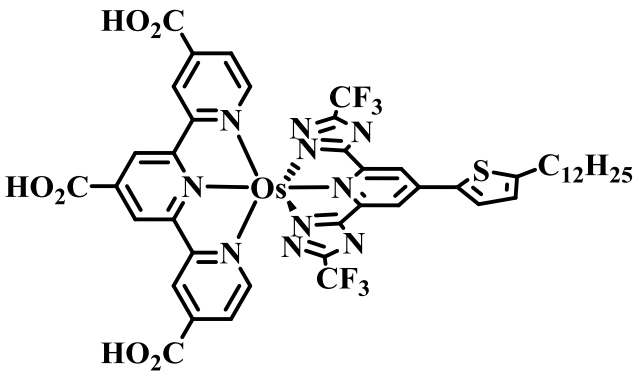

Scheme 7: Os(II) complex with good light harvesting properties.

Research groups are currently exploring Fe(II) dyes with specially designed ligands (often bearing carbene groups) that can shift the energy level of the ^{3}MLCT state[71]. Some achievements in this direction have been made by Wärnmark and colleagues[67], where they could destabilize the ^{3}MLCT state in an Fe(II) complex and prevent intersystem crossing to the low lying ^{3}MC state (Fig. 7)[72]. However, recombination reactions still occurred in an assembled DSSC using their complex and a very low efficiency of 0.13% (relative to 6.1% for an **N719** reference cell) was obtained[73].

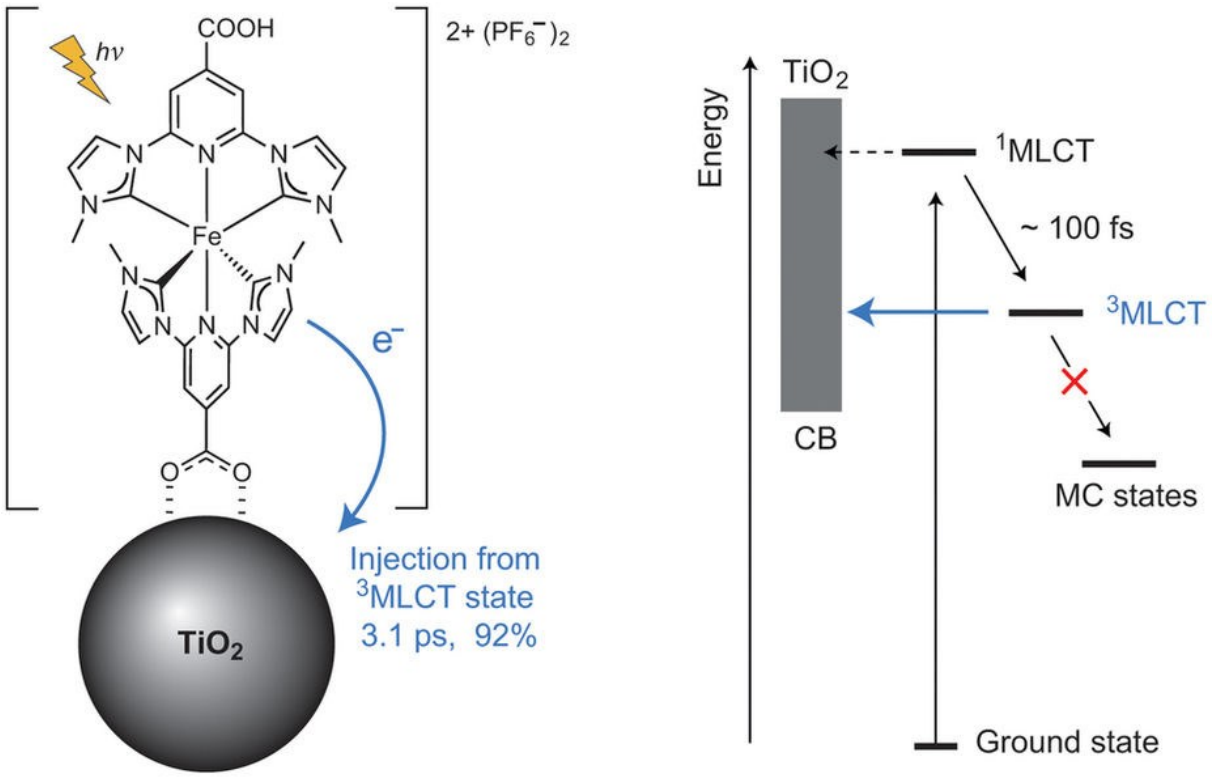

Fig. 7: The complex Wärnmark and colleagues used to sensitize TiO_2 and energetic states and transitions present in the complex. Recombination pathways are not shown. Reproduced from ref.[72] with permission of Springer Nature.

A representation of energetic levels and possible transitions in Ru(II) and Cu(I) complexes shows similarities and illustrates why the incorporation of Cu(I)-complexes into DSSCs is a viable alternative (Fig. 8)[64]. Cu(I) as a d^{10} metal complex can promote electrons to empty π-orbitals of coordinated ligands, either by ligand centred (LC) or by MLCT transitions. LC transitions are high in energy and, thus need high energy photons of the UV part of the light spectrum. These UV photons are few, but photons in the visible spectrum (350 – 700 nm) are more frequent, enabling metal complexes to absorb these photons and to transfer them via MLCT to excited π*-states in the ligand. From there, electrons can be injected into a TiO_2

semiconductor to generate an electrical current. In bisdiimine copper(I) dyes, decay pathways for excited electrons are back to the ground state, or to the electrolyte.

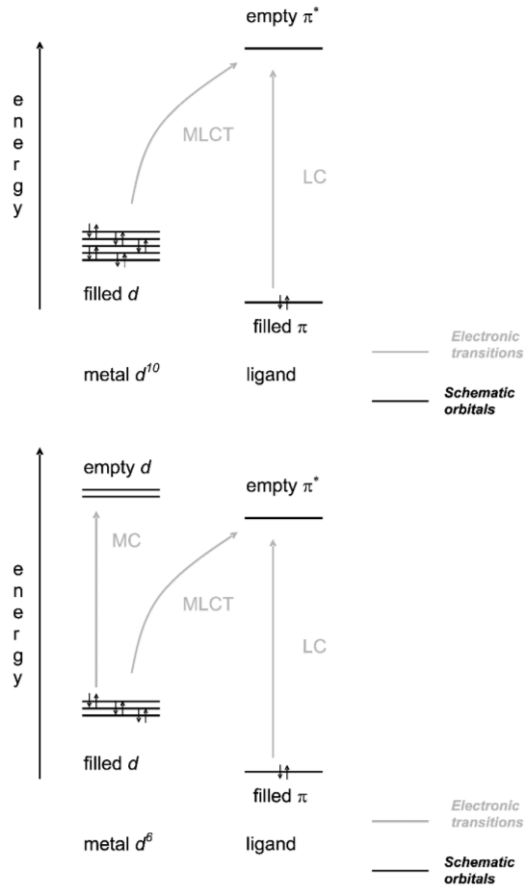

Fig. 8: Comparison of energy transitions in d^{10} (e.g. Cu^{I}) and d^{6} (e.g. Ru^{II}) metal complexes. Reproduced from ref.[64] with permission of Springer Nature.

3.5 Bisdiimine copper(I) dyes

The first Cu(I) complex to be incorporated in a DSSC was reported by Sauvage and coworkers in 1994[74]. They used the sodium salt of a homoleptic [Cu(2,9-bis(4-carboxyphenyl)-1,10-phenanthroline)$_2$](BF_4) dye (Scheme 8) as sensitizer and obtained a working solar cell, but with poor performance (V_{OC} = 0.6 V, J_{SC} = 0.6 mA/cm^{-2}).

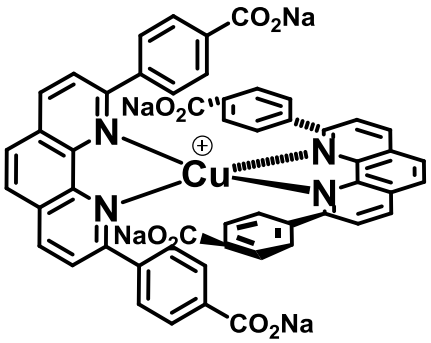

Scheme 8: First working Cu(I) complex, incorporated in a DSSC[74].

The energetics of a bisdiimine copper(I) dye can be tuned by modification of the coordinated ligands. Sauvage and coworkers used a 1,10-phenanthroline ligand, which enables chelating coordination to the metal ion. Chelating coordination is thermodynamically favoured[75] and increases complex stability in contrast to monotopic coordination. Two chelating 1,10-phenanthroline ligands form a distorted tetrahedral complex with Cu(I) salts. The second important feature is substituents at the 2,9-positions of 1,10-phenanthroline. In the case of Sauvage's dye, phenylene groups were incorporated. These groups dramatically increase the stability of bisdiimine copper(I) complexes, by favouring tetrahedral geometry. When a bisdiimine copper(I) complex absorbs a photon, an exciton (electron-hole pair) forms, which can inject its electron into the semiconductor. After this injection, Cu(I) loses an electron and is oxidized to Cu(II), which favours a square planar geometry with a possible 5th coordination site. To prevent, or at least hinder, this conformation change is the purpose of groups on the carbon atom next to coordinating nitrogen atoms.

To apply a bisdiimine copper(I) complex as a dye in a DSSC, an anchoring group is necessary, enabling binding of the complex to the semiconductor. The most common anchoring group is a carboxylic acid or carboxylate salts, as seen in Sauvage's dye or the Ru(II) dye **N719**[58]. More recent studies have shown, that in bisdiimine copper(I) complexes, phosphonic acid anchors outperform carboxylic acid anchors[42].

Substituted 2,2'-bipyridine (6,6'-dimethyl-2,2'-bipyridine) and 1,10-phenanthroline ligands (2,9-dimethyl-1,10-phenanthroline) are the most common ligands found in bisdiimine copper(I) dyes, but other related ligands[76] also show promising performance (Scheme 9).

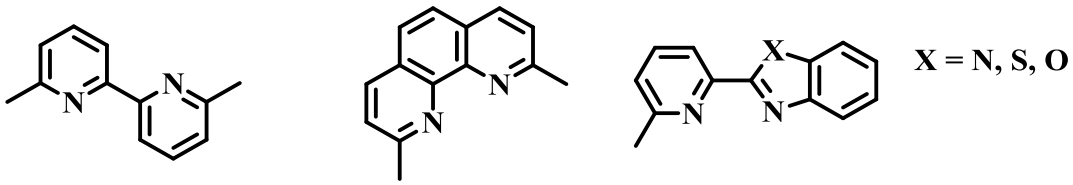

Scheme 9: 6,6'-Dimethyl-2,2'-bipyridine and related ligands used in Cu(I) dyes.

After Sauvage published his first bisdiimine copper(I) dye, researchers realized, that a homoleptic Cu(I) dye is lacking another important feature - the absence of an electronic driving force for electron injection. In a homoleptic complex the highest occupied molecular orbital (HOMO) is equally distributed over the metal and the metal-ligand bonding. The lowest unoccupied molecular orbital (LUMO) is equally distributed over both coordinated ligands, thus an excited electron has a similar probability to be promoted into the remote ligand as into the ligand bound to a semiconductor. Therefore, heteroleptic Cu(I) dyes were developed and a "push-pull" system, similar to organic dyes, was incorporated.

3.5.1 Towards heteroleptic bisdiimine copper(I) complexes

Homoleptic Cu(I) complexes were first applied in DSSCs by Sauvage (see above) and later by Constable and coworkers[77]. Since then research focus mainly lay on the synthesis of heteroleptic complexes, which mimic the "push-pull" systems of organic dyes. Two approaches towards the sensitization of semiconductors with heteroleptic Cu(I) dyes exist.

The HETPHEN approach was developed by Odobel and coworkers[78] in 2013. In their first study, they combined ancillary ligands, with steric demanding groups close to the donor atom, with an anchoring ligand (Scheme 13, bottom right) and obtained a maximum efficiency of 0.71% (relative to 6.55% for an **N719** reference cell). The crux of their approach was to combine Cu(I) metal salts with sterically demanding diimine ligands, that were too bulky to form homoleptic complexes. In a second coordination reaction these Cu(I)-diimine precursors were reacted with a less sterically demanding ligand to form a heteroleptic bisdiimine copper(I) complex in solution. In their second study they combined a sterically demanding anchoring ligand (Scheme 13, top right) with a less demanding ancillary ligand and succeeded in the preparation of a heteroleptic complex (Scheme 10), showing the highest efficiency of $\eta = 4.66\%$ (relative to 7.36% for an **N719** reference cell) for a Cu(I) based dye in DSSC[79].

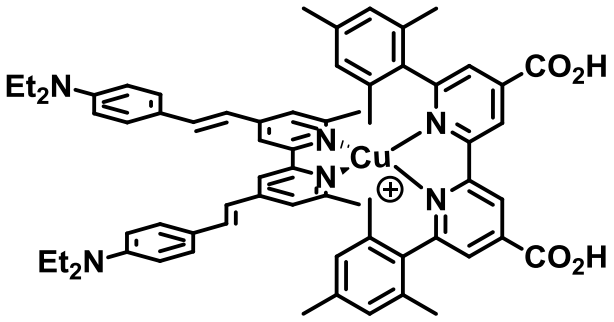

Scheme 10: Best performing bisdiimine copper(I) dye in a DSSC, published by Odobel and coworkers[79].

The second approach uses a stepwise on-surface assembly of the heteroleptic Cu(I)-complex[42]. In the first step the semiconductor is modified by a diimine molecule bearing an anchoring group. The modified surface is then immersed into a dye solution of a homoleptic Cu(I)-complexes. Diimine ligands bound to copper(I) are relatively labile and ligand exchange between the anchoring ligand and the homoleptic Cu(I) complex occurs rapidly. One diimine ligand is released in this process and a surface bound heteroleptic Cu(I) complex formed (Scheme 11). This stepwise assembly can be extended to an additional step, where $[Cu(NCMe)_4][PF_6]$ is introduced first to form a Cu(I)-diimine precursor complex on the surface, followed by one equivalent of ancillary ligand.

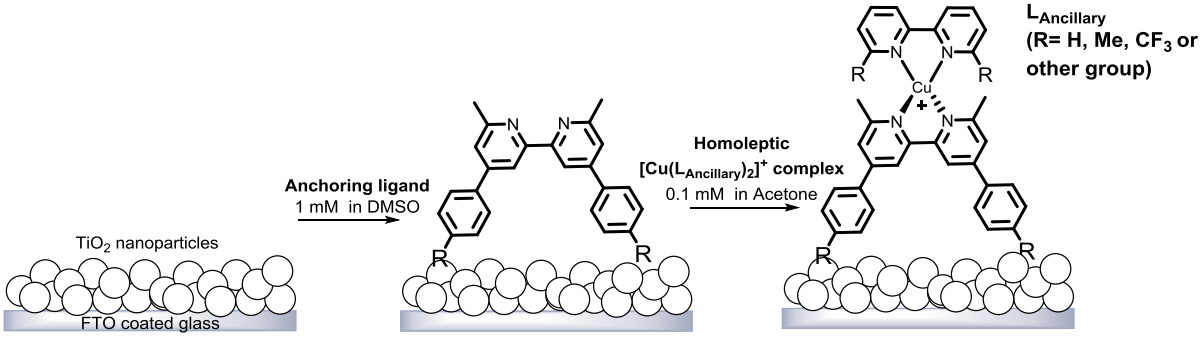

Scheme 11: Stepwise assembly of heteroleptic bisdiimine copper(I) complexes on a semiconductor.

3.5.2 Anchoring ligands in bisdiimine copper(I) complexes

Sauvage and coworkers used a carboxylate anchoring group in their homoleptic Cu(I)-complex (Scheme 8). It substitutes the 4-position of phenyl rings, attached to the 2- and 9- positions of 1,10-phenanthroline. Considering the sterics of this molecule it is not surprising that poor performance was observed. A homoleptic complex lacks the electronic driving force to transfer electrons to the ligand bound to the semiconductor. The position of the anchoring groups is also

not ideal. A maximum of two simultaneously bound anchors can be expected (Scheme 8) and the steric demand of the 1,10-phenanthroline backbone will most likely push the complex away from the surface. Positioning of the anchoring groups para to the N-atom reduces repulsion from the surface, increases binding and electronic coupling is favourable. Scheme 12 shows early examples of anchoring ligands, bearing their anchoring group para to the coordinating N-atom. The homoleptic Cu(I) complexes of these two anchors show promising light harvesting abilities, with solar-to-power conversion efficiencies of 1.9 and 2.3%(relative to 9.7% for an **N719** reference cell)[77]. Scheme 12 also illustrates the conformational change a 2,2'-bipyridine based ligand has to undergo upon coordination to a Cu(I) metal centre. Rotation around the C-C bond connecting both pyridine moieties, enables a 2,2'-bipyridine to transform from its thermodynamically favoured *trans* configuration to a *cis* conformation, necessary for the chelating coordination to a metal.

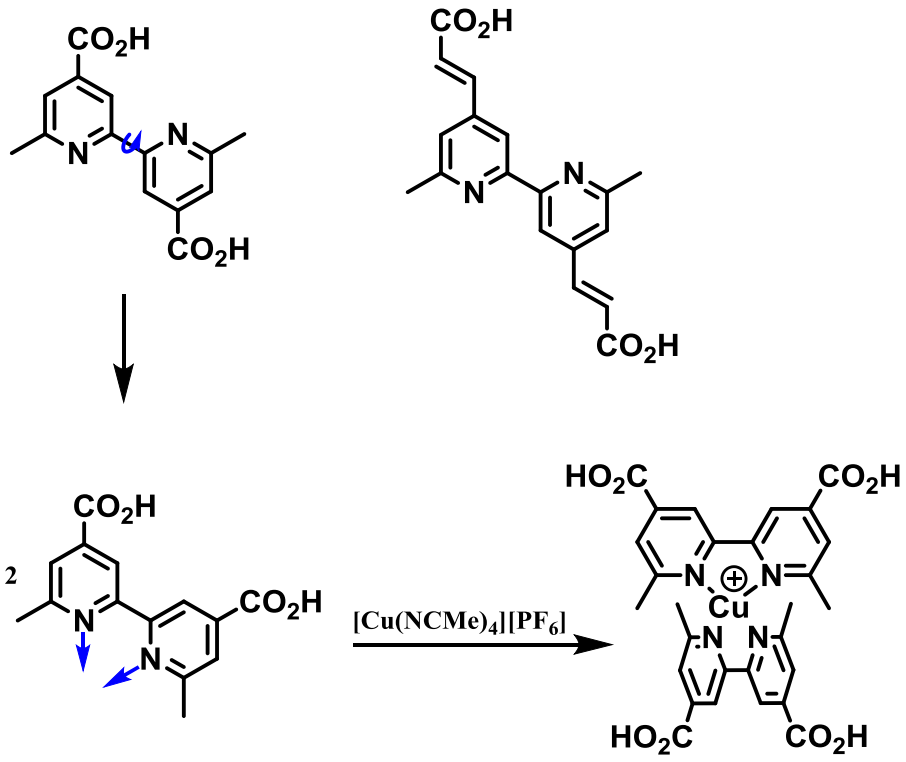

Scheme 12: Carboxylic acid anchoring ligand (top). Conformational change towards a *cis* configuration, necessary for chelating coordination to a Cu(I) metal centre (bottom)[77].

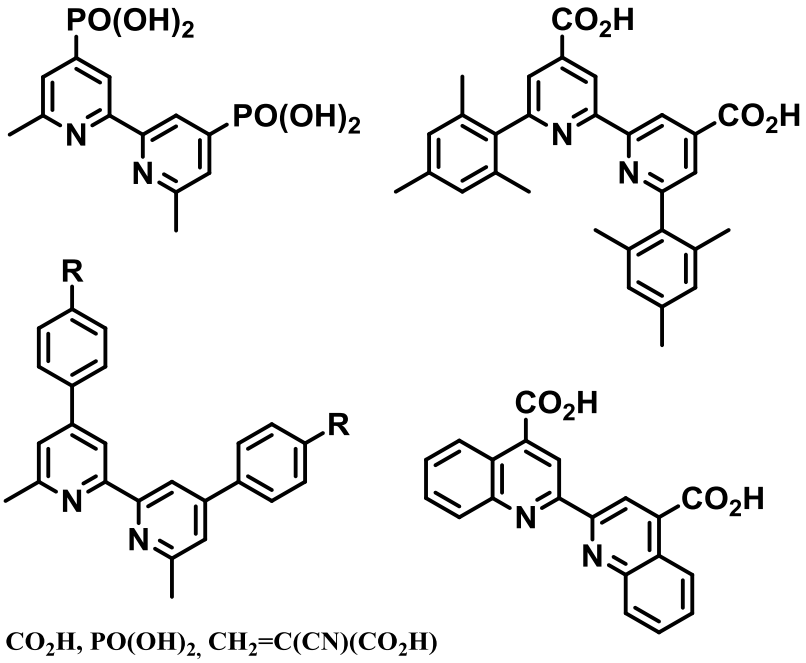

Scheme 13: Anchoring ligands for heteroleptic bisdiimine copper(I) based sensitizers. HETPHEN approach ligands (right side) and on-surface approach ligands (left side).

Over the past years anchoring ligands have been synthesized and tested in Cu(I) based DSSCs (some are displayed in Scheme 13) as anchors in heteroleptic[42, 78-80] and homoleptic[81-82] Cu(I)-complexes. The anchoring ligand is certainly one of the most important parts of a Cu(I) based solar cell, as it enables surface binding to a semiconductor. Studies with 2,2′-biquinoline-4,4′-dicarboxylic acid (Scheme 13, bottom right) as the anchoring ligand have shown that heteroleptic Cu(I) complexes using this anchor[78] outperform the homoleptic Cu(I) complex[82]. Other examples are rare. The ligand 6,6'-dimethyl-[2,2'-bipyridine]-4,4'-diyl)bis(4,1-phenylene))bis(phosphonic acid) (Scheme 13, bottom left, R = $PO(OH)_2$), shows very good performance as an anchoring ligand in heteroleptic bisdiimine copper(I) based DSSCs[16]. An attempt to isolate the homoleptic copper(I) complex of this ligand failed[83], which proves the step-wise on surface approach[16] for the formation of surface bound heteroleptic bisdiimine copper(I) dyes is beneficial in the case of this ligand.

3.5.3 Ancillary ligands in heteroleptic bisdiimine copper(I) complexes

The role of the anchoring ligand has been discussed briefly in the previous section. To complete the assembly of a heteroleptic Cu(I) complex a second diimine ligand, a so-called ancillary ligand, is necessary. The ancillary ligand has two main features. It needs blocking groups on

the C-atom next to the coordinating N, to encapsulate the Cu(I) metal centre and maintain the tetrahedral geometry. It is very important to prevent irreversible oxidation to a square planar Cu(II) complex. The second aspect concerns electron-releasing groups (ERGs), often positioned para to the coordinated N-atom. These ERGs "push" excited electrons towards the anchoring ligand, where they can be injected. A lot of research has been done on the modification of ancillary ligands with the aim of developing more efficient Cu(I) based DSSCs. Halogen groups were incorporated as electron-releasing groups[84]. Large ancillary ligands bearing hole transporting triarylamines have been investigated[85]. The most used 2,2'-bipyridine ligand core was changed to substituted 2,9-dimethyl-1,10-phenanthrolines, bearing various functionalities[86] to identify only a few attempts towards more efficient Cu(I) based DSSCs. Most of these modifications yielded solar cells with improved efficiency compared to non-substituted ligands like 6,6'-dimethyl-2,2'-bipyridine. However, the overall efficiency still lies between 2 and 3% in most of these cases and the big breakthrough using modified ancillary ligand is still awaited.

The modification of the electrolyte in bisdiimine copper(I) DSSCs, leads to an increase in performance compared to the standard iodine electrolyte (LiI (0.1 M), I_2 (0.05 M), 1-methylbenzimidazole (MBI) (0.5 M), 1-butyl-3-methylimidazolinium iodide (BMII) (0.6 M) in 3-methoxypropionitrile (MPN)) used in most studies. A systematic investigation of concentrations and additives in I^-/I_3^- electrolyte was carried out[87] and revealed an optimal composition using I_2 (0.015 M), BMII (0.6 M), and guanidinium thiocyanate (GNCS) (0.01 M) in MPN without addition of LiI. Fürer and coworkers[20] demonstrated the beneficial effect of replacing the I^-/I_3^- redox couple by a $[Co(bpy)_3]^{2+/3+}$ redox couple in the electrolyte. An increase in efficiency from 2.73% using a I^-/I_3^- electrolyte (relative to 8.02% for an **N719** reference cell) to 3.69% (relative to 7.12% for an **N719** reference cell) using a $[Co(bpy)_3]^{2+/3+}$ electrolyte was observed.

The research focus in this PhD thesis concentrates on the modification of anchoring ligands for heteroleptic bisdiimine copper(I) complexes, which has not been examined in great detail to date.

4 CELL-ASSEMBLY AND CHARACTERIZATION

4.1 Chemicals

Chemicals for ligand synthesis were purchased from Sigma-Aldrich, TCI, Acros, Apollo, Fluorochem or Alfa Aesar. Deuterated solvents for NMR spectroscopy were purchased from Cambridge Isotope Laboratories, Inc. HPLC solvents were used for UV-VIS, ESI-MS and electrochemical measurements. Technical dimethyl sulfoxide (DMSO), miliQ water and HPLC solvents were used in the solar cell assembly.

4.2 General

A Biotage Initiator 8 microwave reactor was used for reactions carried out under microwave conditions. Ligands were characterized by ^{1}H, ^{13}C, ^{19}F and ^{31}P-NMR spectroscopy, ESI-MS, high res ESI-MS, MALDI-TOF-MS, melting point, UV-VIS, IR and elemental analysis measurements. 400MHz, 500MHz and 600MHz NMR spectra were measured on Bruker Avance III- 400, DRX-500 or DRX-600 NMR spectrometers with chemical shifts referenced to residual solvent peaks; ^{1}H and ^{13}C δ(TMS) = 0 ppm; ^{31}P δ(85% aqueous H_3PO_4) = 0 ppm; ^{19}F $\delta(CFCl_3)$ = 0 ppm. Electrospray mass spectra were measured on Bruker Esquire 3000^{plus} or Shimadzu LCMS-2020 instruments. High resolution ESI-MS was measured on a Bruker maXis 4G instrument. MALDI-TOF mass spectra were recorded on a Bruker Daltonics Inc. microflex instrument. Solution electronic absorption spectra were recorded on an Agilent 8453 or Cary 5000 spectrophotometer. Solid-state spectra were recorded on a Cary 5000 spectrophotometer. FT-IR spectra were recorded on a Perkin Elmer Spectrum Two instrument.

Single crystal data were collected on a Bruker APEX-II diffractometer. Data reduction, solution and refinement used the programs APEX[88] or CRYSTALS[89]. The structures were analyzed with Mercury[90-91].

4.3 Materials for DSSCs

4.3.1 N-type DSSCs

TiO_2 working electrodes, Pt-electrodes and sealing materials were purchased from Solaronix SA, Aubonne, Switzerland (Test Cell Kit, ref: 74991) and used to assemble most of the DSSCs presented in the next chapters. Self-printed TiO_2 electrodes were used in one study and were prepared by Annika Büttner via the screen-printing technique[34].

Commercially available TiO_2 electrodes have an active TiO_2-area of 36mm^2 on a 4 cm^2 FTO coated glass plate. The mesoporous TiO_2 layer is ~10µm thick, covered with a ~3 µm scattering/blocking layer of larger TiO_2 particles (SEM measurement by Dr. Collin Morris at the University of Basel). The mesoporous layer has a large surface area and enables increased dye uptake, compared to a TiO_2 monolayer. This increase in surface area was the breakthrough for the DSSC technology[14].

The counter electrode is an FTO coated glass (4cm^2) with a thin Pt layer and a hole drilled through the glass. The hole enables addition of electrolyte to the assembled cell, via the vacuum backfilling technique.

Hot melting foil was provided in the solar cell kit from Solaronix SA. A gasket sealing foil was used to glue working and counter electrodes together. A thin glass plate was glued on the hole in the counter electrode using a thin sealing foil. The solar cell is completely closed and stable for weeks.

4.3.2 P-type DSSCs

NiO is a semiconductor material, which can be used as a counter electrode material and can replace the Pt electrode. It can be sensitized with dye molecules, similar to the TiO_2 semiconductor. The working and design principle of p-type DSSCs is described in chapter 10.

NiO working electrodes were prepared by Nathalie Marinakis, using the screen-printing technique according to the literature preparation[92]. A thickness of ~1.0-2.5 µm for the NiO layer was confirmed using focused ion beam (FIB) scanning electron microscopy (REM-FEI Helios NanoLab 650).

The same Pt-electrode used for n-type DSSCs was used in the assembly of p-type solar cells. Hot melting foil was provided in the solar cell kit from Solaronix SA was used to glue both electrodes together and close the hole in the Pt-electrode, used for vacuum backfilling of the electrolyte.

4.3.3 The electrolyte

The electrolyte used for all n-type DSSCs presented in this thesis consists of following components: LiI (0.1 M), I_2 (0.05 M), 1-methylbenzimidazole (0.5 M) and 1-butyl-3-methylimidazolinium iodide (0.6 M) in 3-methoxypropionitrile. The electrolyte can be introduced into the DSSC via vacuum backfilling, explained in the next section.

4.4 Sensitization of TiO_2 and DSSC assembly

Bisdiimine copper(I) based solar cells were attached to a TiO_2 working electrode in a step-wise on surface approach (Fig. 9). The commercial TiO_2 electrodes were washed with miliQ water and HPLC ethanol and sintered for 30 min at 450°C. The electrodes were cooled to 80°C and immersed into an anchoring ligand solution (1 mM in DMSO) for one day. The modified electrodes were washed with DMSO and ethanol and dried under a nitrogen stream or with a heat gun (80°C) and then immersed in a solution containing an homoleptic bisdiimine coper(I) complex (0.1 mM in dichlormethane or acetone) for three days. Ligand exchange reactions take place during that time and an heteroleptic copper(I) complex attached to the TiO_2 surface is formed. The sensitized semiconductor is washed with the solvent of the homoleptic copper(I) dye bath and dried under a nitrogen stream or with a heat gun (80°C).

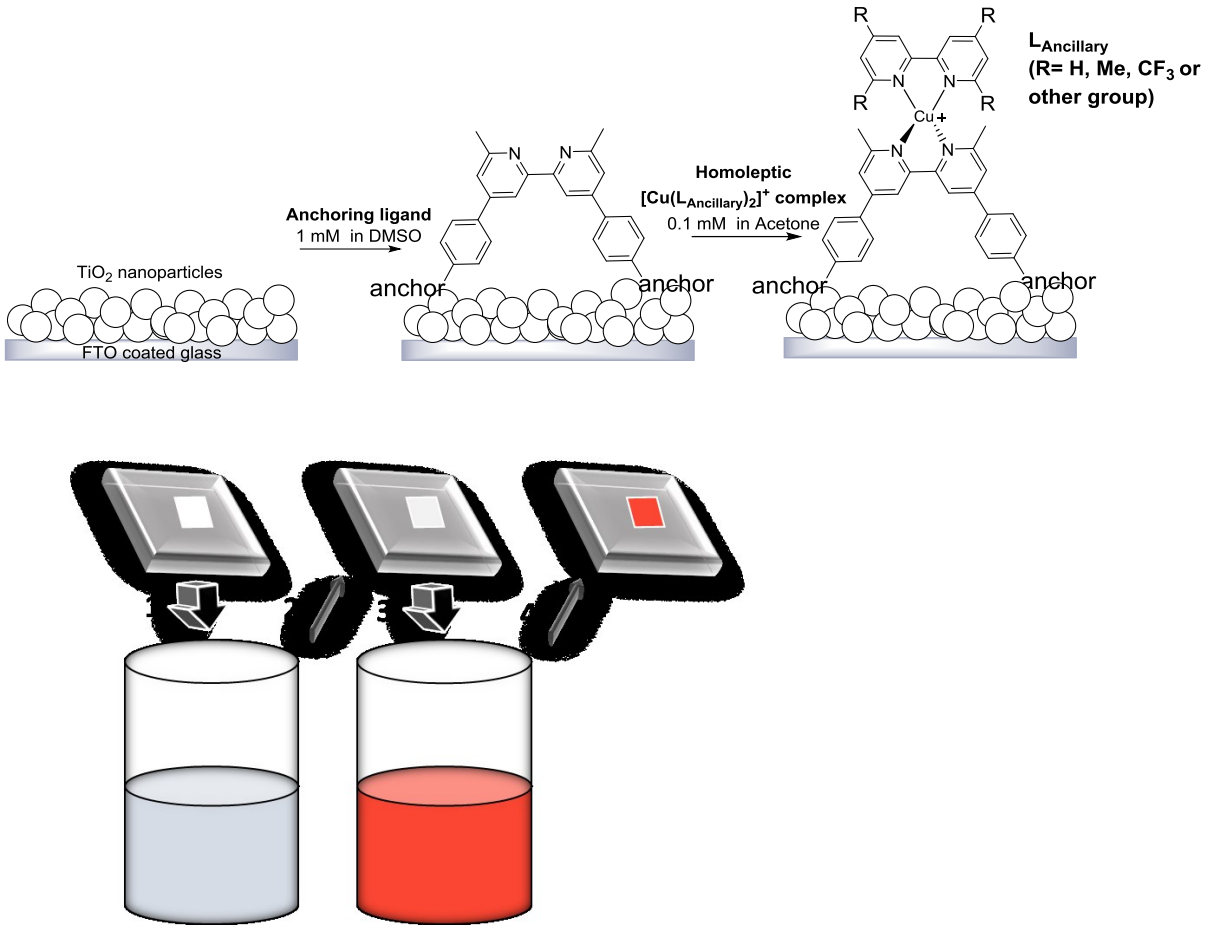

Fig. 9: Step-wise solar cell assembly.

TiO_2 electrodes sensitized with the **N719** dye (0.3 mM in ethanol) and an organic dye (1 mM in DMSO), presented in chapter 9, were dipped into the corresponding dye solutions for 3 days and 1 day, respectively.

The Pt counter electrode was washed with miliQ water and ethanol (HPLC grade) and sintered at 450°C for 30 min and cooled to RT afterwards. The electrodes were glued together using thermoplast hot-melt sealing foil. A soldering iron was pressed on the backside of the counter electrode, while heating the glass to 240 °C and melting the foil between the glass plates. The tip of the soldering iron was modified to match the shape of the sealing foil and not directly heat the dye. The predrilled hole in the counter electrode was positioned within the sealing foil gasket and an Eppendorf pipette tip was placed in the hole. The cell was evacuated and flushed with N_2 three times. Liquid electrolyte was filled into the pipette-tip and the vacuum was carefully increased. N_2 inside the cell was drained out and replaced by the electrolyte ("vacuum-backfilling"). 1-2 back-filling steps were performed to remove all gas from the cell. The tip was

removed, and the cell closed using hot-melt sealing foil and a covering glass. Silver paste was applied to the edges of both electrodes, enabling better contact.

4.5 *J*/*V* measurements

The basic photophysical properties, the voltage and the current were measured under artificial light irradiation with a sun simulator. A LOT Quantum Design LS0811 instrument (AM 1.5, 23 °C) was used and calibrated with a silicon solar cell to 1000 W/cm^2 (1 sun). The sealed solar cells were masked with a copper sheet, minimizing diffuse and reflected light, which enables consistent and reproducible data. The exposed area of the masked solar cell was around 0.0600 cm^2, depending on the used mask. P-type solar cells were not masked and the active area was 0.237 cm^2.

Fig. 10: The LOT Quantum Design LS0811 instrument.

The solar cell was placed under the sun simulator and sun soaked for 20 min. The sun soaking fills all trap states in the semiconductor with electrons (or holes for p-type). The solar cell was fixed on a measuring table under the solar lamp and the output current was measured by applying and external voltage. For p-type solar cells the measuring mode in the instrument software was changed to p-type, which supports the inverted configuration. The measurement was controlled, and data were analyzed using ReRa Tracer 2.0 software.

The *J*/*V* measurement was performed under light irradiation, while the voltage was screened from −0.1 V to 0.7 V. The output current was measured and directly divided by the active surface to give the short circuit current density J_{SC}. The potential where the current becomes 0 is defined as the open circuit voltage V_{OC}. The maximum of the product of voltage times current is the maximum power (P_{max}) point of the solar cell. The voltage at the maximum power point is V_{MP} and the current J_{MP}. The fill factor (*ff*) is the ratio of the rectangles defined by $J_{MP} \cdot V_{MP}$ and $J_{SC} \cdot\cdot V_{OC}$. It's given in % and has a value between 0 and 100.

$$ff = \frac{J_{MP}V_{MP}}{J_{SC}V_{OC}}$$

These values including the power density of the incident light (P_{IN}) can be used to calculate the most important value, the efficiency η of a solar cell.

$$\eta = \frac{J_{SC} \cdot V_{OC} \cdot ff}{P_{IN}}$$

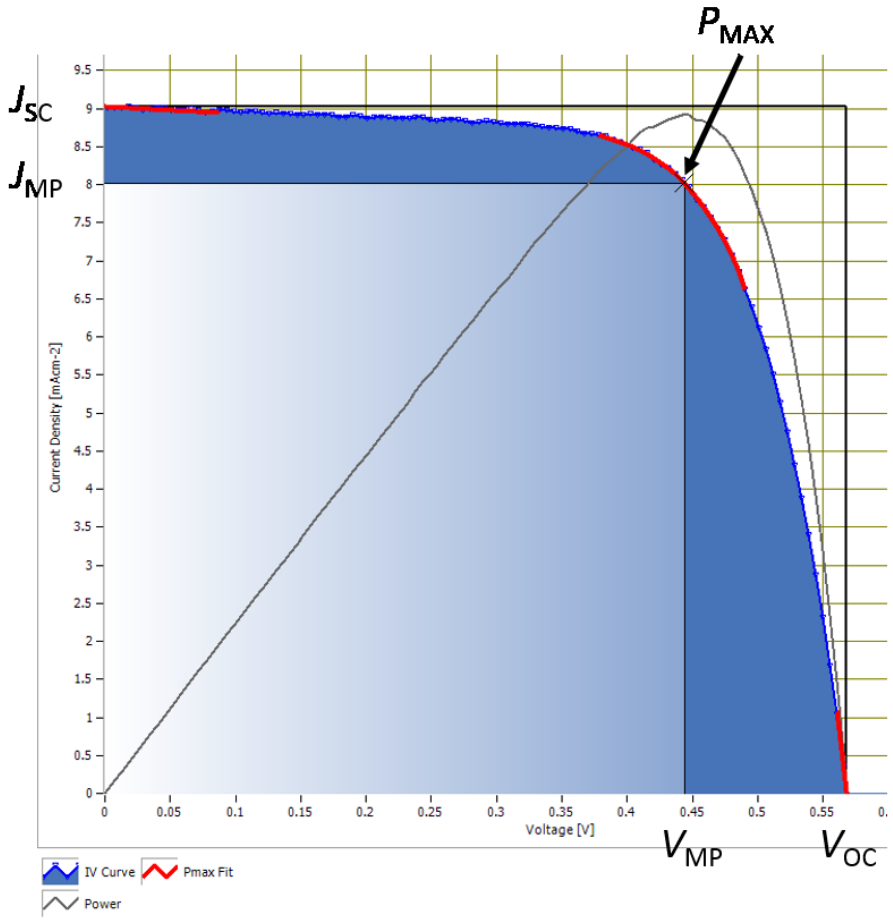

Fig. 11: *J/V* curve obtained from measurement with the LOT Quantum Design LS0811 instrument. Important parameters are highlighted.

4.6 EQE measurements

Photophysical insight into the process of light absorption and injection is gained from external quantum efficiency measurements. This method measures the current output at open circuit conditions in relation to the wavelength of the incident light. The wavelength of the incident light is controlled by a monochromator. The EQE value is defined by the current output (J_{SC}) at a given wavelength (λ), the incident light at that wavelength (P_{IN}) and a correction factor of 1240 to convert eV to nm.

$$E = h \cdot v = \frac{h \cdot c}{\lambda} = \frac{1240\ eVnm}{\lambda(nm)}$$

The formula shows the relation between wavelength and energy; 1nm = 1240 eV.

A photon with a wavelength of 450 nm would have an energy of 2.756 eV. The EQE is defined as:

$$EQE = 1240 \frac{J_{SC}}{\lambda \cdot P_{IN}}$$

External quantum efficiency (EQE) was measured on a Spe-Quest quantum efficiency setup equipped with a 100 W halogen lamp (Rera Systems, Netherlands). The monochromator was a lambda 300 machine from Lot Oriel modulating the light to 3Hz using a chopper wheel (ThorLabs). Data were recorded with a SR830 DSP Lock-In amplifier from Stanford Research.

4.7 EIS measurements

EIS measurements were carried out by Dr. Markus Willgert and Nathalie Marinakis from the University of Basel.

EIS is measured by applying an alternating current of varying frequency close to the V_{OC} of a DSSC. EIS is measured at different light intensities, which enables investigation of different charge transfer and recombination processes in the cell. Charge transfer, resistance and capacitance of the interfaces (TiO_2 / electrolyte and Pt counter electrode / electrolyte) in a DSSC can be extracted from EIS measurements and give important insight into the processes in a solar cell. EIS is a very powerful tool, but also complex and was performed in cooperation with colleagues. It will be discussed briefly in chapters 7 and 8, but is not the main focus of this PhD thesis.

5 PREPARATION OF BISDIIMINE COPPER(I) COMPLEXES FOR DSSCS

5.1 Project Aim

Bisdiimine copper(I) complexes as sensitizers in DSSCs are a research field with great potential (see introduction). They are part of a family of metal-organic complexes with the ability to absorb photons and convert them into electrical current. Compared to other inorganic dyes, mainly ruthenium(II) based complexes, copper(I) complexes benefit from sustainable, cheap and abundant materials. Photophysical properties of bisdiimine copper(I) complexes enable long lived excited states[93], suitable for charge separation and electron injection into a semiconductor. The low oxidation potential[63] (+0.17 V with respect to Fc/Fc^+), combined with a relatively intense MLCT enables these materials to be suitable materials for DSSCs. Upon irradiation bisdiimine copper(I) complexes undergo MLCT transitions and transfer an electron to the antibonding π*-orbital of a bisdiimine ligand. The loss of one electron generates a copper(II) ligand-radical with an electronic d^9 configuration in the excited state. Copper(II) prefers to be five or six coordinated. The geometry of a copper(II) complex is distorted (Jahn-Teller distortion) in an octahedron, as the three electrons in the e_g orbitals can either fully occupy the d_{z^2} or the $d_{x^2-y^2}$ orbital, which causes elongation or compression of the bond length of the axial ligands[62]. Bulky groups (e.g.: methyl, ^{n}butyl, ^{iso}butyl, ^{n}hexyl, phenyl) can be incorporated at the C-atom next to the coordinating N-atom (see Scheme 14 for 6,6'-dimethyl-2,2'-bipyridine)[80]. These substituents give the complex a tendency to stay in a pseudo-tetrahedral geometry and shield the copper atom from nucleophilic attack (e.g. by solvent molecules), which in turn prevents excited state decay. Bisdiimine copper(I) complexes show colours ranging from orange to red to purple.

The Constable/Housecroft group at the University of Basel has investigated different types of ligands for copper(I) based dyes and tested their performances in a solar cells over the last few years[16]. By changing one ligand of the complex, the so-called ancillary ligand, and keeping the anchoring ligand the same, efficiencies of these heteroleptic systems could be increased[84].

In this PhD thesis, all aspects of modification in a bisdiimine copper(I) complex will be discussed. A new type of ancillary ligand bearing a CF_3-group will be introduced, which shows encouraging results. Many intensive studies of ancillary ligands for bisdiimine copper(I) complexes have already been reported from our research group and will not be the main interest in this thesis.

The focus of this PhD thesis lies on the modification of the second diimine ligand in a copper(I)-complex, the anchoring ligand. These ligands bear anchoring groups, which enable binding to a semiconductor like TiO_2, enabling electron injection. Systematic studies of spacers, substitution positions and especially new types of anchoring groups will be presented.

5.2 Design principle of bisdiimine copper(I) complexes

Bisdiimine copper(I) complexes as dyes in DSSC's were discussed in the introduction. The simplest bisdiimine ligand discussed in this thesis is 6,6'-dimethyl-2,2'-bipyridine (**1** ,Scheme 14).

The Constable/Housecroft research group at the University of Basel developed their own approach towards heteroleptic bisdiimine copper(I) complexes anchored to a semiconductor surface. Direct solution synthesis of heteroleptic complexes is difficult, as homoleptic and heteroleptic complexes of bisdiimine ligands equilibrate in solution and their separation is challenging. Thus, a stepwise on surface assembly methodology was developed[42, 94]. This method allows fast and easy screening of different heteroleptic complexes in a solar cell. Cells can be modified with an anchoring ligand and by ligand exchange of the surface bound anchor with homoleptic bisdiimine copper(I) complexes a wide range of heteroleptic complexes can be investigated easily and rapidly. The disadvantage of this assembly method is the lack of characterizations possible. On surface solid state UV-VIS spectroscopy and electrochemical impedance spectroscopy (EIS) are important characterization methods, but standard solution characterization of heteroleptic complexes is not possible. Scheme 15 shows an example of a heteroleptic bisdiimine copper(I) complex bound to a TiO_2-semiconductor surface. It consists of two diimine ligands, with chelating coordination to copper(I) in a tetrahedral geometry. In

this study, substituted 2,2'-bipyridine (bpy) and 1,10-phenanthroline (phen) ligands are discussed and Scheme 15 gets modified, as the results of my PhD work are presented.

On the right side of Scheme 15 the ancillary ligand is displayed. Two important substitution positions are highlighted by R-groups. In the 6 and 6' positions of 2,2'-bipyridine, alkyl and aromatic groups of various length and size can be incorporated to prevent flattening of the tetrahedral geometry of the copper(I) centre. In the 4 and 4' positions, functionalized aromatic groups with various substituents can be easily incorporated by a Kröhnke type reaction mechanism[95]. The highest occupied molecular orbital of a copper(I)-complex should lie on the copper centre and the ancillary ligand side of the complex to promote electronic driving force towards the anchoring ligand. The transfer of excited electrons, that are generated upon irradiation, through a heteroleptic bisdiimine copper(I) complex is influenced by electron withdrawing and releasing substituents on the diimine ligands. To enhance this driving force, electron rich and releasing groups like alcohols, amines and halogens can be incorporated (e.g. in 4 and 4' position of 6,6'-dimethyl-2,2'-bipyridine). Previous studies in the Constable/Housecroft research group highlighted beneficial effects of incorporated halogen[84] and triarylamine[85] substituents compared to the 6,6'-dimethyl-2,2'-bipyridine (Scheme 14) ligand.

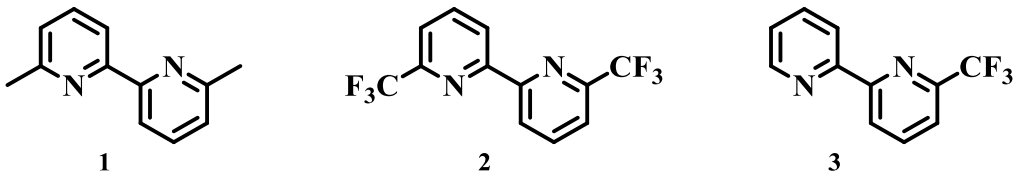

1 2 3

Scheme 14: The 6,6'-dimethyl-2,2'-bipyridine ligand **1** and ancillary ligands **2** and **3** discussed in the next chapter.

A clear trend however is hard to establish, and efficiencies range from 2.5-3.5% in most cases (relative to 7.63% for a **N719** reference cell)[84]. In chapter 6, 2,2'-bipyridine ligands with different groups in the 6 and 6' positions of the ancillary ligand (**2** and **3**, Scheme 14) will be incorporated into copper(I) based solar cells and their efficiencies compared to ligand **1**.

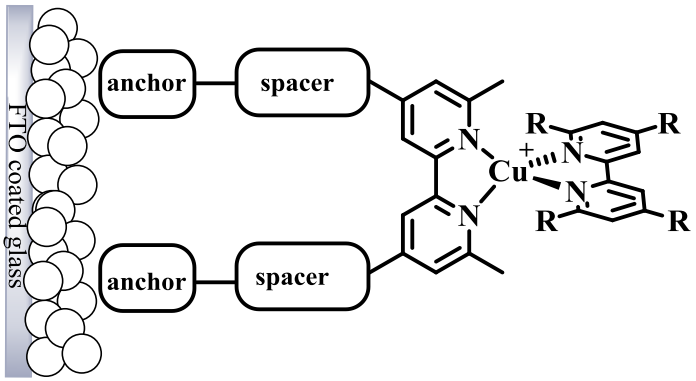

Scheme 15: General structure of a heteroleptic bisdiimine copper(I) complex bound to a TiO_2 semiconductor. The ligand on the right-hand side is the so-called ancillary ligand, the ligand bound to the surface is the so-called anchoring ligand.

On the left-hand side in Scheme 15, the anchoring ligand is displayed. It consists of a 6,6'-dimethyl-2,2'-bipyridine or a 2,9-dimethyl-1,10-phenanthroline core with substituents in the 4 and 4' positions or 4 and 7 positions, respectively. The anchoring ligands discussed in this thesis always possess methyl groups in the 6 and 6' position of 2,2'-bipyridine or in the 2 and 9 positions of 1,10-phenanthroline (trivial name: neocuproine), to prevent distortion of the tetrahedral geometry. Previous studies[42] have shown, that anchoring groups directly attached in the 4 and 4' positions of 6,6'-dimethyl-2,2'-bipyridine show worse performances than those with an anchor separated from the bpy core by a spacer in the 4,4'-positions[42].

The synthesis of the standard and most frequently used anchoring ligand for heteroleptic bisdiimine copper(I) dyes is displayed in Scheme 16. Anchor **4** is synthesized in 4 steps[83]. Steps 1 and 2 highlight the great potential of the pyridine synthesis developed by Kröhnke in 1976[95]. The synthesis follows a general route. In the first step, two equivalents of functionalized aromatic aldehyde are reacted in a double Knoevenagel condensation, with 2,3-butandione in the presence of catalytic amounts of piperidine, to give the 1,6-substituted hexa-1,5-diene-3,4-dione. A wide variety of functional groups attached to the aromatic aldehyde are tolerated, such as amide, alkyl, alkoxy and halogen groups. The second step is the Kröhnke type condensation, where a e.g. 1-(2-oxopropyl)pyridin-1-ium chloride reacts with the hexa-1,5-diene-3,4-dione in the presence of ammonium acetate to yield a 4,4'-substituted 6,6'-dimethyl-2,2'-bipyridine ligand. The wide variety of available aromatic aldehydes combined with the easy preparation of Kröhnke salts (α-pyridinium methyl ketones) enables a fast and beneficial synthesis of otherwise difficult accessible 2,2'-bipyridine ligands. In the specific example in

Scheme 16, the 6,6'-dimethyl-2,2'-bipyridine ligand is substituted in the 4 and 4' position with 4-bromophenyl groups. The bromine functionality allows subsequent modification via Pd-based cross coupling reactions. In a microwave (MW) reaction under dry solvent conditions the dibromo compound reacts with $HPO(OEt)_2$, Cs_2CO_3 and catalytic amounts of $[Pd(PPh_3)_4]$ to give the phosphonic ester (Scheme 16). The ester is easily deprotected by reaction with the electrophile TMS-Br and workup under aqueous conditions yielded anchoring ligand **4** in 80% yield. The synthesis follows a literature preparation[83] with an improved deprotection step[96] to **4**.

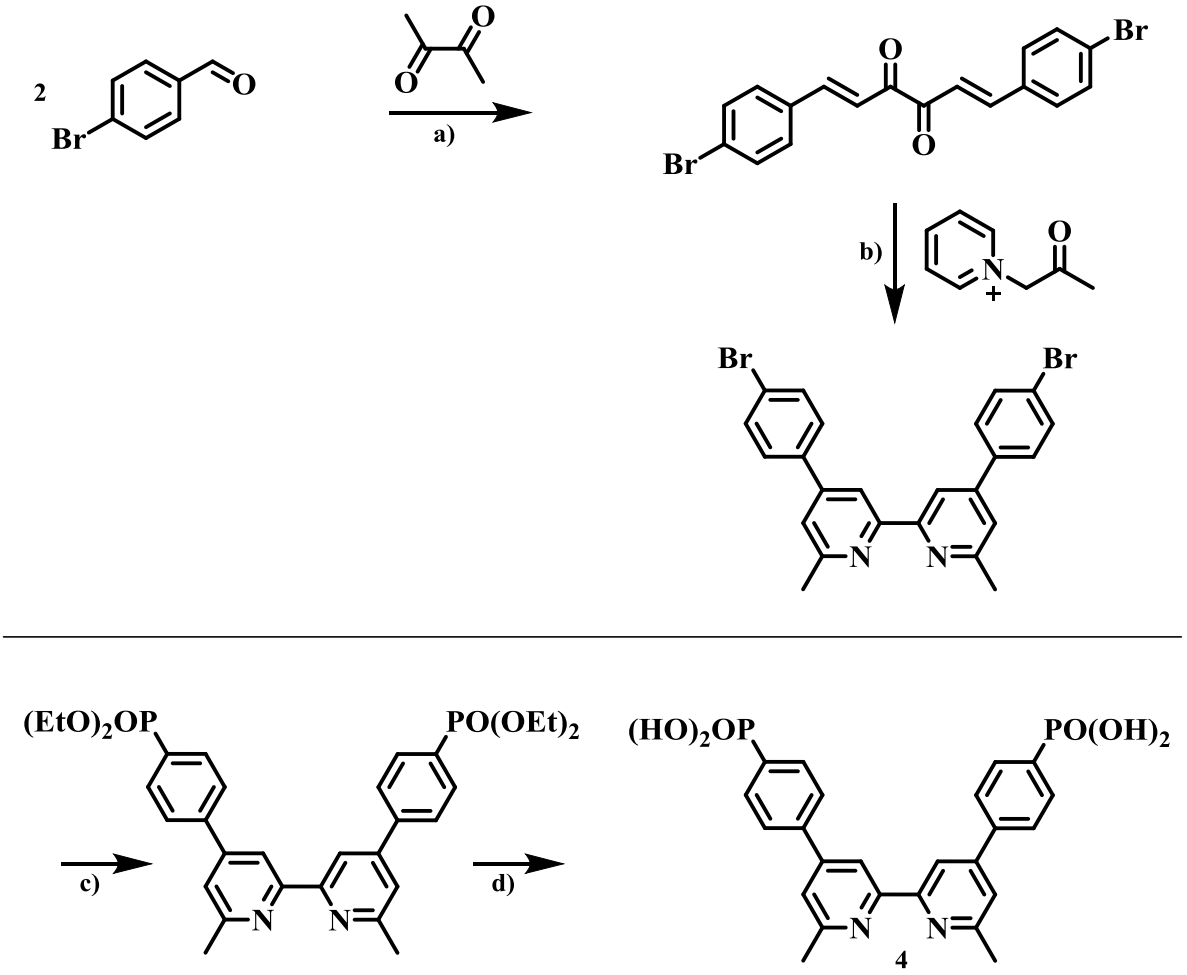

Scheme 16: General route for the synthesis of standard anchor **4**; a) MeOH, piperidine, reflux, 16h, b) NH_4OAc, EtOH, reflux, 4h, c) $HPO(OEt)_2$, $[Pd(PPh_3)_4]$, Cs_2CO_3 in dry THF (110°C, MW radiation, 90min), d) TMS-Br, CH_2Cl_2, RT, aqueous workup.

The spacer in the standard anchoring ligand is a phenylene group (**4**, Scheme 16). It enables electron transport from the copper(I)-bpy core, via conjugation to the anchoring group and the

semiconductor. Spacers enable better charge separation by transferring the excited electron from the MLCT process at the copper(I)-bpy core via the phenylene spacer and the anchoring group into the semiconductor. This spatial separation of the electron generating centre and the charge injection part decreases recombination and the return of the excited state to the ground state, which in turn results in enhanced power output. In chapter 7 the influence of thiophenediyl groups as aromatic spacers and the position of the anchoring group in the thiophenediyl will be discussed.

Another important part of a heteroleptic bisdiimine copper(I) dye is the anchoring group on the anchoring ligand. The standard anchor **4** (Scheme 16) bears a phosphonic acid anchoring group in the 4 position of both phenylene-spacers. Previous studies revealed that phosphonic acid anchors perform better in heteroleptic copper(I)-dyes than the more frequently used carboxylic acid and carboxylate anchors[42] which are popular choices in ruthenium and organic dyes (see introduction).

In the growing field of organic dyes, cyanoacrylic acid anchoring groups are widely used. Common and promising anchoring groups from the fields of inorganic and organic sensitizers were discussed in the introduction. The most promising and widely used are carboxylic acids, carboxylates and phosphonic acids. In chapter 8 four new anchoring ligands, combining 2,2'-bipyridine and 1,10-phenanthroline ligand cores, with phenylene spacers and two different anchoring groups will be discussed, revealing promising performances of the (1-cyanovinyl) phosphonic acid in bisdiimine copper(I) complexes.

Chapter 9 carries on the systematic investigation of anchoring ligands by changing the length of the aromatic spacer. The initial idea was to decrease recombination processes to a minimum, by spatial separation of anchor and charge generating copper(I)-bpy core. This approach is widely used in the design of organic dyes, where a donor-π-bridge-acceptor design leads to an electrical driving force from the donor, through the π-bridge into the acceptor and finally the semiconductor. This principle was discussed in the introduction and is represented in the **MK2** dye (Scheme 17)[97]. The carbazole group acts as the electron donor and is connected to a cyanoacrylic acid group (electron acceptor and anchor) via 4 thiophenediyl spacers. As an additional feature, hexyl groups were incorporated, to shield the semiconductor surface from the electrolyte, thus preventing recombination of injected electrons to the electrolyte.

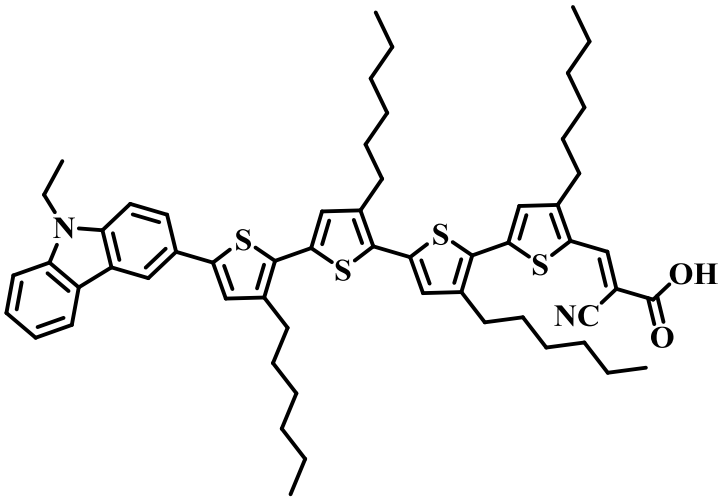

Scheme 17: The organic **MK2** dye[97].

Inspired by this design, an organic dye will be presented, which shows good light harvesting abilities as a stand-alone dye. Its performance in combination with a copper(I) metal centre is discussed in chapter 9.

In section 10 a purely organic dye is presented, which will be tested as a dye in p-type DSSCs.

6 ANCILLARY LIGANDS: CF_3 VS METHYL SUBSTITUTED 2,2'-BIPYRIDINE LIGANDS

In the previous chapter, effects of substitutions on ancillary ligands for bisdiimine copper(I) complexes were discussed. Of great importance are alkyl groups in the 6 and 6' positions of 2,2'-bipyridine ligands which hinder flattening of the tetrahedral geometry upon photo-oxidation of the copper(I) complex. In this chapter the standard anchoring ligand **4** (Scheme 16) was used, bearing methyl groups in the 6 and 6' positions and phosphonic acid substituted phenylene groups in the 4 and 4' positions (left-hand side, Scheme 18). The synthesis of anchoring ligand **4** was described in the previous chapter.

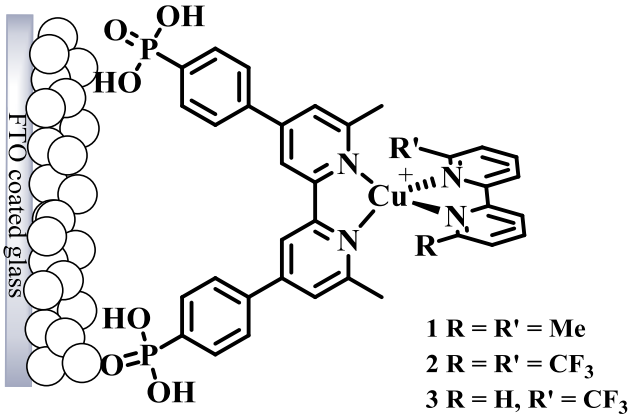

Scheme 18: Bisdiimine copper(I) complexes with **4** as the anchoring ligand and 2,2'-bipyridine ligands substituted in 6 and/or 6' position by a methyl or CF_3 group.

As ancillary ligands 6,6'-dimethyl-2,2'-bipyridine **1** was compared with 6,6'-bis(trifluoromethyl)-2,2'-bipyridine (**2**) and 6-trifluoromethyl-2,2'-bipyridine (**3**) (Scheme 19). Ligands **2** and **3** bear electron withdrawing groups in the 6 and/or 6' position. Although the choice of CF_3 is counterintuitive in terms of a "push-pull" system, these ligands showed better performances in a DSSC than 6,6'-dimethyl-2,2'-bipyridine and highlight, that one CF_3 group in the 6-position is sufficient to prevent a heteroleptic copper(I) complex from irreversible oxidation to copper(II). In addition to the DSSC performance, this chapter highlights some general characteristics of homoleptic bisdiimine copper(I) complexes. NMR spectroscopic assignment, solution UV-VIS absorption spectra, electrochemical measurements and single

crystal X-ray diffraction was carried out to characterize the homoleptic complexes [Cu(**2**)$_2$][PF$_6$]. These characterizations are only presented here, as the following chapters reuse the homoleptic complexes from this chapter in combination with newly synthesized anchoring ligands.

6.1 Synthesis and Characterization

Ligand and complex synthesis, including characterizations, in this chapter were carried out in cooperation with Fabian Brunner, Dr. Sarah Keller and Dr. Collin D. Morris from the Housecroft/Constable group at the University of Basel. Solar cell device fabrication and studies were carried out by myself.

6.1.1 Ancillary ligand and homoleptic complex synthesis

Ancillary ligand **1** is commercially available and was used without further purification (supplier: Sigma-Aldrich). Ancillary ligand **2** was previously published and characterized[98]. The commercially available precursor 2-chloro-6-(trifluoromethyl)pyridine was reacted with dichloridobis(triphenylphosphine)nickel(II) catalyst, zinc and tetraethylammonium iodide in dry THF following the literature preparation[98].

Ligand **3** was prepared via a Negishi cross coupling reaction[99] of commercially available precursors 2-chloro-6-(trifuoromethyl)pyridine and 2-pyridylzinc bromide under microwave conditions in the presence of the Pd(0) catalyst [Pd(PPh$_3$)$_4$]. Compound **3** was obtained in 61% yield and characterized by ^{1}H-, ^{13}C{^{1}H}-, ^{19}F-NMR spectroscopy, ESI-MS, UV-VIS spectroscopy and elemental analysis measurements.

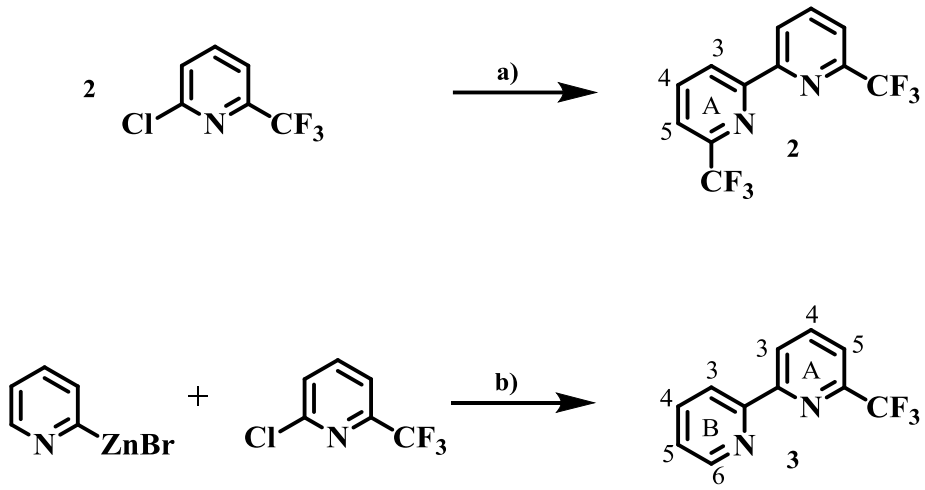

Scheme 19: Synthetic routes towards ancillary ligands **2** and **3**; a) Dichloridobis(triphenylphosphine) nickel(II), zinc and tetraethylammonium iodide in dry THF (60 °C, 22h), b) [$Pd(PPh_3)_4$] in dry THF (110 °, MW radiation, 2h).

The ^{1}H-NMR spectrum of **3** was recorded in $CDCl_3$ and protons on the CF_3 substituted pyridine ring showed similar chemical shifts[98] to those of **2**. A singlet (δ = -68.4 ppm) was observed in the ^{19}F-NMR spectrum, and signals showing J_{CF} coupling patterns in the $^{13}C\{^1H\}$-NMR spectrum for the C^{CF3} group (q, J = 274 Hz) and carbon atoms C^{A6} (q, J = 35 Hz) and C^{A5} (q, J = 2.9 Hz) were obtained. The base peak in the ESI-MS spectrum was assigned to the $[M+H]^+$ species (*m/z* 225.1). Fig. 12 shows the assigned ^{1}H-NMR of compound **3**.

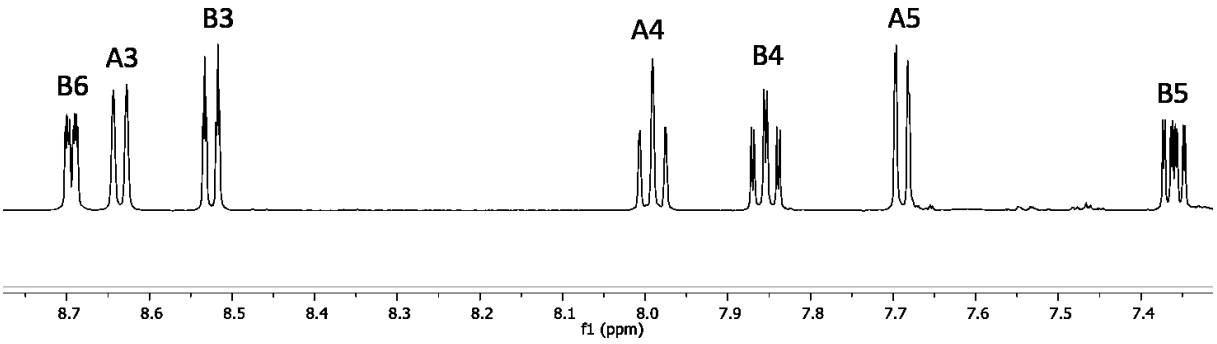

Fig. 12: ^{1}H NMR spectrum of compound **3** (400 MHz in $CDCl_3$). Chemical shifts in δ/ppm, referenced to δ(TMS) = 0 ppm. Labelling according to Scheme 19.

Homoleptic complex synthesis followed the general route described in Scheme 20. Ligands **1**, **2** and **3** were dissolved in dichloromethane and 0.5 eq. of $[Cu(MeCN)_4][PF_6]$ (prepared according to the literature[100]) was added. The solution instantly turned orange/red. Evaporation of the solvent yielded $[Cu(\mathbf{2})_2][PF_6]$ and $[Cu(\mathbf{3})_2][PF_6]$ as red crystals. $[Cu(\mathbf{1})_2][PF_6]$ was

precipitated with diethyl ether from a solution of the complex in acetonitrile according to the literature preparation methodology[63].

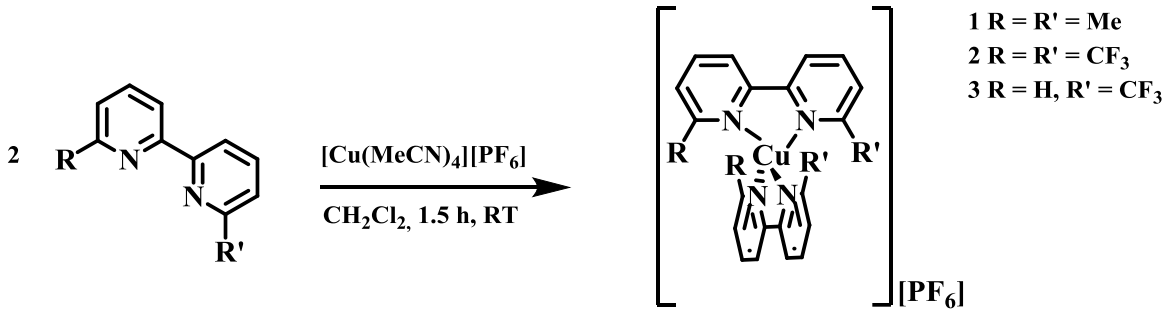

Scheme 20: General synthetic method towards homoleptic [Copper(I)-(bisdiimine)$_2$][PF_6] complexes.

[Cu(**1**)$_2$][PF_6] was previously published and characterized[63] and is used as an homoleptic complex in this and the following chapters. [Cu(**2**)$_2$][PF_6] and [Cu(**3**)$_2$][PF_6] were characterized by MALDI-TOF, ^{1}H-, ^{13}C{^{1}H}-, ^{19}F-, ^{31}P{^{1}H}-NMR spectroscopies, UV-VIS spectroscopy and elemental analysis. ^{1}H and ^{13}C{^{1}H} NMR spectra of [Cu(**2**)$_2$][PF_6] and [Cu(**3**)$_2$][PF_6] were compared with free ligand data and confirmed full conversion towards the according complexes (Fig. 13).

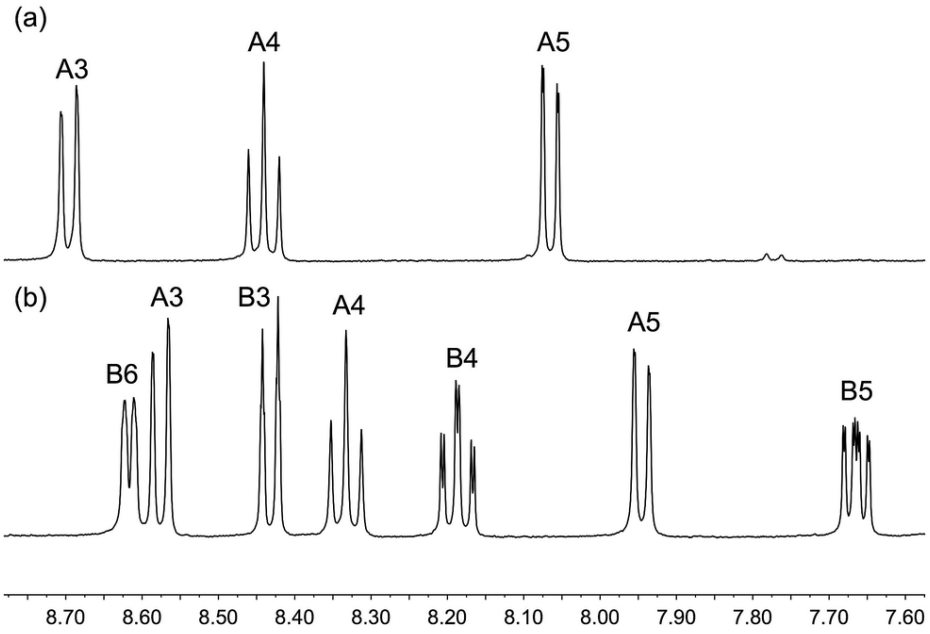

Fig. 13: ^{1}H NMR spectra of complexes [Cu(**2**)$_2$][PF_6] and [Cu(**3**)$_2$][PF_6] (500 MHz in CD_2Cl_2). Chemical shifts in δ/ppm. Labelling according to Scheme 19. Reproduced from ref.[101] with permission of The Royal Society of Chemistry.

The successful synthesis was validated by ^{19}F-NMR spectra. The integral of the signal for the PF_6^- ion was set in relation to the CF_3 signals and revealed four or two CF_3 groups for [Cu(**2**)$_2$][PF_6] and [Cu(**3**)$_2$][PF_6], respectively. Base peaks in the MALDI-TOF mass spectrum were assigned to [Cu(**2**)$_2$]$^+$ (*m/z* 647.2) and [Cu(**3**)$_2$]$^+$ (*m/z* 511.1). Solution UV-VIS spectroscopy of both complexes showed intense absorptions in the UV part of the spectrum, corresponding to ligand based π* ← π transitions. A broad MLCT transition was observed in the visible region with maxima at 445nm for [Cu(**2**)$_2$][PF_6] and 443nm for [Cu(**3**)$_2$][PF_6], responsible for the orange/red colour of the complexes.

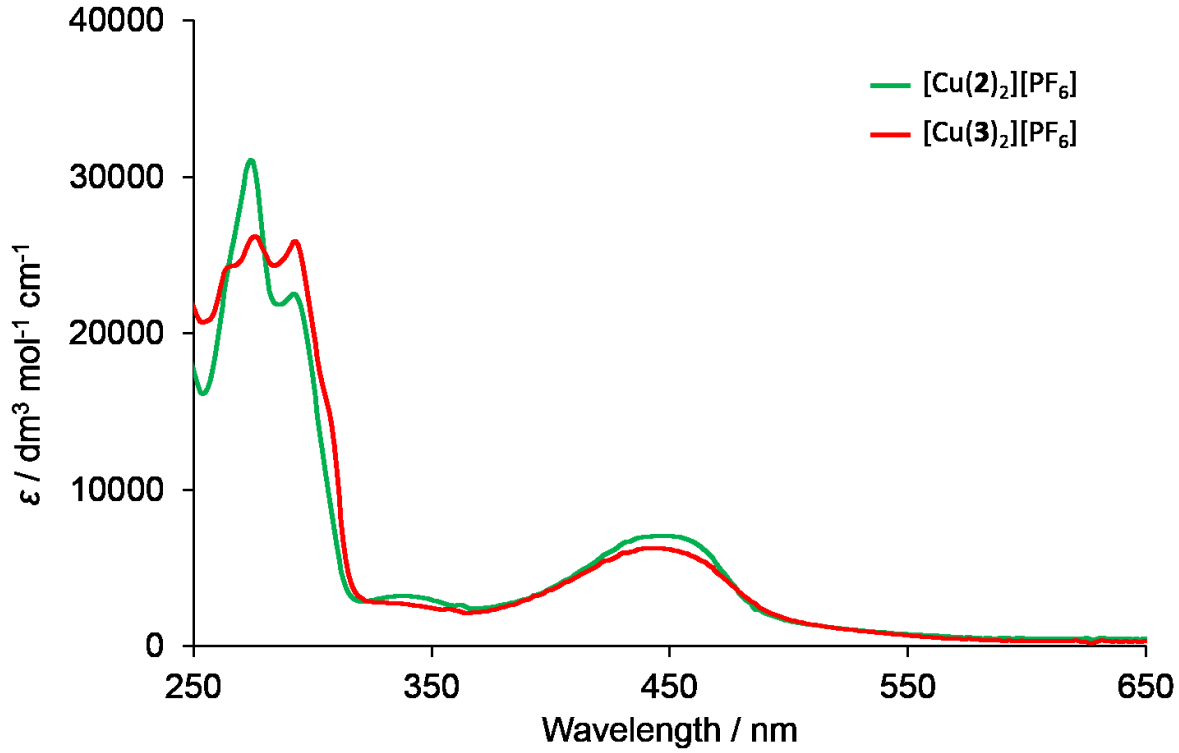

Fig. 14: Solution UV-VIS spectra of complexes [Cu(**2**)$_2$][PF_6] and [Cu(**3**)$_2$][PF_6] in CH_2Cl_2. A characteristic MLCT absorption for bisdiimine copper(I) complexes at ~ 450nm is present for both complexes. Absorptions below 350nm correspond to ligand based π* ← π transitions.

A cyclic voltammogram (CV) of [Cu(**2**)$_2$][PF_6] was measured in dichlormethane. [Cu(**3**)$_2$][PF_6] rapidly decomposed in dichloromethane and a reliable CV could not be measured. Previous studies revealed the effect of coordinating solvents on the Cu^+/Cu^{2+} potential, due to an additional 5th coordination to copper(II)[102]. In this study the coordinating solvent acetonitrile was replaced by the non-coordinating solvent dichloromethane. [Cu(**2**)$_2$][PF_6] shows a reversible oxidation $E_{1/2}^{ox}$ (copper(I) to copper(II)) of +0.72 V *versus* an external Fc/Fc^+

reference, which is a positive shift compared to the reversible oxidation of [Cu(**1**)$_2$][PF$_6$] with +0.44 V.

6.1.2 Crystal structure of [Cu(2)$_2$][PF$_6$]

Single crystals of [Cu(**2**)$_2$][PF$_6$] were obtained from a slow diffusion of diethyl ether into a dichloromethane solution of the complex. The crystal structure was solved by Dr. Alessandro Prescimone from the University of Basel.

The compound crystallizes in the orthorhombic space group $P2_12_12_1$. In the crystal structure the important aspects of the stabilizing groups in 6 and 6' position of the bpy ligand are nicely illustrated (Fig. 15). Both ligands **2** are coordinating to the central copper(I) atom in a tetrahedral geometry, which is slightly distorted with an angle of 84.1° between the planes of each bpy ligand. The crystal structure of [Cu(**2**)$_2$][PF$_6$] is a good representative of bisdiimine copper(I) complexes bearing blocking groups in 6 and 6' position of their ligands. It is important to remember the geometry represented by the structure of [Cu(**2**)$_2$][PF$_6$], as heteroleptic complexes discussed later in this thesis will most likely possess a comparable orientation of ligands around the copper centre; with slight distortions.

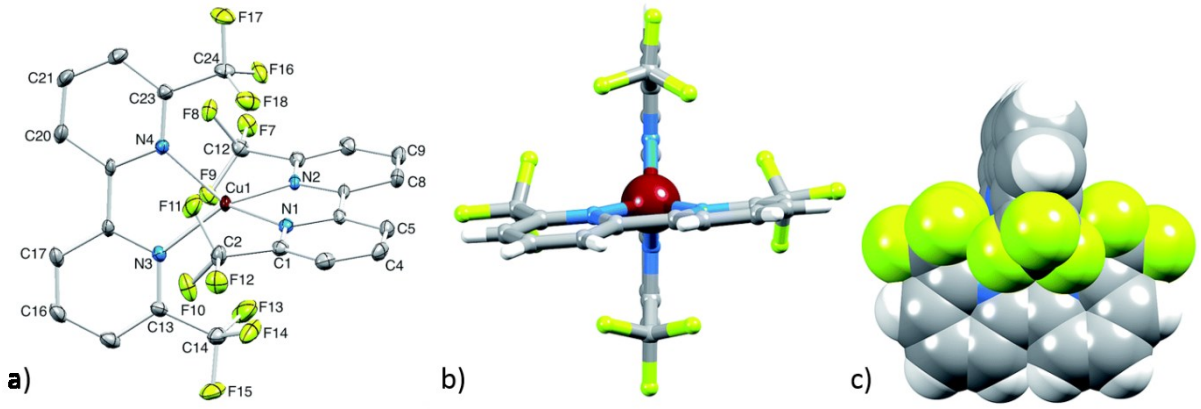

Fig. 15: a) The cation [Cu(**2**)$_2$]$^+$, with H-atoms and the PF$_6^-$ counter ion omitted. Red: copper, green: fluorine, blue: nitrogen, grey: carbon, white: hydrogen. Ellipsoids are plotted at 30% probability level. Bond parameters and angles: Cu1–N1 = 2.036(3), Cu1–N2 = 2.021(3), Cu1–N3 = 2.030(3), Cu1–N4 = 2.027(3) Å; N1– Cu1–N2 = 82.41(11), N1–Cu1–N3 = 124.71(12), N2–Cu1–N3 = 127.02(11), N1–Cu1–N4 = 123.51(11), N2–Cu1–N4 = 122.05(11), N3–Cu1–N4 = 82.85(12)°; C–F bond distances are in the range 1.319(5) to 1.341(4) Å; b) View along one ligand, showing the slight distortion of the tetrahedral geometry, with an angle of 84.1° between the ligands; c) space-filling presentation, highlighting the steric demand of the CF$_3$ groups and the good shielding of the copper(I) centre. Reproduced from ref.[101] with permission of the Royal Society of Chemistry.

6.2 DFT calculations

To examine the electronic structures of the heteroleptic bisdiimine copper(I) complexes containing anchor **4** and ancillary ligands **1**, **2** and **3**, ground state DFT calculations were conducted by Prof. Catherine E. Housecroft from the University of Basel.

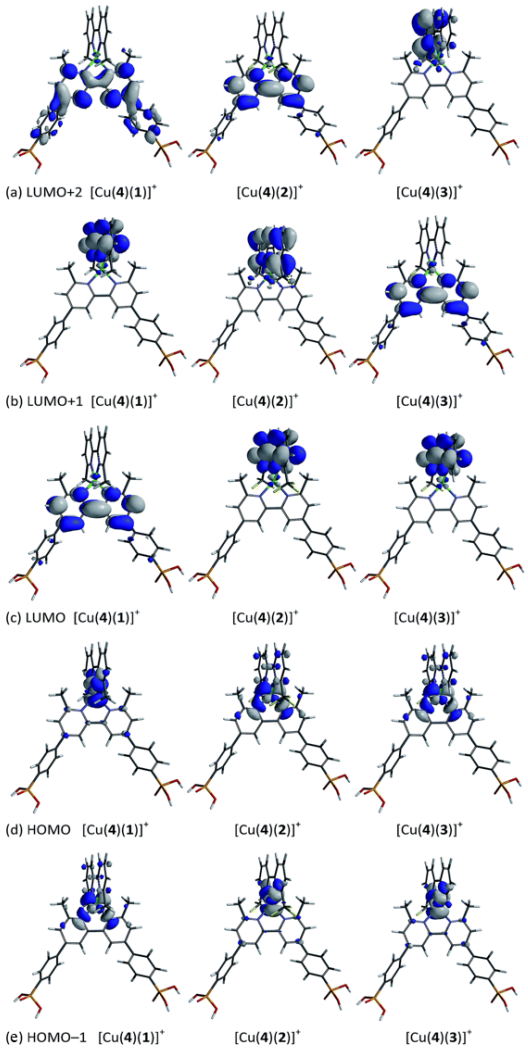

Fig. 16: Molecular orbitals (MOs) of complexes [Cu(**4**)(**1**)]$^+$, [Cu(**4**)(**2**)]$^+$ and [Cu(**4**)(**3**)]$^+$ in their ground state with HOMO and LUMO localizations. Yellow: phosphorus, red: oxygen, grey: carbon, blue: nitrogen, white hydrogen. Anchor **4** is positioned at the bottom, ancillary ligands **1**, **2** and **3** above. a) LUMO+2, b) LUMO+1, c) LUMO, d) HOMO, e) HOMO-1. Reproduced from ref.[101] with permission of the Royal Society of Chemistry.

The structures of the non-isolated, but presumably formed heteroleptic complex [Cu(**4**)(**1**)]$^+$, [Cu(**4**)(**2**)]$^+$ and [Cu(**4**)(**3**)]$^+$ in a DSSC were optimized using DFT calculations. The HOMO of complex [Cu(**4**)(**1**)]$^+$ lies on the side of the ancillary ligand, including the coordination to the copper centre. For all three complexes the HOMO and HOMO−1 are close in energy and taken

together, they show a similar contributions from the copper centre and the ancillary ligands. For [Cu(**4**)(**1**)]$^+$ the desired LUMO location on the anchoring ligand is observed. When all three unoccupied MOs (LUMO, LUMO+1 and LUMO+2) are taken into account a similar distribution over the ancillary ligand and the anchoring ligand is present in the complexes [Cu(**4**)(**1**)]$^+$, [Cu(**4**)(**2**)]$^+$ and [Cu(**4**)(**3**)]$^+$. It should be emphasized that these DFT calculations give information only about the ground sate of each dye as drawn in Fig. 16, but don't give information about the dye bound to the surface and e.g. the protonation state of the dye. It is furthermore important to consider, that energy levels of these complexes shift upon binding of the anchoring ligand to TiO_2 and that the actual HOMO and LUMO energies should be calculated for the excited state of the dye. Nevertheless, are ground state DFT calculations often a good indication of the HOMO and LUMO energies, which implies that the results discussed in the next section rely on a different phenomenon.

6.3 DSSC performance

The general stepwise solar cell assembly described in chapter 4 was used to assemble heteroleptic complexes [Cu(**4**)(**2**)]$^+$ and [Cu(**4**)(**3**)]$^+$ on TiO_2-working electrodes. Therefore, the homoleptic complexes [Cu(**1**)$_2$][PF_6], [Cu(**2**)$_2$][PF_6] and [Cu(**3**)$_2$][PF_6] (Scheme 21) were synthesized and used in the on-surface ligand exchange reaction to obtain the corresponding heteroleptic complexes with anchor **4**. Transparent TiO_2 electrodes with these complexes were obtained in the same manner for use in UV-VIS spectroscopic measurements. The standard II electrolyte (see chapter 4) was used. The solar cells were measured under conditions described in chapter 4 using as light source a LOT Quantum Design LS0811. Solid state UV-VIS and EQE measurements were performed according to chapter 4.

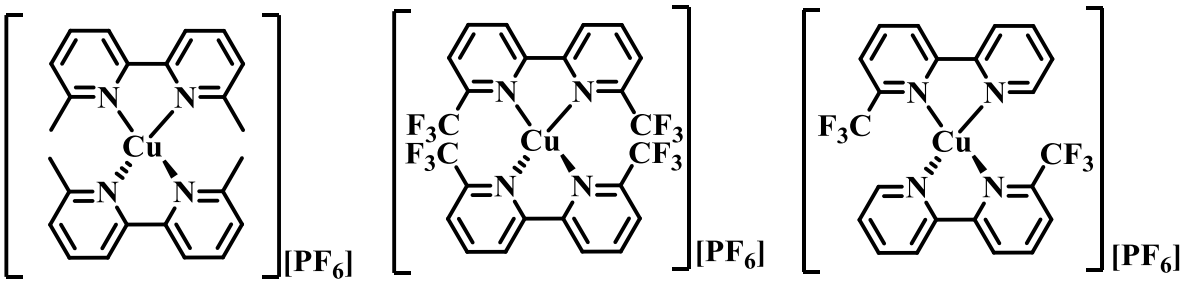

Scheme 21: From left: Homoleptic copper(I)-complexes [Cu(**1**)$_2$][PF_6], [Cu(**2**)$_2$][PF_6] and one enantiomeric form of [Cu(**3**)$_2$][PF_6] investigated in this section.

Transparent electrodes sensitized with $[Cu(\mathbf{4})(\mathbf{2})]^+$ and $[Cu(\mathbf{4})(\mathbf{3})]^+$ showed differences in colour intensity, visible by eye and in the solid state absorption spectra (Fig. 17). Heteroleptic complex $[Cu(\mathbf{4})(\mathbf{3})]^+$ appeared more intense than $[Cu(\mathbf{4})(\mathbf{2})]^+$, which was confirmed by a stronger absorption in the solid state absorption spectrum. Both complexes show an MLCT transition with a maximum at around 455 nm. At wavelengths lower than 380 nm, TiO_2 absorbs photons and makes analysis of this spectral area impossible.

a)

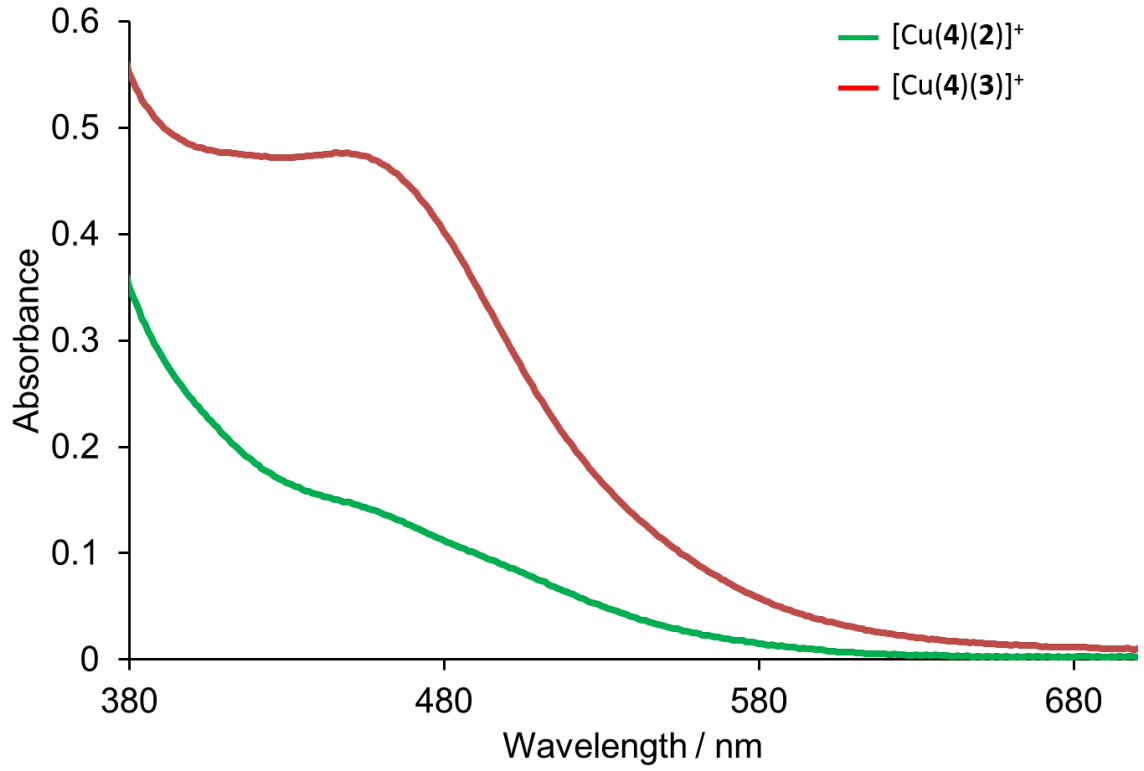

b)

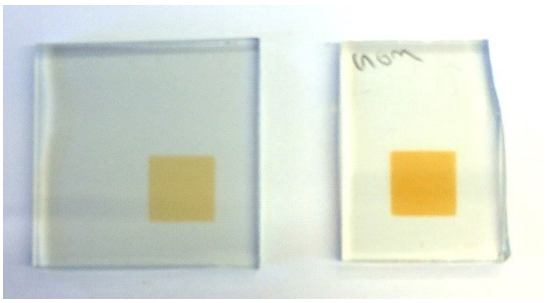

Fig. 17: a) Solid state absorption spectra of complexes $[Cu(\mathbf{4})(\mathbf{2})]^+$ and $[Cu(\mathbf{4})(\mathbf{3})]^+$. b) Difference in colour intensity of complexes $[Cu(\mathbf{4})(\mathbf{2})]^+$ (left) and $[Cu(\mathbf{4})(\mathbf{3})]^+$ (right) on a transparent TiO_2 electrode.

TiO_2 electrodes were sensitized with complexes $[Cu(\mathbf{4})(\mathbf{2})]^+$ and $[Cu(\mathbf{4})(\mathbf{3})]^+$ and their performances in DSSCs compared to previous reported results for $[Cu(\mathbf{4})(\mathbf{1})]^+$[83]. Absolute values for solar cell efficiency measurements tend to vary a lot between different instruments, operators and research groups. The measurements presented in this thesis were all done on the same instrument (LOT Quantum Design LS0811) using always the same measurement conditions (see chapter 4). To keep current/voltage measurements consistent, duplicate cells were built and each solar cell was masked to measure an exact surface area. Masking the solar cells reduces the active surface area exposed to the light of the sun simulator from 0.36 cm^2 to ~ 0.6 cm^2. The smaller surface area is taken into account when the efficiency is calculated. Cell masking is important, to have an accurate exposed area and not an estimated surface area provided by the supplier (Solaronix SA). Another important aspect is the high amount of scattered light in unmasked cells. Glass plates of working and counter electrode and material underneath the solar cell during the measurements scatter the light from the sun simulator and increase the number of photons, that get absorbed by the dye. This leads to higher efficiencies and unprecise results. Masking the solar cell reduces the scattered light and makes these measurements trustworthy[103-104]. Additionally, **N719** solar cells were assembled under the same conditions and efficiencies of Cu-based DSSCs were stated relative to **N719** (Table 1). Fig. 18 shows *J*/*V* curves measured on the day of sealing the cells, corresponding to data in Table 1.

Dye	J_{SC} / mA cm^{-2}	V_{OC} / mV	*ff* / %	η / %	Relative η / %
On the day of sealing the cells					
[Cu(**4**)(**2**)]$^+$	4.81	537	73.5	1.90	31.8
[Cu(**4**)(**2**)]$^+$	4.67	531	71.5	1.78	30.0
[Cu(**4**)(**3**)]$^+$	5.35	530	73.4	2.08	34.8
[Cu(**4**)(**3**)]$^+$	5.40	532	70.3	2.02	33.8
N719	13.65	652	67.0	5.97	100
[Cu(**4**)(**1**)]$^+$	3.79	522	73.8	1.46	24.7[83]
[Cu(**4**)(**1**)]$^+$	3.46	527	74.3	1.35	22.8[83]
N719[83]	12.51	672	70.2	5.91	100
1 day after sealing the cells					
[Cu(**4**)(**2**)]$^+$	4.73	557	73.8	1.95	33.2
[Cu(**4**)(**2**)]$^+$	4.63	550	70.6	1.80	30.6
[Cu(**4**)(**3**)]$^+$	5.45	540	73.0	2.15	36.6
[Cu(**4**)(**3**)]$^+$	5.56	546	70.2	2.13	36.2
N719	13.19	681	65.5	5.88	100
3 days after sealing the cells					
[Cu(**4**)(**2**)]$^+$	4.85	564	73.4	2.00	33.6
[Cu(**4**)(**2**)]$^+$	4.68	559	70.7	1.85	31.1
[Cu(**4**)(**3**)]$^+$	5.17	541	73.2	2.05	34.5
[Cu(**4**)(**3**)]$^+$	5.53	562	70.2	2.18	36.6
N719	13.16	689	65.6	5.95	100
8 days after sealing the cells					
[Cu(**4**)(**2**)]$^+$	4.77	565	73.2	1.97	32.5
[Cu(**4**)(**2**)]$^+$	4.70	556	67.7	1.77	29.2
[Cu(**4**)(**3**)]$^+$	5.48	563	70.8	2.18	35.9
[Cu(**4**)(**3**)]$^+$	5.81	567	68.6	2.26	37.2
N719	12.82	696	68.1	6.07	100

Table 1: Solar cell measurements with values obtained from a LOT Quantum Design LS0811 light source on days 0,1,3 and 8. A **N719** reference cell was built for this study. Values for [Cu(**4**)(**1**)]$^+$ and the corresponding **N719** cell, were taken from the literature[83].

Consistent efficiencies were obtained for **N719** measured on the day of sealing in this thesis and in the previously reported work[83]. All copper(I)-complexes showed good fill factors with values over 70% and open circuit voltages of ~ 530 mV (Fig. 18). The main differences are observed in values J_{SC}. [Cu(**4**)(**1**)]$^+$ showed the lowest current densities with 3.79 and 3.46 mA cm^{-2} for duplicate cells. Of the new heteroleptic complexes [Cu(**4**)(**3**)]$^+$, bearing one CF_3 group, showed the highest J_{SC} with 5.40 mA cm^{-2} for one of the duplicate cells. [Cu(**4**)(**2**)]$^+$ bearing two CF_3 groups showed good J_{SC} values of 4.67 and 4.81 mA cm^{-2}. A clear trend in J_{SC} increase

for the ancillary ligands going from **1** to **3** is identified. To examine long term stability, each cell with dyes $[Cu(\mathbf{4})(\mathbf{2})]^+$ and $[Cu(\mathbf{4})(\mathbf{3})]^+$ was measured on day 1,3 and 8 after sealing the cells. Efficiencies for $[Cu(\mathbf{4})(\mathbf{2})]^+$ remained constant over this period with a maximum efficiency of 2.00% (33.6% relative to **N719**) achieved on day 3. 8 days were necessary for $[Cu(\mathbf{4})(\mathbf{3})]^+$ to reach its maximum efficiency of 2.26% (37.2% relative to **N719**) outperforming $[Cu(\mathbf{4})(\mathbf{1})]^+$ and $[Cu(\mathbf{4})(\mathbf{2})]^+$ by far. This increase in efficiency is caused by a rise in V_{OC} from 532 to 567 mV and a rise in J_{SC} from 5.40 to 5.81 mA cm^{-2}.

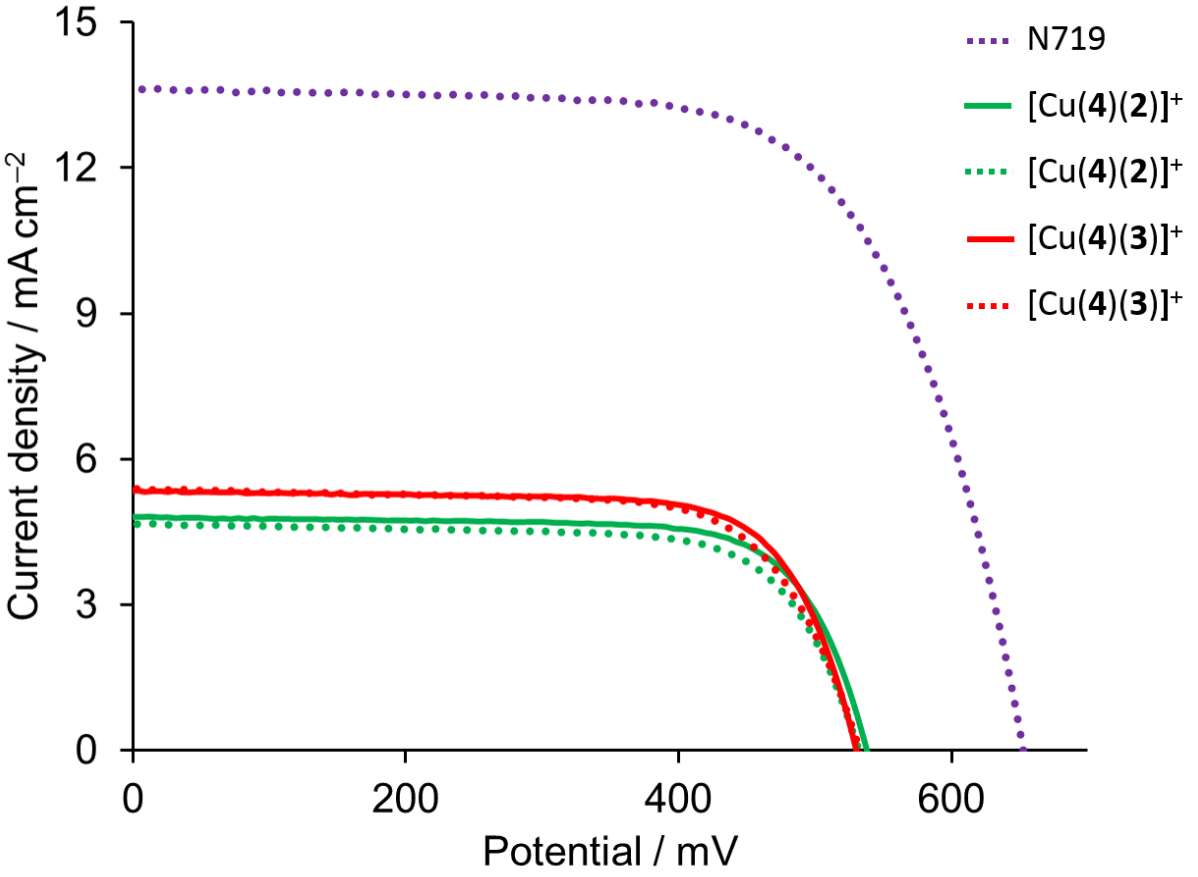

Fig. 18: *J*/*V* curves recorded for the **N719** reference and duplicate cells of complexes $[Cu(\mathbf{4})(\mathbf{2})]^+$ and $[Cu(\mathbf{4})(\mathbf{3})]^+$ on day of sealing the cells.

The processes in a solar cell leading to these changes are not understood, but some flexibility in anchoring ligand binding to TiO_2 together with the lability of the heteroleptic complexes might lead to this efficiency increase over time. In most cases a consistent performance is

observed after 7 days and bisdiimine copper(I) based solar cells can remain stable over several months[105].

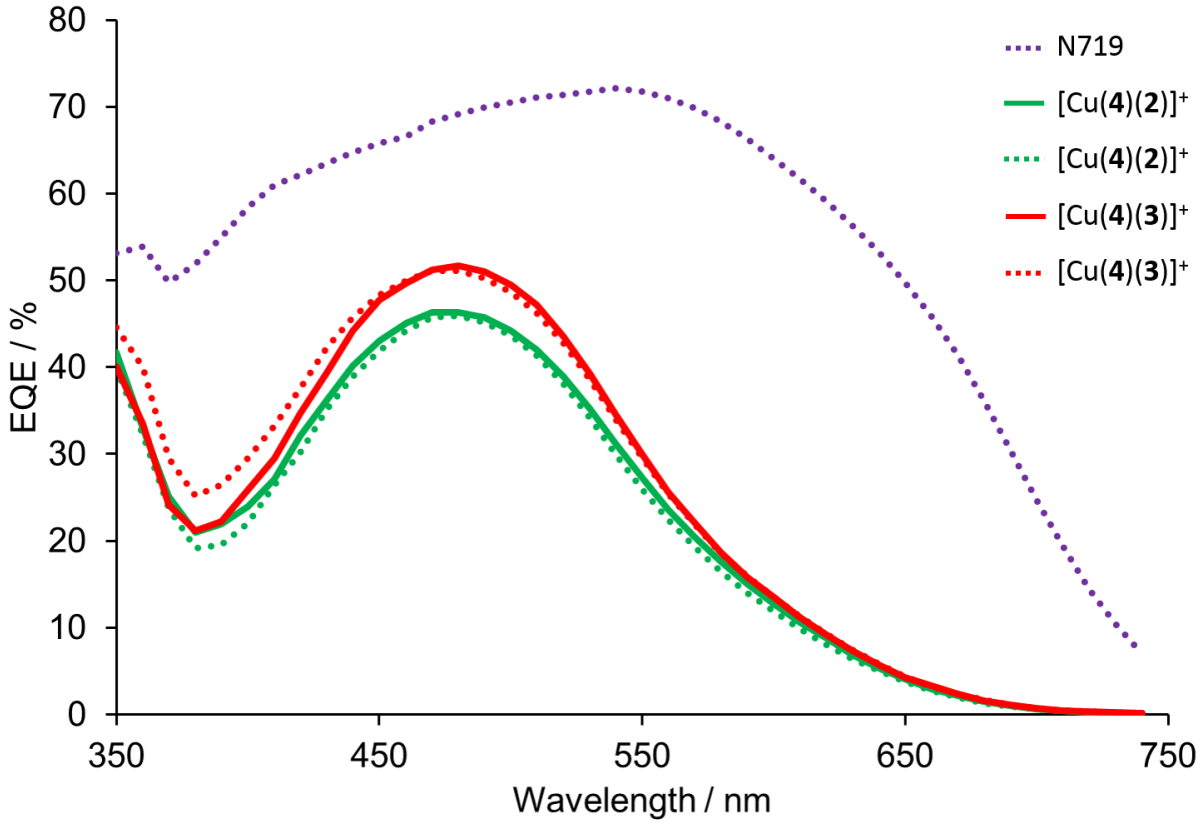

Fig. 19: EQE spectra for the **N719** reference and duplicate cells of complexes [Cu(**4**)(**2**)]$^+$ and [Cu(**4**)(**3**)]$^+$ on the day of sealing the cells.

The EQE spectra (Fig. 19) show a similar trend to the current density/voltage measurements. A broad curve was obtained for the **N719** reference with EQE values above 50% between 350 and 650 nm. [Cu(**4**)(**3**)]$^+$ outperforms [Cu(**4**)(**2**)]$^+$ in this measurement, by showing the highest EQE value of 51% among these copper(I)-complexes. Copper(I) complexes show good light harvesting abilities in the blue/green part of the visible spectrum, but lack absorption in the red part. EQE values for duplicate cells of [Cu(**4**)(**2**)]$^+$ and [Cu(**4**)(**3**)]$^+$ are summarized in Table 2.

	Cell 1		Cell2	
Anchored dye	λ / nm	EQE_{max} / %	λ / nm	EQE_{max} / %
$[Cu(\mathbf{4})(\mathbf{2})]^+$	480	46.3	480	46.0
$[Cu(\mathbf{4})(\mathbf{3})]^+$	480	51.7	480	51.1

Table 2: EQE values of complexes $[Cu(\mathbf{4})(\mathbf{2})]^+$ and $[Cu(\mathbf{4})(\mathbf{3})]^+$ at λ = 480 nm.

6.3.1 Dye bath solvent for homoleptic bisdiimine copper(I) complexes

To form the heteroleptic complex on a TiO_2 surface a ligand exchange reaction (see chapter 4) must take place. This is achieved by dipping a TiO_2 electrode, modified by an anchoring ligand, into a homoleptic bisdiimine copper(I) dye solution. Previous studies have shown, that the solvent of the dye bath can influence the ligand exchange reaction[106]. Less harmful solvents are beneficial in this respect and therefore the solvent for the dye solution was changed from dichloromethane to acetone in this chapter. To verify, that this change in dye bath solvent doesn't influence DSSC performances in a negative way, assembly of heteroleptic complexes $[Cu(\mathbf{4})(\mathbf{1})]^+$, $[Cu(\mathbf{4})(\mathbf{2})]^+$ and $[Cu(\mathbf{4})(\mathbf{3})]^+$ on a TiO_2 surface were repeated with acetone as solvent in homoleptic dye baths. Table 3 shows the results and the same trend with efficiencies increasing in the order $[Cu(\mathbf{4})(\mathbf{1})]^+$ to $[Cu(\mathbf{4})(\mathbf{2})]^+$ to $[Cu(\mathbf{4})(\mathbf{3})]^+$. The acetone dye bath of $[Cu(\mathbf{2})_2][PF_6]$ enhances the efficiency of the corresponding heteroleptic $[Cu(\mathbf{4})(\mathbf{2})]^+$ complex, which is now in the same range as $[Cu(\mathbf{4})(\mathbf{3})]^+$.

Dye	J_{SC} / mA cm^{-2}	V_{OC} / mV	*ff* / %	η / %	Relative η / %
1 day after sealing the cells					
[Cu(**4**)(**2**)]$^+$	4.58	626	68	1.95	33.6
[Cu(**4**)(**2**)]$^+$	4.97	621	67	2.08	35.9
[Cu(**4**)(**3**)]$^+$	4.91	613	67	2.03	35.0
[Cu(**4**)(**3**)]$^+$	4.34	599	71	1.84	31.7
[Cu(**4**)(**1**)]$^+$	3.21	548	69	1.22	21.0
[Cu(**4**)(**1**)]$^+$	3.00	551	71	1.17	20.0
N719	13.55	650	66	5.80	100
3 days after sealing the cells					
[Cu(**4**)(**2**)]$^+$	4.59	620	70	1.99	33.6
[Cu(**4**)(**2**)]$^+$	4.76	614	67	1.97	33.2
[Cu(**4**)(**3**)]$^+$	4.81	613	68	2.00	33.7
[Cu(**4**)(**3**)]$^+$	4.42	609	73	1.96	33.1
[Cu(**4**)(**1**)]$^+$	3.08	540	70	1.17	19.7
[Cu(**4**)(**1**)]$^+$	2.90	556	71	1.15	19.4
N719	13.14	684	66	5.93	100
7 days after sealing the cells					
[Cu(**4**)(**2**)]$^+$	4.49	610	71	1.96	33.2
[Cu(**4**)(**2**)]$^+$	4.81	603	69	2.00	33.9
[Cu(**4**)(**3**)]$^+$	4.74	614	68	1.98	33.6
[Cu(**4**)(**3**)]$^+$	4.48	611	73	2.00	33.9
[Cu(**4**)(**1**)]$^+$	3.04	537	70	1.15	19.5
[Cu(**4**)(**1**)]$^+$	2.82	564	70	1.12	19.0
N719	13.05	691	66	5.90	100

Table 3: Solar cell measurements with values obtained at days 1,3 and 7. The homoleptic complex dye bath solvent was changed from dichloromethane to acetone in this study.

Nevertheless solutions of [Cu(**2**)$_2$][PF$_6$] lose their orange colour within one day in dichloromethane and acetone. [Cu(**3**)$_2$][PF$_6$] appears to be more stable, and there was no bleaching of dye solutions over time. Therefore **3** was selected as the ancillary ligand in the following chapters. *J*/*V* and EQE curves reflect results from the previous study in dichloromethane and will not be displayed here.

The surprisingly good results in solar conversion efficiencies for [Cu(**4**)(**2**)]$^+$ and [Cu(**4**)(**3**)]$^+$, bearing electron withdrawing groups, compared to the standard heteroleptic [Cu(**4**)(**1**)]$^+$, demonstrates the difficulties of predicting the performances of bisdiimine copper(I) complexes as sensitizers in DSSCs. It is counterintuitive to use electron withdrawing groups on the

ancillary ligand of a heteroleptic complex, as electrons should be "pushed" towards the anchoring ligand. A CF_3 group has very different electronic properties, compared to a methyl group, but the steric demand of both groups is comparable[107]. The combination of the anchoring ligand **4**, bearing two methyl groups in the 6 and 6' positions, with ancillary ligand **3**, bearing one CF_3 group in 6 position, is enough to stabilize the heteroleptic copper(I) complex. Two CF_3 groups on the ancillary ligand in $[Cu(\mathbf{4})(\mathbf{2})]^+$ fulfil this requirement as well, but previous studies have shown[80], that too bulky substituents in the 6 and 6' positions can destabilize the complex. The reason for the better performances of $[Cu(\mathbf{4})(\mathbf{2})]^+$ and $[Cu(\mathbf{4})(\mathbf{3})]^+$ compared to $[Cu(\mathbf{4})(\mathbf{1})]^+$ remains unresolved.

6.4 Conclusion

DFT calculations gave no indication why heteroleptic complexes $[Cu(\mathbf{4})(\mathbf{2})]^+$ and $[Cu(\mathbf{4})(\mathbf{3})]^+$ outperform $[Cu(\mathbf{4})(\mathbf{1})]^+$ in a DSSC. Especially $[Cu(\mathbf{4})(\mathbf{3})]^+$ shows outstanding results compared to other previous published "push-pull" copper(I) systems. With an EQE of 51% (on day of sealing) the heteroleptic complex $[Cu(\mathbf{4})(\mathbf{3})]^+$ ranks among the best bisdiimine copper(I) dyes prepared using the stepwise approach. The puzzling results concerning the effect of ancillary ligands on general cell performance lead to the conclusion to concentrate further research efforts on a different part of the heteroleptic bisdiimine copper(I) dyes, namely the anchoring ligand.

This work was published 2015 in *RSC Advances*[101] and data in section 6.3.1 was published 2016 in *Dalton Transactions*[105].

7 ANCHORING LIGANDS WITH THIOPHENEDIYL SPACERS

In chapter 6 the focus of improvement for heteroleptic bisdiimine copper(I) complexes lay on the ancillary ligand. The monosubstituted ancillary ligand **3**, bearing one CF_3 group in the 6 position of 2,2'-bipyridine was identified as a good ancillary ligand and will be used in this and the next chapterss of this thesis. Previously, research into bisdiimine copper(I) complexes mainly focused on modification of the ancillary ligand and little effort had been made in anchoring ligand modification. Two new anchoring ligands will be presented, with promising performances in DSSCs.

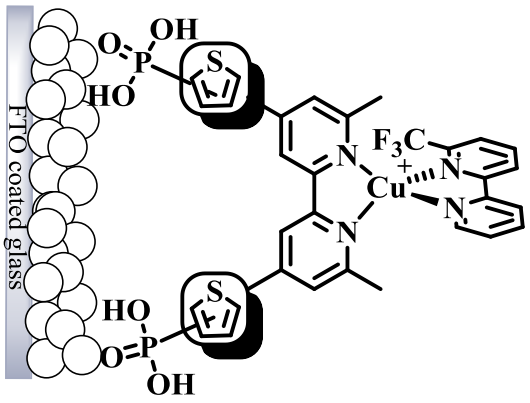

Scheme 22: Bisdiimine copper(I) complexes with anchoring ligands bearing thiophenediyl spacers and the mono CF_3 substituted ancillary ligand **3**.

Scheme 22 shows the updated design of heteroleptic bisdiimine copper(I) complexes discussed in this chapter. On the right side the previously introduced ancillary ligand **3** is displayed. The anchoring ligand on the left side consists of the 6,6'-dimethyl-2,2'-bipyridine core, a phosphonic acid anchoring group and an aromatic spacer. In contrast to anchor **4**, the phenylene spacer is replaced by a thiophenediyl group and the anchoring group is attached to it in either 4 or 5 position.

Thiophenediyl groups are well known as building blocks in the design of light harvesting materials. Thiophenediyl groups have been incorporated into the inorganic ruthenium(II) complexes **CYC-B11** (see introduction Scheme 6), yielding the record efficiency. In organic dyes[108-109] similar groups are often present as spacers (see introduction Scheme 4).

Poly(3,4-ethylenedioxythiophene) polystyrene sulfonate (PEDOT:PSS) is a conductive organic polymer consisting of poly(3,4-ethylenedioxythiophene) and sodium polystyrene sulfonate[110].

Good performing organic dyes and the highly conductive polymer PEDOT:PSS highlight the beneficial effect and outstanding potential of thiophenediyl groups in electron conducting materials. With this inspiration two new anchoring ligands, bearing thiophenediyl spacers were synthesized and their performance in bisdiimine copper(I) dyes was investigated.

7.1 Synthesis and Characterization

Anchoring ligand synthesis and DSSC fabrication and characterization were carried out by myself. EIS measurements were carried out by Dr. Markus Willgert; the main results of the EIS will be briefly presented but are not discussed in detail. Further information about the EIS data can be found in the corresponding publication[105].

7.1.1 Anchoring ligand synthesis

The synthesis of anchoring ligands **5** and **6** (Scheme 23) followed the same synthetic route as for ligand **4** (Scheme 16). As starting material, the commercially available (supplier: Sigma-Aldrich) aromatic aldehydes 5-bromo-2-thiophenecarboxaldehyde and 4-bromo-2-thiophenecarboxaldehyde were used and reacted in the same manner as in Scheme 16 to yield the corresponding 6,6'-dimethyl-2,2'-bipyridines substituted in positions 4 and 4' with 2-thiophenediyl groups in 8.1% and 2.8% yield over two steps, respectively. The bromo substituent on the thiophenediyl residue was converted in a Pd-catalyzed reaction to the phosphonic esters (**5a** and **6a**) in 46.2% and 53.3% yields, respectively. **5a** and **6a** were deprotected with Me_3SiBr to yield the anchoring ligands **5** and **6**, in 66.7% and 80.0% yield respectively.

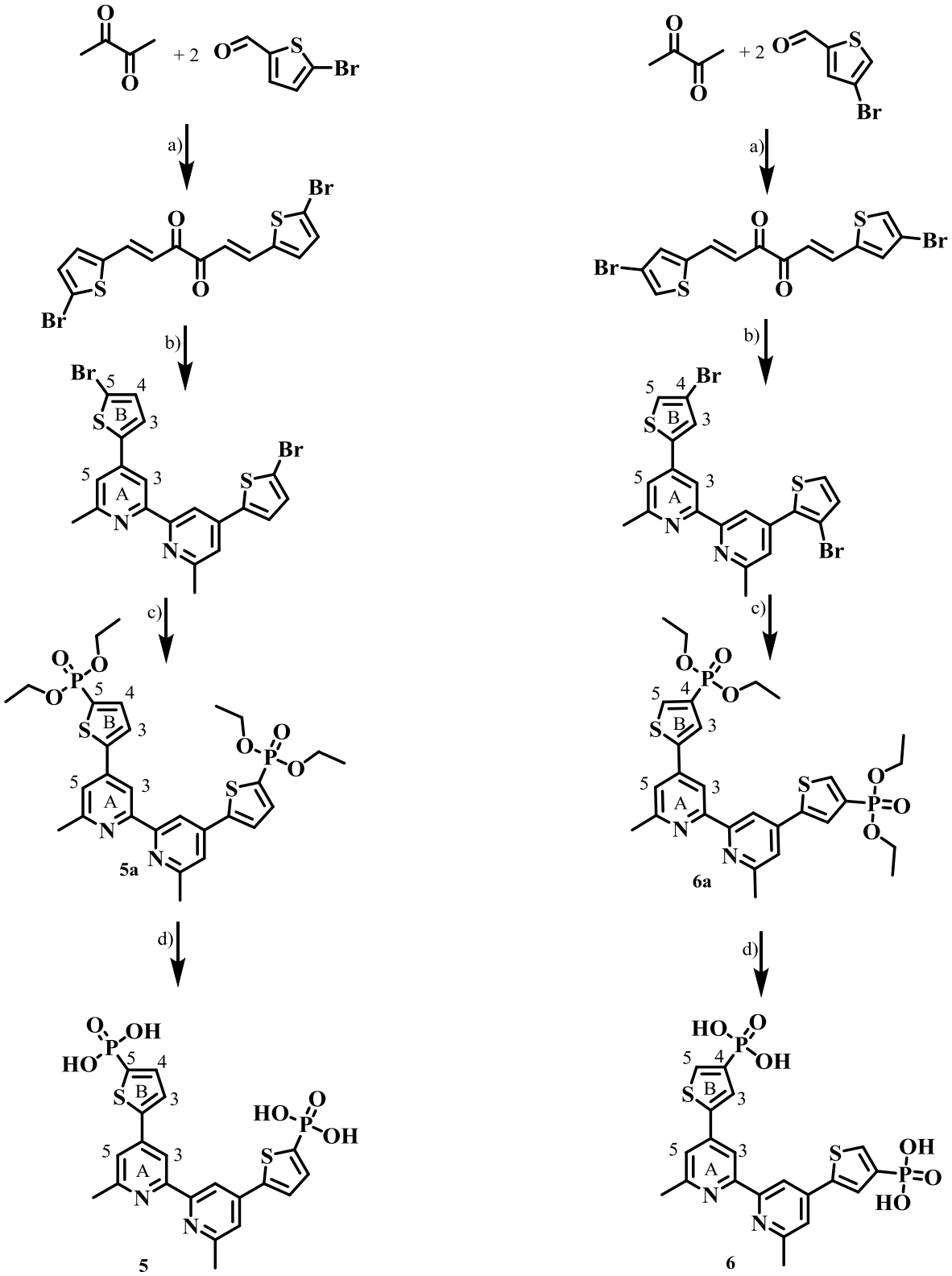

Scheme 23: The synthesis of the phosphonic esters **5a** and **6a** and the corresponding anchoring ligands **5** and **6**, with labels for NMR discussion. a) MeOH, piperidine, reflux, 16h, b) NH_4OAc, EtOH, reflux, 4h, c) $HPO(OEt)_2$, $[Pd(PPh_3)_4]$, Cs_2CO_3 in dry THF (110°C, MW radiation, 90min), d) TMS-Br, CH_2Cl_2, RT, aqueous workup.

Intermediate compounds were characterized by ^{1}H, $^{13}C\{^{1}H\}$ NMR spectroscopies and ESI-MS. Bpy intermediates 4,4'-bis(5-bromothiophen-2-yl)-6,6'-dimethyl-2,2'-bipyridine and 4,4'-bis(4-bromothiophen-2-yl)-6,6'-dimethyl-2,2'-bipyridine showed base peaks in the ESI-MS at *m/z* 506.7 and 506.9, respectively, corresponding to the $[M+H]^+$ molecule ion. ^{1}H, $^{13}C\{^{1}H\}$ NMR spectra of the intermediates were assigned using 2D COSY, NOESY, HMQC and HMBC spectra. NOE cross peaks between H^{Me} and H^{A5} gave a clear distinction of H^{A5} and H^{A3}. H^{A5} and H^{A3} both show a NOE cross peak to H^{B3}. The remaining aromatic signal corresponds to H^{B4} or H^{B5}, respectively. ^{1}H-NMR spectra of the esters **5a** and **6a** and anchoring ligands **5** and **6** were assigned in the same manner and these compounds were further characterized by $^{13}C\{^{1}H\}$ and $^{31}P\{^{1}H\}$ NMR spectroscopies, ESI-MS, high resolution ESI-MS (for **5a**) or elemental analysis. Base peaks in the ESI-MS for **5a** and **6a** appeared at *m/z* 621.1 and those of **5** and **6** appeared at *m/z* 509.1 corresponding to the $[M+H]^+$ species. The formation of **5a** was validated by high resolution ESI-MS with *m/z* 621.1407 corresponding to the $[M+H]^+$ ion (calc. 621.1412). Elemental analysis of compounds **6a**, **5** and **6** showed good agreement with calculated values. For **5** and **6** one and 3.5 molecules of water had to be added to the theoretical values to match the recorded values. Water, used during the workup of the final synthesis step could not be removed completely from the powder, as might be expected by the presence of two hydrophilic phosphonic acid groups. The ^{1}H NMR spectra of **5a** showed phosphorus-proton couplings for protons H^{B3} ($^{3}J_{PH}$ = 3.6Hz) and H^{B4} ($^{2}J_{PH}$ = 8.2Hz). In **6a** a similar coupling was observed for H^{B5} ($^{2}J_{PH}$ = 8.2Hz); H^{B3} showed a broadened signal.

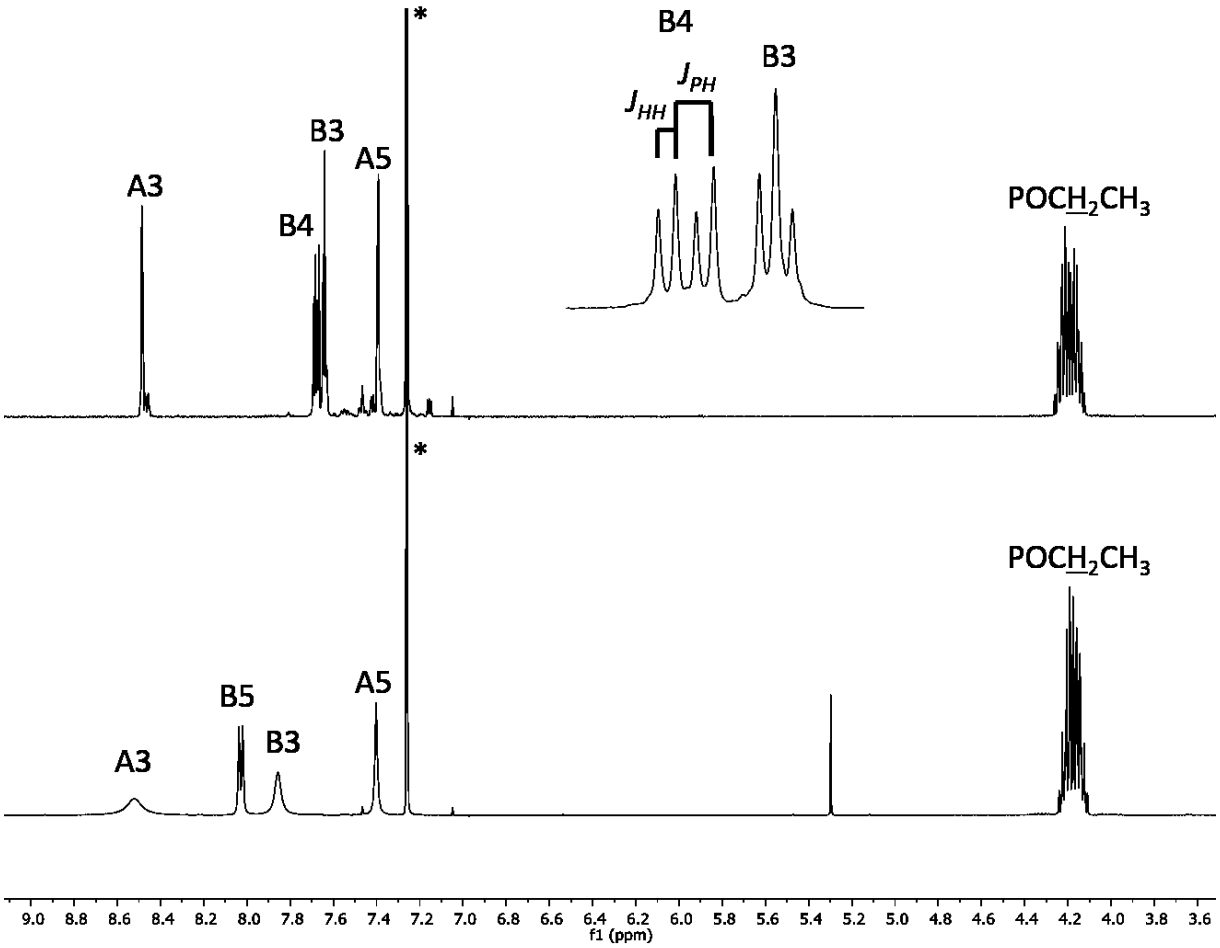

Fig. 20: 400 MHz ^{1}H NMR spectra of **5a** (top) and **6a** (bottom), with J_{PH} and J_{HH} couplings highlighted for H^{B4} in **5a**. $CDCl_3$ was used as solvent (*) and chemical shifts were referenced to δ (TMS) = 0 ppm.

The $^{13}C\{^{1}H\}$ NMR spectra of **5a** and **6a** showed characteristic doublets for the carbon atoms C^{B5} and C^{B4} substituted with a phosphorus atom, with $^{1}J_{PC}$ coupling constants of 201Hz and 197Hz, respectively. Phosphonic ester ethyl and methyl carbon atoms in **6a** showed $^{2}J_{PC}$ and $^{3}J_{PC}$ coupling constants of 5.4 and 6.5 Hz, respectively. The $^{31}P\{^{1}H\}$ spectra of **5a** and **6a**, showed singlets at +10.8 ppm and +12.0 ppm, respectively. These signals shift to +4.0 ppm and +6.1 ppm in the corresponding phosphonic acid compounds **5** and **6**, respectively. ^{1}H-NMR spectra of **5** and **6** were measured in DMSO-*d6* due to low solubility of the compounds in other solvents. In **5** a doublet of doublets was observed for the proton in the the 4 position of the thiophenediyl ring (H^{B4}) next to the phosphorus atom. One doublet with a coupling constant of J = 3.7 Hz corresponds to a $^{3}J_{HH}$ coupling with proton H^{B3}. The second doublet is a $^{3}J_{PH}$ coupling with a coupling constant of 8.0 Hz. Broader peaks were obtained in **6** and coupling constants were not resolved (Fig. 21). $^{13}C\{^{1}H\}$-NMR spectra were assigned using 2D DEPT,

COSY, NOESY, HMQC and HMBC spectra. The NMR samples were less concentrated and fully assigned using HMQC and HMBC spectra. $^{2}J_{PC}$ and $^{3}J_{PC}$ coupling constants could not be obtained for **5** and **6**.

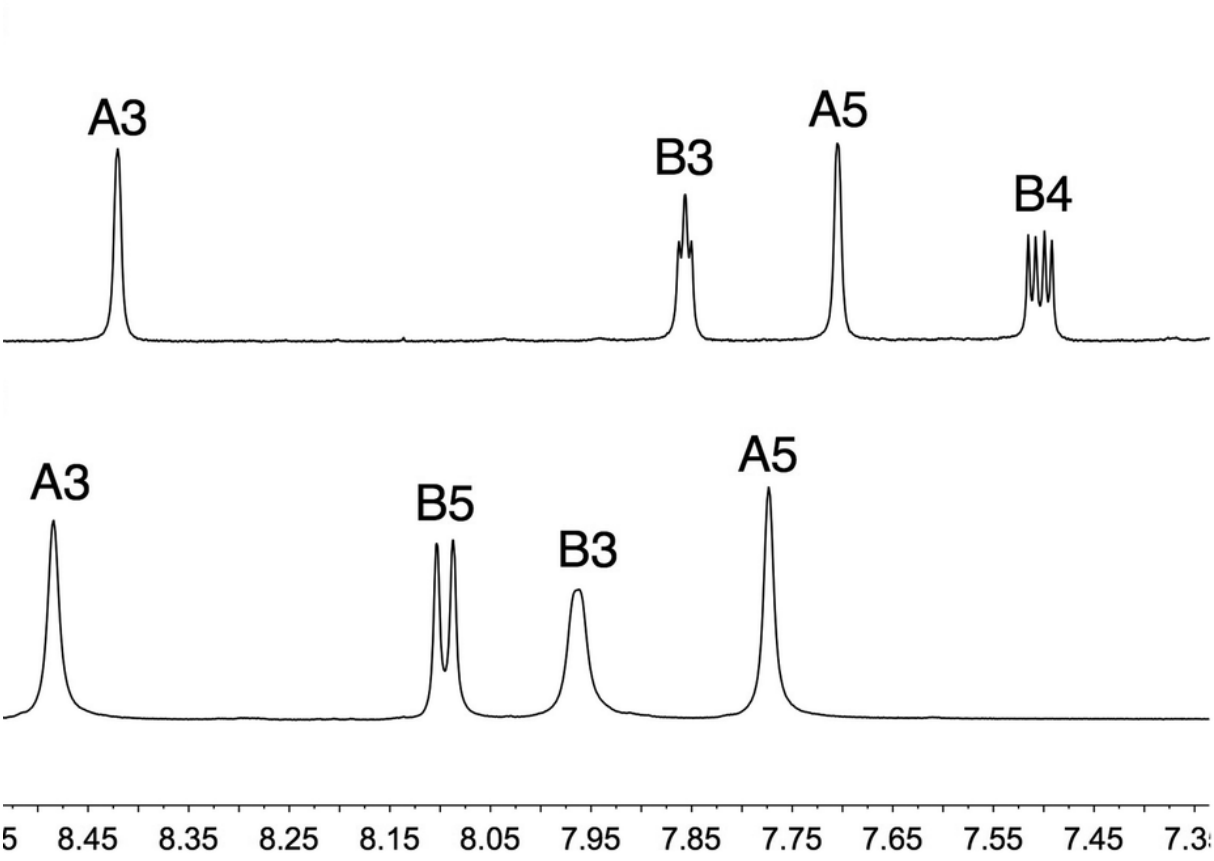

Fig. 21: 400 and 500 MHz ^{1}H-NMR spectra of the aromatic region of ligands **5** (top) and **6** (bottom) in DMSO-d_6.

5 has a phosphonic acid anchoring group attached in the 5 position of each thiophenediyl (C^{B5}). This position is the most reactive position of thiophenes towards bromination and lithiation[111], thus polythiophenes are mostly connected in 5,2 positions. Substitution of thiophenes, including spacers and the anchoring group are predominantly in the 2 or 5 positions[112]. The Kröhnke-type pyridine synthesis demonstrates its beneficial methodology, as the bromine functionality in the 4 position of the thiophenediyl could be carried through the reaction sequence from the 4-bromo-2-thiophenecarboxaldehyde starting material to the Pd-coupling step. The unusual anchor position makes ligand **6** an interesting candidate in comparison to ligand **5**.

7.1.2 Crystallography

Single crystals of the phosphonic ester **5a** were obtained from slow evaporation of an acetone/cyclohexane solution and the structure of the compound was determined by Dr. Alessandro Prescimone. The ligand crystallized in the monoclinic space group $P2_1/c$. Fig. 22 shows the structure in its favoured *trans* conformation, where N lone pairs have least repulsion. To coordinate to copper(I) a rotation around the C-C bond between the pyridine rings has to occur.

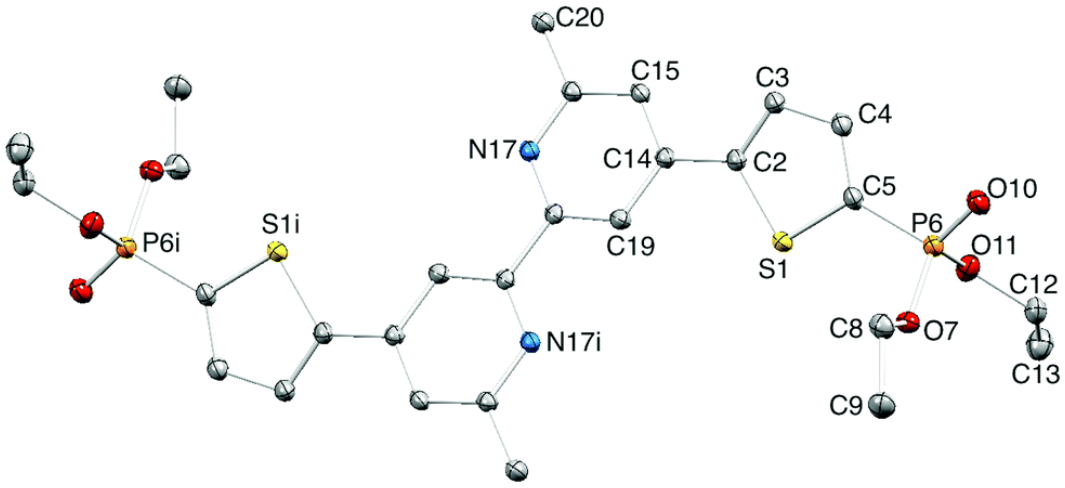

Fig. 22: Single crystal structure of phosphonic ester **5a**. H atoms are omitted and ellipsoids plotted at 40% probability level. Symmetry code i = 1–*x*, –*y*, 1–*z*. Selected bond parameters: S1–C2 = 1.731(2), S1–C5 = 1.718(2), C5–P6 = 1.780(2), P6–O7 = 1.5782(17), P6–O10 = 1.4644(18), P6–O11 = 1.5726(18) Å; C2–S1–C5 = 91.86(11), C5–P6–O7 = 107.07(10), C5–P6–O10 = 112.57(11), O7–P6–O10 = 115.04(10), C5–P6–O11 = 101.27(10), O7–P6–O11 = 101.80(9), O10–P6–O11 = 117.54(10)°. reproduced from ref.[101] with permission of The Royal Society of Chemistry.

The structure is centrosymmetric and the inversion centre in the middle of the C-C bond connecting both pyridine rings. The bpy ligand core has to be planar by symmetry and the thiophenediyl rings are slightly twisted (22.2°) with respect to the pyridine rings.

7.2 DSSC performance

The same routine as in chapter 6 was applied here. Anchors **4**, **5** and **6** were combined with the homoleptic copper(I)-complexes ($[Cu(\mathbf{L})_2][PF_6]$, **L** = **1**, **3**, **7**, Scheme 24) to form heteroleptic bisdiimine copper(I) complexes on a TiO_2 surface. $[Cu(\mathbf{7})_2][PF_6]$ was prepared according to a previous publication[42]. Acetone was used as the dye bath solvent, according to results presented in chapter 6. Transparent electrodes were prepared for solid state absorption

measurements. Duplicate solar cells were masked and their performance documented with current density/voltage and EQE measurements. The results were compared and fixed relative to relation to an **N719** cell for consistency.

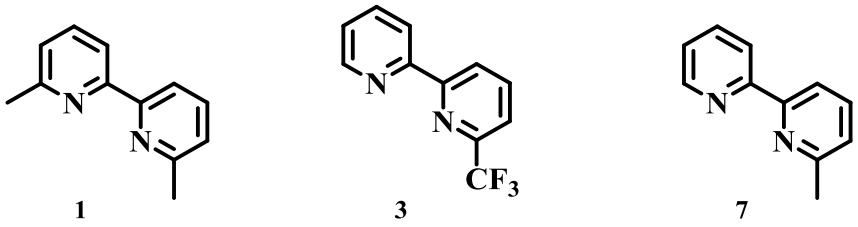

1 **3** **7**

Scheme 24: Ancillary ligands investigated in this series.

7.2.1 DSSCs of anchors 4,5 and 6 combined with ancillary ligand 3

The general stepwise solar cell assembly described in chapter 4 was used to assemble heteroleptic complexes of $[Cu(\mathbf{4})(\mathbf{3})]^+$, $[Cu(\mathbf{5})(\mathbf{3})]^+$ and $[Cu(\mathbf{6})(\mathbf{3})]^+$ on TiO_2-working electrodes. Transparent TiO_2 electrodes with all complexes were obtained in the same manner for solid-state absorption spectroscopy. Standard II electrolyte (see chapter 4) was used as a charge carrier between working- and counter electrode. The solar cells were measured according to conditions described in chapter 4.

Transparent TiO_2-electrodes showed similar colour, confirmed by solid state absorption spectra (Fig. 23). All complexes show an MLCT transition with a maximum at around 460 nm. The maximum for $[Cu(\mathbf{5})(\mathbf{3})]^+$ and $[Cu(\mathbf{6})(\mathbf{3})]^+$ is slightly redshifted to 470 nm, which is also observed in the EQE spectra (Fig. 25).

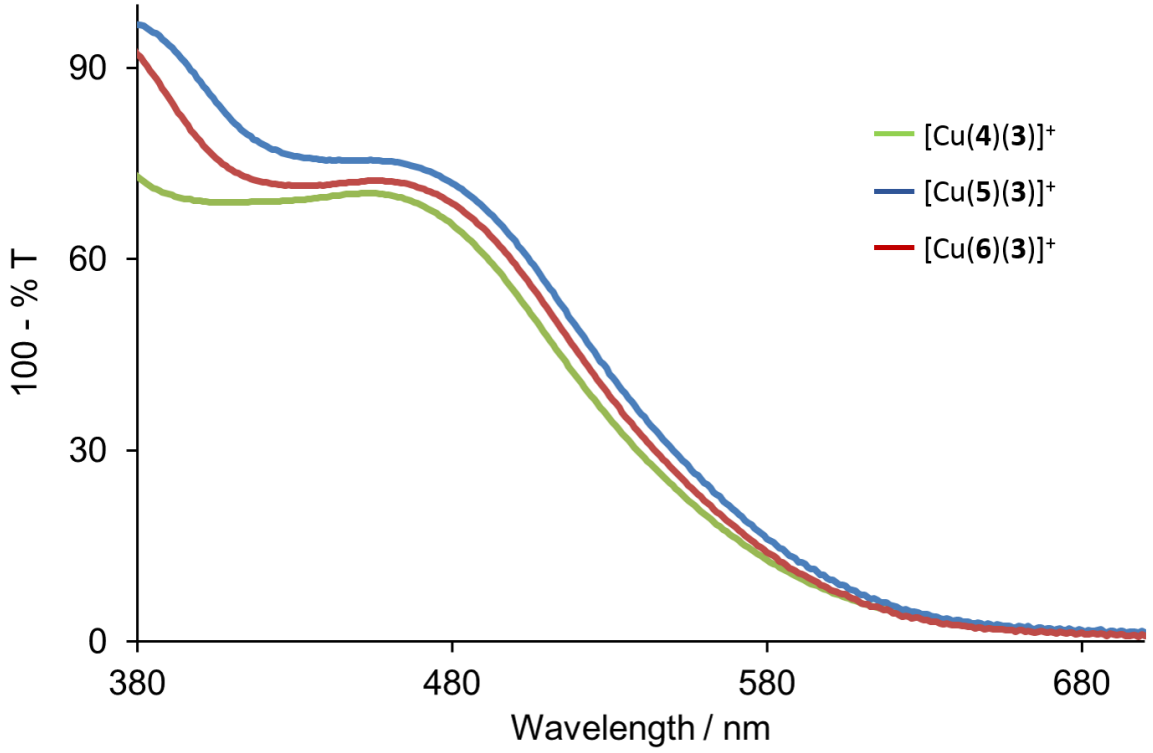

Fig. 23: Solid state absorption spectra of complexes $[Cu(\mathbf{4})(\mathbf{3})]^+$, $[Cu(\mathbf{5})(\mathbf{3})]^+$ and $[Cu(\mathbf{6})(\mathbf{3})]^+$ on a transparent TiO_2-electrode measured in the transmission mode.

TiO_2 electrodes were sensitized with complexes $[Cu(\mathbf{4})(\mathbf{3})]^+$, $[Cu(\mathbf{5})(\mathbf{3})]^+$ and $[Cu(\mathbf{6})(\mathbf{3})]^+$ and their performance set in relation to a **N719** reference cell. Results from the solar simulator measurements are displayed in Table 4.

Dye	J_{SC} / mA cm^{-2}	V_{OC} / mV	*ff* / %	η / %	Relative η / %
On the day of sealing the cells					
[Cu(**4**)(**3**)]$^+$	5.45	606	69	2.26	39.2
[Cu(**4**)(**3**)]$^+$	5.16	582	74	2.22	38.5
[Cu(**5**)(**3**)]$^+$	5.90	535	67	2.13	37.0
[Cu(**5**)(**3**)]$^+$	5.28	535	68	1.91	33.2
[Cu(**6**)(**3**)]$^+$	5.87	589	64	2.23	38.7
[Cu(**6**)(**3**)]$^+$	6.02	591	67	2.40	41.7
N719	13.64	636	66	5.76	100
3 days after sealing the cells					
[Cu(**4**)(**3**)]$^+$	4.81	613	68	2.00	33.7
[Cu(**4**)(**3**)]$^+$	4.42	609	73	1.96	33.1
[Cu(**5**)(**3**)]$^+$	5.46	552	64	1.93	32.5
[Cu(**5**)(**3**)]$^+$	4.98	557	67	1.86	31.4
[Cu(**6**)(**3**)]$^+$	5.25	611	65	2.08	35.1
[Cu(**6**)(**3**)]$^+$	5.66	600	67	2.29	38.6
N719	13.14	684	66	5.93	100
7 days after sealing the cells					
[Cu(**4**)(**3**)]$^+$	4.74	614	68	1.98	33.6
[Cu(**4**)(**3**)]$^+$	4.48	611	73	2.00	33.9
[Cu(**5**)(**3**)]$^+$	5.43	566	68	2.09	35.4
[Cu(**5**)(**3**)]$^+$	4.93	564	68	1.90	32.2
[Cu(**6**)(**3**)]$^+$	5.10	619	67	2.10	35.6
[Cu(**6**)(**3**)]$^+$	5.42	601	69	2.25	38.1
N719	13.05	691	66	5.90	100

Table 4: Solar cell measurements with values obtained at days 0, 3 and 7. Ancillary ligand **3** was used in every complex and the performance of new anchors **5** and **6** where compared to standard anchor **4**.

Data displayed in Table 4 show good reproducibility of duplicate solar cells for each of the three heteroleptic complexes. All cells have good fill factors between 64 and 74%. The V_{OC} of complexes with standard anchor **4** and the new anchor **6**, bearing the phosphonic acid anchoring group in the 4 position of the thiophenediyl spacer, are comparable and show good V_{OC} values around 610 mV. In contrast the heteroleptic complex [Cu(**5**)(**3**)]$^+$ has a V_{OC} lowered by roughly 50-60 mV compared to [Cu(**4**)(**3**)]$^+$ and [Cu(**6**)(**3**)]$^+$. The J_{SC} values for complexes with anchors **5** and **6**, using a thiophenediyl spacer, are always higher than those for standard anchor **4**. This is the first evidence of improvement by this new class of anchoring ligands. The heteroleptic complex [Cu(**6**)(**3**)]$^+$, outperforms [Cu(**5**)(**3**)]$^+$ in terms of V_{OC} and outperforms [Cu(**4**)(**3**)]$^+$ in terms of J_{SC} leading to the record efficiency of 2.40% (41.7% compared to a **N719** reference cell) at the day of sealing the cells. Over the following days the efficiency of all cells decreased

slightly, but [Cu(**6**)(**3**)]$^+$ remained the best performing complex. This is seen in the *J*/*V* curves displayed in Fig. 24 where the best performing cell with complex [Cu(**6**)(**3**)]$^+$ shows the highest J_{SC} and a high V_{OC} as well (red curve). The lower V_{OC} on going from [Cu(**6**)(**3**)]$^+$ to [Cu(**5**)(**3**)]$^+$ (blue curve) is clearly displayed in this graph.

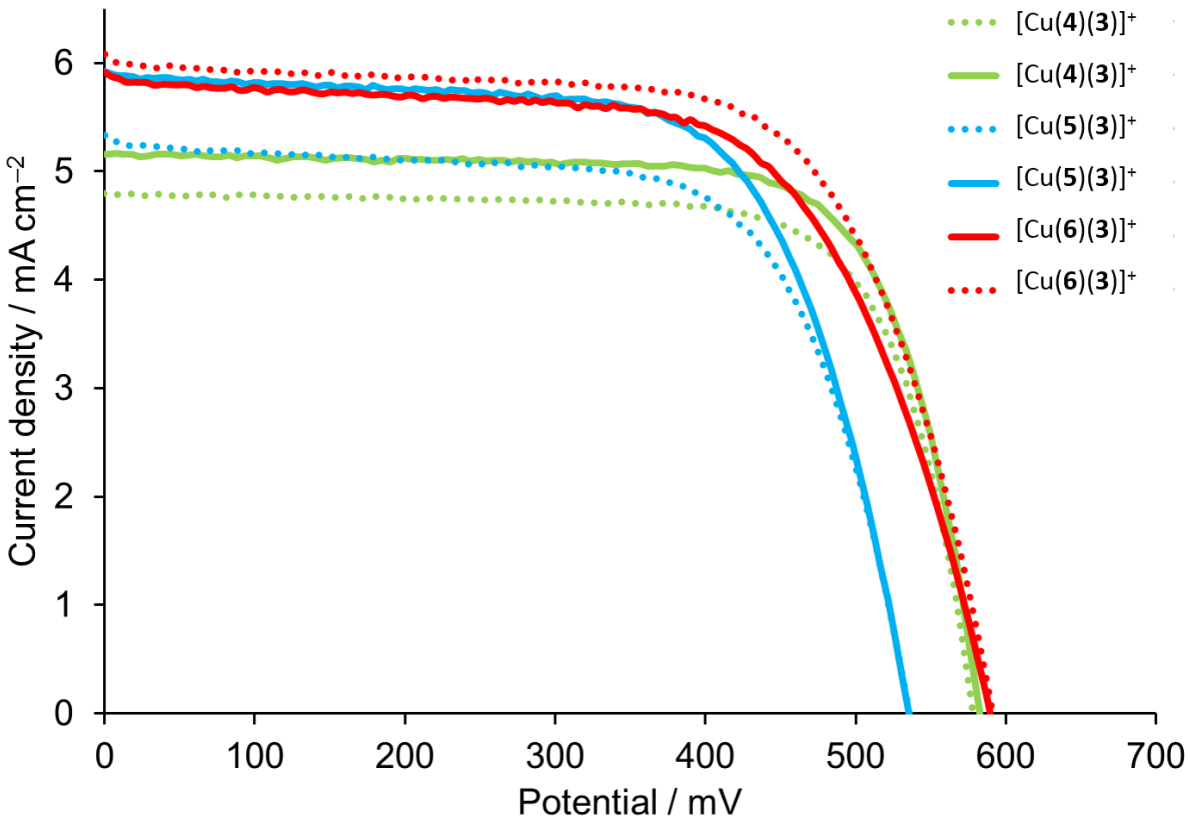

Fig. 24: *J*/*V* curves recorded for duplicate cells of complexes [Cu(**4**)(**3**)]$^+$, [Cu(**5**)(**3**)]$^+$ and [Cu(**6**)(**3**)]$^+$ on the day of sealing the cells.

The EQE spectra of complexes [Cu(**4**)(**3**)]$^+$, [Cu(**5**)(**3**)]$^+$ and [Cu(**6**)(**3**)]$^+$ are similar to most bisdiimine copper(I) complexes, which normally show a maximum at λ = 480nm. It is noteworthy, that heteroleptic complexes [Cu(**5**)(**3**)]$^+$ and [Cu(**6**)(**3**)]$^+$, containing a thiophenediyl spacer in the anchoring ligand, have a broader spectrum and benefit from increased photon absorption in the red part of the visible region (Fig. 25). This parallels the redshifted absorption observed in the solid state UV-VIS measurement.

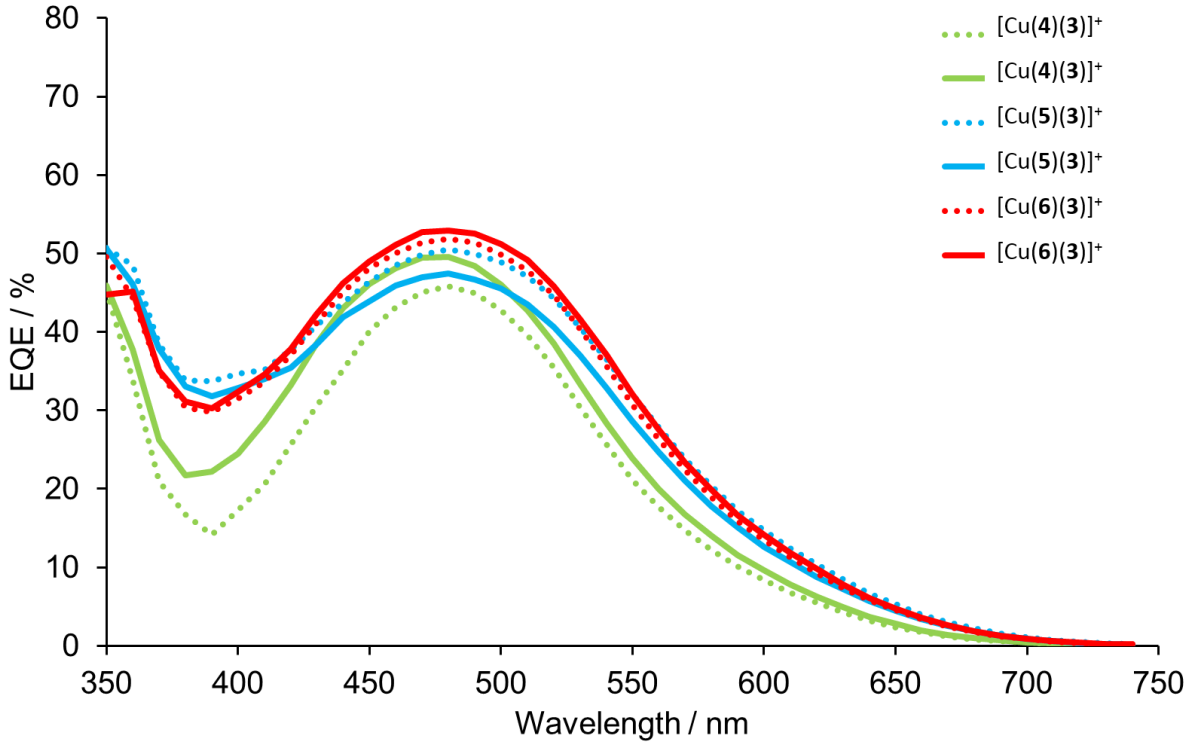

Fig. 25: EQE spectra for duplicate cells of complexes $[Cu(\mathbf{4})(\mathbf{3})]^+$, $[Cu(\mathbf{5})(\mathbf{3})]^+$ and $[Cu(\mathbf{6})(\mathbf{3})]^+$ on day of sealing the cells. Broader EQE curves were obtained for complexes $[Cu(\mathbf{5})(\mathbf{3})]^+$ and $[Cu(\mathbf{6})(\mathbf{3})]^+$ supporting their increased solar cell performance.

Complexes $[Cu(\mathbf{5})(\mathbf{3})]^+$ and $[Cu(\mathbf{6})(\mathbf{3})]^+$ show higher EQE_{max} values of 50.5 and 52.9%, respectively, surpassing $[Cu(\mathbf{4})(\mathbf{3})]^+$ (EQE_{max} = 49.6%). The values are summarized in Table 5 and further highlight the beneficial effects of new anchors **5** and **6**, over the standard anchor **4**.

	Cell 1		Cell2	
Anchored dye	λ / nm	EQE_{max} / %	λ / nm	EQE_{max} / %
$[Cu(\mathbf{4})(\mathbf{3})]^+$	480	45.8	480	49.6
$[Cu(\mathbf{5})(\mathbf{3})]^+$	480	50.5	480	47.4
$[Cu(\mathbf{6})(\mathbf{3})]^+$	480	51.8	480	52.9

Table 5: EQE values of complexes $[Cu(\mathbf{4})(\mathbf{3})]^+$, $[Cu(\mathbf{5})(\mathbf{3})]^+$ and $[Cu(\mathbf{6})(\mathbf{3})]^+$ at λ = 480 nm.

7.2.2 Home-made vs commercial TiO_2-electrodes

Home-made TiO_2 electrodes were made by Annika Büttner from the Constable/Housecroft research group in Basel, by the screen-printing technique.

Previous studies in our group showed increased device stability and reproducibility of home-made TiO_2 electrodes over commercially available ones. To validate results achieved for complexes [Cu(**5**)(**3**)]$^+$ and [Cu(**6**)(**3**)]$^+$, especially the difference in V_{OC}, duplicate cells were fabricated using home-made TiO_2 electrodes. The overall DSSC performance increased for [Cu(**5**)(**3**)]$^+$ with a record J_{SC} at day 0 of 6.53 mA cm^{-2}. The trend in V_{OC} of [Cu(**5**)(**3**)]$^+$ being 50-60 mV lower than in [Cu(**6**)(**3**)]$^+$ was confirmed. Over the following days, cell performance decreased and at day 7, the performance of both complexes was similar for commercial (Table 4) and home-made TiO_2 electrodes (Table 6).

Dye	J_{SC} / mA cm^{-2}	V_{OC} / mV	*ff* / %	η / %	Relative η / %
On the day of sealing the cells					
[Cu(**5**)(**3**)]$^+$	6.18	539	69	2.31	40.1
[Cu(**5**)(**3**)]$^+$	6.53	535	69	2.41	41.8
[Cu(**6**)(**3**)]$^+$	5.91	596	67	2.37	41.1
[Cu(**6**)(**3**)]$^+$	5.75	595	69	2.38	41.3
N719	13.64	636	66	5.76	100
3 days after sealing the cells					
[Cu(**5**)(**3**)]$^+$	5.90	535	67	2.13	35.9
[Cu(**5**)(**3**)]$^+$	5.28	535	68	1.91	32.2
[Cu(**6**)(**3**)]$^+$	5.87	589	64	2.23	37.6
[Cu(**6**)(**3**)]$^+$	6.02	591	67	2.40	40.5
N719	13.14	684	66	5.93	100
7 days after sealing the cells					
[Cu(**5**)(**3**)]$^+$	5.72	548	69	2.16	36.6
[Cu(**5**)(**3**)]$^+$	5.95	541	68	2.20	37.3
[Cu(**6**)(**3**)]$^+$	5.53	626	68	2.36	40.0
[Cu(**6**)(**3**)]$^+$	5.61	603	69	2.35	39.8
N719	13.05	691	66	5.90	100

Table 6: Solar cell measurements of complexes [Cu(**5**)(**3**)]$^+$ and [Cu(**6**)(**3**)]$^+$ with values obtained at days 0, 3 and 7. Home-made TiO_2 electrodes were used in this study. Data for the **N719** reference cell was taken from the previous chapter.

The EQE spectra of $[Cu(\mathbf{5})(\mathbf{3})]^+$ and $[Cu(\mathbf{6})(\mathbf{3})]^+$ mirror those discussed in the previous section, with slightly increased EQE_{max} values. It is very important to state an efficiency relative to an external reference like **N719**, as different research groups use different setups, yielding different results for **N719**. This is even the case in our own research laboratory where two sun simulators are used for measurements and efficiencies vary significantly between them. This makes efficiencies relative to **N719** the only reliable value to validate the performance of a DSSC. $[Cu(\mathbf{6})(\mathbf{3})]^+$ ranges among the best bisdiimine copper(I) based dyes (using an I^-/I_3^- based electrolyte) fabricated in our research laboratory with an efficiency of 41.7% relative to a **N719** reference cell (Table 4) and an EQE_{max} of 52.9%.

7.2.3 Long term stability of bisdiimine copper(I) based DSSCs

Bisdiimine copper(I) based dyes show a very good stability over a long period. The cells were not exposed to sun-light except for the sun simulator measurements, and were otherwise kept in the dark. Their performance was measured 41 and 46 days after fabrication and compared with corresponding values obtained after 7 days. Results displayed in Table 7 highlight the long-term stability of complexes $[Cu(\mathbf{5})(\mathbf{3})]^+$ and $[Cu(\mathbf{6})(\mathbf{3})]^+$ in a DSSC fabricated with either commercial or home-made TiO_2 electrodes. Comparison of J_{SC}, V_{OC}, *ff* and η values 7 days after fabrication (Table 4 and Table 6) with values obtained after 41 and 46 days, respectively, revealed little differences. Long term stability of a device is equally important to its efficiency, as researchers aim for commercialization of DSSCs in the long term. The stability of bisdiimine copper(I) based dyes in DSSCs highlights their great potential for future applications, if efficiencies can be increased.

Dye	**Age** of the DSSC / days	J_{SC} / mA cm^{-2}	V_{OC} / mV	*ff* / %	η / %
		Commercial TiO_2 electrodes			
[Cu(**5**)(**3**)]$^+$	**46**	5.23	572	70	2.10
[Cu(**5**)(**3**)]$^+$	**46**	4.70	568	71	1.90
[Cu(**6**)(**3**)]$^+$	**46**	5.08	615	69	2.15
[Cu(**6**)(**3**)]$^+$	**46**	5.07	613	72	2.22
		Home-made TiO_2 electrodes			
[Cu(**5**)(**3**)]$^+$	**41**	5.65	549	70	2.17
[Cu(**5**)(**3**)]$^+$	**41**	5.82	545	69	2.19
[Cu(**6**)(**3**)]$^+$	**41**	5.39	625	69	2.32
[Cu(**6**)(**3**)]$^+$	**41**	5.41	616	70	2.34

Table 7: Long-term stability measurement of heteroleptic complexes [Cu(**5**)(**3**)]$^+$ and [Cu(**6**)(**3**)]$^+$ in commercial and home-made TiO_2 electrodes.

7.2.4 Anchors 5 and 6 with different ancillary ligands

In the previous sections, focus was set on the different performances of anchoring ligands **4**, **5** and **6** with the same ancillary ligand **3**. The results illustrated the increased device performance on going from **4** and **5** to anchor **6**, showing the best efficiency of 2.40% for heteroleptic complex [Cu(**6**)(**3**)]$^+$. To validate and establish anchor **6** as a better, and general, standard anchor for heteroleptic bisdiimine copper(I) based dyes, studies of anchors **4**, **5** and **6** with ancillary ligands **1** and **7** were performed. The same trend as with ancillary ligand **3** was observed in complexes [Cu(**4**)(**1**)]$^+$, [Cu(**5**)(**1**)]$^+$ and [Cu(**6**)(**1**)]$^+$, as well as in [Cu(**4**)(**7**)]$^+$, [Cu(**5**)(**7**)]$^+$ and [Cu(**6**)(**7**)]$^+$. The characteristic V_{OC} increase of ~ 50 mV on going from anchor **5** to **6**, was confirmed as well as the red shifting properties of thiophenediyl anchors in the EQE. Among these 6 new heteroleptic complexes, the ones with anchor **6** showed the overall highest performance.

7.3 Electrochemical impedance spectroscopy

EIS was measured by Dr. Markus Willgert from the University of Basel. EIS can be a very useful method to understand transport and recombination processes occurring in an operating solar cell. The systematic investigation of three different anchors (**4**, **5** and **6**) with the ancillary

ligand **1**, **3** and **7** revealed the trends in J_{SC} and V_{OC} discussed in the previous sections. These trends help in the validation of the EIS measurements and EIS nicely complements the trends found in the *J*/*V* measurements.

7.3.1 Anchor 4 with ancillary ligands 1, 3 and 7

In this first EIS study the standard anchor **4** was combined with the methyl-substituted ancillary ligands **1** and **7**, as well as with the CF_3-substituted ancillary ligand **3**. **1** bears two methyl groups in 6 and 6' position and **7** bears one. In the *J*/*V* measurements $[Cu(\mathbf{4})(\mathbf{1})]^+$ and $[Cu(\mathbf{4})(\mathbf{7})]^+$ perform in a similar range, with $[Cu(\mathbf{4})(\mathbf{7})]^+$ showing slightly larger values in J_{SC} and V_{OC}. In $[Cu(\mathbf{4})(\mathbf{3})]^+$ a slightly higher J_{SC} was obtained, but the main performance gain was in the V_{OC}, that increased from ~ 550 mV for ancillaries **1** and **7** to 582-606 mV for ancillary **3**.

EIS measurements can be carried out at different light intensities. At low light intensities (2.4 mW cm^{-2}, Table 8) the transport resistance (R_t) in the TiO_2 semiconductor is measured, as the V_{OC} is lower and R_t is easier to obtain. R_t then only depends on the surface modification by dye molecules and possibly present electrolyte molecules. The CB level (and the Fermi level) of the TiO_2 is affected by dye molecules and additives, like Li^+-ions, in the electrolyte. When the fermi level of the CB shifts to more positive potentials a reduced V_{OC} is the consequence, as the V_{OC} is defined by the potential difference between the fermi level of the CB and the redox potential of the electrolyte. The V_{OC} and the R_t are closely related in these terms, because the lifetime of the electrons is comparable. The higher the V_{OC} of a dye in this closely related series is, the lower the R_t. This is nicely confirmed in the series $[Cu(\mathbf{4})(\mathbf{1})]^+$ (440 mV, R_t = 288.6 Ω) vs. $[Cu(\mathbf{4})(\mathbf{7})]^+$ (493 mV, R_t = 228.0 Ω) vs. $[Cu(\mathbf{4})(\mathbf{3})]^+$ (550 mV, R_t = 104.3 Ω). The highest V_{OC} and consequently the lowest R_t was obtained for $[Cu(\mathbf{4})(\mathbf{3})]^+$, which contributes to the best overall performance of this complex in the series.

	R_s / Ω	R_t / Ω	R_{rec} / Ω	C_μ / μF	R_{Pt} / Ω	C_{Pt} / μF	τ / ms	L_d/L	V_{OC} / mV
[Cu(**4**)(**1**)]$^+$	7.0	288.6	2420.0	88.3	91.2	6.9	213.6	2.9	440
[Cu(**4**)(**7**)]$^+$	13.0	228.0	1723.0	130.1	16.0	8.6	224.1	2.7	493
[Cu(**4**)(**3**)]$^+$	11.7	104.3	1242.0	158.5	52.8	4.7	196.9	3.5	550

Table 8: Low light intensity impedance measurements (2.4 mW cm^{-2}) 3 days after DSC assembly.

At higher light intensities (22 mW cm^{-2}, Table 9) the chemical capacitance (C_μ) of the TiO_2/electrolyte interface, the recombination resistance (R_{rec}) and the lifetime of the electron τ are measured. The length of the electron diffusion (L_d) and the thickness of the porous active layer (L) can also be obtained from this measurement.

	R_s / Ω	R_{rec} / Ω	C_μ / μF	R_{Pt} / Ω	C_{Pt} / μF	τ / ms	V_{OC} / mV	η / %[a]
[Cu(**4**)(**1**)]$^+$	9.3	316.0	183.3	53.3	4.7	57.9	530	1.15
[Cu(**4**)(**7**)]$^+$	15.4	250.5	201.4	14.2	4.6	50.4	553	1.53
[Cu(**4**)(**3**)]$^+$	12.2	204.3	276.1	47.4	5.2	56.4	620	2.00

Table 9: High light intensity impedance measurements (22 mW cm^{-2}) 3 days after DSC assembly.

The series of compounds [Cu(**4**)(**1**)]$^+$ vs. [Cu(**4**)(**7**)]$^+$ vs. [Cu(**4**)(**3**)]$^+$ was investigated. [Cu(**4**)(**1**)]$^+$ and [Cu(**4**)(**7**)]$^+$ show high R_{rec} values of 316.0 and 250.5Ω, respectively, that is higher than in [Cu(**4**)(**3**)]$^+$ (204.3 Ω). Another important parameter is the chemical capacitance and this is highest for [Cu(**4**)(**3**)]$^+$. This implies, that [Cu(**4**)(**3**)]$^+$ injects more electrons into TiO_2 than [Cu(**4**)(**1**)]$^+$ and [Cu(**4**)(**7**)]$^+$. When more electrons are injected, the R_{rec} increases. In summary [Cu(**4**)(**3**)]$^+$ has the highest C_μ and the lowest R_t, which implies more electron injection and faster transport of the injected electrons through the semiconductor to the

electrode and confirms the higher J_{SC}. R_t is lower than R_{rec}, which states, that injected electrons get transferred to the electrode faster than they recombine. R_{rec} is still relatively high and R_t is lowest for [Cu(**4**)(**3**)]$^+$ in this series which confirms the higher V_{OC}.

7.3.2 Anchors 4, 5 and 6 with ancillary ligand 3

In the second EIS study the performances of [Cu(**4**)(**3**)]$^+$, [Cu(**5**)(**3**)]$^+$ and [Cu(**6**)(**3**)]$^+$ were investigated. [Cu(**6**)(**3**)]$^+$ showed the highest efficiency. The V_{OC} of [Cu(**4**)(**3**)]$^+$ and [Cu(**6**)(**3**)]$^+$ was comparable, but [Cu(**5**)(**3**)]$^+$ showed a decrease in V_{OC} by ~50mV.

The relation between V_{OC} and R_t at low light intensities (Table 10) is demonstrated by data presented in Table 10. In this series τ has to be taken into account as it decreases in going from [Cu(**4**)(**3**)]$^+$ to [Cu(**6**)(**3**)]$^+$ to [Cu(**5**)(**3**)]$^+$. The high R_t and very short τ in [Cu(**5**)(**3**)]$^+$ causes the low V_{OC}. [Cu(**4**)(**3**)]$^+$ and [Cu(**6**)(**3**)]$^+$, both very similar in V_{OC} also show comparable values for R_t and τ. [Cu(**6**)(**3**)]$^+$ has the lowest R_t.

At higher light intensities (Table 11) [Cu(**4**)(**3**)]$^+$ and [Cu(**6**)(**3**)]$^+$ show higher R_{rec} and C_μ. These two findings combined with the lower R_t and longer τ confirm the better overall performance of these tow complexes compared to [Cu(**5**)(**3**)]$^+$. Between [Cu(**4**)(**3**)]$^+$ and [Cu(**6**)(**3**)]$^+$, shows [Cu(**6**)(**3**)]$^+$ a higher C_μ and slightly lower R_{rec}. Combined with the lower R_t is [Cu(**6**)(**3**)]$^+$ able to outperform [Cu(**4**)(**3**)]$^+$ and shows the best efficiency in this series.

	R_s / Ω	R_t / Ω	R_{rec} / Ω	C_μ / μF	R_{Pt} / Ω	C_{Pt} / μF	τ / ms	L_d/L	V_{OC} / mV
[Cu(**4**)(**3**)]$^+$	11.7	104.3	1242.0	158.5	52.8	4.7	196.9	3.5	550
[Cu(**5**)(**3**)]$^+$	12.3	251.2	738.0	93.2	59.0	5.8	68.8	1.7	510
[Cu(**6**)(**3**)]$^+$	16.4	67.8	917.4	182.0	35.3	4.4	166.9	3.7	520

Table 10: Low light intensity impedance measurements (2.4 mW cm^{-2}) 3 days after DSC assembly.

	R_s / Ω	R_{rec} / Ω	C_μ / μF	R_{Pt} / Ω	C_{Pt} / μF	τ / ms	V_{OC} / mV	η / %[a]
[Cu(**4**)(**3**)]$^+$	12.2	204.3	276.1	47.4	5.2	56.4	620	2.00
[Cu(**5**)(**3**)]$^+$	13.7	94.1	197.0	54.5	4.8	18.5	582	1.93
[Cu(**6**)(**3**)]$^+$	18.6	150.8	309.1	31.7	4.7	46.6	594	2.29

Table 11: High light intensity impedance measurements (22 mW cm^{-2}) 3 days after DSC assembly.

7.4 Conclusion

Results from all sections are summarized in Fig. 26 and a clear trend is observed. Anchoring ligands **4** and **5** perform in a similar efficiency range. Ligand **4** has a higher V_{OC} which is compensated by ligand **5** showing higher J_{SC} values. Ligand **6** outperforms **4** in J_{SC} and **5** in V_{OC}, being the best anchoring ligand in this series and most important better than the standard anchor **4**. EIS measurements revealed low transport resistance, high capacitance, relative high recombination resistance and a long lifetime for complex [Cu(**6**)(**3**)]$^+$. High efficiencies were obtained for the combination of anchor **6** and ancillary ligand **3**, in the heteroleptic complex [Cu(**6**)(**3**)]$^+$.

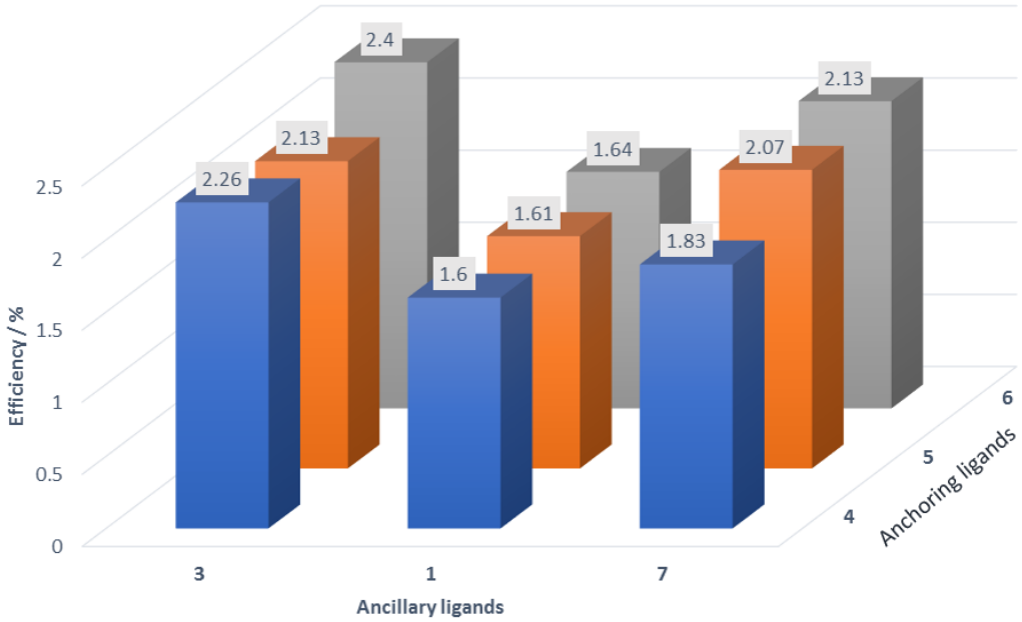

Fig. 26: Summary of solar cell efficiencies, combining anchoring ligands **4**-**6** with ancillary ligands **1**, **3** and **7**.

The results confirm the beneficial effect of thiophenediyl groups. The substitution position of the phosphonic acid group on the thiophenediyl spacer has a big impact on the electron transport and the recombination. A substitution in 4 position of the thiophenediyl is beneficial compared to a substitution in 5 position.

This work was published 2016 in *Dalton Transactions*[105].

8 CYANOACRYLIC ACID VS. (1-CYANOVINYL)PHOSPHONIC ACID IN BISDIIMINE BASED ANCHORS

In chapter 7 the focus of improvement for heteroleptic bisdiimine copper(I) complexes lay on the spacer in the anchoring ligand. The monosubstituted ancillary ligand **3**, bearing one CF_3 group in the 6 position of 2,2'-bipyridine was beneficial in terms of overall performance and will be used in this chapter as well. The spacer between the bpy-ligand core and the phosphonic acid anchoring group was altered from a phenylene to a thiophenediyl group. Good results were obtained for the 4-thiophenediyl substituted anchor **6**, already outperforming the standard anchor **4**. Before the attention is drawn back to thiophenediyl spacers in DSSCs in chapter 9; this chapter will illustrate a new class of anchoring groups for heteroleptic bisdiimine copper(I) complexes. The established cyanoacrylic acid anchor was presented in the introduction, and its beneficial properties were discussed. Its less common phosphonic acid analogue, (1-cyanovinyl)phosphonic acid, is now introduced as an anchoring ligand. In this study both anchors are covalently connected at the 4-position of a phenylene substituted 6,6'-dimethyl-2,2'-bipyridine and/or neocuproine ligand core (Scheme 25).

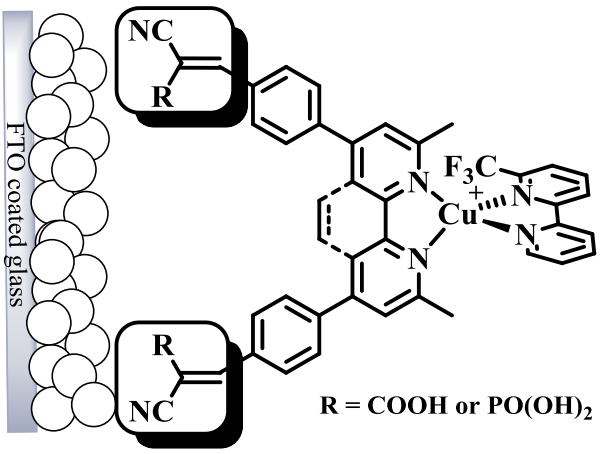

Scheme 25: Bisdiimine copper(I) complexes with 6,6'-dimethyl-2,2'-bipyridine and/or neocuproine based anchoring ligands bearing cyanoacrylic acid or (1-cyanovinyl)phosphonic acid anchoring groups. Ligand **3** was used as the ancillary ligand.

Cyanoacrylic acid is one of the most used anchoring group in organic dyes (see introduction) and it benefits from two aspects. The cyano group acts as an electron withdrawing group and

enhances the electron pulling abilities of the anchoring group. It is possible that the CN group itself anchors to the surface via N-Ti coordination. The main anchoring ability however is generated through H-bonding and O-Ti coordination of the carboxylic acid group. Fast electron injection and reduced recombination of injected electrons back to the dye are advantages of this group over a simple carboxylic acid group. Two anchoring ligands incorporating cyanoacrylic acid anchors (**8** and **10**, Scheme 27), connected to either a 6,6'-dimethyl-2,2'-bipyridine or a neocuproine (Scheme 26) will be discussed in this chapter. The 6,6'-dimethyl-2,2'-bipyridine based anchor **8** was published previously, but only as a homoleptic bisdiimine copper(I) complex[81]. The homoleptic complex $[Cu(\mathbf{8})_2]^+$ showed an efficiency of 2.2% (relative to 7.8% for a **N719** reference cell). It was resynthesized for this study and tested in our heteroleptic system.

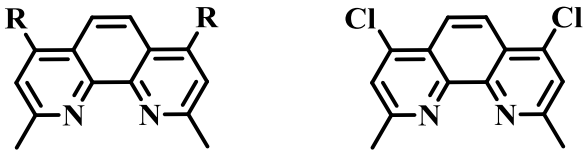

Scheme 26: Left: Neocuproine, with possible substitutions in 4 and 7 positions, highlighted by R-groups. Right: 4,7-Dichloro-2,9-dimethyl-1,10-phenanthroline used as starting material for the synthesis of anchors **10** and **11**.

Previous studies have shown that neocuproine based ancillary ligands show good performance in heteroleptic bisdiimine copper(I) complexes[86]. To reverse the position of the neocuproine core in the complex from the ancillary to the anchoring site was one goal of this study.

The second aim was to incorporate a new type of anchoring group into the system. Carboxylic acid groups are widely used in organic and inorganic dyes (see introduction). Bisdiimine copper(I) based dyes however, show relatively poor performances with this anchoring group[42]. It was assumed that cyanoacrylic acid anchors would perform equally poorly, but the results of Yuan *et al.*[81] obtained for the homoleptic complex $[Cu(\mathbf{8})_2]^+$ encouraged us to resynthesise ligand **8** and test the performance of cyanoacrylic acid based anchors in heteroleptic bisdiimine copper(I) based dyes. Phosphonic acids anchors however improve cell performance of bisdiimine copper(I) based dyes[16, 42], thus the phosphonic acid analogu0e of the cyanoacrylic acid was incorporated into the system. (1-cyanovinyl)phosphonic acid was connected to a phenylene group attached to a 6,6'-dimethyl-2,2'-bipyridine and a neocuproine ligand core (**9**

and **11**, Scheme 27). In total four (three of them new) anchoring ligands were synthesized and their solar cell performance compared relative to the standard anchor **4**.

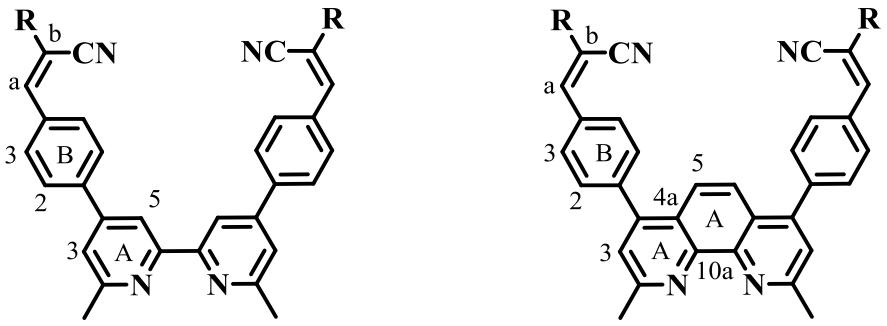

Scheme 27: Anchoring ligands discussed in this chapter, with labels for NMR assignment.

8.1 Synthesis and Characterization

Anchoring ligand synthesis and solar cell measurements were carried out in cooperation with the Wahlpraktikum student Yann Baumgartner. EIS measurements were carried out by Dr. Markus Willgert; the main results of EIS will be briefly presented, but are not discussed in detail. Further information about EIS data can be found in the corresponding publication[113].

8.1.1 Anchoring ligand synthesis

The synthesis of anchoring ligands **8** and **9** is displayed in Scheme 28. 4,4'-Dibromo-6,6'-dimethyl-2,2'-bipyridine was synthesized following a literature procedure[114]. In the first synthetic step, a double Suzuki coupling of the dibromo compound with two equivalents of (4-formylphenyl)boronic acid, in the presence of $[Pd(PPh_3)_4]$ and Cs_2CO_3 was performed. The microwave assisted reaction yielded 4,4'-(6,6'-dimethyl-[2,2'-bipyridine]-4,4'-diyl)dibenzaldehyde in 74.0% yield after recrystallization from a mixture of $CHCl_3$/EtOH. In general 6,6'-dimethyl-2,2'-bipyridine based ligands are not soluble, or only weakly soluble in ethanol, making recrystallizations from chloroform and ethanol very rewarding. The dialdehyde intermediate was condensed in a Knoevenagel type reaction with cyanoacetic acid in the presence of piperidine to give the anchoring ligand **8** in a good yield of 84.3%. A second batch

of dialdehyde was condensed in the same way with diethyl cyanomethylphosphonate to yield the intermediate **9a** in 78.4% yield. The final step towards anchoring ligand **9** was carried out in dichloromethane in the presence of Me_3SiBr. Addition of water to the reaction mixture lead to the formation of compound **9**, which precipitated and was filtered off in 35.0% yield.

The synthesis of anchors **10** and **11** followed the same general procedure, but using 4,7-dichloro-2,9-dimethyl-1,10-phenanthroline as the precursor (Scheme 26). It was prepared according to a literature method[115]. The coupling reaction of the dichloro compound with (4-formylphenyl)boronic acid was not very efficient with a yield of 12.0%. This might be due to the fact that chloro groups are less reactive in Pd-based cross coupling reactions than to bromo or iodo substituents. The condensation reaction from the dialdehyde to ligand **10** yielded the desired compound in 69.8% yield. The corresponding condensation with diethyl cyanomethylphosphonate to the phosphonic ester precursor **11a** and the following deprotection with Me_3SiBr yielded anchoring ligand **11**, in 24.8% yield over both steps.

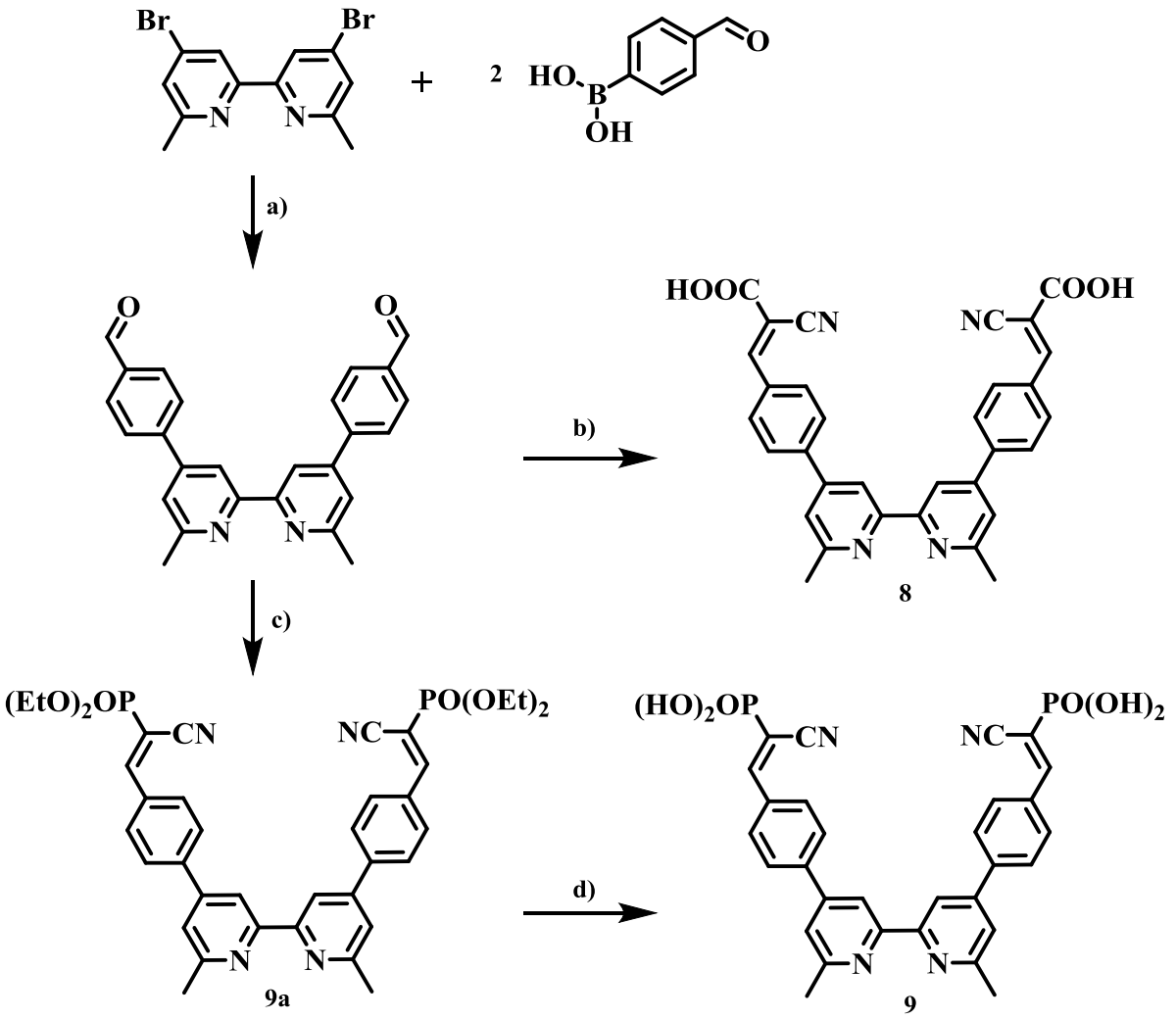

Scheme 28: General synthetic route towards anchoring ligands **8**-**11**, schematically represented by the synthesis of **8** and **9**. For **10** and **11** the educt in the first step was 4,7-Dichloro-2,9-dimethyl-1,10-phenanthroline. Conditions: a) [$Pd(PPh_3)_4$], Cs_2CO_3, microwave reactor, THF/H2O, 90°C, 4h; b) cyanoacetic acid, piperidine, $CHCl_3$, 70 °C, 16 h; c) diethyl cyanomethylphosphonate, piperidine, $CHCl_3$, 70 °C, 16 h; d) Me_3SiBr, CH_2Cl_2, room temperature, 56 h, followed by H_2O.

Ligands **8**-**11** were characterized by ^{1}H, $^{13}C\{^{1}H\}$ and $^{31}P\{^{1}H\}$ NMR spectroscopies, FT-IR, ESI-MS, MALDI-TOF and high resolution ESI-MS. Carboxylic acid anchors **8** and **10** were only soluble in DMSO and could be assigned using 2D-NMR methods. NOE crosspeaks between H^{A3} / H^{B2} and H^{B3} / H^{a} gave clear evidence for the proton assignment (see Scheme 27 for labelling). The FT-IR spectra of **8** and **10** show a characteristic band of the CN-group at 2218 cm^{-1} and a very strong band of the carboxyclic acid group at 1598 cm^{-1}. The stereochemistry of the cyanoacrylic acid, as well as the (1-cyanovinyl)phosphonic acid group is very likely to be as drawn in Scheme 27. It is not clear if the stereochemistry is introduced during the reaction or afterwards, as Kloo and coworkers have shown that isomerization of this

group can occur under irradiation[116]. Carboxylic acid anchors **8** and **10** showed base peaks in the ESI-MS at *m/z* 527.07 and *m/z* 551.34, respectively, corresponding to the $[M+H]^+$ species.

The phosphonic ester precursors **9a** and **11a** were fully assigned by 2D-NMR methods. In the $^{31}P\{^1H\}$ spectrum of **9a** and **11a** a singlet was obtained at δ +10.9 and +10.7 ppm, respectively. Upon deprotection of the phosphonic ester **9a** to give the phosphonic acid **9** a shift to δ +4.55 ppm was observed. A similar phenomenon for phosphonic acid **11** could not be investigated, due to low solubility of the compound in common solvents and DMSO-*d6*. The ^{1}H-NMR spectrum of **11** could be recorded in DMSO-*d6*, but peaks appeared very broad and made assignments impossible. One important information however could be extracted from this spectrum, the disappearance of ethylester signals at δ 4.27 and 3.02 ppm, present in **11a**. This spectral information, together with mass peaks found in MALDI-TOF and high resolution ESI-MS lead to the conclusion that compound **11** was successfully synthesized. ^{1}H-NMR spectra were assigned in the same manner as **8** and **10**. Proton H^a showed a singlet in **8** and **10**, but the presence of the phosphorus in **9a**, **11a** and **9** leads to a splitting of the signal into a doublet with a characteristic coupling constant of around 20 Hz. The $^{13}C\{^1H\}$ NMR spectrum of **9** showed a $^1J_{PC}$ coupling of 182.9 Hz for proton H^b, similar to $^1J_{PC}$ coupling constants obtained in chapter 7 for ligands **5** and **6**. In **9a** a weak coupling of C^{Et} and C^{Me} to the phosphorus atom with coupling constants of 5.8 and 6.4 Hz, respectively was observed. ESI mass spectra of phosphonic acids **9** and **11** could only be obtained in basic aqueous media and revealed base peaks of *m/z* 297.88 and *m/z* 309.95, respectively, which correspond to the $[M-2H]^{2-}$ ion.

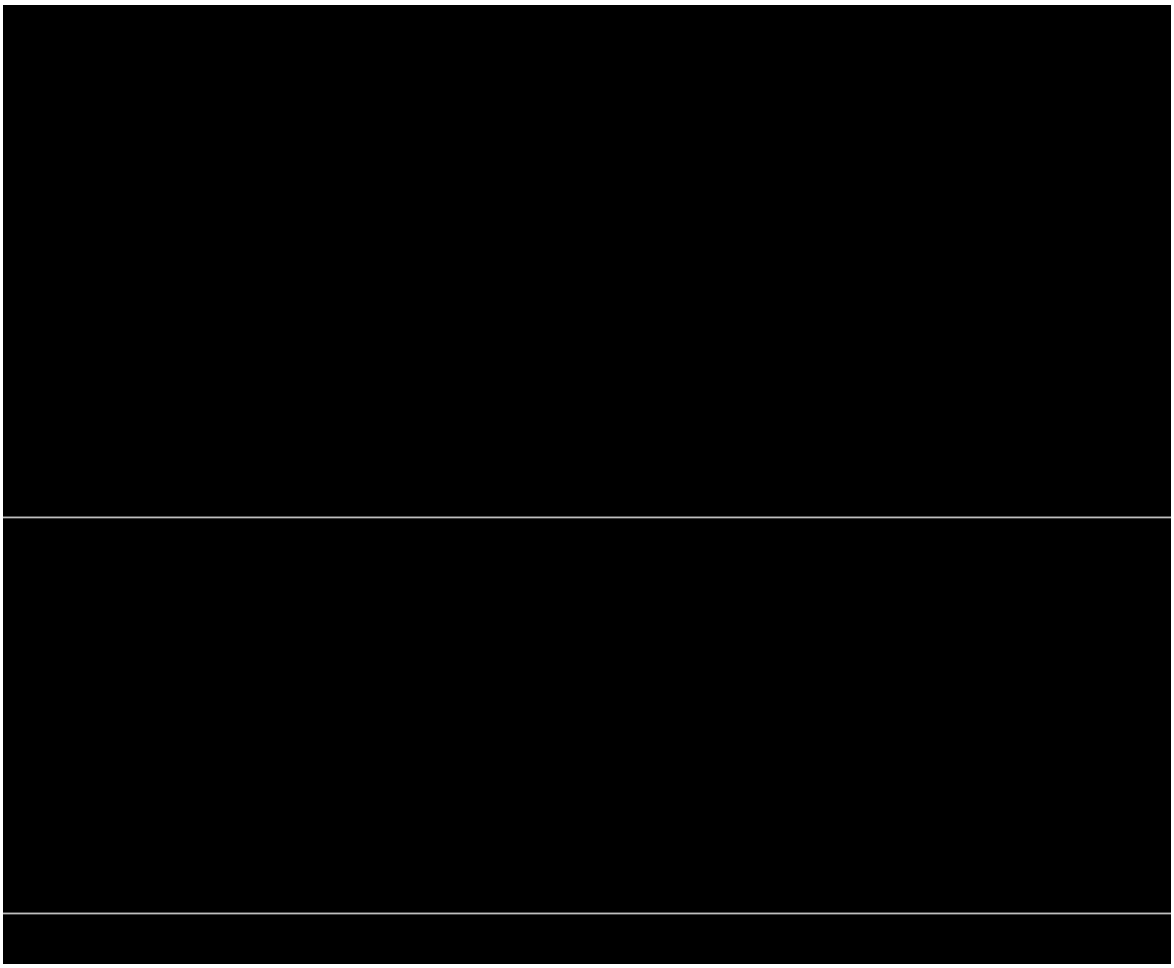

Fig. 27: 500 MHz ^{1}H NMR spectrum of anchoring ligand **9** in DMSO-d_6 (*). a) Spectrum over the whole range with the methyl signal at δ 2.82 ppm; b) The zoomed in aromatic region of **9** with H^a showing a doublet with a large J_{PH} coupling constant of 19.7 Hz.

8.2 DSSC performance

The same routine as in chapter 4 was applied here. Anchors **4** and **8-11** were combined with homoleptic copper(I)-complexes ([Cu(**L**)$_2$][PF_6], **L**= **1**,**3**) from previous chapters to form heteroleptic bisdiimine copper(I) complexes on a TiO_2 surface. Transparent electrodes were prepared for solid state absorption measurements. Duplicate solar cells were masked and their performance documented with current/voltage and EQE measurements. The results were compared and set in relation to a **N719** cell for consistency.

8.2.1 DSSCs of anchors 8 - 11 combined with ancillary ligand 1

The general stepwise solar cell assembly described in chapter 4 was used to attach heteroleptic complex of $[Cu(\mathbf{8})(\mathbf{1})]^+$, $[Cu(\mathbf{9})(\mathbf{1})]^+$, $[Cu(\mathbf{10})(\mathbf{1})]^+$ and $[Cu(\mathbf{11})(\mathbf{1})]^+$ to a TiO_2 surface. Ligand **1** was chosen to identify a general trend between the new anchoring ligands, before ancillary ligand **3** was incorporated to verify trends and aim for higher efficiencies. Acetone dye bath solutions of homoleptic complexes $[Cu(\mathbf{1})_2][PF_6]$ and $[Cu(\mathbf{3})_2][PF_6]$ were used for the ligand exchange reaction on the modified TiO_2 surface. Table 12 displays results from sun simulator measurements of heteroleptic complexes $[Cu(\mathbf{8})(\mathbf{1})]^+$, $[Cu(\mathbf{9})(\mathbf{1})]^+$, $[Cu(\mathbf{10})(\mathbf{1})]^+$ and $[Cu(\mathbf{11})(\mathbf{1})]^+$, relative to a **N719** reference cell on the day of sealing the cells. From this first measurement a clear trend of the newly synthesized anchoring ligands can be observed. The heteroleptic complex $[Cu(\mathbf{9})(\mathbf{1})]^+$ performs the best among these complexes with an efficiency of 1.91% (32.0% relative to **N719**). The second best anchor is ligand **11** (0.93%), followed by **8** (0.60%) and **10** (0.47%), which perform in a similar range. Anchors **9** and **11** both use a (1-cyanovinyl)phosphonic acid group to anchor to the surface and clearly outperform their related ligands **8** and **10**, which bear cyanoacrylic acid groups. This is the first trend in this chapter, resembling previous studies[16, 42], where phosphonic acids outperformed carboxylic acids as anchors in bisdiimine copper(I) based dyes. The second trend concerns the ligand core. Anchors with the more flexible 2,2'-bipyridine part (**8** and **9**) outperform the anchors with the rigid neocuproine (**10** and **11**) in terms of efficiency. 2,2'-bipyridine enables free rotation along the C-C bond connecting both pyridine rings. This enables anchors, bearing such a ligand core, to anchor to the surface in many different conformations. It is possible, that the more flexible ligands **8** and **9** anchor to the surface in the thermodynamic and steric most favourable way, which leads to a high surface coverage and strong binding. It isn't necessarily the best orientation to form a chelating coordination with a copper(I) centre, nevertheless, surface modification remains labile, with anchoring groups detaching and reattaching to the surface. This lability enables the anchoring ligands to re-orientate on the surface in such a way, that both N-atoms are positioned *cis* to each other and enable chelating coordination to copper(I), as drawn in Scheme 25. The heteroleptic complexes then probably undergo a dynamic process, to find their most favourable and stable connection to the TiO_2 surface. This could be the reason why efficiencies of bisdiimine copper(I) based DSSCs tend to vary within the first seven days after fabrication of the solar cells.

Dye	J_{SC} / mA cm^{-2}	V_{OC} / mV	*ff* / %	η / %	Relative η / %
On the day of sealing the cells					
[Cu(**8**)(**1**)]$^+$	2.01	388	49	0.38	6.4
[Cu(**8**)(**1**)]$^+$	2.61	424	54	0.60	10.1
[Cu(**9**)(**1**)]$^+$	4.67	511	73	1.75	29.4
[Cu(**9**)(**1**)]$^+$	5.09	511	73	1.91	32.0
[Cu(**10**)(**1**)]$^+$	1.06	412	71	0.31	5.2
[Cu(**10**)(**1**)]$^+$	1.59	410	72	0.47	7.9
[Cu(**11**)(**1**)]$^+$	2.95	423	72	0.90	15.1
[Cu(**11**)(**1**)]$^+$	3.06	421	72	0.93	15.6
N719	13.75	641	68	5.96	100

Table 12: Solar cell measurements of complexes [Cu(**8**)(**1**)]$^+$, [Cu(**9**)(**1**)]$^+$, [Cu(**10**)(**1**)]$^+$ and [Cu(**11**)(**1**)]$^+$ with values obtained at the day of sealing the cells.

Anchoring ligands **10** and **11**, with the rigid neocuproine ligand core, can only coordinate to a surface in their conformation drawn in Scheme 27. It is very likely, that already attached anchoring ligands (of the same molecule) hinder the binding of following molecules, which leads to an obstruction over the surface. Another disadvantage could be increased π-π interactions between anchored molecules, which will be stronger in the less flexible neocuproine based ligands **10** and **11**, compared to the 2,2'-bipyridine based anchors **8** and **9**, simply by considering the relative flexibility of the anchors. π-π stacking of dye molecules is disadvantageous, as it enables additional excited state decay pathways. In bisdiimine copper(I) based dyes another problem arises, as close stacked anchoring ligands attached to the surface could sterically hinder the complexation with a copper(I) centre and the ancillary ligand. A bit of flexibility is given by the anchoring group itself, but in general ligands **10** and **11** are expected to bind less efficiently and strongly to a TiO_2 surface, than **8** and **9**. The corresponding *J*/*V* curves are displayed in Fig. 28. The best performing dye is [Cu(**9**)(**1**)]$^+$ with the highest V_{OC} and J_{SC} values. The second best dye is [Cu(**11**)(**1**)]$^+$ with decreased values for V_{OC} and J_{SC}. Both [Cu(**9**)(**1**)]$^+$ and [Cu(**11**)(**1**)]$^+$ use a (1-cyanovinyl)phosphonic acid anchoring group, which clearly outperforms the cyanoacrylic acid anchors present in [Cu(**8**)(**1**)]$^+$ and [Cu(**10**)(**1**)]$^+$. The solar cell performance of [Cu(**8**)(**1**)]$^+$ and [Cu(**10**)(**1**)]$^+$ is mainly influenced by the anchoring group and not so much by the ligand core, as both perform in a similar range. A reason could be the less strong binding of carboxylic acids to TiO_2 in our stepwise assembly procedure. Fewer anchoring molecules attached to the surface cancel out possible stacking of **10** and the lability of the anchoring group possibly leads to the poor cell performance. It is noteworthy,

that [Cu(**8**)(**1**)]$^+$ and [Cu(**9**)(**1**)]$^+$, both constructed with a 2,2'-bipyridine ligand core, show J_{SC} values almost doubled compared to their neocuproine based analogues [Cu(**10**)(**1**)]$^+$ and [Cu(**11**)(**1**)]$^+$. This validates, that the flexibility present in 2,2'-bipyridine based anchoring ligands, enhances the performance of heteroleptic bisdiimine copper(I) based dyes, due to increased electron injection into the semiconductor surface. The increased V_{OC} of [Cu(**9**)(**1**)]$^+$, compared to the other heteroleptic dyes could be due to decreased recombination in this complex.

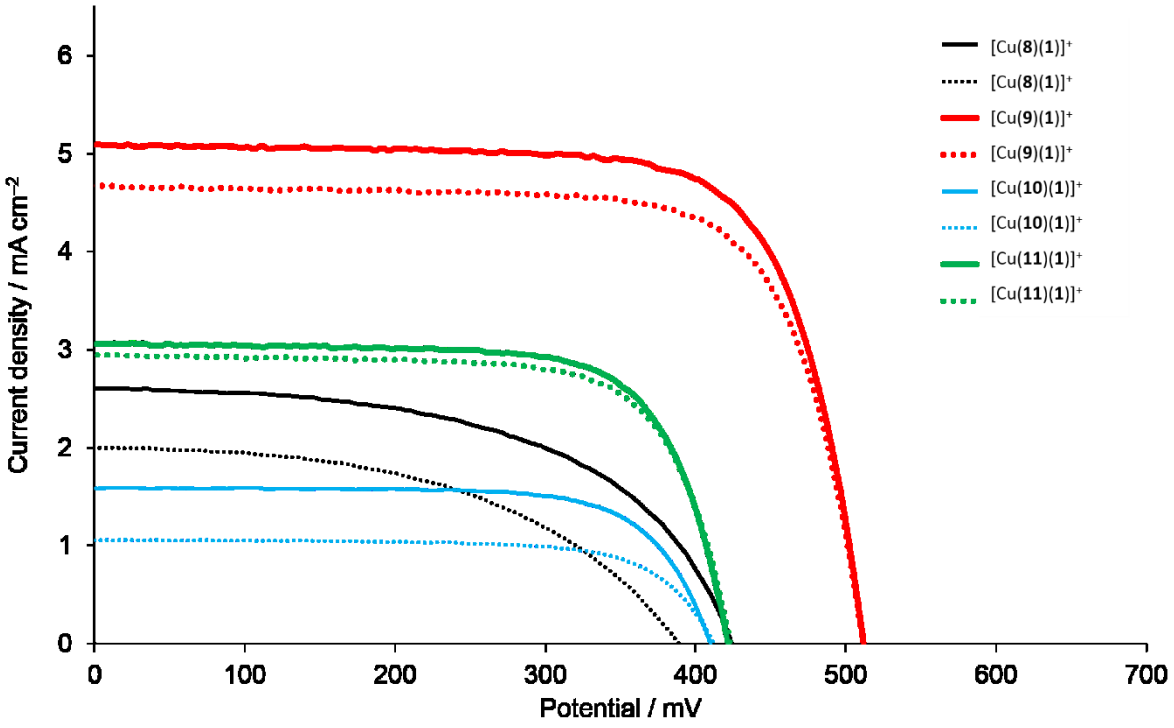

Fig. 28: *J*/*V* curves recorded for duplicate cells of complexes [Cu(**8**)(**1**)]$^+$, [Cu(**9**)(**1**)]$^+$, [Cu(**10**)(**1**)]$^+$ and [Cu(**11**)(**1**)]$^+$ on the day of sealing the cells.

The electron injection behaviour of dyes on a TiO_2 surface can be monitored by EQE measurements. Fig. 29 displays the EQE spectra of complexes [Cu(**8**)(**1**)]$^+$, [Cu(**9**)(**1**)]$^+$, [Cu(**10**)(**1**)]$^+$ and [Cu(**11**)(**1**)]$^+$ (duplicate cells are omitted) and validates beneficial effects of a 2,2'-bipyridine a ligand core with a (1-cyanovinyl)phosphonic acid present in [Cu(**9**)(**1**)]$^+$. Increased electron injection trough the anchoring ligand, leads to the highest EQE value (42.7%) in this series. Additionally, a slight redshift of the EQE_{max} to 490 nm is observed.

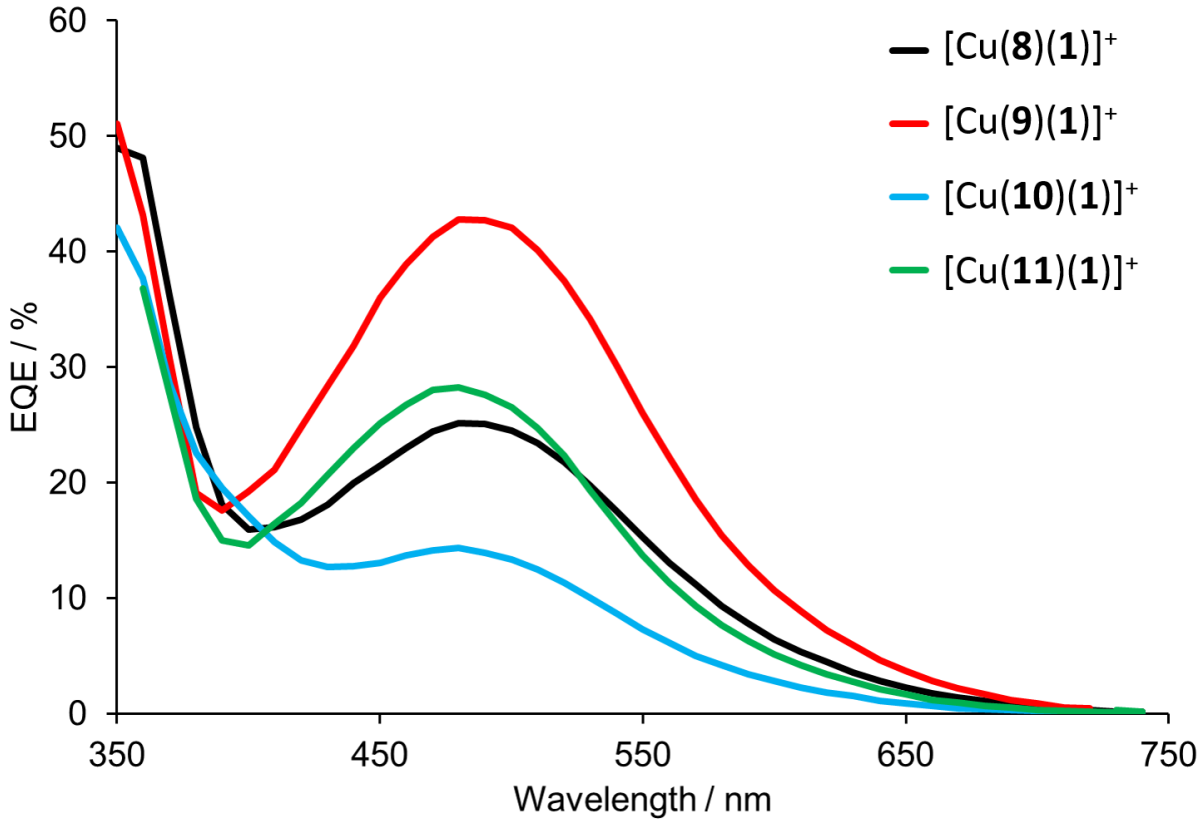

Fig. 29: EQE spectra for duplicate cells of complexes [Cu(**8**)(**1**)]$^+$, [Cu(**9**)(**1**)]$^+$, [Cu(**10**)(**1**)]$^+$ and [Cu(**11**)(**1**)]$^+$ on day of sealing the cells.

In conclusion a 2,2'-bipyridine ligand core is advantageous over a neocuproine ligand core and phosphonic acid anchoring groups outperform carboxylic acid anchoring groups in bisdiimine copper(I) based dyes. Both these findings agree with reported results. Especially neocuproine based ligands, which were rarely studied as anchors in copper(I)-based dyes can be neglected for future studies, although their great potential as ancillary ligands was demonstrated in previous studies[20, 86].

8.2.2 Anchors 8, 9, 10 and 11 combined with ancillary ligand 3

In previous chapters, the beneficial effect of introducing CF_3 groups on the ancillary ligand side were discussed. Increased J_{SC} values were obtained by using ancillary ligand **3** (Scheme 19), bearing one CF_3 group in 6 position of 2,2'-bipyridine. This ligand is used in the current section to validate trends found for anchoring ligands **8**, **9**, **10** and **11** combined with the simple ancillary ligand **1**. It is expected, that the general trend among anchors remains the same, with

anchor **9** outperforming the others by far. Data from solar simulator measurements on the day of sealing the cells is displayed in Table 13.

Dye	J_{SC} / mA cm^{-2}	V_{OC} / mV	*ff* / %	η / %	Relative η / %
On the day of sealing the cells					
[Cu(**8**)(**3**)]$^+$	2.84	447	70	0.90	15.1
[Cu(**8**)(**3**)]$^+$	2.17	427	69	0.64	10.7
[Cu(**9**)(**3**)]$^+$	6.59	547	71	2.56	43.0
[Cu(**9**)(**3**)]$^+$	6.59	548	70	2.52	42.3
[Cu(**10**)(**3**)]$^+$	1.89	461	71	0.62	10.4
[Cu(**10**)(**3**)]$^+$	1.51	438	70	0.46	7.7
[Cu(**11**)(**3**)]$^+$	3.53	445	70	1.09	18.3
[Cu(**11**)(**3**)]$^+$	2.30	432	69	0.68	11.4
N719	13.75	641	68	5.96	100

Table 13: Solar cell measurements of complexes [Cu(**8**)(**3**)]$^+$, [Cu(**9**)(**3**)]$^+$, [Cu(**10**)(**3**)]$^+$ and [Cu(**11**)(**3**)]$^+$ with values obtained at the day of sealing the cells.

The general trend from the previous section is confirmed by this study. Anchor **9** forms a heteroleptic copper(I) complex with ancillary ligand **3** and outperforms the other anchor by far. It shows an increased J_{SC} (6.59 mA cm^{-2}) and V_{OC} (547 mV) compared to the heteroleptic complex [Cu(**9**)(**1**)]$^+$ from the previous study. Consistent efficiencies for duplicate cells of [Cu(**9**)(**3**)]$^+$ were obtained with values of 2.56% (43.0% relative to **N719**) and 2.52% (42.3% relative to **N719**).

8.2.3 Standard anchor 4 vs. (1-cyanovinyl)phosphonic acid anchor 9

The last study of this series of new anchors highlights a comparison of standard anchor **4** with the best of the four new anchoring ligands, anchor **9**. Anchors **4** and **9** both consist of the same ligand backbone and only vary in terms of their anchoring domain. Both use a phosphonic acid to anchor to a semiconductor surface, but anchor **9** has a slightly longer spacer via the vinyl group and benefits from the electron withdrawing properties of the cyano group. Enhanced binding via C≡N–TiO_2 coordination might be possible[43]. Table 14 shows results of the comparison of [Cu(**9**)(**3**)]$^+$ with [Cu(**4**)(**3**)]$^+$.

Dye	J_{SC} / mA cm^{-2}	V_{OC} / mV	*ff* / %	η / %	Relative η / %
On the day of sealing the cells					
[Cu(**9**)(**3**)]$^+$	6.59	547	71	2.56	43.0
[Cu(**9**)(**3**)]$^+$	6.59	548	70	2.52	42.3
[Cu(**4**)(**3**)]$^+$	6.30	585	68	2.51	42.1
[Cu(**4**)(**3**)]$^+$	6.01	576	66	2.28	38.3
N719	13.75	641	68	5.96	100

Table 14: Solar cell measurements of complexes [Cu(**9**)(**3**)]$^+$ and [Cu(**4**)(**3**)]$^+$ with values obtained at the day of sealing the cells.

[Cu(**9**)(**3**)]$^+$ outperforms [Cu(**4**)(**3**)]$^+$ in terms of J_{SC} (6.59 mA cm^{-2} vs. 6.30 mA cm^{-2}), but shows a slightly lower V_{OC} (547 mV vs. 585 mV). Fill factors of all duplicate cells are similar, differences in J_{SC} and V_{OC} values compensate for each other and overall, both heteroleptic complexes show very similar efficiencies of 2.56% and 2.51% (42.3 and 43.0% relative to a **N719** reference cell).

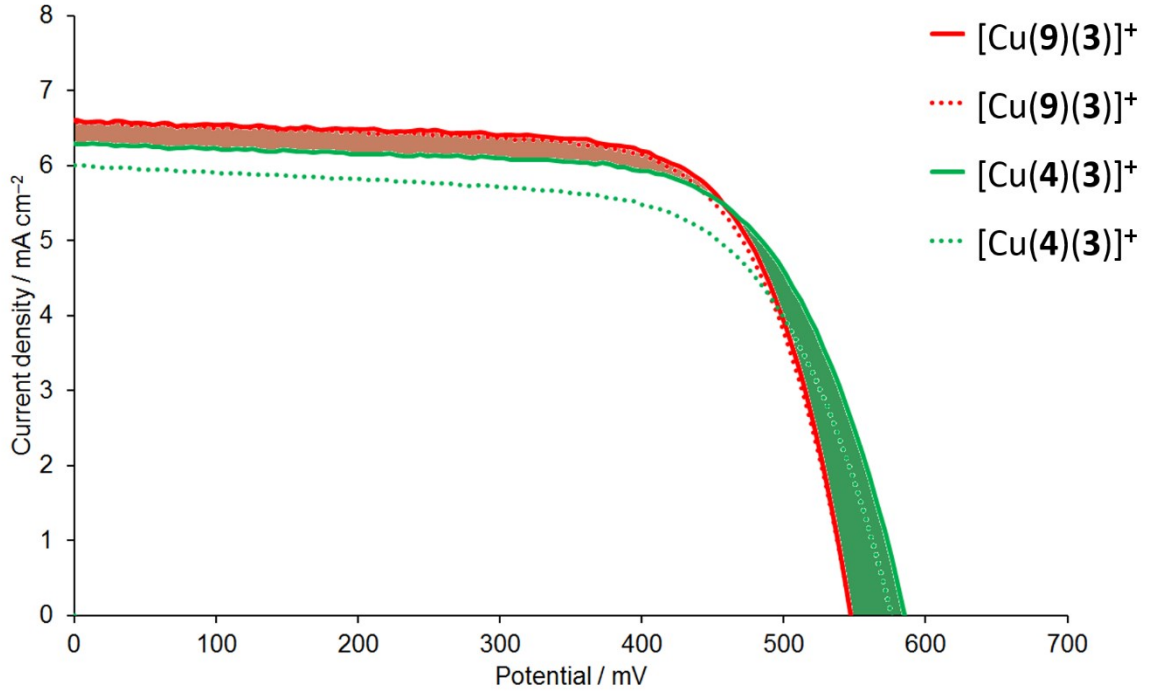

Fig. 30: *J*/*V* curves recorded for duplicate cells of complexes [Cu(**9**)(**3**)]$^+$ and [Cu(**4**)(**3**)]$^+$ on the day of sealing the cells. The red filling highlights the gain in J_{SC} for [Cu(**9**)(**3**)]$^+$ and the green filling the gain in V_{OC} for [Cu(**4**)(**3**)]$^+$. The area of the red and green filling is similar, which leads to similar efficiencies obtained for both complexes.

The *J*/*V* curves visualize the increase in J_{SC} for [Cu(**9**)(**3**)]$^+$, which is compensated by a loss in V_{OC} (Fig. 30) compared to [Cu(**4**)(**3**)]$^+$. [Cu(**4**)(**3**)]$^+$ has a higher EQE_{max} of 53.43% at 490 nm

and is balanced out by $[Cu(\mathbf{9})(\mathbf{3})]^+$ having a broader absorption and a slight red-shift, with an EQE_{max} = 50.28% at 490 nm (Fig. 31).

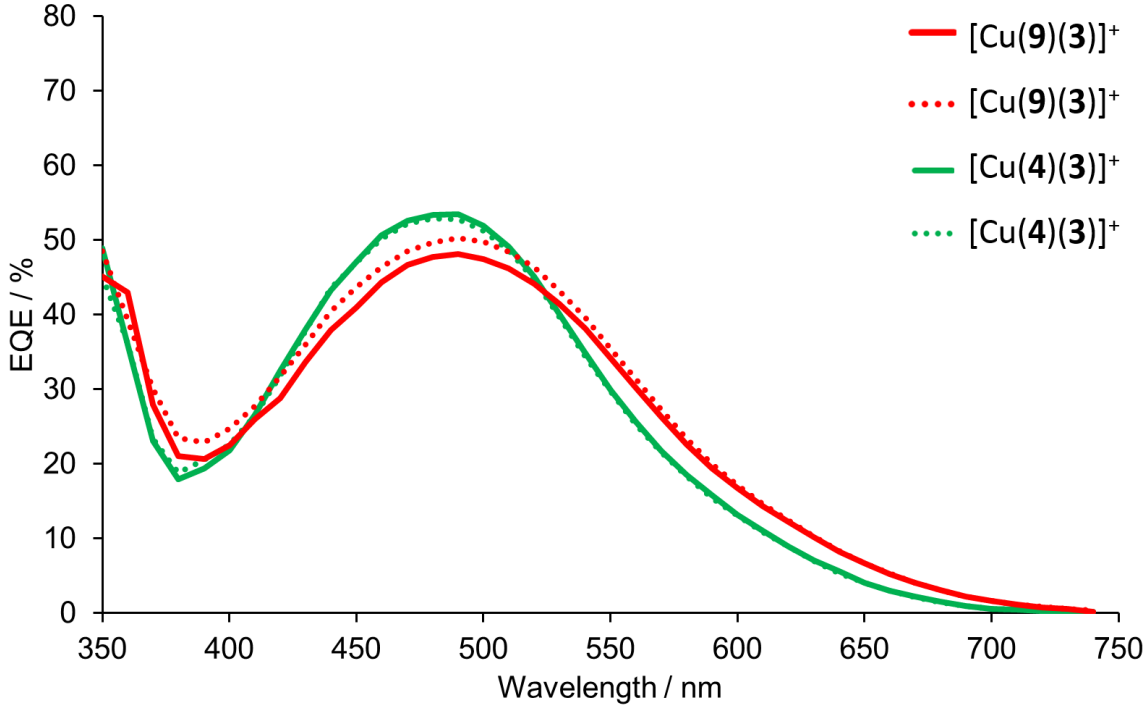

Fig. 31: EQE spectra for duplicate cells of complexes $[Cu(\mathbf{4})(\mathbf{3})]^+$ and $[Cu(\mathbf{9})(\mathbf{3})]^+$ on day of sealing the cells. $[Cu(\mathbf{9})(\mathbf{3})]^+$ benefits from a red-shift and broader absorption compared to $[Cu(\mathbf{4})(\mathbf{3})]^+$.

8.2.4 Electrochemical impedance spectroscopy

To understand the improved performance of anchor **9** (bpy-core, (1-cyanovinyl)phosphonic acid) compared to **8**, **10** and **11**, EIS measurements of the corresponding complexes with ancillary ligand **3** were done. The beneficial effect of carboxylic acid anchoring groups was discussed in the introduction. Cyanoacrylic acids are known for their good charge injection abilities, but show weaker anchoring abilities compared to phosphonic acids. In bisdiimine copper(I) dyes, assembled in the step wise fashion carboxylic acids are always outperformed by their phosphonic acid counter parts. This trend was confirmed in the *J*/*V* measurements and is supported by the EIS measurements. Complexes $[Cu(\mathbf{8})(\mathbf{3})]^+$ and $[Cu(\mathbf{10})(\mathbf{3})]^+$ anchoring to the surface via carboxylic acids should show high electron injection, thus a high capacitance. When reflecting the J_{SC} and V_{OC} values and the overall performance, it is clear, that this assumption is not appropriate. Indeed $[Cu(\mathbf{8})(\mathbf{3})]^+$ and $[Cu(\mathbf{10})(\mathbf{3})]^+$ show a low C_μ, which implies, that few electrons got injected into the semiconductor. The reason for this low injection

could be weaker binding and less dye coverage. The other important parameters the recombination resistance and the transport resistance also resemble the weak performance of carboxylic anchor complexes. It is difficult to attribute values found in EIS measurements to the structural properties of a given anchor, when important parameters, like dye coverage and binding strength of anchoring ligands is not known. The DSSC efficiencies of complexes $[Cu(\mathbf{8})(\mathbf{3})]^+$, $[Cu(\mathbf{9})(\mathbf{3})]^+$, $[Cu(\mathbf{10})(\mathbf{3})]^+$ and $[Cu(\mathbf{11})(\mathbf{3})]^+$ differs tremendously from 0.46% (for $[Cu(\mathbf{10})(\mathbf{3})]^+$) to 2.56% (for $[Cu(\mathbf{9})(\mathbf{3})]^+$), which is most likely due to the stronger binding phosphonic acid anchoring group and the more flexible bpy ligand core.

Referring to the EIS studies of chapter 7, it is much more effective to compare two dyes, that perform in a similar efficiency range. Table 15 illustrates EIS data from the heteroleptic complexes $[Cu(\mathbf{4})(\mathbf{3})]^+$ (**4** = the standard phosphonic acid anchor) and $[Cu(\mathbf{9})(\mathbf{3})]^+$ (**9** = the new (1-cyanovinyl)phosphonic acid anchor). The differences in the *J*/*V* measurements can be brought back to mind by looking at Fig. 30. $[Cu(\mathbf{4})(\mathbf{3})]^+$ outperforms $[Cu(\mathbf{9})(\mathbf{3})]^+$ in V_{OC}, but shows a lower J_{SC}. The higher V_{OC} of $[Cu(\mathbf{4})(\mathbf{3})]^+$ is mainly related to the increased R_{rec}, which is almost doubled compared to $[Cu(\mathbf{9})(\mathbf{3})]^+$. The increase in J_{SC} for $[Cu(\mathbf{9})(\mathbf{3})]^+$ is related to the lower R_t. Similar to V_{OC} and J_{SC} in *J*/*V* measurements, are R_t and R_{rec} compensating for each other in the EIS measurements and both complexes show a similar DSSC efficiency.

Dye	R_t / Ω	R_{rec} / Ω	C_μ / µF	R_{Pt} / Ω	C_{Pt} / µF	τ / ms	L_d/L
$[Cu(\mathbf{4})(\mathbf{3})]^+$ cell 1	57	151	460	52	5	70	1.6
$[Cu(\mathbf{4})(\mathbf{3})]^+$ cell 2	62	156	388	52	4	60	1.6
$[Cu(\mathbf{9})(\mathbf{3})]^+$ cell 1	36	83	325	28	5	27	1.5
$[Cu(\mathbf{9})(\mathbf{3})]^+$ cell 2	51	86	346	42	5	30	1.3

Table 15: High light intensity impedance measurements (22 mW cm^{-2}).

8.3 Conclusion

Four new anchoring ligands **8-11** were synthesized and their performance as heteroleptic copper(I) dyes combined with two ancillary ligands **1** and **3** was investigated. A general trend was found, for anchors bearing 2,2'-bipyridine ligand cores (**8** and **9**) outperforming those with neocuproine ligand cores (**10** and **11**). Anchors **9** and **11**, substituted with a (1-cyanovinyl)phosphonic acid group showed increased photon to current efficiencies compared to their analogues anchors **8** and **10**, which use a cyanoacrylic acid as anchoring domain. The ancillary ligand has a big impact on the performance of all anchors as heteroleptic copper(I) dyes. Ancillary ligand **1** combined with the best anchoring ligand **9**, reached an efficiency of 1.91% (32.0% relative to **N719**) on the day of sealing the cells. Changing the ancillary ligand to the previous introduced mono CF_3 ligand **3** boosted the efficiency of all heteroleptic complexes and especially $[Cu(\mathbf{9})(\mathbf{3})]^+$ showed a high efficiency of 2.56% (43.0% relative to **N719**) and a broader EQE-curve towards the red end of the visible spectrum. A comparison of the new anchor **9** with the standard anchor **4** revealed similar overall efficiencies. **9** out performs **4** by a higher J_{SC}, which is compensated by **4** yielding a higher V_{OC}. This series shows that changing the anchoring group has a big impact on the performance of heteroleptic bisdiimine copper(I) complexes as dyes in DSSCs. Changes in anchor architecture can increase cell parameters like J_{SC} and V_{OC}, but the long-awaited replacement of the standard anchor **4** in bisdiimine copper(I) based dyes was not achieved.

In the previous chapters, impact of ancillary ligands, anchors with thiophenediyl spacers, anchors using flexible or rigid ligand cores and different types of anchoring groups were discussed. To complete this systematic investigation of bisdiimine based anchoring ligands, the next chapter will focus on the elongation of the spacer, between ligand core and anchoring group. Additionally, the alkyl groups are attached to these spacers, which are known to reduced electron recombination and dye aggregation[50].

This work was published 2016 in *RSC Advances*[113].

9 LONG SPACERS – TOWARDS ORGANIC 2,2'-BIPYRIDINE BASED SENSITIZERS

In previous chapters a wide range of new anchoring ligands for bisdiimine copper(I) based dyes was presented. Spacers, ligand core and anchoring groups were systematically changed and investigated. The best anchors from each series showed similar overall efficiencies in a heteroleptic copper(I)-complex bound to a TiO_2-semiconductor.

This chapter focuses on another promising modification possible in such a system, the elongation of the spacer, connecting ligand core and anchoring group. It is known, especially from studies of organic sensitizers, that a spatial separation of the electron generating centre and the electron injecting anchoring group can enhance device performance tremendously (see introduction). Upon irradiation an exciton forms. The electron and a positive hole have to be separated to make a solar cell work. The electron should move towards the semiconductor, where it can be injected, and the hole should move in the opposite direction, towards the electrolyte, where the ground state of the dye gets regenerated. If this separation of electron and hole gets larger in terms of space, the probability of recombination between electron and hole decreases. This results in an increased current output, open-circuit voltage and overall efficiency. Organic “push-pull” dyes described in the introduction, were taken as an inspiration. They consist of an electron pushing part, often a triarylamine or a carbazole group and a pulling anchoring group, mainly cyanoacrylic acid, which was introduced in the introduction. Between the pushing and pulling centres, up to six 3-hexyl-thiophenediyl spacers are normally incorporated to decrease recombination[35]. Hexyl chains on the spacers are introduced to increase solubility and more importantly, prevent aggregation of the dyes on the surface, which could lead to additional charge recombination pathways. Another advantage of these groups is their ability to cover the semiconductor surface and decrease vacancies. The steric demanding hexyl chains keep adjacent molecules at a distance, that decreases electronic interactions between these molecules and hinders this decay pathway. One can imagine that hexyl chains interact via van-der-Waals interactions and form net-like arrangements between neighboring molecules on the surface. This decreases vacant sites on TiO_2 and hinders contact between the

semiconductor surface and the electrolyte, which decreases recombination of injected electrons to the electrolyte.

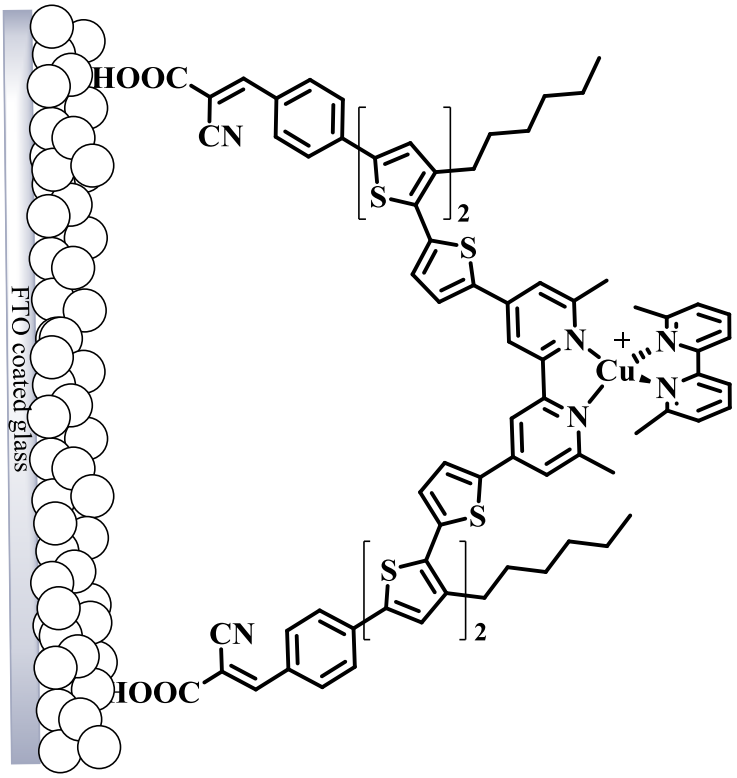

Scheme 29: Bisdiimine copper(I) complexes with a 6,6'-dimethyl-2,2'-bipyridine ligand core, three thiophene-2,5-diyl spacers, a phenylene spacer on each pyridine side and a cyanoacrylic acid anchoring groups. Ligand **1** was tested as the ancillary ligand.

Scheme 29 shows the new modifications to the existing system of heteroleptic bisdiimine copper(I) dyes.

The aim of this study was to use a heteroleptic copper(I) complex as the electron generating and donating centre, which is linked to an anchoring group via 3-hexyl-thiophenediyl spacers. This molecule can be considered a organic-inorganic dye, combining beneficial properties of both systems. Multiple attempts towards the synthesis of anchors with more than two 3-hexyl-thiophenediyls connected to each other (see Scheme 29) were made, but purification was a significant problem and only the synthesis of compound **12** (Scheme 30) was successfully achieved. Compound **12** has a dark red colour and was tested as a purely organic dye and combined with ancillary **1** ligand in a DSSC.

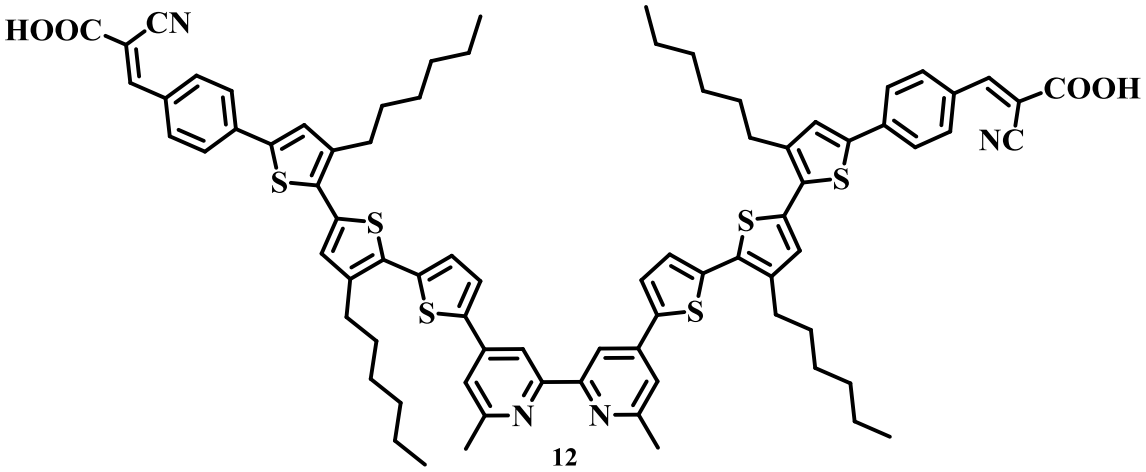

Scheme 30: Compound **12** investigated in this chapter. The bpy core can be considered the electron "pushing" centre and the cyanoacrylic acid acts as the electron "pulling" anchoring group. Both centres are separated by three thiophene-2,5-diyl spacers and a phenylene spacer, which should enhance electron injection and reduce recombination.

9.1 Synthesis and Characterization

Compound **12** was synthesized in 8 steps (Scheme 31 and Scheme 32). In the first two steps the Kröhnke-type pyridine synthesis described in chapter 7 was used to form 4,4'-bis(5-bromothiophen-2-yl)-6,6'-dimethyl-2,2'-bipyridine. The bromine atoms on both thiophenediyl groups enable modifications via Pd-based cross coupling reactions. A double Suzuki-Miyaura coupling with 2.5 equivalents of 3-hexylthiophene-2-boronic acid pinacol ester in the presence of $[Pd(PPh_3)_4]$ and Cs_2CO_3 in dry toluene (microwave radiation, 120 °C, 4h) yielded the first intermediate **12a** in 96.7% yield. Thiophenes are known for their strong reactivity towards electrophilic aromatic substitution[111] with *N*-bromosuccinimide (NBS). Reacting two equivalents of NBS with **12a** in a mixture of DMF/$CHCl_3$ (1/1) at room temperature gave exclusively the α brominated species **12b** in 90.0% yield. Both steps, Pd-cross coupling and NBS bromination, were repeated with **12b** to yield compound **12d** in 68.6% yield over both steps.

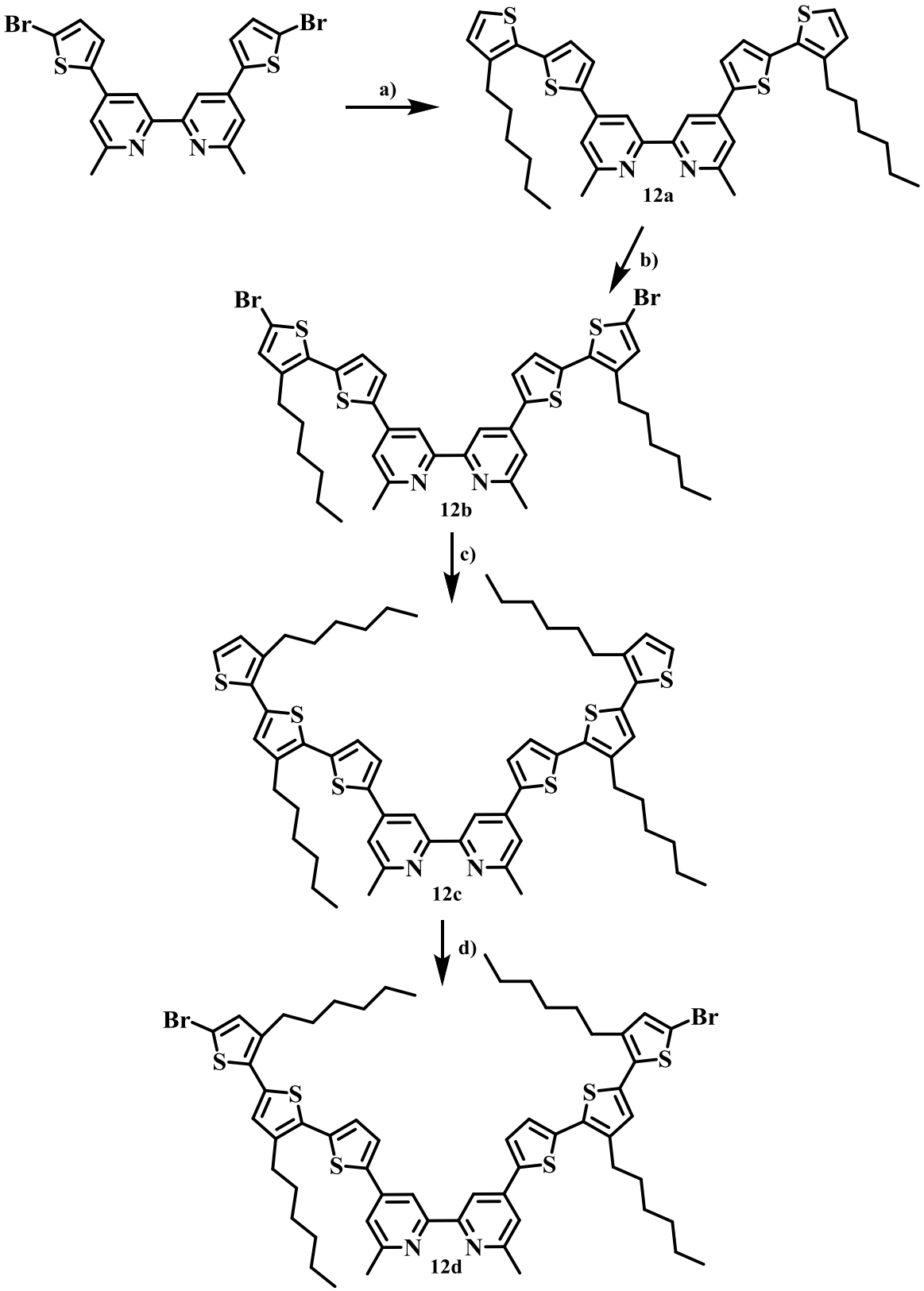

Scheme 31: Synthesis of precursor **12d**; a) 3-hexylthiophene-2-boronic acid pinacol ester, $[Pd(PPh_3)_4]$, Cs_2CO_3 in dry toluene (120 °C, MW radiation, 4h), b) NBS in DMF/$CHCl_3$ (1/1), c) conditions from previous step (a), d) conditions from previous step (b).

Another Suzuki-Miyaura cross coupling reaction of **12d** with 2.5 equivalents of 4-formylphenylboronic acid, in the presence of $[Pd(PPh_3)_4]$ and Cs_2CO_3 using a THF/water mixture as solvent (microwave radiation, 90°C, 2h) yielded the dialdehyde **12e** in 72.6% yield. In chapter 8, condensation reactions of aldehydes with cyanoacetic acid, in the presence of piperidine were discussed and the same conditions were applied in the last step of this synthesis to yield compound **12** in 67.7% yield.

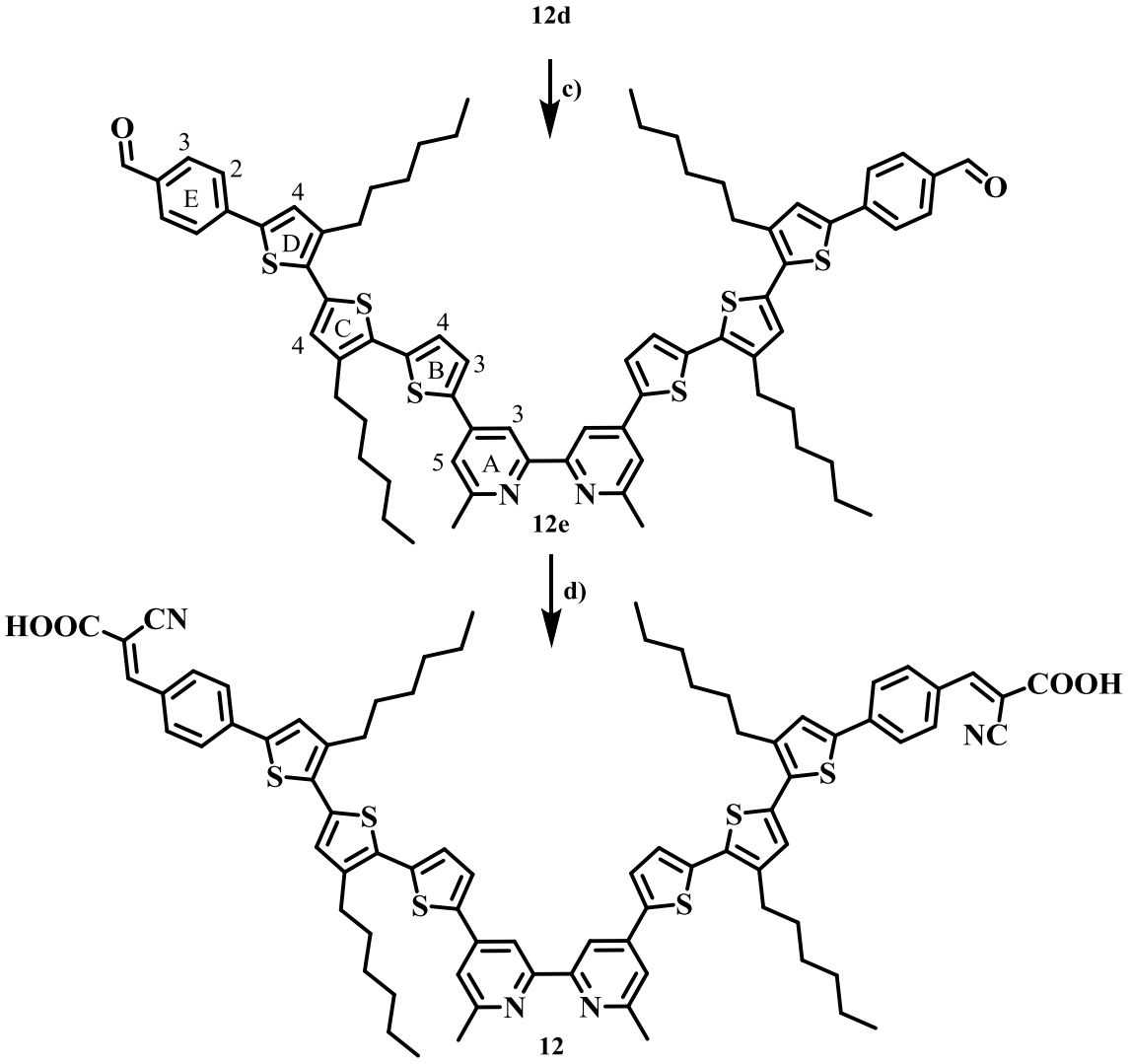

Scheme 32: Synthesis of compound **12**, starting from precursor **12d**. a) 4-formylphenylboronic acid, $[Pd(PPh_3)_4]$, Cs_2CO_3 in THF/water (90 °C, MW radiation, 2h), b) cyanoacetic acid, piperidine in $CHCl_3$.

It is noteworthy, that cross-coupling reaction and NBS bromination worked very well, with isolated yields ranging from 70 to 96%. The slight excess of boronic acid pinacol ester in the cross-coupling reactions lead to almost quantitative conversion and the remaining pinacol ester

educts could easily be removed via crystallization from a mixture of $CHCl_3$/EtOH. Each step was purified via recrystallization from $CHCl_3$/EtOH and column chromatography could be avoided, making the synthetic route towards anchor **12** resource saving and time efficient.

Anchor **12** is only poorly soluble in organic solvents and an NMR spectrum in DMSO-*d6* showed broad peaks, which made assignment of the signals difficult (Fig. 32).

Fig. 32: The 500 MHz ^{1}H NMR spectrum of **12** in DMSO-d_6. Assignment of the peaks was not possible, due to broad peaks and low concentration of the sample. The missing aldehyde signal at $\delta \sim 10$ ppm indicates complete conversion from **12e** to **12**.

A good indication for the formation of **12** is the disappearance of aldehyde signals in the NMR spectrum and the observation of the $[M+H]^+$ ion with *m/z* = 1356.59 in the MALDI-TOF spectrum. All intermediates were fully characterized by ^{1}H NMR spectroscopy and MALDI-TOF mass spectrometry. $^{13}C\{^1H\}$ NMR assignments were possible up to precursor **12b**. Other intermediate compounds couldn't be assigned in the $^{13}C\{^1H\}$ NMR spectra, as multiple signals appeared for equivalent carbon atoms and overlapping signals in the HMBC couldn't be distinguished. For a representative ^{1}H NMR discussion, the precursor **12e** was selected (Fig. 33).

Fig. 33: The 500 MHz ^{1}H NMR spectrum of the dialdehyde **12e** in $CDCl_3$ (*). Chemical shifts were referenced to δ (TMS) = 0 ppm.

NOE cross peaks in the 2D-NOESY spectrum showed coupling of the aldehyde protons to H^{E3}. Following 2D-COSY cross peaks from H^{E3} to H^{E2} and NOEs from H^{E2} to H^{D4}, continuing along the backbone to H^{C4} and H^{B4}, the ^{1}H-spectrum could be readily assigned. Aliphatic protons from alkyl chains located in rings C and D showed overlap and could not be fully assigned. The characteristic methyl singlet of 6,6'-dimethyl-2,2'-bipyridines was observed with a shift of δ 2.72 ppm. Intermediates **12a-12d** were characterized in the same manner and their $[M+H]^+$ molecule ions were confirmed by MALDI-TOF MS. Compounds **12c-12** all showed an intense red colour, due to thiophenediyl groups extending the aromatic π-system. Solution UV-VIS absorption spectra of compound **12** in DMSO at different concentrations revealed aggregation of molecules at concentrations > 0.025 mM (Fig. 34).

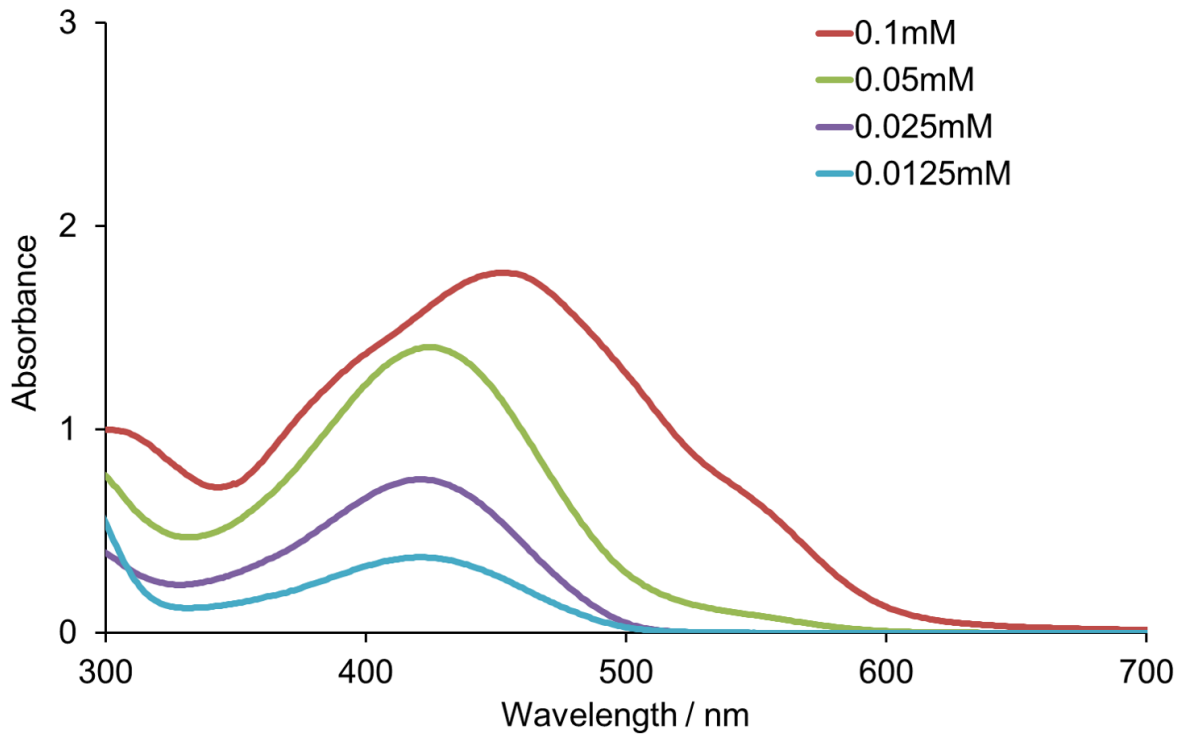

Fig. 34: Solution UV-VIS absorption spectra of compound **12** in DMSO and various concentrations (red: 0.1 mM, green: 0.05 mM, purple: 0.025 mM, blue: 0.0125 mM). At concentrations higher than 0.025 mM a broadening of the absorption into the red region of the spectrum is observed. This effect is most likely due to aggregation of molecules of **12**.

The extinction coefficient for **12** was determined using the 0.025 mM concentration (Fig. 35). An ε_{max} of 30113.8 dm^3 mol^{-1} cm^{-1} at 421 nm was obtained. The absorption maximum of **12** is in a similar region as most $[Cu(bpy)_2]^+$ complexes, but **12** has a roughly three times higher extinction coefficient than the homoleptic complex $[Cu(\mathbf{3})_2][PF_6]$ (see chapter 6). This indicates, that compound **12** has strong light harvesting abilities. A drawback is that compound **12** and most bisdiimine copper(I) complexes absorb at $\lambda \sim 450$ nm. A heteroleptic dye using **12** as an anchoring ligand, combined with an ancillary ligand and copper(I) will most likely benefit little from the MLCT transitions in the copper(I) complex.

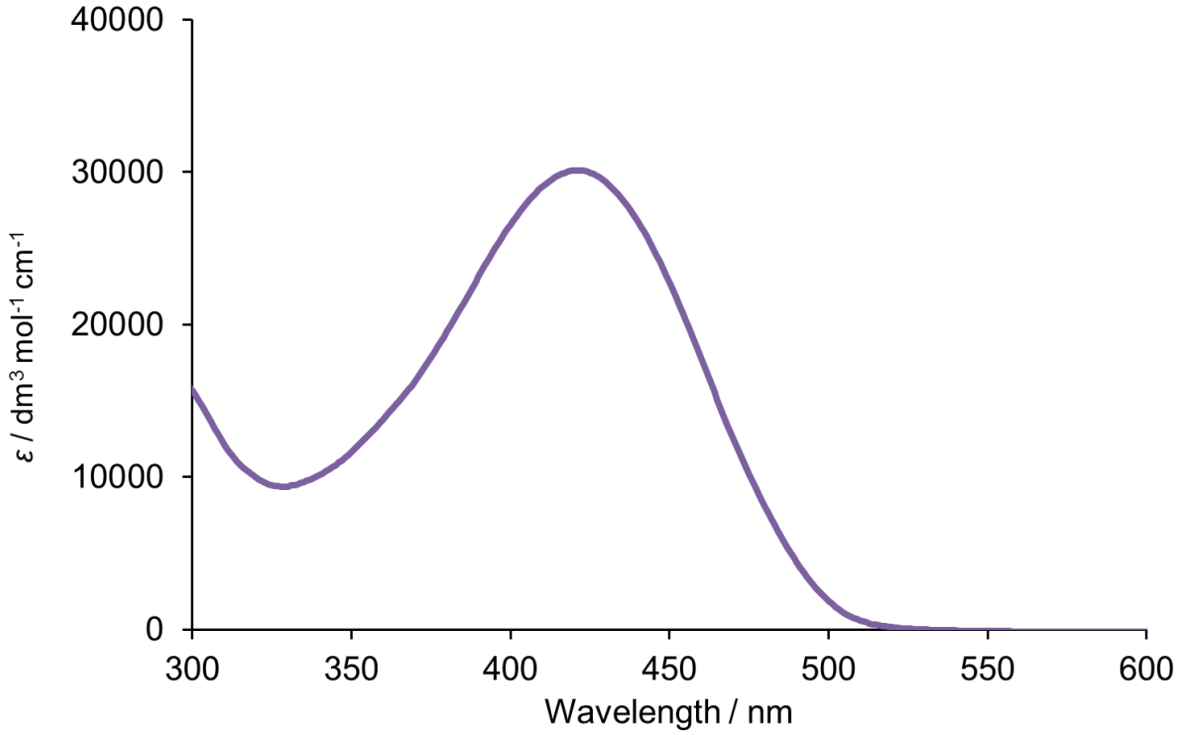

Fig. 35: Solution UV-VIS absorption spectra of compound **12** in DMSO at 0.025 mM concentration. Aggregation is not observed at this concentration. E_{max} = 30113.8 dm^3 mol^{-1} cm^{-1} at 421 nm.

9.2 DSSC performance

The same strategy for DSSC assembly as in chapter 4 was applied. A 1mM solution of compound **12** was used to modify a TiO_2 surface. The intense red colour of the sensitized semiconductor (Fig. 36), lead to an extension of the original plan to investigate **12** as a new anchoring ligand for heteroleptic bisdiimine copper(I) based dyes. The solid state UV-VIS spectra shows some noise for absorptions above 3, due to instrument limitations. In the first experiment the performance of anchor **12** as a purely organic sensitizer is examined and in the following study its performance as an anchor in a heteroleptic bisdiimine copper(I) complex with ancillary ligand **1** is investigated.

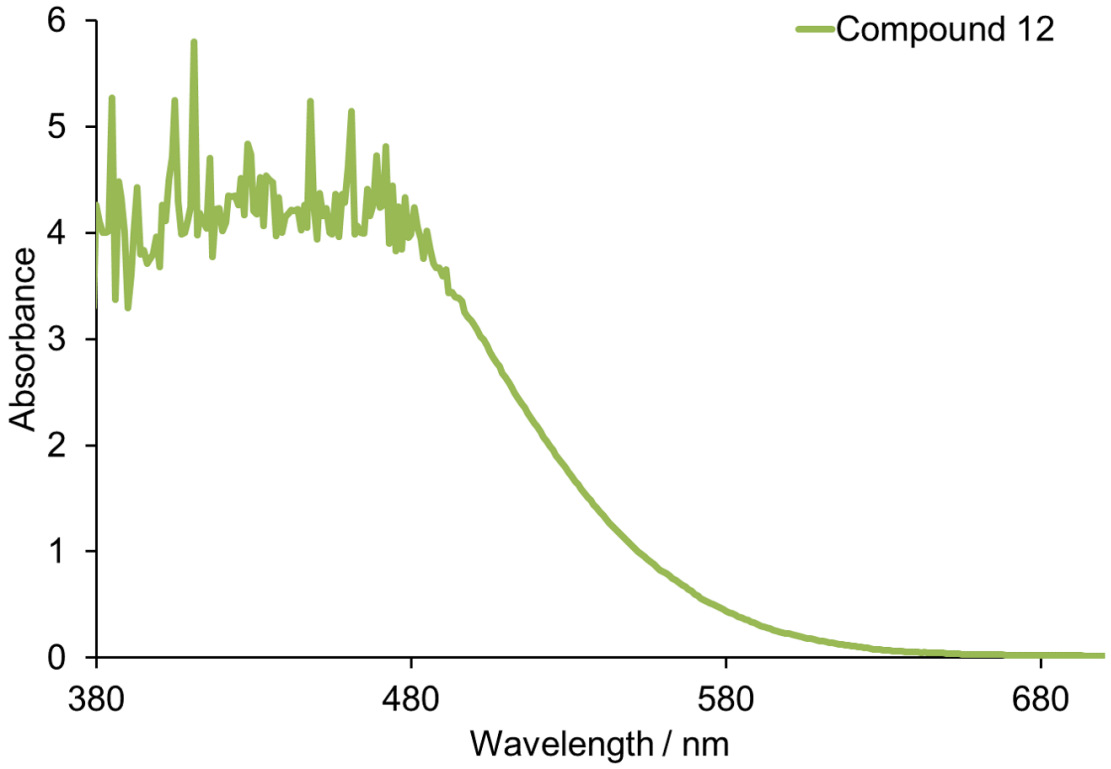

Fig. 36: Solid state absorption spectrum of compound **12**.

9.2.1 Compound 12 as an organic dye in a DSSC

Solar cells sensitized with dye **12** were measured on the day of sealing the cells and 3, 7, 17 and 34 days afterwards. Technical problems with the sun simulator on day 3 lead to inconsistent results and these measurements are excluded here. On day 7, one cell performed very poorly and remained so on days 17 and 34. The reason for the poor performance is illustrated by the fill factor, which decreases over time and can be an indication of cell degradation or leakage. What causes this phenomenon is unclear. Table 16 displays parameters obtained from sun simulator measurements for compound **12** and the **N719** reference cell from the previous chapter.

Dye	J_{SC} / mA cm^{-2}	V_{OC} / mV	*ff* / %	η / %	Relative η / %
On the day of sealing the cells					
Compound **12**	9.38	551	61	3.15	52.9
Compound **12**	9.08	539	63	3.09	51.8
N719	13.75	641	68	5.96	100
7 days after sealing the cells					
Compound **12**	9.52	591	47	2.66	42.4
Compound **12**	9.58	583	64	3.59	57.3
N719	12.80	702	70	6.27	100
17 days after sealing the cells					
Compound **12**	9.30	589	52	2.81	
Compound **12**	9.63	586	67	3.77	
34 days after sealing the cells					
Compound **12**	9.24	592	53	2.90	
Compound **12**	9.68	585	67	3.77	

Table 16: Solar cell measurements of compound **12** with values obtained at days 0, 7, 17 and 34. Efficiencies are set relative to a **N719** reference cell. No reference was measured on days 17 and 34, which should simply highlight the long-term stability of the dye.

Compound **12** performs very well and efficiently as an organic dye in a DSSC. On the day of sealing both duplicate cells reached a J_{SC} of over 9 mA cm^{-2}, which increased for the champion cell (second entry in Table 16) to the highest value on day 34 (9.68 mA cm^{-2}). V_{OC} for duplicate cells range between 539 and 592 mV, which is comparable to values obtained for copper(I) based dyes and in an acceptable range for an I^-/I_3^- electrolyte. The fill factor however, is slightly lower than in bisdiimine copper(I) based DSSCs with values between 63 and 67% for the champion cell. The first cell in this series of duplicate cells (entry 1 in Table 16) performs well on the day of sealing (η = 3.15%, 52.9% relative to **N719**, Fig. 37), but encounters long term stability problems and especially the fill factor drops to ~ 50% in the following measurements. The other cell remains stable over 34 days and all parameters improved during this period to yield the highest J_{SC} (9.68 mA cm^{-2}), an improved V_{OC} (585 mV) and a good fill factor (67%). This leads to an improved overall performance of compound **12**, exhibiting an efficiency of 3.77%, which was reached after 17 days and remained constant up to 34 days after sealing the cells.

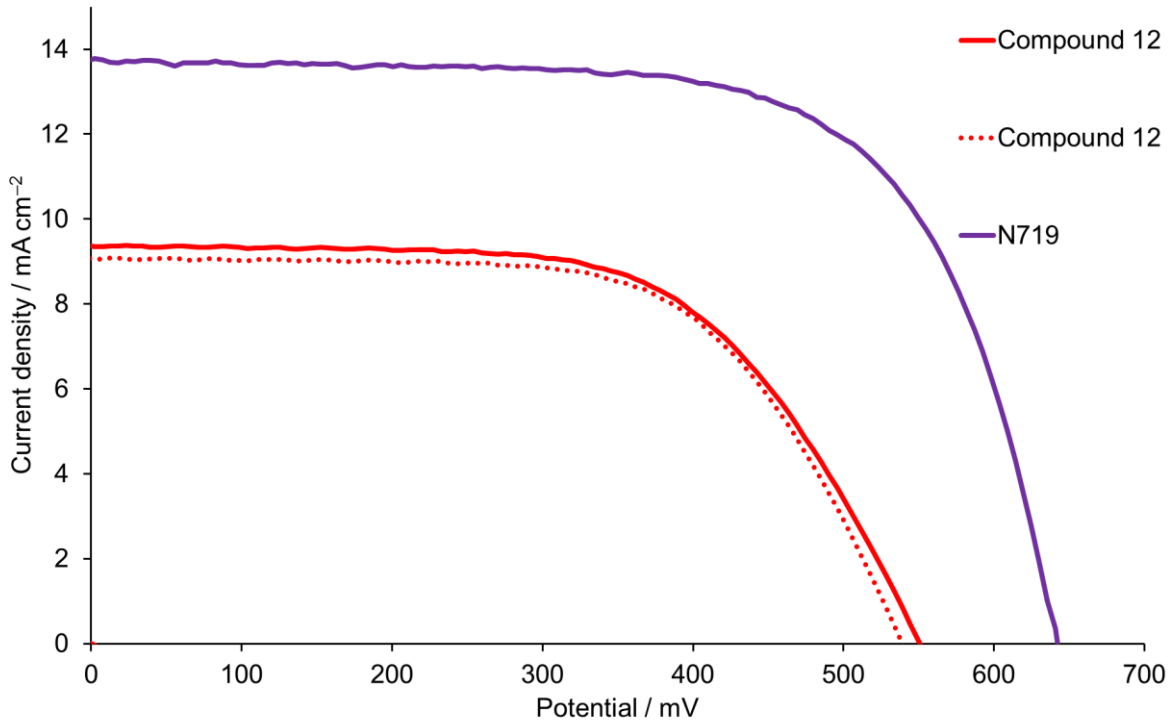

Fig. 37: *J*/*V* curves recorded for duplicate cells of l compound **12** and the **N719** reference cell, on the day of sealing the cells.

The EQE spectra of duplicate cells for DSSCs using compound **12** as dye are displayed in Fig. 38. A broad photon to current conversion over almost the whole visible range was observed (350 – 650 nm), with an EQE_{max} of 72.9% at 450nm. A plateau with EQE values of over 60% ranges from 350 to 550 nm, which highlights the good light harvesting and electron injecting properties of **12**.

Following these promising results, compound **12** was used as an anchoring ligand and combined in an on-surface ligand exchange reaction with ancillary compound **1** and copper(I), to further improve the spectral response.

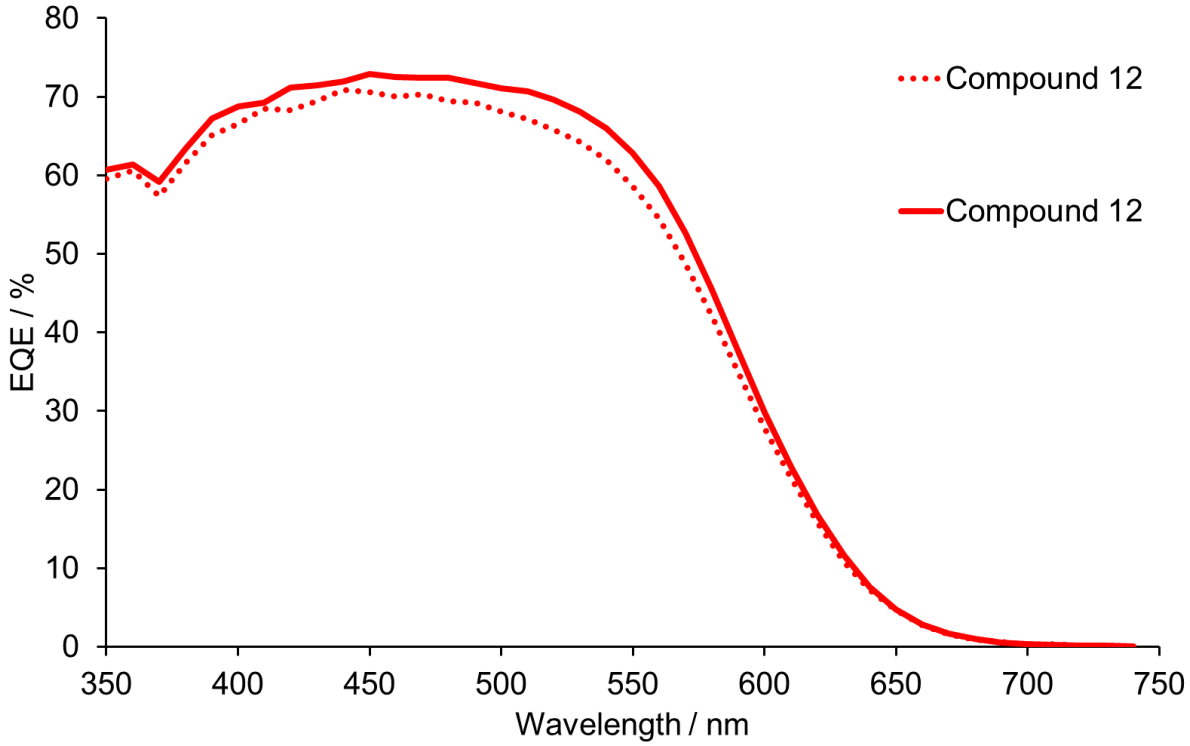

Fig. 38: EQE spectra for duplicate cells of compound **12** on the day of sealing the cells.

9.2.2 An heteroleptic copper(I) complex combining anchor 12 and ancillary ligand 1

DSSCs containing **12** as the dye show good light harvesting abilities. The DSSCs are dark red, similar in colour to heteroleptic bisdiimine copper(I) complexes and exhibit a broader and higher EQE spectrum, than any here presented bisdiimine copper(I) dye. From these considerations it is doubtful, if a system combining two dyes absorbing light in the same range of the visible spectrum (350 – 500 nm) can work together as organic-inorganic bisdiimine copper(I) sensitizer. Another aspect to consider is the conformation of ligand **12**. Being very large with 4 aromatic spacers, it is very unlikely that **12** is orientated on a TiO_2 surface as drawn in Scheme 31. It will probably be twisted around the C-C bond connecting both pyridine units and for such a large molecule a reorientation on the surface towards a *cis* conformation (of the pyridine N atoms) is very improbable. This orientation, however is necessary to form a heteroleptic bisdiimine copper(I) complex of ligand **12**, copper(I) and an ancillary ligand. The last consideration for this system concerns energetics. With these preliminary results it not possible to say, what the energy level the excited state LUMO of ligand **12** and especially of

the excited MLCT state of the theoretical heteroleptic copper(I) centre is. The excited state of ligand **12** is based on photon absorption of the conjugated aromatic π-system, whereas an excited state in a heteroleptic bisdiimine copper(I) complex is a MLCT transition. The MLCT transition should be higher in energy than the organic π*←π transition. This would allow generated electrons to cross from the excited MLCT to the π* state, from where they can be injected into the semiconductor.

Table 17 shows results obtained from combining anchoring ligand **12** with the homoleptic complex [Cu(**1**)$_2$][PF_6] in an on surface ligand exchange reaction described in chapter 4. A colour change of the fabricated solar cells, compared to the ones of ligand **12** only, was not observed, but this is an ambiguous result because **12** has a similar colour to a typical $[Cu(bpy)_2]^+$ chromophore. There is, therefore, no evidence for the formation of a complex $[Cu(\mathbf{12})(\mathbf{1})]^+$ and the copper-containing DSSC had lower efficiencies than the cells with **12** as the dye.

Dye	J_{SC} / mA cm^{-2}	V_{OC} / mV	*ff* / %	η / %	Relative η / %
On the day of sealing the cells					
Compound **12**	9.38	551	61	3.15	52.9
Compound **12**	9.08	539	63	3.09	51.8
"$[Cu(\mathbf{12})(\mathbf{1})]^+$"	7.66	552	66	2.81	47.1
"$[Cu(\mathbf{12})(\mathbf{1})]^+$"	8.03	558	64	2.85	47.8
N719	13.75	641	68	5.96	100

Table 17: Solar cell measurements of compound **12** compared to theoretically formed $[Cu(\mathbf{12})(\mathbf{1})]^+$ on the day of sealing the cells.

9.3 Conclusion and Outlook

Considering the fact, that these are first preliminary results and that the system was not optimized in terms of electrolyte, an efficiency of 3.77% is remarkable for the organic dye **12**. Changing the electrolyte to Co^{2+}/Co^{3+} or the recent studied Cu^{2+}/Cu^+ redox couples, will most likely increase the V_{OC}. The formation of an organic-inorganic bisdiimine copper(I) sensitizer has to be carefully investigated in terms of synthesis and energetic levels of the organic π-system and the metal MLCT. Electrochemical measurements and/or DFT calculations should be carried out to understand the energetics and possibly design a working bisdiimine copper(I) dye.

These aspects will be examined in future studies, as well as the exchange of the cyanoacrylic acid anchoring group in **12** towards the beneficial (1-cyanovinyl)phosphonic acid group from chapter 8 will be investigated.

10 AN ORGANIC P-TYPE DYE BEARING A PHOSPHONIC ACID ANCHORING GROUP

In the previous chapters the research focus lay on the modification of a TiO_2 semiconductor with n-type dyes, to enable photon to electron conversion. These generated electrons are injected into the semiconductor and generate electric current. The hole formed in this process recombines with electrons delivered by the redox electrolyte. The oxidized electrolyte is regenerated by electrons provided by the Pt-counter electrode.

In this chapter a modification of the counter electrode will be discussed. The Pt-electrode is replaced by a NiO-semiconductor, which can be sensitized with a dye, similar to TiO_2 sensitization. The anchored p-type dye on NiO must work in exactly the opposite way as a n-type dye. It has to drain electrons from the semiconductor and deliver them to the redox electrolyte. When this process is viewed in reverse, a p-type dye transports holes from the electrolyte to the NiO semiconductor and injects them there (Scheme 33). The V_{OC} of a p-type solar cell is defined as the potential between the electrolyte and the valence band (VB) of NiO. The J_{SC} is generated by injected holes, which draw electrons into the NiO semiconductor, thus generating electric current. The counter electrode in a p-type solar cell is a Pt-electrode, which now fulfils the role of oxidizing the electrolyte, which can be considered as injecting electrons from the electrolyte into the Pt or injecting holes from the Pt into the electrolyte. The electric circuit is closed, and a p-type solar cell can be measured with the same equipment as for n-type solar cells.

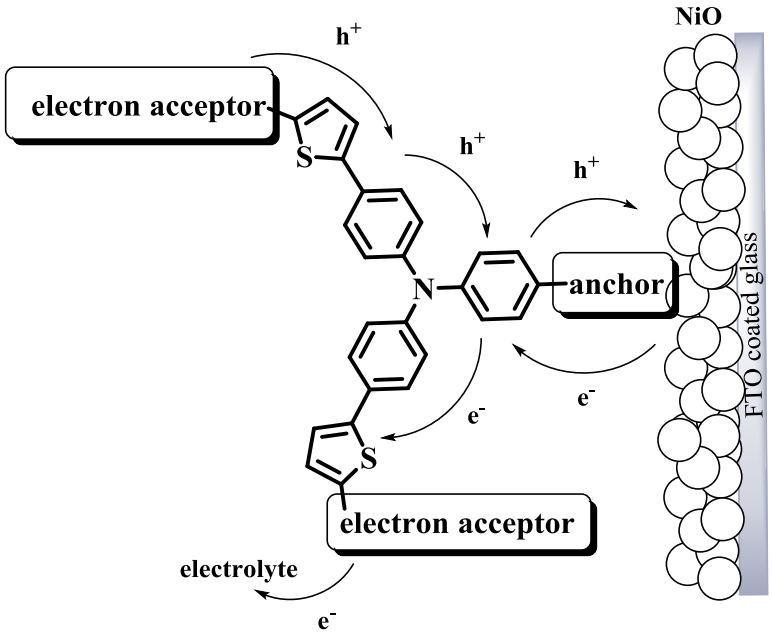

Scheme 33: P-type dye anchored to the photo-cathode (NiO semiconductor). Electron "pushing groups" are close to the surface and electrons are "pulled" away from the semiconductor by electron accepting groups (malononitrile). Reverse transport way is given for hole injection.

In the long term, sensitized p-type and n-type semiconductors can be combined within one cell to generate a so-called tandem solar cell. These tandem solar cells require both n- and p-type dyes to exhibit similar J_{SC} values and a redox electrolyte with a potential between the conduction band of TiO_2 and the valence band of NiO. In an ideal case, the J_{SC} of such a system should increase or at least remain constant, but both V_{OC} of TiO_2 and NiO are combined to the maximum possible V_{OC}. It is defined by energetic niveaus of the CB and the VB and has a theoretical value of 0.9 V. It will boost the overall efficiency of a tandem solar cell, outperforming its single n- or p-type components. Another advantage is the spectral response of this double junction system. Each dye can absorb photons of different wavelengths and convert them into electrons or holes. This increases the theoretical efficiency of a tandem solar cell to over 40%[11].

The main drawback in this technology is the low efficiency and J_{SC} of the p-type solar cell. The main research in both p-type and tandem solar cells is focussed on synthesizing new p-type dyes with increased J_{SC}. Some attempts have been made by the Constable/Housecroft research group towards new p-type dyes. A Ru(II) based inorganic dye $[Ru(bpy)_2(H\mathbf{L})]$ (**L** = (4-(2-phenylpyridin-4-yl)phenyl)phosphonate) has been successfully synthesized and outperforms the standard p-type dye **P1** (Scheme 34)[92]. **P1** is a standard organic p-type dye, with a "push-

pull" architecture optimized for p-type purposes. It anchors to NiO, via a carboxylic acid group. The anchoring group is attached in the 4 position of one phenylene ring of a triphenylamine core. The other phenylene rings are substituted in the 4 position by a thiophenediyl spacer, bearing an electron withdrawing malononitrile group. Upon irradiation, electrons are donated from the triarylamine unit, through the thiophenediyl spacer towards the electron pulling malononitrile group. In reverse, a hole hops from the malononitrile, via the spacer to the triarylamine and gets injected into the NiO semiconductor. The inorganic complex $[Ru(bpy)_2(H\mathbf{L})]$ differs from **P1** in its architecture and especially in the anchoring group. In contrast to **P1** it anchors to the NiO semiconductor via a phosphonic acid and not via a carboxylic acid. **P1** shows a maximum efficiency of 0.057% and $[Ru(bpy)_2(H\mathbf{L})]$ exhibits a maximum of 0.116% on the day of sealing the cells. The Ru(II) dye clearly outperforms **P1**, which might be due to increased absorption of dye on the surface using a phosphonic acid.

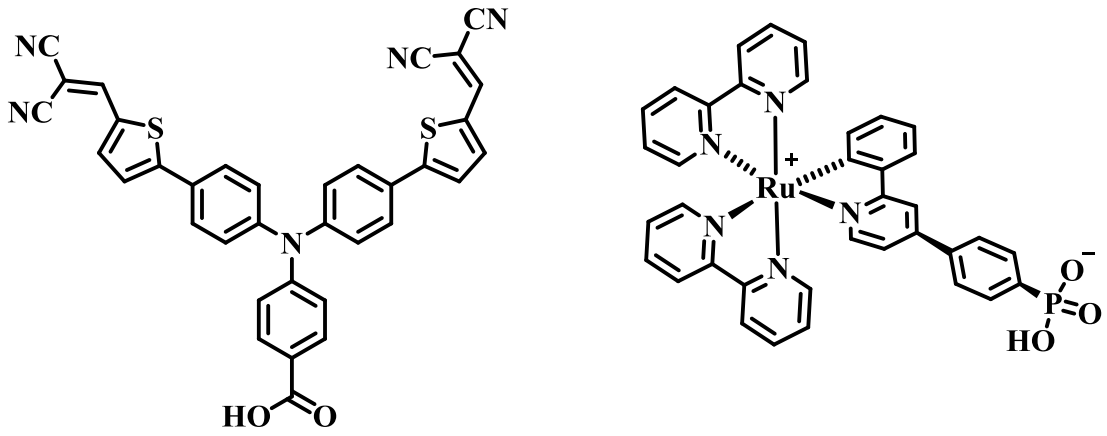

P1 **[Ru(bpy)$_2$(HL)]**

Scheme 34: Structure of the p-type dyes **P1** and $[Ru(bpy)_2(H\mathbf{L})]$ (**L** = (4-(2-phenylpyridin-4-yl)phenyl)phosphonate).

To establish, that phosphonic acid anchoring groups outperform carboxylic acid anchoring groups not only in n-type bisdiimine copper(I) solar cells, but might also work in p-type solar cells was the aim of this study. The analogous molecule to **P1** (compound **13,** Scheme 35), in which we exchanged the carboxylic by a phosphonic acid group, was synthesized and will be investigated in solar cells.

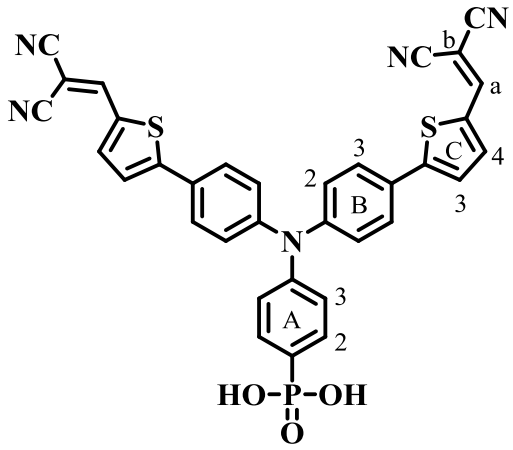

13

Scheme 35: Ligand **13** bearing a phosphonic acid anchoring group and only differs to **P1** in this substitution.

10.1 Synthesis and Characterization

Anchoring ligand **13** was synthesized in 5 steps (Scheme 36). In the first step 4-bromotriphenylamine was reacted with $HPO(OEt)_2$ in a Pd-based cross coupling reaction, using Cs_2CO_3 and catalytic amounts of $[Pd(PPh_3)_4]$ (5 mol%) in dry THF (microwave radiation, 120 °C, 20 min) to yield the phosphonic ester **13a** in 48.8% yield. Phosphonic esters are relatively stable functional groups and don't interfere in the following bromination, coupling or condensation reactions. However, yields for these C-P couplings are rather low (~ 50%), which makes the incorporation of the phosphonic ester functionality in the beginning of the synthesis advantageous. The second step was an NBS bromination in THF at 60°C, which yielded the desired product **13b** in 56.9% yield. The para position of phenyl rings in triphenylamines is most reactive towards bromination with NBS, due to the +M effect of the N atom. In the third step a double Suzuki-Miyaura coupling with 4 equivalents of **L1** (Scheme 36) in the presence of $[Pd(PPh_3)_4]$ and Cs_2CO_3 in dry toluene (microwave radiation, 120 °C, 4h) yielded the dialdehyde intermediate **13c**. Aldehyde groups were transformed into the electron withdrawing methylene-malononitrile functionality, by condensing **13c** with 2.2 equivalent of malononitrile and 4 drops of triethylamine in dry acetonitrile. Compound **13d** was obtained in 68.7% yield as an orange/red oil. The final compound **13** (Scheme 35) was obtained in 68.9% yield after deprotection of the phosphonic ester group to the free phosphonic acid using TMS-Br and aqueous workup.

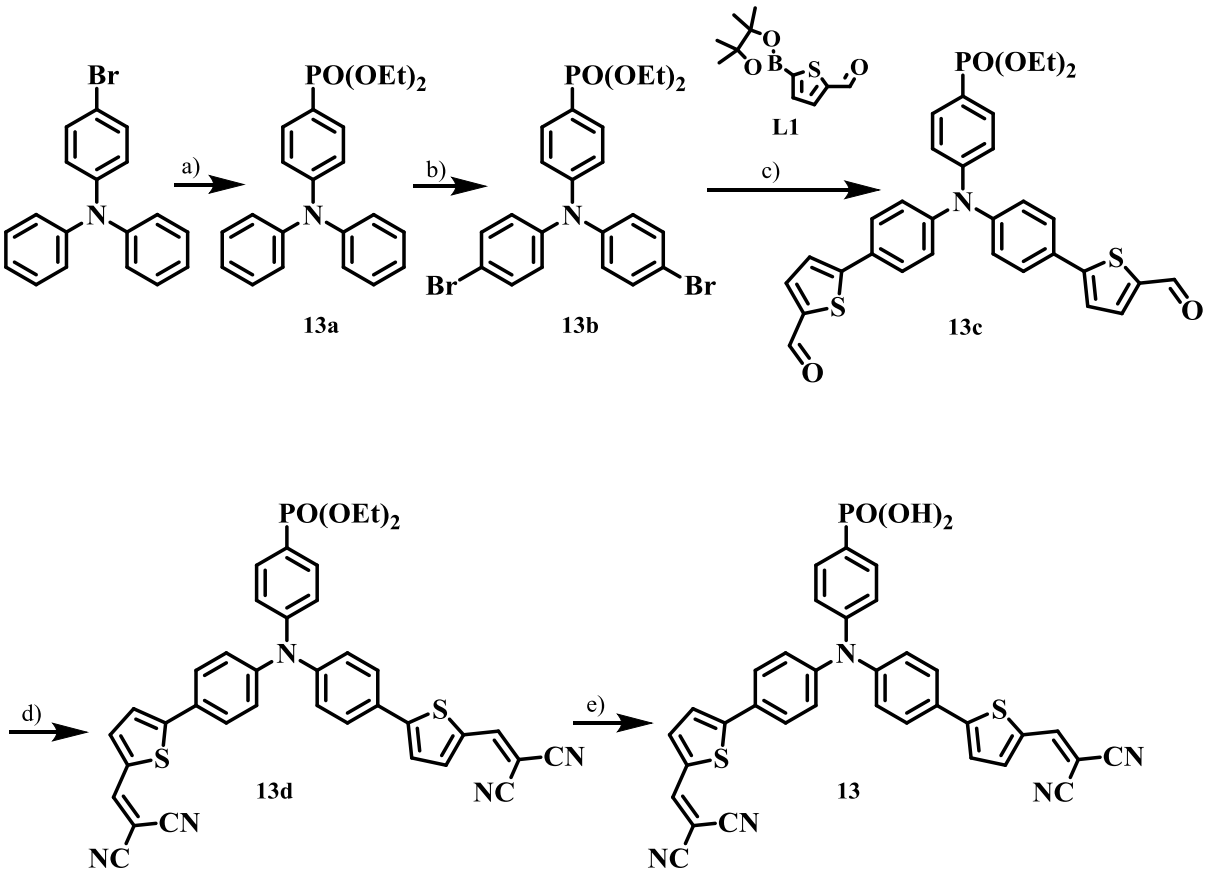

Scheme 36: Synthetic route towards ligand **13**; a) $HPO(OEt)_2$, Cs_2CO_3, $[Pd(PPh_3)_4]$ in dry THF (MW radiation, 120 °C, 20min); b) NBS, THF, 60°C; c) **L1**, Cs_2CO_3, $[Pd(PPh_3)_4]$ in dry toluene (MW radiation, 120 °C, 4h); d) malononitrile, triethylamine (4 drops) in dry acetonitrile; e) Me_3SiBr, CH_2Cl_2, room temperature, 12 h, followed by H_2O.

The organic dye **13** and intermediate steps **13a-13d** were characterized by ^{1}H, $^{13}C\{^{1}H\}$ and $^{31}P\{^{1}H\}$ NMR spectroscopy, ESI-MS, MALDI-TOF and high resolution ESI-MS. ^{1}H NMR assignments benefited from characteristic J_{PH} couplings present in phenylene ring A (Scheme 35). Protons H^{A2} and H^{A3} observed as doublets of doublets with J_{HH} coupling constants of 8.6 Hz between neighbouring protons and J_{PH} coupling constants of 12.7 and 3.4 Hz, respectively. This makes distinguishing between phenylene rings straight forward. Thiophenediyl ring C show doublet signals for H^{C3} and H^{C4} with J_{HH} coupling constants of 4.0 Hz. A singlet with δ = 7.79 ppm is obtained for H^{a}. The ^{1}H NMR assignment was supported by 2D-NOESY and COSY spectra. NOE cross peaks between H^{a}/H^{C4}, H^{C3}/H^{B3} and H^{B2}/H^{A3} completed the assignment.

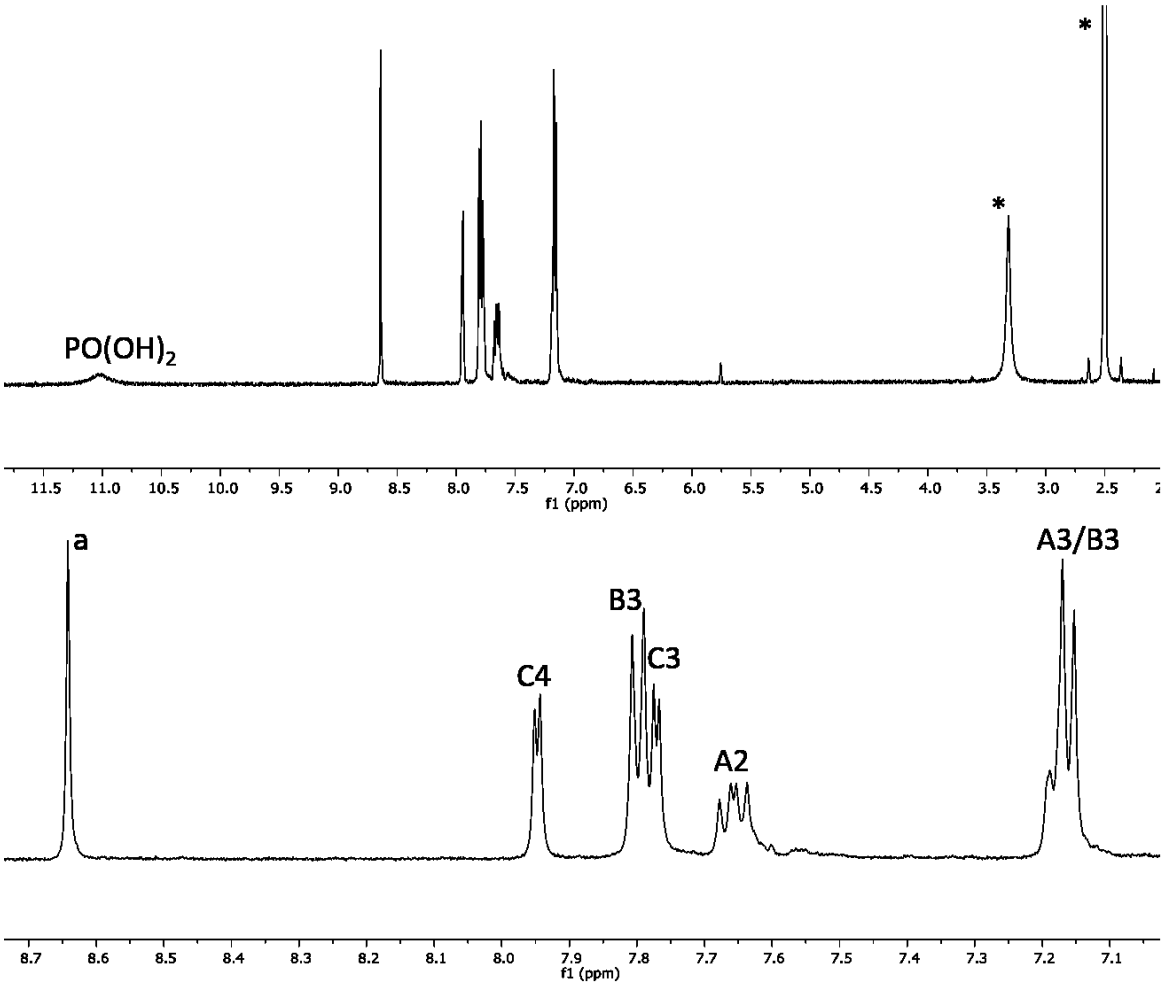

Fig. 39: The 500 MHz ^{1}H NMR spectrum of **13** in DMSO-d_6 (*). Top: Full spectrum with a broad peak for the phosphonic acid protons at δ = 11.03 ppm. Bottom: Zoom into the aromatic region. H^{A2} shows a dd signal, which arises from J_{PH} and J_{HH} couplings.

$^{13}C\{^{1}H\}$ NMR assignment benefited from the phosphorous substituent on ring A, showing doublet signals with J_{PC} coupling constants of 194.2, 15.5, 10.8 and 3.5 Hz for C^{A1}, C^{A2}, C^{A3} and C^{A4}, respectively. The $^{31}P\{^{1}H\}$ NMR spectra of phosphonic ester intermediates **13a-13d** showed a singlet signal between δ 18-20 ppm, which shifted to δ 25.49 ppm in the final compound **13**. All intermediates showed $[M+H]^+$ molecule ion peaks in the MALDI-TOF mass spectrum. An ESI-MS and high resolution ESI-MS of **13** was measured in acetone and basic acetone/water media which revealed a base peak of *m/z* 639.99, corresponding to the $[M-H]^-$ ion. Compound **13** possesses an orange/red colour, which is displayed in the solution UV-VIS spectrum (Fig. 40). **13** has a λ_{max} = 504 nm, which is in a similar range as the reported **P1** dye (λ_{max} = 468 nm in acetonitrile)[117].

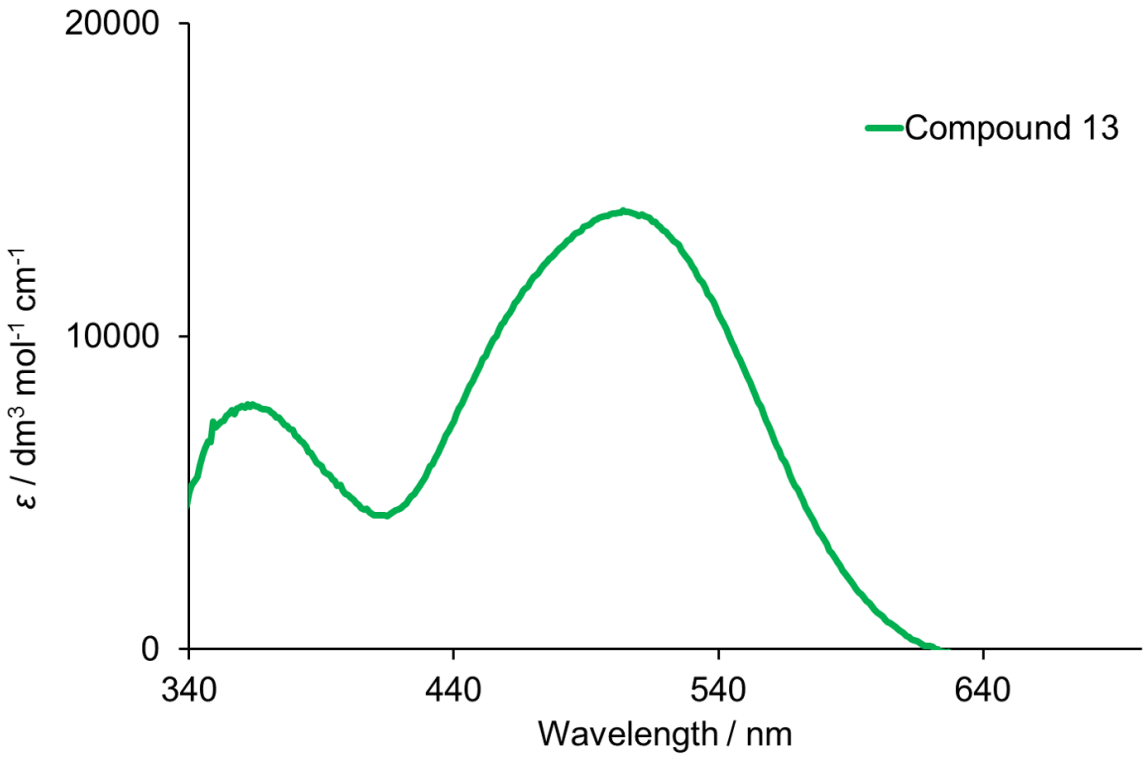

Fig. 40: Solution UV-VIS absorption spectra of compound **13** in acetone at 0.0025 mM concentration.

P-type solar cell investigation will be carried out by Nathalie Marinakis.

11 SUMMARY AND OUTLOOK

The aim of the dye-sensitized solar cell part of this thesis was the investigation of alternative anchoring ligands for bisdiimine copper(I) dyes. The standard anchoring ligand **4** showed good anchoring and electron injection properties on a TiO_2 semiconductor, in the stepwise on-surface approach. Before new anchoring ligands were investigated, a series of unusual ancillary ligands was studied.

As ancillary ligands 6,6'-dimethyl-2,2'-bipyridine (**1**) ligand was compared to the 6,6'-bis(trifluoromethyl)-2,2'-bipyridine (**2**) and 6-trifluoromethyl-2,2'-bipyridine (**3**) ligands. Ligands **2** and **3** showed improved performance in J_{SC}, V_{OC} and η, compared to **1**. These results were surprising as **2** and **3**, bearing electron withdrawing CF_3 group, are counterintuitive to the recommended "push-pull" system for bisdiimine copper(I) dyes. Ligand **3** performed the best among the three ancillary ligands and showed a maximum efficiency of 2.26% (37.2% relative to **N719**) in the heteroleptic complex $[Cu(\mathbf{4})(\mathbf{3})]^+$. It also showed that one blocking group in the 6-position of a 2,2'-bipyridine ancillary ligand is enough to stabilize the distorted tetrahedral geometry in a heteroleptic copper(I) complex bound to a semiconductor surface. The reason for this puzzling performance was not found. Better interaction with the electrolyte, and thus faster dye regeneration might be possible. The more positively shifted oxidation potential of $[Cu(\mathbf{3})_2][PF_6]$, compared to $[Cu(\mathbf{1})_2][PF_6]$ might have a similar effect on the ground state energy level of the corresponding heteroleptic complex and influence recombination and electron lifetimes. Ligand **3** was incorporated as a good performing ancillary ligand in the following studies.

Anchoring ligand **4** has a design principle consisting of three parts. The ligand core is a 6,6'-dimethyl-2,2'-bipyridine, with methyl groups stabilizing the tetrahedral geometry of the copper(I) centre. Phenylene spacers are incorporated in the 4 and 4' positions of the 6,6'-dimethyl-2,2'-bipyridine and each bears a phosphonic acid anchoring group in the 4 positions. The phenylene separates the electron generating centre from the electron injecting anchoring group, enhances electron lifetime and hinders recombination of injected electrons and the corresponding holes. The phosphonic acid anchoring group has a strong affinity for the TiO_2 semiconductor and shows increased binding compared to the more common carboxylic acid. This increase in binding strength seems to affect the performance of bisdiimine copper(I) dyes

significantly. A systematic comparison of cyanoacrylic acid anchoring groups with their analogues (1-cyanovinyl)phosphonic acids confirmed the improved performance of phosphonic acid anchors.

Between ligands, bearing phosphonic acid anchoring groups, a systematic study concerning spacer, ligand core (rigid or flexible) and the incorporation of electron withdrawing cyano groups next to the anchor were investigated. In the first study the phenylene spacer, present in **4**, was changed to a thiophenediyl spacer, substituted with a phosphonic acid group in 4- or 5-position of the thiophenediyl. The position effected J_{SC} and V_{OC} and the best performance in this series was obtained for the 4-thiophenediyl substituted anchoring ligand **6**. It outperformed anchors **4** in J_{SC} and **5** (5-thiophenediyl substituted) in V_{OC} and showed an efficiency of 2.40% (41.7% relative to a **N719**) for the complex [Cu(**6**)(**3**)]$^+$.

The ligand core was changed from a 6,6'-dimethyl-2,2'-bipyridine to a neocuproine to investigate the effect of the flexibility in the anchoring ligand on the performance of a bisdiimine copper(I) DSSC. The studies revealed a clear trend, that flexible anchoring ligands (6,6'-dimethyl-2,2'-bipyridine) outperform rigid ones (neocuproine) by far. The reason might be better anchor coverage and less aggregation for the flexible 6,6'-dimethyl-2,2'-bipyridine based anchors.

The anchoring ligand was changed from a phosphonic acid to a (1-cyanovinyl)phosphonic acid, keeping the phenylene spacer the same. The 1-cyanovinyl)phosphonic acid is the phosphonic acid analogue of the cyanoacrylic acid and it was proposed, that it should benefit from the electron withdrawing cyano group in combination with the strongly binding phosphonic acid functionality. This anchoring group showed a good performance in the bisdiimine copper(I) complex [Cu(**9**)(**3**)]$^+$ with an efficiency of 2.56% (43.0% relative to **N719**), being the highest in the whole series of investigated anchors.

During this systematic investigation the efficiencies for [Cu(**4**)(**3**)]$^+$ (**4** = standard anchor) remained high and were always were close to the efficiencies of the champion cells of the newly synthesized complexes [Cu(**6**)(**3**)]$^+$ (**6** = 4-thiophenediyl phosphonic acid anchor) and [Cu(**9**)(**3**)]$^+$ (**9** = 1-cyanovinyl)phosphonic acid anchor). The two newly synthesized anchors **6** and **9** show good performance in bisdiimine copper(I) based solar cells but are not significantly better than the standard anchor **4**. It is concluded, that phosphonic acids are still the best

anchoring groups for a stepwise on-surface assembly of heteroleptic copper(I) complexes, but, changing the spacers (from **4** to **6**) and incorporating additional electron withdrawing cyano groups (from **4** to **9**) has little positive effect on the overall efficiency of the DSSC. A possible improvement might be the development of a new type of anchoring group, that still has to be found, or the successful incorporation of the silyl anchoring group, discussed in the introduction.

The two outlier studies about long thiophenediyl spacers on 6,6'-dimethyl-2,2'-bipyridine (**12**) and the synthesis of the p-type dye **13**, should expose my joy and affection for multistep organic dye synthesis. Both projects were successful. Ligand **12** was originally designed as an anchoring ligand, where light harvesting of the anchor should be combined with the coordinated copper(I) centre to generate increased J_{SC}. Preliminary results revealed that **12** works very well as an organic dye with an efficiency of 3.59% (57.3% relative to **N719**) on day 3 and 3.77% (no **N719** reference measured) on day 17. In combination with the homoleptic complex $[Cu(\mathbf{1})_2][PF_6]$ a decreased performance was obtained, but evidence for the formation of the heteroleptic complex $[Cu(\mathbf{12})(\mathbf{1})]^+$ was not found. A more detailed investigation is planned, and the promising results will be further investigated.

The second outlier project concerned p-type dyes. A new p-type dye, bearing a phosphonic acid anchoring group was synthesized (**13**). Apart from the anchoring group, **13** is identical to the standard p-type dye **P1** (carboxylic acid anchoring group), making this comparison interesting in terms of a general trend. The DSSC measurements have to be conducted in the future. Further studies in this direction are considered of great importance, as better p-type dyes can be incorporated into tandem solar cells, enhancing their potential tremendously. Better p-type dyes are the most important research field for both technologies and bear a lot of potential for improvement and investigation.

12 EXPERIMENTAL PART

12.1 Ligand summary for bisdiimine copper(I) DSSCs

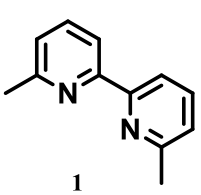

1

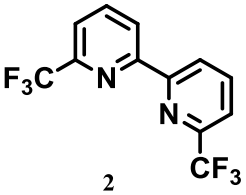

2

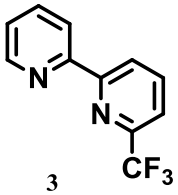

3

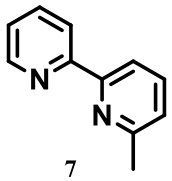

7

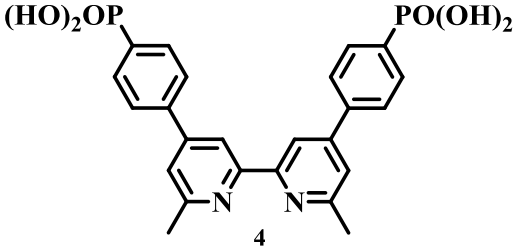

4

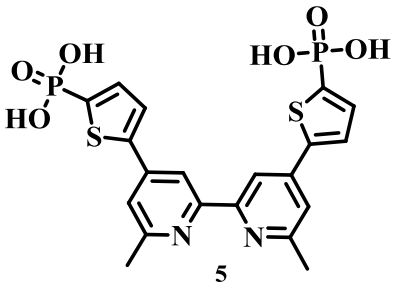

5

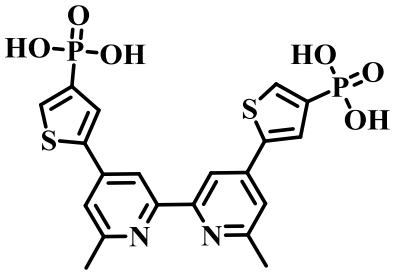

6

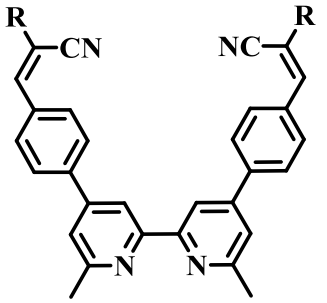

8 R = COOH
9 R = PO(OH)$_2$

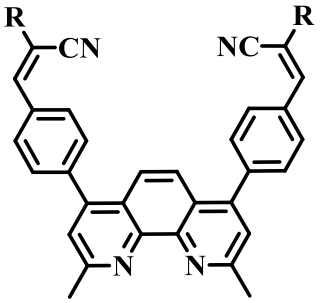

10 R = COOH
11 R = PO(OH)$_2$

Ancillary ligand **1** was commercially available. Ancillary ligands **2**[98] and **7**[42] and anchoring ligand **4**[83] were prepared according to the literature. Complexes [Cu(**1**)$_2$][PF$_6$][63] and [Cu(**7**)$_2$][PF$_6$][42] were prepared according to the literature.

12.2 Ancillary ligands and homoleptic complexes

The synthesis of **3**, [Cu(**2**)$_2$][PF_6] and [Cu(**3**)$_2$][PF_6] was performed in collaboration with Fabian Brunner and Dr. Sarah Keller.

12.2.1 Ancillary ligand 3

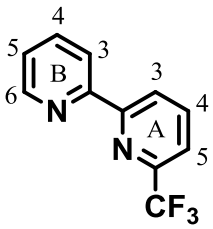

Solid 2-chloro-6-(trifluoromethyl)pyridine (423 mg, 2.33 mmol) and [$Pd(PPh_3)_4$] (135 mg, 0.12 mmol) were added to a 10-20 ml vial, and the tube was then evacuated and refilled with N_2 three times. Dry THF (5 ml) and a solution of 2-pyridylzinc bromide (0.5 M in THF, 7 ml, 3.50 mmol) were added, and then the tube was sealed, and heated in a microwave reactor at 110 °C for 2 h. The reaction mixture was poured into a separating funnel and saturated aqueous $NaHCO_3$ was added. The mixture was extracted with CH_2Cl_2 (3 × 50 ml), and then the combined organic layers were washed with water (2 × 100 ml) and dried over $MgSO_4$. The solvent was removed and the brown crude material was redissolved in CH_2Cl_2 and filtered over silica. The solvent was removed to give **3** as a white solid (318 mg, 1.42 mmol, 61%). ^{1}H NMR (400 MHz, $CDCl_3$) δ/ppm 8.69 (ddd, J = 4.7, 1.8, 0.9 Hz, 1H, H^{B6}), 8.64 (dt, J = 8.0, 0.8 Hz, 1H, H^{A3}), 8.53 (dt, J = 7.9, 1.1 Hz, 1H, H^{B3}), 7.99 (td, J = 7.8, 0.7 Hz, 1H, H^{A4}), 7.85 (td, J = 7.7, 1.8 Hz, 1H, H^{B4}), 7.69 (dd, J = 7.8, 1.0 Hz, 1H, H^{A5}), 7.36 (ddd, J = 7.5, 4.7, 1.2 Hz, 1H, H^{B5}). ^{13}C{^{1}H} NMR (126 MHz, $CDCl_3$) δ/ppm 156.7 (C^{A2}), 154.8 (C^{B2}), 149.3 (C^{B6}), 148.0 (q, J_{CF} = 35 Hz, C^{A6}), 138.4 (C^{A4}), 137.3 (C^{B4}), 124.6 (C^{B5}), 123.6 (C^{A3}), 121.8 (C^{B3}), 121.7 (q, J = 274 Hz, C^{CF3}), 120.3 (q, J_{CF} = 2.9 Hz, C^{A5}). ^{19}F NMR (376 MHz, CD_2Cl_2) δ/ppm –68.4. ESI MS m/z 225.1 $[M+H]^+$ (base peak, calc. 225.2). UV-Vis (CH_2Cl_2, 2.5 × 10^{-5} mol dm^{-3}): λ/nm (ε/dm^3 mol^{-1} cm^{-1}) 238 (10600), 245sh (9400), 282 (12600), 295sh (6700). Found C 59.31, H 3.41, N 12.46; $C_{11}H_7F_3N_2$ requires C 58.93, H 3.15, N 12.50%.

12.2.2 Complex $[Cu(2)_2][PF_6]$

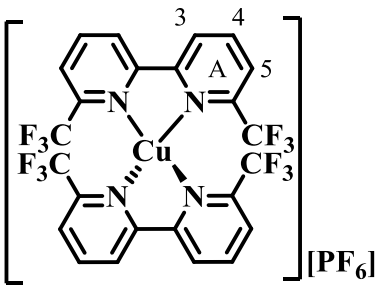

$[Cu(MeCN)_4][PF_6]$ (93 mg, 0.25 mmol) was dissolved in CH_2Cl_2 (25 ml) and **2** (146 mg, 0.50 mmol) was added. The mixture was stirred for 2 h at room temperature and then the orange solution was filtered and the solvent from the filtrate was removed under reduced pressure. The crude product was washed with Et_2O and cyclohexane to give $[Cu(\mathbf{2})_2][PF_6]$ (86.0 mg, 0.108 mmol, 43.2%) as an orange crystalline solid. ^{1}H NMR (500 MHz, CD_2Cl_2) δ/ppm 8.70 (dd, J = 8.2, 1.0 Hz, 4H, H^{A3}), 8.44 (t, J = 8.0 Hz, 4H, H^{A4}), 8.07 (dd, J = 7.9, 1.0 Hz, 4H, H^{A5}). ^{13}C{^{1}H} NMR (126 MHz, CD_2Cl_2) δ/ppm 152.8 (C^{A6}), 146.8 (C^{A2}) 141.3 (C^{A4}), 126.7 (C^{A3}), 125.0 (C^{A5}), 121.3 (q, J = 273 Hz, C^{CF3}). ^{19}F NMR (376 MHz, CD_2Cl_2) δ/ppm –68.2 (F^{CF3}), –73.3 (d, J_{PF} = 710 Hz, F^{PF6}). ^{31}P NMR (162 MHz, CD_2Cl_2) δ/ppm –144.0 (septet, J_{PF} = 710 Hz). MALDI–TOF MS *m/z* 647.2 $[M–PF_6]^+$ (base peak, calc. 647.0). UV-Vis (CH_2Cl_2, 2.5 × 10^{-5} mol dm^{-3}): λ/nm (ε/dm^3 mol^{-1} cm^{-1}) 273 (30500), 295 (23000), 340 (2980), 445 (7050). Found C 36.63, H 1.98, N 7.39; $C_{24}H_{12}CuF_{18}N_4P$ requires C 36.36, H 1.53, N 7.07%.

12.2.3 Complex $[Cu(3)_2][PF_6]$

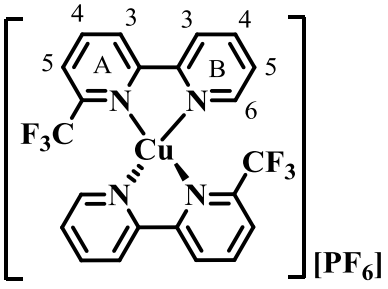

$[Cu(MeCN)_4][PF_6]$ (93 mg, 0.25 mmol) and **3** (112.0 mg, 0.50 mmol) were dissolved in CH_2Cl_2 (25 ml) and the mixture was stirred for 1.5 h at room temperature. After filtration, the filtrate was collected and the solvent removed under reduced pressure. $[Cu(\mathbf{3})_2][PF_6]$ was isolated as an orange crystalline solid (147 mg, 0.224 mmol, 89.6%). ^{1}H NMR (500 MHz, CD_2Cl_2) δ/ppm

8.62 (m, 2H, H^{B6}), 8.58 (dd, J = 8.3, 1.0 Hz, 2H, H^{A3}), 8.43 (dt, J = 8.3, 1.0 Hz, 2H, H^{B3}), 8.33 (t, J = 8.0 Hz, 2H, H^{A4}), 8.19 (td, J = 7.9, 1.7 Hz, 2H, H^{B4}), 7.95 (dd, J = 7.8, 1.1 Hz, 2H, H^{A5}), 7.66 (ddd, J = 7.6, 5.1, 1.2 Hz, 2H, H^{B5}). $^{13}C\{^1H\}$ NMR (126 MHz, CD_2Cl_2) δ/ppm 154.2 (C^{A6}), 151.0 (C^{B6}), 149.9 (C^{B2}), 146.4 (C^{A2}), 140.9 (C^{A4}), 139.2 (C^{B4}), 127.9 (C^{B5}), 125.5 (C^{A3}), 123.6 (C^{A5}), 123.4 (C^{B3}), 120.9 (q, J = 274 Hz, C^{CF3}). ^{19}F NMR (376 MHz, CD_2Cl_2) δ/ppm –68.5 (F^{CF3}), –73.3 (d, J_{PF} = 710 Hz, F^{PF6}). ^{31}P NMR (162 MHz, CD_2Cl_2) δ/ppm –144.0 (septet, J_{PF} = 710 Hz). MALDI–TOF MS m/z 511.1 $[M–PF_6]^+$ (base peak, calc. 511.0). UV-Vis (CH_2Cl_2, 2.5 × 10^{-5} mol dm^{-3}): λ/nm (ε/dm^3 mol^{-1} cm^{-1}) 263 (24400), 273 (25800), 293 (26200), 340 (2940), 443 (6580). Found C 40.94, H 2.51, N 8.53; $C_{22}H_{14}CuF_{12}N_4P$ requires C 40.23, H 2.15, N 8.53%.

12.3 Anchoring ligand **5**

12.3.1 (1*E*,5*E*)-1,6-Bis(5-bromothiophen-2-yl)hexa-1,5-diene-3,4-dione

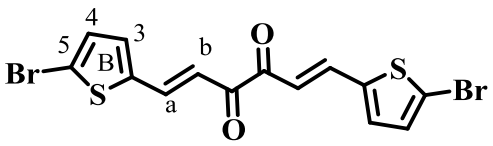

2,3-Butanedione (3.68 g, 42.1 mmol), 5-Bromo-2-thiophenecarboxaldehyde (16.1 g, 84.2 mmol) and piperidine (0.72 g, 8.4 mmol) were dissolved in MeOH (200 mL) and the reaction mixture was refluxed for 2h. A precipitate started to form after 30 min. The reaction mixture was cooled at -19 °C (refrigerator) over night. The resulting precipitate was filtered off and washed with cold MeOH (2 × 10 mL). The product was isolated as a brown powder (3.8 g, 8.8 mmol, 20.9%). Decomp. > 155 °C. ^1H NMR (500 MHz, $CDCl_3$) δ/ppm 7.84 (d, J = 15.8, 2H, H^a), 7.16 (overlapping d, J = 15.7 Hz and J = 3.9 Hz, 4H, H^{b+B3}), 7.08 (d, J = 3.9 Hz, 2H, H^{B4}). $^{13}C\{^1H\}$ NMR (126 MHz, CD_2Cl_2) δ/ppm 187.5 ($C^{C=O}$), 141.8 (C^{B2}), 138.7 (C^a), 133.5 (C^{B3}), 131.6 (C^{B4}), 118.5 (C^{B5}), 118.3 (C^b).

12.3.2 4,4'-Bis(5-bromothiophen-2-yl)-6,6'-dimethyl-2,2'-bipyridine

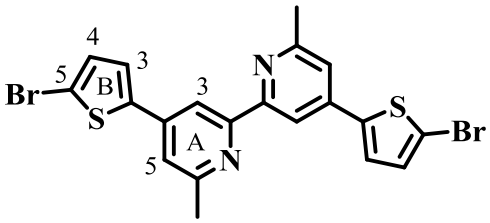

(1*E*,5*E*)-1,6-Bis(5-bromothiophen-2-yl)hexa-1,5-diene-3,4-dione (2.00 g, 4.63 mmol), 1-(2-oxopropyl)pyridin-1-ium chloride (1.99 g, 11.6 mmol) and NH_4OAc (5.00 g, 64.8 mmol) were dissolved in EtOH (100 mL) and the reaction mixture was heated at reflux for 4h. The reaction mixture was concentrated by solvent removal in vacuo and cooled at –19 °C (refrigerator) until a precipitate formed. The precipitate was removed by filtration and was washed with cold MeOH (2 × 15 mL). 4,4'-Bis(5-bromothiophen-2-yl)-6,6'-dimethyl-2,2'-bipyridine was isolated as an off-white powder (0.91 g, 1.8 mmol, 38.9%). M.p. 233 °C. ^{1}H NMR (500 MHz, $CDCl_3$) δ/ppm 8.35 (d, J = 1.6 Hz, 2H, H^{A3}), 7.37 (d, J = 3.9 Hz, 2H, H^{B3}), 7.26 (m, 2H, H^{A5}), 7.10 (d, J = 3.9 Hz, 2H, H^{B4}), 2.67 (s, 6H, H^{Me}). $^{13}C\{^1H\}$ NMR (126 MHz, $CDCl_3$) δ/ppm 159.0 (C^{A6}), 156.5 (C^{A2}), 143.4 ($C^{A4/B2}$), 141.8 ($C^{A4/B2}$), 131.3 (C^{B4}), 125.8 (C^{B3}), 119.2 (C^{A5}), 114.6 (C^{A3}), 114.1 (C^{B5}), 24.8 (C^{Me}). ESI MS *m/z* 506.7 $[M+H]^+$ (calc. 506.9).

12.3.3 Compound 5a

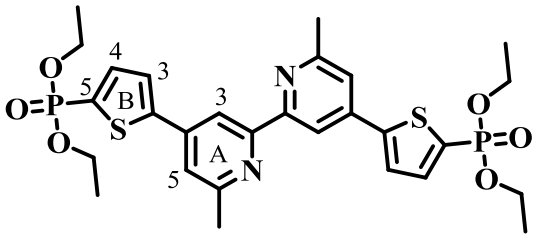

4,4'-Bis(5-bromothiophen-2-yl)-6,6'-dimethyl-2,2'-bipyridine (64.8 mg, 0.13 mmol), Cs_2CO_3 (116 mg, 0.36 mmol) and $[Pd(PPh_3)_4]$ (7.4 mg, 0.006 mmol) were added to a microwave vial. The vial was evacuated and flushed with N_2 three times. Then dry THF (5 mL) was added and N_2 was bubbled through the solution for 30 min. Diethyl phosphite (79.0 mg, 0.57 mmol) was added and the N_2 flow continued for 5 min. The reaction mixture was heated in a microwave reactor at 90 °C for 2h. The resulting mixture was filtered over Celite and the solvent from the

filtrate was removed. Compound **5a** was purified by flash column chromatography (SiO_2, cyclohexane/Acetone (3/2), Rf: 0.1) and isolated as a pale yellow powder (38 mg, 0.06 mmol, 46.2%). M.p. 198 °C. ^{1}H NMR (500 MHz, $CDCl_3$) δ/ppm 8.49 (d, J = 1.6 Hz, 2H, H^{A3}), 7.68 (dd, J_{PH} = 8.2 Hz, J_{HH} = 3.7 Hz, 2H, H^{B4}), 7.64 (dd, J_{PH} = 3.6 Hz, J_{HH} = 3.6 Hz, 2H, H^{B3}), 7.39 (d, J = 1.7 Hz, 2H, H^{A5}), 4.28–4.08 (m, 8H, $H^{Et\text{-}CH2}$), 2.70 (s, 6H, H^{Me}), 1.37 (m, 12H, $H^{Et\text{-}CH3}$). ^{13}C{^{1}H} NMR (126 MHz, $CDCl_3$) δ/ppm 158.1 (C^{A6}), 156.4 (C^{A2}), 149.7 ($C^{A4/B2}$), 141.3 ($C^{A4/B2}$), 137.5 (C^{B4}), 129.0 (d, J_{PC} = 201 Hz, C^{B5}), 126.0 (C^{B3}), 119.8 (C^{A5}), 115.1 (C^{A3}), 62.8 ($C^{Et\text{-}CH2}$), 24.7 (C^{Me}), 16.2 ($C^{Et\text{-}CH3}$). ^{31}P{^{1}H} NMR (162 MHz, $CDCl_3$) δ/ppm +10.8. ESI-MS *m/z* 621.1 $[M+H]^+$ (calc. 621.1). High resolution ESI-MS *m/z* 621.1407 $[M+H]^+$ (calc. 621.1412). UV-VIS (MeCN, 2.5×10^{-5} M) λ/nm (ε/dm^3 mol^{-1} cm^{-1}): 275 (51600), 299 (59500). Satisfactory elemental analysis could not be obtained.

12.3.4 Anchoring Ligand 5

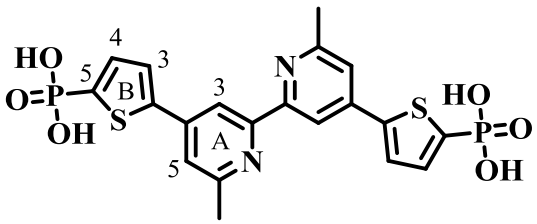

Compound **5a** (20.0 mg, 0.03 mmol) was dissolved in CH_2Cl_2 (5 mL), then Me_3SiBr (98.6 mg, 0.64 mmol) was added and the solution stirred at room temperature overnight. Water (15 mL) was added and the solution stirred for 30 min. A white precipitate formed, was separated by filtration and dried *in vacuo*. Compound **5** (10 mg, 0.02 mmol, 66.7%) was obtained as an off-white powder. Decomp > 275 °C. ^{1}H NMR (600 MHz, DMSO-d_6) δ/ppm 8.41 (s, 2H, H^{A3}), 7.85 (m, 2H, H^{B3}), 7.70 (s, 2H, H^{A5}), 7.50 (dd, J_{PH} = 8.0 Hz, J_{HH} = 3.7 Hz, 2H, H^{B4}), 2.65 (s, 6H, H^{Me}). ^{13}C{^{1}H} NMR (151 MHz, DMSO-d_6) δ/ppm 159.4 (C^{A6}), 155.4 (C^{A2}), 146.0 (C^{A4}), 141.7 (C^{B5}), 137.5 (C^{B2}), 135.0 (C^{B4}), 127.2 (C^{B3}), 119.9 (C^{A5}), 114.2 (C^{A3}), 24.7 (C^{Me}). ^{31}P{^{1}H} NMR (162 MHz, DMSO-d_6) δ/ppm +4.0. ESI-MS *m/z* 509.1 $[M+H]^+$ (calc. 509.0). Found C 45.06, H 3.84, N 5.44; $C_{20}H_{18}N_2O_6P_2S_2 \cdot H_2O$ requires C 45.63, H 3.83, N 5.32%.

12.4 Anchoring Ligand **6**

12.4.1 (1*E*,5*E*)-1,6-Bis(4-bromothiophen-2-yl)hexa-1,5-diene-3,4-dione

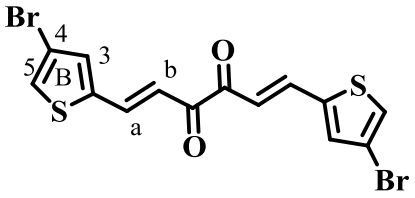

The method was as for (1*E*,5*E*)-1,6-Bis(5-bromothiophen-2-yl)hexa-1,5-diene-3,4-dione (section 12.3.1) but starting with 2,3-butanedione (2.37 g, 27.5 mmol), 4-bromothiophene-2-carboxaldehyde (10.5 g, 55.0 mmol) and piperidine (0.47 g, 5.5 mmol) in MeOH (150 mL). The product was isolated as a yellow powder (1.60 g, 3.7 mmol, 13.5%). Decomp. > 208 °C. ^{1}H NMR (500 MHz, CD_2Cl_2) δ/ppm 7.87 (d, J = 15.8 Hz, 2H, H^{a}), 7.37 (m, 2H, H^{B5}), 7.32 (m, 2H, H^{B3}), 7.29 (d, J = 15.8 Hz, 2H, H^{b}). ^{13}C{^{1}H} NMR (126 MHz, CD_2Cl_2) δ/ppm 187.2 ($C^{C=O}$), 141.0 (C^{B2}), 138.4 (C^{a}), 134.6 (C^{B3}), 127.3 (C^{B5}), 119.1 (C^{b}), 111.7 (C^{B4}).

12.4.2 4,4'-Bis(4-bromothiophen-2-yl)-6,6'-dimethyl-2,2'-bipyridine

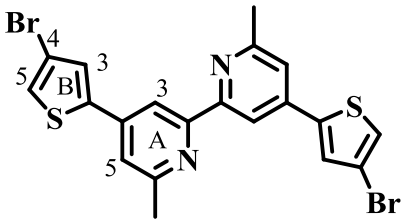

The method was as for 4,4'-bis(5-bromothiophen-2-yl)-6,6'-dimethyl-2,2'-bipyridine (section 12.3.2), but starting with (1*E*,5*E*)-1,6-bis(4-bromothiophen-2-yl)hexa-1,5-diene-3,4-dione (0.99 g, 2.29 mmol), 1-(2-oxopropyl)pyridin-1-ium chloride (0.98 g, 5.73 mmol) and NH_4OAc (2.65 g, 34.4 mmol) in EtOH (70 mL). 4,4'-Bis(4-bromothiophen-2-yl)-6,6'-dimethyl-2,2'-bipyridine was isolated as an off-white powder (0.24 g, 0.47 mmol, 20.5%). M.p. 228 °C. ^{1}H NMR (500 MHz, $CDCl_3$) δ/ppm 8.40 (d, J = 1.6 Hz, 2H, H^{A3}), 7.52 (d, J = 1.4 Hz, 2H, H^{B3}), 7.32 (d, J = 1.7 Hz, 2H, H^{A5}), 7.31 (d, J = 1.4 Hz, 2H, H^{B5}), 2.69 (s, 6H, H^{Me}). ^{13}C{^{1}H} NMR (126 MHz, $CDCl_3$) δ/ppm 159.1 (C^{A6}), 156.5 (C^{A2}), 143.0 ($C^{A4/B2}$), 141.4 ($C^{A4/B2}$), 128.0 (C^{B3}),

124.0 (C^{B5}), 119.4 (C^{A5}), 114.8 (C^{A3}), 111.2 (C^{B4}), 24.8 (C^{Me}). ESI MS *m/z* 506.9 $[M+H]^+$ (calc. 506.9).

12.4.3 Compound 6a

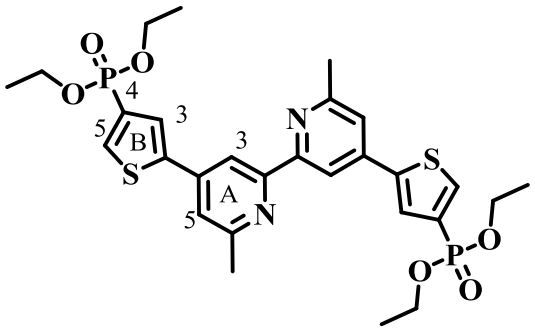

The method was as for **5a** (section 12.3.3) starting with 4,4'-bis(4-bromothiophen-2-yl)-6,6'-dimethyl-2,2'-bipyridine (74.9 mg, 0.15 mmol), Cs_2CO_3 (169 mg, 0.52 mmol), $[Pd(PPh_3)_4]$ (8.6 mg, 0.007 mmol) and diethyl phosphite (81.8 mg, 0.59 mmol). Compound **6a** was obtained as a pale yellow powder (50 mg, 0.08 mmol, 53.3%). M.p. 188 °C. ^{1}H NMR (500 MHz, $CDCl_3$) δ/ppm 8.50 (br, 2H, H^{A3}), 8.02 (dd, J_{PH} = 8.2 Hz, J_{HH} = 1.2 Hz, 2H, H^{B5}), 7.83 (br. d, 2H, H^{B3}), 7.38 (broadened, 2H, H^{A5}), 4.30–4.01 (m, 8H, $H^{Et\text{-}CH2}$), 2.72 (s, 6H, H^{Me}), 1.36 (m, 12H, $H^{P\text{-}Me}$). $^{13}C\{^1H\}$ NMR (126 MHz, $CDCl_3$) δ/ppm 158.9 (C^{A6}), 156.1 (C^{A2}), 144.0 ($C^{B2/A4}$), 141.6 ($C^{B2/A4}$) 136.0 (C^{B5}), 131.2 (d, J_{PC} = 197 Hz, C^{B4}), 127.2 (C^{B3}), 119.9 (C^{A5}), 115.2 (C^{A3}), 62.4 (d, J_{PC} = 5.4 Hz, $C^{Et\text{-}CH2}$), 24.6 (C^{Me}), 16.4 (d, J_{PC} = 6.5 Hz, $C^{Et\text{-}CH3}$). $^{31}P\{^1H\}$ NMR (202 MHz, $CDCl_3$) δ/ppm +12.0. UV-VIS (MeCN, 2.5 × 10^{-5} M) λ/nm (ε/dm^3 mol^{-1} cm^{-1}): 269 (35000), 293 (34500). ESI-MS *m/z* 621.1 [M+H] (calc. 621.1). Found C 54.44, H 5.89, N 4.40; $C_{28}H_{34}N_2O_6P_2S_2$ requires C 54.19, H 5.52, N 4.51%.

12.4.4 Anchoring ligand 6

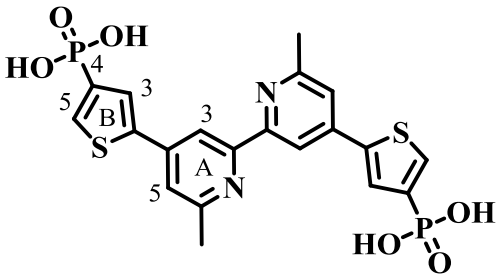

The method was as for **5a** (section 12.3.4), starting with **6a** (60 mg, 0.10 mmol) in CH_2Cl_2 (10 mL) and Me_3SiBr (296 mg, 1.93 mmol). Compound **36** (40 mg, 0.08 mmol, 80.0%) was isolated as an off-white powder. Decomp >290 °C. ^{1}H NMR (600 MHz, DMSO-d_6) δ/ppm 8.46 (s, 2H, H^{A3}), 8.08 (br. d, J = 8.1 Hz, 2H, H^{B5}), 7.93 (br. m, 2H, H^{B3}), 7.75 (s, 2H, H^{A5}), 2.67 (s, 6H, H^{Me}). ^{13}C{^{1}H} NMR (151 MHz, DMSO-d_6) δ/ppm 159.3 (C^{A6}), 142.1 (C^{A4}), 137.9 (C^{B4}), 135.0 (C^{B5}), 128.4 (C^{B3}), 120.3 (C^{A5}), 114.5 (C^{A3}), 24.5 (C^{Me}); C^{A2} and C^{B2} not resolved. ^{31}P{^{1}H} NMR (202 MHz, DMSO-d_6) δ/ppm +6.1. ESI-MS m/z 509.1 $[M+H]^+$ (calc. 509.0). Found C 42.08, H 4.37, N 5.17; $C_{20}H_{18}N_2O_6P_2S_2 \cdot 3.5H_2O$ requires C 42.03, H 4.41, N 4.90%.

12.5 Anchoring ligands **8** and **9**

Anchors **8** and **9** were synthesized in collaboration with the Wahlpraktikum student Yann Baumgartner.

12.5.1 4,4'-(6,6'-Dimethyl-[2,2'-bipyridine]-4,4'-diyl)dibenzaldehyde

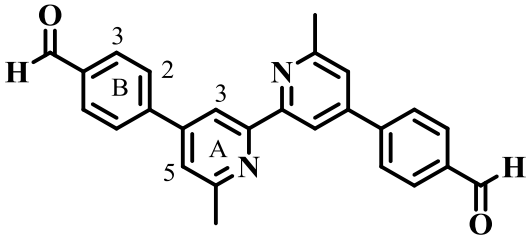

The method is adapted from a literature preparation[81]. Cs_2CO_3 (1.14 g, 3.51 mmol) was dissolved in water (2 mL) and the solution was degassed with N_2 for 10 min. 4,4'-Dibromo-6,6'-dimethyl-2,2'-bipyridine (200 mg, 0.585 mmol), (4-formylphenyl)boronic acid (263 mg,

1.75 mmol) and a catalytic amount of [$Pd(PPh_3)_4$] (33.8 mg, 0.090 mmol) were dissolved in THF (15 mL) in a microwave vial and the solution was degassed with N_2 for 10 min. The aqueous solution of Cs_2CO_3 was then added to the reaction mixture which was then heated at 90 °C for 4h in a microwave reactor. The reaction mixture was allowed to cool to room temperature and then water (25 mL) was added. The reaction mixture was extracted with CH_2Cl_2 (3 × 25 mL) and the combined organic layers were dried over $MgSO_4$. The solvent was removed under reduced pressure and the crude product was recrystallized (EtOH/$CHCl_3$). The product was obtained as a white solid (170 mg, 0.433 mmol, 74.0%). The previous literature report of this compound gave only ^{1}H NMR spectroscopic data for a DMSO-d_6 solution[81]. M.p. 232.2 °C. ^{1}H NMR (500 MHz, $CDCl_3$) δ/ppm 10.11 (s, 2H, H^{CHO}), 8.55 (d, J = 1.3 Hz, 2H, H^{A5}), 8.03 (m, 4H, H^{B3}), 7.92 (m, 4H, H^{B2}), 7.44 (d, J = 1.3 Hz, 2H, H^{A3}), 2.74 (s, 6H, H^{Me}). ^{13}C{^{1}H} NMR (126 MHz, $CDCl_3$) δ/ppm 191.9 (C^{CHO}), 159.0 (C^{A6}), 156.6 (C^{A2}), 148.3 (C^{B1}), 144.9 (C^{A4}), 136.5 (C^{B4}), 130.5 (C^{B3}), 128.1 (C^{B2}), 121.6 (C^{A5}), 116.9 (C^{A3}), 24.9 (C^{Me}). ESI-MS *m/z* 415.04 $[M+Na]^+$ (calc. 415.14).

12.5.2 Anchoring ligand 8

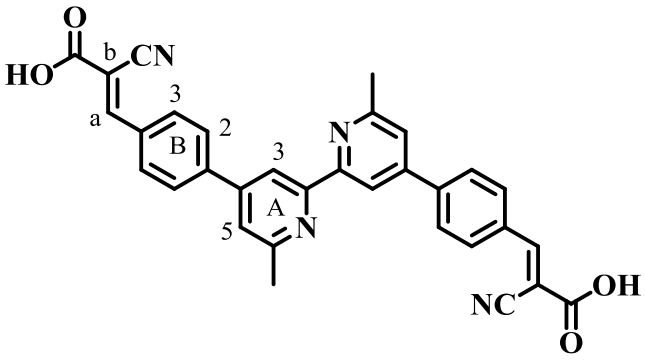

Piperidine (32.7 µL, 0.331 mmol), cyanoacetic acid (84.5 mg, 0.993 mmol) and 4,4'-(6,6'-dimethyl-[2,2'-bipyridine]-4,4'-diyl)dibenzaldehyde (130 mg, 0.331 mmol) were dissolved in $CHCl_3$ (20 mL) and the reaction mixture was heated at reflux for ~15 h. The reaction mixture was allowed to cool to room temperature and was filtered. The product was washed with CH_2Cl_2 (2 × 10 mL) to obtain **8** as a white solid (147 mg, 0.331 mmol, 84.3%). M.p. 234.4 °C. ^{1}H NMR (500 MHz, DMSO-d_6) δ/ppm 8.68 (br, 2H, H^{OH}), 8.54 (s, 2H, H^{A3}), 8.31 (s, 2H, H^{a}), 8.17 (m, 4H, H^{B3}), 8.04 (m, 4H, H^{B2}), 7.75 (s, 2H, H^{A5}), 2.68 (s, 6H, $H^{Me.}$). ^{13}C{^{1}H} NMR (126 MHz, DMSO-d_6) δ/ppm 163.1 (C^{COOH}), 158.7 (C^{A6}), 155.5 (C^{A2}), 151.3 (C^{a}), 147.2 (C^{A4}), 141.0 (C^{B1}), 132.7 (C^{B4}), 131.1 (C^{B3}), 127.6 (C^{B2}), 121.2 (C^{A5}), 117.3 (C^{CN}), 115.4 (C^{A3}), 79.2 (C^{b}), 24.4

(C^{Me}). IR (solid, ν/cm^{-1}) ~3000 (v br), 2218 (w), 1710 (m), 1595 (s), 1543 (m), 1382 (m), 1340 (m), 1275 (m), 1215 (m), 1191 (s), 830 (vs), 754 (s), 717 (vs). ESI-MS *m/z* 527.07 $[M+H]^+$ (calc. 527.17). HR ESI-MS *m/z* 527.1713 $[M+H]^+$ (calc. 527.1714). Satisfactory elemental analysis could not obtained.

12.5.3 Compound 9a

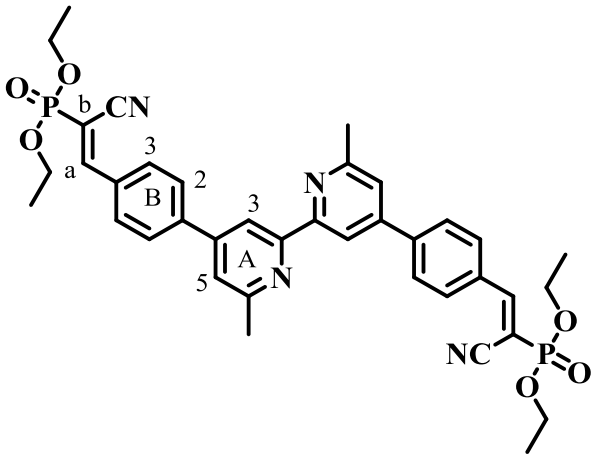

Piperidine (7.91 µL, 0.080 mmol), diethyl cyanomethylphosphonate (38.6 µL, 0.240 mmol) and 4,4'-(6,6'-dimethyl-[2,2'-bipyridine]-4,4'-diyl)dibenzaldehyde (31.4 mg, 0.080 mmol) were dissolved in $CHCl_3$ (20 mL) and the reaction mixture was heated at reflux for ~15 h. The reaction mixture was allowed to cool to room temperature and CH_2Cl_2 (30 mL) was added. The organic layer was washed with water (3 × 25 mL) and brine (3 × 25 mL), dried over $MgSO_4$ and the solvent was removed under reduced pressure. The crude product was purified by column chromatography (3:2 cyclohexane/acetone) and the solvent from the fraction collected was removed under reduced pressure. Ester **9a** was isolated as a white solid (44.6 mg, 0.0628 mmol, 78.4%). ^{1}H NMR (500 MHz, $CDCl_3$) δ/ppm 8.55 (d, J = 1.2 Hz, 2H, H^{A3}), 8.11 (m, 4H, H^{B3}), 8.07 (d, J_{PH} ~ 21 Hz, 2H, H^a), 7.90 (m, 4H, H^{B2}), 7.44 (d, J = 1.3 Hz, 2H, H^{A5}), 4.27 (m, 8H, H^{Et}), 2.74 (s, 6H, $H^{Me\text{-}bpy}$), 1.44 (m, 12H, H^{Et}). $^{13}C\{^1H\}$ NMR (126 MHz, $CDCl_3$) δ/ppm 159.0 (C^{A6}), 158.0 (d, J_{PC} = 6.7 Hz, C^a),156.6 (C^{A2}), 147.9 (C^{A4}), 143.3 (C^{B1}), 132.9 (C^{B4}), 131.4 (C^{B3}), 128.2 (C^{B2}), 121.4 (C^{A5}), 116.8 (C^{A3}), 115.6 (C^{CN}), 63.9 (d, J_{PC} = 5.8 Hz, C^{Et}), 24.4 ($C^{Me\text{-}bpy}$), 16.4 (d, J_{PC} = 6.4 Hz, C^{Et}), signal for C^b was not resolved. $^{31}P\{^1H\}$ NMR (202 MHz, $CDCl_3$) δ/ppm: +10.9. ESI-MS: *m/z* 711.12 $[M+H]^+$ (calc. 711.25). HR ESI-MS *m/z* 711.2497 $[M+H]^+$ (calc. 711.2496). Satisfactory elemental analysis could not obtained.

12.5.4 Anchoring ligand 9

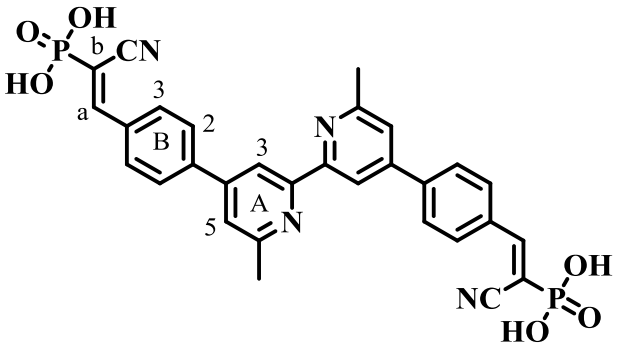

Me_3SiBr (0.639 mL, 4.84 mmol) and **9a** (44.6 mg, 0.0628 mmol) were dissolved in CH_2Cl_2 (20 mL). The reaction mixture was stirred for 2.5 days at room temperature. Water (20 mL) was added to the reaction mixture and a precipitate formed. The product was filtered, and washed with water (10 mL), EtOH (2 × 10 mL) and CH_2Cl_2 (2 × 10 mL). Compound **9** was isolated as a pale yellow solid (13.3 mg, 0.022 mmol, 35.0%).^{1}H NMR (500 MHz, DMSO-d_6) δ/ppm 8.81 (d, J = 1.8 Hz, 2H, H^{A3}), 8.22 (m, 4H, H^{B2}), 8.17 (m, 4H, H^{B3}), 8.15 (s, 2H, H^{A5}), 7.99 (d, J = 19.7 Hz, 2H, H^{a}), 2.82 (s, 6H, H^{Me}). $^{13}C\{^{1}H\}$ NMR (126 MHz, DMSO-d_6) δ/ppm 157.88 (C^{A6}), 152.9 (d, J = 6.1 Hz C^{a}), 149.8 (C^{A4}), 138.7 (C^{B1}), 134.6 (C^{B4}), 130.3 (C^{B3}), 128.3 (C^{B2}), 123.6 (C^{A5}), 118.4 (C^{A3}), 116.7 (C^{CN}), 107.6 (d, J_{PC} = 182.9 Hz, C^{b}), 22.6 (C^{Me}); signal for H^{A3} was not resolved. $^{31}P\{^{1}H\}$ NMR (202 MHz, DMSO-d_6) δ/ppm: +4.55. IR (solid, ν/cm^{-1}) ~3000 (br), 2209 (w), 1623 (sh), 1597 (s), 1394 (m), 1163 (sh), 1050 (s), 920 (s), 828 (vs), 616 (s) 564 (vs). MALDI-MS *m/z* 599.07 $[M+H]^+$ (calc. 559.12). ESI-MS (**9** in aqu. NH_3) *m/z* 297.88 $[M–2H]^{2–}$ (calc. 298.05). HR ESI-MS *m/z* 298.0515 $[M–2H]^{2–}$ (calc. 298.0513). Satisfactory elemental analysis could not be obtained.

12.6 Anchoring ligands **10** and **11**

Anchors **10** and **11** were synthesized in collaboration with the Wahlpraktikum student Yann Baumgartner.

12.6.1 4,4'-(2,9-Dimethyl-1,10-phenanthroline-4,7-diyl)dibenzaldehyde

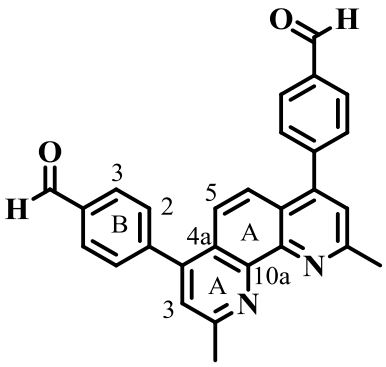

Cs_2CO_3 (3.52 g, 10.8 mmol) was dissolved in water (2 mL) and the solution degassed with N_2 for 10 min. 4,7-Dichloro-2,9-dimethyl-1,10-phenanthroline (500 mg, 1.80 mmol), (4-formylphenyl)boronic acid (810 mg, 5.40 mmol) and a catalytic amount of $[Pd(PPh_3)_4]$ (104 mg, 0.090 mmol) were dissolved in THF (15 mL) in a microwave vial and the solution was degassed with N_2 for 10 min. The aqueous solution was then added to the THF solution and the reaction was heated at 90 °C for 4h in a microwave reactor. After the mixture had cooled to ambient temperature, water (25 mL) was added. The mixture was extracted with CH_2Cl_2 (3 × 25 mL) and the combined organic layers were dried over $MgSO_4$. Solvent was then removed under reduced pressure and the crude product was recrystallized from EtOH/$CHCl_3$. 4,4'-(2,9-Dimethyl-1,10-phenanthroline-4,7-diyl)dibenzaldehyde was isolated as a pale yellow solid (90.1 mg, 0.216 mmol, 12.0%). Decomp > 300 °C. ^{1}H NMR (500 MHz, $CDCl_3$) δ/ppm 10.13 (s, 2H, H^{CHO}), 8.04 (d, 4H, J = 8.3 Hz, H^{B3}), 7.70 (d, 4H, J = 8.3, H^{B2}), 7.68 (s, 2H, H^{A5}), 7.48 (s, 2H, H^{A3}), 3.01 (s, 6H, H^{Me}). $^{13}C\{^1H\}$ NMR (126 MHz, $CDCl_3$, δ/ppm) δ/ppm 191.8 (C^{CHO}), 159.3 (C^{A2}), 147.3 (C^{A4}), 146.1 (C^{A10a}), 144.4 (C^{B1}), 136.2 (C^{B4}), 130.5 (C^{B2}), 136.0 (C^{B3}), 124.4 (C^{A4a}), 124.0 (C^{A3}), 123.0 (C^{A5}), 26.1 (C^{Me}). ESI-MS *m/z* 417.06 $[M+H]^+$ (calc. 417.16), 439.04 $[M+Na]^+$ (calc. 439.04).

12.6.2 Anchoring ligand 10

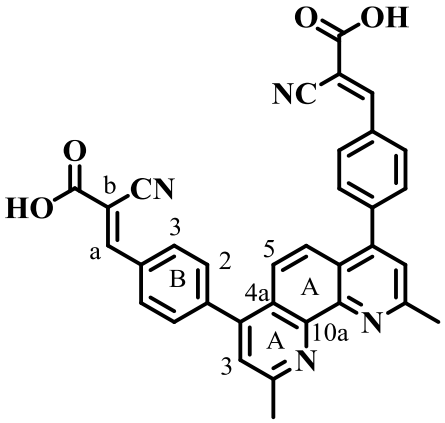

Piperidine (14.3 µL, 0.145 mmol), cyanoacetic acid (37.0 mg, 0.435 mmol) and 4,4'-(2,9-dimethyl-1,10-phenanthroline-4,7-diyl)dibenzaldehyde (60.3 mg, 0.145 mmol) were dissolved in $CHCl_3$ (20 mL) and the reaction mixture was heated at reflux for ~15 h. The reaction mixture was allowed to cool down to room temperature, then was filtered and the solid product was washed with CH_2Cl_2 (2 × 10 mL). Compound **10** was isolated as a pale yellow solid (55.7 mg, 0.101 mmol, 69.8%). Decomp > 300 ºC. ^{1}H NMR (500 MHz, DMSO-d_6) δ/ppm 8.44 (s, 2H H^a), 8.23 (d, J = 8.4 Hz, 4H, H^{B3}), 7.80 (d, J = 8.4 Hz, 4H, H^{B2}), 7.75 (s, 2H, H^{A3}), 7.67 (s, 2H, H^{A5}), 2.87 (s, 6H, H^{Me}). $^{13}C\{^1H\}$ NMR (126 MHz, DMSO-d_6) δ/ppm 163.0 (C^{COOH}), 158.1 (C^{A2}), 153.0 (C^a), 146.3 (C^{A4}), 145.4 (C^{A10a}), 141.7 (C^{B1}), 131.7 (C^{B4}), 130.7 (C^{B3}), 130.3 (C^{B2}), 123.7 (C^{A5}), 122.6 (C^{A3}), 116.8 (C^{CN}), 24.8 (C^{Me}); signals for C^b, C^{4a} were not resolved. IR (ν/cm^{-1}) ~3000 (br), 2218 (w), 1703 (m), 1598 (vs), 1554 (m), 1328 (m), 1259 (m), 1190 (s), 838 (vs), 711 (vs). MALDI-MS *m/z* 551.34 $[M+H]^+$ (calc. 551.17). ESI-MS *m/z* 551.08 $[M+H]^+$ (calc. 551.17). High resolution ESI-MS *m/z* 551.1712 $[M+H]^+$ (calc. 551.1714). Satisfactory elemental analysis could not be obtained.

12.6.3 Compound 11a

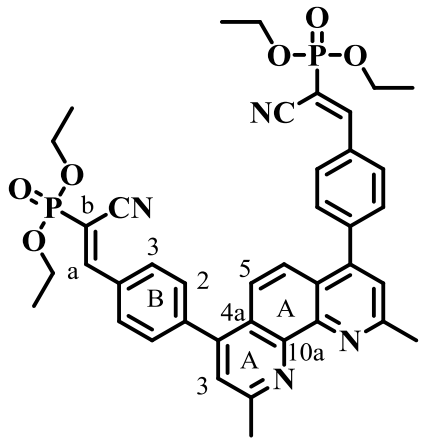

Piperidine (16.8 µL, 0.170 mmol), diethyl cyanomethylphosphonate (82.1 µL, 0.510 mmol) and Dimethyl-1,10-phenanthroline-4,7-diyl)dibenzaldehyde (70.7 mg, 0.170 mmol) were dissolved in $CHCl_3$ (20 mL) and the reaction mixture was heated at reflux for ~15 h. After cooling the mixture to room temperature, CH_2Cl_2 (30 mL) was added and the organic layer was washed with water (3 × 25 mL) followed by brine (3 × 25 mL), dried over $MgSO_4$ and the solvent was removed under reduced pressure. The crude product was purified by column chromatography (3:2 cyclohexane/acetone) and the solvent from the fractions collected was removed under reduced pressure. Ester **11a** was isolated as a pale yellow solid (61.4 mg, 0.0836 mmol, 49.2%). ^{1}H NMR (500 MHz, $CDCl_3$) δ/ppm 8.11 (m, 6H, H^{B3+a}), 7.71 (s, 2H, H^{A5}), 7.67 (d, 4H, J = 8.2 Hz, H^{B2}), 7.47 (s, 2H, H^{A3}), 4.27 (m, 8H, H^{Et}), 3.02 (s, 6H, $H^{Me\text{-}phen}$), 1.44 (t, 12H, 7.2 Hz, H^{Et}). $^{13}C\{^{1}H\}$ NMR (126 MHz, $CDCl_3$) δ/ppm 159.2 (C^{A2}), 157.8 (C^{a}), 146.9 (C^{A4}), 146.1 (C^{A10a}), 142.8 (C^{B1}), 132.5 (C^{B4}), 130.6 (C^{B3}), 130.5 (C^{B2}), 124.2 (C^{A4a}), 123.9 (C^{A3}), 122.9 (C^{A5}), 115.3 (C^{CN}), 101.2 (d, J_{PC} = 258 Hz, C^{b}), 63.9 (d, J_{PC} = 5.8 Hz, C^{Et}), 26.0 ($C^{Me\text{-}bpy}$), 16.5 (d, J_{PC} = 6.3 Hz, C^{Et}). $^{31}P\{^{1}H\}$ NMR (202 MHz, $CDCl_3$) δ/ppm +10.7. ESI-MS *m/z* 735.1 $[M+H]^+$ (calc. 735.25). HR ESI-MS *m/z* 735.2500 $[M+H]^+$ (calc. 735.2496). Satisfactory elemental analysis could not be obtained.

12.6.4 Anchoring ligand 11

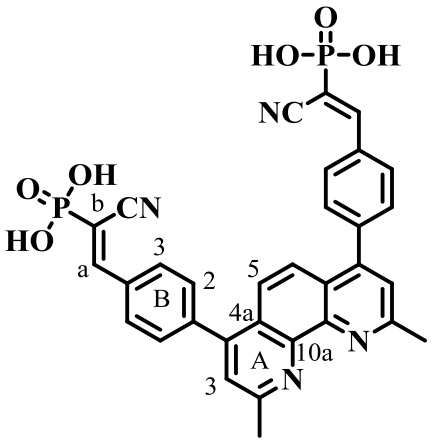

Me_3SiBr (0.718 mL, 5.44 mmol) and **11a** (61.4 mg, 0.0836 mmol) were dissolved in CH_2Cl_2 (20 mL) and the reaction mixture was stirred for 3 days at room temperature. Water (20 mL) was added to the reaction mixture and the precipitate that formed was collected by filtration, and was washed with water (10 mL), EtOH (2 × 10 mL) and CH_2Cl_2 (2 × 10 mL). **11** was isolated as a pale yellow solid (26.3 mg, 0.0422 mmol, 50.5%). Only a broadened ^1H NMR spectrum could be recorded. MALDI-MS *m/z* 622.92 $[M+H^+]$ (calc. 623.12). ESI-MS (**11** in aqu. NH_3) *m/z* 309.95 $[M–2H]^{2–}$ (calc. 310.05). HR ESI-MS *m/z* 310.0514 $[M–2H]^{2–}$ (calc. 310.0513). IR (ν/cm^{-1}): ~3000 (br), 2206 (w), 1616 (s), 1597 (s), 1557 (m), 1402 (w), 1158 (sh), 1062 (vs), 920 (s), 838 (vs), 622 (s) 566 (vs). Satisfactory elemental analysis could not be obtained.

12.7 Anchor molecule **12**

12.7.1 Compound 12a

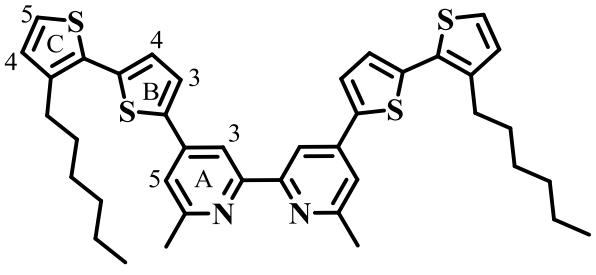

4,4'-bis(5-bromothiophen-2-yl)-6,6'-dimethyl-2,2'-bipyridine (0.653 g, 1.29 mmol), $[Pd(PPh_3)_4]$ (0.074 g, 0.065 mmol) and Cs_2CO_3 (2.522 g, 7.74 mmol) were added to a

microwave vial and the vial was evacuated and flushed with N_2 three times. 3-Hexylthiophene-2-boronic acid pinacol ester (0.965 mL, 0.949 g, 3.22 mmol) was dissolved in dry toluene (18 mL) and N_2 was bubbled through the solution for 20 min. The degassed solution was added to the microwave vial, sealed and heated in a microwave reactor at 120°C for 4 h. Water (15mL) and dichloromethane (50mL) were added. The organic phase was extracted, dried over $MgSO_4$ and the solvent removed under reduced pressure. The crude product was purified by recrystallization (chloroform/ethanol). Compound **12a** was isolated as a yellow solid (850 mg, 1.247 mmol, 96.7%). ^{1}H NMR (500 MHz, $CDCl_3$) δ/ppm 8.44 (dd, J = 1.7, 0.6 Hz, 2H, H^{A3}), 7.59 (d, J = 3.8 Hz, 2H, H^{B3}), 7.37 (dd, J = 1.7, 0.5 Hz, 2H, H^{A5}), 7.22 (d, J = 5.2 Hz, 2H, H^{C5}), 7.15 (d, J = 3.8 Hz, 2H, H^{B4}), 6.97 (d, J = 5.2 Hz, 2H, H^{C4}), 2.85 – 2.79 (m, 4H, H^{Ca}), 2.73 – 2.66 (m, 6H, H^{Me}), 1.74 – 1.63 (m, 4H, H^{Cb}), 1.46 – 1.37 (m, 4H, H^{Cc}), 1.36 – 1.29 (m, 8H, H^{Cd+e}), 0.94 – 0.85 (m, 3H, H^{Cf}). ^{13}C{^{1}H} NMR (126 MHz, $CDCl_3$) δ/ppm 158.81 (C^{A6}), 156.60 (C^{A2}), 142.40 (C^{A4}), 141.29 (C^{B2}), 140.42 (C^{C3}), 138.02 (C^{B5}), 130.41 (C^{C2}), 130.32 (C^{C4}), 126.99 (C^{B4}), 125.92 (C^{B3}), 124.35 (C^{C5}), 119.23 (C^{A5}), 114.70 (C^{A3}), 31.83 (C^{Cd+e}), 30.77 (C^{Cb}), 29.49 (C^{Ca}), 29.37 (C^{Cc}), 24.88 (C^{Me}), 22.78 (C^{Cd+e}), 14.25 (C^{Cf}). MALDI-MS *m/z* 681.56 $[M+H]^+$ (calc. 681.25).

11.1 Compound 12b

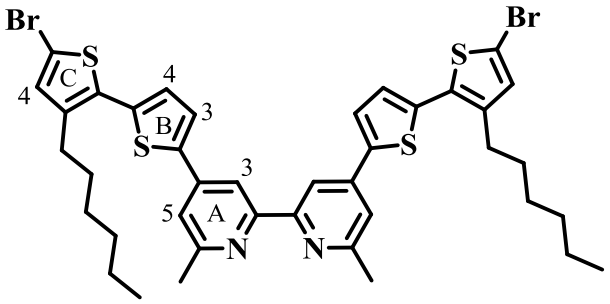

Compound **12a** (0.623 g, 0.915 mmol) was dissolved in chloroform/dimethylformamide (50 mL, 1/1) and N-bromosuccinimide (0.326 g, 1.83 mmol) was added in one portion. The solution was stirred at ambient conditions for 16h. Aq. HCl (20 mL, 1M) was added and the mixture extracted with dichloromethane (3 × 50mL) . The organic phases were combined, dried over $MgSO_4$ and the solvent removed under reduced pressure. The crude product was purified by recrystallization (chloroform/ethanol). Compound **12b** was isolated as an orange solid (691 mg, 0.824 mmol, 90.0%). ^{1}H NMR (500 MHz, CD_2Cl_2) δ/ppm 9.16 (s, 2H, H^{A3}), 8.25 (d, J = 3.7 Hz, 2H, H^{B3}), 7.54 (s, 2H, H^{A5}), 7.19 (d, J = 3.6 Hz, 2H, H^{B4}), 6.97 (s, 2H, H^{C4}), 2.97 (s, 6H,

H^{Me}), 2.77 (t, J = 7.8 Hz, 4H, H^{Ca}), 1.75–1.56 (m, 4H, H^{Cb}), 1.45–1.37 (m, 4H, H^{Cc}), 1.35–1.30 (m, 8H, H^{Cd+e}), 0.93 – 0.81 (m, 6H, H^{Cf}). $^{13}C\{^1H\}$ NMR (126 MHz, CD_2Cl_2) δ/ppm 157.95 (C^{A6}), 147.72 (C^{A2}), 142.66 (C^{C3}), 141.08(C^{B2}), 138.34(C^{B5}), 133.89 (C^{C4}), 132.02 (C^{C2}), 131.73 (C^{B3}), 128.52 (C^{B4}), 122.07 (C^{A5}), 119.07 (C^{A3}), 112.61 (C^{C5}), 32.20 (C^{Cd+e}), 30.86 (C^{Cb}), 30.04 (C^{Ca}), 29.68 (C^{Cc}), 23.17 (C^{Cd+e}), 22.54 (C^{Me}), 14.44 (C^{Cf}). C^{A4} was not resolved. MALDI-MS *m/z* 839.54 $[M+H]^+$ (calc. 839.07).

12.7.2 Compound 12c

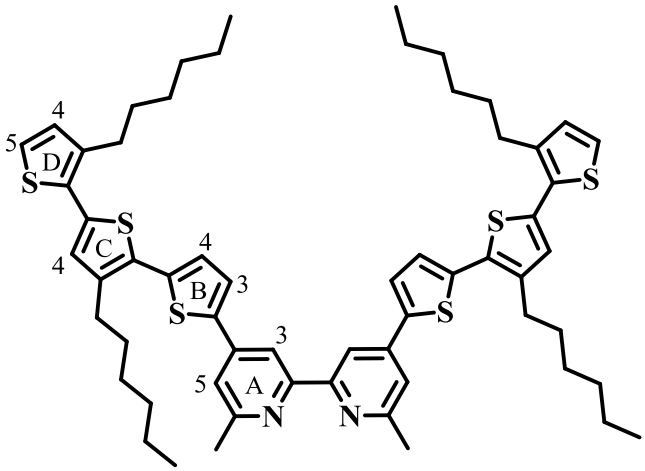

Compound **12b** (0.299 g, 0.357 mmol), $[Pd(PPh_3)_4]$ (0.021 g, 0.018 mmol) and Cs_2CO_3 (0.698 g, 2.14 mmol) were added to a microwave vial and the vial was evacuated and flushed with N_2 three times. 3-Hexylthiophene-2-boronic acid pinacol ester (0.267 mL, 0.263 g, 0.893 mmol) was dissolved in dry toluene (18 mL) and N_2 was bubbled through the solution for 20 min. The degassed solution was added to the microwave vial, sealed and heated in a microwave reactor at 120°C for 4 h. Water (15mL) and dichloromethane (50mL) were added. The organic phase was extracted, dried over $MgSO_4$ and the solvent removed under reduced pressure. The crude product was purified by recrystallization (chloroform/ethanol). Compound **12c** was isolated as a red solid (290 mg, 0.286 mmol, 80.1%). ^1H NMR (500 MHz, $CDCl_3$) δ/ppm 9.52 (s, 2H, H^{A3}), 8.65 (d, J = 4.1 Hz, 2H, H^{B3}), 7.58 (s, 2H, H^{A5}), 7.33 (d, J = 4.1 Hz, 2H, H^{B4}), 7.21 (d, J = 5.1 Hz, 2H, H^{D5}), 6.99 (s, 2H, H^{C4}), 6.95 (d, J = 5.1 Hz, 2H, H^{C5}), 3.17 (s, 6H, H^{Me}), 2.88–2.71 (m, 8H, H^{Ca+Da}), 1.77–1.60 (m, 8H, H^{Cb+Db}), 1.49–1.29 (m, 24H, H^{CH2}), 0.96–0.83 (m, 12H, H^{Cf+Df}). $^{13}C\{^1H\}$ NMR (126 MHz, $CDCl_3$) δ/ppm 157.12 (C^{A6}), 144.94 (C^{B2}), 142.70 (C^{C3}), 140.62 (C^{D2}), 136.99 (C^{D3}), 135.53 (C^{B3}), 130.47 (C^{D4}), 129.97 (C^{C5}), 129.25 (C^{C4}), 128.30 (C^{B4}), 124.52 (C^{D5}), 122.08 (C^{A5}), 120.94 (C^{A3}), 31.84 (C^{CH2}), 31.83 (C^{CH2}), 30.74 (C^{CH2}), 30.37

(C^{CH2}), 30.01 (C^{CH2}), 29.56 (C^{CH2}), 29.42 (C^{CH2}), 29.39 (C^{CH2}), 22.78 (C^{CH2}), 22.77, 21.11 (C^{Me}), 14.27 (C^{CH3}). C^{A2}, C^{A4}, C^{B5} and C^{C2} could not be assigned. MALDI-MS *m/z* 681.56 $[M+H]^+$ (calc. 681.25).

12.7.3 Compound 12d

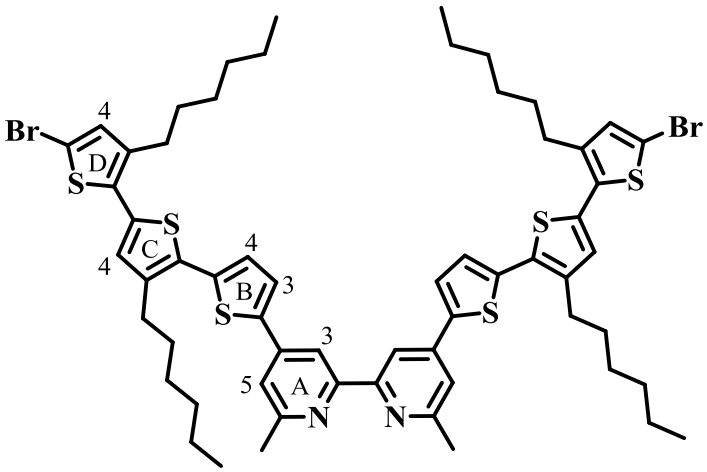

Compound **12c** (0.283 g, 0.279 mmol) was dissolved in chloroform/dimethylformamide (50 mL, 1/1) and N-bromosuccinimide (0.099 g, 0.558 mmol) was added in one portion. The solution was stirred at ambient conditions for 16h. Aq. HCl (20 mL, 1M) was added and the mixture extracted with dichloromethane (3 × 50mL). The organic phases were combined, dried over $MgSO_4$ and the solvent removed under reduced pressure. The crude product was purified by recrystallization (chloroform/ethanol). Compound **12d** was isolated as a red solid (280 mg, 0.239 mmol, 85.7%). ^{1}H NMR (500 MHz, CD_2Cl_2) δ/ppm 9.13 (s, 2H, H^{A3}), 8.15 (d, J = 3.5 Hz, 2H, H^{B3}), 7.52 (d, J = 1.5 Hz, 2H, H^{A5}), 7.26 (d, J = 3.9 Hz, 2H, H^{B4}), 6.95 (s, 2H, $H^{C4/D4}$), 6.94 (s, 2H, $H^{C4/D4}$), 2.93 (s, 6H, H^{Me}), 2.86–2.79 (m, 4H, H^{CH2}), 2.76–2.71 (m, 4H, H^{CH2}), 1.75–1.67 (m, 4H, H^{CH2}), 1.67–1.59 (m, 4H, H^{CH2}), 1.49–1.42 (m, 4H, H^{CH2}), 1.41–1.29 (m, 24H, H^{CH2}), 0.97–0.86 (m, 12H, H^{CH3}). $^{13}C\{^1H\}$ NMR (126 MHz, CD_2Cl_2) δ/ppm 157.42 (C^{A6}), 141.48, 133.62 ($C^{C4/D4}$), 132.18, 131.11 (C^{B3}), 130.52, 129.94 ($C^{C4/D4}$), 127.97 (C^{B4}), 121.62 (C^{A5}), 111.19, 32.25 (C^{CH2}), 32.19 (C^{CH2}), 31.02 (C^{CH2}), 30.88 (C^{CH2}), 30.18 (C^{CH2}), 29.84 (C^{CH2}), 29.80 (C^{CH2}), 29.67 (C^{CH2}), 23.21 (C^{CH2}), 23.19 (C^{Me}), 14.45 (C^{CH3}). Assignment of other carbon atoms was not possible, due to overlapping signals. MALDI-MS *m/z* 1171.58 $[M+H]^+$ (calc. 1171.23).

12.7.4 Compound 12e

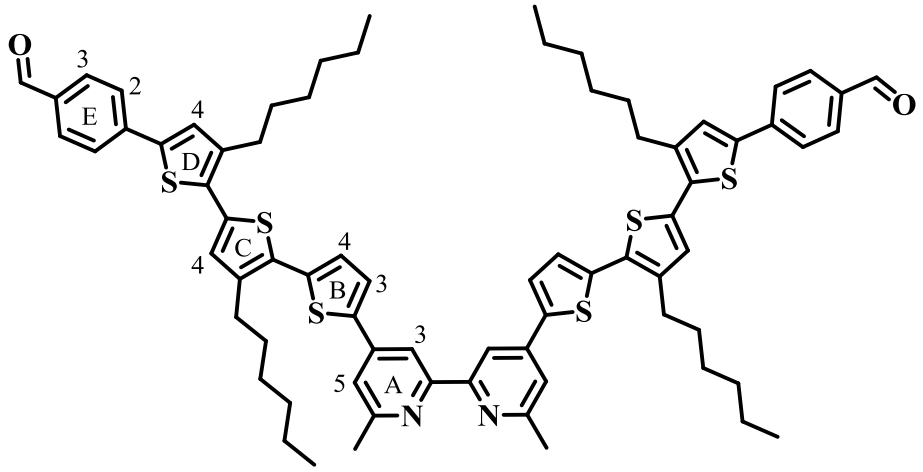

Compound **12d** (0.198 g, 0.169 mmol), 4-formylphenylboronic acid (0.063 g, 0.423 mmol), $[Pd(PPh_3)_4]$ (0.010 g, 0.008 mmol) and Cs_2CO_3 (0.330 g, 1.01 mmol) were added to a microwave vial and the vial was evacuated and flushed with N_2 three times. THF/water (18 mL/1mL) was added to a flask and N_2 was bubbled through the solvents for 20 min. The degassed solution was added to the microwave vial, sealed and heated in a microwave reactor at 90°C for 2 h. Water (15mL) and dichloromethane (50mL) were added. The organic phase was extracted, dried over $MgSO_4$ and the solvent removed under reduced pressure. The crude product was purified by recrystallization (chloroform/ethanol). Compound **12e** was isolated as a red solid (150 mg, 0.123 mmol, 72.6%). ^{1}H NMR (500 MHz, $CDCl_3$) δ/ppm 10.00 (s, 2H, H^{Ald}), 8.46 (d, J = 1.6 Hz, 2H, H^{A3}), 7.89 (d, J = 8.4 Hz, 4H, H^{E3}), 7.74 (d, J = 8.3 Hz, 4H, H^{E2}), 7.61 (d, J = 3.8 Hz, 2H, H^{B3}), 7.38 (d, J = 1.7 Hz, 2H, H^{A5}), 7.32 (s, 2H, H^{D4}), 7.20 (d, J = 3.8 Hz, 2H, H^{B4}), 7.06 (s, 2H, H^{C4}), 2.88–2.78 (m, 8H, H^{CH2}), 2.72 (s, 6H, H^{Me}), 1.78–1.66 (m, 8H, H^{CH2}), 1.51–1.41 (m, 8H, H^{CH2}), 1.41–1.29 (m, 16H, H^{CH2}), 0.98–0.84 (m, 12H, H^{CH3}). $^{13}C\{^1H\}$ NMR (126 MHz, $CDCl_3$) δ/ppm 191.50 (C^{Ald}), 158.83 (C^{A6}), 156.58, 142.28, 141.48, 141.24, 140.75, 140.06, 139.86, 137.43, 135.17, 134.23, 132.51, 130.88, 130.63 (C^{E3}), 129.20 (C^{C4}), 128.34 (C^{D4}), 126.93 (C^{B4}), 126.05 (C^{B3}), 125.72 (C^{E2}), 119.22 (C^{A5}), 114.67 (C^{A3}), 31.84 (C^{CH2}), 30.68 (C^{CH2}), 30.62 (C^{CH2}), 29.77 (C^{CH2}), 29.65 (C^{CH2}), 29.42 (C^{CH2}), 29.40 (C^{CH2}), 24.89 (C^{Me}), 22.79 (C^{CH2}), 14.28 (C^{CH3}). Assignment of other carbon atoms was not possible, due to overlapping signals. MALDI-MS *m/z* 1221.88 $[M+H]^+$ (calc. 1221.46).

12.7.5 Anchor molecule 12

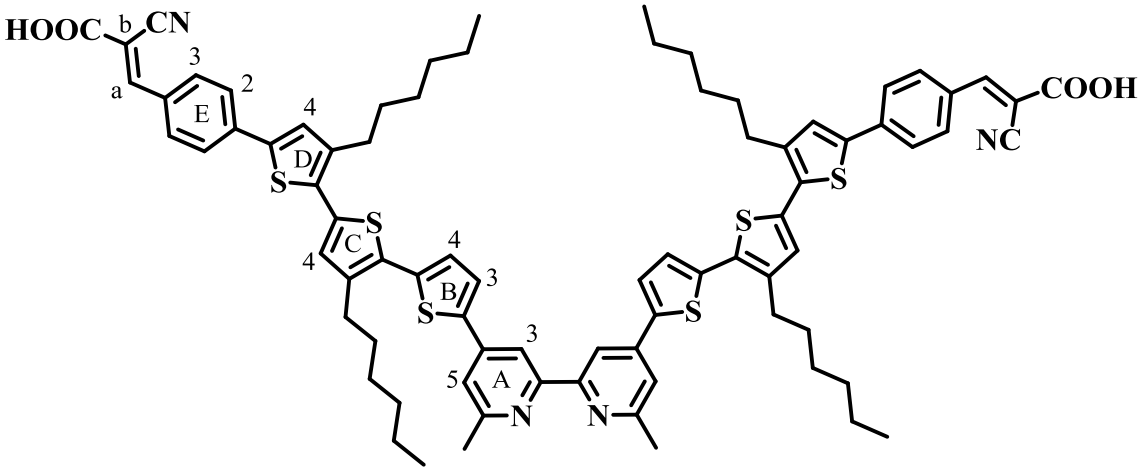

Compound **12e** (0.04 g, 0.033 mmol), cyanoacetic acid (0.008 g, 0.098 mmol), and a drop of piperidine were dissolved in chloroform. The mixture was refluxed for 16h and the precipitate collected by filtration. Compound **12** was isolated as a red solid (30 mg, 0.022 mmol, 67.7%). ^{1}H NMR (500 MHz, DMSO-d_6) δ/ppm 8.42 (s, 2H), 8.31 (s, 2H), 7.97–7.85 (m, 8H), 7.78 (d, J = 8.2 Hz, 4H), 7.70 (s, 2H), 7.63 (s, 2H), 7.37 (d, J = 4.0 Hz, 2H), 7.22 (s, 2H). The aliphatic region between 0-4 ppm showed broad signals and could not be assigned. ^{13}C{^{1}H} NMR data could not be obtained, due to peak broadening (aggregation, see discussion part) at higher concentrations. MALDI-MS *m/z* 1356.59 $[M+H]^+$ (calc. 1355.47).

12.8 P-type dye **13**

12.8.1 Compound 13a

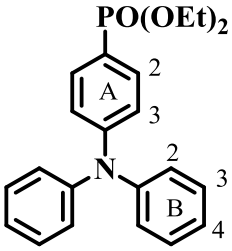

4-Bromotriphenylamine (1.0 g, 3.08 mmol), $Pd(PPh_3)_4$ (0.178 g, 0.154 mmol) and Cs_2CO_3 (1.5 g, 4.62 mmol) were added to a microwave vial and the vial was evacuated and flushed with N_2 three times. Diethyl phosphite (0.591 mL, 0.638 g, 4.62 mmol) was dissolved in dry THF (18 mL) and N_2 was bubbled through the solution for 20 min. The degassed solution was added to

the microwave vial, sealed and heated in a microwave reactor at 120°C for 20 min. Water (15mL) and dichloromethane (50mL) were added. The organic phase was extracted, dried over $MgSO_4$ and the solvent removed under reduced pressure. The crude product was purified by column chromatography (SiO_2, 3 : 2 cyclohexane/ethylacetate, Rf = 0.1). Compound **13a** was isolated as a yellow oil (573 mg, 1.503 mmol, 48.8%). ^{1}H NMR (500 MHz, $CDCl_3$) δ/ppm 7.59 (dd, J = 12.7, 8.4 Hz, 2H, H^{A2}), 7.29 (t, J = 7.7 Hz, 4H, H^{B3}), 7.16 – 7.07 (m, 6H, $H^{B2/B4}$), 7.01 (dd, J = 8.6, 3.4 Hz, 2H, H^{A3}), 4.20–4.01 (m, 4H, $H^{PO(O\underline{CH2}CH3)2}$), 1.32 (t, J = 7.1 Hz, 6H, $H^{PO(OCH2\underline{CH3})2}$). ^{13}C{^{1}H} NMR (126 MHz, $CDCl_3$) δ/ppm 151.60 (d, J_{PC} = 3.3 Hz, C^{A4}), 146.67 (C^{B1}), 133.01 (d, J_{PC} = 11.1 Hz, C^{A2}), 129.64 (C^{B3}), 125.87 (C^{B2}), 124.50 (C^{B4}), 120.28 (d, J_{PC} = 15.6 Hz, C^{A3}), 118.91 (d, J_{PC} = 195.7 Hz, C^{A1}), 62.03 (d, J_{PC} = 5.4 Hz, $C^{PO(O\underline{CH2}CH3)2}$), 16.45 (d, J_{PC} = 6.6 Hz, $C^{PO(OCH2\underline{CH3})2}$). ^{31}P NMR (202 MHz, $CDCl_3$) δ/ppm +20.06. MALDI-MS *m/z* 381.31 $[M+H]^+$ (calc. 382.16).

12.8.2 Compound 13b

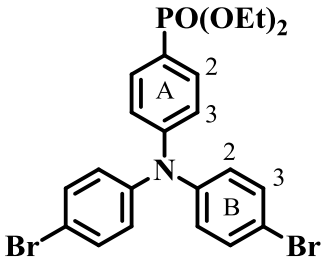

Compound **13b** (1.145 g, 3.0 mmol) was dissolved in THF and N-bromosuccinimide (1.335 g, 7.5 mmol) was added in one portion. The solution was heated at 60°C for 16h. Aq. Na_2CO_3 (20 mL, 10 %) was added and the mixture extracted with ethylacetate (3 × 50mL). The organic phases were combined, dried over $MgSO_4$ and the solvent removed under reduced pressure. The crude product was purified by column chromatography (SiO_2, 2:3 cyclohexane/ethylacetate, Rf = 0.4). Compound **13b** was isolated as a yellow oil (920 mg, 1.71 mmol, 56.9%). ^{1}H NMR (500 MHz, $CDCl_3$) δ/ppm 7.68–7.57 (m, 2H, H^{A2}), 7.44–7.36 (m, 4H, H^{B3}), 7.02 (dd, J = 8.6, 3.3 Hz, 2H, H^{A3}), 7.00–6.95 (m, 4H, H^{B2}), 4.21–3.96 (m, 4H, $H^{PO(O\underline{CH2}CH3)2}$), 1.33 (t, J = 7.1 Hz, 6H, $H^{PO(OCH2\underline{CH3})2}$). ^{13}C{^{1}H} NMR (126 MHz, $CDCl_3$) δ/ppm 150.69 (d, J_{PC} = 3.3 Hz, C^{A4}), 145.56 (C^{B1}), 133.29 (d, J_{PC} = 11.0 Hz, C^{A2}), 132.90 (C^{B3}), 127.03 (C^{B2}), 121.32 (d, J_{PC} = 15.6 Hz, C^{A3}), 120.91 (d, J_{PC} = 194.9 Hz, C^{A1}), 117.46 (C^{B4}), 62.19 (d,

J_{PC} = 5.5 Hz, $C^{PO(O\underline{CH2}CH3)2}$), 16.51 (d, J_{PC} = 6.5 Hz, $C^{PO(OCH2\underline{CH3})2}$). ^{31}P NMR (202 MHz, $CDCl_3$) δ/ppm +19.28. MALDI-MS *m/z* 540.13 $[M+H]^+$ (calc. 539.2).

12.8.3 Compound 13c

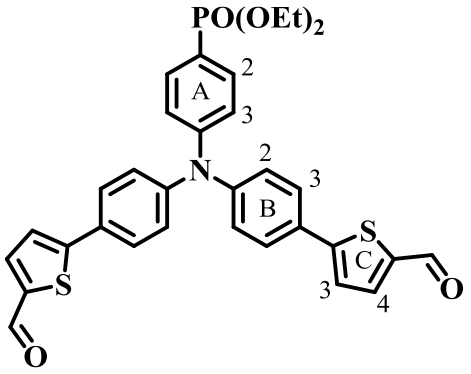

5-(4,4,5,5-tetramethyl-1,3,2-dioxaborolan-2-yl)thiophene-2-carbaldehyde (1.029 g, 4.32 mmol), $Pd(PPh_3)_4$ (0.125 g, 0.108 mmol) and Cs_2CO_3 (2.111 g, 6.48 mmol) were added to a microwave vial and the vial was evacuated and flushed with N_2 three times. Compound **13b** (0.582 g, 1.08 mmol) was dissolved in dry toluene (18 mL) and N_2 was bubbled through the solution for 20 min. The degassed solution was added to the microwave vial, sealed and heated in a microwave reactor at 120°C for 4h. Water (15mL) and ethylacetate (50mL) were added. The organic phase was extracted, dried over $MgSO_4$ and the solvent removed under reduced pressure. The crude product was purified by column chromatography (SiO_2, ethylacetate, Rf = 0.4). Compound **13c** was isolated as a yellow oil (402 mg, 0.668 mmol, 61.9%). ^1H NMR (500 MHz, $CDCl_3$) δ/ppm 9.88 (s, 2H, H^{Ald}), 7.74 (d, J = 4.0 Hz, 2H, H^{C4}), 7.70 (dd, J = 12.8, 8.6 Hz, 2H, H^{A2}), 7.61 (d, J = 8.6 Hz, 4H, H^{B3}), 7.36 (d, J = 3.9 Hz, 2H, H^{C3}), 7.20–7.14 (m, 6H, $H^{B2/A3}$), 4.28–3.96 (m, 4H, $H^{PO(O\underline{CH2}CH3)2}$), 1.35 (t, J = 7.1 Hz, 6H, $H^{PO(OCH2\underline{CH3})2}$). $^{13}C\{^1H\}$ NMR (126 MHz, $CDCl_3$) δ/ppm 182.82 (C^{Ald}), 153.63 (C^{C2}), 150.32 (d, J_{PC} = 3.4 Hz, C^{A4}), 147.45 (C^{B1}), 142.28 (C^{C5}), 137.71 (C^{C4}), 133.40 (d, J_{PC} = 11.0 Hz, C^{A2}), 127.85 (C^{B3}), 125.40 (C^{B2}), 123.85 (C^{C3}), 122.84 (d, J_{PC} = 15.6 Hz, C^{A3}), 122.07 (d, J_{PC} = 195.0 Hz, C^{A1}) 62.35 (d, J_{PC} = 5.5 Hz, $C^{PO(O\underline{CH2}CH3)2}$), 16.53 (d, J_{PC} = 6.5 Hz, $C^{PO(OCH2\underline{CH3})2}$), C^{B4} could not be resolved. ^{31}P NMR (202 MHz, $CDCl_3$) δ/ppm +18.97. MALDI-MS *m/z* 601.54 $[M+H]^+$ (calc. 602.12).

12.8.4 Compound 13d

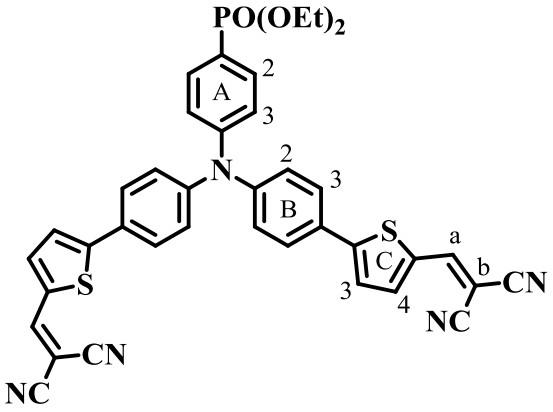

Compound **13c** (0.349 g, 0.58 mmol) was dissolved in anhydrous acetonitrile (30mL). Malononitrile (0.084 g, 1.28 mmol) and trimethylamine (4 drops) were added and the mixture was refluxed at 85 °C for 16h. Dichloromethane (50 mL) was added and the organic phase was washed with water (3 × 30mL), dried over $MgSO_4$ and the solvent removed under reduced pressure. The crude product was purified by column chromatography (SiO_2, ethylacetate, Rf = 0.3). Compound **13d** was isolated as a red oil (278 mg, 0.398 mmol, 68.7%). ^{1}H NMR (500 MHz, $CDCl_3$) δ/ppm 7.79 (s, 2H, H^{a}), 7.76–7.70 (m, 4H, $H^{A2/C4}$), 7.64–7.62 (m, 4H, C^{B3}), 7.40 (d, J = 4.1 Hz, 2H, C^{C3}), 7.21–7.15 (m, 6H, $C^{A3/B2}$), 4.23–4.07 (m, 4H, $H^{P(O)(O\underline{CH2}CH3)}$), 1.35 (t, J = 7.1 Hz, 6H, $H^{P(O)(OCH2\underline{CH3})}$). $^{13}C\{^{1}H\}$ NMR (126 MHz, $CDCl_3$) δ/ppm 155.74 (C^{a}), 150.56 (C^{C2}), 149.85 (d, J_{PC} = 3.5 Hz, C^{A4}), 147.98 (C^{B1}), 140.40 (C^{C4}), 134.08 (C^{C5}), 133.48 (d, J_{PC} = 10.8 Hz, C^{A2}), 128.13 (C^{B3}), 125.16 (C^{B2}), 124.34 (C^{C3}), 123.55 (d, J_{PC} = 15.5 Hz, C^{A3}), 123.16 (d, J_{PC} = 194.2 Hz, C^{A1}), 114.35 (C^{CN}), 113.55 (C^{CN}), 76.41 (C^{b}), 62.34 (d, J_{PC} = 5.6 Hz, $C^{P(O)(O\underline{CH2}CH3)}$), 16.52 (d, J_{PC} = 6.5 Hz, $C^{P(O)(OCH2\underline{CH3})}$). C^{B4} could not be resolved. ^{31}P NMR (202 MHz, $CDCl_3$) δ/ppm +18.57. MALDI-MS *m/z* 697.78 $[M+H]^{+}$ (calc. 698.14).

12.8.5 P-type dye 13

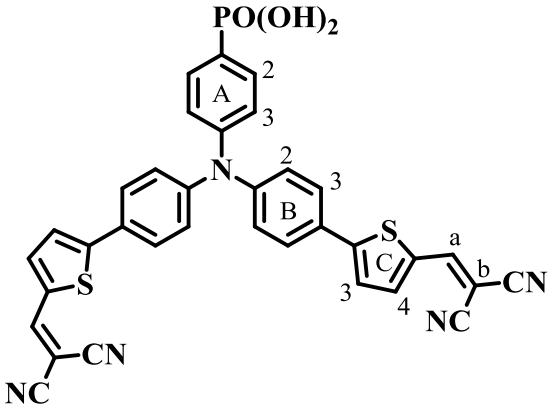

Compound **13d** (0.06 g, 0.086 mmol) was dissolved in anhydrous dichloromethane (30mL). Bromotrimethylsilane (0.227 mL, 0.263 g, 1.72 mmol) was added and the solution stirred at room temperature for 16h. Water (20mL) and dichloromethane (20 mL) were added and the organic phase was washed with water (3 × 30mL), dried over $MgSO_4$ and the solvent removed under reduced pressure. The crude product was recrystallized from ethanol/cyclohexane. Compound **13** was isolated as a red solid (38 mg, 0.059 mmol, 68.9%). ^{1}H NMR (500 MHz, DMSO-d_6) δ/ppm 11.03 (s, 2H, $H^{P(O)(OH)2}$), 8.64 (s, 2H, H^{a}), 7.95 (d, J = 4.1 Hz, 2H, H^{C4}), 7.80 (d, J = 8.4 Hz, 4H, H^{B3}), 7.77 (d, J = 4.1 Hz, 2H, H^{C3}), 7.66 (dd, J = 12.4, 8.1 Hz, 2H, H^{A2}), 7.21–7.13 (m, 6H, $H^{A3/B2}$). ^{13}C{^{1}H} NMR (126 MHz, $CDCl_3$) δ/ppm 155.09 (C^{C2}), 152.96 (C^{a}), 148.17, 143.12 (C^{C4}), 133.26 (C^{A2}), 128.48 (C^{B3}), 127.41, 125.42 (C^{C3}), 124.63 ($C^{A2/B2}$), 115.20 (C^{CN}). Other C-atoms could not be assigned, due to low concentration in the NMR sample and peak broadening upon increase of the concentration. ^{31}P NMR (202 MHz, $CDCl_3$) δ/ppm +25.49. ESI-MS *m/z* 639.99 $[M-H]^-$ (calc. 640.07).

13 REFERENCES

[1] U.S. Energy Information Administration / Annual Energy Review 2009, retrieved 21 January 2018, https://www.eia.gov/totalenergy/data/annual/.

[2] Natural Resources Canada, Energy Sources and Distribution 2016, retrieved 21 January 2018, https://www.nrcan.gc.ca/energy/oil-sands/18089.

[3] NASA/Goddard Institute for Space Studies, 2016 Climate Trends Continue to Break Records, retrieved 21 January 2018, https://www.giss.nasa.gov/research/news/20160719/.

[4] United Nations, Paris Agreement on Climate Change 2016, retrieved 21 January 2018, http://bigpicture.unfccc.int/#content-the-paris-agreemen.

[5] PBL Netherlands Environmental Assessment Agency, Trends in Global CO_2 emission 2016, retrieved 21 January 2018, http://www.pbl.nl/en/publications/trends-in-global-co2-emissions-2016-report.

[6] R. Perez, M. Perez, *A fundamental look at energy reserves for the planet, Vol. 50*, **2009**.

[7] W. Shockley, H. J. Queisser, *J. Appl. Phys.* **1961**, *32*, 510-519.

[8] A. Hagfeldt, G. Boschloo, L. Sun, L. Kloo, H. Pettersson, *Chem. Rev.* **2010**, *110*, 6595-6663.

[9] D. C. Jordan, S. R. Kurtz, *Prog. Photovolt: Res. Appl.* **2013**, *21*, 12-29.

[10] M. A. Green, K. Emery, Y. Hishikawa, W. Warta, E. D. Dunlop, D. H. Levi, A. W. Y. Ho-Baillie, *Prog. Photovolt: Res. Appl.* **2017**, *25*, 3-13.

[11] M. C. Hanna, A. J. Nozik, *J. Appl. Phys.* **2006**, *100*, 074510.

[12] W. S. Yang, B.-W. Park, E. H. Jung, N. J. Jeon, Y. C. Kim, D. U. Lee, S. S. Shin, J. Seo, E. K. Kim, J. H. Noh, S. I. Seok, *Science* **2017**, *356*, 1376-1379.

[13] G. Grancini, C. Roldán-Carmona, I. Zimmermann, E. Mosconi, X. Lee, D. Martineau, S. Narbey, F. Oswald, F. De Angelis, M. Grätzel, M. K. Nazeeruddin, *Nat. Commun.* **2017**, *8*, 15684.

[14] B. O'Regan, M. Grätzel, *Nature* **1991**, *353*, 737.

[15] J. Wang, K. Liu, L. Ma, X. Zhan, *Chem. Rev.* **2016**, *116*, 14675-14725.

[16] C. E. Housecroft, E. C. Constable, *Chem. Soc. Rev.* **2015**, *44*, 8386-8398.

[17] M. A. M. Al-Alwani, A. B. Mohamad, N. A. Ludin, A. A. H. Kadhum, K. Sopian, *Renew. Sust. Energ. Rev.* **2016**, *65*, 183-213.

[18] M. S. Su'ait, M. Y. A. Rahman, A. Ahmad, *Sol. Energy* **2015**, *115*, 452-470.

[19] Y. Cao, Y. Saygili, A. Ummadisingu, J. Teuscher, J. Luo, N. Pellet, F. Giordano, S. M. Zakeeruddin, J. E. Moser, M. Freitag, A. Hagfeldt, M. Grätzel, *Nat. Commun.* **2017**, *8*, 15390.

[20] S. O. Fürer, B. Bozic-Weber, T. Schefer, C. Wobill, E. C. Constable, C. E. Housecroft, M. Willgert, *J. Mater. Chem. A* **2016**, *4*, 12995-13004.

[21] A. Colombo, G. Di Carlo, C. Dragonetti, M. Magni, A. Orbelli Biroli, M. Pizzotti, D. Roberto, F. Tessore, E. Benazzi, C. A. Bignozzi, L. Casarin, S. Caramori, *Inorg. Chem.* **2017**, *56*, 14189-14197.

[22] J. Nowotny, M. A. Alim, T. Bak, M. A. Idris, M. Ionescu, K. Prince, M. Z. Sahdan, K. Sopian, M. A. Mat Teridi, W. Sigmund, *Chem. Soc. Rev.* **2015**, *44*, 8424-8442.

[23] C. Dette, M. A. Pérez-Osorio, C. S. Kley, P. Punke, C. E. Patrick, P. Jacobson, F. Giustino, S. J. Jung, K. Kern, *Nano Lett.* **2014**, *14*, 6533-6538.

[24] M. K. Nazeeruddin, A. Kay, I. Rodicio, R. Humphry-Baker, E. Mueller, P. Liska, N. Vlachopoulos, M. Grätzel, *J. Am. Chem. Soc.* **1993**, *115*, 6382-6390.

[25] K. Kakiage, H. Osada, Y. Aoyama, T. Yano, K. Oya, S. Iwamoto, J.-i. Fujisawa, M. Hanaya, *Sci. Rep.* **2016**, *6*, 35888.

[26] B. Roose, S. Pathak, U. Steiner, *Chem. Soc. Rev.* **2015**, *44*, 8326-8349.

[27] C. Zhang, S. Chen, L. e. Mo, Y. Huang, H. Tian, L. Hu, Z. Huo, S. Dai, F. Kong, X. Pan, *J. Phys. Chem. C* **2011**, *115*, 16418-16424.

[28] M. Saito, S. Fujihara, *Energy Environ. Sci.* **2008**, *1*, 280-283.

[29] O.-A. Boateng, K. Shoji, K. Asoka, O. Masayuki, M. Kenji, K. Akinori, T. Kirthi, *Jpn. J. Appl. Phys.* **2005**, *44*, L731.

[30] G. Boschloo, H. Lindström, E. Magnusson, A. Holmberg, A. Hagfeldt, *J. Photochem. Photobiol., A* **2002**, *148*, 11-15.

[31] S. E. Koops, B. C. O'Regan, P. R. F. Barnes, J. R. Durrant, *J. Am. Chem. Soc.* **2009**, *131*, 4808-4818.

[32] N. Kopidakis, K. D. Benkstein, J. van de Lagemaat, A. J. Frank, *J. Phys. Chem. B* **2003**, *107*, 11307-11315.

[33] A. Yella, H.-W. Lee, H. N. Tsao, C. Yi, A. K. Chandiran, M. K. Nazeeruddin, E. W.-G. Diau, C.-Y. Yeh, S. M. Zakeeruddin, M. Grätzel, *Science* **2011**, *334*, 629-634.

[34] B. Bozic-Weber, E. C. Constable, S. O. Fürer, C. E. Housecroft, L. J. Troxler, J. A. Zampese, *Chem. Commun.* **2013**, *49*, 7222-7224.

[35] K. Kakiage, Y. Aoyama, T. Yano, K. Oya, J.-i. Fujisawa, M. Hanaya, *Chem. Commun.* **2015**, *51*, 15894-15897.

[36] Y. Bai, Q. Yu, N. Cai, Y. Wang, M. Zhang, P. Wang, *Chem. Commun.* **2011**, *47*, 4376-4378.

[37] M. Magni, R. Giannuzzi, A. Colombo, M. P. Cipolla, C. Dragonetti, S. Caramori, S. Carli, R. Grisorio, G. P. Suranna, C. A. Bignozzi, D. Roberto, M. Manca, *Inorg. Chem.* **2016**, *55*, 5245-5253.

[38] K. Kakiage, T. Tokutome, S. Iwamoto, T. Kyomen, M. Hanaya, *Chem. Commun.* **2013**, *49*, 179-180.

[39] E. Galoppini, *Coord. Chem. Rev.* **2004**, *248*, 1283-1297.

[40] P. Pechy, F. P. Rotzinger, M. K. Nazeeruddin, O. Kohle, S. M. Zakeeruddin, R. Humphry-Baker, M. Grätzel, *J. Chem. Soc., Chem. Commun.* **1995**, 65-66.

[41] H. Park, E. Bae, J.-J. Lee, J. Park, W. Choi, *J. Phys. Chem. B* **2006**, *110*, 8740-8749.

[42] B. Bozic-Weber, E. C. Constable, C. E. Housecroft, P. Kopecky, M. Neuburger, J. A. Zampese, *Dalton Trans.* **2011**, *40*, 12584-12594.

[43] Y. Ooyama, Y. Shimada, Y. Kagawa, Y. Yamada, I. Imae, K. Komaguchi, Y. Harima, *Tetrahedron Lett.* **2007**, *48*, 9167-9170.

[44] J. Idigoras, M. Godfroy, D. Joly, A. Todinova, P. Maldivi, G. Oskam, R. Demadrille, J. A. Anta, *RSC Adv.* **2015**, *5*, 68929-68938.

[45] D. Daphnomili, G. Landrou, S. Prakash Singh, A. Thomas, K. Yesudas, B. K, G. D. Sharma, A. G. Coutsolelos, *RSC Adv.* **2012**, *2*, 12899-12908.

[46] T. Michinobu, N. Satoh, J. Cai, Y. Li, L. Han, *J. Mater. Chem. C* **2014**, *2*, 3367-3372.

[47] C. Li, J.-H. Yum, S.-J. Moon, A. Herrmann, F. Eickemeyer, N. G. Pschirer, P. Erk, J. Schöneboom, K. Müllen, M. Grätzel, M. K. Nazeeruddin, *ChemSusChem* **2008**, *1*, 615-618.

[48] S.-F. Li, X.-C. Yang, M. Cheng, J.-H. Zhao, Y. Wang, L.-C. Sun, *Tetrahedron Lett.* **2012**, *53*, 3425-3428.

[49] L. Wang, X. Yang, S. Li, M. Cheng, L. Sun, *RSC Adv.* **2013**, *3*, 13677-13680.

[50] K. Omata, S. Kuwahara, K. Katayama, S. Qing, T. Toyoda, K.-M. Lee, C.-G. Wu, *Phys. Chem. Chem. Phys.* **2015**, *17*, 10170-10175.

[51] K. Kakiage, Y. Aoyama, T. Yano, T. Otsuka, T. Kyomen, M. Unno, M. Hanaya, *Chem. Commun.* **2014**, *50*, 6379-6381.

[52] K. Y. Chiu, T. T. Ha Tran, S. H. Chang, T.-F. Yang, Y. O. Su, *Dyes Pigm.* **2017**, *146*, 512-519.

[53] C. Zhang, S. Wang, Y. Li, *Sol. Energy* **2017**, *157*, 94-102.

[54] M. K. Nazeeruddin, P. Pechy, M. Grätzel, *Chem. Commun.* **1997**, 1705-1706.

[55] C.-C. Chou, K.-L. Wu, Y. Chi, W.-P. Hu, S. J. Yu, G.-H. Lee, C.-L. Lin, P.-T. Chou, *Angew. Chem., Int. Ed.* **2011**, *50*, 2054-2058.

[56] M. Tuikka, P. Hirva, K. Rissanen, J. Korppi-Tommola, M. Haukka, *Chem. Commun.* **2011**, *47*, 4499-4501.

[57] T. Privalov, G. Boschloo, A. Hagfeldt, P. H. Svensson, L. Kloo, *J. Phys. Chem. C* **2009**, *113*, 783-790.

[58] M. K. Nazeeruddin, S. M. Zakeeruddin, R. Humphry-Baker, M. Jirousek, P. Liska, N. Vlachopoulos, V. Shklover, C.-H. Fischer, M. Grätzel, *Inorg. Chem.* **1999**, *38*, 6298-6305.

[59] P. Wang, S. M. Zakeeruddin, J. E. Moser, M. K. Nazeeruddin, T. Sekiguchi, M. Grätzel, *Nat. Mater.* **2003**, *2*, 402.

[60] C.-Y. Chen, M. Wang, J.-Y. Li, N. Pootrakulchote, L. Alibabaei, C.-h. Ngoc-le, J.-D. Decoppet, J.-H. Tsai, C. Grätzel, C.-G. Wu, S. M. Zakeeruddin, M. Grätzel, *ACS Nano* **2009**, *3*, 3103-3109.

[61] Rare Metals Prices and Charts, retrieved 09 January 2018, https://www.quandl.com/collections/markets/rare-metals.

[62] C. E. Housecroft, A. G. Sharpe, in *Inorganic Chemistry, 3rd edn*, Pearson, **2008**, p. 738.

[63] B. Bozic-Weber, V. Chaurin, E. C. Constable, C. E. Housecroft, M. Meuwly, M. Neuburger, J. A. Rudd, E. Schönhofer, L. Siegfried, *Dalton Trans.* **2012**, *41*, 14157-14169.

[64] N. Armaroli, G. Accorsi, F. Cardinali, A. Listorti, in *Photochemistry and Photophysics of Coordination Compounds I* (Eds.: V. Balzani, S. Campagna), Springer Berlin Heidelberg, Berlin, Heidelberg, **2007**, pp. 69-115.

[65] K.-L. Wu, S.-T. Ho, C.-C. Chou, Y.-C. Chang, H.-A. Pan, Y. Chi, P.-T. Chou, *Angew. Chem., Int. Ed.* **2012**, *51*, 5642-5646.

[66] T. Higashino, H. Imahori, *Dalton Trans.* **2015**, *44*, 448-463.

[67] T. C. B. Harlang, Y. Liu, O. Gordivska, L. A. Fredin, C. S. Ponseca Jr, P. Huang, P. Chábera, K. S. Kjaer, H. Mateos, J. Uhlig, R. Lomoth, R. Wallenberg, S. Styring, P. Persson, V. Sundström, K. Wärnmark, *Nat. Chem.* **2015**, *7*, 883.

[68] A. Barbieri, G. Accorsi, N. Armaroli, *Chem. Commun.* **2008**, 2185-2193.

[69] M. Alebbi, C. A. Bignozzi, T. A. Heimer, G. M. Hasselmann, G. J. Meyer, *J. Phys. Chem. B* **1998**, *102*, 7577-7581.

[70] G. Sauvé, M. E. Cass, G. Coia, S. J. Doig, I. Lauermann, K. E. Pomykal, N. S. Lewis, *J. Phys. Chem. B* **2000**, *104*, 6821-6836.

[71] M. Pastore, T. Duchanois, L. Liu, A. Monari, X. Assfeld, S. Haacke, P. C. Gros, *Phys. Chem. Chem. Phys.* **2016**, *18*, 28069-28081.

[72] E. Galoppini, *Nat. Chem.* **2015**, *7*, 861.

[73] T. Duchanois, T. Etienne, C. Cebrián, L. Liu, A. Monari, M. Beley, X. Assfeld, S. Haacke, P. C. Gros, *Eur. J. Inorg. Chem.* **2015**, *2015*, 2469-2477.

[74] N. Alonso-Vante, J.-F. Nierengarten, J.-P. Sauvage, *J. Chem. Soc., Dalton Trans.* **1994**, 1649-1654.

[75] C. E. Housecroft, A. G. Sharpe, in *Inorganic Chemistry, 4th edn*, Pearson, **2012**, chapter 7.

[76] F. J. Malzner, A. Prescimone, E. C. Constable, C. E. Housecroft, M. Willgert, *J. Mater. Chem. A* **2017**, *5*, 4671-4685.

[77] T. Bessho, E. C. Constable, M. Grätzel, A. Hernandez Redondo, C. E. Housecroft, W. Kylberg, M. K. Nazeeruddin, M. Neuburger, S. Schaffner, *Chem. Commun.* **2008**, 3717-3719.

[78] M. Sandroni, M. Kayanuma, A. Planchat, N. Szuwarski, E. Blart, Y. Pellegrin, C. Daniel, M. Boujtita, F. Odobel, *Dalton Trans.* **2013**, *42*, 10818-10827.

[79] M. Sandroni, L. Favereau, A. Planchat, H. Akdas-Kilig, N. Szuwarski, Y. Pellegrin, E. Blart, H. Le Bozec, M. Boujtita, F. Odobel, *J. Mater. Chem. A* **2014**, *2*, 9944-9947.

[80] B. Bozic-Weber, S. Y. Brauchli, E. C. Constable, S. O. Fürer, C. E. Housecroft, F. J. Malzner, I. A. Wright, J. A. Zampese, *Dalton Trans.* **2013**, *42*, 12293-12308.

[81] Y.-J. Yuan, Z.-T. Yu, J.-Y. Zhang, Z.-G. Zou, *Dalton Trans.* **2012**, *41*, 9594-9597.

[82] K. A. Wills, H. J. Mandujano-Ramirez, G. Merino, D. Mattia, T. Hewat, N. Robertson, G. Oskam, M. D. Jones, S. E. Lewis, P. J. Cameron, *RSC Adv.* **2013**, *3*, 23361-23369.

[83] F. J. Malzner, S. Y. Brauchli, E. Schönhofer, E. C. Constable, C. E. Housecroft, *Polyhedron* **2014**, *82*, 116-121.

[84] F. J. Malzner, S. Y. Brauchli, E. C. Constable, C. E. Housecroft, M. Neuburger, *RSC Adv.* **2014**, *4*, 48712-48723.

[85] B. Bozic-Weber, S. Y. Brauchli, E. C. Constable, S. O. Fürer, C. E. Housecroft, I. A. Wright, *Phys. Chem. Chem. Phys.* **2013**, *15*, 4500-4504.

[86] S. O. Fürer, B. Bozic-Weber, M. Neuburger, E. C. Constable, C. E. Housecroft, *RSC Adv.* **2015**, *5*, 69430-69440.

[87] S. O. Fürer, L. Y. N. Luu, B. Bozic-Weber, E. C. Constable, C. E. Housecroft, *Dyes Pigm.* **2016**, *132*, 72-78.

[88] Bruker Analytical X-ray Systems, Inc., APEX2, version 2 User Manual, M86-E01078, Madison, WI, 2006.

[89] P. W. Betteridge, J. R. Carruthers, R. I. Cooper, K. Prout, D. J. Watkin, *J. Appl. Crystallogr.* **2003**, *36*, 1487.

[90] I. J. Bruno, J. C. Cole, P. R. Edgington, M. Kessler, C. F. Macrae, P. McCabe, J. Pearson, R. Taylor, *Acta Crystallogr., Sect. B* **2002**, *58*, 389-397.

[91] C. F. Macrae, I. J. Bruno, J. A. Chisholm, P. R. Edgington, P. McCabe, E. Pidcock, L. Rodriguez-Monge, R. Taylor, J. van de Streek, P. A. Wood, *J. Appl. Crystallogr.* **2008**, *41*, 466-470.

[92] F. Brunner, N. Marinakis, C. Wobill, M. Willgert, C. D. Ertl, T. Kosmalski, M. Neuburger, B. Bozic-Weber, T. Glatzel, E. C. Constable, C. E. Housecroft, *J. Mater. Chem. C* **2016**, *4*, 9823-9833.

[93] M. W. Mara, K. A. Fransted, L. X. Chen, *Coord. Chem. Rev.* **2015**, *282-283*, 2-18.

[94] S. Y. Brauchli, F. J. Malzner, E. C. Constable, C. E. Housecroft, *RSC Adv.* **2015**, *5*, 48516-48525.

[95] F. Kröhnke, *Synthesis* **1976**, *1976*, 1-24.

[96] V. Spampinato, N. Tuccitto, S. Quici, V. Calabrese, G. Marletta, A. Torrisi, A. Licciardello, *Langmuir* **2010**, *26*, 8400-8406.

[97] Z.-S. Wang, N. Koumura, Y. Cui, M. Takahashi, H. Sekiguchi, A. Mori, T. Kubo, A. Furube, K. Hara, *Chem. Mater.* **2008**, *20*, 3993-4003.

[98] K. S. Chan, A. K. S. Tse, *Synth. Commun.* **1993**, *23*, 1929-1934.

[99] E. Negishi, *Angew. Chem., Int. Ed.* **2011**, *50*, 6738-6764.

[100] G. J. Kubas, B. Monzyk, A. L. Crumbliss, in *Inorganic Syntheses*, John Wiley & Sons, Inc., **2007**, pp. 90-92.

[101] F. Brunner, Y. M. Klein, S. Keller, C. D. Morris, A. Prescimone, E. C. Constable, C. E. Housecroft, *RSC Adv.* **2015**, *5*, 58694-58703.

[102] M. Magni, A. Colombo, C. Dragonetti, P. Mussini, *Electrochim. Acta* **2014**, *141*, 324-330.

[103] S. Ito, M. K. Nazeeruddin, P. Liska, P. Comte, R. Charvet, P. Péchy, M. Jirousek, A. Kay, S. M. Zakeeruddin, M. Grätzel, *Prog. Photovolt: Res. Appl.* **2006**, *14*, 589-601.

[104] H. J. Snaith, *Energy Environ. Sci.* **2012**, *5*, 6513-6520.

[105] Y. M. Klein, M. Willgert, A. Prescimone, E. C. Constable, C. E. Housecroft, *Dalton Trans.* **2016**, *45*, 4659-4672.

[106] S. Y. Brauchli, B. Bozic-Weber, E. C. Constable, N. Hostettler, C. E. Housecroft, J. A. Zampese, *RSC Adv.* **2014**, *4*, 34801-34815.

[107] M. T. Miller, P. K. Gantzel, T. B. Karpishin, *Angew. Chem., Int. Ed.* **1998**, *37*, 1556-1558.

[108] P. Shen, Y. Liu, X. Huang, B. Zhao, N. Xiang, J. Fei, L. Liu, X. Wang, H. Huang, S. Tan, *Dyes Pigm.* **2009**, *83*, 187-197.

[109] G. Li, K.-J. Jiang, Y.-F. Li, S.-L. Li, L.-M. Yang, *J. Phys. Chem. C* **2008**, *112*, 11591-11599.

[110] L. Groenendaal, F. Jonas, D. Freitag, H. Pielartzik, J. R. Reynolds, *Adv. Mater.* **2000**, *12*, 481-494.

[111] J. Clayden, N. Greeves, S. Warren, P. Wothers, in *Organic Chemistry*, Oxford University Press, **2001**, pp. 1160-1161.

[112] C.-P. Lee, R. Y.-Y. Lin, L.-Y. Lin, C.-T. Li, T.-C. Chu, S.-S. Sun, J. T. Lin, K.-C. Ho, *RSC Adv.* **2015**, *5*, 23810-23825.

[113] Y. Baumgartner, Y. Maximilian Klein, E. C. Constable, C. E. Housecroft, M. Willgert, *RSC Adv.* **2016**, *6*, 86220-86231.

[114] D. O. Kirsanov, N. E. Borisova, M. D. Reshetova, A. V. Ivanov, L. A. Korotkov, I. I. Eliseev, M. Y. Alyapyshev, I. G. Spiridonov, A. V. Legin, Y. G. Vlasov, V. A. Babain, *Russ. Chem. Bull.* **2012**, *61*, 881-890.

[115] A. F. Larsen, T. Ulven, *Org. Lett.* **2011**, *13*, 3546-3548.

[116] B. Zietz, E. Gabrielsson, V. Johansson, A. M. El-Zohry, L. Sun, L. Kloo, *Phys. Chem. Chem. Phys.* **2014**, *16*, 2251-2255.

[117] P. Qin, H. Zhu, T. Edvinsson, G. Boschloo, A. Hagfeldt, L. Sun, *J. Am. Chem. Soc.* **2008**, *130*, 8570-8571.

Part II

Coordination polymers

TABLE OF CONTENTS

1 ABSTRACT

The careful choice of building blocks, the consideration of their geometry, topology and their influence on the crystal packing interactions enables control of the self-assembly processes in coordination polymer synthesis. When these aspects are well understood the specific construction of various multidimensional motifs, by self-assembly of building blocks can be achieved. The building blocks are often easily accessible in the form of metal salts and organic ligands, that often require few synthetic steps to synthesize. Screening of building blocks for the creation of multidimensional motifs on the nano to micro scale is an important research field.

The building blocks self-assemble and form these structures without further influence of the scientist. With the right selection of building blocks and by careful consideration of conditions, like temperature and concentration it is possible to predefine the outcome of the self-assembly process.

Organic ligands based on 4,2':6',4"- and 3,2':6',3"-terpyridine were synthesized and the control of the self-assembly process of these linkers with various metal centres was investigated.

Rigid ditopic 4,2':6',4"-terpyridines proved to be the most reliable ligand in this respect. In combination with linear two-connecting metal centres, 1D zig-zag chains were the dominant motif. With metal centres, like Co(II) (and to some extent Cd(II)), that have a connectivity of four, the dominant motif was the formation of 2D (4,4) nets.

Tetratopic bis(4,2':6',4"-terpyridines) and bis(3,2':6',3"-terpyridines) were used to assemble 2D networks, 3D frameworks and MOFs. 3D frameworks are known for their potential applications in gas-sorption, guest exchange, drug-delivery etc. Their formation was not predictable, but the change from ditopic linkers to tetratopic linkers increased the probability to obtain these 3D motifs. A 2-fold interpenetrating MOF with ~65% void space, relative to the total volume, was obtained with a tetratopic bis(4,2':6',4"-terpyridine) ligand in combination with $ZnBr_2$, which highlights the great potential of this ligand class.

A collection of ~30 multidimensional structures is presented in this thesis and should give an indication how one might be able to control self-assembly processes in coordination polymers with 4,2':6',4"- and 3,2':6',3"-terpyridines as linkers.

Chapter 3 is the general introduction of coordination polymers and MOFs.

Chapter 4 gives a perspective of recent coordination polymers obtained with 4,2':6',4"- and 3,2':6',3"-terpyridines.

Chapter 5 discusses characterization methods.

Chapter 6 describes ligand design and synthesis of ligands presented in this thesis.

Chapter 7 shows two single crystal structures of ligands.

Chapter 8 displays discrete cyclic structures.

Chapters 9 and **10** discuss with 1D coordination chains and ladders.

Chapter 11 illustrates 2D networks.

Chapter 12 presents 3D frameworks and a MOF.

Chapters 13 and **14** are the conclusion and outlook, respectively.

Chapters 15 and **16** contain the experimental part including PXRD spectra.

Chapter 17 contains the crystallographic data.

Chapter 18 contains the reprints of the publications (see below) for detailed structure discussion.

Chapter 19 is the literature reference list.

The work presented in this thesis has been published (chronological order) and the printed versions of these papers can be found in chapter **18** of this thesis:

4'-(Pyrimidin-5-yl)- and 4'-(2-methylpyrimidin-5-yl)- 4,2':6',4"-terpyridines: selective coordination to zinc(II) through the 4,2':6',4"-terpyridine domain
Y. Maximilian Klein, E. C. Constable, C. E. Housecroft, J. A. Zampese, *Polyhedron* **2014**, *81*, 98–104. DOI: 10.1016/j.poly.2014.05.058.

A 3-dimensional $\{4^2.8^4\}$ lvt net built from a ditopic bis(3,2':6',3"-terpyridine) tecton bearing long alkyl tails
Y. M. Klein, A. Prescimone, E. C. Constable, C. E. Housecroft, *CrystEngComm* **2015**, *17*, 6483–6492. DOI: 10.1039/C4CE02347A.

Manipulating connecting nodes through remote alkoxy chain variation in coordination networks with 4'-alkoxy-4,2':6',4"-terpyridine linkers
Y. Maximilian Klein, E. C. Constable, C. E. Housecroft, A. Prescimone, *CrystEngComm* **2015**, *17*, 6483-6492. DOI: 10.1039/C5CE01115A.

Constructing chiral MOFs by functionalizing 4,2':6',4"-terpyridine with long-chain alkoxy domains: rare examples of neb nets
Y. M. Klein, A. Prescimone, M. B. Pitak, S. J.Coles, E. C. Constable, C. E. Housecroft, *CrystEngComm* **2016**, *18*, 4704–4707. DOI: 10.1039/C6CE00939E.

A double-stranded 1D-coordination polymer assembled using the tetravergent ligand 1,1'-bis(4,2':6',4"-terpyridin-4'-yl)ferrocene
Y. M. Klein, A. Prescimone, E. C. Constable, C. E. Housecroft, *Inorg. Chem. Commun.* **2016**, *70*, 118–120. DOI: 10.1016/j.inoche.2016.05.027.

2-Dimensional networks assembled using 4'-functionalized 4,2':6',4"-terpyridines and $Co(NCS)_2$
Y. M. Klein, A. Prescimone, E. C. Constable, C. E. Housecroft, *Polyhedron* **2016**, *103*, 58–65. DOI: 10.1016/j.poly.2015.08.005.

Coordination behaviour of 1-(4,2':6',4"-terpyridin-4'-yl)ferrocene and 1-(3,2':6',3"-terpyridin-4'-yl)ferrocene: predictable and unpredictable assembly algorithms
Y. M. Klein, A. Prescimone, E. C. Constable, C. E. Housecroft, *Aust. J. Chem.* **2017**, *70*, 468–477. DOI: 10.1071/CH16527.

Coordination behavior of 1-(3,2′:6′,3″-terpyridin-4′-yl)ferrocene: Structure and magnetic and electrochemical properties of a tetracopper dimetallomacrocycle
Y. M. Klein, A. Lanzilotto, A. Prescimone, K. W. Krämer, S. Decurtins, S.-X. Liu, E. C. Constable, C. E. Housecroft, *Polyhedron* **2017**, *129*, 71–76. DOI: 10.1016/j.poly.2017.03.030.

What a difference a tail makes: 2D->2D parallel interpenetration of sheets to interpenetrated nbo networks using ditopic-4,2':6',4"-terpyridine ligands
Y. M. Klein, A. Prescimone, M. Neuburger, E. C. Constable, C. E. Housecroft, *CrystEngComm* **2017**, *19*, 2894–2902. DOI: 10.1039/C7CE00686A.

4,2':6',4"- and 3,2':6',3"-terpyridines: the conflict between well-defined vectorial properties and serendipity in the assembly of 1D-, 2D- and 3D-architectures
Y. M. Klein, A. Prescimone, E. C. Constable, C. E. Housecroft, *Mater.* **2017**, *10*, 728.

The different faces of 4'-pyrimidinyl functionalized 4,2':6',4"-terpyridines: metal organic assemblies from solution and on Au(111) and Cu(111) surface platforms
T. Nijs, Y. M. Klein, S. F. Mousavi, A. Ahsan, S. Nowakowska, E. C. Constable, C. E. Housecroft, T. A. Jung, *J. Am. Chem. Soc.* **2018**, *just accepted*. DOI: 10.1021/jacs.7b12624.

2 ABBREVIATIONS

1D	One dimensional
2D	Two dimensional
3D	Three dimensional
Å	Angström
$AgCF_3SO_3$	Silver(I) triflate
Bpy	4,4'-Bipyridine
$Cd(NO_3)_2$	Cadmium(II) nitrate
$Cd(OAc)_2$	Cadmium(II) acetate
$Co(NCS)_2$	Cobalt(II) thiocyanate
COSY	Homonuclear correlation spectroscopy
$Cr(NO_3)_3.9H_2O$	Chromium(III) nitrate nonahydrate
CSD	Cambridge Structural Database
$CuCl_2$	Copper(II) chloride
$Cu(OSO_2CF_3)_2$	Copper(II) triflate
CV	Cyclic voltammetry
δ	Chemical shift
DMF	Dimethylformamide
EtOH	Ethanol
ESI-MS	Electrospray ionization mass spectrometry
Fc	Ferrocene
Fc^+	Ferrocenium
FT-IR	Fourier-transform infrared spectroscopy
GCMS	Gas chromatography – mass spectrometry
HMBC	Heteronuclear multiple bond correlation
HMQC	Heteronuclear multiple-quantum correlation
KOH	Potassium hydroxide
MALDI-TOF	Matrix-assisted laser desorption/ionization – time of flight
MeOH	Methanol
MHz	Megahertz
MOF	Metal organic framework
m/z	Mass to charge ratio

n-BuLi	*n*-Butyl lithium
NCS^-	Thiocyanate anion
NMR	Nuclear magnetic resonance
NOESY	Nuclear Overhauser effect spectroscopy
Ppm	Parts per million
SBU	Secondary building block
T	Temperature
TGA	Thermal gravimetric analysis
Tpy	Terpyridine
TTF	Tetrathiafulvalene
UV-VIS	Ultraviolet-visible
$\chi_m T$	Magnetic susceptibility
XRD	Single crystal X-ray diffraction
$Zn(acac)_2$	Znic (II) acetylacetonate
$ZnBr_2$	Zinc(II) bromide
$ZnCl_2$	Zinc(II) chloride
ZnI_2	Zinc(II) iodide
$Zn(OAc)_2$	Zinc(II) acetate

3 INTRODUCTION

3.1 Coordination chemistry

The development of well-designed compounds with defined functionalities is one of the major aims in material science. One approach to this field is via coordination chemistry, where metal ions are combined with multitopic organic ligands to yield multidimensional compounds with a huge diversity of shapes and properties[1]. The building blocks are held together by coordination bonds. A coordination bond is formed between a metal or metal ion and the lone pair of an organic ligand[2]. The metal centre is an ion in all cases discussed in this thesis, even though coordination between neutral metals and organic ligands exist, as in Pd(0)-phosphine complexes[3]. The metal ion acts as a Lewis acid and the ligand acts as a Lewis base. A coordination bond is formed, when the Lewis base donates a pair of electrons to the metal[2]. The combination of multitopic ligands with metal ions, having multiple connectivity, can lead to formation of one, two- and three-dimensional (1D, 2D and 3D) structures. The combination of building blocks with distinct topologies, the control of the coordination bond formation, the control of the geometry of these building blocks and the ability to direct the multi-dimensional assembly and packing is known as crystal engineering.

3.1.1 Terminologies

MOF vs. coordination polymer

The term coordination polymer was first used in 1964 by J. C. Bailar[4] and for many decades it was the most-frequently used term to describe multidimension assemblies formed from coordination bonds between metal centres and organic ligands.

In recent years a big debate arose concerning the terms coordination polymer and metal organic framework (MOF). When the term MOF was still relative new, scientists either ignored one term and for example only used coordination polymer[5], or they used the terms 3D coordination polymer and MOF for the same type of assembly[6-7]. Nowadays, many definitions exist and two are common. In one definition 3D coordination polymers are described as MOFs when they are porous[8-9] but a stricter definition was given by Yaghi and coworkers in 2009[10]. According to Yaghi a MOF is defined as a 3D, often porous assembly of polynuclear secondary building

blocks (SBUs) and organic ligands, mainly bearing carboxylate groups. The strength of e.g. a Zn-O bond in a MOF (~ 360 kJ mol^{-1}) is close to that of a C-C single bond. In contrast 3D coordination polymers are assembled using mostly mononuclear building blocks and organic ligands, often bearing N-atoms. The Zn-N bond strength is significantly weaker (~ 100-150 kJ mol^{-1}) and this weaker coordination bond is said to be characteristic for coordination polymers. Metals ions, that allow labile coordination bonds to form are good candidates for metal building blocks in coordination polymers. d^5 (e.g. Mn(II)) and d^{10} metals (Zn(II), Cd(II), Hg(II) and Cu(I)) usually have a spherical symmetric distribution of charge around the metal centre, which allows these ions to form reversible coordination bonds with organic ligands and to respond to crystal packing interactions[11]. The angles of ligands around a "pseudo tetrahedral" Zn(II) metal ion can vary a lot from the ideal 109.5° of a tetrahedron, demonstrating the flexibility of this metal ion. Other metal ions, like Co(II) (d^7) and Cu(II) (d^9) are also suitable candidates as building blocks in coordination polymers and several examples incorporating these metal ions are presented in this thesis. The number of coordination bonds, that have to be broken to deconstruct a network is another indication if a structure is a coordination polymer or a MOF. In MOFs the SBUs are multiatomic and a larger number of bonds has to be broken compared to a coordination polymer. Yaghi's definition specifies, that the infinite structures presented in the main part of this thesis should be called 1D, 2D and 3D coordination polymers. Referring to Yaghi's definition[10], 1D and 2D structures should be always called coordination polymers and can never be MOFs. However, most applications of MOFs are attributed to their porous character and 3D coordination polymers, that do not fulfil Yaghi's rules, but show a porous character will be called MOFs in this thesis.

Coordination and connectivity

Another important terminology concerns the bond formation at a metal centre. A metal salt e.g. $Co(NCS)_2$ is often six-coordinate in a metal complexes. When neutral organic ligands (e.g. oligopyridines) with more than one donor atom are combined with $Co(NCS)_2$ a connectivity of four is frequently observed for the Co(II) centre. The term connectivity in a coordination polymer refers to the connections formed by a metal centre, with ligands, that extend the coordination polymer. Ligands that do not extend the assembly are ignored in this terminology. To balance the charge of the Co(II) ion two NCS^- can be present in the complex and occupy the axial positions of the octahedral Co(II). In principle other anionic ligands with an additional donor atom could replace NCS^-, which would balance the charge and could increase the

connectivity of Co(II) to six. One example is presented in this thesis, where the charge of the metal centre is balanced by a non-coordinating triflate anion incorporated into the structure. It is also possible, that solvent molecules like MeOH or water coordinate to the Co(II) centre, which can reduce the connectivity. Examples are discussed in the main part of this thesis

Bidentate, two-donating or ditopic?

The terminology used for organic ligands described in this thesis is briefly defined in this paragraph. The term bidentate should only be used when a ligand, bearing two donor atoms, coordinates to the same metal ion with both donor atoms. A ligand such as 2,2'-bipyridine would be called bidentate, two-donating and monotopic. The term monotopic, ditopic, tritopic, tetratopic and multitopic describes the ability of an organic ligands to build a connection to one, two, three, four or multiple different metal ions, respectively (Scheme 1). In this respect the terms two-donating and ditopic will be used in this thesis, to describe the coordination properties of organic ligands, but ditopic is the more precise description[8].

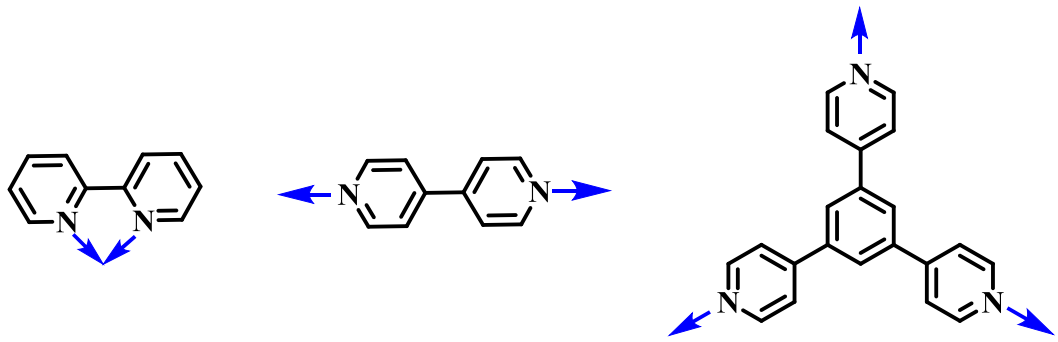

Scheme 1: Examples for a monotopic (left), ditopic (middle) and tritopic (right) ligand.

Topology, term symbol and Schläfi symbol

A 2D network, that consists of 4-connecting nodes and where four of these nodes form the smallest circuit in the network, has the term symbol (4,4). The first number represents the smallest possible circuit and the second number stands for the connectivity of the node. The topology of the (4,4) net is independent of its geometry and is only defined by the connectivity of the nodes in the network.

For 3D frameworks another symbol, the vertex symbol or Schläfi symbol is used. In a Schläfi symbol the connectivity of a node is not explicitly stated but can be derived from the symbol. The topology of a 3D framework is defined by the number of possible circuits, that can be formed between nodes, considering different linkers. Nodes can be connected in a different way by these linkers and each possible circuit is counted. A 3D net, were nodes are connected by 2 four-membered rings and 4 six-membered rings have the Schläfi symbol $\{4^2.6^4\}$. The connectivity of the node defines the number of possible circuits using the following formula:

$$No.of\ circuits = p * (p-1)/2$$

Solving this formula for 6 circuits, gives a p of 4, hence the framework consists of 4-connecting nodes. When more nodes are present in a framework, double Schläfi symbols can be used to describe it[12].

3.2 Self-assembly

Self-assembly in crystal engineering is the reversible process of coordination bond formation between metal building blocks and organic ligands, that eventually leads to the formation of ordered crystalline structures.

The formation of every crystalline material can be attributed to a self-assembly process and crystallization is one of the best examples of this phenomenon[13]. Self-assembly of coordination polymers is a very powerful tool to generate multidimensional structures, that would be otherwise very difficult and time consuming to obtain by conventional organic chemical processes involving sequential covalent bond formation.

The control of the self-assembly process can lead to the formation of multidimensional structures which can possess various properties, including gas storage[14], gas separation[15], luminescence[16], magnetism[17], optical properties[18], electrical conductivity[19], enantioselectivity[20], heterogeneous catalysis[21], negative thermal expansion[22] and spin crossover[23]. The construction of materials with specific properties is one of the aims of crystal engineering.

The key point in coordination polymer and MOF research is to control the self-assembly process. Self-assembly of coordination polymers is strongly influenced by the metal centre and the organic ligands, which have to react with each other to form the structure.

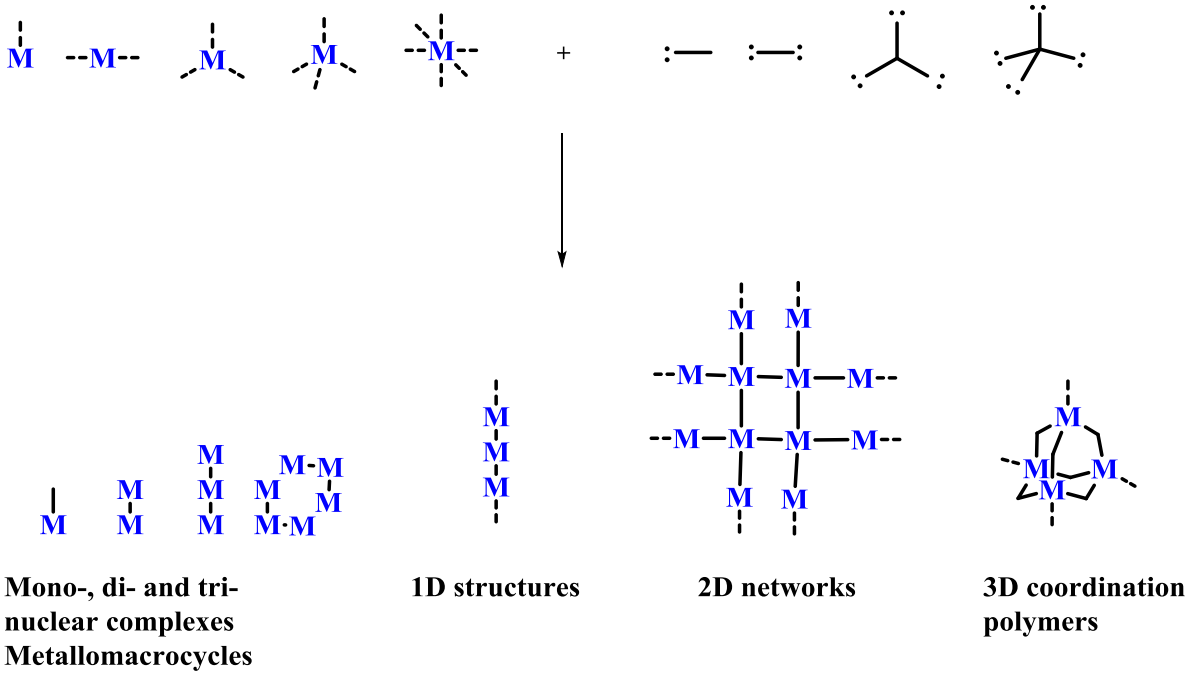

Scheme 2: Top: Schematic presentation of metal centres with multiple connectivity (left) and multitopic organic ligands (right). Bottom: Some structural motifs that can be obtained by combining various building blocks.

The number of possible coordination bonds between metal ions and organic ligands can favour the formation of 3D structures over the formation of 2D or 1D structures. Scheme 2 illustrates the most common building blocks for coordination polymers and their possible structures after the self-assembly process. The top row of Scheme 2 shows metal ions with the most common connectivity (one, two, three, four) and organic ligands which can be mono, di, tri, tetratopic (or higher).

The complexation of a monotopic ligand with a metal ion, that has a connectivity of one can only lead to the formation of a discrete mononuclear complex. The combination of a ligand with two donor sites with two metal ions, both having a connectivity of one can lead to a discrete dinuclear complex. When organic ligands, that have at least two donor atoms, are combined with metal ions, that have a connectivity of two or more, multidimensional structures can form. The topology of the building blocks, that are connected in a coordination polymer influences the outcome of the dimensionality. Coordination polymers, where metal ions with a

connectivity of two are bridged by two-donor linkers will be called 1D. Structures, where metal ions with multiple connectivity are combined with multitopic ligands, which leads to connection of the metal ions in two dimensions will be called 2D. The same combination of building blocks can lead to a 3D assembly, when metal ions are linked by ligands into all three dimensions.

3.3 Crystal engineering

The careful choice of building blocks, the consideration of their geometry, topology and their influence on the crystal packing interactions enables control of the self-assembly processes. When these aspects are well understood the specific construction of various multidimensional motif, by self-assembly of building blocks can be achieved. Design principles of 3D structures using self-assembly and crystal engineering were discussed in many reviews[5-6, 10, 24-28]. The more flexible the building blocks (especially the organic ligands), the more coincidental are the resulting coordination polymer structures. Crystal engineering starts with the choice of the building blocks. Many metal ions (e.g. in zinc(II) halides, $Co(NCS)_2$) have a favoured coordination geometry, which enables some control over the outcome of coordination polymer structure.

3.3.1 Building block 1: Selected metal ions

Table 1 presents the coordination numbers of some metal complexes and metal complex ions and shows their corresponding favoured geometries. Examples of a metal complexes for each geometry is given[29].

Coordination No.	**Geometry**	**Examples**
2	Linear:	$[Au(CN)_2]^-$, $[Ag(NH_3)_2]^+$, $Hg(CN)_2$
3	Trigonal planar:	$[Cu(CN)_3]^{2-}$, $[Ag(PPh_3)_3]^+$, $[HgI_3]^-$
4	Tetrahedral: Square planar:	$[FeCl_4]^-$ $[PdCl_4]^{2-}$, $[PtCl_4]^{2-}$, $[AuCl_4]^-$,
5	Trigonal bipyramidal: Square based pyramidal:	$[CdCl_5]^{3-}$, $[CuCl_5]^{3-}$, $[NbCl_4(O)]^-$ $[Cu(bpy)\{NH(CH_2CO_2)_2]$
6	octahedral	$[Cu(NO_2)_6]^{4-}$, $[Zn(OH_2)_6]^{2+}$, $[Co(OH_2)_6]^{2+}$
7	Pentagonal bipyramidal	$[V(CN)_7]^{4-}$, $[NbF_7]^{3-}$, $[ZrF_7]^{3-}$,
8	Dodecahedral: Square antiprismatic: Hexagonal bipyramidal:	$[Y(OH_2)_8]^{3+}$ $[Zr(acac)_4]$ $[CdBr_2(18\text{-crown-}6)]$
9	Tricapped trigonal prismatic	$[Y(OH_2)_9]^{3+}$

Table 1: Coordination numbers and corresponding geometries in some metal complexes and complex ions.

Coordination numbers from 2 to 9 are observed for transition metals[29]. The most common ones are four-coordinating and six-coordinating metal ions. Four-coordinating metal ions can have limiting square-planar or tetrahedral geometries of the coordinated ligands. The ligands in a

six-coordinated metal ion often adopt a distorted octahedral geometry. Some metal units used as building blocks in this PhD thesis are summarized in Table 2 and their connectivity is highlighted by the single N-atoms.

The connectivity of a metal ion like Zn(II) strongly relies on the number of anionic ligands and how many coordination sites they occupy. The dinuclear coordination unit $\{Zn_2(OAc)_4\}$ (Table 2 top left) is formed *in situ* from two $Zn(OAc)_2$ units. Each zinc centre is coordinated to four oxygen atoms of each of four bridging two donor acetate ligands. Each Zn(II) centre has an additional coordination site available oriented along the Zn…Zn vector. The building block has a connectivity of two. This motif is frequently observed[30], but structures exist in which a zinc(II) ion is coordinated by two acetate ligands and the remaining coordination sites are occupied by organic linkers[31]. This influences the geometry of the coordination to an organic ligand. When coordinating solvents, like water or methanol are used during crystallization, they will most likely occupy coordination sites on the metal ion and are either sequentially replaced by organic ligands or remain as a ligand in the final structure[32]. In complexes using $ZnCl_2$ and ZnI_2 a pseudo tetrahedral geometry is favoured around the Zn(II) centre; the zinc atom is a four-coordinating building block with a connectivity of two. $Co(NCS)_2$ units typically show an overall six-coordinate geometry in coordination polymers. Usually the NCS^- ligands are mutually *trans*, with four accessible equatorial coordination sites, and $Co(NCS)_2$ can be a square planar building block with a connectivity of four. Some metal salts tend to form clusters or dimers, demonstrated in the entry for $Zn(OAc)_2$, $Cd(OAc)_2$ and $CuCl_2$. Often, pairs of $Cd(OAc)_2$ units assemble as shown in Table 2 (top right) and the building block so-formed gives a connectivity of four. Dimerization in $CuCl_2$ complexes is a well-documented phenomenon[33]. Two Cu atoms can be bridged by up to two chlorido ligands. Two accessible coordination sites on each Cu atom, make this a building block with a connectivity of four. For $Cd(NO_3)_2$, monotopic or chelating coordination of NO_3^- groups to Cd(II) is possible. Two monotopic NO_3^- ions can coordinate to the axial positions of a six-coordinate Cd(II) leaving equatorial coordination sites accessible, which makes $Cd(NO_3)_2$ a four-connecting square-planar building block. Alternatively, Cd(II) can be seven-coordinate with two chelating NO_3^- groups coordinating to the metal centre. The building block then has a connectivity of three. All building blocks in Table 2 are taken from published structures obtained during my Master and PhD studies.

Metal salt	Geometry in the complex	Metal salt	Geometry in the complex
$Zn(OAc)_2$	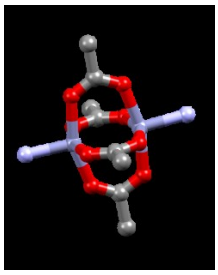	$Cd(OAc)_2$	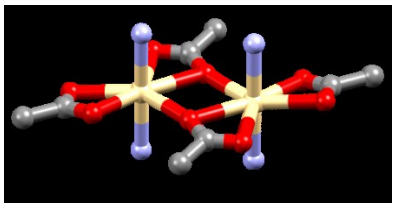
$ZnCl_2$	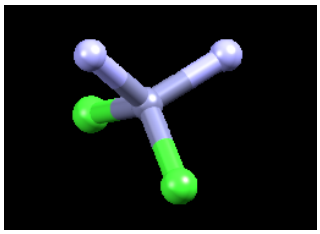	$Cd(NO_3)_2$	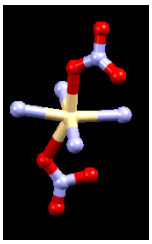
ZnI_2	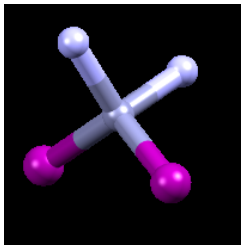	$Cd(NO_3)_2$	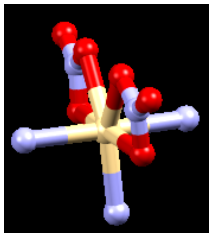
$Co(NCS)_2$	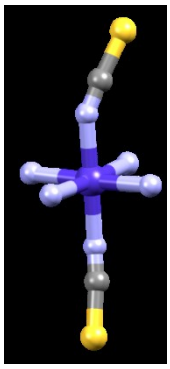	$CuCl_2$	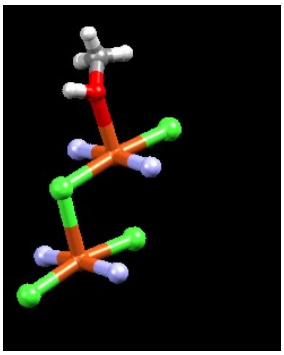

Table 2: Selection of metal salts and their corresponding connectivity in coordination polymers presented in this thesis. Colour code: grey = C, blue = N, white = H, orange = Cu, dark-yellow = S, light-yellow = Cd, red = O, purple = Co, grey-blue = Zn.

This short overview illustrates some of the important considerations that have to be taken into account, when a metal building block is to be incorporated into a coordination polymer.

Coordination numbers 4 (tetrahedral, square planar) and 6 (octahedral) are very common and allow some prediction for the outcome of a coordination polymer structure, if a rigid ligand like 4,4'-bipyridine (bpy) is incorporated. The coordinating N-atoms in the 4 and 4' positions of 4,4'-bipyridine make this ligand ditopic linear (Scheme 3).

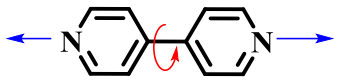

Scheme 3: The ligand 4,4'-bipyridine with two donor sites. Blue arrows indicate possible coordination. The red arrow illustrates, that 4,4'-bipyridine keeps its linear geometry upon rotation around the C-C bond.

An overview of different organic ligands will be given in the next section, but 4,4'-bipyridine is presented here as an example to illustrate how metal geometries and connectivity can influence the formation of coordination polymers.

A Cambridge Structural Database[34] (CSD version 5.39) using Conquest v. 1.20[35] revealed 4380 structures containing 4,4'-bipyridine. The combination of 4,4'-bipyridine with $Co(NO_3)_2$ lead to the formation of a 2D ladder like structure (Fig. 1, CSD refcode: LEFSOH)[36]. Two NO_3^- anions form a chelating coordination to Co(II), occupying four coordination sites. The cobalt centre is seven coordinate in the final structure with a connectivity of three, which enables coordination of three 4,4'-bipyridine ligands to Co(II).

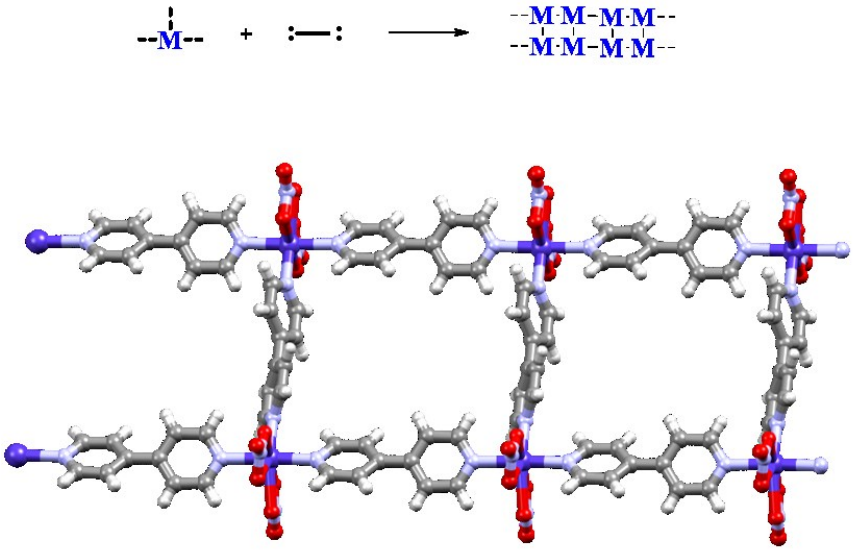

Fig. 1: Top: Schematic presentation of the $Co(NO_3)_2$ building block in the structure and the organic ligand, which form the ladder like structure $[Co(bpy)_{1.5}(NO_3)_2]_n$ upon coordination. Bottom: The X-ray structure published by Rajak *et al.*[36]. Colour code: grey = C, blue = N, white = H, purple = Co, red = O. CSD refcode: LEFSOH.

In another example, 4,4'-bipyridine is combined with copper(II) triflate $Cu(OSO_2CF_3)_2$. The metal centre in $Cu(OSO_2CF_3)_2$ is six-coordinate in the product with the axial positions occupied by triflate anions. $Cu(OSO_2CF_3)_2$ has a connectivity of four in the structure and 4,4'-bipyridines coordinate to the equatorial positions of the copper centre. The combination of the two donor ligand with the four-connecting $Cu(OSO_2CF_3)_2$ node leads to a (4,4)-net structure (Fig. 2, CSD refcode: NECNAN)[37].

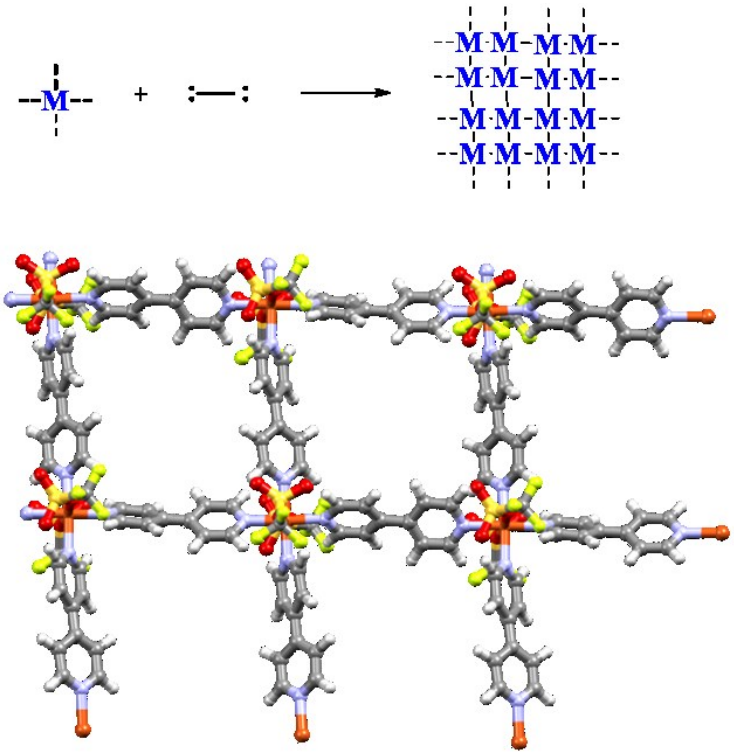

Fig. 2: Top: Schematic presentation of the connectivity four metal node and the organic linker, which form a 4,4-net 2D structure upon coordination. Bottom: The X-ray structure of $[Cu(bpy)_2(OTf)_2]_n$ published by Li *et al.*[37]. Colour code: grey = C, blue = N, white = H, orange = Cu, yellow = F, red = O. CSD refcode: NECNAN.

To further increase the dimensionality of coordination polymers, a number of possibilities exist: 4,4'-bipyridine can be replaced by a different ligand with more donor atoms or a metal building block with a connectivity of more than four can be used. A third possibility is the combination of two ligands with one metal centre as presented in the example in Fig. 3[38]. In this case the cobalt ion is coordinated by 5 ligands. Three 4,4'-bipyridine ligands extend the polymer structure in two dimensions. In the third dimension, metal centres are bridged by two mandelic acid (**L1**, Fig. 3) ligands, of which one is coordinated to Co(II) via one donor atom and another one is forming a chelating coordination to Co(II) with two donor atoms. Co(II) is six-coordinate in the structure.

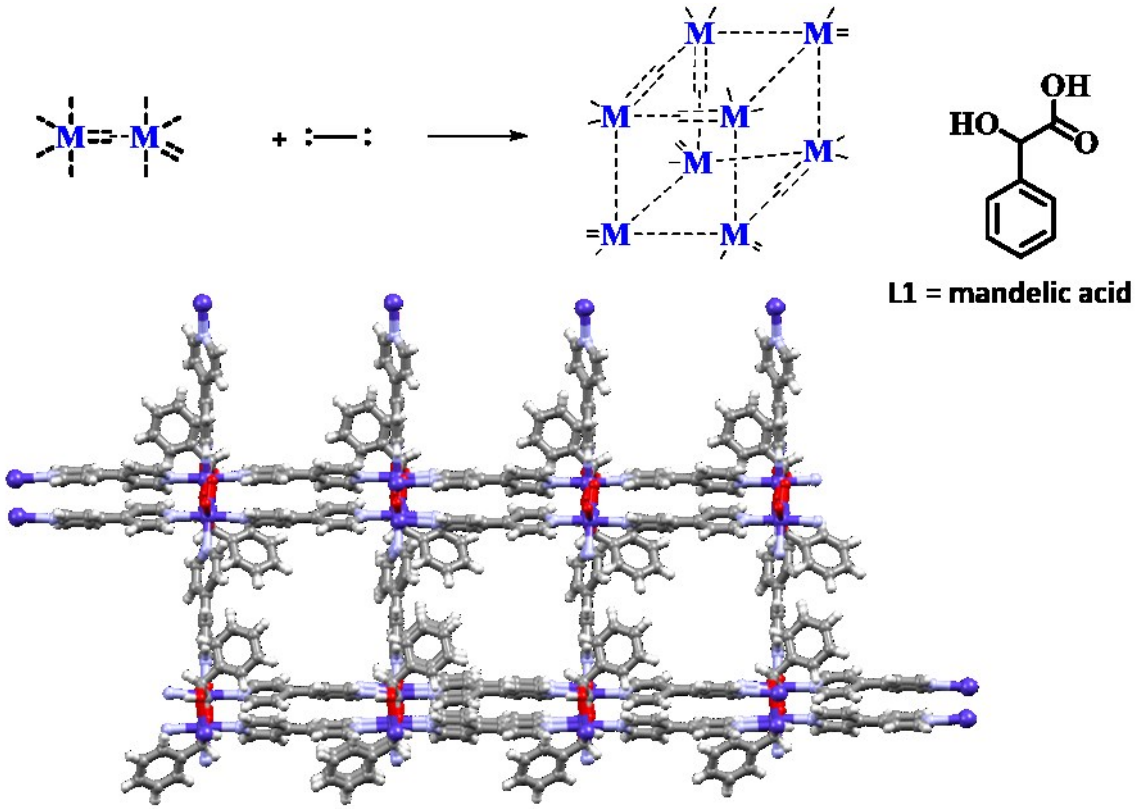

Fig. 3: Top: Schematic presentation of the Co(**L1**)$_n$ building block and the organic ligand, which form a 3D framework [{$Co_2(bpy)_2$(**L1**)$_2$}·$2CF_3SO_3$·$^n C_{10}H_{18}O$]$_n$ upon coordination. Bottom: The X-ray published by Zhang *et al.*[38]. Colour code: grey = C, blue = N, white = H, purple = Co. CSD refcode: NEHGOZ.

The rigid linear 4,4'-bipyridine is a good compound to demonstrate how connectivity and geometry of metal building blocks can influence or dictate the formation of coordination polymers. By changing the number of donor atoms on a ligand to three, four or more, an increase in the variety of multidimensional structures can be expected. The predictability of structural motifs, using multitopic ligands will decrease with the increase in donor atoms on a ligand and flexibility in coordination. Some common organic ligands with various donor atoms are summarized in the next section

3.3.2 Building Block 2: Selected organic linkers

An organic ligand can be either anionic, cationic (rarely present) or neutral and acts as a Lewis base. Covalently-bonded elements like N, P, O, S, Se, F, Cl, Br and I that have free lone pairs can act as donors in the formation of coordination polymers. In the previous section 4,4'-bipyridine and mandelic acid were introduced as linkers. N-donors and carboxylates are among the most common groups in organic ligands for coordination polymers. Some ligands, successfully incorporated into coordination polymers, are displayed in Scheme 4.

Oligopyridines and polycarboxylates are common classes of organic ligands. Pyridines (unless functionalized with additional charged substituents) are neutral Lewis bases and form coordination bonds via their nitrogen lone pair. Coordination polymers with 4,4'-bipyridine were discussed in the previous section. Phosphines, like triphenylphosphine are common ligands in Pd catalysts for cross-coupling reactions[3] and enable the formation of coordination polymers. Wang and coworkers[39] synthesized a 3-(3,5-bis(diphenylphosphino)phenyl)pyridine ligand (**L2**, Scheme 4) and combined it with $AgCF_3SO_3$ to form the coordination polymer $[Ag\mathbf{L2}(CF_3SO_3)]_n$ (CSD refcode: VUPSAB) displayed in Fig. 4. **L2** has three donor atoms and coordinates to two Ag metals via two phosphine groups and to another Ag metal via the pyridine. The phosphines connect the metal ions in one dimension and the pyridine lets the structure propagate into the second dimension. $[Ag\mathbf{L2}(CF_3SO_3)]_n$ is a 2D network.

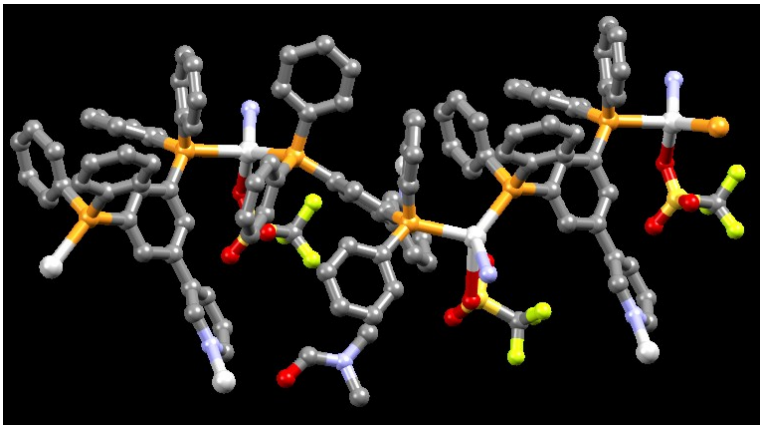

Fig. 4: The single crystal X-ray structure of $[Ag\mathbf{L2}(CF_3SO_3)]_n$.[39] N-atoms pointing into and away from the viewer are part of **L2** and extend the structure in the second dimension. Colour code: grey = C, blue = N, white = Ag, orange = P, yellow = F, red = O. CSD refcode: VUPSAB.

Small ligands

Halido ligands: F^-, Cl^-, Br^-, I^-

CN^-, CO, SCN^-, NH_3, OH_2,
$[NO_3]^-$, $[CO_3]^{2-}$, $[PO_4]^{3-}$,$[SO_4]^{2-}$,

Neutral organic ligands

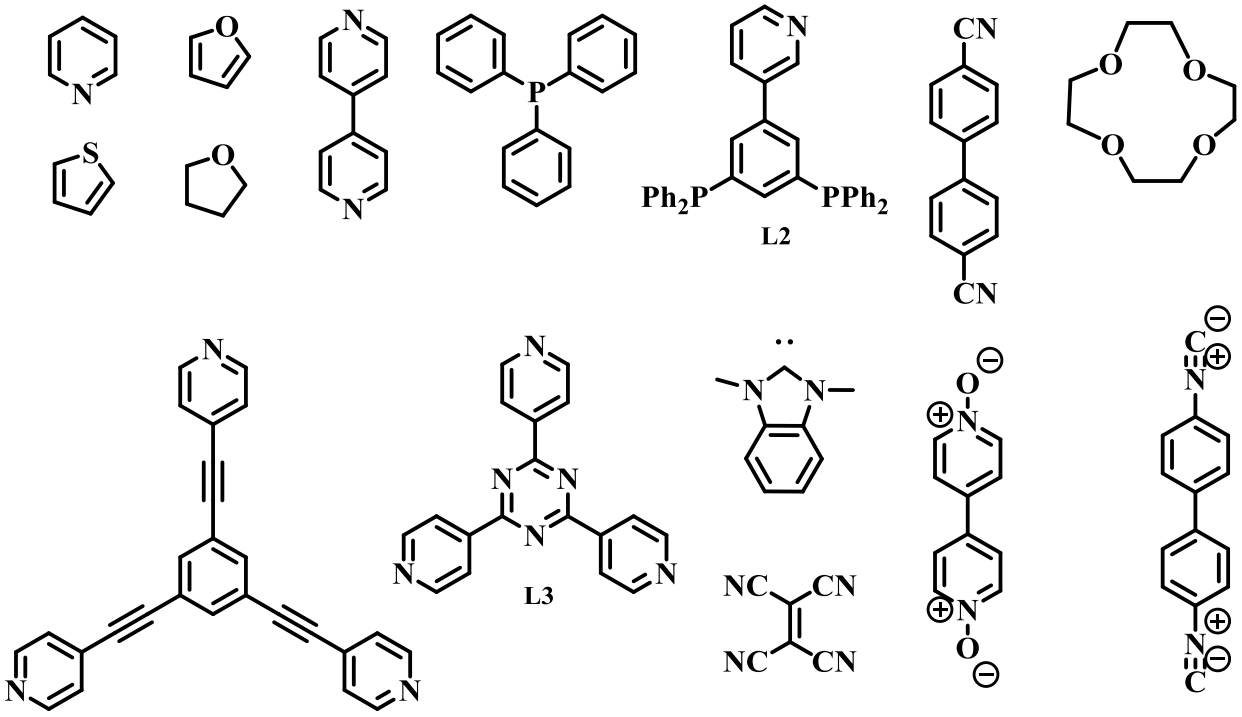

Anionic organic ligands

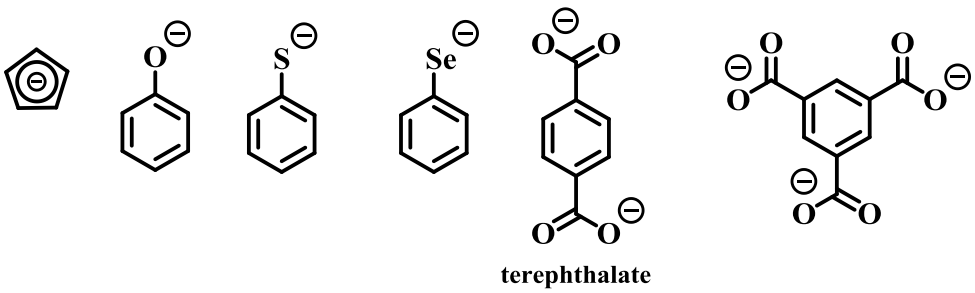

Scheme 4: Representation of some linkers used in crystal engineering.

Neutral organic linkers can be furans[40], thiophenes[41], ethers (crown-ethers)[42], cyanides[43] and carbenes[44]. Zwitter-ions like N-oxides[45] and isonitriles[46] form coordination bonds to metals and are known in coordination polymers.

Anionic organic ligands can bear cyclopentadienyl, alkoxy[47], thiolate[48], selenolate[49] and carboxylate groups.

Polycarboxylates are a large group of anionic organic ligands. A Cambridge Structural Database[34] (CSD version 5.39) using Conquest v. 1.20[35] revealed 5579 structures containing terephthalate (Scheme 4) as a ligand. Férey *at al.*[50] combined terephthalate with $Cr(NO_3)_3 \cdot 9H_2O$ to obtain a MOF (MIL-101) with "giant" pores.

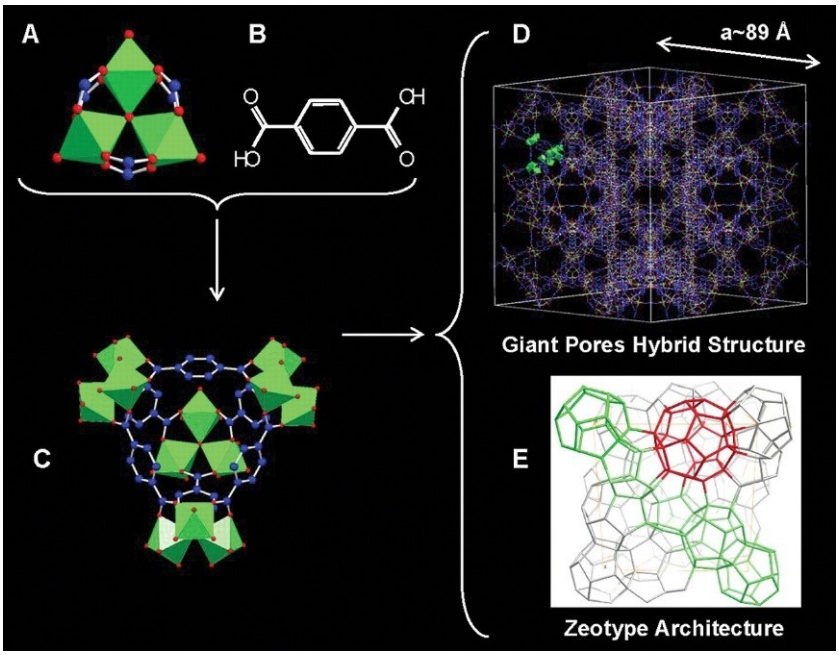

Fig. 5: The structure of the chromium terephthalate MOF $[Cr_3F(H_2O)_2O\{(O_2C)\text{-}C_6H_4\text{-}(CO_2)\}^3 \cdot nH_2O]_n$ (MIL-101). Reproduced from ref.[50] with permission from The American Association for the Advancement of Science.

Possible applications of this material and other porous networks are discussed in the next section.

3.4 Applications of porous coordination assemblies

Porous materials have applications in separation, gas storage, heterogenous catalysis, host-guest exchange and can act as nanoreactors[5]. Three types of porous materials exist nowadays, but until the mid 1990s only two were studied intensively, namely zeolites and activated carbon. These materials will not be discussed in this thesis.

In recent years the research in the field of coordination polymers and MOFs increased and many 3D porous structures were published. Two of them will be briefly discussed in this section.

3.4.1 The porous 3D framework MIL-101

MIL-101 (Fig. 5) is a porous 3D framework with large pores of 30 – 34 Å diameter. These pores enable gas uptake and N_2 sorption into the pores proved to be successful. Guest uptake was tested for MIL-101 and the Keggin cluster $K_7PW_{11}O_{40}\cdot nH_2O$ was successfully incorporated into the pores. The van der Waals radius of ~ 13.1 Å is significantly less than the pore diameter, and the presence of an NMR active ^{31}P-nucleus in the Keggin cluster, allowed uptake to be monitored based on shifting of the ^{31}P NMR resonance. The guest uptake was confirmed by thermal gravimetric analysis (TGA), single crystal X-ray diffraction (XRD), solid state ^{31}P NMR spectroscopy and IR spectroscopy. MIL-101 with its large pore size is a good candidate for further investigations of gas storage and host-guest chemistry.

3.4.2 Crystalline "sponges"

An important contribution concerning host-guest chemistry in coordination polymers / MOFs was made by Fujita and coworkers[51]. They constructed a 3D dimensional coordination assembly (**a1** in Fig. 6) combining an organic 2,4,6-*tris*(4-pyridyl)-1,3,5-triazine (**L3**, Scheme 4) ligand with a $Co(NCS)_2$ metal salt. In a previous study[52], they used the same ligand in combination with $[Pd(en)(NO_3)_2]$ (en = ethylendiamine) to obtain a discrete metallocage (**a2** in Fig. 6).

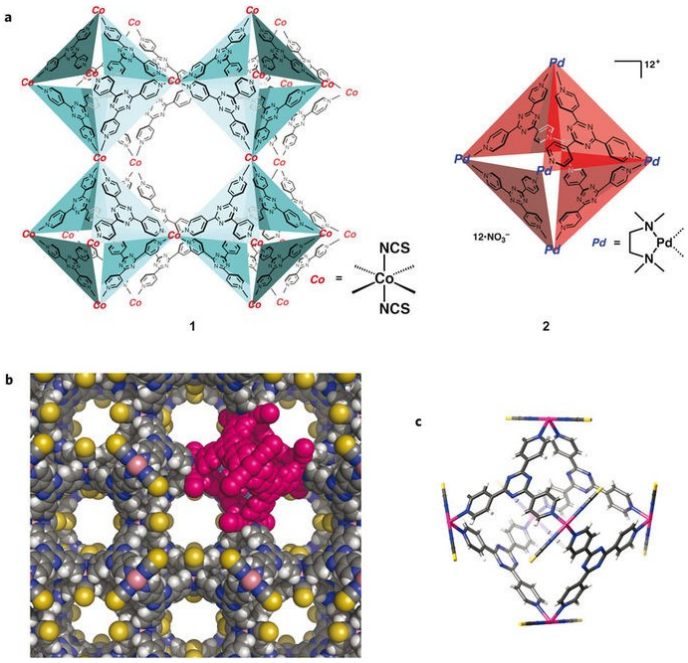

Fig. 6: The X-ray single crystal structures of the 3D coordination assembly $[\{(Co(SCN)_2)_3(\mathbf{L3})_4\}\cdot x(\mathbf{G})]_n$ **1** (**G** = guest molecules) (**a1**) and the discrete cage (**a2**). The 3D structure has large channels (**b**), that enable guest uptake. Structure **a1** is built of $M_6\mathbf{L3}_4$ cages (pink in **b**, represented as the stick model in **c**), that are connected via coordination bonds. Colour code: grey = C, blue = N, white = H, pink = Co, yellow = S. Reproduced from ref.[51] with permission from Springer Nature.

Guest uptake of the porous network was investigated and tetrathiafulvalene (TTF) and fullerene C_{60} could be successful incorporated. The inclusion of TTF in the 3D network was confirmed by single crystal X-ray diffraction and four TTF molecules were observed in each $M_6\mathbf{L3}_4$ unit (Fig. 7, CDS refcode: PUZLUS).

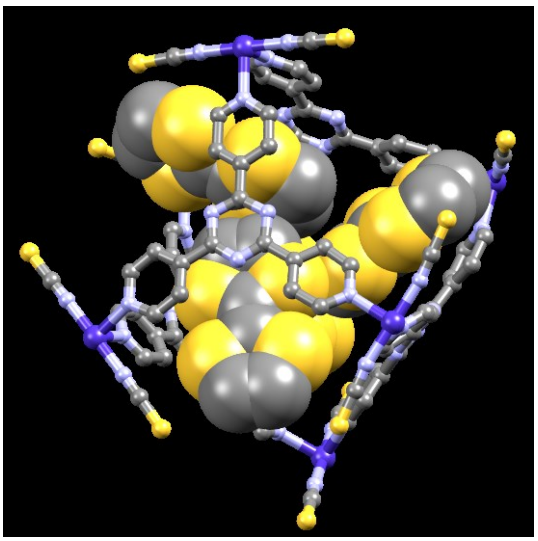

Fig. 7: A $Co_6\mathbf{L3}_4$ cage of the 3D coordination polymer filled with four TTF guest molecules. Colour code: grey = C, blue = N, yellow = S, purple = Co. CDS refcode: PUZLUS.

This method of including a guest molecule into a porous framework and obtaining its structure by single crystal X-ray diffraction is a very powerful tool. Fujita and coworkers carried on the research of these porous materials and introduced the term "crystalline sponge". They were able to obtain crystal structures of guests inside their "sponge" by guest exchange, what made a conventional crystallization evitable[53-54]. This method is an important discovery and is often referred to as: "crystal-free crystallography". The term has to be used with caution, as a single crystal is always needed in single crystal X-ray diffraction. The "crystalline sponge" is crystalline and the ordered structure of the host material can lead to the incorporation of ordered guest molecules, that occupy the void space in the host material in a regular periodicity. The structure of the guest molecules can be solved inside the structure of the "crystalline sponge".

The potential of Fujitas "sponge" for the uptake of larger guests was demonstrated by the incorporation of fullerene C_{60}. The channels between adjacent Co_6**L3**$_4$ cages have a diameter of 11.5 Å, which is wide enough for C_{60} (10.3 Å) to penetrate the network. Presence of C_{60} in the structure was confirmed by a colour change of the crystals from orange to black (Fig. 8) and by observation of pure C_{60} after destruction of the modified network with aqueous HCl.

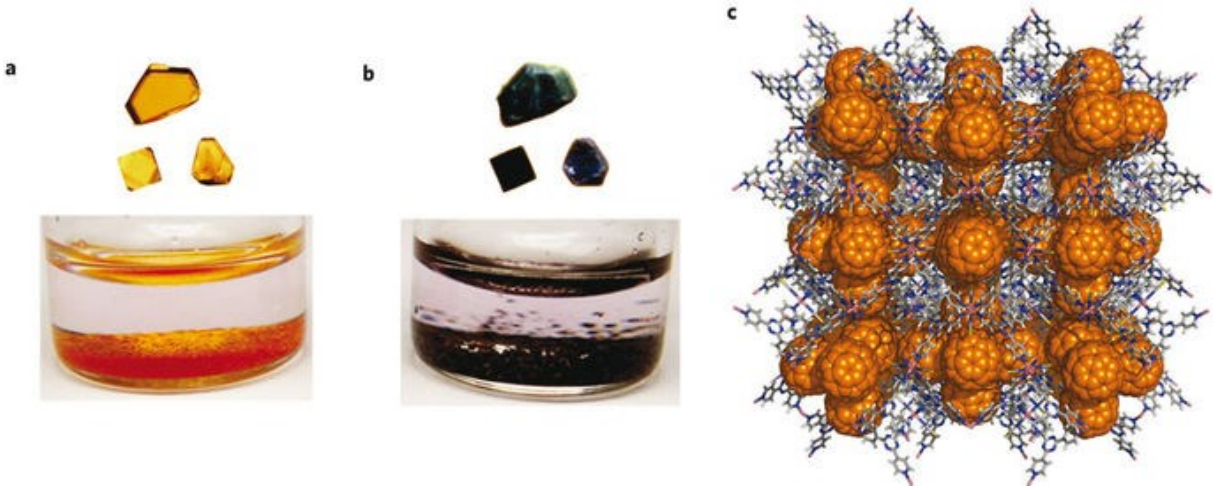

Fig. 8: a) Crystals of the 3D-network, b) Crystals of the network after one week in a saturated toluene solution of C_{60}, c) An optimized model of C_{60} guests in the channels between Co_6**L3**$_4$ cages. Reproduced from ref.[51] with permission from Springer Nature.

The 2,4,6-*tris*(4-pyridyl)-1,3,5-triazine ligand used by Fujita is very similar to the 6'-(pyridin-4-yl)-4,2':6',4"-terpyridine ligand (Scheme 5), used by the Constable/Housecroft group[55] and other research groups[56-64] to study coordination assemblies. The next chapter shows some coordination polymers using 4,2':6',4"-terpyridine and 3,2':6',3"-terpyridine ligands as linkers.

In the main chapter of this thesis, the emergence of new 4,2':6',4"-terpyridine and 3,2':6',3"-terpyridine based ligands for the assembly of coordination polymers will be discussed.

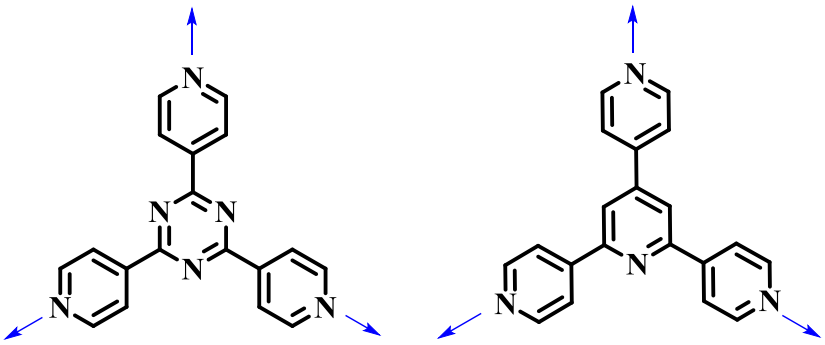

Scheme 5: 2,4,6-*Tris*(pyridine-4-yl)-1,3,5-triazine (left) and 6'-(pyridin-4-yl)-4,2':6',4"-terpyridine (right). The N atoms in the inner ring normally remain uncoordinated and both ligands are tritopic. Blue arrows indicate coordination.

4 4,2':6',4"- AND 3,2':6',3"-TERPYRIDINES

Terpyridine (tpy) has 48 isomers[11]. The most common isomer is the bis-chelating 2,2':4',2"-terpyridine, which forms discrete complexes with octahedral metal ions, like Ru(II), Os(II) and Fe(II). Several examples of 2,2':6',2"-terpyridine ligands were discussed in the DSSC part of this thesis (Scheme 6 left).

Two less common isomers of tpy are 4,2':6',4"- and 3,2':6',3"-terpyridines. As unsubstituted ligands they are neutral ditopic linkers. The N atom on the central ring of both ligands remains uncoordinated in most cases. 4,2':6',4"-terpyridine is a bent rigid ligands, with a V-shaped coordination geometry. The less common isomer 3,2':6',3"-terpyridine has a far greater flexibility in coordination, due to rotation along the C-C bonds connecting the pyridine rings (Scheme 6).

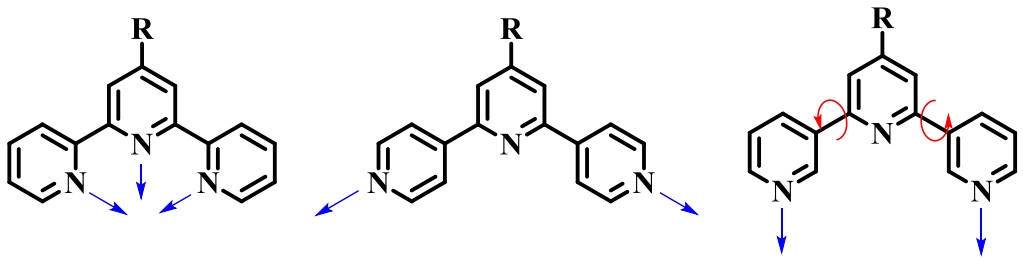

Scheme 6: Three isomers of tpy. From left: 2,2':6',2"-, 4,2':6',4"- and 3,2':6',3"-terpyridine. The R group highlights a possible and most common substitution position. Blue arrows indicate coordination and red arrows illustrate rotational freedom.

A Cambridge Structural Database[34] search (CSD version 5.39) using Conquest v. 1.20[35] revealed 251 coordination polymers, where 4,2':6',4"-terpyridine bridges at least two metal ions. For coordination polymers containing 3,2':6',3"-terpyridine 40 structures were found. A large number of these structures were published by the Constable/Housecroft group in Basel over the last years.

The aim of this PhD work was the advancement of previously reported 4,2':6',4"-terpyridines and 3,2':6',3"-terpyridine ligands towards multitopic ligands and the incorporation of these ligands into coordination polymers. The structures of these polymers give new insights into crystal engineering, possible with these ligands and trends in structural motifs are discussed in the main chapter. Selected 4,2':6',4"-terpyridine and 3,2':6',3"-terpyridine ligands and their

corresponding coordination polymer structures reported in the literature are presented in this chapter.

4.1 Structural motifs obtained with 4,2':6',4''-terpyridines

The majority of substituted 4,2':6',4''-terpyridine ligands for coordination polymers are summarized in Scheme 7. Coordination polymers with labelled ligands are presented in the following sections.

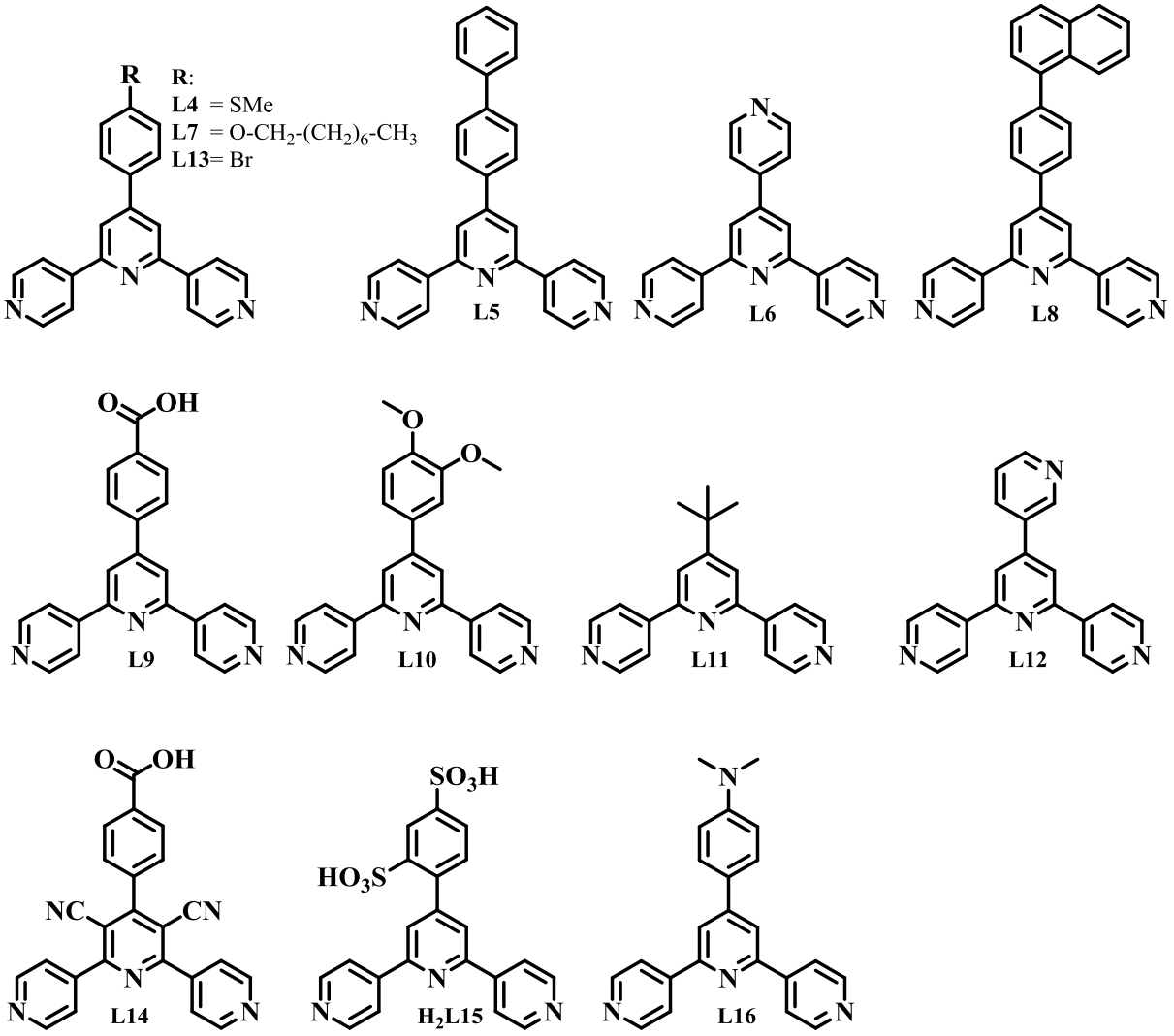

Scheme 7: A selection of 4,2':6',4''-terpyridine ligands used in coordination polymers.

The following sections show structural motifs, obtained with these ligands and illustrate how their assembly is influenced by metal ions and the number of donor atoms associated with the linkers.

4.1.1 Dinuclear structures, metallocycles and metallocages

A dinuclear structure has been observed in the reaction between a Zn(II) salt and ligand **L4** (CSD refcodes: CECTUB)[65]. In a reaction between **L5** and Zn(II) salts metallocycles (CSD refcodes: CISVUX, CISWEI, JAGZAV)[66] were observed. It is counterintuitive to expect that a ligand with two donor atoms can form a dinuclear complex, as most metal ions have a connectivity of at least two. It is important to note, that metallocycles, combining two donor linkers and metal ions with a connectivity of two can be formed. These structures can be cyclic (e.g. squares, pentagons and hexagons) or multidimensional cages and capsules. A cage combining ligand **L3**, having three donor atoms, with a two-connecting Pd(II) metal ion is displayed in Fig. 6. An example of a metallohexacyclic structure is displayed in Fig. 9b. The ligand with two donor sites **L5** reacted with the two-connecting $ZnBr_2$ to form this structural motif (CSD refcode:)[66]. Both building blocks are bent, due to the rigid nature of the V-shaped 4,2':6',4"-terpyridine ligand and $ZnBr_2$, which favours a pseudo tetrahedral geometry with ligands in the structure. In the structure the 4,2':6',4"-terpyridine building blocks form an alternating up-down arrangement. The structure in Fig. 9b is a discrete molecule and constructed of **L4** and a two-connecting $Zn(acac)_2$ building blocks[67]. Zinc(II) ions are 5 coordinated in this complex but are known to form 6 coordination bonds. It is unclear why the sixth coordination site on the zinc is not coordinated and why the structure is a discrete complex. Conditions, including solvent, concentration and temperature can have an influence on the crystal formation. Sometimes crystals of different assemblies form together under the same conditions in the same environment, as demonstrated by Constable and coworkers[68].

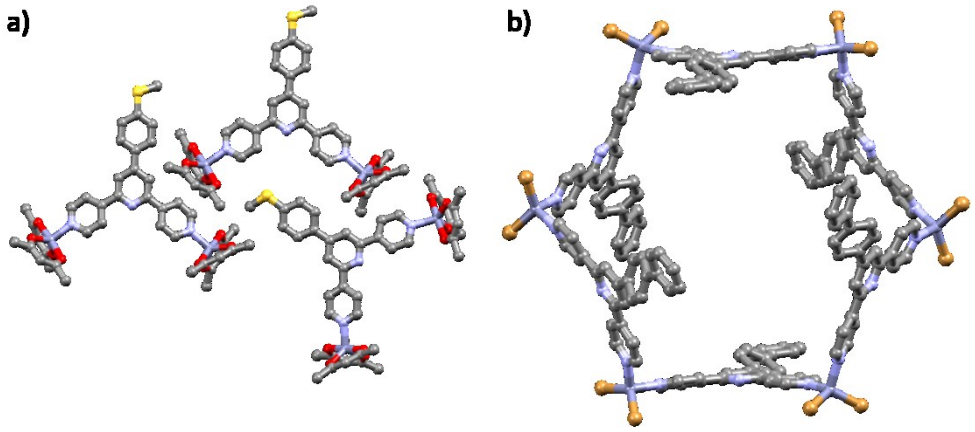

Fig. 9: a) The structure of the discrete two-nuclear complex $[Zn_2(acac)_4$**L4**$]$ (CSD refcode: CECTUB)[65]; b) The structure of a discrete hexacycle $[\{ZnBr_2($**L5**$)\}_6]$ (CSD refcode: CISVUX)[66]. Colour code: grey = C, blue = N, yellow = S, grey-blue = Zn, brown = Br, red = O.

In section 3.4.2 about Fujitas "sponge" a metallocage motif was briefly mentioned, where **L6**, having three donor atoms was combined with $[Pd(en)(NO_3)_2]$ (en = ethylendiamine), which has a connectivity of two. The metallocage (**a2** in Fig. 6) was constructed of 6 Pd(II) ions and 4 ligands **L3**[52]. Another metallocage was obtained for a combination of ligand **L16**, having two donor atoms, with a $\{Fe_2NiO(RCOO)_6\}$ (R = tert-butyl) metal cluster, which has a connectivity of three (Fig. 10, CSD refcode: CANZAU)[69]. The metallocage contains 8 metal clusters, that are connected by 12 ligands **L16**.

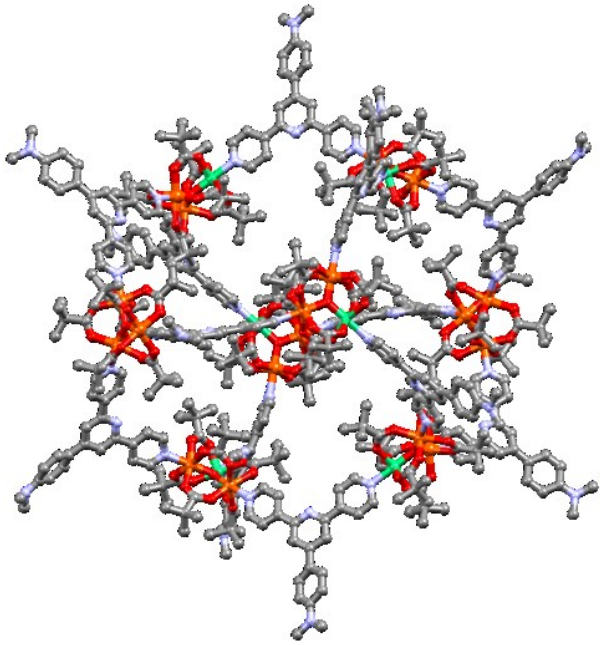

Fig. 10: The metallocage $[\{Fe_2NiO(Piv)_6\}_8\{$**L16**$\}_{12}]$ (Piv = pivalate) obtained with **L16**, published by Dorofeeva and coworkers (CSD refcode: CANZAU)[69].

4.1.2 1D-structures

Apart from the hexagon described in the previous section, 1D coordination polymers are the most frequent motifs obtained with a two donor 4,2':6',4"-terpyridine ligand and a two-connecting metal ion. Some examples are displayed in Fig. 11.

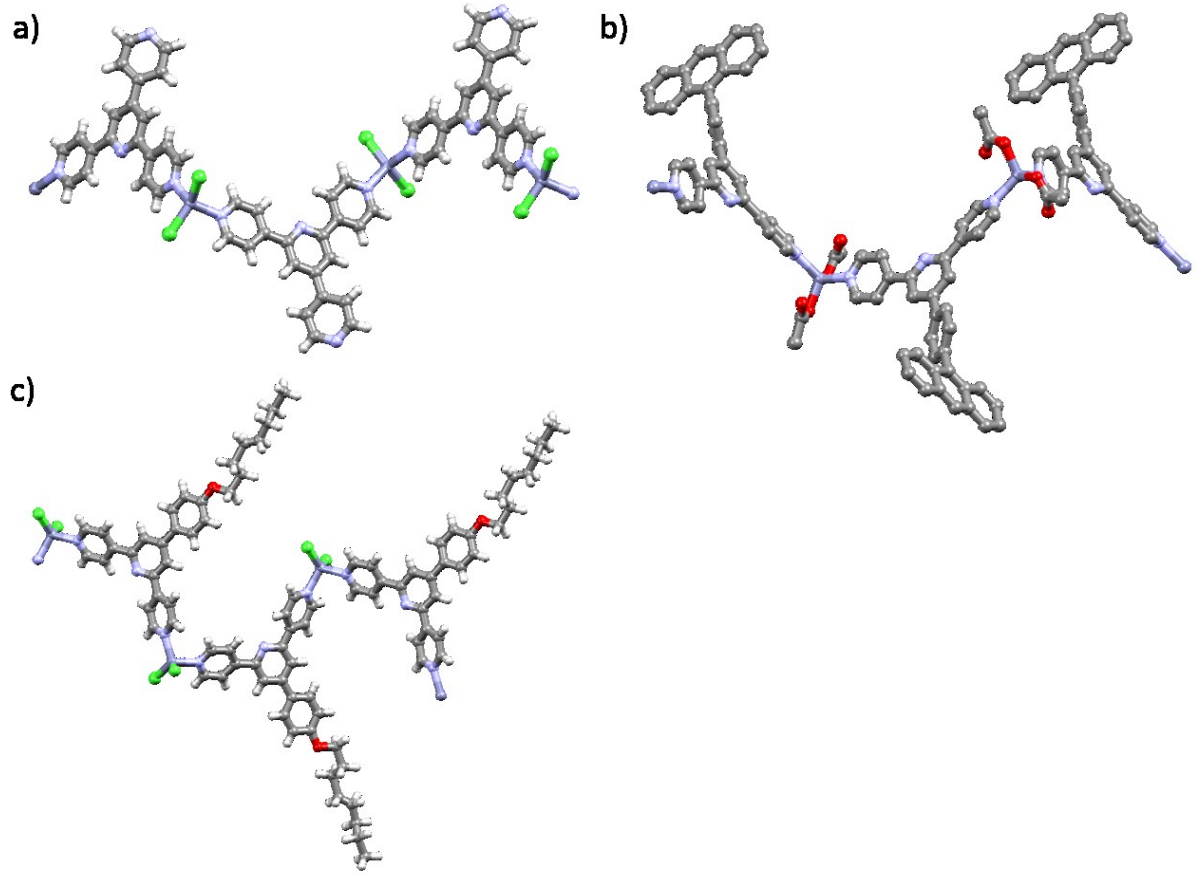

Fig. 11: X-ray structures of $[ZnCl_2(\mathbf{L6})]_n$ (a, CSD refcode: AGUPEY)[56], $[ZnCl_2(\mathbf{L7})]_n$ (b, CSD refcode: OFIWEH)[70] and $[ZnCl_2(\mathbf{L8})]_n$ (c, CSD refcode: AJURIG)[66]. Colour code: grey = C, blue = N, green = Cl, grey-blue = Zn, red = O, white = H.

All structures in Fig. 11 use zinc(II) as the metal centre. Zinc halides ($ZnCl_2$, $ZnBr_2$, ZnI_2) are normally two-connecting and have a tetrahedral geometry in the final structure. In a methanol solution zinc chloride can be present in different forms, such as $ZnCl_3^-$, $ZnCl_4^{2-}$ and $[Zn(MeOH)_6]^{2+}$ confirmed by Raman spectroscopy[71]. In combination with 4,2':6',4"-terpyridine ligands the Zn(II) species are predominately two-connecting as two coordination sites are occupied by halido ligands in the final structure. Helical 1D coordination chains are frequently obtained, e.g, in the compounds $[ZnCl_2(\mathbf{L6})]_n$ (CSD refcode: AGUPEY)[56], $[ZnCl_2(\mathbf{L7})]_n$ (CSD refcode: OFIWEH)[70] and $[ZnCl_2(\mathbf{L8})]_n$ (CSD refcode: AJURIG)[66].

In one structure $ZnCl_2$ is two-connecting and ligand **L12** has three donor atoms. However, this structure is not 2D, but can be described as a 1D ladder[72], with central Zn(II) centres being the rungs (Fig. 12a, CSD refcode: ZOKFAI). The structure presented in Fig. 12b shows a connectivity, which leads to the formation of a triple chain. Each Mn(II) centre has a connectivity of two in the final structure, where ligands with two donor atoms like **L13** can coordinate. This would in principle lead to a 1D structure, but three metal ions are connected via bridging acetate ligands, which increases the connectivity of the metal cluster to six and extends the structure to triple chain (CSD refcode: CUXCII)[73].

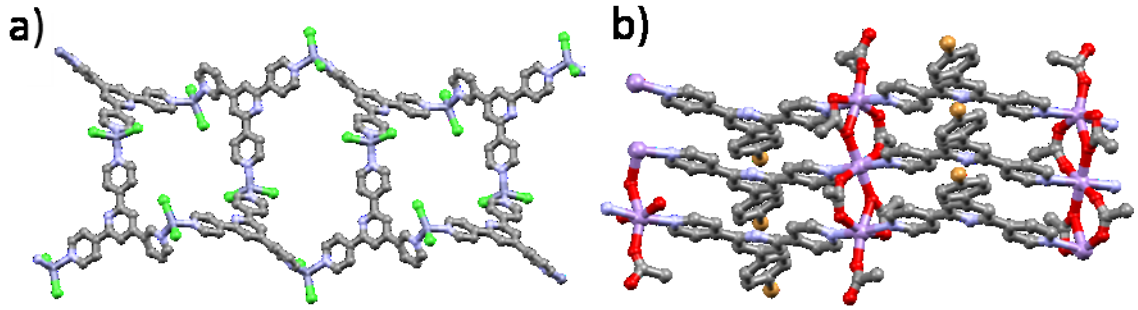

4.1.2.1 Fig. 12: a) The 1D coordination ladder $[\{Zn_3(\mathbf{L12})_2Cl_6\}\cdot nH_2O]_n$ obtained with **L12** (CSD refcode: ZOKFAI). b) The triple chain $[\{Mn_3(\mathbf{L13})_3(OAc)_6\}\cdot 0.8MeOH\cdot 2.2H_2O]_n$ obtained with **L13** (CSD refcode: CUXCII). Colour code: grey = C, blue = N, green = Cl, grey-blue = Zn, purple = Mn, brown = bromine.

4.1.3 2D networks

The dimensionality of coordination polymers can be increased, when metal ions with a connectivity of more than two are combined with 4,2':6',4"-terpyridine ligands having more than two donor atoms. An exception was described in the previous section, where a 1D ladder was observed.

The incorporation of additional coordinating groups on the 4,2':6',4"-terpyridine ligand **L9** lead to an increase in dimensionality towards 2D coordination nets. In the structure, displayed in Fig. 13c (CSD refcode: DIRMAU), a three connectivity Co(II), is combined with **L9**, having three donor atoms. A net-like structure forms, which consist of triangles defined by three Co(II) ions and three ligands **L9**[74].

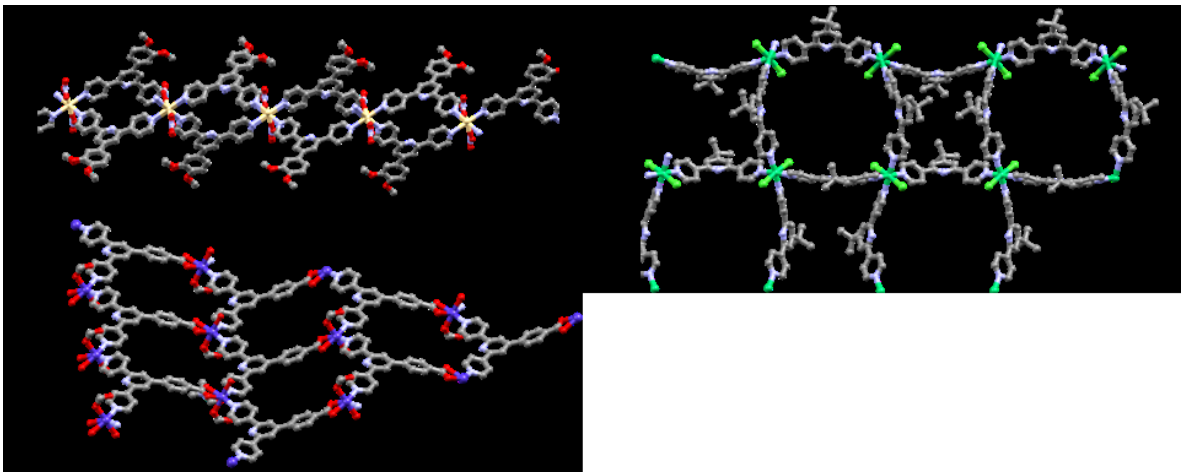

Fig. 13: a) The 2D net [Cd(**L9**)$_2$(NO$_3$)$_2$]. b) The 2D net [4{Ni$_2$Cl$_4$(**L10**)$_4$}·13(1,2-Cl$_2$C$_6$H$_4$)·30H$_2$O]$_n$. c) The 2D net [Co(**L11**)(HCOO)(H$_2$O)]$_n$·nDMF. CSD refcodes = a) COGWEC, b) GALGOR, c) DIRMAU. Colour code: grey = C, blue = N, green = Cl, dark-green = Ni, grey-blue = Zn, red = O, yellow = Cd.

Structures a and b in Fig. 13 have four-connecting Cd(II) and Ni(II) nodes, combined with ligands **L10** (CSD refcode: COGWEC)[75] and **L11**(CSD refcode: GALGOR)[76] which have two donor atoms. A 2D structure is a common motif obtained when linkers with two donor atoms are combined with four-connecting nodes and some examples will be presented in the main part of this thesis. The topology of the net is defined by the connectivity of the nodes. In Fig. 13b the Ni centres are the nodes of the (4,4) net. The first number in the term (4,4) is defined by the shortest circuit, that can be formed by connecting nodes with linkers. The second term is defined by the connectivity of the node (the Ni centre is 4-coordinate). The structures in Fig. 13c is a (3,6) net. 3 for the shortest circuit of nodes connected by linkers and 6 for the connectivity of the node.

4.1.4 3D-structures

4,2':6',4"-Terpyridines with more than two donor atoms can be combined with multi-connecting metal ions to form 3D structures. In section 3.4 some applications of porous coordination polymers were discussed, and it is one goal of the crystal engineering presented in this thesis to synthesize 3D structures using 4,2':6',4"-terpyridine ligands. Some examples exist in the literature, where researchers achieved the formation of 3D motifs.

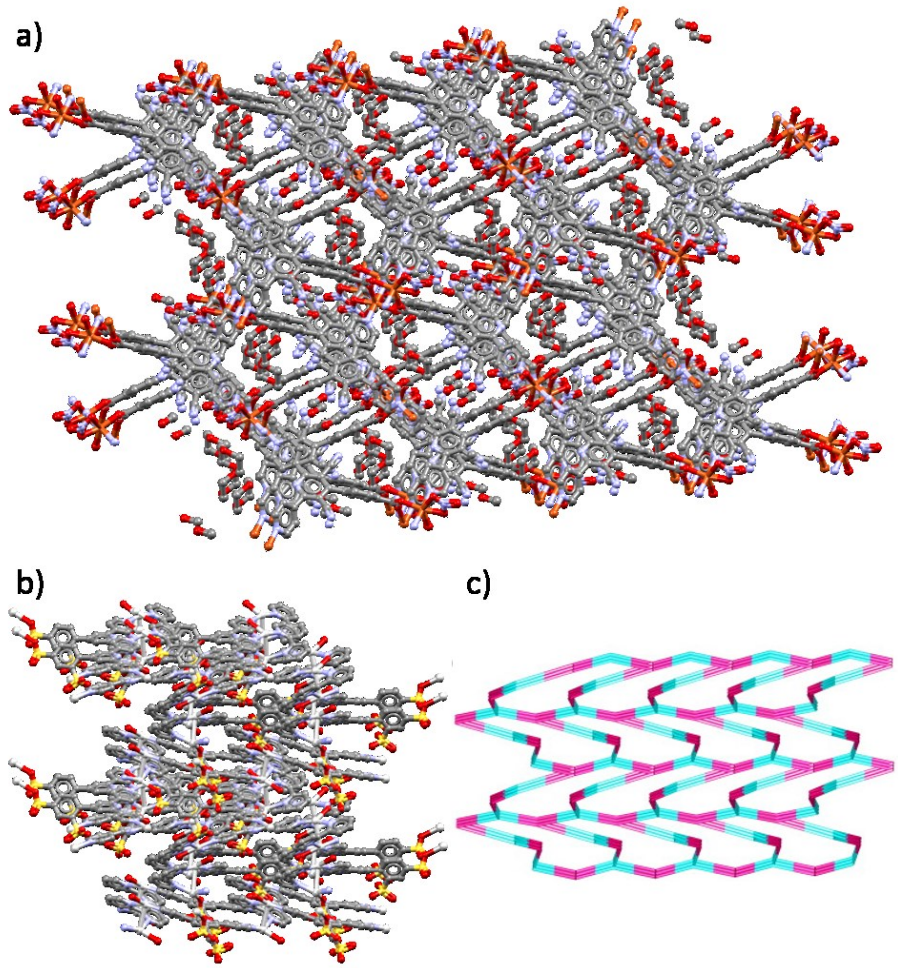

Fig. 14: The 3D structures [{Cu(**L14**)(NO_3)}·0.5MeOH·0.5dioxane]$_n$ (a, CSD refcode: CIVTEH) and [Ag_2(**L15**)(2,2′-bpy)(H_2O)]$_n$ (b, CSD refcode: DOZYEY). c) Scaffold representation of the 3D **ths** net in [Ag_2(**L15**)(2,2′-bpy)(H_2O)]$_n$, reproduced from ref.[77] with permission of Elsevier. Colour code: grey = C, blue = N, silver = Ag, red = O, orange = Cu, yellow = S.

In structures a (CSD refcode: CIVTEH)[78] and b (CSD refcode: DOZYEY)[77] in Fig. 14 ligands **L14** and H_2**L15**, which have more than two donor atoms, were combined with metal centres of four (Cu(II)) and three (Ag(I)) connectivity, respectively. For the reader it is very difficult to understand and visualize the connection pattern in 3D structures by looking at a 2D image, but some tools exist that help visualization. The scaffold displayed in Fig. 14c gives a better understanding of the connectivity in the framework displayed in Fig. 14b. How such a scaffold can be generated from a crystal structure will be discussed at the end of this chapter.

4.1.5 A tetratopic bis(4,2':6',4''-terpyridine) ligand

The total number of donor atoms in a 4,2':6',4''-terpyridine can easily be increased by the incorporation of functional groups possessing donor atoms in the 4' position (see **L6**, **L9**, **L15** in Scheme 7) using Wang and Hanan's[79] one-pot synthesis. 4'-Substituted 4,2':6',4''-terpyridines can be for example synthesized from aromatic aldehydes and 4-acetylpyridine. The aromatic group is attached in the 4'-position of 4,2':6',4''-terpyridines. The detailed reaction is presented in chapter 6. The incorporation of more than one functional group was achieved in ligand **L15**, bearing two sulfonic acid groups, but only one sulfonic acid took part in the coordination to a Ag(I) centre (Fig. 14c). This could be partly due to an increased steric demand of two functional groups on one phenyl ring. One approach towards ligands with four donor atoms, and potentially more donor atoms, is the elongation of the ligand backbone and the incorporation of a second 4,2':6',4''-terpyridine molecule. Yoshida and coworkers published the first bis(4,2':6',4''-terpyridine) ligand in a coordination polymer in 2013. The ligand is constructed from two 4,2':6',4''-terpyridine units, linked via the 1 and 3 positions of a phenylene spacer (**L17**, Fig. 15)[80]. A 2D triple interpenetrating network was obtained when **L17** was combined with a two-connecting cobalt(II) ion (CSD refcode: DEXVOT). For a better visualization the TOPOS[81] overlay and the scaffold of the network was generated using TOPOS[81] (Fig. 15). The net topology is defined by the node, which is the centroid of two Co(II) ions (Co1 and Co1i in Fig. 15a). The nodes are connected by two "half-ligands **L17**" (half-ligand are one 4,2':6',4''-terpyridine unit in **L17**) which also coordinate to a second distinct Co(II) ions (Co2 in Fig. 15a). Each node is four-connecting and the net consists of squares, defined by four nodes (4,4-net, Fig. 15b and c). Other bis(4,2':6',4''-terpyridine) ligands were reported[82], but a 3D coordination polymer using these tetratopic ligands was never reported. Examples with tetratopic bis(4,2':6',4''-terpyridine) ligands which were successfully used to create 3D frameworks are presented in this thesis.

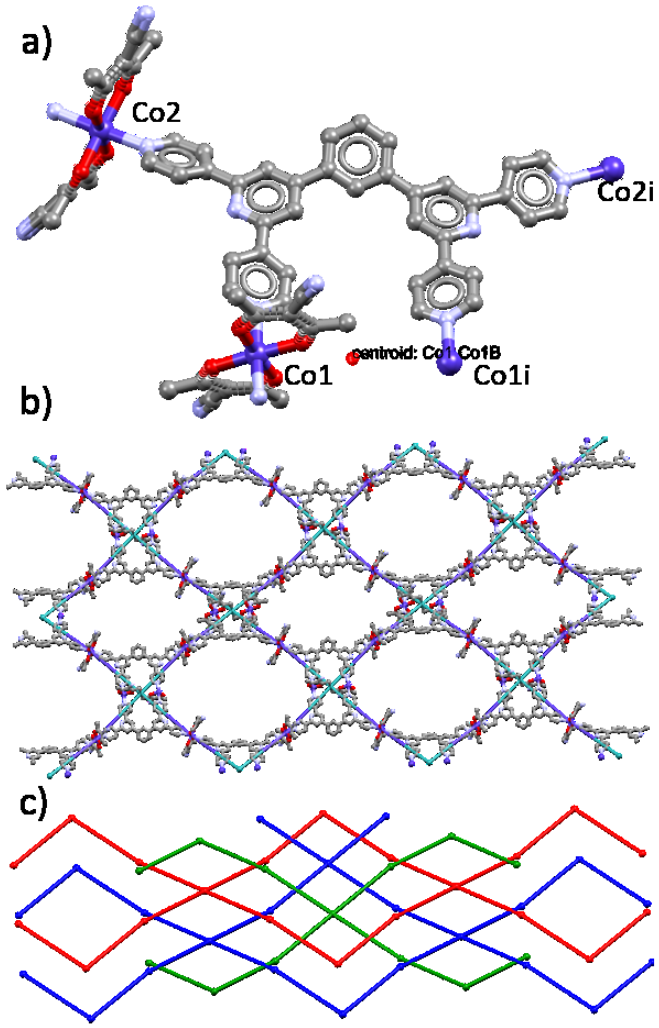

Fig. 15: a) The repeat unit in the structure $[\{Co(CNacac)_2\}_2(\mathbf{L17})\cdot(CHCl_3)\cdot(CH_3OH)]_n$ published by Yoshida and coworkers (CSD refcode: DEXVOT)[80]. b) The superimposed structure using TOPOS[81]/ Mercury[83]. c) The scaffold of the 2D (4,4) triple interpenetrating net, generated with TOPOS[81]. Interpenetrating nets are coloured in red, blue and green. Colour code in a) and b): grey = C, blue = N, white = H, red = O, purple = Co.

4.2 Structural motifs obtained with 3,2':6',3"-terpyridine

A selection of published 3,2':6',3"-terpyridine ligands (**L18-L26**)[57, 84-91] in coordination polymers is displayed in Scheme 8. A similar comparison of structural motifs as in section 4.1 is presented here.

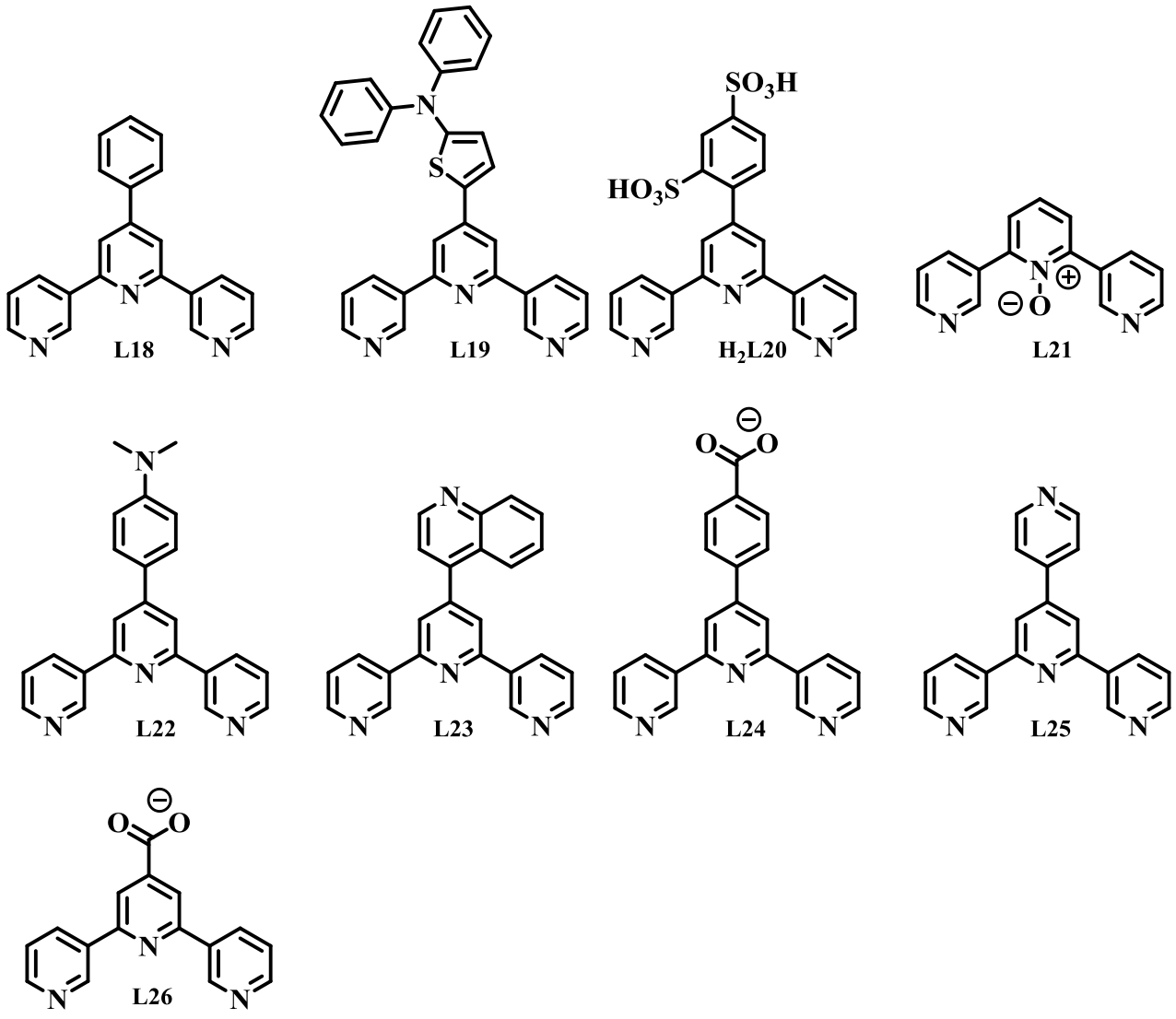

Scheme 8: A selection of 3,2':6',3"-terpyridine ligands incorporated into coordination polymers.

4.2.1 Dinuclear and multinuclear structures

Two dinuclear structures are presented in Fig. 16 using ligands **L18**[84] and **L19**[85] (see Scheme 8).

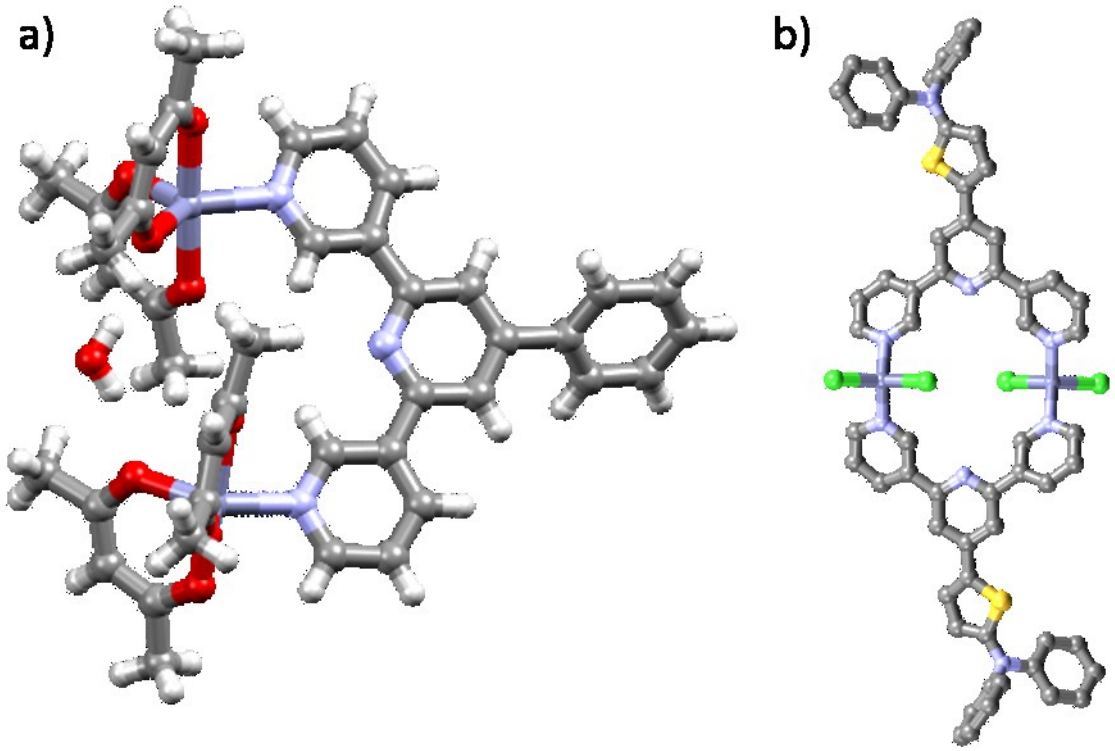

Fig. 16: The dinuclear discrete structure [{Zn_2(**L18**)$(acac)_4$}·H_2O] obtained with ligand **L18**(a, CSD refcode: COMVIK). The dinuclear discrete structure [Zn_2(**L19**)$_2$·Cl_4] (b, CSD refcode: ELAMUB). Colour code: grey = C, blue = N, white = H, red = O, yellow = S, grey-blue = Zn, green = Cl.

The structure in Fig. 16a (CSD refcode: COMVIK) has two five coordinated Zn ions, bridged by **L18** and the metal building block is connected through a single coordination site, like in the structure displayed in Fig. 9a. The $Zn(acac)_2$ building block seems to sterically hinder the second coordination site in both structures, even though a Cambridge Structural Database[34] (CSD version 5.39) using Conquest v. 1.20[35] revealed 152 structures, where the zinc centres in $Zn(acac)_2$ units are six coordinate. A dimeric structure of a compound obtained with $ZnCl_2$ and **L19** is displayed in Fig. 16b (CSD refcode: ELAMUB) and further new examples of discrete structures using zinc halides with 4,2':6',4"-terpyridine and 3,2':6',3"-terpyridine ligands are presented in this thesis.

4.2.2 1D structures

Some 1D structures of coordination polymers using ligands **L20** – **L23** are displayed in Fig. 17[86-89].

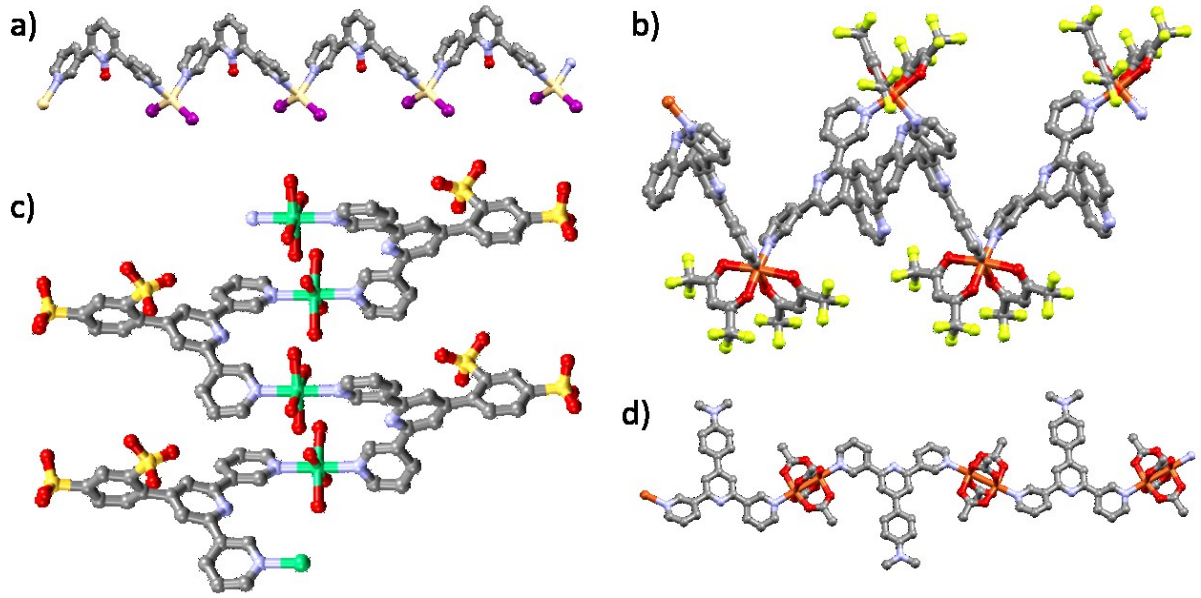

4.2.2.1 Fig. 17: 1D coordination chains constructed of two-connecting metal ions and ligand with two donor atoms **L20** – **L23**. Structures of $[Cd(\mathbf{L21})I_2]_n$ (a)), $[Cu(\mathbf{L23})(hfacac)_2]_n$ (hfacac = hexafluoroacetylacetone) (b)), $[\{Ni(\mathbf{L20})(H_2O)_4\}\cdot 3H_2O]_n$ (c)) and $[Cu_2(\mathbf{L22})(OAc)_4]_n$ (d)). Colour code: grey = C, blue = N, red = O, yellow = S, bright-yellow = F, purple = I, light yellow = Cd, green = Ni, orange = Cu. CSD refcodes: a) HATFOA, b) SAZSAQ, c) DUWCUV, d) SADBEH.

The structure in Fig. 17a (CSD refcode: HATFOA) is a 1D coordination polymer with a 2-fold rotation axis through the O and inner pyridine ring. The chains in the structures in Fig. 17b and c are built up by a screw axis and the chain in structure Fig. 17d is built up by a glide plane. The greater flexibility (Scheme 9) in the way of coordination for 3,2':6',3"-terpyridines dictates the assembly of these chains. When 4,2':6',4"-terpyridines, with two donor atoms are combined with zinc halides (e.g.: $ZnCl_2$, ZnI_2, $ZnBr_2$), which have a connectivity of two in the crystal (see Fig. 11a and c), helical 1D polymer chains can form. Examples and a comparison of 1D chains incorporating 4,2':6',4"-terpyridines and 3,2':6',3"-terpyridines with a connectivity of two and zinc halides will be presented in the main part of this thesis.

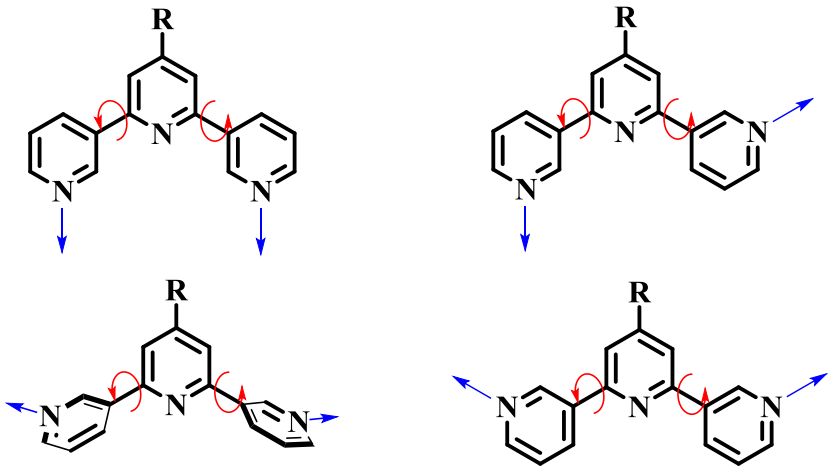

Scheme 9: 4'-substituted 3,2':6',3"-terpyridine in some possible conformations. The R group highlights a possible and most common substitution position. Blue arrows indicate coordination and red arrows illustrate rotational freedom.

A good example for the influence of the ligand coordination on the structural assembly is displayed in Fig. 17c (CSD refcode: DUWCUV). Both coordinating N atoms in **L20** coordinate in a parallel fashion (Scheme 9 top left) to a linear two-connecting Ni building block. A left-right alternating 1D coordination polymer is formed. A different orientation of the coordinating N atoms is observed in structures Fig. 17b and d (CSD refcodes: SAZSAQ and SADBEH). The external pyridine rings are twisted by 180° (Scheme 9 bottom right) with respect to the two previous structures. 1D coordination polymers are obtained, but why the ligand orientation changes, especially on comparing the structures in Fig. 17b and d, both of which have a linear two-connecting metal building block is not easy to understand. One reason could be the larger $Cu_2(OAc)_4$ building block, compared to the less sterically demanding $Ni(OH_2)_4^{2+}$ centre. Other interactions, including π-stacking of ligands and hydrogen-bonding between SO_3^{2-} and H_2O also have to be considered and can influence the assembly of a structure. The structure in Fig. 17b consists of **L23** and Cu(hexafluoroacetylacetonate)$_2$ building blocks.

4.2.3 2D networks

A 2D structure incorporating **L24** is displayed in Fig. 18[90].

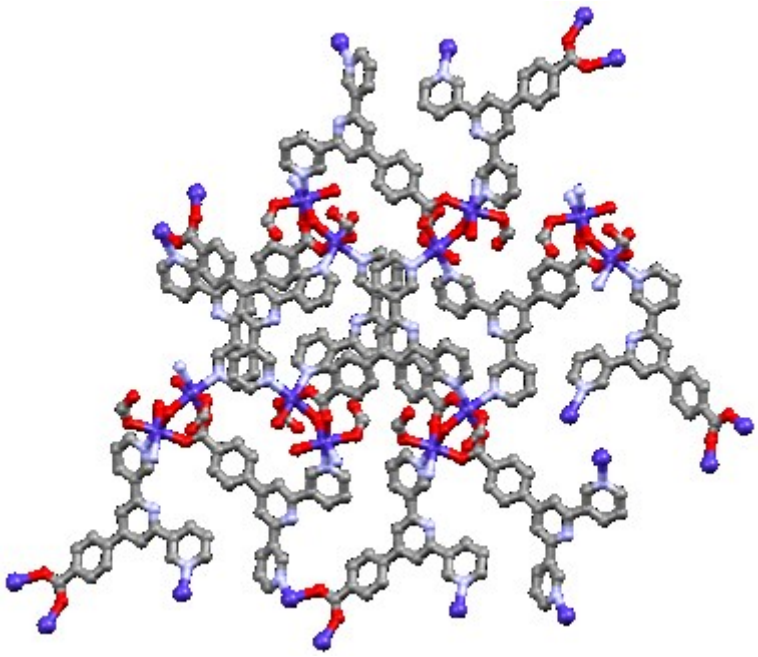

Fig. 18: The 2D structure $[Co_4(\mathbf{L24})_4(HCOO)_4(H_2O)_2]_n$ obtained with **L24**, having four donor atoms. Colour code: grey = C, blue = N, red = O, purple = Co. CSD refcode: DIRMIC.

The structure in Fig. 18 (CSD refcode: DIRMIC) uses **L24** and a Co dimer as the metal building block, where two Co centres are bridged via mono-coordination of a carboxylate group of one molecule of **L24**. Each Co also coordinates to two N atoms of different **L24** molecules. The other positions are coordinated by formate and water molecules. Two kinds of Co dimers and two kinds of ligands **L24** were identified in the net and the structure is described as (3,6) net, constructed of triangles (three Co dimers are connected via three ligands **L24**) and each Co dimer node is 6-connecting[90].

A 2D structure was obtained with **L25**[57] in combination with $Cu(CN)_2$. Fig. 20 (CSD refcode: COXGEC) displays one sheet of the 2D net structure. Each Cu ion has a connectivity of three and each ligand **L25** has three donor atoms. Cu ions are bridged by $Cu(CN)_2$.

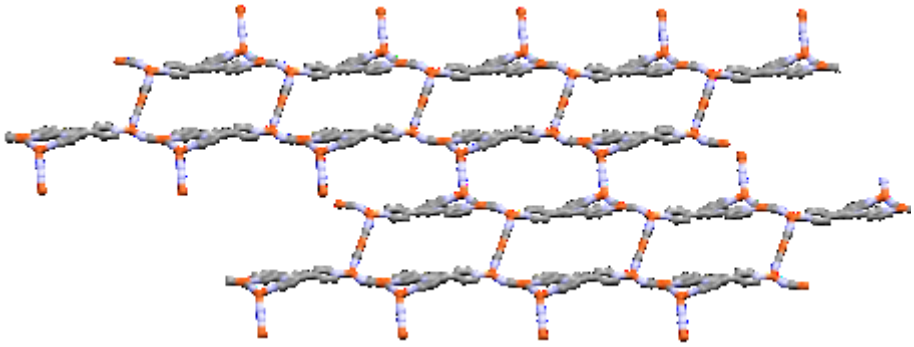

Fig. 19: A 2D sheet present in $[(CuCN)_4(\mathbf{L25})]_n$ (CSD refcode: COXGEC). Colour code: grey = C, blue = N, orange = Cu.

4.2.4 3D structure

A 3D structure was obtained with **L26**[91]. The structure in Fig. 20 (CSD refcode: XEWGAJ) is constructed from a four-donor ligand **L26**, which bridges two Cd centres via the carboxylate group. Three Cd centres form a cluster, which is connected via carboxylate groups, bridging water molecules and a benzene-1,2,4-tricarboxylate ligand.

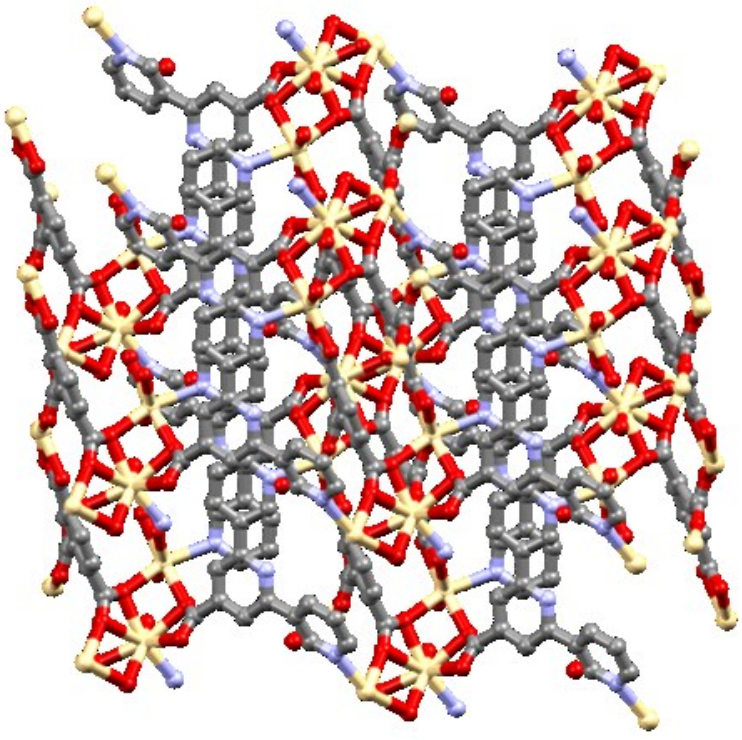

Fig. 20: The 3D structure $[\{Cd_4(\mathbf{L26})_2(2\text{-btc})_2(H_2O)_2\}_n\, nH_2O]$ (2-btc = 1,3,5-benzenetricarboxylic acid) obtained with ligand **L26** (CSD refcode: XEWGAJ). Colour code: grey = C, blue = N, red = O, light yellow = Cd.

4.2.5 A tetratopic bis(3,2':6',3''-terpyridine) ligand

Yoshida and coworkers published ligand **L27** in the same study as the tetratopic bis(4,2':6',4"-terpyridine) (Fig. 15)[80]. **L27** has four donor atoms and was combined with a Co(II) centre (connectivity of two in the structure) and a (4,4)-net structure was obtained (CSD refcode: DEXVIN). Four Co(II) centres and four ligands define the shortest circuit of the net (Fig. 21). The node in this network is the centroid of the phenylene ring in **L27**. The node has a connectivity of four and defines the topology of the net. The Co(II) units are the linkers.

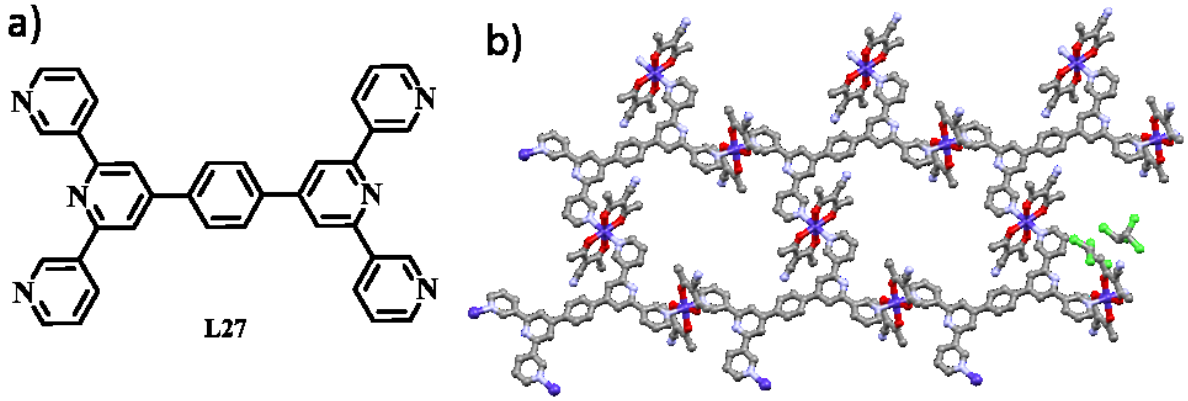

Fig. 21: The 2D (4,4) net [{Co(CNacac)$_2$(**L27**)$_{1/2}$}·(tetrachloroethane)$_{3/2}$]$_n$ obtained with the tetratopic ligand **L27** and a two-connecting Co(II) centre. Colour code: grey = C, blue = N, white = H, red = O, purple = Co. CSD refcode: DEXVIN.

4.3 Visualizing and analyzing 3D structures with TOPOS[81]

In the last section examples of 3D structures were displayed. Some of these structures are complicated to evaluate in 2D representation, as they could be interpenetrating or have multiple substituents, which makes visualization difficult. Even for a crystallographer and crystal engineer it is often challenging to understand coordination patterns and describe the topology of structure. Topologies of coordination networks were nicely described by Stuart Batten, Suzanne Neville and David Turner in their book "Coordination polymers" [12] and this approach can be used to describe 3D structures and assign them to a specific group. The analysis is based upon the assignment of a net type, three types of which are displayed in Fig. 22. One example

is the most common net type for tetrahedral nodes, the diamond structure (**dia**). Ligands with four donor atoms and four connectivity metal ions are connected and form an adamantane like subunits (Fig. 22 b). It is often very difficult to identify the nodes and or even match the nodes to an atomistic model. Even if they are identified, it is not simple to understand how they are connected and what net type is present. Throughout this thesis and in the associated publications, 2D and 3D structures were examined, analyzed and visualized with the program TOPOS[81] in combination with Mercury v.3.10[83]. This section will give short and quick guidelines how to use TOPOS[81] and how crystal structure data can be modified, analyzed and most importantly simplified to obtain the topology.

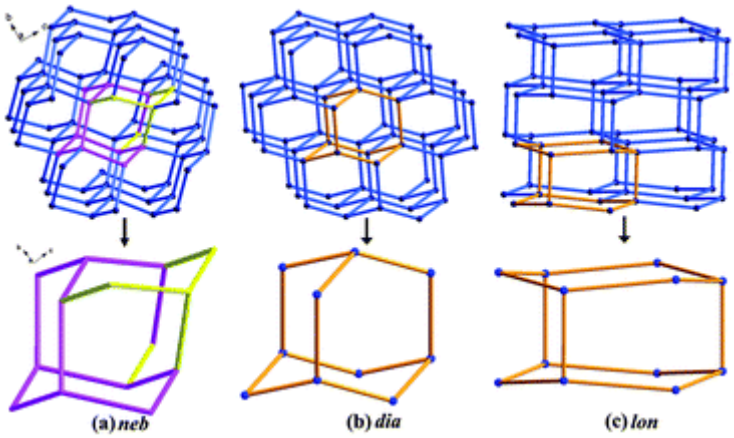

Fig. 22: Three common 3D-net topologies **neb**, **dia** and **los** used to describe and categorize 3D networks. Reproduced from ref.[92] with permission from the Royal Society of Chemistry.

TOPOS[81] is free for non-commercial use and the program and can be downloaded here: http://topospro.com/software/

The structure $[\{Zn_3(\mathbf{L12})_2Cl_6\}\cdot nH_2O]_n$ from section 4.1.3 is taken as an example. The aim is to visualize the coordination pattern in this structure for the viewer and provide information about the topology of the coordination polymer. A combination of the programs Mercury v.3.10[83] and TOPOS[81] is recommended for this purpose.

1) Identification of the nodes in the coordination framework

The first step is to open the structure in Mercury v.3.10[83] and analyze its coordination pattern. In some structures the nodes in a framework are conventially identified as the metal centres, in others the ligand acts as a node. This part of the analysis is subjective and relies upon chemical intuition and experience. Fig. 23 illustrates the nodes and the distances of the nodes identified

after viewing the structure (CSD refcode: ZOKFAI) with Mercury. Sometimes a node is not an atom, but the centroid of a ring or cluster. In this case study, one node (the centroid of the central pyridine ring) was identified to represent the 1D ladder type structure. If a centroid is generated, Mercury can display its coordinates (/Display/More information/centroids list). A centroid can also be generated using the subprogram IsoCryst in TOPOS[81] and, as the subsequent steps will be done with TOPOS[81] it is recommended to use the coordinates obtained with IsoCryst. The centroid coordinates are important for the subsequent steps and should be written down.

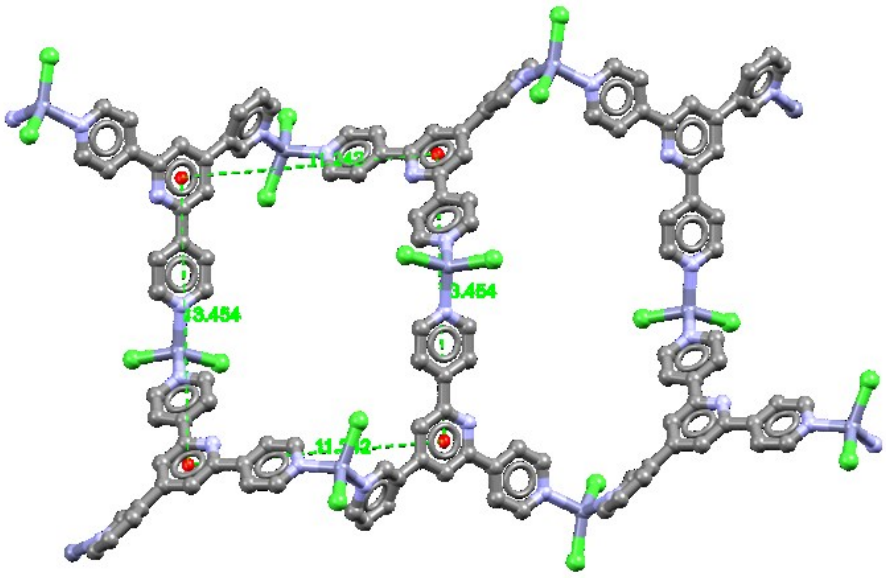

Fig. 23: The centroids (red dots) of **L12** are the nodes in this structure of the compound $[\{Zn_3(\mathbf{L12})_2Cl_6\}\cdot nH_2O]_n$. Centroids have a distance of 11.242 Å and 13.454 Å.

2) Generating virtual bonds between nodes

A good way to visualize coordination patterns is to connect the nodes and either overlay them with the structure or delete every atom except the nodes to visualize the scaffold of the framework. This can be done easily with TOPOS[81].

I) Import of the structure into TOPOS: database/import/choose cif file; create database – click yes; user code: 1.

II) Generate dummy atom (e.g. Ru) at the centroid position if needed: double click the name of the structure, go to atoms, scroll to the bottom and fill in the centroid coordinates from Mercury v.3.10[83] or IsoCryst, save.

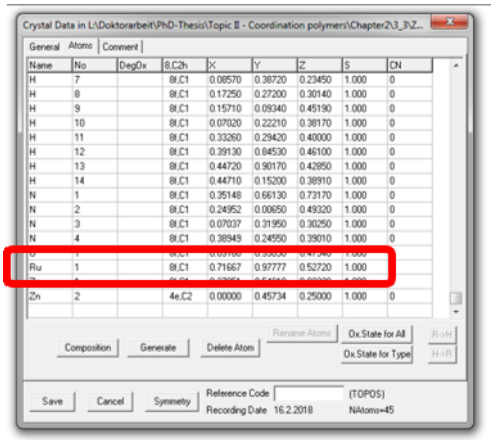

III) Check if the insertion was successful: open IsoCryst in TOPOS[81] 

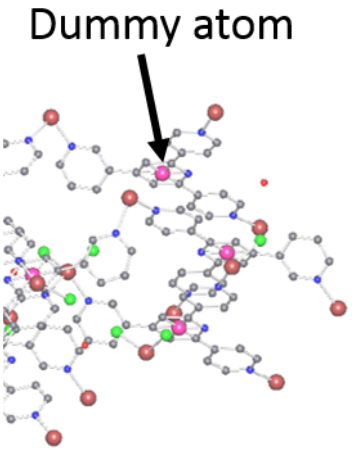

The new dummy atom (pink) is at the centroid position of the inner pyridine ring of **L12**.

IV) Measure the distance between the nodes using Mercury v.3.10[83] (see Fig. 23) or IsoCryst.

V) Define a bond between nodes in TOPOS[81]: open “Run AutoCN” and click options.

Go to 'matrix' and choose ranges. Type in the range in which bonds are drawn between certain atoms. Type in “Ru-Ru 12.241:12.243” in this format and TOPOS[81] will draw bonds between all Ru atoms between 12.241 and 12.243 Å. Press okay and press **Run**. The TOPOS[81] output shows which atoms are connected. The Ru dummy atom has three connections to other Ru dummy atoms. Always check, that no “wrong” bonds are drawn to adjacent molecules, chains or layers.

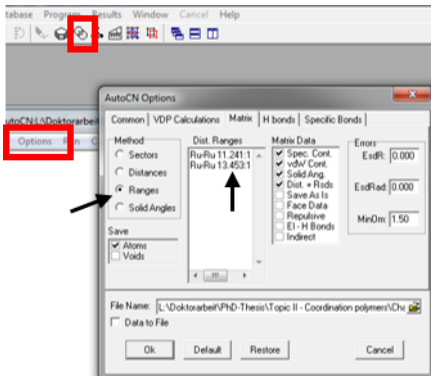

VI) Grow the structure in IsoCryst (it is possible to grow from specific atoms by selecting them and then press grow or *ctrl* w) and save it as a pdb file. By deleting all atoms except the nodes in IsoCryst, the scaffold of the network can be saved as a pdb file.

VII) Open the pdb files in Mercury and generate pictures.

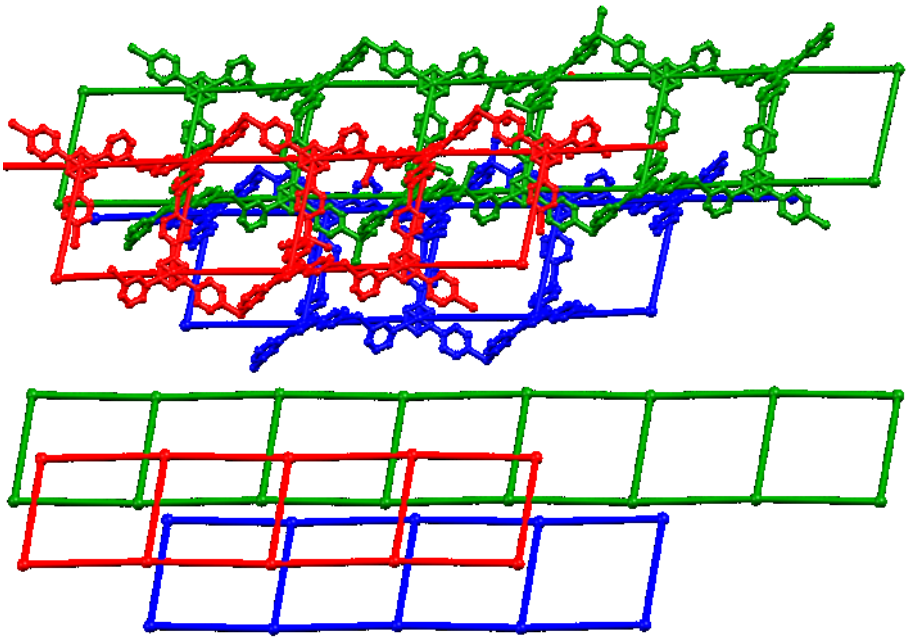

VIII) Topology of the net

Click on "Run Ads" in TOPOS[81] and press run. Choose and select (*Ctrl* + click) the nodes (here both dummy atoms) and press okay. TOPOS[81] analyzes the structure and outputs the topology (here: a 1D chain).

TOPOS[81] in combination with Mercury v.3.10[83] is a great set of tools for the topological analysis and modification of crystal structures. In particular 3D structures and interpenetrating nets can be nicely visualized by overlaying the nodal connections with the original structure. The scaffold of the structure can be generated using TOPOS[81] and topologies of structures calculated. Many examples, where this has been used are presented in the following chapters.

5 MATERIALS AND METHODS

5.1 Chemicals

Chemicals for ligand synthesis were purchased from Sigma-Aldrich, TCI, Acros, Apollo, Fluorochem and Alfa Aesar. Deuterated solvents for NMR spectroscopy were purchased from Cambridge Isotope Laboratories, Inc. HPLC solvents were used for UV-VIS and ESI-MS measurements.

5.2 General

Ligands were characterized by ^{1}H and $^{13}C\{^{1}H\}$, spectroscopy, ESI-MS, high res ESI-MS, MALDI-TOF-MS, melting point, UV-VIS spectroscopy, IR spectroscopy and elemental analysis. 400MHz, 500MHz and 600MHz NMR spectra were measured on a Bruker Avance III- 400, DRX-500 or DRX-600 NMR spectrometers with chemical shifts referenced to residual solvent peaks; ^{1}H and ^{13}C δ(TMS) = 0 ppm. Electrospray mass spectra were measured on Bruker Esquire 3000^{plus} or Shimadzu LCMS-2020 instrument. High resolution ESI-MS was measured on a Bruker maXis 4G instrument. MALDI-TOF mass spectra were recorded on a Bruker Daltonics Inc. microflex instrument. For GC/MS analysis, a Shimadzu GCMS/QP2010 SE gas chromatograph system with ZB-5HT inferno column (30 m × 0.25 mm × 0.25 mm), at 1 mL min^{-1} He-Flow rate (split = 20:1) with a Shimadzu mass detector (EI 70 eV) was used. Solution electronic absorption spectra were recorded on an Agilent 8453 or Cary 5000 spectrophotometer. Solid-state spectra were recorded on a Cary 5000 spectrophotometer. FT-IR spectra were recorded on a Perkin Elmer Spectrum Two instrument.

5.3 Single crystal X-ray diffraction - XRD

Single crystal data were collected on a Bruker APEX-II diffractometer or a STOE StadiVari diffractometer equipped with a Pilatus300K detector and with a Metaljet D2 source. Data reduction, solution and refinement used the programs APEX[93], STOE X-AREA, STOE X-RED[94], APEX2, SuperFlip[95] and CRYSTALS[96] respectively. SQUEEZE[97] was used on some of the structures if solvent molecules could not be refined in a satisfactory manner. The structures were analyzed with Mercury v.3.10[83] and TOPOS[81].

Fig. 24: The APEX-II X-ray diffractometer (zoomed in on the goniometer head) used for analysing most of the single crystal structures reported in this thesis. The top part is the nitrogen gas, low temperature cryostat, underneath is a microscope and the X-ray source is at left-hand side of the image. X-rays hit the crystal mounted on the goniometer in the centre of the picture and diffracted X-rays get detected by the detector (right-hand side).

Single crystal X-ray data was collected, solved and refined in collaboration with three crystallographers Dr. Markus Neuburger, Dr. Jennifer Zampese and Dr. Alessandro Prescimone. Dr. Mateusz Pitak and Prof. Dr. Simon J. Coles from the University of Southampton solved three crystal structures[98]. Structures published in *JACS*[99] 2018 were collected, solved and refined by myself.

5.4 Powder X-ray diffraction – PXRD

Powder X-ray diffraction was used to analyze the bulk material of a crystallization experiment. PXRDs were measured on a Stoe Stadi P powder diffractometer. PXRD data can be found in the experimental section at the end of the thesis. One PXRD spectrum was measured by Dr. Karl Krämer from the University of Bern[100].

5.5 Crystallization experiments

Single crystals of the compounds presented in this thesis were obtain by the slow evaporation or layering techniques.

In the slow evaporation technique, a vial with dissolved compound is exposed to air and the solvent allowed to evaporate. The concentration of the dissolved compound increases accordingly and as the concentration exceed the solubility, single crystals (often of ligands) are obtained.

The layering technique was used for self-assembly of pyridine ligands with more than one donor atom with various metal salts. The general setup is exemplified in Fig. 25.

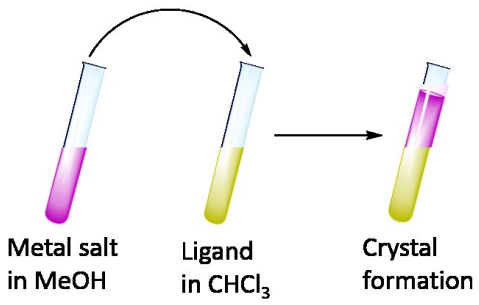

Fig. 25: Crystal growth by the layering technique, e.g. $Co(NCS)_2$ dissolved in MeOH is pink.

This technique is useful to grow crystals which are normally insoluble in the solvent used after formation, which means that the slow evaporation technique cannot be used. The conditions for this technique, such as solvents and concentrations of material have to be chosen carefully in order to obtain crystals.

The organic ligand (~ 20µmol) is dissolved in a halogenated solvent (~5mL, e.g. chloroform or dichlorobenzene) and added to a long test-tube. Halogenated solvents have the advantage to be denser than other organic solvents, thus mixing with other non-halogenated solvents is slow and diffusion controlled. A thin layer of methanol is carefully layered on top of the chloroform or dichlorobenzene layer (~ 1mL) and mixing of both solvents should be avoided. Most metal salts are soluble in methanol, which makes it a good general choice (other solvents might work as well). Metal salts (~ 20µmol) were dissolved in methanol (3-5 mL) and the solution was very careful layered over the thin methanol layer in the test-tube. The test-tube was closed with a stopper and is ideally placed in a dark and cold place. Vibrations of the test-tube can hinder crystal formation and the test-tubes should be placed in a quiet place and not touched for at least one week. Most crystals of coordination polymers were obtained with this technique within 2-4 weeks.

In some cases, when no crystal formed after 2-4 weeks, the test-tube was opened and the solvents allowed to evaporate slowly, which sometimes lead to crystal formation.

Crystallization experiments are presented in the experimental section.

6 LIGAND DESIGN AND CHARACTERIZATION

The synthesis of ligands for coordination polymers presented in the following chapters is discussed here. 3,2':6',3"-Terpyridines and 4,2':6',4"-terpyridines were synthesized in most cases from aromatic aldehydes and 3-acetylpyridine or 4-acetylpyridine, respectively, in the presence of KOH and aqueous ammonia. The reaction is one-pot, using Wang and Hanan's[79] methodology. The one-pot synthesis and the availability of many commercial aromatic aldehydes made screening of a large number of ligands straight forward (Scheme 10).

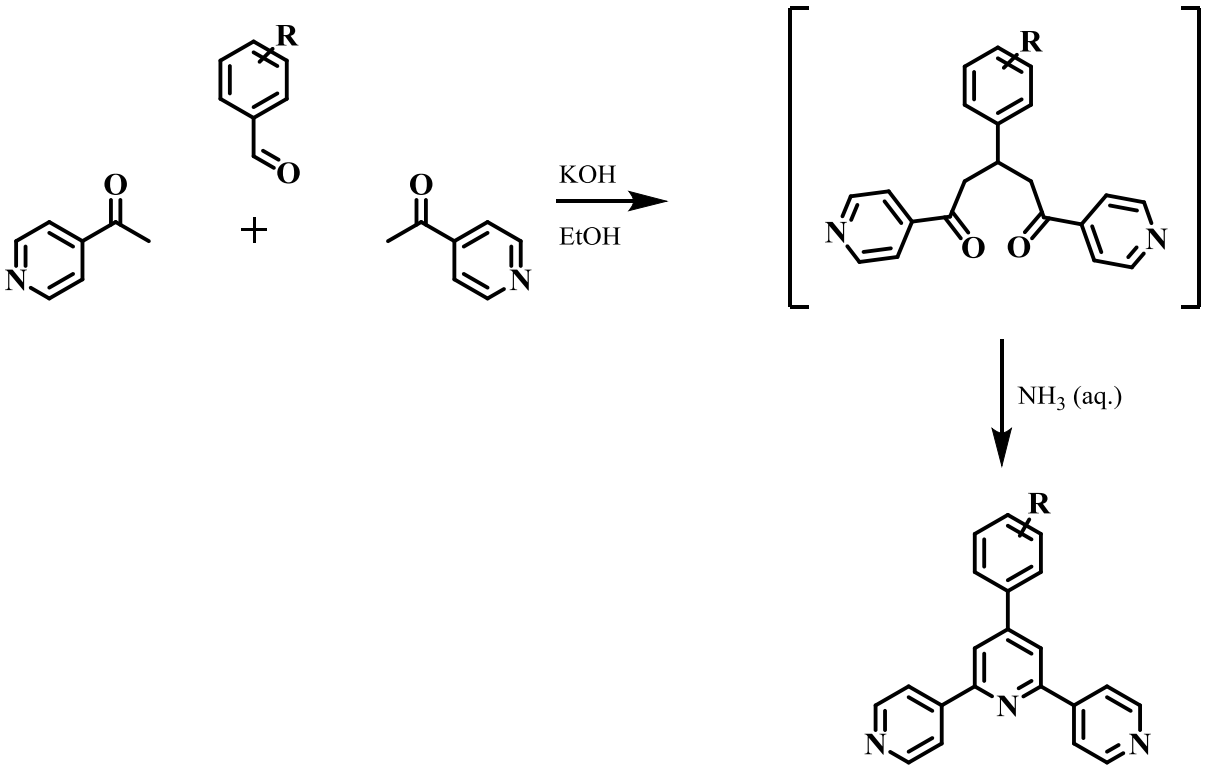

Scheme 10: Wang and Hanan's one-pot synthesis[79], represented by a substituted benzaldehyde and 4-acetylpyridine. The reaction was complete within one day, while stirring at ambient conditions.

The first step is an aldol addition, followed by a Michael addition. The enolate of 4-acetylpyridine is formed by the addition of KOH and attacks the aldehyde. A second enolate of 4-acetylpyridine attacks the α,β-unsaturated ketone and forms the intermediate (Scheme 10), which is normally not isolated (one exception is presented in this thesis). Addition of aqueous ammonia leads to a ring closing reaction and the formation of the inner pyridine ring. A wide

range of aromatic aldehydes and bulky aliphatic aldehydes (e.g. trimethylacetaldehyd, leading to the formation of **6** in Scheme 11) are tolerated. The product of the Wang and Hanan one-pot reaction is poorly soluble in EtOH/water and precipitates out of solution.

6.1 Ditopic ligands

4'-Substituted 3,2':6',3"-terpyridines and 4,2':6',4"-terpyridines presented in this thesis are displayed in Scheme 11. They were synthesized according to Scheme 10 from 4-acetylpyridine or 3-acetylpyridine and the corresponding aldehydes.

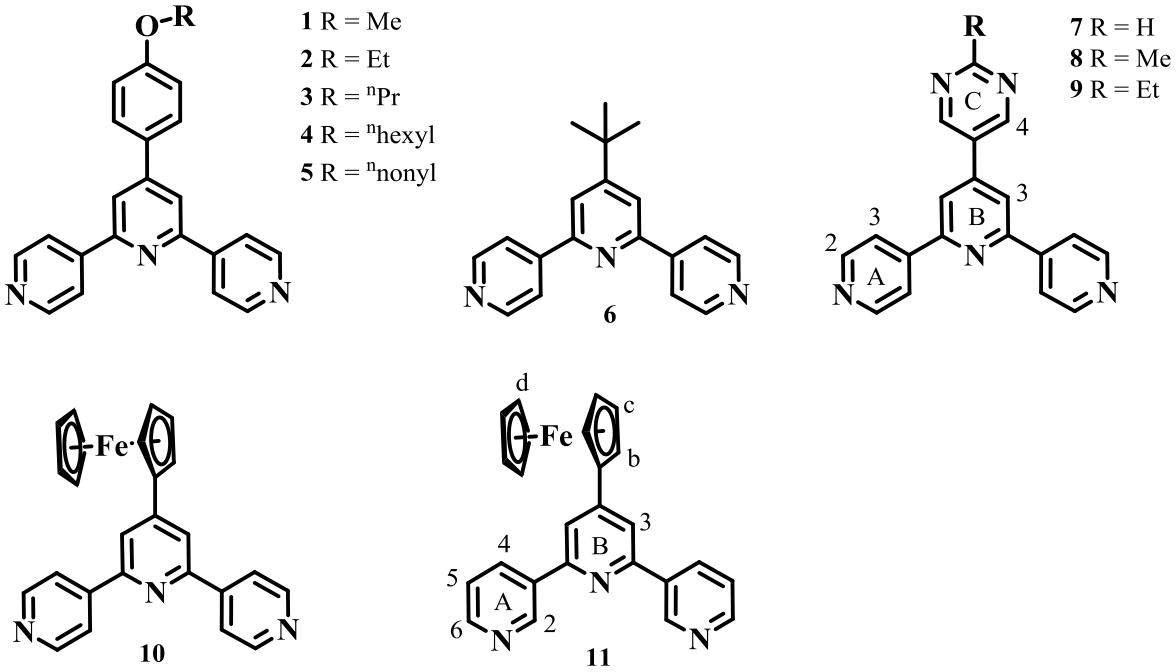

Scheme 11: Substituted 3,2':6',3"-terpyridines and 4,2':6',4"-terpyridines incorporated into coordination polymers and discrete complexes.

Ligands **1**-**5** were synthesized during my Master studies in the Constable/Housecroft group in Basel and their preparation can be found in the according publication[30]. Ligands were characterized by ^{1}H, and $^{13}C\{^{1}H\}$ spectroscopy, ESI-MS, high-resolution ESI-MS, melting point, UV-VIS spectroscopy and elemental analysis. The ^{1}H NMR spectrum of ligand **9** is shown in Fig. 26, representative for other 4,2':6',4"-terpyridines. The ^{1}H NMR spectrum was readily assigned by 2D-COSY and 2D-NOESY spectroscopy. NOE cross peaks from H^{A3} to H^{B3} and from H^{B3} to H^{C4} were used for the assignment. $^{13}C\{^{1}H\}$ NMR spectra were assigned using 2D-HMQC and 2D-HMBC spectroscopies.

Fig. 26: The 400 MHz ^{1}H NMR spectrum of ligand **9** with assigned peaks corresponding to Scheme 11. The solvent is $CDCl_3$ and shifts were references to $\delta(CHCl_3)$ = 7.26 ppm (*).

Ligand **11** is the only monotopic 3,2':6',3''-terpyridine ligand prepared and shows a different NMR spectroscopic signature (Fig. 27). One ferrocenyl proton (H^b) showed a NOE cross peak to one aromatic proton (H^{B3}). NOE cross peaks from H^{B3} to H^{A4} and to H^{A2}, in combination with the singlet observed for H^{A2} allowed assignment of these protons on ring A. The remaining protons H^{A5} and H^{A6} were assigned by 2D-COSY spectroscopy.

Fig. 27: The 500 MHz ^{1}H NMR spectrum of ligand **11** with assigned peaks corresponding to Scheme 11. The solvent is methanol-d_4 and shifts were references to $\delta(CHD_2OD)$ = 4.87ppm (*).

6.2 Bis(3,2':6',3"-terpyridines) and bis(4,2':6',4"-terpyridines)

2,5-Bis(octyloxy)terephthalaldehyde (precursor for **17** and **15**) and 1,1'-ferrocenedicarboxaldehyde (precursor for **18**) were purchased from Sigma-Aldrich.

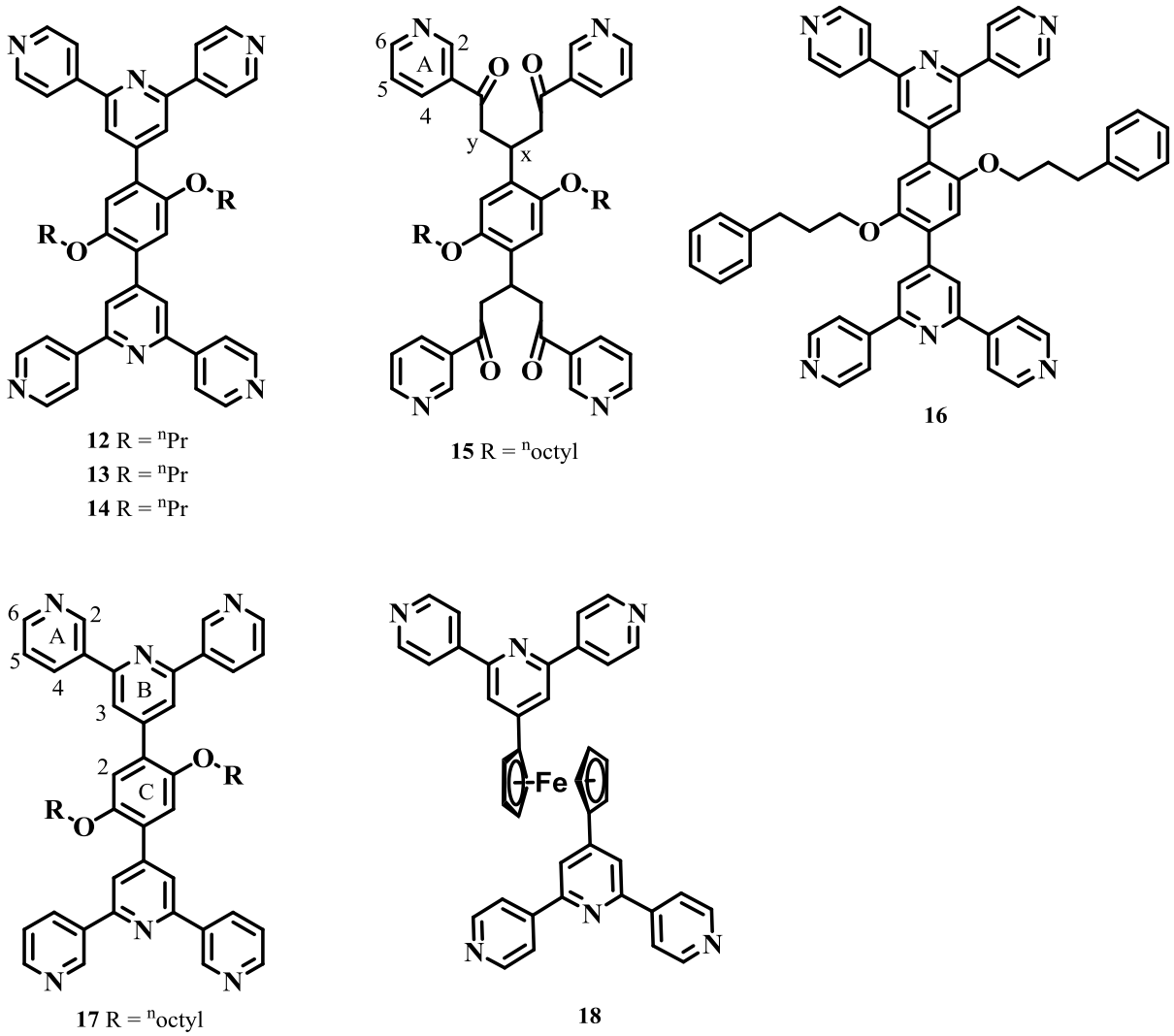

Scheme 12: Tetratopic bis(3,2':6',3"-terpyridines) and bis(4,2':6',4"-terpyridines) and the structure of the bis(1,5-di(pyridin-3-yl)pentane-1,5-dione) ligand **15**.

All other dicarboxaldeyhdes were synthesized in two steps from 2,5-dibromohydroquinone and the corresponding 1-bromoalkanes (Scheme 13) to yield the intermediate compounds **12a** (**R** = propyloxy), **13a** (**R** = *n*hexyloxy), **14a** (**R** = *n*decyloxy) and **16a** (**R** = propylbenzene). **12a**-**14a** and **16a** were reacted with *n*-BuLi in dry diethylether at 0°C for 6h. The reaction mixture was

quenched with dry DMF to yield the 2,5-bis(**R**)terephthalaldehydes (**12b**: **R** = propyloxy, **13b**: **R** = *n*hexyloxy, **14b**: **R** = *n*decyloxy and **16b**: **R** = propylbenzene). Commercial and synthesized dicarboxaldehydes were transformed into the bis(3,2':6',3"-terpyridine) **17** and into the bis(4,2':6',4"-terpyridines) **12-16** and **18** in a double Wang and Hanan[79] one-pot reaction. In one reaction the intermediate compound **15** of the one-pot synthesis of 2,5-bis(octyloxy)terephthalaldehyde with 3-acetylpyridine was obtained and the reaction was repeated without addition of aqueous ammonia to verify the formation of the targeted compound **15**.

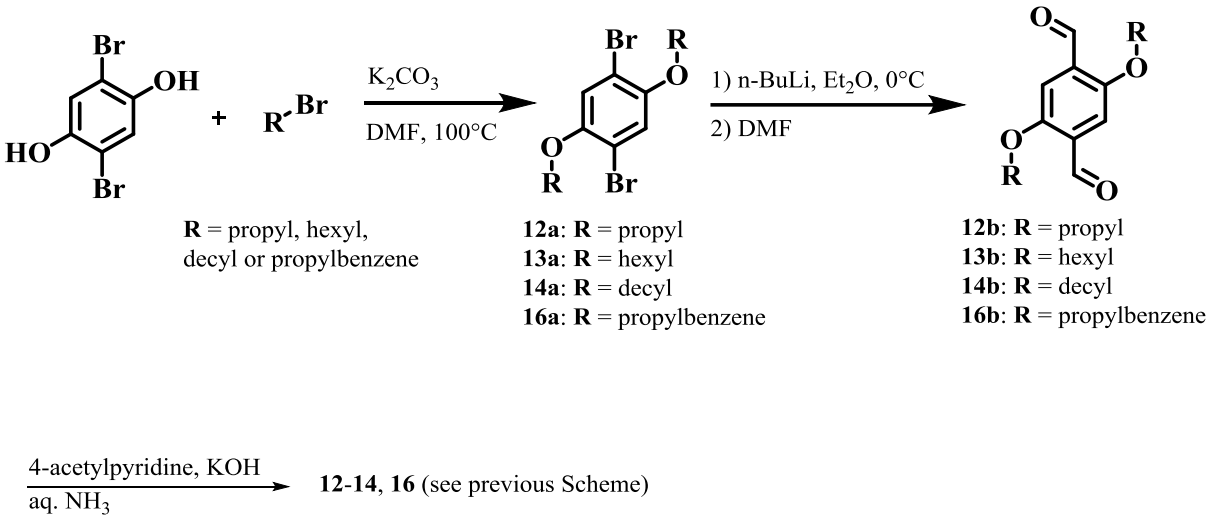

Scheme 13: Synthetic route towards bis(4,2':6',4"-terpyridines) **12-14** and **16**. Other ligands in Scheme 12 were synthesized from the according dicarboxalydes in the Wang and Hanan one-pot reaction.

The ^{1}H NMR spectrum of the tetratopic ligand **17** is displayed in Fig. 28. The assignment follows the same routine as described for ditopic 3,2':6',3"-terpyridine and ^{1}H NMR shifts for protons in rings A and B are similar in both di- and tetratopic pairs of ligands.

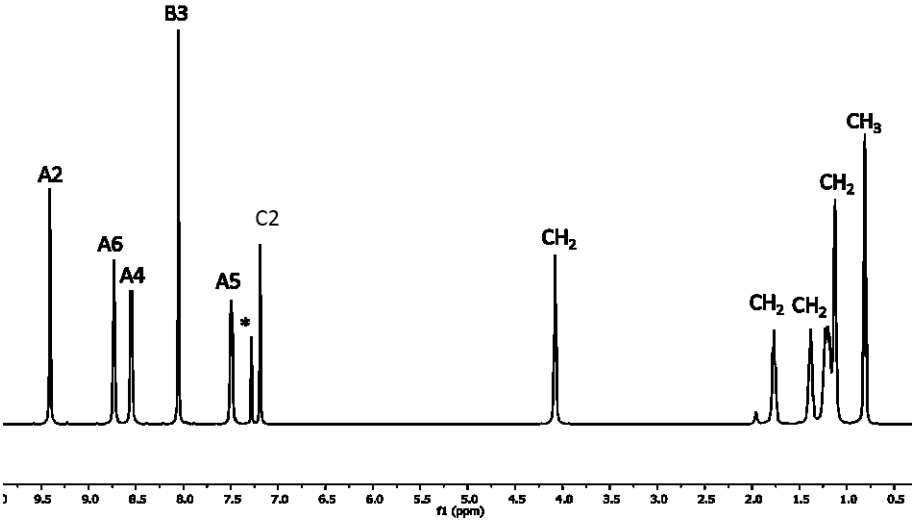

Fig. 28: The 500 MHz ^{1}H NMR spectrum of ligand **17** with assigned peaks corresponding to Scheme 12. The solvent is $CDCl_3$ and shifts were references to $\delta(CHCl_3)$ = 7.26 ppm (*).

The ^{1}H NMR spectrum of the **15** is displayed in Fig. 29.

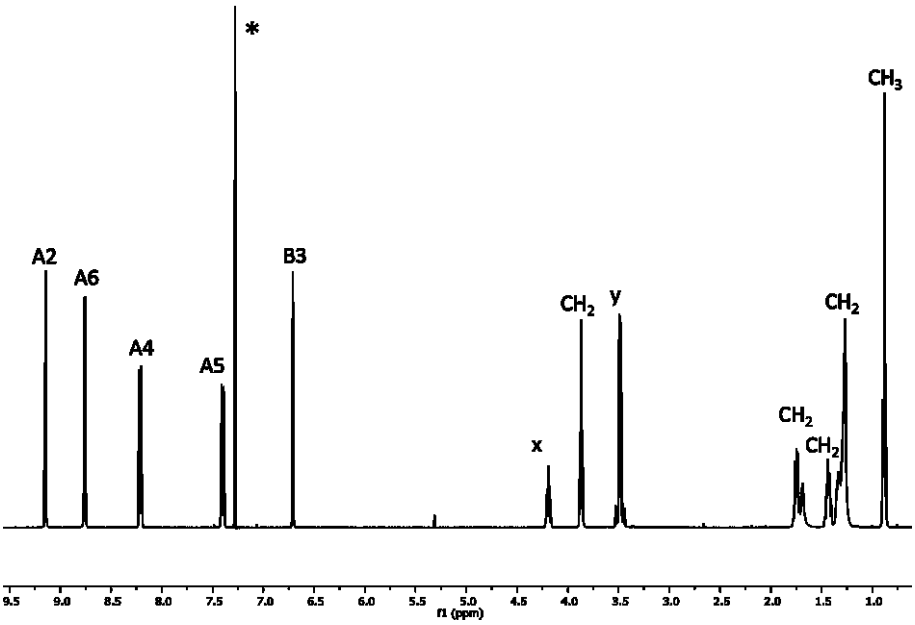

Fig. 29: The 500 MHz ^{1}H NMR spectrum of ligand **15** with assigned peaks corresponding to Scheme 12. The solvent is $CDCl_3$ and shifts were references to $\delta(CHCl_3)$ = 7.26 ppm (*).

15 was synthesized on purpose via the Hanan and Wang one-pot synthesis without addition of aqueous ammonia. Proton signals of ring A were readily assigned using 2D-COSY and 2D-

NOESY spectroscopy. NOE cross peaks from H^y to H^{A2} and H^{A4} were used to identify these protons. H^{A2} was distinguished from H^{A4} by the multiplicity of the signals.

The ligands were characterized by ^1H, and $^{13}C\{^1H\}$ spectroscopies, ESI-MS, high-resolution ESI-MS, melting point, UV-VIS spectroscopy and elemental analysis. Roughly 30 crystal structures were obtained with the ligands displayed in Scheme 11 and Scheme 12. An ordered presentation and comparison of the crystal engineering using these ligands is presented in the next chapters.

7 LIGAND STRUCTURES

Ligand structures were obtained for **8** and **11**.

7.1 Ligand **8**

Single crystals of ligand **8** were obtained during an attempt to react **8** with iron(II) perchlorate in MeOH. **8** crystallizes in the space group $Pmn2_1$. The asymmetric unit contains half a molecule of **8**, the second half is generated by a mirror plane. The structure of **8** is displayed in Fig. 30 and the planar orientation implies intermolecular interactions with other molecules.

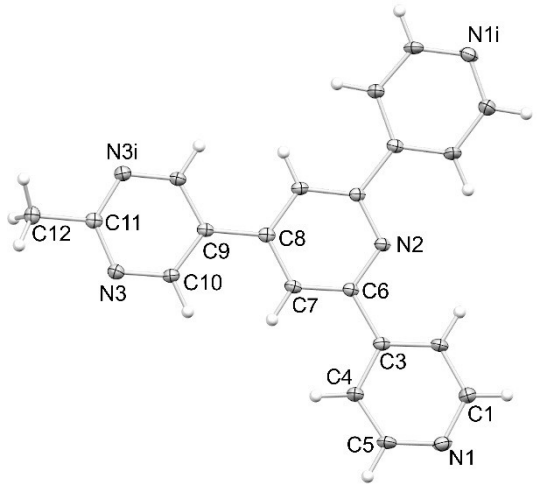

Fig. 30: Structure of molecule **8** with ellipsoids plotted at the 40% probability level. Symmetry code i = 2–*x*, *y*, *z*. Selected bond parameters: N1–C5 = 1.335(2), N1–C1 = 1.337(2), N2–C6 = 1.3402(19), N3–C10 = 1.336(2), N3–C11 = 1.3395(17) Å; C5–N1–C1 = 116.12(15), C6–N2–$C6^i$ = 118.19(19), C10–N3–C11 = 116.69(14)°. Reproduced from ref.[101], published by Elsevier.

Fig. 31 illustrates the packing of **8**, where neighbouring molecules stack and form face-to-face π-π interactions between all pyridine and pyrimidine rings. A second layer of stacked molecules is twisted by 90° and adjacent layers interact via hydrogen-bonds between C7-H…N(pyrimidine) (2.521 Å) and C7/C10…N (2.744 Å and 2.518 Å, respectively).

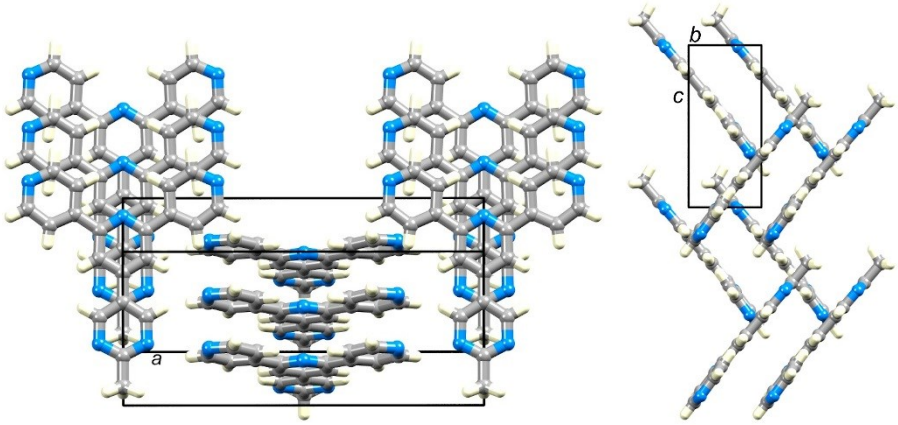

Fig. 31: Packing of **8**. Molecules are slipped with respect to one another, which enables π-π interactions between pyridine and pyrimidine rings. Reproduced from ref.[101], published by Elsevier.

Additional information can be found in the printed publication (section 18.1).

7.2 Ligand **11**

Single crystals of **11** were obtained serendipitously from a slow evaporation of a chloroform solution of **11**. **11** crystallizes in the chiral space group $P2_12_12_1$. The ferrocenyl group is slightly twisted with respect to the inner pyridine ring (28.8(4)°) and the pyridine ring containing N3 is twisted by 35° in respect to the inner pyridine ring (Fig. 32a and b).

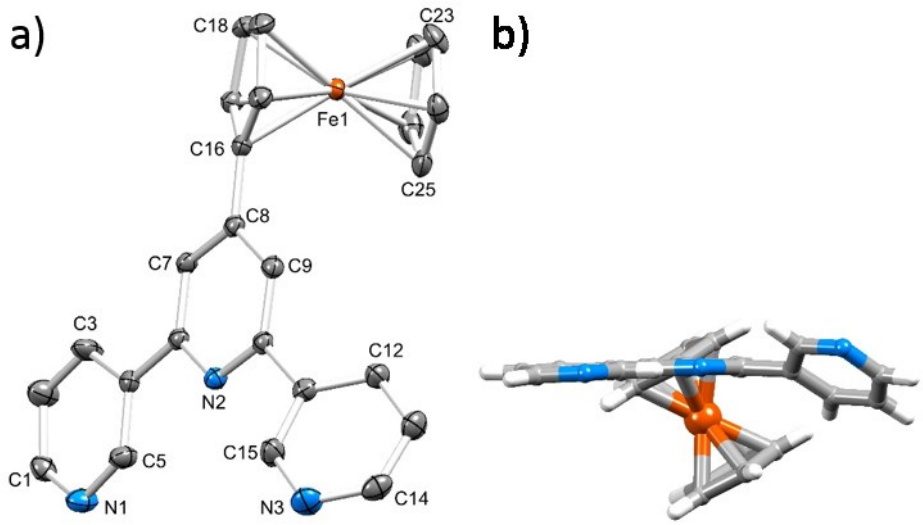

Fig. 32: a) Structure of compound **11**; H atoms omitted for clarity and ellipsoids plotted at 40% probability level. Important bond distances: C8 –C16 = 1.468(4), C1–N1 = 1.328(4), C5–N1 = 1.337(4), C6–N2 = 1.349(4), C10–N2 = 1.348(4), C14–N3 = 1.329(4), C15–N3 = 1.342(4) Å. b) View along the 3,2':6',3"-terpyridine, visualizing twists in ferrocenyl group and pyridine ring. Reproduced from ref.[31], published by CSIRO Publishing.

The twist in the pyridine and ferrocenyl group hinders efficient stacking of adjacent molecules in the lattice. Outer pyridine rings of adjacent molecules **11** (rings containing N1 and N3) show some face-to-face π-π interactions (red and blue in Fig. 33) and weak edge-to-face π-π interactions are observed between the inner pyridine ring (green in Fig. 33) and the outer pyridine ring containing N3 (blue in Fig. 33).

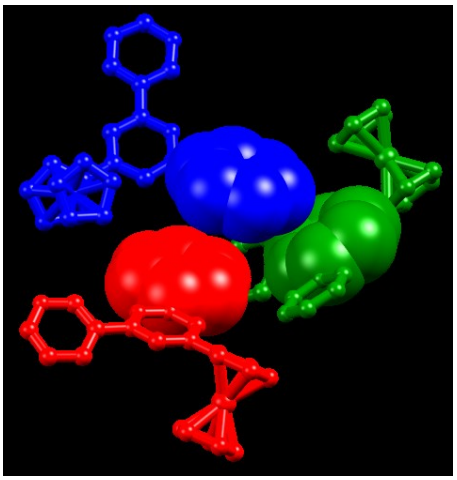

Fig. 33: Face-to-face π-π interactions (red and blue) and weak edge to face π-π interactions (blue and green in Fig. 33).

Additional information can be found in the printed publication (section 18.2).

8 DISCRETE CYCLIC STRUCTURES

Building blocks that favour the formation of mononuclear, dinuclear and cyclic complexes were discussed in chapter 4. Metallocycles were obtained with ligands **10** and **11**. The building blocks leading to these assemblies are summarized in Table 3.

Ligand	**Metal salts and their connectivity**	**Structure motif**
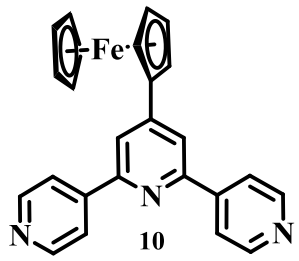 **10**	ZnI_2  (bent two-connecting)	Discrete metallosquare 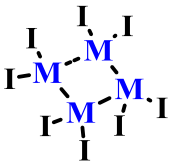
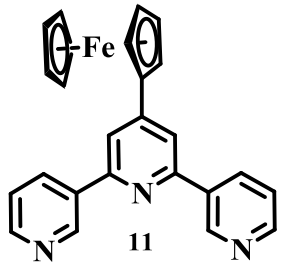 **11**	$ZnCl_2$  (bent two-connecting)	Discrete metallosquare 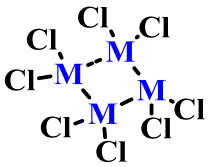
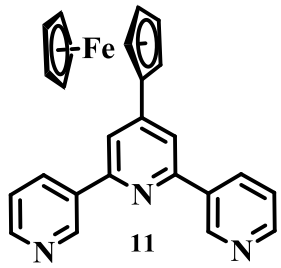 **11**	$CuCl_2$ 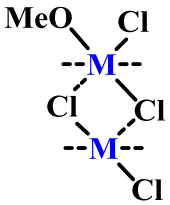 (dinuclear four connectivity)	Discrete double decker 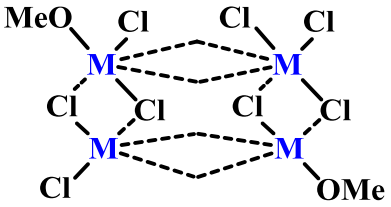

Table 3: Overview of the building blocks for structures discussed in this chapter

8.1 [{ZnI_2(**10**)}$_4$·1.4MeOH·0.8H_2O]

ZnI_2 reacted with the potentially two-donor ligand **10** and formed the discrete metallosquare [{ZnI_2(**10**)}$_4$·1.4MeOH·0.8H_2O] (Fig. 34). In the complex ZnI_2 two-connecting. The structure consists of four ZnI_2 and four ligands **10** and crystallizes in the space group *P*-1, which is centrosymmetric (inversion centre in the centre of the square). The experimental PXRD pattern gave a good match to the pattern predicted from the single crystal data of [{ZnI_2(**10**)}$_4$·1.4MeOH·0.8H_2O].

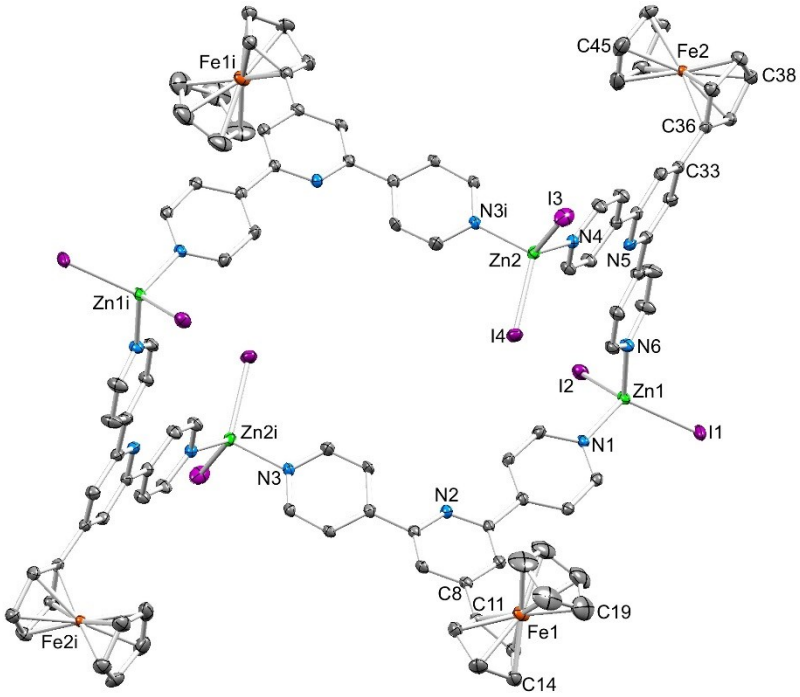

Fig. 34: Structure of the {ZnI_2(**10**)}$_4$ metallosquare in [{ZnI_2(**10**)}$_4$·1.4MeOH·0.8H_2O]; H atoms omitted for clarity and ellipsoids plotted at 40% probability level. Symmetry code i = –*x*, –*y*, –*z*. Selected bond lengths and angles: Zn1–I1 = 2.5318(7), Zn1–I2 = 2.5455(8), Zn1–N1 = 2.043(4), Zn1–N6 = 2.056(4), Zn2–I3 = 2.5456(7), Zn2–I4= 2.5458(7), Zn2–N3i = 2.081(4), Zn2–N4 = 2.039(4) Å; I1–Zn1–I2 = 117.46(3), I3–Zn2–I4 = 115.08(3), N1–Zn1–N6 = 102.00(16), N3–Zn2–N4 = 99.64(15)°. Reproduced from ref.[31], published by CSIRO Publishing.

The pseudo tetrahedral geometry of ligands around the Zn(II) centre in the complex introduces a coordination angle of ~ 100° between the two connection sites. The 4,2':6',4"-terpyridine unit in **10** is almost planar and retains its V-shaped orientation with an angle (N6…centroid of inner pyridine…N4) of ~ 106°. The connection angles of both building blocks and most of all the orientation of the coordinated ligand **10** lead to a square shaped structure. The structure consists of two distinct 4,2':6',4"-terpyridines (containing Fe1 and Fe2 respectively) and two distinct Zn(II) centres (Zn1 and Zn2) displayed in Fig. 34. The 4,2':6',4"-terpyridine units on opposite

sides of the square are inverted to one another, by symmetry. Two π-π interactions between adjacent molecules are present in the structure. Fig. 35a shows the metallosquare viewed along the c-axis with face-to-face π-π interactions between outer pyridine rings (rings containing N1 and N3) of 4,2':6',4''-terpyridines in adjacent molecules. Fig. 35b illustrates the face-to-face π-π interactions between pyridine (rings containing N4 and N5) and ferrocenyl units (ferrocenyl containing Fe2) of the second 4,2':6',4''-terpyridine unit (containing atoms N4, N5; N6 and Fe2) in neighbouring molecules (Fig. 35b). Molecules pack efficiently in the lattice, with few solvent molecules present (omitted in the pictures).

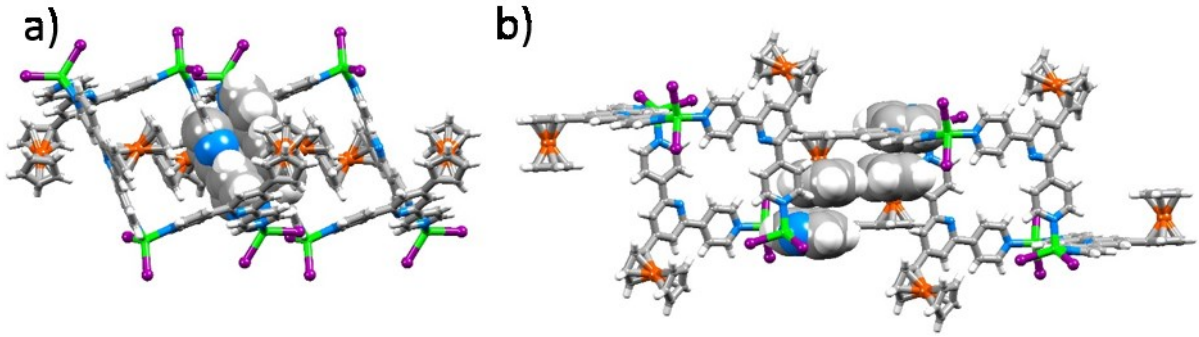

Fig. 35: a) View down the crystallographic *c*-axis with π-stacking between neighbouring $\{ZnI_2(\mathbf{10})\}_4$ molecules. b) Ferrocenyl-pyridine π-stacking interaction. Reproduced from ref.[31], published by CSIRO Publishing.

The second distinct 4,2':6',4''-terpyridine unit (containing N1, N2, N3 and Fe1) shows a twist of the inner pyridine ring in respect to the ferrocenyl group (angle of the planes through the pyridine and cyclopentadienyl rings = 30.67°). The twist in the ferrocenyl unit hinders efficient π-π interactions to neighbouring molecules and these ferrocenyl units (containing Fe2, blue in Fig. 36) and iodine ligands from another adjacent molecule (green in Fig. 36) occupy the space in the squares (space-filling representation).

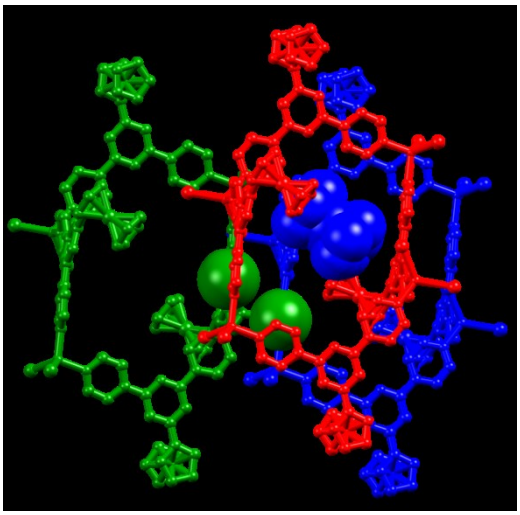

Fig. 36: Three adjacent {ZnI_2(**10**)}$_4$ metallosquares. Ferrocenyl groups (blue) and iodine ligands (green) occupy the space inside the adjacent metallosquare (red), highlighted in space-filling representation.

Additional information can be found in the printed publication (section 18.2).

8.2 [{$ZnCl_2$(**11**)}$_4$·3$CHCl_3$·3MeOH]

A similar combination of a zinc halide ($ZnCl_2$) with a ferrocenyl-substituted 3,2':6',3''-terpyridine also lead to the formation of a discrete metallosquare. The more flexible coordination ability of 3,2':6',3''-terpyridines (see Scheme 9) in respect to 4,2':6',4''-terpyridines allows a different arrangement of the building blocks. Four $ZnCl_2$ units and four ligands **11** form the structure [{$ZnCl_2$(**11**)}$_4$·3$CHCl_3$·3MeOH] (Fig. 37). It crystallizes in the space group *Pccn*.

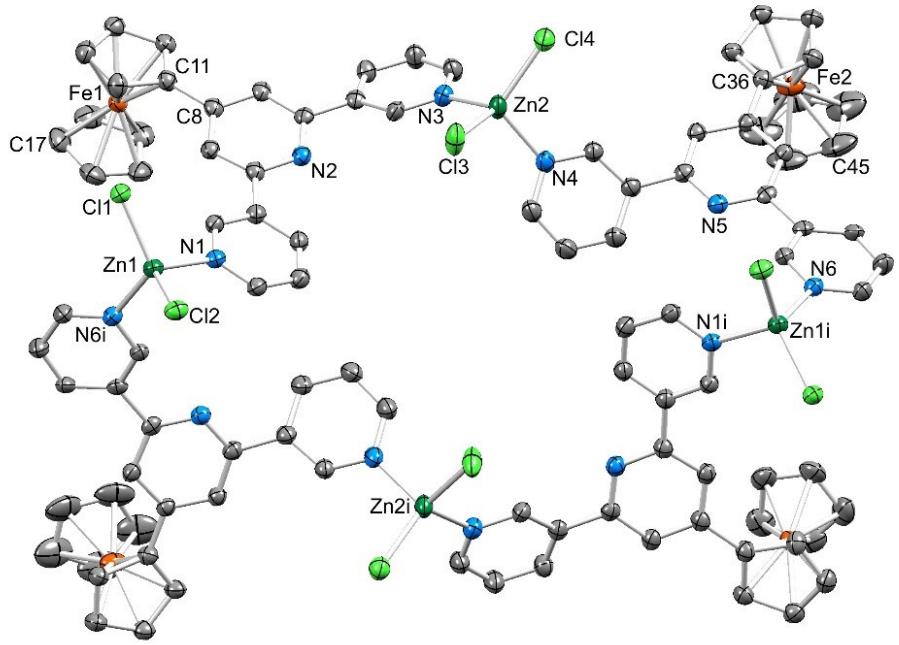

Fig. 37: Structure of the $\{ZnCl_2(\mathbf{11})\}_4$ molecule in $[\{ZnCl_2(\mathbf{11})\}_4 \cdot 3CHCl_3 \cdot 3MeOH]$; H atoms and solvent molecules are omitted and ellipsoids plotted at 30% probability level. Symmetry code i = $^1/_2–x$, $^1/_2–y$, z. Selected bond distances: Zn1–N6^i = 2.063(8), Zn1–Cl1 = 2.202(2), Zn1–Cl2 = 2.235(3), Zn1–N1 = 2.074(8), Zn2–Cl3 = 2.243(3), Zn2–Cl4 = 2.224(3), Zn2–N3 = 2.043(8), Zn2–N4 = 2.038(9) Å. Reproduced from ref.[31], published by CSIRO Publishing.

Ferrocenyl groups in $[\{ZnCl_2(\mathbf{11})\}_4 \cdot 3CHCl_3 \cdot 3MeOH]$ all point in the same direction (in contrast to the up-down-up-down orientation of **10** in the previous section) and the structure can be imagined as a bowl. The Zn(II) centres and 3,2':6',3"-terpyridine cores form the base and ferrocenyl groups represent the rim of the bowl. Adjacent molecules interact via face-to-face π-stacking of pyridine rings (Fig. 38).

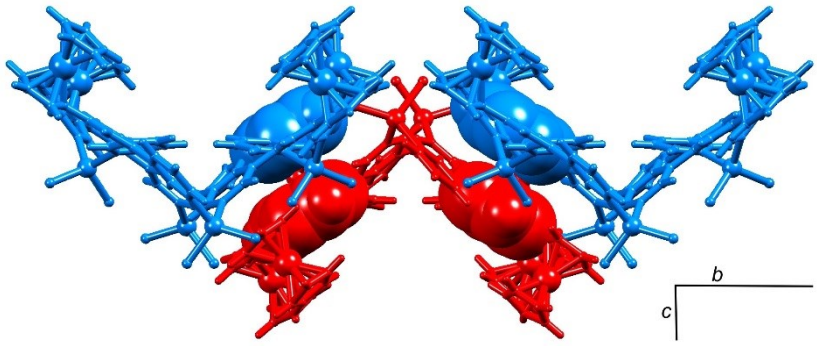

Fig. 38: π-stacking between pyridine rings of adjacent molecules $[\{ZnCl_2(\mathbf{11})\}_4 \cdot 3CHCl_3 \cdot 3MeOH]$, view along the a-axis. Reproduced from ref.[31], published by CSIRO Publishing.

Additional information can be found in the printed publication (section 18.2).

8.3 $[Cu_4Cl_8(\mathbf{11})_4(MeOH)_2]$

An interesting structure was obtained when ligand **11** was combined with $CuCl_2$. Two $CuCl_2$ molecules form a dinuclear four connecting building block. $CuCl_2$ units are bridged via two Cl (μ-Cl) ligand. The outer positions on Cu1 (Fig. 39) is occupied by a Cl^- ligand and Cu1 is five coordinated, with a connectivity of two. The outer positions on Cu2 are coordinated by a Cl^- and a MeOH ligand. Cu2 also shows a weak interaction to Cl4i (symmetry code i = 1−x, 1−y, −z) with a distance of 3.158(2) Å. Cu2 is five coordinate and has a connectivity of two. The connecting sites are opposite to one another on one Cu atom and parallel in respect to the bridged Cu. Ligand **11** is flexible enough to adopt a coordination geometry, where both N-lone pairs point in the same direction (Scheme 14).

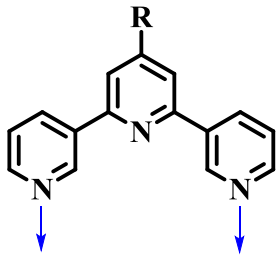

Scheme 14: Orientation of the donor atoms in ligand **11** in the complex $[Cu_4Cl_8(\mathbf{11})_4(MeOH)_2]$.

The combination of these building blocks lead to the double-decker structure $[Cu_4Cl_8(\mathbf{11})_4(MeOH)_2]$ consisting of four Cu ions doubly bridged by ligands **11** in one direction and μ-Cl ligands in a second direction perpendicular to the 4,2':6',4"-terpyridine unit. Two layers, containing two ligands **11** form the two decks of the double-decker motif.

8.3.1 Single crystal data of $[Cu_4Cl_8(11)_4(MeOH)_2]$

The distance between Cu_2Cl_4 dimers is defined by the scope of **11**, more precise the distance (~ 6.9Å) between coordinating N-atoms. The bulk material was analyzed by Dr. Karl Krämer from the University of Bern and revealed, that the bulk material is composed of the same compound as that found in the single crystal.

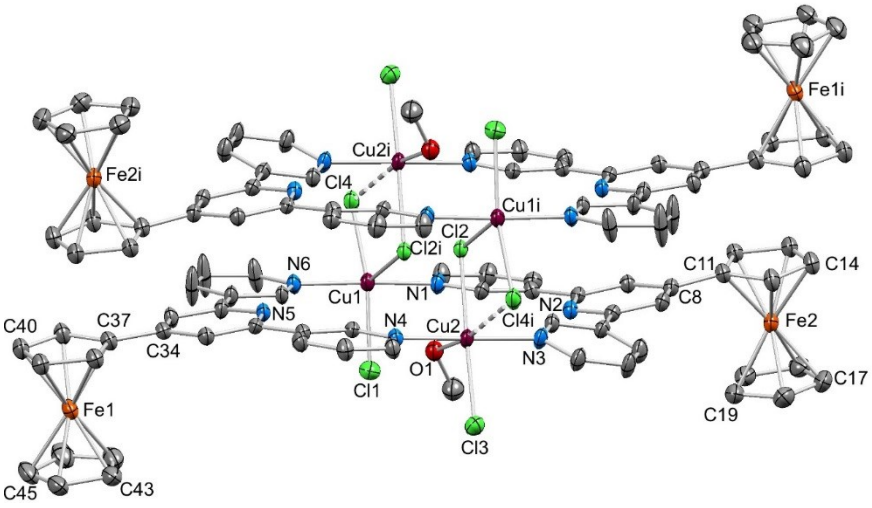

Fig. 39: Structure of the $[Cu_4Cl_8(\mathbf{11})_4(MeOH)_2]$ molecule in $[\{Cu_4Cl_8(\mathbf{11})_4(MeOH)_2\}\cdot 0.7CHCl_3\cdot 1.8MeOH]$. Hydrogen atoms are omitted and ellipsoids are plotted at 30% probability level. Symmetry code $i = 1-x, 1-y, -z$. Selected bond distances and angles: Cu1–Cl1 = 2.269(2), Cu1–Cl4 = 2.3201(19), Cu1–Cl2^i = 2.5459(19), Cu2–Cl2 = 2.3471(17), Cu2–Cl3 = 2.309(2), Cu1–N1 = 2.018(6), Cu1–N6 = 2.007(5), Cu2–N3 = 2.016(5), Cu2–N4 = 2.024(5), Cu2–O1 = 2.287(5) Å; N1–Cu1–N6 = 173.1(3), N3–Cu2–N4 = 174.2(3), Cl2–Cu2–Cl3 = 177.24(8), Cl4^i–Cu1–Cl1 = 157.32(9) Cu1^i–Cl2–Cu2 = 97.03(6)°. Reproduced from ref.[100], published by Elsevier.

The two decks of the double decker are held together by μ-Cl ligands and face-to-face π-π interactions between pyridine rings and ferrocenyl units are present (Fig. 40).

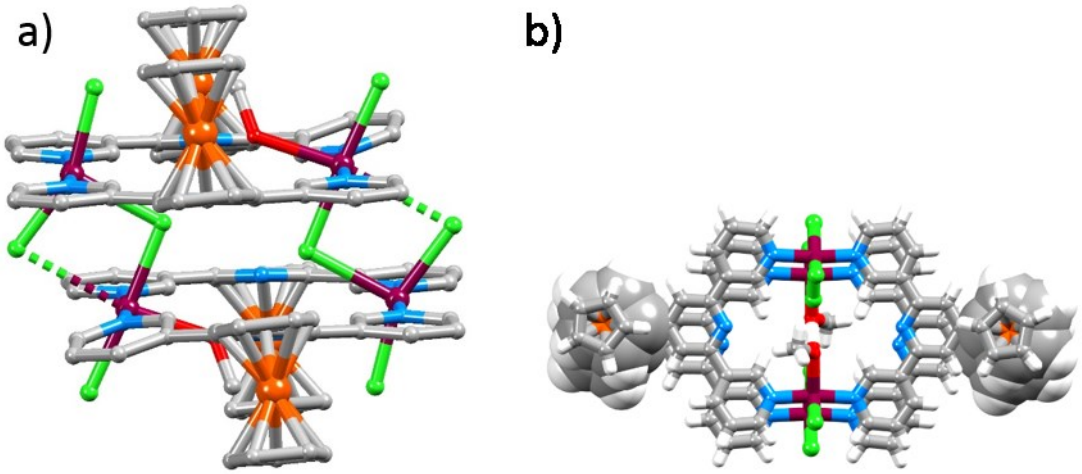

Fig. 40: a) View of the double decker unit $[Cu_4Cl_8(\mathbf{11})_4(MeOH)_2]$ along the N-Cu-N coordination bond. Parallel cp rings in ferrocenyl units are slightly shifted with respect to one another, enabling π-stacking displayed in b). Reproduced from ref.[100], published by Elsevier.

The intermolecular interactions in $[\{Cu_4Cl_8(\mathbf{11})_4(MeOH)_2\}\cdot 0.7CHCl_3\cdot 1.8MeOH]$ are dominated by face-to-face π-stacking of ferrocenyl groups and 4,2':6',4"-terpyridine units of

adjacent molecules. This interaction can be imagined like a locking of the teeth in a zipper (the zipper is represented by the red π-stacking motif in Fig. 41).

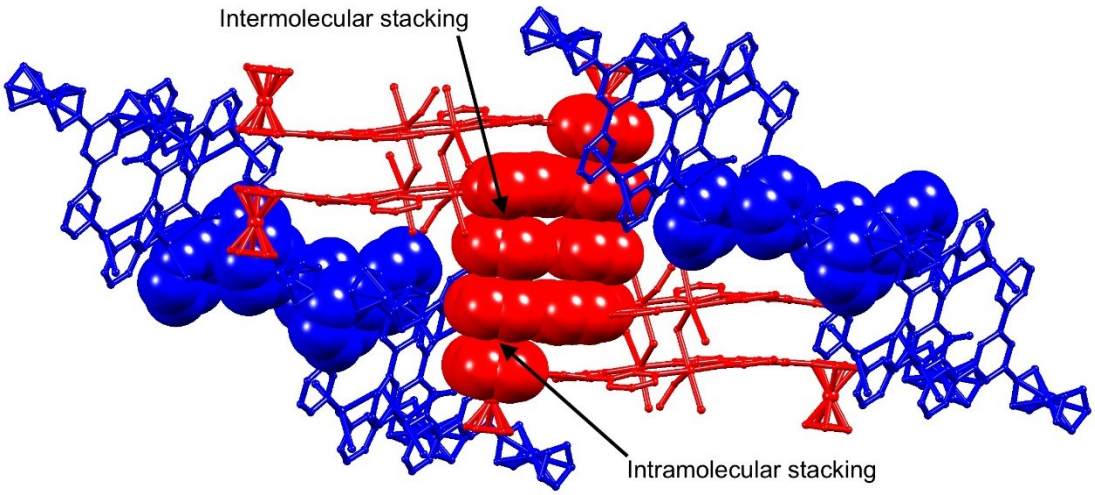

Fig. 41: Inter- and intramolecular π-stacking between ferrocenyl groups and ferrocenyl and pyridine rings of adjacent double-deckers, respectively. Reproduced from ref.[100], published by Elsevier.

8.3.2 Magnetic susceptibility measurements

The close distance (3.668(1) Å, Cl bridged and 6.703(1) Å, ligand **11** bridged) of the copper(II) ions (d^9) could result in magnetic coupling of the spins and the complex was therefore investigated by magnetic susceptibility measurements ($\chi_m T$) in cooperation with the group of Prof. Silvio Decurtins from the University of Bern. It is important to note, that the Cu_2Cl_4 in [{Cu_4Cl_8(**11**)$_4$(MeOH)$_2$}·0.7$CHCl_3$·1.8MeOH] is considered mono-bridged as the Cu2-Cl4i distance is quite large. In the literature, double μ-Cl Cu_2Cl_4 dimers[102-103] and polymers[104-105] are reported, which show magnetic coupling The $\chi_m T$ measurement of [{Cu_4Cl_8(**11**)$_4$(MeOH)$_2$}·0.7$CHCl_3$·1.8MeOH] revealed antiferromagnetic exchange interactions and weak coupling between Cu(II) ions, through the mono bridging Cl ligands at temperatures below 50 K. The results are comparable to values obtained for double μ-Cl Cu(II) compounds in the literature[105] and coupling between Cu(II) ions via the bridging ligands **11** could not be confirmed. Fig. 42 shows the plot of $\chi_m T$ vs. T illustrating the antiferromagnetic exchange interactions caused by the μ-Cl ligand.

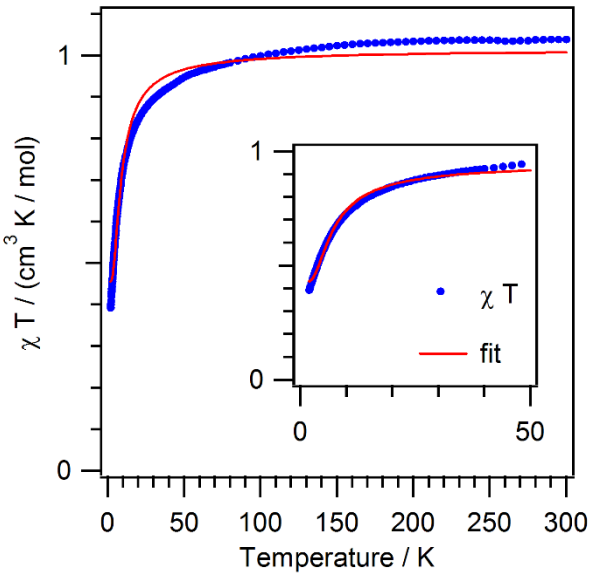

Fig. 42: $\chi_m T$ vs. T graph for [{Cu_4Cl_8(**11**)$_4$(MeOH)$_2$}·0.7$CHCl_3$·1.8MeOH] (per two Cu(II) ions). The inset highlights the 50 to 1.9 K region. Solid lines represent fitted curves. Reproduced from ref.[100], published by Elsevier.

8.3.3 Electrochemistry

Cyclic voltammograms (CV) of complex [{Cu_4Cl_8(**11**)$_4$(MeOH)$_2$}·0.7$CHCl_3$·1.8MeOH] and ligand **11** were measured in propylene carbonate containing [^{n}Bu$_4$N][PF_6] as the electrolyte. It was not clear if the complex dissolved in propylene carbonate or decomposed because only free ligand **11** appeared to be present in the solution. The comparison of the CV from the dissolved complex and free ligand **11** revealed the same electrochemical behaviour (Fig. 43). Both compounds show a reversible oxidation at +0.12 V (referenced to external Fc/Fc^+) and a reversible reduction at -2.44 V, presumably based on the ferrocenyl-functionalized 3,2':6',3''-terpyridine.

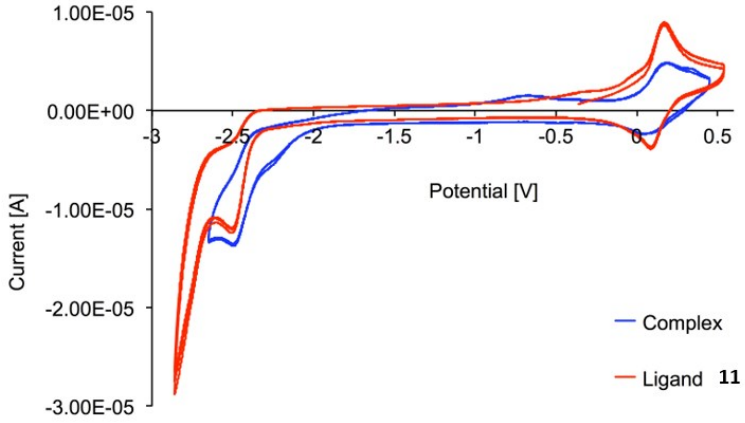

Fig. 43: CVs of complex [{Cu_4Cl_8(**11**)$_4$(MeOH)$_2$}·0.7$CHCl_3$·1.8MeOH] and ligand **11**. Reproduced from ref.[100], published by Elsevier.

8.3.4 Quasi-solid-state electrochemistry

Another attempt was made to measure the CV of [{Cu_4Cl_8(**11**)$_4$(MeOH)$_2$}·0.7$CHCl_3$·1.8MeOH] using a quasi-solid-state setup in collaboration with Dr. Angelo Lanzilotto and Prof. Dr. Edwin C. Constable. The complex was ground and added as a suspension (in propylene carbonate with [^{n}Bu$_4$N][PF_6]) between two FTO-glass plates (resembling the architecture of a dye-sensitized solar cell). One FTO glass plate was coated with Pt and the CV of the complex in this quasi-solid-state configuration was measured in five consecutive cycles (Fig. 44). The CV showed a reversible (presumably iron centred) oxidation at +0.01 V, which was assigned to [{Cu_4Cl_8(**11**)$_4$(MeOH)$_2$}·0.7$CHCl_3$·1.8MeOH].

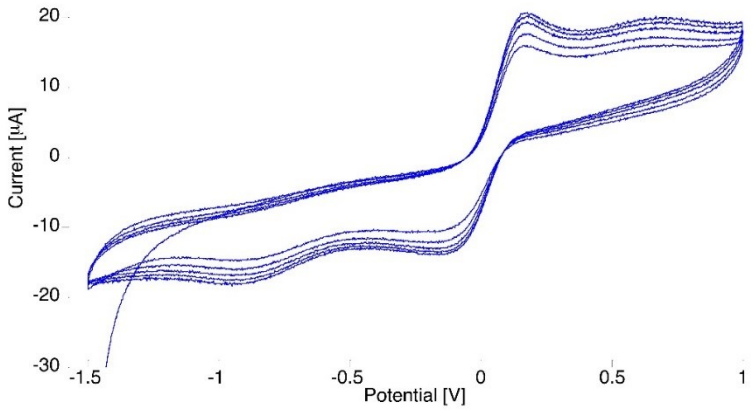

Fig. 44: Quasi-solid-state CV of a suspension of [{Cu_4Cl_8(**11**)$_4$(MeOH)$_2$}·0.7$CHCl_3$·1.8MeOH] in propylene carbonate (with addition of [^{n}Bu$_4$N][PF_6]) measured between an FTO- and a FTO-Pt-glass electrode. Reproduced from ref.[100], published by Elsevier.

8.3.5 Spectroelectrochemistry of ligand 11

The spectroelectrochemical measurements (done by Dr. Angelo Lanzilotto) of **11** were obtained by increasing the voltage of a propylene carbonate solution containing [$^{n}Bu_4N$][PF_6] and **11** from 0.1 V to 1.5 V and back to 0 V. An absorption spectrum of the solution was measured every 0.1 V step and the 2D-plot is displayed in Fig. 45.

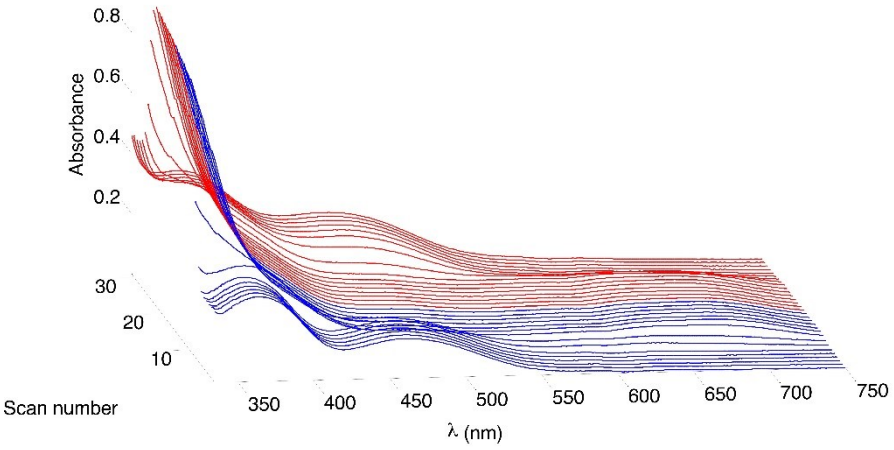

Fig. 45: Spectroelectrochemistry measurement of [{Cu_4Cl_8(**11**)$_4$(MeOH)$_2$}·0.7$CHCl_3$·1.8MeOH] with a voltage screening between 0 V and 1.5 V. UV-VIS absorption spectra were collected every 0.1 V steps. Reproduced from ref.[100], published by Elsevier.

The data in Fig. 45 should be viewed starting at scan number 0 (= 0.1 V). At this potential, **11** is not oxidized and the orange colour, corresponding to the ferrocenyl group is present. The absorption spectrum shows a λ_{max} = 461 nm. By increasing the potential (up to scan number 10) the oxidation of the ferrocenyl takes place and the absorption band at 461 nm disappears. A new broad band at ~ 660 nm appears, which corresponds to a ferrocenium ion (Fc^+). The process is reversible and the absorption of **11** at scan number 0 and 30 is the same.

Additional information can be found in the printed publication (section 18.3).

8.4 Comparison of structural motifs

This chapter has so far illustrated the formation of discrete multinuclear and cyclic structures using ligands with two donor atoms and two-connecting metal building blocks. One similarity is noticeable straight away, the presence of the ferrocenyl group in all ligands presented here.

The ferrocenyl group in ligands **10** and **11** seems to favour the formation of the discrete structures over the formation of 1D polymer chains, that are more frequent obtained with other monotopic 3,2':6',3"-terpyridines and 4,2':6',4"-terpyridines. The ferrocenyl group introduces bulkiness and steric demand compared to e.g. phenylene groups presented in the next chapter. The ferrocenyl group also exhibits strong π-interactions with pyridine rings of adjacent ligands in the structures. The combination of bulkiness and π-stacking leads to different intermolecular interactions compared to 1D coordination polymers and favours the formation of discrete cyclic structures in the cases presented in this chapter. This phenomenon has been observed in other studies and discrete metallohexacycles were obtained when zinc halides were combined with ligand **10**[106] or with other bulkier, aromatic ligands (**L5**, **L8** Scheme 7)[66]. It is noteworthy that Xiao and coworkers used ligand **10** and ZnI_2 in the same manner as it was presented in this chapter, but they obtained a 1D coordination polymer instead of a discrete metallosquare. The formation of non-polymeric complexes[66, 85, 106] and 1D coordination chains[56, 106] using Zn(II) halides and ditopic 3,2':6',3"-terpyridines and 4,2':6',4"-terpyridines has been reported in the literature. The structures we obtained with the combination of these ligands and Zinc(II) halides are presented in this chapter and the following one and confirm, that a prediction, if a metallosquare or 1D chains forms is not possible in this case.

9 1D COORDINATION CHAINS

The building blocks discussed in the last chapter lead to the formation of metallosquares. This chapter illustrates, that similar building blocks can also lead to the formation of 1D structures. An overview of the building blocks and structures discussed in this chapter is displayed in Table 4.

Ligands	**Metal salts and their connectivity**	**Structure motif**
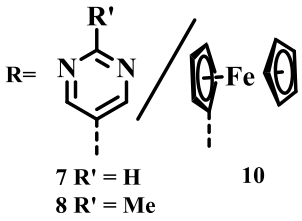 7 R' = H 8 R' = Me 10 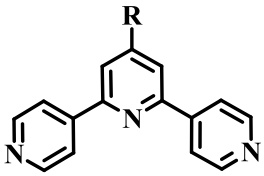 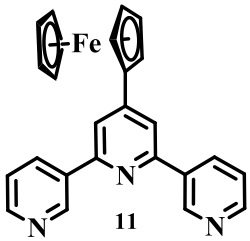 11	$ZnCl_2$, ZnI_2, $ZnBr_2$, $Zn(OAc)_2$  (bent two-connecting)	Alternating 1D polymer chain 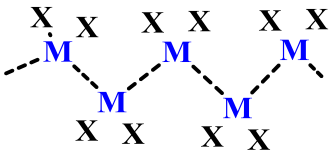
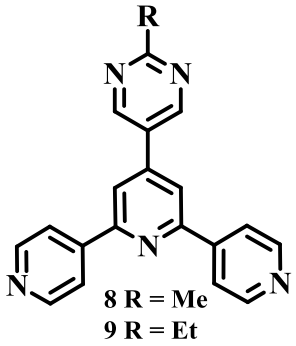 8 R = Me 9 R = Et	$Co(NCS)_2(MeOH)_2$ / $Cu_2(OAc)_4$ 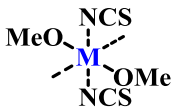  (linear two-connecting)	Linear 1D polymer chain 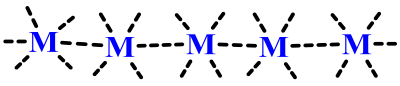

Table 4: Overview of ligands, metal salts and structure motifs discussed in this chapter.

9.1 $[ZnCl_2(\mathbf{7})]_n$ and $[ZnI_2(\mathbf{8})\cdot MeOH]_n$

The structures presented in this section were obtained during my master studies, but their structural motifs nicely complement the series of structures presented in this chapter.

The reaction of the zinc halides $ZnCl_2$ and ZnI_2 with ligands **7** and **8** lead to the formation of 1D coordination polymers. Ligands **7** and **8** only differ in their substituent on the pyrimidine ring, **7** bears a hydrogen and **8** a methyl group (see Scheme 7 and Table 4).

Structures $[ZnCl_2(\mathbf{7})]_n$ and $[ZnI_2(\mathbf{8})\cdot MeOH]_n$ both crystallize in the space group $P2_1/n$, are similar and will be discussed together. Their repeat units are displayed in Fig. 46 and Fig. 47. Both ligands coordinate to the ZnX_2 unit via the outer pyridine rings. The inner pyridine ring and the pyrimidine N-atoms are not coordinated. Both ligands are almost planar in the structures and $[ZnI_2(\mathbf{8})\cdot MeOH]_n$ also has one MeOH molecule in the asymmetric unit, that forms a hydrogen-bond to pyrimidine N5 (OH…N5 distance = 2.026 Å).

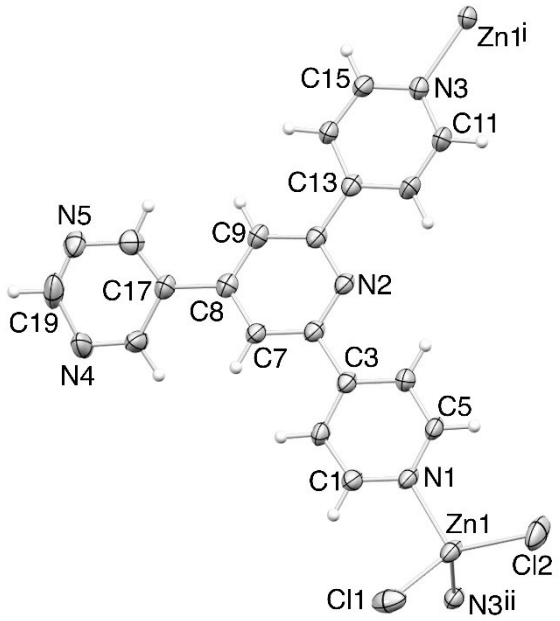

Fig. 46: Repeat unit in $[ZnCl_2(\mathbf{7})]_n$; symmetry codes: i = $^1/_2-x$, $-^1/_2+y$, $^3/_2-z$; ii = $^1/_2-x$, $^1/_2+y$, $^3/_2-z$) and ellipsoids plotted at the 40% probability level. Selected bond parameters: Zn1–N1 = 2.046(3), Zn1–N3^{ii} = 2.054(4), Zn1–Cl2 = 2.1996(15), Zn1–Cl1 = 2.2384(17) Å; N1–Zn1–N3^{ii} = 107.15(15), N1–Zn1–Cl2 = 111.25(12), N3^{ii}–Zn1–Cl2 = 110.22(11), N1–Zn1–Cl1 = 103.37(12), N3^{ii}–Zn1–Cl1 = 101.46(12), Cl2–Zn1–Cl1 = 122.15(8)°. Reproduced from ref.[101], published by Elsevier.

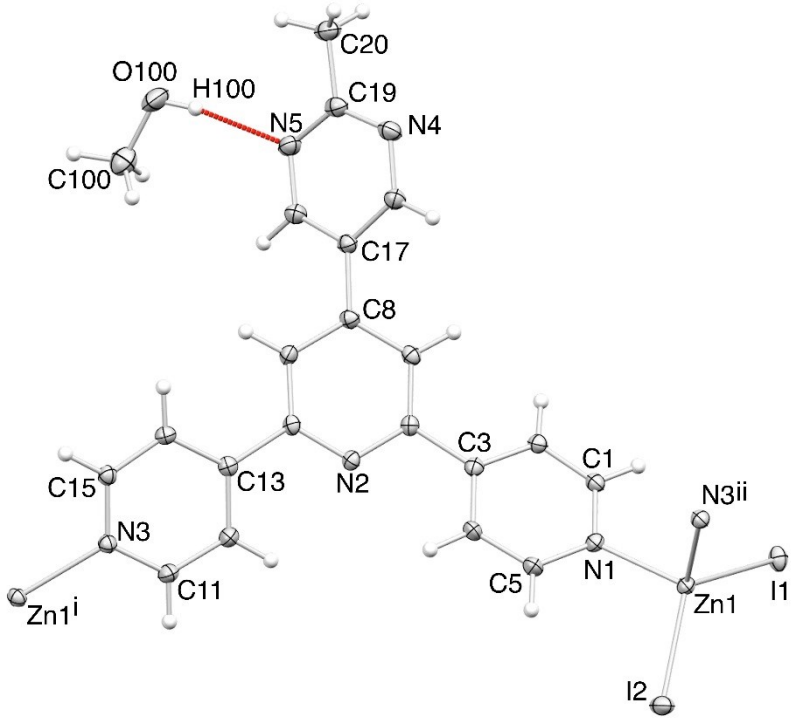

Fig. 47: Repeat unit in $[ZnI_2(\mathbf{8})\cdot MeOH]_n$; symmetry codes: i = $-^1/_2+x$, $^1/_2-y$, $-^1/_2+z$; ii = $^1/_2+x$, $^1/_2-y$, $^1/_2+z$, ellipsoids plotted at the 40% probability level. Reproduced from ref.[101], published by Elsevier.

The structures differ in the propagation of their chains. In $[ZnCl_2(\mathbf{7})]_n$ the pyrimidine units point in opposite directions (up-down-up-down, Fig. 48b) when viewed along the zinc atoms in the chain. This leads to a helical structure (the pitch of the helix is 19.194 Å) and the crystal contains 1D coordination polymers of opposite chirality. The orientation of the ligands leads to a twist in the pyridine rings coordinating to Zn with a torsion angle of 30.53° (highlighted by the yellow selected atoms in Fig. 48b).

In $[ZnI_2(\mathbf{8})\cdot MeOH]_n$ the methylpyrimidine rings point in the same direction (up-up-up, Fig. 48a) and the coordinating pyridine rings are not twisted with respect to each other (torsion angle is ~ 0°, yellow selected atoms in Fig. 48a). The chains in this structure are not chiral and Zn1 centres (measured from Zn1 to Zn1 after the next one) are separated by 18.649 Å, which is comparable to the pitch in $[ZnCl_2(\mathbf{7})]_n$. The differences in chain propagation are displayed in Fig. 48 and the reason for different motifs relies on the orientations of the ligands.

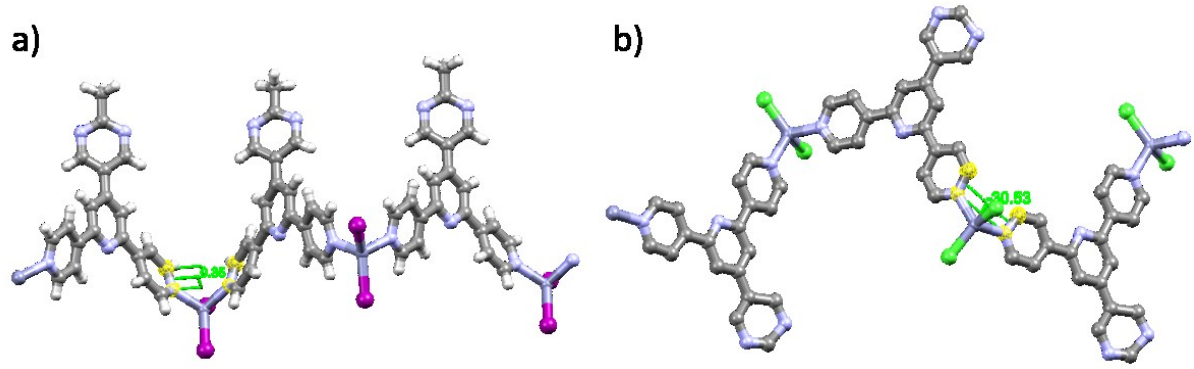

Fig. 48: a) 1D polymer chains of $[ZnI_2(\mathbf{8})]_n$ highlighting the torsion angle between coordinating pyridine rings (yellow selected atoms) and the up-up-up orientation of the methylpyrimidine rings. b) 1D polymer chain of $[ZnCl_2(\mathbf{7})]_n$ with a torsion angle of 30.53° (yellow selected atoms) and the up-down-up orientation of the pyrimidine rings.

The packing in both structures is comparable and dominated by double face-to-face π-π interactions between pyridine rings. In $[ZnCl_2(\mathbf{7})]_n$ (Fig. 49) rings containing N1 and N2 (blue) stack with rings containing N1 and N2 (red) of one adjacent chain. The inner pyridine ring has another π-π interactions to the pyridine ring, containing N3, of the next adjacent chain. $[ZnI_2(\mathbf{8})]_n$ (Fig. 50) shows a similar double face-to-face π-π motif. The chirality of $[ZnCl_2(\mathbf{7})]_n$ is visualized by the colours red and blue in Fig. 49. When a red chain is viewed from the right side of the figure a right-handed helix is observed and for a blue polymer a left-handed helix is observed. The structure is a racemate (non-chiral space group) and contains helices of both handiness.

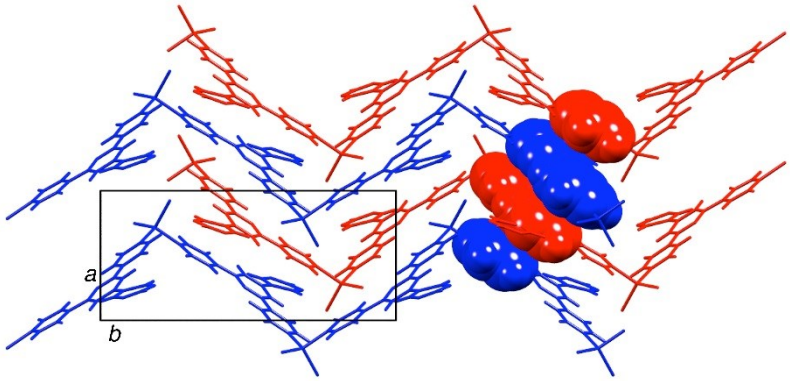

Fig. 49: Face-to-face π-stacking interactions in $[ZnCl_2(\mathbf{7})]_n$ involve all pyridine rings. Pyrimidine rings are not part of the π-stacking interactions. Red and blue chains represent helices of opposite chirality. Reproduced from ref.[101], published by Elsevier.

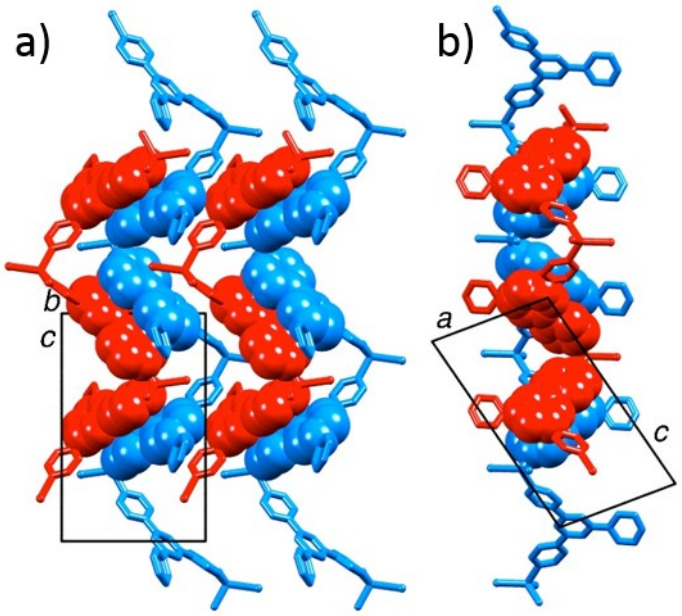

Fig. 50: a) π-stacking interactions between adjacent chains in $[ZnI_2(\mathbf{8})]_n$, view along the a-axis. b) π-stacking interactions viewed along the b-axis. Methylpyrimidine rings are not participating in the π-stacking. Reproduced from ref.[101], published by Elsevier.

Additional information can be found in the printed publication (section 18.1).

9.2 $[\{Zn(OAc)_2(\mathbf{10})\}\cdot MeOH\cdot H_2O]_n$

$Zn(OAc)_2$ was used with ligand **10** to form a linear (in respect to the metal atoms) 1D coordination chain (Fig. 51). $[\{Zn(OAc)_2(\mathbf{10})\}\cdot MeOH\cdot H_2O]_n$ crystallizes in the space group *Pbca*. $Zn(OAc)_2$ building blocks are known to form $Zn_2(OAc)_4$ paddlewheel dimers, where two zinc atoms are bridged by four acetate groups. In fact, this is the most common arrangement of this building block in coordination polymers as demonstrated in previous studies[30, 73, 76, 107]. In the structure discussed in this section the $Zn(OAc)_2$ unit does not form a dinuclear paddlewheel but acts as a two-connecting centre, similar to zinc halides. Why this (for zinc acetate) unusual motif is obtained in this structure is unclear.

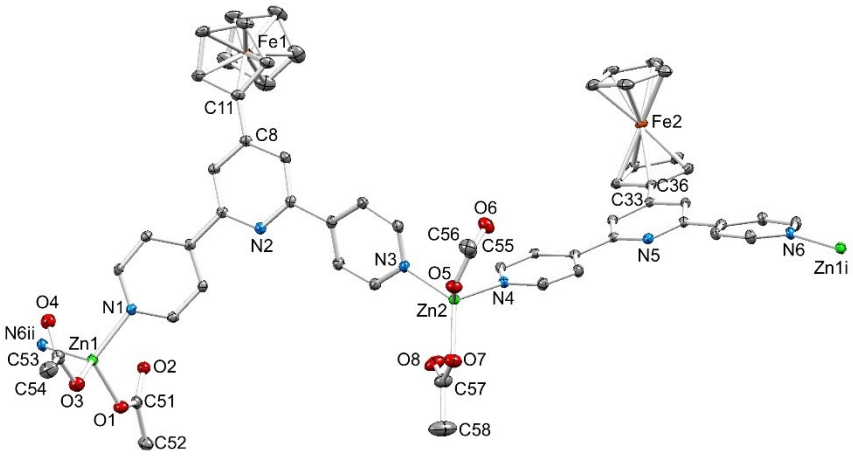

Fig. 51: Structure of the repeat unit in [{Zn(OAc)$_2$(**10**)}·MeOH·H$_2$O]$_n$ with symmetry-generated atoms; H atoms and solvent molecules are omitted and ellipsoids plotted at 30% probability level. Symmetry code i = –1+*x*, *y*, *z*, ii = 1+*x*, *y*, *z*. Selected bond distances: Zn1–N6^{ii} = 2.033(2), Zn1–N1 = 2.030(2), Zn1–O1 = 1.9403(19), Zn1–O3 = 1.955(2), Zn2–N3 = 2.036(2), Zn2–N4 = 2.028(2), Zn2–O5 = 1.936(2), Zn2–O7 = 1.947(2) Å. Reproduced from ref.[31], published by CSIRO Publishing.

The chain propagates slightly differently to the other zinc halide structures in the previous sections. All zinc atoms are in line (with respect to one another), and ligands adopt a left-right-left orientation relative to this line (Fig. 52a). Zn1 centres within one chains are separated by 24.342 Å. Intermolecular face-to-face π-stacking between ferrocenyl groups and pyridine rings (rings containing N1 and N4) are the dominating forces in the crystal packing. Pyridine rings containing N3 and N6 are not participating in the π-stacking, as acetate ligands block these sites (space-filling representation in Fig. 52b).

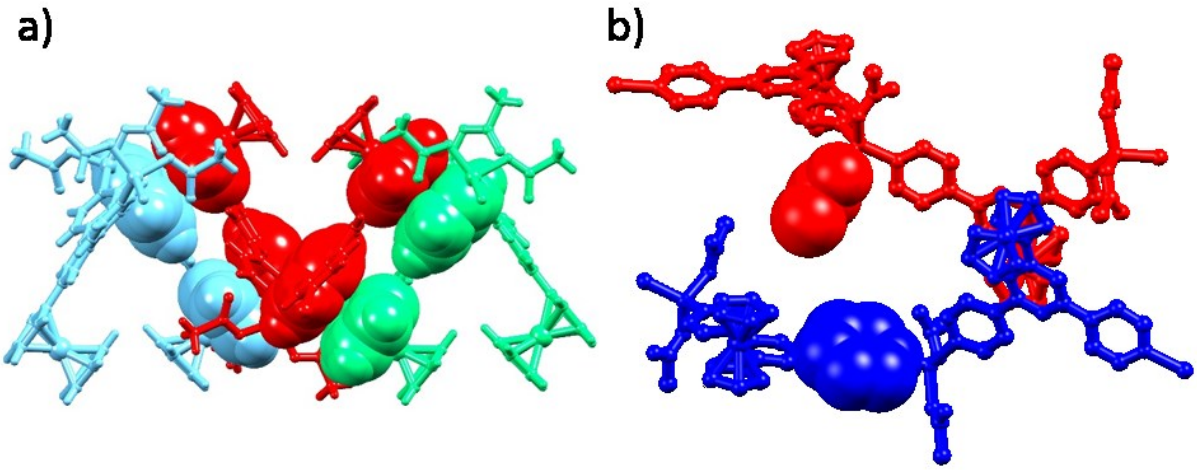

Fig. 52: a) The space filling representation illustrates π-stacking interactions of ferrocenyl and pyridine rings in three adjacent chains in [{Zn(OAc)$_2$(**10**)}·MeOH·H$_2$O]$_n$. b) Acetate ligands (red, highlighted in space-filling) occupy the space close to pyridine rings containing N3 and N6 and prevent π-stacking. Reproduced from ref.[31], published by CSIRO Publishing.

Additional information can be found in the printed publication (section 18.2).

9.3 $[\{ZnBr_2(\mathbf{11})\}\cdot MeOH]_n$

Another unusual structure was obtained with the ferrocenyl substituted ligand **11** and $ZnBr_2$. Ligand **11** is the only 3,2':6',3''-terpyridine ligand in this series of 1D coordination chains, and forces a change in chain propagation, compared to the structures in the previous sections. $[\{ZnBr_2(\mathbf{11})\}\cdot MeOH]_n$ crystallizes in the space group *P*-1 and the structure is displayed in Fig. 53.

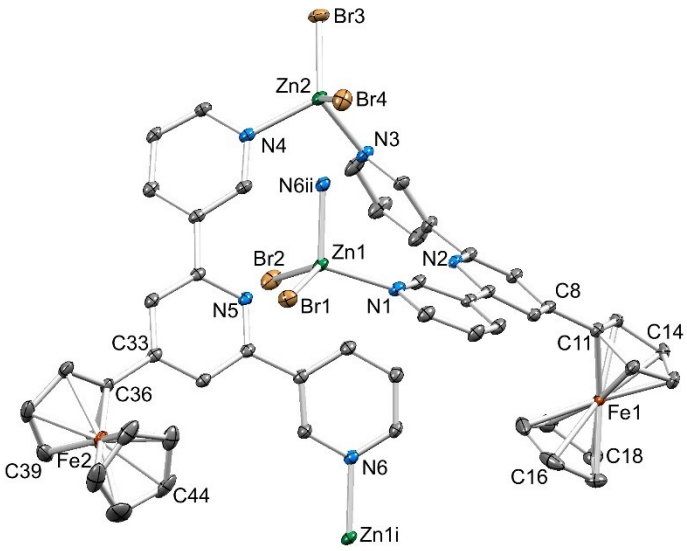

Fig. 53: Structure of the repeat unit in $[\{ZnBr_2(\mathbf{11})\}\cdot MeOH]_n$ with symmetry-generated atoms; ellipsoids are plotted at 30% probability level, and H atoms and solvent molecules are omitted. Symmetry code i = 1–*x*, *y*, *z*, ii = –1+*x*, *y*, *z*. Selected bond distances: Zn1–N6^{ii} = 2.038(3), Zn1–Br1 = 2.3504(6), Zn1–Br2 = 2.3587(6), Zn1–N1 = 2.041(3), Zn2–Br3 = 2.3515(6), Zn2–Br4 = 2.3455(6), Zn2–N3 = 2.050(3), Zn2–N4 = 2.059(3) Å. Reproduced from ref.[31], published by CSIRO Publishing.

The 1D coordination chain is helical and the flexibility in the 3,2':6',3''-terpyridine coordination allows that ligands within the same chain come close to one another. The result is intramolecular face-to-face π-stacking, which is observed for the first time in this series of 1D structures (Fig. 54). The intramolecular π-stacking is present in every second ligand **11** within one polymer chain, between the ferrocenyl group and pyridine rings (containing N1 and N2). The pitch of the helix (from Zn1 to Zn1 centre) is 8.788 Å.

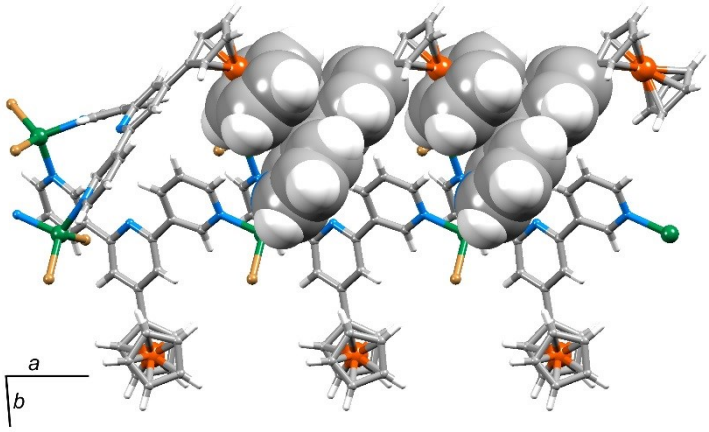

Fig. 54: View of a helical chain in [{$ZnBr_2$(**11**)}·MeOH]$_n$ (solvent molecules are omitted) along the c-axis. The chain propagates along the *a*-axis. Intramolecular face-to-face π-stacking interactions are shown in space-filling representation. Reproduced from ref.[31], published by CSIRO Publishing.

Weak face-to-face π-stacking of outer pyridine rings (containing N1) of adjacent chains (red and blue in Fig. 55) and edge-to-face π-stacking of ferrocenyl groups are the intermolecular interactions in this structure. The chain propagation and pitch of the helix is strongly influenced by the orientation of the donor atoms on **11**. It is noteworthy, that the helix in [{$ZnBr_2$(**11**)}·MeOH]$_n$ is a lot more interwoven compared to the helix [{$ZnCl_2$(**7**)}$_n$] from section 9.1, clearly represented by the differences in the helical pitch (19.194 Å in [{$ZnCl_2$(**7**)}$_n$] compared to 8.788 Å in [{$ZnBr_2$(**11**)}·MeOH]$_n$)

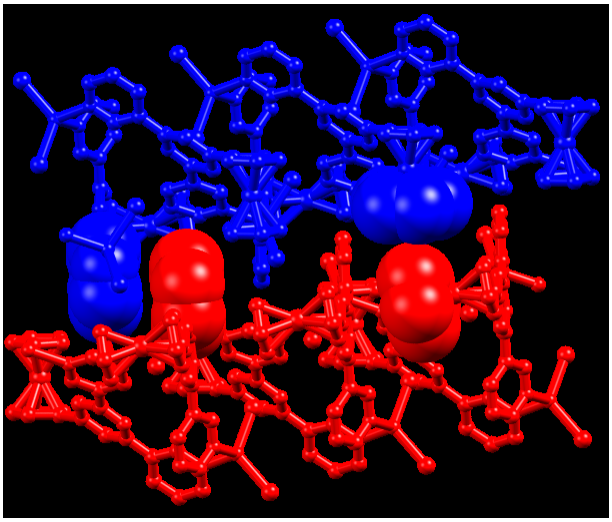

Fig. 55: Face-to-face π- π interactions between adjacent chains (red and blue) and edge-to-face π-stacking between ferrocenyl units.

Additional information can be found in the printed publication (section 18.2).

9.4 $[\{Co_2(NCS)_4(MeOH)_4(\mathbf{8})_2\}\cdot 2MeOH\cdot 8H_2O]_n$

Ligand **8** was combined with $Co(NCS)_2$, which lead to the formation of the 1D polymer chain $[\{Co_2(NCS)_4(MeOH)_4(\mathbf{8})_2\}\cdot 2MeOH\cdot 8H_2O]_n$. The space group is *P*-1 and the ligand is the same as in $[\{ZnI_2(\mathbf{8})\cdot MeOH\}_n]$ (section 9.1). The main difference in chain propagation arises from the linear building block $Co(NCS)_2(MeOH)_2$, which has a connectivity of two in the structure. Co is six coordinate and has a connectivity of four in all structures presented in the following chapters. Among the series of structures presented in this thesis this is the only one, where only two (instead of four) sites in a $Co(NCS)_2$ unit are coordinated by N-donors from 4,2':6',4''-terpyridine units. In $[\{Co_2(NCS)_4(MeOH)_4(\mathbf{8})_2\}\cdot 2MeOH\cdot 8H_2O]_n$ two coordination sites are occupied by coordinating methanol molecules (Fig. 56) which block propagation of anything of dimensionality higher than one. The distance of Co(II) centres (from Co1 to Co1) is 26.350 Å.

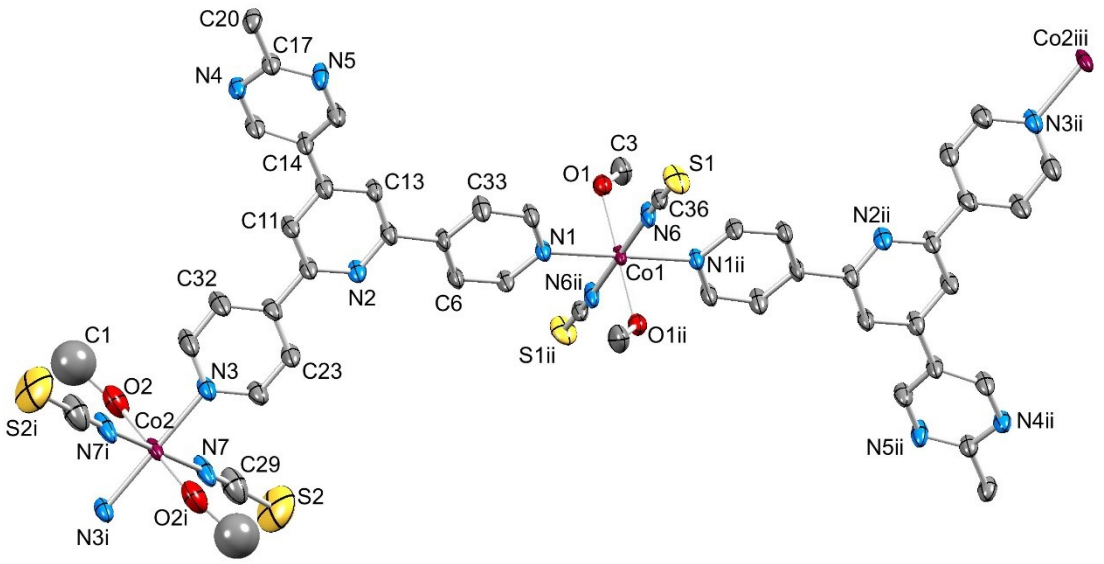

Fig. 56: Structure of the repeat unit in $[\{Co_2(NCS)_4(MeOH)_4(\mathbf{8})_2\}\cdot 2MeOH\cdot 8H_2O]_n$ with symmetry generated atoms; H atoms and solvent molecules are omitted. Ellipsoids are plotted at 40% probability; atom C1 was refined isotropically. Symmetry codes: i = 1–*x*, 2–*y*, 1–*z*; ii = 1–*x*, –*y*, 2–*z*; iii = *x*, –2+*y*, 1+*z*. Selected bond parameters: Co1–N1 = 2.189(6), Co1–N6 = 2.095(7), Co1–O1 = 2.098(6), Co2–N3 = 2.154(6), Co2–N7 = 2.069(7), Co2–O2 = 2.077(9) Å; N1–Co1–N6 = 88.8(2), N1–Co1–O1 = 86.5(2), N3–Co2–N7 = 90.1(2), N3–Co2–O2 = 91.8(3), N7–Co2–O2 = 90.9(4)°. Reproduced from ref.[32], published by MDPI.

The chain propagates in an up-down-up-down orientation of the ligands (illustrated in Fig. 57a), coordinating to the linear two connecting Co(II) centre. There is almost no twist (~ 5°) in the torsion angle between coordinated pyridine rings and the 4,2':6',4''-terpyridine is almost planar.

All Co(II) centres are in line when viewed along the chain (Fig. 57b) and the structure can be described as a zig-zag polymer chain.

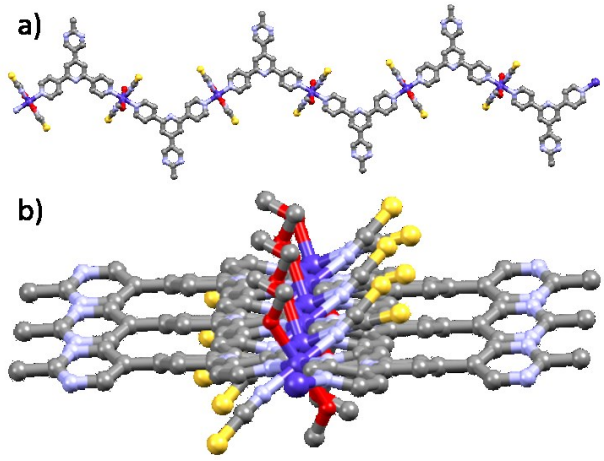

Fig. 57: a) The zig-zag chain motif obtained from the up-down-up-down orientation of ligands **8**. b) View along the chain, highlighting, the almost planar orientation of the ligands and the Co(II) centres stringed together in line.

Chains interact with the chains above (red in Fig. 58) via face-to-face π-π interactions of pyrimidine and pyridine (containing N1) rings (Fig. 58). This π-stacking motif is present in every second ligand **8** within one chain. The other ligands **8** (blue in Fig. 58) interact in the same manner with the next chain underneath, what leads to a staircase-like face-to-face π-stacking motif through the lattice.

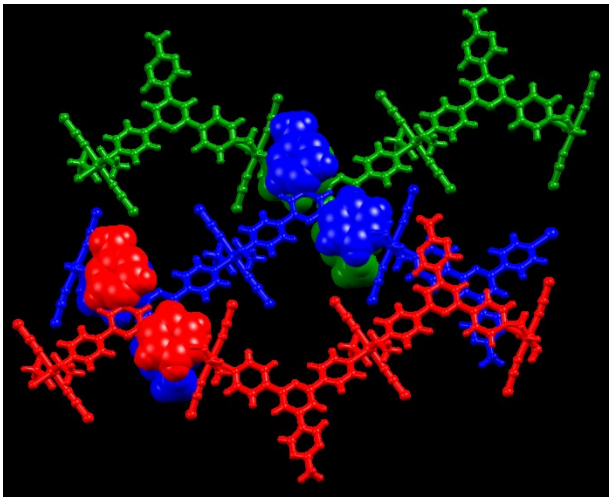

Fig. 58: Two adjacent zig-zag chains of $[\{Co_2(NCS)_4(MeOH)_4(\mathbf{8})_2\}\cdot 2MeOH\cdot 8H_2O]_n$, interacting via face-to-face π-stacking of pyridine (containing N1) and pyrimidine rings.

Chains within the same layer show CH…S interactions (2.817 Å) between the proton on C11/C13 and the S atom of the NCS^- ligand. The methyl group on the pyrimidine ring points towards the V-shaped cavity of the 4,2':6',4"-terpyridine of the neighbouring chain. The space in the cavity is limited and the pyrimidine ring is slightly twisted with respect to the 4,2':6',4"-terpyridine. The pyrimidine ring slips over the inner pyridine ring (Fig. 59) of the neighbouring 4,2':6',4"-terpyridine, which enables closer interchain distance (N…N distance of inner pyridine rings is 10.720(8) Å).

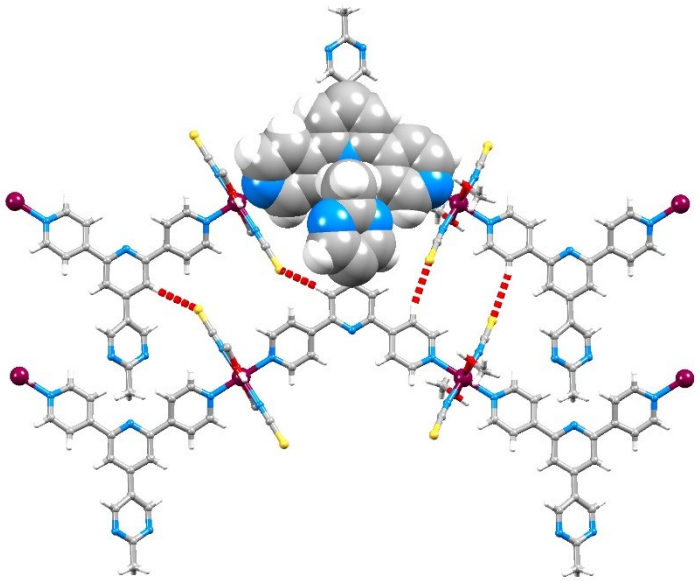

Fig. 59: Interactions of chains within one layer, with CH…S contacts and the slipping of pyrimidine rings over the 4,2':6',4"-terpyridine of the neighbouring chain. Reproduced from ref.[32], published by MDPI.

A zig-zag chain motif is very frequently obtained, when two donor 4,2':6',4"-terpyridine ligands are combined with linear two-connecting metal building blocks, like $Co(NCS)_2(MeOH)_2$, $Zn_2(OAc)_4$[30] and $Cu_2(OAc)_4$[99]. Another example of this motif is presented in the next section.

Additional information can be found in the printed publication (section 18.4).

9.5 $[Cu_2(OAc)_4(\mathbf{9})]_n$

Ligand **9** reacted with $Cu(OAc)_2$ to yield a 1D zig-zag chain, similar to the one discussed in the last section. Two $Cu(OAc)_2$ units dimerize and from a two-connecting $Cu_2(OAc)_4$ building block. $[Cu_2(OAc)_4(\mathbf{9})]_n$ crystallizes in the space group $C2/c$ (Fig. 60). The asymmetric unit contains half a ligand and half a metal building block. The second half of the ligand is generated by a 2-fold rotation axis defined by the symmetry of the space group. The ethylpyrimidine group is slightly twisted (torsion angle C7-C8-C9-C10 = 34.67°) with respect to the inner pyridine ring.

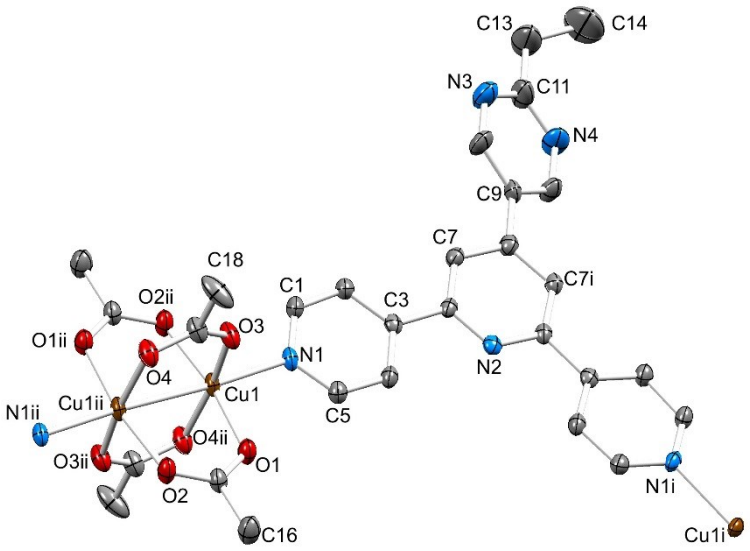

Fig. 60: Structure of the repeat unit (with symmetry generated Cu1i and N1ii atoms) in $[Cu_2(OAc)_4(\mathbf{9})]_n$ (ellipsoids plotted at 40% probability level and H atoms omitted); the ring containing N3 and N4 is disordered. Symmetry codes: i = 1–x, y, $^3/_2$–z; ii = $^3/_2$–x, $^3/_2$–y, 1–z. Selected bond parameters: Cu1–N1 = 2.141(2), Cu1–O1 = 1.972(2), Cu1–O3 = 1.9750(19), Cu1–$O4^{ii}$ = 1.9879(19), Cu1–$O2^{ii}$ = 1.967(2), Cu1–$Cu1^{ii}$ = 2.6096(7) Å; $O4^{ii}$–Cu1–N1 = 98.87(8), $O2^{ii}$–Cu1–N1 = 95.33(8), O1–Cu1–N1 = 95.67(8), O3–Cu1–N1 = 92.31(8)°. Reprinted with permission from ref.[99], copyright 2018 American Chemical Society.

The chain propagation is similar to the one from the previous section and is displayed in Fig. 61. The N…N distance of inner pyridine rings in adjacent chains is 14.869 Å, which is significantly larger than the distance measured in $\{[Co_2(NCS)_4(MeOH)_4(\mathbf{8})_2]\cdot 2MeOH\cdot 8H_2O\}_n$. The dinuclear $Cu_2(OAc)_4$ building block, with its four acetate groups, is bulkier than $Co(NCS)_2(MeOH)_2$ and doesn't allow closer interchain distances or slipping of the pyrimidine ring over the inner pyridine ring of the next chain. The ethyl groups on the pyrimidine ring point directly into the V-shaped cavity of the 4,2':6',4"-terpyridine of the adjacent chain, "pushing" it away (Fig. 61b). Chains of different layers interact via face-to-face π-stacking of

pyridine rings (containing N1 and N2 Fig. 61c). Pyrimidine rings are not participating in the π-stacking. In $[Cu_2(OAc)_4(\mathbf{9})]_n$ one ligand **9** within one chain shows π-stacking interactions to adjacent chains above and underneath, which stands in contrast to the staircase like π-stacking motif observed in the structure presented in the last section.

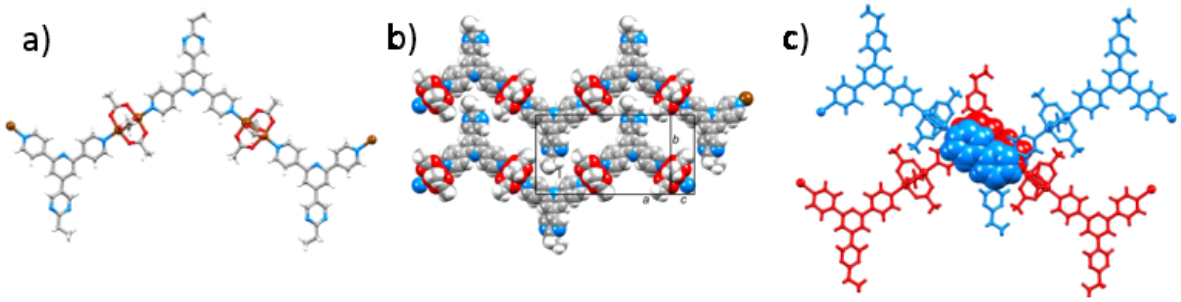

Fig. 61: a) The zig-zag chain motif of $[Cu_2(OAc)_4(\mathbf{9})]_n$. b) Space-filling mode highlighting the interactions between the ethyl group and the V-shaped cavity of the next adjacent chain. c) π-stacking interactions between pyridine rings of chains in different layers. Reprinted with permission from ref.[99], copyright 2018 American Chemical Society.

A detailed study[30] of the related $Zn_2(OAc)_4$ paddlewheel building block with 4'-(4-ROC_6H_4)-4,2':6',4"-terpyridines bearing alkoxy chains of different lengths (R = Me to *n*decyl) revealed, that the adjacent zig-zag chains can be pushed away and that longer alkoxy chains (up to *n*hexyloxy) can curl up and fit into the V-shaped cavity. *n*Octyloxy chains or longer chains further increase the steric demand in the cavity and the formation of discrete complexes is favoured over the formation of coordination polymers. The described study[30] and the findings in this and the last section clearly display a favoured motif achieved by crystal engineering of 4,2':6',4"-terpyridines with short residues on the phenylene/pyrimidine rings and metal centres, that favour a linear connectivity of two in the solid state.

Additional information can be found in the printed publication (section 18.5).

9.6 Comparison of the structural motifs

Five 1D coordination polymer chains were discussed in this chapter. All structures consist of two-connecting metal building blocks and ligands with two donor atoms. The connection of the building blocks and the relative orientation of the ligands in the lattice defines the propagation of the chains and the differences in the structural motifs, which can lead to e.g. helical or zig-zag chains. The best predictable case is a combination of a metal building block, that favours a linear connectivity of two ($Co(NCS)_2(MeOH)_2$, $Cu_2(OAc)_4$ etc.) in the solid state with a rigid V-shaped two donor 4,2':6',4"-terpyridine ligand. The clear orientation of the connecting centres in both building blocks will predominately lead to the formation of a zig-zag chain. The variation in chain propagation increases, when the metal building block, favouring a pseudo-tetrahedral two-connecting geometry (e.g. zinc halides) in the solid state is used. Two possibilities for chain propagation using Zn(II) centres are described in this chapter. The ligands can all point in the same direction, which leads to the formation of a regular polymer chain. The other possibility is, that the ligands are pointing in different directions (up-down-up-down). This alternating ligand orientation combined with the pseudo-tetrahedral geometry of ligands around the Zn(II) centre can lead to the formation of a helical polymer chain. When zinc halides are combined with a more flexible ligand (in respect to a 4,2':6',4"-terpyridine) with two donor sites (e.g. a 3,2':6',3"-terpyridine) the outcome of the chain propagation is a lot more difficult to forecast.

10 1D COORDINATION LADDERS

The structures presented in this chapter are 1D coordination polymers. Their unusual double chain motifs can be considered as 1D coordination ladders, an uncommon structural motif for 4,2':6',4"-terpyridine based ligands. Two different types of ladders/ double chains are presented in this chapter (summarized in Table 5).

Ligands	Metal salts and their connectivity	Structure motif
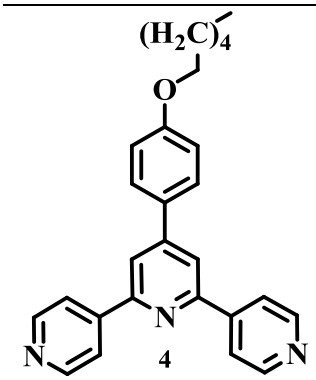	$Cd(NO_3)_2$ 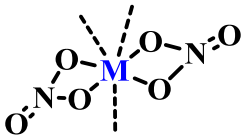 (three connecting)	1D ladder 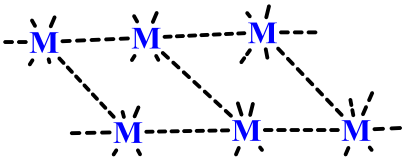
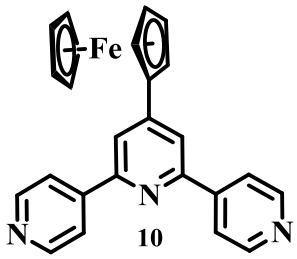	$CuCl_2$ 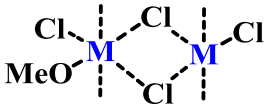 (dinuclear four connecting)	1D double chain/ narrow ladder 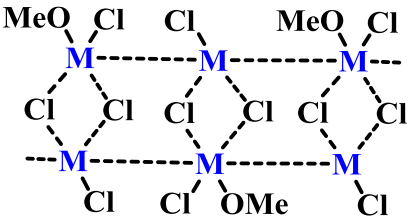
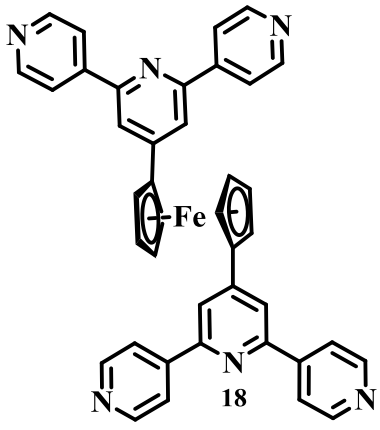	$ZnCl_2$  (bent two connecting)	1D ladder (special case of a very narrow ladder) 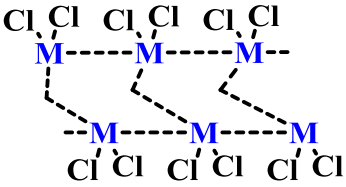

Table 5: 1D coordination ladders/double chains and their corresponding building blocks.

One possibility to construct a coordination ladder is to use a metal centre, which favours a connectivity of three in the coordination polymer and to combine it with a ligand with two donor sites. Metal centres are connected in two positions by ligands, forming the rail of the ladder and the rungs are formed by a ligand, bridging metals of two different rails.

The second motif in Table 5 is best described as a 1D double chain, but can be considered a very narrow ladder, where bridging chlorido ligands are the rungs of the ladder. The motif is obtained when a dinuclear building block has a connectivity of four and is combined with an organic ligand with two donor atoms. The ligands can be considered the rails of the ladder and form a double chain. The rungs are the chloride ligands, which connect the double chains (rails).

The third motif in Table 5 is a special case of a 1D ladder. Topographically entries 1 and 3 in Table 5 are identical, however is the separation of the rails in the third motif very small considering the large tetratopic bis(4,2':6',4"-terpyridine) ligand **18**. The 4,2':6',4"-terpyridine units are parallel to each other, possible due to the ferrocenediyl group as the backbone (entry 3, Table 5). Each 4,2':6',4"-terpyridine units bridges two-connecting metal centres, which forms the rails of the ladder. The ferrocenediyl group defines the separation of the rails which leads to a very narrow ladder (4.678 Å distance for the rails). When the Fe centres are considered to be the rungs, the ladder can be best described as a narrow corded ladder.

10.1 $[Cd_2(NO_3)_4(MeOH)(\mathbf{4})_3]_n$

A regular ladder was constructed from $Cd(NO_3)_2$, which has a connectivity of three in the structure and the two-donor 4,2':6',4"-terpyridine **4**. $[Cd_2(NO_3)_4(MeOH)(\mathbf{4})_3]_n$ (Fig. 62) crystallizes in the space group *P*-1. The experimental PXRD pattern gave a good match to the pattern predicted from the single crystal data of $[Cd_2(NO_3)_4(MeOH)(\mathbf{4})_3]_n$.

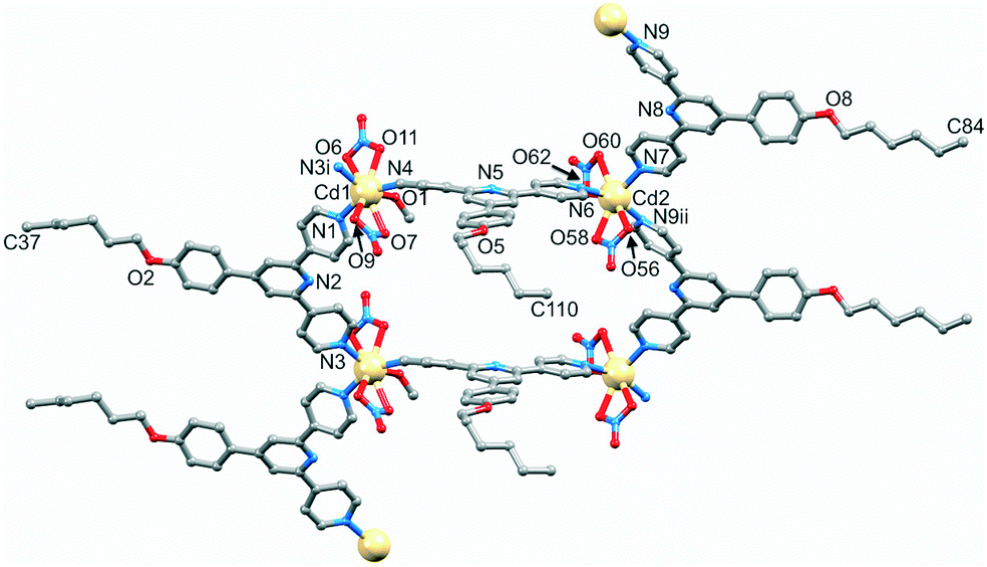

Fig. 62: Part the polymer chain in $[Cd_2(NO_3)_4(MeOH)(\mathbf{4})_3]_n$. Atoms in the asymmetric unit are labelled; symmetry codes: i = −1 + x, y, z; ii = 1 + x, y, z. Hydrogen atoms are omitted for clarity. Reproduced from ref.[108], published by The Royal Society of Chemistry.

Ligands **4**, representing one rail of the ladder are pointing in the same direction, with an up-up-up arrangement and their *n*hexyloxy chains are almost linear extended on one side of the ladder and slightly squeezed together on the other side (right-hand side and left-hand side in Fig. 62, respectively). 4,2':6',4''-terpyridine units forming the rails are almost parallel to one another and the bridging ligand is points out of a plane defined by the Cd atoms with an angle of 28° relative to it. The bridging ligands form the rungs of the ladder and a TOPOS[81] representation (the Cd(II) centres are the nodes) of the scaffold is displayed in Fig. 63b.

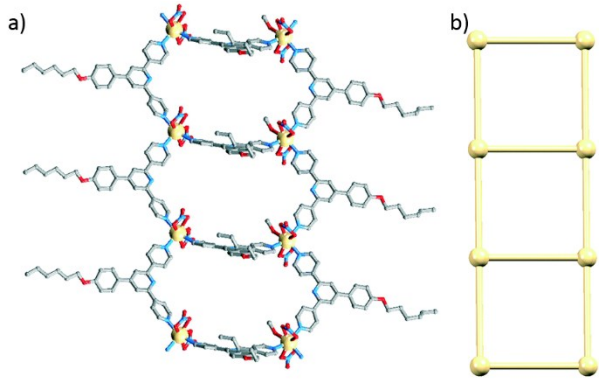

Fig. 63: a) View of the $[Cd_2(NO_3)_4(MeOH)(\mathbf{4})_3]_n$ ladder along the b-axis. b) TOPOS[81] scaffold representation of the ladder (Cd(II) centres are the nodes). Reproduced from ref.[108], published by The Royal Society of Chemistry.

The packing of adjacent molecules is dominated by face-to-face π-stacking of inner pyridine rings (green with purple in Fig. 64) and to some extend by van der Waals interactions between extended *n*hexyloxy chains of the ligands forming the rails of the ladder (Fig. 64).

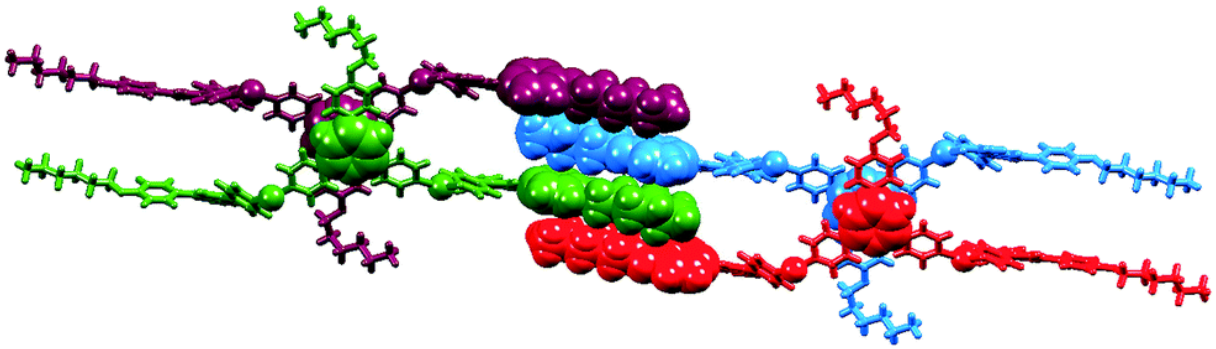

Fig. 64: Face-to-face π-stacking interactions and van-der-Waals interactions present in $[Cd_2(NO_3)_4(MeOH)(\mathbf{4})_3]_n$. Reproduced from ref.[108], published by The Royal Society of Chemistry.

Additional information can be found in the printed publication (section 18.6).

10.2 $[\{Cu_2Cl_4(\mathbf{10})_2(MeOH)\}\cdot 2.25MeOH\cdot H_2O\cdot CHCl_3]_n$

The $CuCl_2$ salt was introduced in chapter 8 and two $CuCl_2$ units dimerized to form the dinuclear building block Cu_2Cl_4, with a connectivity of four. In combination with a 4'-ferrocenyl substituted 3,2':6',3"-terpyridine a discrete double-decker structure was obtained. The double decker motif is formed by four ligands **11** and two Cu_2Cl_4 units. The Cu_2Cl_4 units are bridged by two ligands **11** to form two decks of 3,2':6',3"-terpyridine ligands, parallel to each other, which can be described as a double-decker.

In this section the same metal building block is combined with the analogues 4'-ferrocenyl substituted 4,2':6',4"-terpyridine ligand **10**. The rigid V-shaped coordination of **10** doesn't allow a formation of a double-decker structure, because the Cu_2Cl_4 unit has linear connecting sites. Two parallel zig-zag chains, bridged by two μ-Cl ligands, form. The zig-zag chain motif is common for 4,2':6',4"-terpyridines with linear two-connecting metal building blocks (see previous chapter). The 4,2':6',4"-terpyridines form a double chain, which can be considered the rails of a very narrow ladder. The μ-Cl ligands bridge the chains and can be considered the

rungs. The repeat unit of $[\{Cu_2Cl_4(\mathbf{10})_2(MeOH)\}\cdot 2.25MeOH\cdot H_2O\cdot CHCl_3]_n$ is displayed in Fig. 65 – the structure crystallizes in the space group $P2_1/n$.

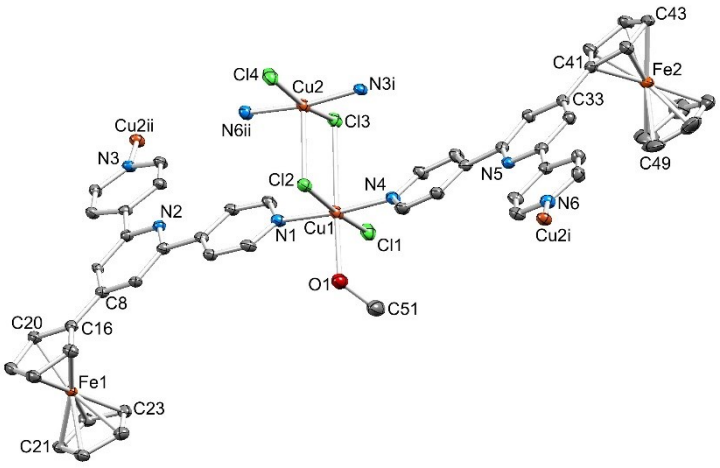

Fig. 65: Structure of the repeat unit in $[\{Cu_2Cl_4(\mathbf{10})_2(MeOH)\}\cdot 2.25MeOH\cdot H_2O\cdot CHCl_3]_n$ with symmetry-generated atoms; H atoms and solvent molecules are omitted and ellipsoids plotted at 30% probability level. Symmetry code i = $^1/_2-x$, $-^1/_2+y$, $^1/_2-z$, ii = $^1/_2-x$, $^1/_2+y$, $^1/_2-z$. Selected bond distances: Cu1–Cl1 = 2.3406(15), Cu1–Cl2 = 2.3688(14), Cu1–Cl3 = 3.0436(14), Cu1–N1 = 1.996(4), Cu1–N4 = 1.992(4), Cu1–O1 = 2.319(4), Cu2–N6^{ii} = 2.001(4), Cu2–N3^{i} = 2.000(4), Cu2–Cl2 = 2.6392(13), Cu2–Cl3 = 2.3008(14), Cu2–Cl4 = 2.3333(16) Å. Reproduced from ref.[31], published by CSIRO Publishing.

Fig. 66a and b show the double chain along the a- and c-axis, respectively and highlight the close distance between ligands **10** in parallel chains (distance of the N-atoms in the inner pyridine rings = 3.511 Å). Adjacent ladders pack via face-to-face π-π interactions of ligands **10** (all pyridine rings and one ferrocenyl ring participate in the stacking).

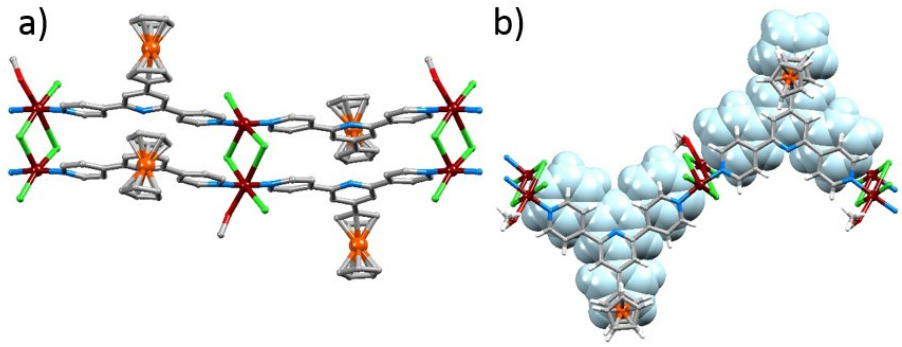

Fig. 66: a) View of the narrow $[\{Cu_2Cl_4(\mathbf{10})_2(MeOH)\}\cdot 2.25MeOH\cdot H_2O\cdot CHCl_3]_n$ ladder along the a-axis. b) Space-filling presentation of ligands **10** in the back chain, with **10** in the front showing good π-stacking overlap. Reproduced from ref.[31], published by CSIRO Publishing.

Ferrocenyl groups point into the V-shaped cavities of next adjacent chains, interlocking the double chains (Fig. 67a). Adjacent chains interact via face-to-face π-stacking of outer pyridine rings (Fig. 67b).

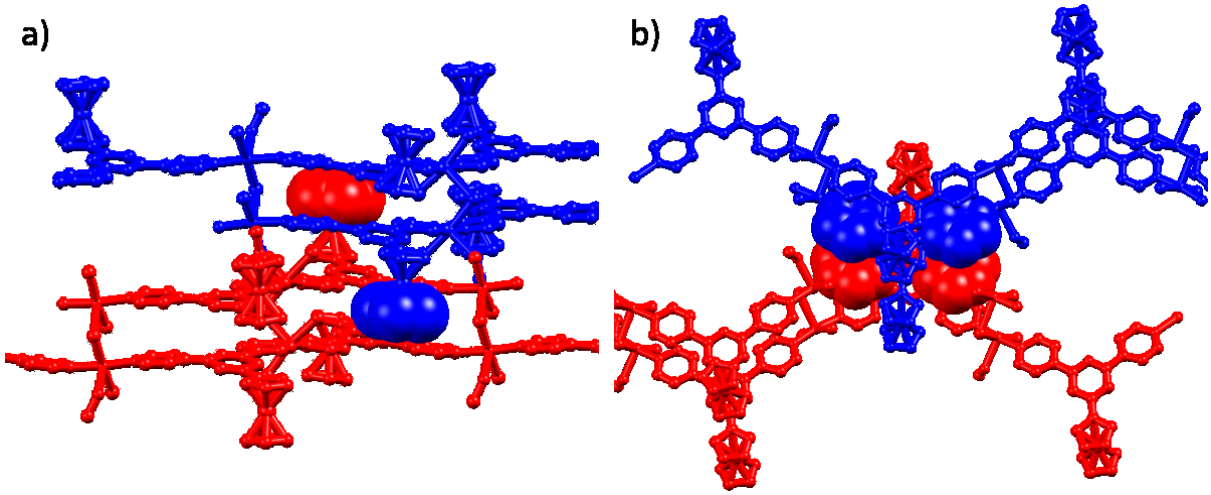

Fig. 67: a) Ferrocenyl groups pointing into the V-shaped cavities of the adjacent double chain. b) Face-to-face π-stacking of outer pyridine rings in two adjacent double chains.

Additional information can be found in the printed publication (section 18.2).

10.3 $[\{Zn_2(\mathbf{18})Cl_4\}\cdot 3CHCl_3]_n$

The last structure in this series of 1D structures is formed from the tetratopic bis(4,2':6',4''-terpyridine) ligand **18** and $ZnCl_2$. A ferrocenediyl group is substituted on both cyclopentadienyl rings via the 4' position of 4,2':6',4''-terpyridine. The metallocene enables rotation of the 4,2':6',4''-terpyridines by 360° with respect to one another. The structure $[\{Zn_2(\mathbf{18})Cl_4\}\cdot 3CHCl_3]_n$ (Fig. 68) crystallizes in the space group $P2_1/n$.

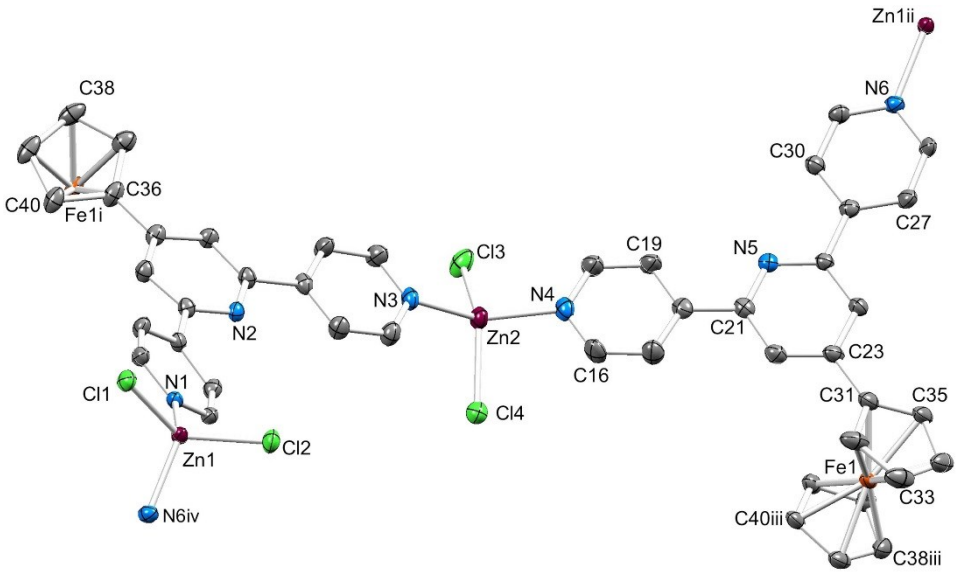

Fig. 68: The asymmetric unit in $[\{Zn_2(\mathbf{18})Cl_4\}\cdot 3CHCl_3]_n$ with symmetry-generated atoms; H atoms and solvent molecules are omitted for clarity. Symmetry codes: *I* = 3/2–x, − ½ + y, 3/2–z; ii = x, 1 + y, z; iii = 3/2–x, ½ + y, 3/2–z; iv = x, − 1 + y, z. Selected bond distances: Zn1–N6iv = 2.042(4), Zn1–N1 = 2.035(4), Zn1–Cl1 = 2.2453(13), Zn1–Cl2 = 2.2435(13), Zn2–N3 = 2.076(4), Zn2–N4 = 2.079(4), Zn2–Cl3 = 2.2499(15), Zn2–Cl4 = 2.2708(14) Å. Reproduced from ref.[109], published by Elsevier.

In $[\{Zn_2(\mathbf{18})Cl_4\}\cdot 3CHCl_3]_n$ both 4,2':6',4"-terpyridine units point in the same direction, are parallel to one another (Scheme 15).

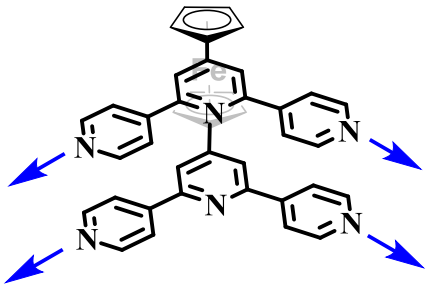

Scheme 15: Orientation of the 4,2':6',4"-terpyridine units of **18** in the structure $[\{Zn_2(\mathbf{18})Cl_4\}\cdot 3CHCl_3]_n$. The coordination geometry is highlighted by the blue arrows.

One ligand **18** is coordinated by four $ZnCl_2$ units and a double stranded zig-zag coordination polymer or very narrow ladder is observed. Topologically this structure and the structure in section 10.1 are the same. Ligand **18** can be considered the rung in this narrow "corded ladder". A zig-zag motif is normally not observed with zinc halides, that favour a pseudo tetrahedral geometry of coordinated ligands with a connectivity of two (if a helix is not considered zig-zag shaped) as demonstrated by the structures in the previous chapter. The way ligand **18** coordinates to the Zn(II) centres dictates this motif and does not allow the formation of a helix.

The pseudo tetrahedral geometry of the $ZnCl_2$ is retained (Fig. 69) and the view along the c-axis shows a wave-like double stranded zig-zag motif. There is some restrain in the structure as the 4,2':6',4''-terpyridine unit is bent (~25° angle between a coordinating pyridine ring and the central one) and the nitrogen atoms are not pointing directly towards the metal atoms. This flexibility in the coordination geometry around the Zn(II) centres (d^{10}) allows the formation of this motif.

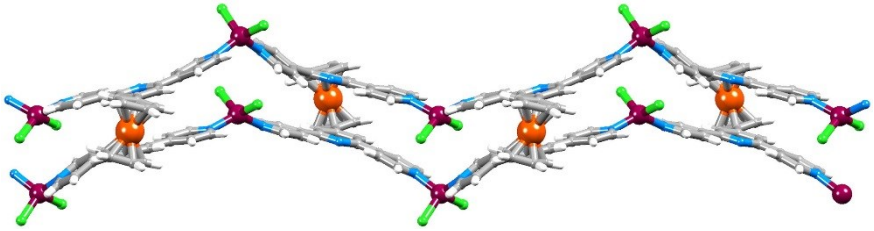

Fig. 69: Part of one chain in $[\{Zn_2(\mathbf{18})Cl_4\}\cdot 3CHCl_3]_n$. Reproduced from ref.[109], published by Elsevier.

Neighbouring chains (blue in Fig. 70) point their ferrocenediyl unit into the V-shaped cavity of the next double chain. A close interaction is not observed and the void space between ferrocenediyl units and V-shaped cavity of the next double chain is filled with chloroform molecules (omitted in Fig. 70).

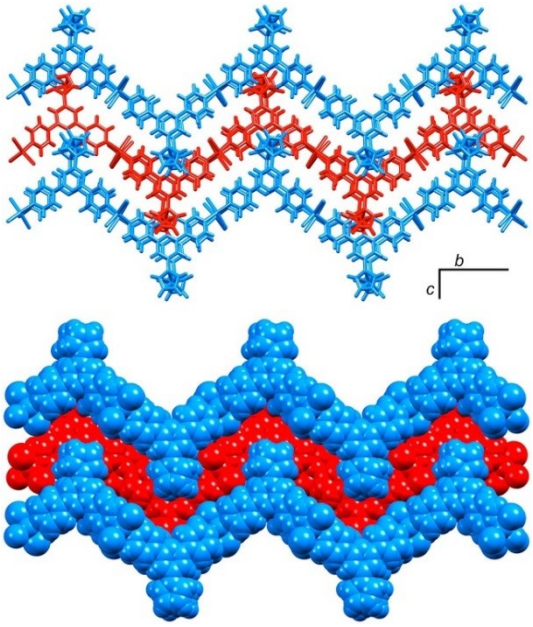

Fig. 70: Packing in $[\{Zn_2(\mathbf{18})Cl_4\}\cdot 3CHCl_3]_n$. Blue double chains are part of the same sheet and interact with the double chain underneath (red) via π-stacking. The space-filling representation illustrates void space between double-chains in the same layer, which is occupied by solvent (chloroform, omitted in the pictures) molecules. Reproduced from ref.[109], published by Elsevier.

Face-to-face π-stacking between ferrocenediyl groups and outer pyridine rings (e.g. ring containing N6) of the adjacent chain underneath (blue in Fig. 71) (or above) is the major intermolecular interaction.

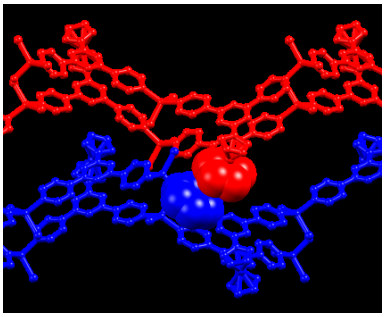

Fig. 71: Face-to-face π-stacking between a ferrocenediyl group and an outer pyridine ring in $[\{Zn_2(\mathbf{18})Cl_4\}\cdot 3CHCl_3]_n$.

Additional information can be found in the printed publication (section 18.7).

11 2D COORDINATION NETWORKS

The construction of 2D dimensional structures requires additional coordination bonds, that have to be formed between ligands and metal centres. A very rewarding metal salt in this respect is $Co(NCS)_2$. $Co(NCS)_2$ is six coordinate in most structures and the axial positions are normally coordinated by NCS^- ligands. The equatorial coordination sites are rarely coordinated by solvent molecules in coordination polymers, like MeOH (see section 9.4) and $Co(NCS)_2$ acts as square planar metal centre with a connectivity of four in the following structures. $Co(NCS)_2$ is also the dominating metal salt in this and the next chapter. Other metal salts like zinc halides are also present in the structures to come, but their connectivity of two requires a combination with ligands, that have more than two donor atoms to form 2D and 3D assemblies. One of such a tetratopic bis(4,2':6',4"-terpyridine) ligand was discussed in section 10.3. **18** consists of two 4,2':6',4"-terpyridine units linked via a ferrocenediyl group. Other bis(4,2':6',4"-terpyridine) and bis(3,2':6',3"-terpyridine) ligands are incorporated into the following structures and their four-donor atom design leads to the formation of 2D and 3D structures with metal centres, that are at least two connecting. 3D structures were mainly obtained with tetratopic ligands, with one exception, where the combination of a two-donor 4,2':6',4"-terpyridine with the four connectivity $Co(NCS)_2$ lead to the formation of a rare **neb** net structure. It is impossible to predict if a combination of the mentioned building blocks will lead to the formation of a 2D or 3D assembly. This and the next chapter present an overview of the possible motifs and gives preferences, which building blocks can favour the formation of a certain motif.

11.1 Two-donor 4,2':6',4"-terpyridines with $Co(NCS)_2$

Linking metal centres, that favour a square planar four connecting geometry (e.g. $Co(NCS)_2$), with two-donor V-shaped 4,2':6',4"-terpyridines can lead to the formation of (4,4)-nets. These chess board like structures consist of metallosquares built out of four metal centres and four bridging ligands. The $Co(NCS)_2$ unit is twisted out of the chess-board plane to allow coordination of the 4,2':6',4"-terpyridines to Co(II) from above and underneath the plane, defined by the Co atoms). A net structure is obtained, where two ligands per square are pointing upwards and two ligands per square are pointing downwards. The result is an almost planar (in respect to the Co-nodes) chess-board structure. The ligands successfully incorporated into this

structure motif are summarized in the following scheme and one structure is discussed in more detail and represents the others.

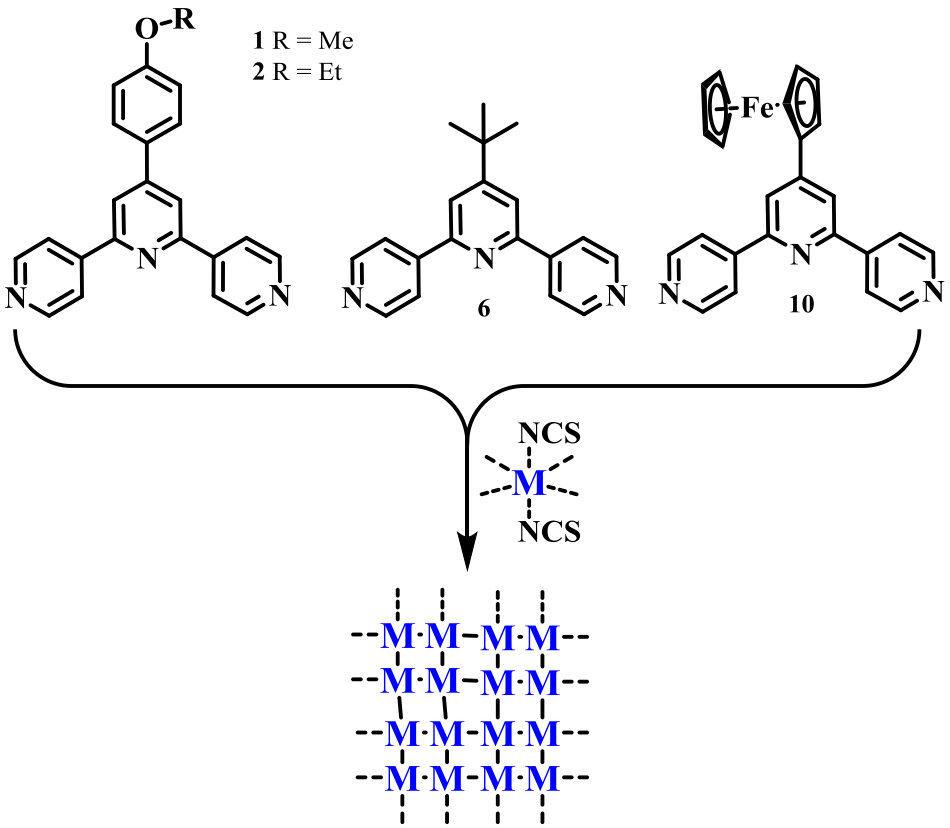

Scheme 12: Ligands, that were combined with $Co(NCS)_2$ and lead to 2D chess board structures. NCS^- ligands not shown in the net scheme at the bottom.

Ligand **10** was present in many previous discussed structures and it was selected as the representative among ligands displayed in Scheme 12. **10** reacted with $Co(NCS)_2$ to form $[\{Co(NCS)_2(\mathbf{10})_2\}\cdot 4CHCl_3]_n$ (Fig. 72). $[\{Co(NCS)_2(\mathbf{10})_2\}\cdot 4CHCl_3]_n$ crystallized in the space group $P2_1/n$. The repeat unit contains one $Co(NCS)_2$ unit and two ligands **10**. The up-down arrangement (zig-zag like) of ligands **10** is visible in the repeat unit. The experimental PXRD pattern gave a good match to the pattern predicted from the single crystal data of $[\{Co(NCS)_2(\mathbf{10})_2\}\cdot 4CHCl_3]_n$.

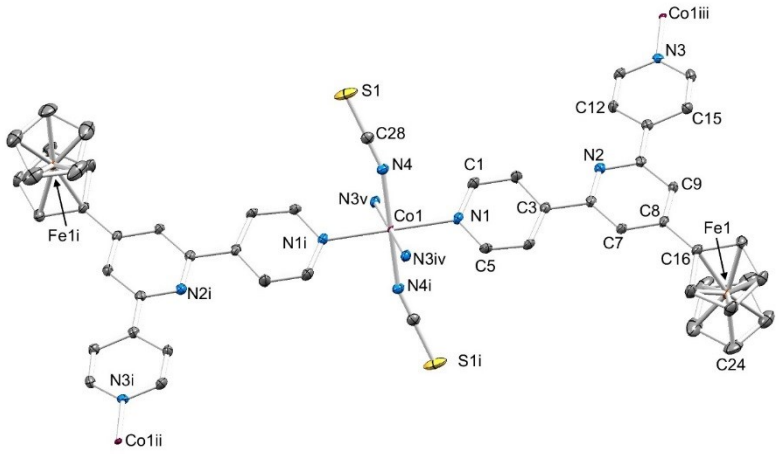

Fig. 72: Structure of the repeat unit in $[\{Co(NCS)_2(\mathbf{10})_2\}\cdot 4CHCl_3]_n$ with symmetry generated atoms; H atoms and solvent molecules are omitted. Ellipsoids are plotted at 50% probability. Symmetry codes: i = $-x$, $1-y$, $1-z$; ii = $-{}^1/_2+x$, ${}^3/_2-y$, $-{}^1/_2+z$; iii = ${}^1/_2+x$, ${}^1/_2-y$, ${}^1/_2+z$; iv = $-{}^1/_2+x$, ${}^1/_2-y$, $-{}^1/_2+z$; v = ${}^1/_2-x$, ${}^1/_2+y$, ${}^3/_2+z$. Important bond parameters: Co1–N1 = 2.183(2), Co1–N3^{iv} = 2.183(2), Co1–N4 = 2.083(2), C8–C16 = 1.472(3) Å; N–Co1–N angles are in the range 86.77(8)– 93.23(8)°. Reproduced from ref.[32], published by MDPI.

The net is built of zig-zag chains, that propagate in 2 dimensions. Each Co(II) centre is part of two chains, which propagate perpendicular to each other. This leads to the formation of a planar (concerning the Co-nodes) chess-board motif displayed in Fig. 73a. The metallocycles are almost rectangular, with angles of 86.82° and 93.18° (measured between the Co(II) nodes of the metallocycle). The length of the edges (12.723 Å) in the metallocycles is defined by the scope of the rigid V-shaped ligand **10**. The zig-zag chain motif (Fig. 73b), influenced by the V-shaped ligand and the linear connecting geometry of the Co(II) centre, causes a tilt in the Co(II) centres which enables ligands to adopt an up-down-up-down arrangement, relative to the chess-board plane (Fig. 73b). A TOPOS[81] overlay helps visualizing the nodes (Co-centres) and connections within the (4,4)-net (Fig. 73a).

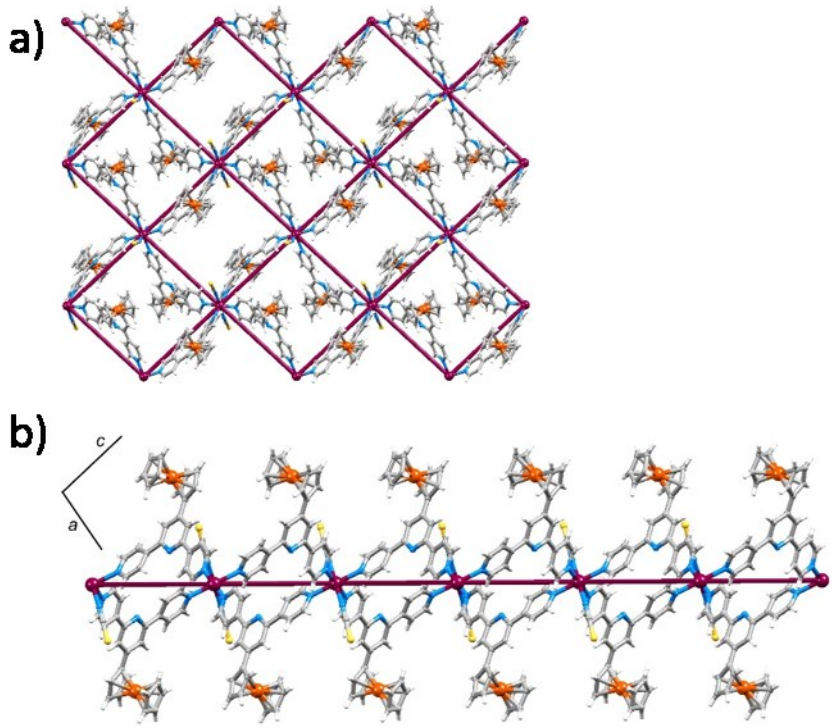

Fig. 73: a) The chess-board motif observed in [{Co(NCS)$_2$(**10**)$_2$}·4CHCl$_3$]$_n$ with TOPOS[81] overlay, connecting the Co-nodes. b) View along the b-axis illustrating the tilted Co(NCS)$_2$ building block and the alternating up-down arrangement of ligands above or underneath the plane (through the Co-atoms). Reproduced from ref.[32], published by MDPI.

Outer pyridine rings (red in Fig. 74) and ferrocenyl groups (blue in Fig. 74) of adjacent sheets interact via face-to-face π-stacking, a common motif observed and discussed in previous chapters.

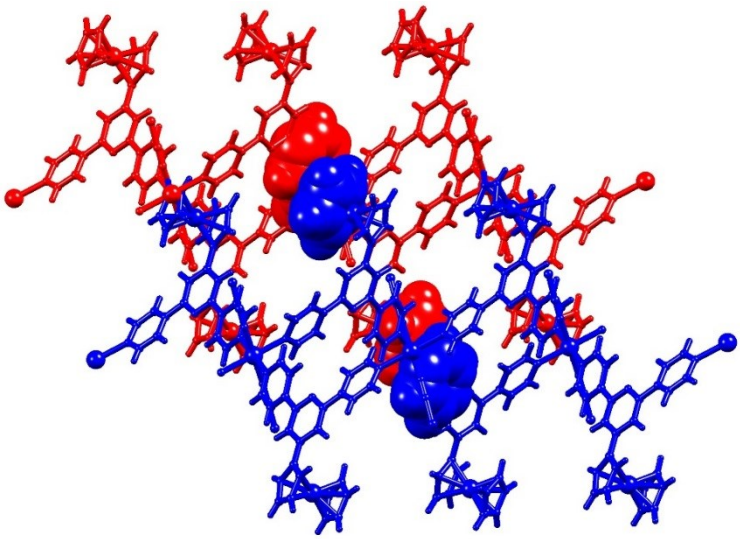

Fig. 74: Intermolecular interactions between two sheets (red and blue) of [{Co(NCS)$_2$(**10**)$_2$}·4CHCl$_3$]$_n$. ferrocenyl groups and pyridine rings interact via π-stacking. Reproduced from ref.[32], published by MDPI.

Three related structures were obtained with the ligands displayed in Scheme 12 and $Co(NCS)_2$. The (4,4)-nets in these structures are constructed the same way (perpendicular zig-zag chains connected by Co centres with a connectivity of four) and form almost planar (in respect to the Co-atoms) chess-board structures, with ligands alternating above and below the plane. The TOPOS[81] overlays of the structures $[\{Co_2(NCS)_4(\mathbf{1})_4\}\cdot 2CHCl_3\cdot 1.5MeOH]_n$, $[\{Co(NCS)_2(\mathbf{2})_2\}\cdot 4CHCl_3]_n$ and $[\{Co(NCS)_2(\mathbf{6})_2\}\cdot 0.5H_2O]_n$ are presented in Fig. 75. The common motif is retained, and the structures differ slightly in the way they pack and how the ligands point out of the planes. In Fig. 75a, b and c the squares are compressed to rhombuses, with angles of 51.37° and 128.63° in $[\{Co_2(NCS)_4(\mathbf{1})_4\}\cdot 2CHCl_3\cdot 1.5MeOH]_n$, angles of 76.43° and 103.57° in $[\{Co(NCS)_2(\mathbf{2})_2\}\cdot 4CHCl_3]_n$ and angles of 53.39° and 128.46° in $[\{Co(NCS)_2(\mathbf{6})_2\}\cdot 0.5H_2O]_n$. The corresponding lengths of the edges in each metallocycle are 13.637/13.193 Å (in a)), 12.913 Å (in b)) and 13.198/13.414 Å (in c)). The values are in a similar range, caused by the rigid V-shaped ligands **1**, **2** and **6**. The experimental PXRD patterns gave a good match to the patterns predicted from the single crystal data of $[\{Co_2(NCS)_4(\mathbf{1})_4\}\cdot 2CHCl_3\cdot 1.5MeOH]_n$, $[\{Co(NCS)_2(\mathbf{2})_2\}\cdot 4CHCl_3]_n$ and $[\{Co(NCS)_2(\mathbf{6})_2\}\cdot 0.5H_2O]_n$.

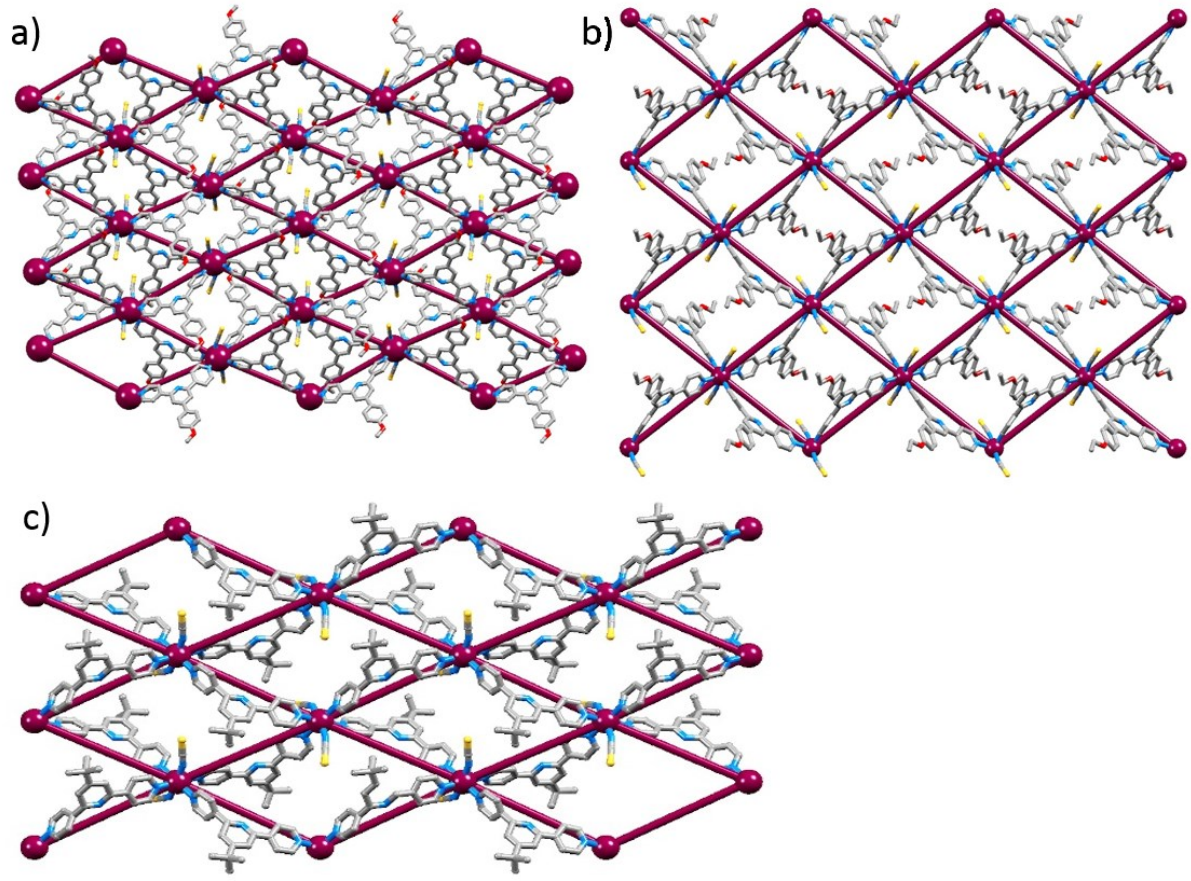

Fig. 75: TOPOS[81] overlay of $[\{Co_2(NCS)_4(\mathbf{1})_4\}\cdot 2CHCl_3\cdot 1.5MeOH]_n$ (a)), $[\{Co(NCS)_2(\mathbf{2})_2\}\cdot 4CHCl_3]_n$ (b)) and $[\{Co(NCS)_2(\mathbf{6})_2\}\cdot 0.5H_2O]_n$ (c)). Co-atoms are the nodes that represent the (4,4)-nets and ligands adopt alternating positions above and underneath the plane. Reproduced from ref.[110] published by The Royal Society of Chemistry.

The packing of the structures is illustrated in Fig. 76 and reveals similarities. In $[\{Co_2(NCS)_4(\mathbf{1})_4\}\cdot 2CHCl_3\cdot 1.5MeOH]_n$ adjacent layers (distance 8.376 Å, measured between a Co(II) centres and a plane through the Co(II) centres of the adjacent layer) interact via face-to-face π-stacking of the inner pyridine rings with phenylene rings (Fig. 76a). In $[\{Co(NCS)_2(\mathbf{2})_2\}\cdot 4CHCl_3]_n$ face-to-face π-stacking is observed between outer pyridine rings and phenylene rings (Fig. 76b). An inter-layer distance of 9.229 Å was observed in the structure. In $[\{Co(NCS)_2(\mathbf{6})_2\}\cdot 0.5H_2O]_n$ the inter-layer distance is the shortest with 3.524 Å (distance measured from one Co(II) centre to and an adjacent plane, through the Co(II) centres) among these structures. Adjacent layers interact via face-to-face π-stacking of inner pyridine rings (Fig. 76c).

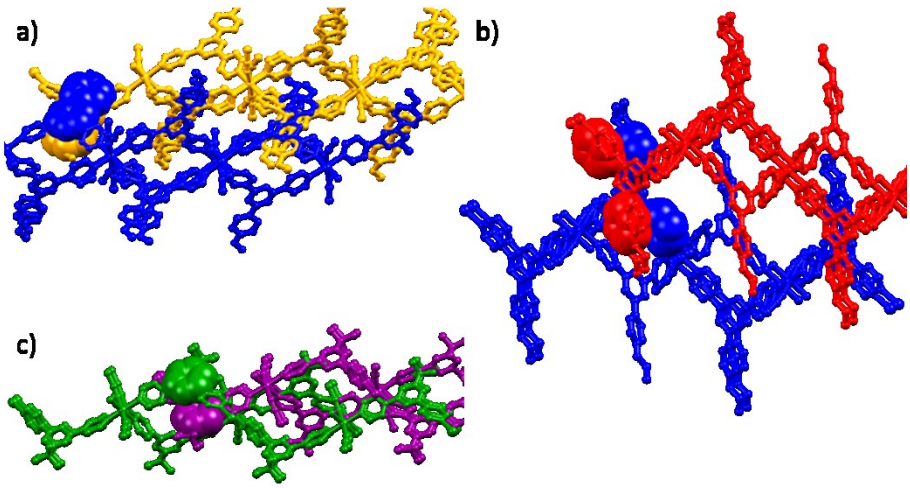

Fig. 76: a) Face-to-face π-π interactions between inner pyridine rings and phenylene rings in $[\{Co_2(NCS)_4(\mathbf{1})_4\}\cdot 2CHCl_3\cdot 1.5MeOH]_n$. b) Face-to-face π-π interactions between outer pyridine rings and phenylene rings in $[\{Co(NCS)_2(\mathbf{2})_2\}\cdot 4CHCl_3]_n$. c) Face-to-face π-π interactions between inner pyridine rings in $[\{Co(NCS)_2(\mathbf{6})_2\}\cdot 0.5H_2O]_n$.

The "length" of the backbone on the 4,2':6',4"-terpyridine ligands **1**, **2** and **6** influences the spacing between adjacent layers. The shorter the backbone (**6** has the shortest group substituted in the 4' position of the 4,2':6',4"-terpyridine) the shorter the separation of the layers. The correlation between ligand design and intermolecular interactions in the lattice packing is an important finding and is an example for crystal engineering.

In $[\{Co(NCS)_2(\mathbf{6})_2\}\cdot 0.5H_2O]_n$ two packing motifs are present. Two chains pack closely with face-to-face π-π interactions between inner pyridine rings, but the next adjacent double sheets is further away (Fig. 77c). This phenomenon of two double sheets stands in contrast to previous reported results for the compound $[\{4Co(SCN)_2(\mathbf{6})\cdot CH_3OH\}\cdot H_2O]_n$ (CSD refcode: FAKRIU)[76], which uses the same metal centre and ligand **6** and also leads to the formation of a (4,4)-net. To assemble the structure $[\{4Co(SCN)_2(\mathbf{6})\cdot CH_3OH\}\cdot H_2O]_n$, a slightly different solvent combination (1,2-dichlorobenzene and MeOH) was used in contrast to chloroform and MeOH for the assembly of $[\{Co(NCS)_2(\mathbf{6})_2\}\cdot 0.5H_2O]_n$. A regular separation of the layers was observed in the literature network $[\{4Co(SCN)_2(\mathbf{6})\cdot CH_3OH\}\cdot H_2O]_n$ and this comparison should highlight how little changes in e.g. the solvent conditions can influence the self-assembly processes and the packing motifs in a lattice.

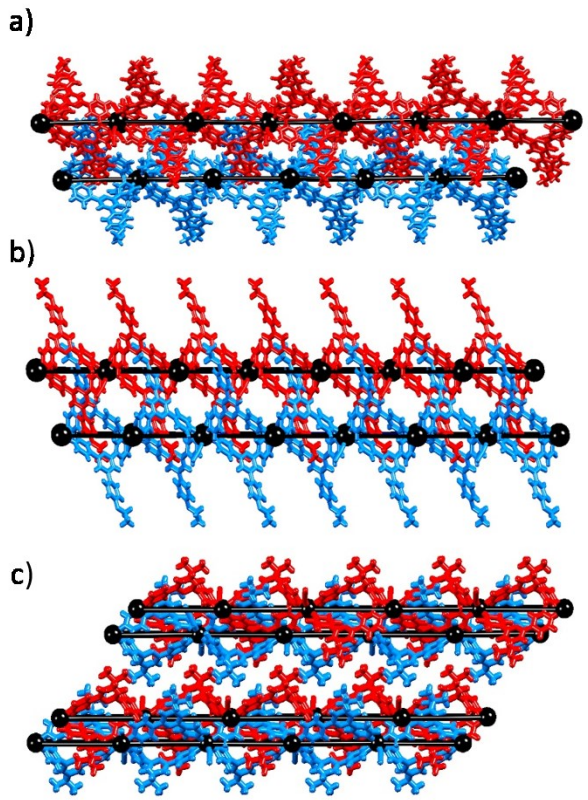

Fig. 77: Packing in $[\{Co_2(NCS)_4(\mathbf{1})_4\}\cdot 2CHCl_3\cdot 1.5MeOH]_n$ (a)), $[\{Co(NCS)_2(\mathbf{2})_2\}\cdot 4CHCl_3]_n$ (b)) and $[\{Co(NCS)_2(\mathbf{6})_2\}\cdot 0.5H_2O]_n$ (c)). Co-atoms form a planar sheet and sheets interact via π-stacking of pyridine and phenyl rings. In a) and b) adjacent sheets have the same distance, in c) double sheets are observed and the distance between pairs of sheets varies. Reproduced from ref.[110] published by The Royal Society of Chemistry.

Additional information can be found in the printed publications (sections 18.4 and 18.8).

11.2 Two-donor 4,2':6',4''-terpyridines with $Cd(NO_3)_2$

In this section 4,2':6',4''-terpyridine ligands with two donor atoms are combined with $Cd(NO_3)_2$. Four 2D networks were obtained with the ligands **3**, **4**, **19** and **20** (synthesized during my master studies; the characterization can be found in the according publication[30]) shown in Scheme 16. The ligands are substituted with propyloxy, ^{n}hexyloxy, ^{n}pentyloxy and ^{n}heptyloxy in the 4 position of the phenylene ring, respectively. How the alkyloxy chains can influence the structural motif and how diverse the geometry and connectivity of $Cd(NO_3)_2$ can be, is presented in this section.

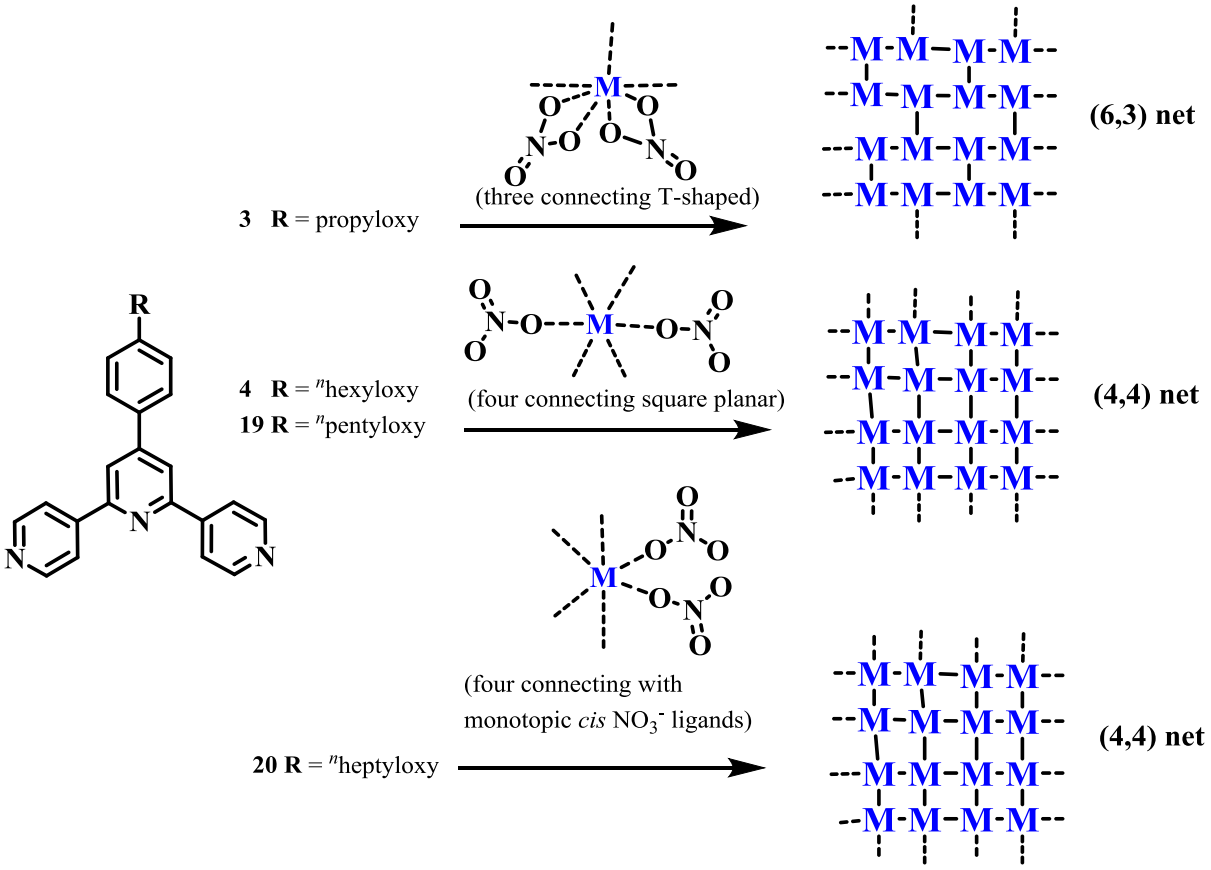

Scheme 16: Schematic presentation of the ligands, metal centres and 2D-networks discussed in this section.

11.2.1 $Cd(NO_3)_2$ with ligand 3

The first structure in this series was constructed from $Cd(NO_3)_2$ and ligand **3** (see Scheme 16). The structure $[\{Cd_2(NO_3)_4(\mathbf{3})_3\}\cdot 3CHCl_3]_n$ crystallized in the space group $P2_1/n$ and $Cd(NO_3)_2$ is seven coordinate. Two NO_3^- ligands coordinate to Cd in a bidentate chelating fashion, occupying four coordination sites. Cd(II) has a connectivity of three in the structure and a T-shaped connecting geometry (Fig. 78).

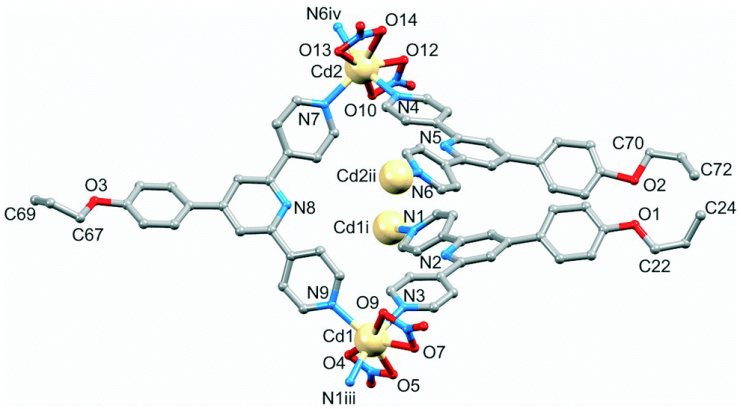

Fig. 78: The asymmetric unit (with symmetry generated atoms) in $[\{Cd_2(NO_3)_4(\mathbf{3})_3\}\cdot 3CHCl_3]_n$; H atoms omitted. Symmetry codes: i = 1/2 − x, 1/2 + y, 3/2 − z; ii = 1/2 − x, −1/2 + y, 1/2 − z; iii = 1/2 − x, −1/2 + y, 3/2 − z; iv = 1/2 − x, 1/2 + y, 1/2 − z. Selected bond distances: Cd1–O4 = 2.400(7), Cd1–O5 = 2.467(7), Cd1–O7 = 2.394(7), Cd1–O9 = 2.489(7), Cd1–N1^{iii} = 2.314(8), Cd1–N3 = 2.338(8), Cd1–N9 = 2.333(8), Cd2–O10 = 2.447(9), Cd2–O12 = 2.408(8), Cd2–O13 = 2.405(7), Cd2–O14 = 2.521(8), Cd2–N4 = 2.325(10), Cd2–N6 = 2.295(9), Cd2–N7 = 2.341(8) Å. Reproduced from ref.[108], published by The Royal Society of Chemistry.

The network is constructed of Cd(II) centres acting as three connecting nodes. The Cd centres are bridged by ligands, which point almost perpendicular up and down out of the sheet (defined by the Cd nodes, Fig. 79). Six Cd centres from a cycle, thus the net is described as (6,3). In Fig. 79a the scaffold of two networks in $[\{Cd_2(NO_3)_4(\mathbf{3})_3\}\cdot 3CHCl_3]_n$ are displayed (in purple and yellow) using TOPOS[81]. The hexacycles, nicely visualized in the scaffold are squeezed and the impression arises that the net is constructed of 1D chains (defined by the long side of each hexacycle in Fig. 79), where Cd centres along one imaginary chain are alternately bridged to the next adjacent chain above or underneath via one ligand **3**. Within the chains (the long side of each hexacycle) the ligands adopt an alternating up-down-up-down orientation. The connecting ligands have an alternating up-up-down-down orientation (underlined orientations are ligands that interconnect the chains) between the chains. The vertical orientations of the ligands relative to the (6,3) net are displayed in Fig. 79b and the interactions between adjacent networks are highlighted in different colours. The blue network lies two layers underneath the red one (with the purple one in between) and the propyloxy groups of the blue net point though the purple net into the V-shaped cavity of a ligand **3** in the red network. Space is limited in this cavity and a systematic study of alkyloxy chains of different lengths incorporated in 4,2':6',4''-terpyridines in combination with $Zn_2(OAC)_4$ revealed, that longer chains can disrupt the packing motifs, what can lead to the transformation of 1D chains to discrete complexes[30]. In the case of $[\{Cd_2(NO_3)_4(\mathbf{3})_3\}\cdot 3CHCl_3]_n$ enough space is available in the V-shaped cavity and preliminary unpublished data of the ^{n}butyloxy analogue of **3** with $Cd(NO_3)_2$ revealed a similar structural motif. ^{n}Butyloxy chains were also able to occupy the space in the V-shaped cavity.

The purple chain in Fig. 79 overlaps with the red and blue one and 4,2':6',4"-terpyridine units interact via face-to-face π-stacking of outer pyridine rings.

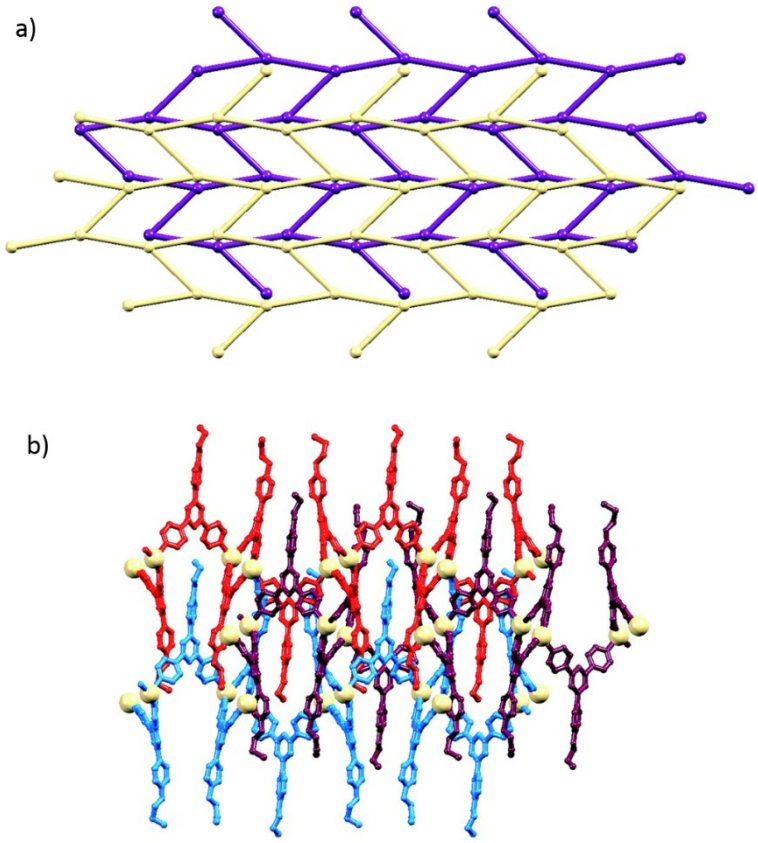

Fig. 79: a) TOPOS[81] representation of the scaffold of two adjacent (6,3) nets in $[\{Cd_2(NO_3)_4(\mathbf{3})_3\}\cdot 3CHCl_3]_n$. The nodes are the Cd(II) centres. b) View of the nets from the side. Reproduced from ref.[108], published by The Royal Society of Chemistry.

The intermolecular interaction is face-to-face π-stacking between the phenyl and inner pyridine ring of two adjacent networks (e.g. purple with red and purple with blue). The sandwich type π-stacking motif is displayed in Fig. 80 and the propyloxy chain interaction with the V-shaped cavity is illustrated in green.

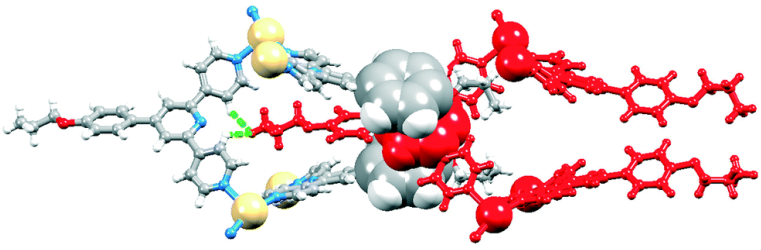

Fig. 80: Intermolecular interaction between propyloxy groups and the V-shaped cavity of the layer after the next one. π-stacking interactions between pyridine and phenyl rings forms a sandwich like motif. Reproduced from ref.[108], published by The Royal Society of Chemistry.

The following structures use ligands with longer alkyloxy chains and a different topology and orientation of the ligands is observed, which can be attributed to the increased steric demand of the alkyloxy chains. The Cd(II) centre seems to compensate for this increased steric demand with a flexible connectivity and geometry.

11.2.2 Cd(II) centres with a connectivity of four

Two NO_3^- ligands, incorporated into the crystal assembly via the $Cd(NO_3)_2$ salt are present in every structure discussed in this thesis. NO_3^- have several possibilities to coordinate to Cd(II) and Cd(II) can have different coordination numbers and geometries. In the previous section Cd(II) was seven coordinate and had a connectivity of three, as four coordination sites were occupied by two bidentate chelating NO_3^- ligands. In this section Cd(II) is seven and six coordinate and has a connectivity of four. However, does the geometry of the four connecting positions on a Cd(II) centre change as well.

$Cd(NO_3)_2$ was combined with ligands **4** (^{n}hexyloxy)and **19** (^{n}pentyloxy) to form the 2D networks $[\{Cd_2(NO_3)_4(\mathbf{4})_4\}\cdot CHCl_3\cdot MeOH]_n$ and $[\{Cd_2(NO_3)_4(\mathbf{19})_4\}\cdot 3CHCl_3]_n$. Both structures crystallize in the space group $P2_1/c$ are very similar and $[\{Cd_2(NO_3)_4(\mathbf{4})_4\}\cdot CHCl_3\cdot MeOH]_n$ will be discussed in detail here (Fig. 81). The experimental PXRD patterns gave a good match to the patterns predicted from the single crystal data of $[\{Cd_2(NO_3)_4(\mathbf{4})_4\}\cdot CHCl_3\cdot MeOH]_n$ and $[\{Cd_2(NO_3)_4(\mathbf{19})_4\}\cdot 3CHCl_3]_n$.

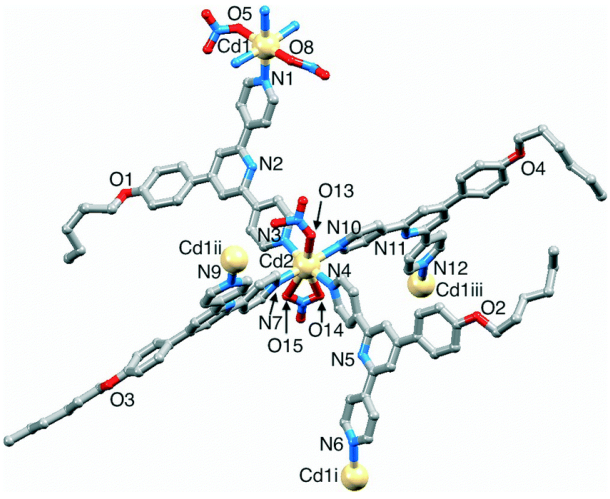

Fig. 81: The asymmetric unit (with symmetry generated atoms) in $[\{Cd_2(NO_3)_4(\mathbf{4})_4\}\cdot CHCl_3\cdot MeOH]_n$; H atoms and solvent molecules omitted. Symmetry codes: i = 1 + x, y, z; ii = 2 − x, −1/2 + y, 3/2 − z; iii = 2 − x, 1/2 + y, 3/2 − z. Reproduced from ref.[108], published by The Royal Society of Chemistry.

The asymmetric unit contains two ligands **4** and two Cd centres. The Cd centre has a connectivity of four and is almost square planar regarding his connecting sites. The axial positions are occupied by a monodentate and a bidentate chelating NO_3^- ligand. The ligands adopt an up-up-down-down orientation around the metal centre and this motif is reflected on the orientations of the ligands in the (4,4) net (Fig. 82b). Each metallomacrocycle is formed by four Cd(II) centres and four ligands, that adopt an up-up-up-down orientation. The TOPOS[81] overlay in Fig. 82a nicely illustrates the connectivity in the (4,4) net, formed by Cd(II) nodes. The V-shaped rigid linkers **4** and **19** combined with the pseudo square planar four connecting Cd(II) leads to a wave like chess-board motif. This stands in contrast to the more regular chess boards observed with 4,2':6',4"-terpyridines and $Co(NCS)_2$.

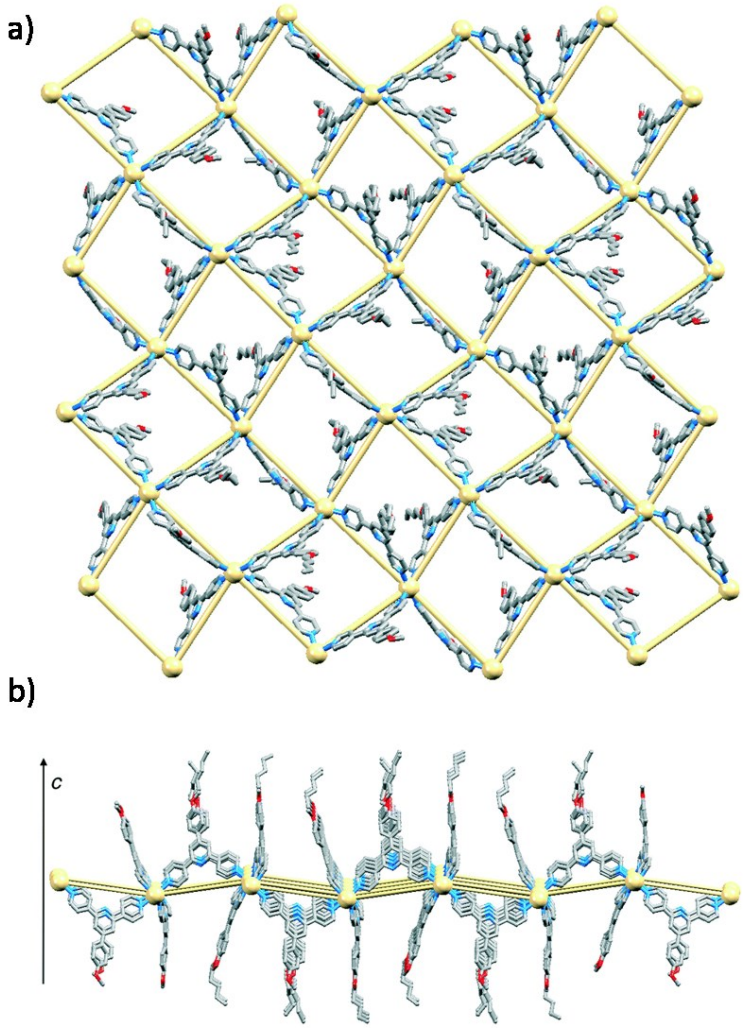

Fig. 82: a) Superimposed TOPOS[81] representation of the (4,4) net. The Cd(II) centres are the nodes. b) Alternating up-down-up-down orientation of ligands **4** along the c-axis. Ligands are point almost perpendicular out of the network. Reproduced from ref.[108], published by The Royal Society of Chemistry.

The alkoxy chain length increased from propyloxy in the last section to *n*pentyloxy and *n*hexyloxy in this section and regarding the packing interactions between propyloxy chain and the V-shaped cavity of the adjacent network a change in the structural motif (from a (6,3) net to a (4,4) net) might be attributed to the influence of the alkyloxy chain. Fig. 83 displays, that the steric demand in $[\{Cd_2(NO_3)_4(\mathbf{4})_4\}\cdot CHCl_3\cdot MeOH]_n$ has been compensated otherwise. The alkyloxy chains are almost linear extended and point into the metallosquare of the next adjacent network (Fig. 83a and b) interlocking the networks. Face-to-face π-π stacking of inner pyridine rings is the dominant intermolecular interaction in these networks.

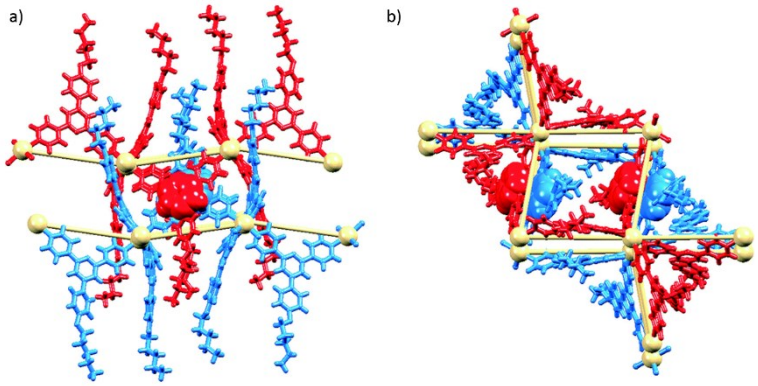

Fig. 83: Packing interactions in $[\{Cd_2(NO_3)_4(\mathbf{4})_4\}\cdot CHCl_3\cdot MeOH]_n$ with π-stacking between pyridine rings of adjacent networks and almost linear extended alkyloxy chains pointing into the mesh of the next adjacent layer. Reproduced from ref.[108], published by The Royal Society of Chemistry.

11.2.3 $Cd(NO_3)_2$ with *n*heptyloxy ligand 20

Another interesting structure was obtained in this series combining ligand **20** (*n*heptyloxy group) with $Cd(NO_3)_2$. It was demonstrated before, that Cd(II) is quite flexible in its coordination number and geometry. Here Cd(II) is six-coordinate with a pseudo octahedral geometry and NO_3^- ligands occupying two equatorial positions (they are *cis* to one another) of the octahedron in a monodentate way. Cd(II) has a connectivity of four with a distorted trigonal pyramidal connecting geometry (Fig. 84). The ligands adopt an up-down-up-down arrangement around a Cd(II) centre and the structure is a (4,4) net and similar to the (4,4) nets from the previous section, with minor differences. The experimental PXRD patterns gave a good match to the patterns predicted from the single crystal data of $[\{Cd(NO_3)_2(\mathbf{20})_2\}\cdot 2MeOH]_n$.

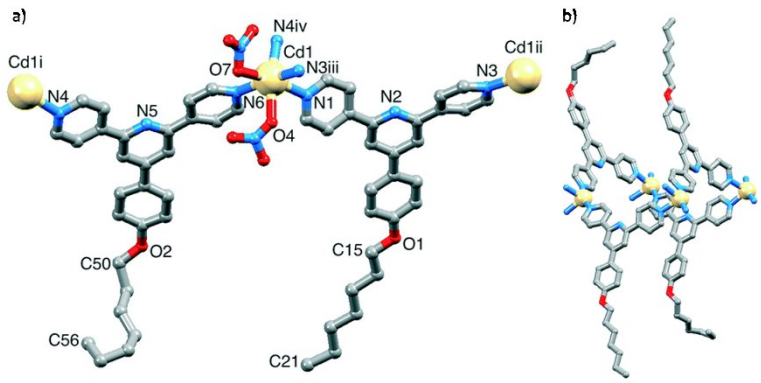

Fig. 84: a) The asymmetric unit (with symmetry generated atoms) in $[\{Cd(NO_3)_2(\mathbf{20})_2\}\cdot 2MeOH]_n$; H atoms and solvent molecules omitted. Symmetry codes: i = 1/2 − x, −1/2 + y, 1/2 − z; ii = 1/2 − x, 1/2 + y, 3/2 − z; iii = 1/2 − x, −1/2 + y, 3/2 − z; iv = 1/2 − x, 1/2 + y, 1/2 − z. Selected bond parameters: Cd1–O4 = 2.363(8), Cd1–O6 = 3.030(10), Cd1–O7 = 2.440(8), Cd1–N1 = 2.399(9), Cd1–$N3^{iii}$ = 2.317(8), Cd1–$N4^{iv}$ = 2.359(9), Cd1–N6 = 2.341(8) Å; O4–Cd1–O7 = 86.0(3); N1–Cd1–N6 = 98.7(3), O7–Cd1–N1 = 165.2(3), O4–Cd1–$N4^{iv}$ = 163.2(3)°. b) A metallomacrocycle in the structure constructed of four Cd atoms and four ligands **20**, adopting an up-down-up-down orientation. Reproduced from ref.[108], published by The Royal Society of Chemistry.

One difference concerns the orientation of the ligands forming the metallocycle in the (4,4) net. In this structure the ligands adopt an up-down-up-down orientation, in contrast to the up-up-down-down arrangement in $[\{Cd_2(NO_3)_4(\mathbf{4})_4\}\cdot CHCl_3\cdot MeOH]_n$. The TOPOS[81] scaffold and the superimposed representation are displayed in Fig. 85a and b. The (4,4) net is defined by the Cd(II) centres, which are the nodes in the network. In contrast to the previous section is this (4,4) net much more regular, which is strongly influenced by the pseudo octahedral geometry of the Cd(II) centres in the structure. The metallocycles have edge lengths of 12.63 Å and 19.938 Å and angles of 86.47° and 94.77°. Alkoxy chains have the possibility to penetrate the metallocycles of the next adjacent network and this orientation of the chains is similar to the one obtained in the previous section. The (4,4) net obtained with $Cd(NO_3)_2$ and the (4,4) nets obtained with $Co(NCS)_2$ are very similar in the dimension of the metallocycle, highlighting, that crystal engineering can lead to similar motifs, when different metal centres (e.g. Co(II) and Cd(II)) have a similar connectivity and geometry in the lattice.

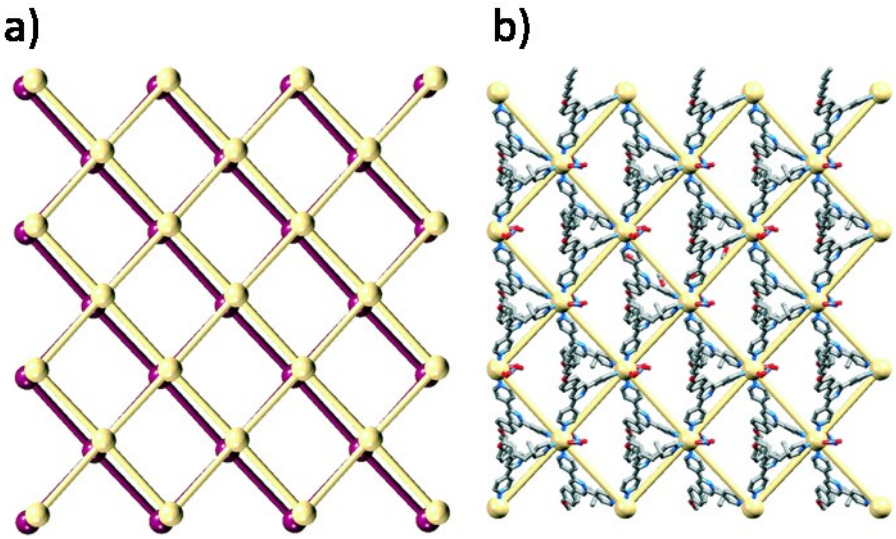

Fig. 85: a) TOPOS[81] representation of the scaffold of [{Cd(NO$_3$)$_2$(**20**)$_2$}·2MeOH]$_n$ representing a (4,4) net. The next adjacent net underneath (purple) is slightly displayed, what allows ″heptyloxy chains to penetrate the adjacent network. b) Superimposed TOPOS[81] representation. Reproduced from ref.[108], published by The Royal Society of Chemistry.

It can be assumed, that ligands with longer alkyloxy chains adopt a similar structural motif, where steric effects of the alkyloxy chains are diminished by "storing" them in them metallocycle of the next adjacent network. The intermolecular interactions of this network are also similar to the ones from the previous section and face-to-face π-stacking of the inner pyridine rings is observed (Fig. 86).

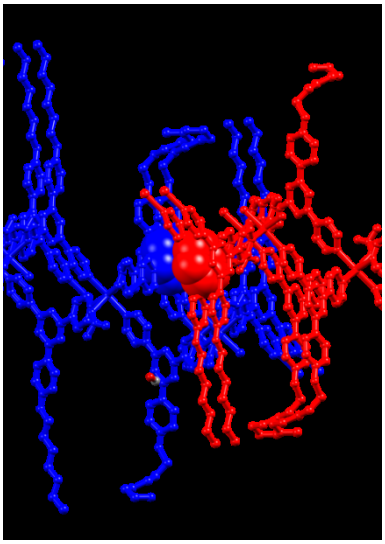

Fig. 86: Face-to-face π-stacking of inner pyridine rings of two adjacent layers in [{Cd(NO$_3$)$_2$(**20**)$_2$}·2MeOH]$_n$.

Additional information can be found in the printed publications (section 18.6).

11.3 [{Cu(**9**)(OMe)(MeOH)}{CF_3SO_3}·MeOH]$_n$

The Cu(I) salt $Cu_2(CF_3SO_3)_2·C_7H_8$ was combined with ligand **9** to obtain the 2D network [{Cu(**9**)(OMe)(MeOH)}{CF_3SO_3}·MeOH]$_n$. The experimental PXRD patterns gave a good match to the patterns predicted from the single crystal data of [{Cu(**9**)(OMe)(MeOH)}{CF_3SO_3}·MeOH]$_n$. Ligand **9** is part of the pyrimidine ligand family and was presented in chapter 9 (1D coordination chains) in combination with $Cu(OAC)_2$. In combination with $Cu(OAC)_2$ a 1D zig-zag chain was obtained. With $Cu_2(CF_3SO_3)_2·C_7H_8$ the attempt was to incorporate a Cu(I) centre into a coordination polymer and to investigate how the preferred coordination number and geometry of Cu(I) influence the self-assembly process. The structure of the repeat unit is displayed in Fig. 87 and reveals that Cu(I) was oxidized to Cu(II) *in situ* and is five-coordinate in the structure with roughly a square base pyramidal geometry around the metal centre. One triflate ion is present in the structure and MeO^- anions bridge two Cu(II) centres. The axial position on each Cu(II) centre is coordinated by a MeOH ligand and each Cu(II) ion has a connectivity of two. The dimer, formed by two Cu(II) centres, bridged by a MeOH and a water ligand, can be considered as one building block, is four connecting and has a distorted square planar connecting geometry.

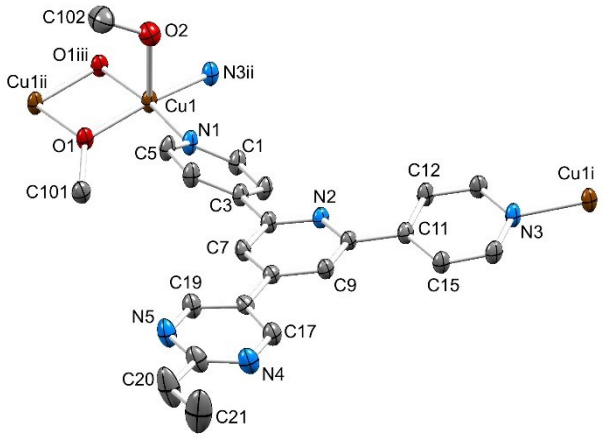

Fig. 87: Structure of the repeat unit (with symmetry generated atoms) in [{Cu(**9**)(OMe)(MeOH)}{CF_3SO_3}·MeOH]$_n$ (ellipsoids plotted at 40% probability level and H atoms omitted). Symmetry codes: i = $^3/_2$–x, $^1/_2$+y, $^1/_2$–z; ii = $^3/_2$–x, –$^1/_2$+y, $^1/_2$–z; iii = 2–x, 1–y, –z. Selected bond parameters: Cu1–$N3^{ii}$ = 2.008(3), Cu1–O1 = 1.944(2), Cu1–$O1^{iii}$ = 1.946(2), Cu1– N1 = 2.008(2), Cu1–O2 = 2.301(3), Cu1–$Cu1^{ii}$ = 3.0454(8) Å; N1–Cu1–O1 = 93.69(10), N1–Cu1–O2 = 87.27(11), O1–Cu1–O2 = 105.10(10), $N3^{ii}$–Cu1–$O1^{iii}$ = 92.67(9), $N3^{ii}$–Cu1–N1 = 97.14(10), $O1^{iii}$–Cu1–O1 = 76.95(9), $N3^{ii}$–Cu1–O2 = 94.15(11), $O1^{iii}$–Cu1–O2 = 92.25(10), $N3^{ii}$–Cu1–O1 = 158.33(11), $O1^{iii}$–Cu1–N1 = 170.18(10)°. Reprinted with permission from ref.[99], copyright 2018 American Chemical Society.

Each ligand **9** bridges two Cu-dimer centres (the centroid between both Cu(II) centres acts as the nodes in the network) which leads to the formation of a (4,4) net. The TOPOS[81] superimposed structure of the net is displayed in Fig. 88a and a regular chess board motif with square shaped metallocycles is obtained (angles in the metallocycle are 85.04° and 94.96°). The ligands are almost flat with respect to the network scaffold and the cavity inside each metallocycle is occupied by two ligands **9** which slip over each other and interact via face-to-face π-stacking of the inner pyridine and the pyrimidine ring of both ligands (Fig. 88b). This stands in contrast to the (4,4) nets obtained with $Co(NCS)_2/CdNO_3$ (connectivity of four) and the ditopic 4,2':6',4"-terpyridines **1**, **2**, **6** and **10** (section 11.1). The Cu-dimer in $[\{Cu(\mathbf{9})(OMe)(MeOH)\}\{CF_3SO_3\}\cdot MeOH]_n$ leads to larger metallocycles (length of the edges in a metallocycle are 14.227 Å) compared to the (4,4) nets obtained with $Co(NCS)_2$ (edge lengths range between 12.913 Å and 13.637Å). The larger metallocycles in the network of $\{[Cu(\mathbf{9})(OMe)(MeOH)][CF_3SO_3]\cdot MeOH\}_n$ allows ligands **9** to occupy the space in the meshes. It can be assumed, that bulkier ligands bearing e.g. *n*hexyloxy or *n*heptyloxy chains (**4** and **20**) would lead to a change in the ligand orientation, as the space in the metallocycle is limited. A disruption of the topology, the packing or the whole assembly could be the result.

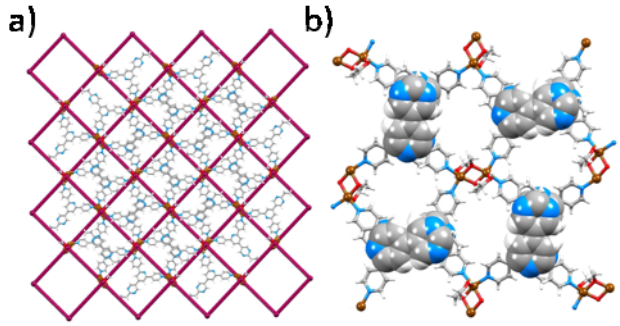

Fig. 88: a) The TOPOS[81] superimposed representation of the (4,4) net in $[\{Cu(\mathbf{9})(OMe)(MeOH)\}\{CF_3SO_3\}\cdot MeOH]_n$. b) Intrachain π-stacking of ligands, occupying the cavity inside the metallocycle (formed by four Cu-dimer nodes). Reprinted with permission from ref.[99], copyright 2018 American Chemical Society.

Adjacent networks in in $[\{Cu(\mathbf{9})(OMe)(MeOH)\}\{CF_3SO_3\}\cdot MeOH]_n$ interact via hydrogen-bonding of coordinating MeOH molecule with the MeOH molecule (OH…H distance = 1.9 Å) present as a guest in the structure. The guest MeOH molecules also form hydrogen-bonds to the N-atom of a pyrimidine ring (OH…N distance = 2.101 Å). Both hydrogen-bonds are highlighted in green in Fig. 89.

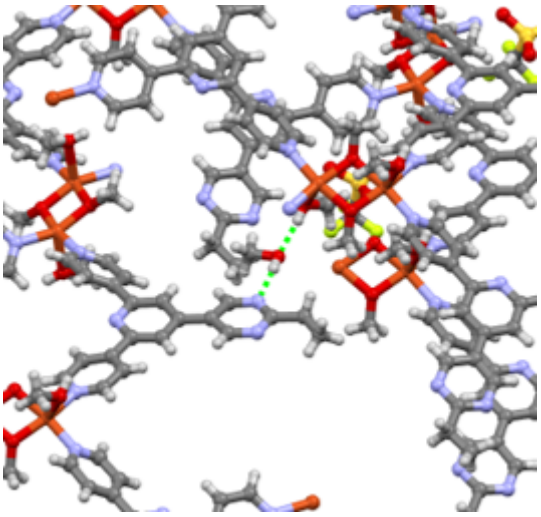

Fig. 89: Intermolecular hydrogen-bonding of coordinating MeOH molecule with the MeOH molecule present as a guest in the structure and the N-atom of a pyrimidine ring.

Additional information can be found in the printed publications (section 18.5).

11.4 $[Zn_2Cl_4(\mathbf{13})]_n$ and $[Zn_2Cl_4(\mathbf{14})\cdot 2MeOH]_n$

The construction of a 2D coordination net with $ZnCl_2$, which prefers a pseudo tetrahedral geometry and often has a connectivity of two in the lattice, requires a ligand with more than two donor atoms. Ligand **13** is a bis(4,2':6',4"-terpyridine), with the central benzyl ring substituted in the 1 and 4 positions by a 4,2':6',4"-terpyridine unit und in the 2 and 5 positions by ^{n}hexyloxy chains. The ^{n}hexyloxy chains hinder π-stacking of molecules of **13** in solution and increase the solubility of the compound in halogenated solvents (e.g. chloroform, dichlorobenzene) tremendously. This is the main reason why these chains were incorporated but thinking in terms of host guest interactions, it could be useful to have the alcohol functionality on the phenylene ring available, to incorporate substituents, which can interact with guests in the lattice. This idea will be discussed in the outlook of this thesis. Ligand **14** is analogous to **13** but bears ^{n}decyloxy chains instead of ^{n}hexyloxy. Their corresponding structures with $ZnCl_2$ are similar and $[Zn_2Cl_4(\mathbf{14})\cdot 2MeOH]_n$ will be presented in more detail. The experimental PXRD patterns gave a good match to the patterns predicted from the single crystal data of $[Zn_2Cl_4(\mathbf{14})\cdot 2MeOH]_n$.

Ligand **13** has four donor atoms and coordinates four $ZnCl_2$ units in the structure. The repeat unit of $[Zn_2Cl_4(\mathbf{13})]_n$ is displayed in Fig. 90. Each side of the tetratopic ligand retains its rigid V-shaped coordination, but both 4,2':6',4"-terpyridines in ligand **13** are very flexible with

respect to one another. Any angle of rotation between 0 and 360° around the C-C bonds, connecting the phenylene spacer and 4,2':6',4"-terpyridine unit, is possible. $[Zn_2Cl_4(\mathbf{13})]_n$ crystallizes in the space group *C*2/*c* and the asymmetric unit contains one $ZnCl_2$ and half a ligand **13**. In $[Zn_2Cl_4(\mathbf{13})]_n$ both 4,2':6',4"-terpyridines are in plane (by symmetry) and the inner phenylene ring is slightly twisted out of this plane (Fig. 90). ^{n}Hexyloxy chains are linear extended and large ellipsoids indicate movement and vibration of these chains in the solid state.

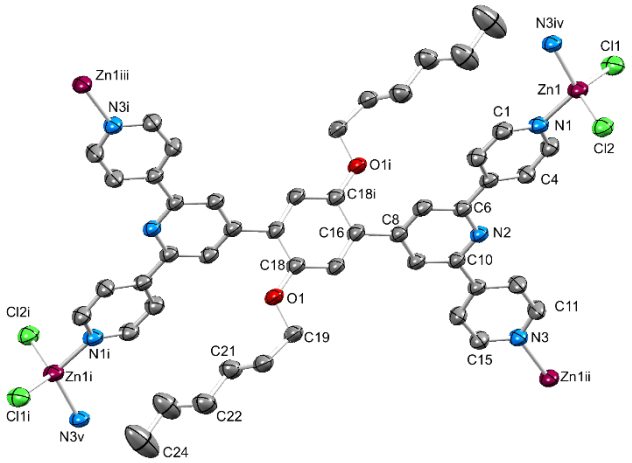

Fig. 90: The repeat unit (with symmetry generated atoms) in $[Zn_2Cl_4(\mathbf{13})]_n$ (H atoms omitted; ellipsoids plotted at 40% probability level). Symmetry codes: i = 1–*x*, –*y*, –*z*; ii = *x*, 1–*y*, $-^1/_2$+*z*; iii = 1–*x*, 1+*y*, $^1/_2$–*z;* iv = *x*, 1–*y*, $^1/_2$+*z;* v = 1–*x*, –1+*y*, $-^1/_2$–*z*. Selected bond parameters: Zn1–N1 = 2.026(3), Zn1–N3^{iv} = 2.034(3), Zn1–Cl1 = 2.2137(11), Zn1–Cl2 = 2.2445(12), O1–C18 = 1.361(4), O1–C19 = 1.439(4) Å; N3^{iv}–Zn1–Cl1 = 107.06(9), N3^{iv}–Zn1–Cl2 = 106.02(10), Cl1–Zn1–Cl2 = 123.64(5), N3^{iv}–Zn1–N1 = 112.07(12), Cl1–Zn1–N1 = 104.68(9), Cl2–Zn1–N1 = 103.35(9), C18–O1–C19 = 118.8(3)°. Reproduced from ref.[111], published by The Royal Society of Chemistry.

The 2D sheets observed in $[Zn_2Cl_4(\mathbf{13})]_n$ consist of metallocycles defined by four Zn atoms bridged via two 4,2':6',4"-terpyridine units (yellow in Fig. 92a) and two pyridine rings of opposite 4,2':6',4"-terpyridines in one ligand **13** ("half ligands" are coloured blue in Fig. 92a). The pseudo tetrahedral connecting geometry of the Zn(II) centre and the orientation of the ligands induces an up-up-up orientation of 4,2':6',4"-terpyridine units in the bottom part of the layer (yellow in Fig. 91) and a down-down-down orientation of 4,2':6',4"-terpyridine units in the top part of the sheet (purple in Fig. 91). An imaginary chain is formed by 4,2':6',4"-terpyridine units with Zn(II) centres.

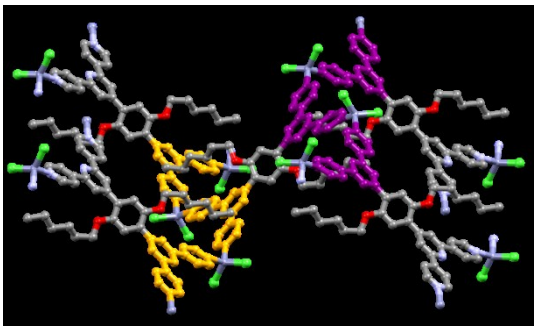

Fig. 91: Construction of the 2D sheet in $[Zn_2Cl_4(\mathbf{13})]_n$ visualized by two 4,2':6',4"-terpyridine units per ligand **13** pointing either up (yellow) or down (purple) in the sheets.

The blue coordination motif (Fig. 92a) connects the "imaginary" chains and lets them propagate into the second dimension. Fig. 92b and c show the layers from the side and highlight alignment of ^{n}hexyloxy chains in $[Zn_2Cl_4(\mathbf{13})]_n$ and ^{n}decyloxy chains in $[Zn_2Cl_4(\mathbf{14})\cdot 2MeOH]_n$.

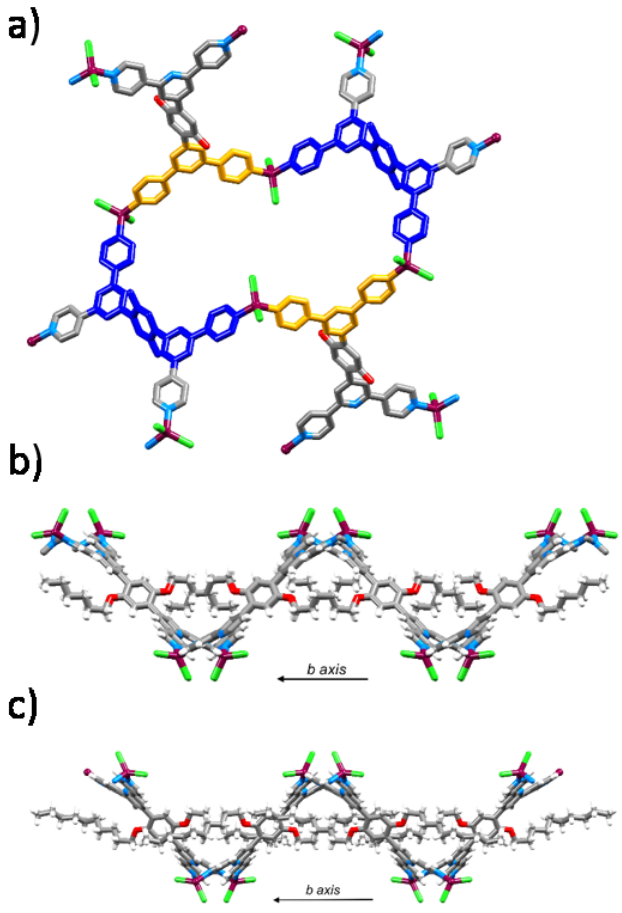

Fig. 92: (a) One metallocycle within the network in $[Zn_2Cl_4(\mathbf{13})]_n$ contains four Zn atoms, two complete 4,2':6',4"-tpy domains (orange) and two 'half-ligands' (blue). ^{n}Hexyloxy chains and H atoms are omitted for clarity. One part of the nets in (b) $[Zn_2Cl_4(\mathbf{13})]_n$ and (c) $[Zn_2Cl_4(\mathbf{14})\cdot 2MeOH]_n$ showing the wave like motif and the aligned ^{n}hexyloxy (in (b)) and ^{n}decyloxy (in (c)) chains along to the *b*-axis. Reproduced from ref.[111], published by The Royal Society of Chemistry.

The connectivity of the nodes (centroid of the phenylene ring in **13**) is nicely represented by the TOPOS[81] images in Fig. 93. The scaffold of $[Zn_2Cl_4(\mathbf{13})]_n$ is illustrated and the colours (red and blue in Fig. 93) represent two parallel interpenetrating nets. The structure is a (4,4) two-fold interpenetrating network.

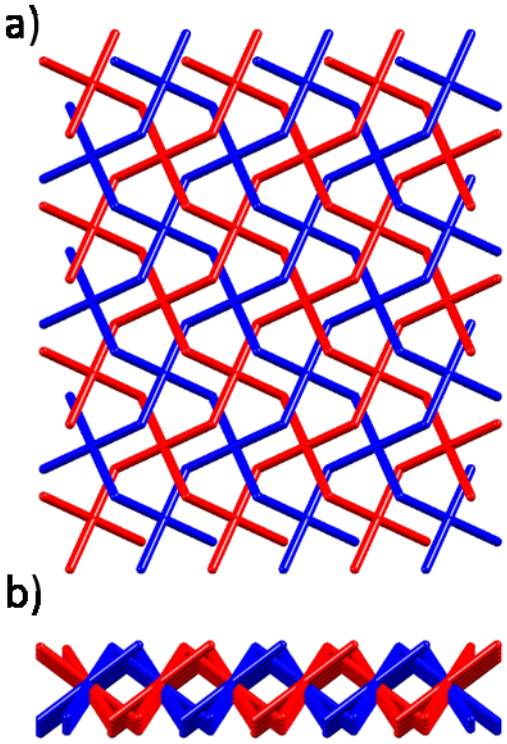

Fig. 93: The scaffold of $[Zn_2Cl_4(\mathbf{13})]_n$ generated with TOPOS[81]. a) View from top, showing two 2D interpenetrating networks. b) view of the networks from the side. Reproduced from ref.[111], published by The Royal Society of Chemistry.

The interpenetrating layers show van der Waals interactions of *n*hexyloxy chains (space-filling representation in red and blue, Fig. 94). Adjacent layers interact via face-to-face π-stacking of inner and outer pyridine rings of 4,2':6',4''-terpyridine units (blue and green in Fig. 94).

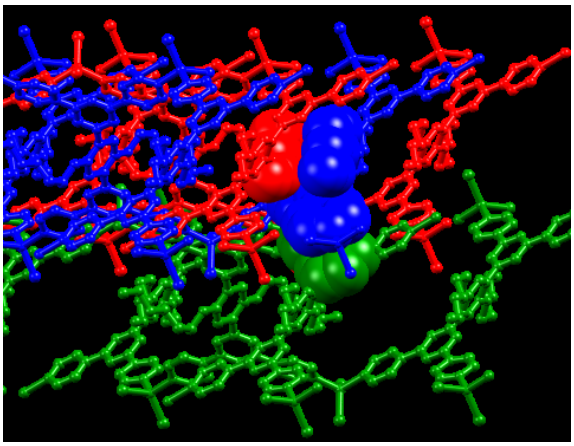

Fig. 94: Intermolecular interactions present in $[Zn_2Cl_4(\mathbf{13})]_n$. Interpenetrating layers (red and blue) interact via van der Waals forces between ^{n}hexyloxy chains and adjacent layers (blue and green) interact via double face-to-face π-stacking of outer and inner pyridine rings.

Additional information can be found in the printed publications (section 18.9).

11.5 $[\{Co(NCS)_2(\mathbf{15})\}\cdot 2CHCl_3]_n$

Ligand **15** is the outsider in this series of ligands, as it is neither a 4,2':6',4"-terpyridine nor a 3,2':6',4"-terpyridine. Ligand **15** was synthesized on purpose using Wang and Hanan's one-pot synthesis[79] without the addition of aqueous ammonia in the last step. Ligand **15** is constructed of a phenylene ring, substituted in the 2 and 5 positions with ^{n}octyloxy chains. The chains are linear extended and well resolved in the crystal structure (Fig. 95). The 1 and 4 positions are substituted by two 1,5-di(pyridin-3-yl)pentane-1,5-dione units. Each unit consist of two pyridine-3-yl rings, that enable coordination similar to a 3,2':6',3"-terpyridine, but with even greater flexibility in the direction of their coordination. Ligand **15** was combined with $Co(NCS)_2$, which often shows a connectivity of four in coordination polymers, and the 2D planar chess board structure $[\{Co(NCS)_2(\mathbf{15})\}\cdot 2CHCl_3]_n$ was obtained (Fig. 95). $[\{Co(NCS)_2(\mathbf{15})\}\cdot 2CHCl_3]_n$ crystallizes in the space group *P*-1 and the asymmetric unit contains half a ligand molecule. The experimental PXRD patterns gave a good match to the patterns predicted from the single crystal data of $[\{Co(NCS)_2(\mathbf{15})\}\cdot 2CHCl_3]_n$.

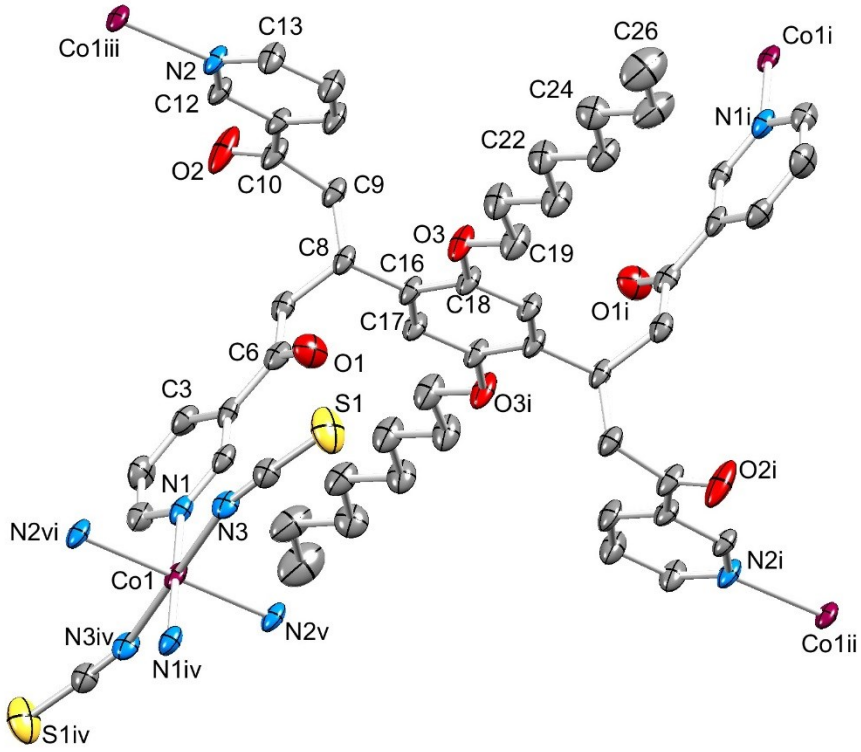

Fig. 95: Structure of the repeat unit in $[\{Co(NCS)_2(\mathbf{15})\}\cdot 2CHCl_3]_n$ with symmetry generated atoms; H atoms and solvent molecules are omitted. Ellipsoids are plotted at 40% probability. Symmetry codes: i = –1+*x*, 1+*y*, 1+*z*; ii = –1+*x*, *y*, 1+*z*; iii = *x*, –1+*y*, *z*; iv = 2–*x*, 3–*y*, –*z*; v = *x*, 1+*y*, *z*; vi = 2–*x*, 2–*y*, –*z*. Selected bond parameters: Co1–N1 = 2.196(4), Co1–N3 = 2.070(4), Co1–N2^{v} = 2.199(4), O1–C6 = 1.216(6), O2–C10 = 1.193(7), O3–C18 = 1.383(6), O3–C19 = 1.413(6) Å; N1–Co1–N3 = 91.13(17), N_{tpy}–Co1–N_{tpy} range 87.68(16)–92.32(16)°. Reproduced from ref.[32], published by MDPI.

The formation of the 2D sheet is different to the structure from the previous section. The increased flexibility allows **15** to adopt an almost flat orientation between Co(II) centres. The nodes of the net are the centroid of the phenylene ring (green in Fig. 96) in **15** and the Co-atom (purple in Fig. 96). A chess board motif, similar to the structures presented in section 11.1 is obtained, with the difference, that the chess board in $[\{Co(NCS)_2(\mathbf{15})\}\cdot 2CHCl_3]_n$ is built by two nodes and not by one. Each node is four connecting and almost square planar and all nodes are part of one plane forming a (4,4) net. The edges of the metallocycle are in 9.054 Å and 10.176 Å in length and the angles are 70.72° and 109.28°. The metallocycles are a lot smaller, than the ones obtained for two-donor 4,2':6',4"-terpyridines combined with $Co(NCS)_2$ (section 11.1), which showed edge lengths of ~ 13 Å.

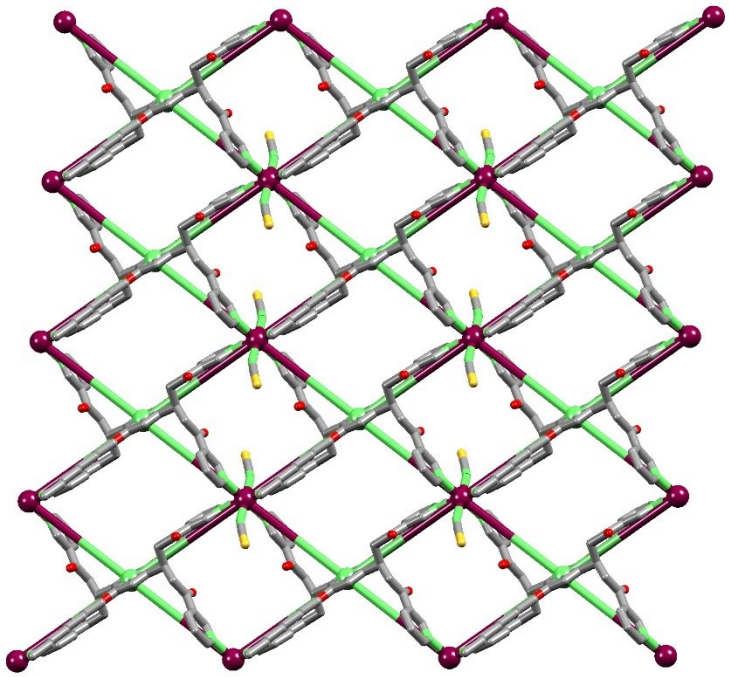

Fig. 96: TOPOS[81] structure overlay of [{Co(NCS)$_2$(**15**)}·2CHCl$_3$]$_n$. ^{n}Octyloxy chains and solvent molecules are omitted for clarity. Reproduced from ref.[32], published by MDPI.

The packing of the chess-boards is displayed in Fig. 97. Linear extended ^{n}octyloxy chains interact via van der Waals interactions and these interactions are the dominating intermolecular forces.

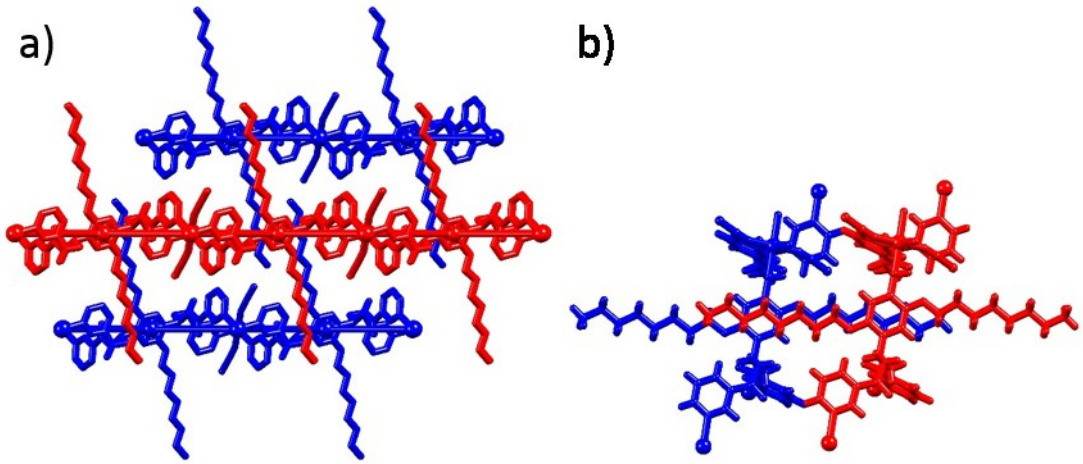

Fig. 97: a) Three adjacent chess boards of [{Co(NCS)$_2$(**15**)}·2CHCl$_3$]$_n$, with alignment of ^{n}octyloxy chains (van der Waals interactions). b) A closer view of the ^{n}octyloxy interactions between neighbouring sheets. Reproduced from ref.[32], published by MDPI.

It is noteworthy, that a structure constructed of centres with a connectivity of four and ligands with four donor atoms can forms a 2D sheet. In the next chapter examples will be presented,

where this combination of building blocks predominantly leads to the formation of 3D structures. One reason for the structural motifs observed in $[\{Co(NCS)_2(\mathbf{15})\}\cdot 2CHCl_3]_n$ can be the high flexibility in coordination of **15** compared to multitopic 4,2':6',4"-terpyridine and 3,2':6',3"-terpyridine ligand. Some rigidity in the linkers appears to be beneficial in the formation of 3D structures and in the control of the self-assembly process. How these structures are constructed is discussed in the next chapter.

Additional information concerning the compound $[\{Co(NCS)_2(\mathbf{15})\}\cdot 2CHCl_3]_n$ can be found in the printed publications (section 18.4).

11.6 Comparison of the structural motifs

The prediction of a 2D structure motif is a lot less reliable, than it was for 1D structures. In this chapter a series of two donor rigid ligands was combined with $Co(NCS)_2$ which favours a square planar four connecting geometry. This combination of building blocks seems to introduce enough control over the self-assembly process, that 2D chess board structures are predominantly obtained. $Cd(NO_3)_2$ is a very flexible metal centre in terms of coordination number and coordination geometry. Differences in connectivity, metal to ligand ratio and connecting geometry lead to the formation of three different 2D motifs, with rather similar ditopic ligands. In the case of $[\{Cd(NO_3)_2(\mathbf{20})_2\}\cdot 2MeOH]_n$ (section 11.2.3) the Cd(II) centres have a similar almost square planar connectivity, like the Co(II) centres (section 11.1). Both metal centres were combined with 4,2':6',4"-terpyridine ligands of comparable size and (4,4) nets with similar edge lengths (~ 13 Å in the Co(II) nets and 12.63/12.938 Å in the Cd(II) net) and angles of the metallocycles were obtained. Concerning crystal engineering, the choice of metal centre has a big influence on the predictability of structural motifs. Metal centres, like Co(II) can favour an octahedral coordination geometry and favour a connectivity of four in a coordination polymer allow some control of the self-assembly processes. The flexibility in coordination geometry, connectivity and coordination number of the Cd(II) centre in the coordination polymers presented in section 11.2 demonstrated, that $Cd(NO_3)_2$ is not recommended as a reliable metal salt for the control of the self-assembly processes. When tetratopic ligands are combined with metal centres, having a connectivity of two or four, a clear trend, which structural motif is obtained can't be observed at all. Even though rigid 4,2':6',4"-terpyridine units are used in the tetratopic ligands, the free rotation of these groups along the C-C bond connecting phenylene rings and 4,2':6',4"-terpyridine units enables too many ligand

geometries and connection possibilities to predict a structure outcome. In some discussed structures 4,2':6',4"-terpyridine ligands with alkyloxy chains of varying length were incorporated. Alkyloxy chains have an influence on the packing interaction. As their bulkiness increases a respond in the packing motifs of the corresponding networks is. This was demonstrated in the $Cd(NO_3)_2$ networks, where the shorter propyloxy chain favoured a (6,3) net and with larger chains (^{n}pentyloxy, ^{n}hexyloxy and ^{n}heptyloxy) a (4,4) net was observed. In tetratopic bis(4,2':6',4"-terpyridine) ligands, combined with $ZnCl_2$ similar very similar structural motifs were observed, even though chains of different length (^{n}hexyloxy and ^{n}decyloxy) were incorporated. The best control and predictability towards 2D (4,4) nets was achieved with ditopic 4,2':6',4"-terpyridines and $Co(NCS)_2$.

12 3D COORDINATION FRAMEWORKS

Four 3D structures are presented in this chapter. It was discussed in the previous chapter, that the control of the self-assembly processes decreases tremendously on going from 1D to 2D structures. For 3D structures a predictability of the outcome of the motif is not possible with the ligands presented. A tendency towards the formation of 3D structures can be attributed to the fact, that metal centres with a connectivity of four are combined with tetratopic ligands.

12.1 $[Co(NCS)_2(\mathbf{17})\cdot 4CHCl_3]_n$

The last structure of the previous chapter used the intermediate step of the Wang and Hanan synthesis **13** as the ligand. The synthesis of the corresponding tetratopic bis(3,2':6',3"-terpyridine) was repeated and ligand **17** was successfully synthesized at the second attempt. Ligands **13** and **17** have the same bridging phenylene ring, have four donor atoms and differ in the flexibility of the donor atoms to coordinate to metal ions. The flexibility decreases, when changing the ligand from **13** to **17** and this affects the assembly of the building blocks and the outcome of the structural motif. Ligand **17** reacted with $Co(NCS)_2$ (has a connectivity of four in the structure) and the 3D structure $[Co(NCS)_2(\mathbf{17})\cdot 4CHCl_3]_n$ (Fig. 98) was obtained. The space group is $Pna2_1$ and the asymmetric unit contains one ligand **17** and one $Co(NCS)_2$ unit. The 3,2':6',3"-terpyridine units are twisted with respect to one another by 23.55° (angle between the planes through the inner pyridine rings of each 3,2':6',3"-terpyridine unit). The ^{n}octyloxy chains are bent and embrace the 3,2':6',3"-terpyridine units.

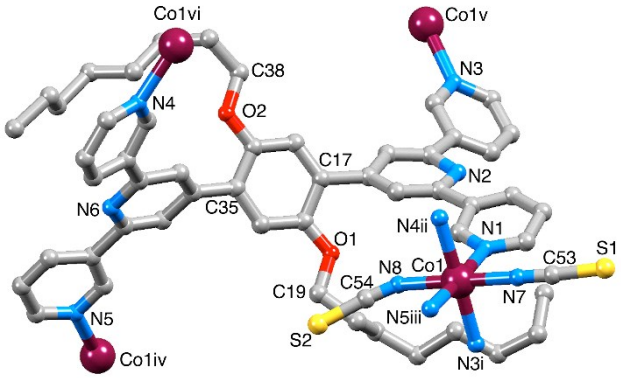

Fig. 98: The repeat unit (with symmetry generated Co atoms) in $[Co(NCS)_2(\mathbf{17})\cdot 4CHCl_3]_n$ (H atoms and solvent molecules omitted). Symmetry codes: i = $^1/_2+x$, $^1/_2-y$, z; ii = $-x$, $1-y$, $-^1/_2+z$; iii = $^1/_2-x$, $^1/_2+y$, $^1/_2-z$; iv = $^1/_2-x$, $-^1/_2+y$, $^1/_2+z$; v = $-^1/_2+x$, $^1/_2-y$, z; vi = $-x$, $1-y$, $^1/_2+z$. Selected bond parameters: Co1–N1 = 2.185(8), Co1–N3i = 2.212(7), Co1–N4ii = 2.204(8), Co1–N5iii = 2.181(8), Co1–N7 = 2.096(8), Co1–N8 = 2.079(8) Å; Co1–N7–C53 = 161.0(8), Co1–N8–C54 = 151.2(8), N1–Co1–N5iii = 176.2(3), N3i–Co1–N4ii = 178.6(3)°. Reproduced from ref.[112], published by The Royal Society of Chemistry.

The 3D-assembly is constructed of [2+2] metallomacrocycles, which are formed by two Co(II) centres and two "half ligands" (yellow in Fig. 99a and b). Metallomacrocycles propagate as a beam in one dimension (view along the a-axis in Fig. 99b). Two coordination sites on each Co(II) centre are used for this propagation, which leaves two connection sites available to coordinate to adjacent [2+2] metallomacrocycles above and underneath. This leads to the 3D assembly motif displayed in Fig. 99b (metallomacrocycles in yellow).

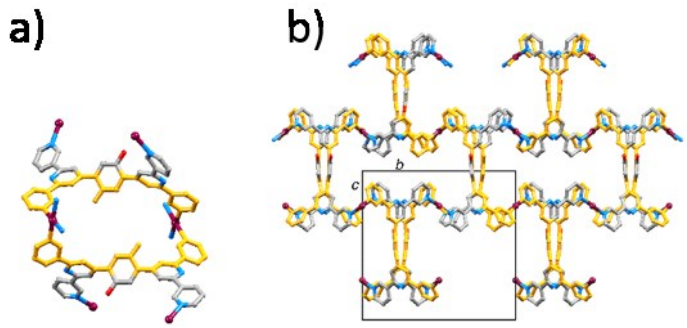

Fig. 99: a) Two Co atoms and two "half ligands" of **17**, forming a [2+2] metallomacrocycle. b) Metallomacrocycles are propagating in one dimension (along the a-axis) and connect metallomacrocyles in the second (along the b-axis) and the third (along the c-axis) dimension. Reproduced from ref.[112], published by The Royal Society of Chemistry.

In the last chapter the use of TOPOS[81] overlay representations was used to represent the connectivity and scaffold of a 2D net. For 3D structures a good visualization relies even more on TOPOS[81] and the scaffold of $[Co(NCS)_2(\mathbf{17})\cdot 4CHCl_3]_n$, is displayed in Fig. 100. The nodes of the 3D net are the centroid of the phenylene ring in ligand **17** and the Co atoms. The Co

nodes are four-connecting square planar and ligand **17** is a tetrahedral four-connecting node. In Fig. 100 only the nodes (centroid of **17** in green, Co in purple) are displayed and the scaffold obtained could be further analyzed with TOPOS[81]. TOPOS[81] described the structure as a $\{4^2.8^4\}$ net and a comparison with net topologies in Stuart Batten's book[12] revealed the **lvt** net topology for $[Co(NCS)_2(\mathbf{17})\cdot 4CHCl_3]_n$.

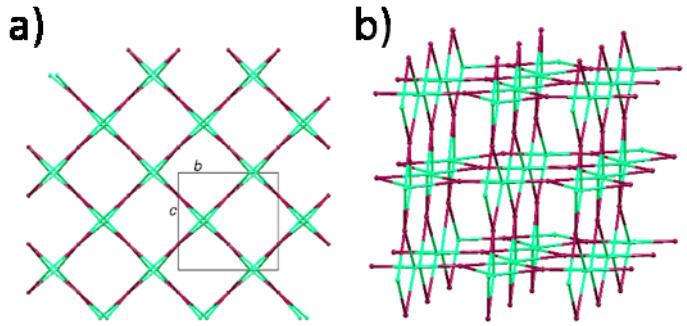

Fig. 100: TOPOS[81] representations of the $\{4^2.8^4\}$ **lvt** net in $[Co(NCS)_2(\mathbf{17})\cdot 4CHCl_3]_n$. a) view down the a-axis. b) Illustration of the 4- and 8-membered metallomacrocycles, described by the Schläfi term $\{4^2.8^4\}$. Reproduced from ref.[112], published by The Royal Society of Chemistry.

Intermolecular interactions are not observed in the 3D structure and the space inside the [2+2] metallomacrocycles is occupied by *n*octyloxy chains and chloroform molecules. The Co…Co distances in the [2+2] metallomacrocycles is 11.53 Å, which is shorter than the Co…Co distance obtained by a bridging 3,2':6',3"-terpyridine unit (13.3 Å).

Additional information can be found in the printed publications (section 18.10).

12.2 $[\{Co(NCS)_2(\mathbf{12})_2\}\cdot 2C_6H_4Cl_2]_n$

The structure in this section was constructed using similar building blocks, namely the tetratopic bis(4,2':6',4"-terpyridine) **12**, which has four donor atoms $Co(NCS)_2$, which has a connectivity of four in the structure. **12** is more rigid and less flexible in its coordination, compared to **17**, which leads to the formation of a different 3D structure. Ligand **12** bears two propyloxy chains on the connecting phenylene ring and two solvent molecules (1,2-dichlorobenzene) are present in the asymmetric unit. A 3D framework was obtained for a combination of **12** and $Co(NCS)_2$ and the repeat unit of $[\{Co(NCS)_2(\mathbf{12})_2\}\cdot 2C_6H_4Cl_2]_n$ is displayed in Fig. 101. $[\{Co(NCS)_2(\mathbf{12})_2\}\cdot 2C_6H_4Cl_2]_n$ crystallizes in the space group $P2_1/c$ and half a ligand **12** is present in the asymmetric unit. The second half is generated via an inversion centre in the centre

of the phenylene ring. The experimental PXRD pattern gave a good match to the pattern predicted from the single crystal data of $[\{Co(NCS)_2(\mathbf{12})_2\}\cdot 2C_6H_4Cl_2]_n$.

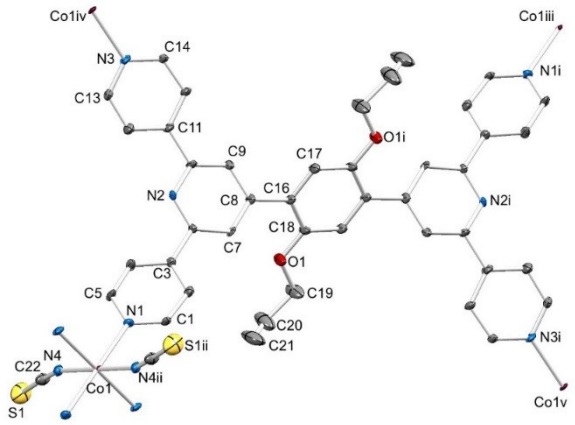

Fig. 101: Structure of the repeat unit in $[\{Co(NCS)_2(\mathbf{12})_2\}\cdot 2C_6H_4Cl_2]_n$ with symmetry generated atoms; H atoms and solvent molecules are omitted. Ellipsoids are plotted at 40% probability. Symmetry codes: i = –*x*, 2–*y*, 1–*z*; ; ii = 1–*x*, 1–*y*, 1–*z*; iii = –1+*x*, 1+*y*, *z*; iv = *x*, $^3/_2$–*y*, $-^1/_2$+*z*; v = –1+*x*, $^3/_2$+*y*, $^1/_2$+*z*. Selected bond parameters: Co1–N1 = 2.173(2), Co1–N4 = 2.047(3), Co1^{iv}–N3 = 2.193(2), O1–C18 = 1.361(4), O1–C19 = 1.431(4) Å; N1–Co1–N4 = 90.47(10)°. Reproduced from ref.[32], published by MDPI.

The nodes in this framework are the same as in the last structure, but here both nodes are square planar (Fig. 102), whereas in the previous section the ligand node was tetrahedral. The topology of the resulting network is defined by the geometry of ligand **12**. This leads to a different net topology and with the help of the TOPOS[81] scaffold representation a $\{6^5.8\}$ **cds** net was identified for $[\{Co(NCS)_2(\mathbf{12})_2\}\cdot 2C_6H_4Cl_2]_n$. The scaffold of $[\{Co(NCS)_2(\mathbf{12})_2\}\cdot 2C_6H_4Cl_2]_n$ is displayed in Fig. 102.

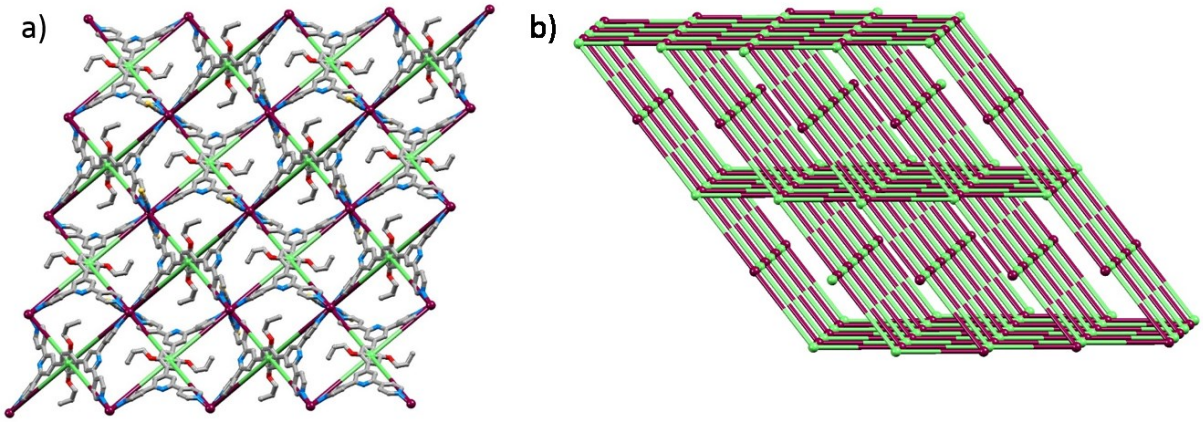

Fig. 102: a) TOPOS[81] structure overly for $[\{Co(NCS)_2(\mathbf{12})_2\}\cdot 2C_6H_4Cl_2]_n$ illustrating connectivity of the square planar nodes. b) Scaffold of the framework generated with TOPOS[81] representing a **cds** topology. Reproduced from ref.[32], published by MDPI.

The cavities in the framework are occupied by 1,2-dichlorobenze molecules and propyloxy chains.

Additional information can be found in the printed publications (section 18.4).

12.3 $[Zn_2Br_4(\mathbf{16})\cdot H_2O]_n$

The two previous structures used two 4-connecting nodes to generate the 3D framework. In this section the organic linker is again a tetratopic bis(4,2':6',4"-terpyridine) with four donor atoms (and acts as the 4-connecting node), but the metal centre is only two connecting ($ZnBr_2$). Ligand **16** is similar to ligand **12** from the previous section but differs in the alkyloxy substitution on the phenylene ring. **16** bears 3-phenylpropoxyl substituents on the phenylene ring. The phenyl ring on the chain was incorporated to introduce π-stacking into the framework, which could lead to host-guest interactions. The incorporation of guests in the framework was not achieved. $[Zn_2Br_4(\mathbf{16})\cdot H_2O]_n$ (Fig. 103) crystallizes in the space group *R*-3 and the asymmetric unit contains half a ligand **16**. The second half is generated by an inversion centre in the centre of the connecting phenylene ring.

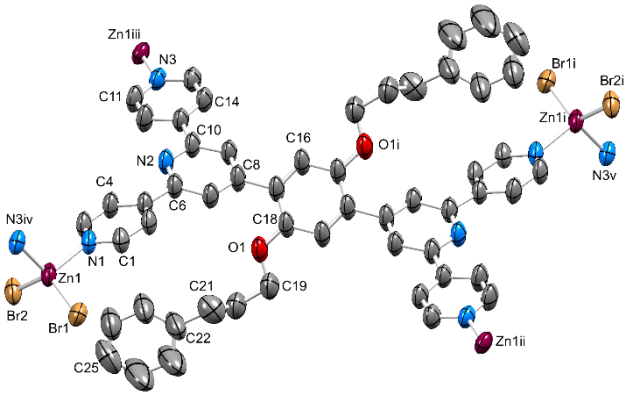

Fig. 103: The repeat unit (with symmetry generated atoms) in $[Zn_2Br_4(\mathbf{16})\cdot H_2O]_n$ (H atoms and water molecule omitted; ellipsoids plotted at 40% probability level). Symmetry codes: i = 1–*x*, 1–*y*, 2–*z*; ii = $^1/_3$–*x*+*y*, $^2/_3$–*x*, $^2/_3$+*z*; iii = $^2/_3$+*x*+*y*, $^1/_3$+*x*, $^4/_3$–*z*; iv = –$^1/_3$+*y*, $^1/_3$–*x*+*y*, $^4/_3$–*z*; v = $^4/_3$–*y*, $^2/_3$+*x*–*y*, $^2/_3$+*z*. Selected bond parameters: Zn1–N3^{iv} = 2.052(4), Zn1–Br1 = 2.3635(8), Zn1–Br2 =2.3462(8), Zn1–N1 = 2.058(3), O1–C18 = 1.382(6), O1–C19 = 1.435(8) Å; N3^{iv}–Zn1–Br1 = 104.90(11), N3^{iv}–Zn1–Br2 = 106.83(10), Br1–Zn1–Br2 = 126.32(4), N3^{iv}–Zn1–N1 = 105.99(15), Br1–Zn1–N1 = 105.36(11), Br2–Zn1–N1 = 105.97(11), C18–O1–C19 = 119.4(4)°. Reproduced from ref.[111], published by The Royal Society of Chemistry.

The centroid of the linking phenylene ring acts as the node in the 3D framework and the metal ions take the role as linkers. Two interpenetrating 3D frameworks were identified in

$[Zn_2Br_4(\mathbf{16})\cdot H_2O]_n$ and TOPOS[81] described the net with the Schläfi symbol $\{6^4\cdot8^2\}$ (Fig. 104). A **nbo** net topology was identified for $[Zn_2Br_4(\mathbf{16})\cdot H_2O]_n$.

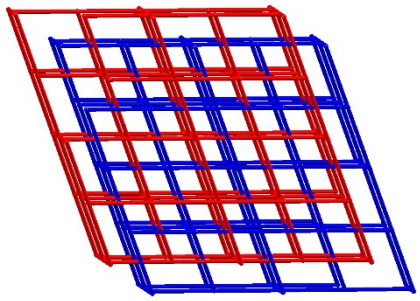

Fig. 104: The scaffold of two interpenetrating $\{6^4\cdot8^2\}$ **nbo** nets in $[Zn_2Br_4(\mathbf{16})\cdot H_2O]_n$, represented by TOPOS[81]. Reproduced from ref.[111], published by The Royal Society of Chemistry.

The *R*-3 space group contains a 3-fold rotation symmetry element, which lead to the formation of hexagonal channels presented in Fig. 105. Phenyl rings of 3-phenylpropoxyl are located inside the channel and interact with pyridine rings of **16** in the next channel via face-to-face π-stacking (Fig. 105a). The colours red and blue are illustrating the interactions between the two neighbouring channels in the framework. Adjacent channels lead to the formation of a honey-comb motif (viewed down the c-axis in Fig. 105a). The void space in the channels (Fig. 105b) was calculated with Mercury v.3.7[83] to be ~65% of the total volume. The void space is occupied by solvent molecules, that could not be resolved. Several attempts to replace the solvent molecules with bigger aromatic guests (fullerene-C_{60}, anthracene, naphthalene, pyrene) were unsuccessful. $[Zn_2Br_4(\mathbf{16})\cdot H_2O]_n$ might be tested in gas-sorption experiments, but more material has to be synthesized.

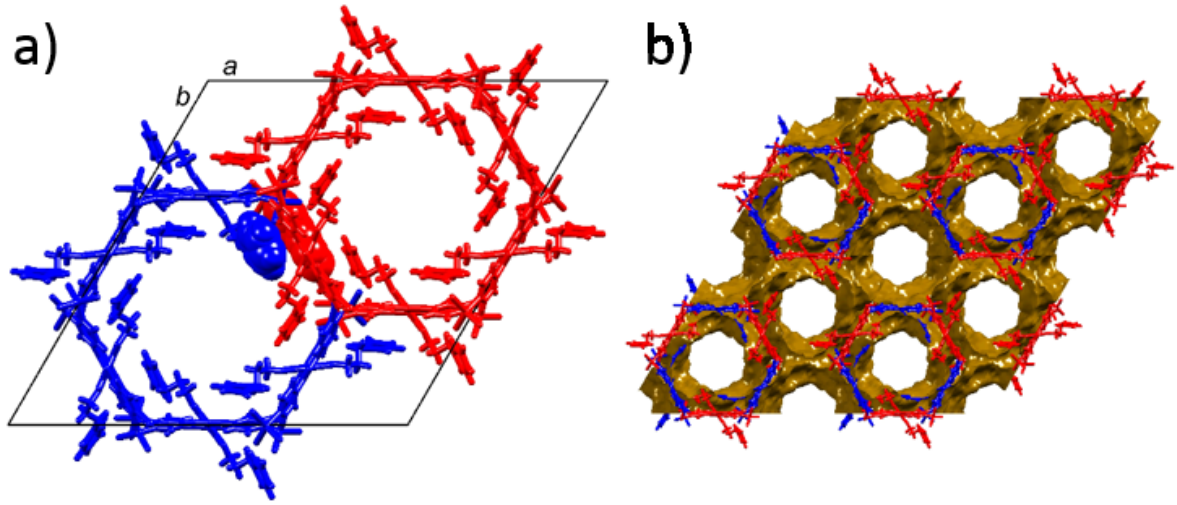

Fig. 105: a) Two interpenetrating (red and blue) frameworks of $[Zn_2Br_4(\mathbf{16})\cdot H_2O]_n$ viewed down the c-axis. Hexagonal channels were observed, and face-to-face π-stacking (space-filling representation) between the phenyl ring of 3-phenylpropoxyl and two pyridine rings of adjacent frameworks.. b) The honey-comb motif observed in $[Zn_2Br_4(\mathbf{16})\cdot H_2O]_n$ with a solvent occupied void space of ~65% of the total volume. Reproduced from ref.[111], published by The Royal Society of Chemistry.

Of all 3D materials presented in this thesis $[Zn_2Br_4(\mathbf{16})\cdot H_2O]_n$ can be viewed as a MOF. A void space of ~ 65% is remarkable for a 3D two-fold interpenetrating structure and this makes it the most promising of all structures presented in this thesis. Interpenetration in 3D materials is frequently observed[24, 113-115] when the organic ligand is relatively large and leads to a large grid in the network[5]. Interpenetration can increase the void space[116] and enhance the stability of the framework[5, 117-118]. Stability and large pore size are two very important properties of a MOF.

Additional information can be found in the printed publications (section 18.9).

12.4 $[Co_2(NCS)_4(\mathbf{4})_4]_n$ and $[\{Co_2(NCS)_4(\mathbf{5})_4\}\cdot 2CHCl_3\cdot MeOH]_n$

The two final structures of this thesis are costructed using the reverse building block approach from the previous section. Two donor 4,2':6',4''-terpyridines, substituted in the 4' position with 4-(^{n}hexyloxy)benzene (**4**) or 4-(^{n}nonyloxy)benzene (**5**), were combined with $Co(NCS)_2$. The NCS^- ligands are *trans* and Co(II) has a square planer connectivity of four. 3D structures of $[Co_2(NCS)_4(\mathbf{4})_4]_n$ (Fig. 106) and $[\{Co_2(NCS)_4(\mathbf{5})_4\}\cdot 2CHCl_3\cdot MeOH]_n$ were obtained in collaboration with Dr. Mateusz B. Pitak and Prof. Dr. Simon J.Coles from the University of Southampton, UK, who collected and solved the structures. In the bulk material of $[Co_2(NCS)_4(\mathbf{4})_4]_n$ two different crystals were picked and their structures were solved. $[Co_2(NCS)_4(\mathbf{4})_4]_n$ crystallized in the space groups $P4_12_12$ and $P4_32_12$, which are enantiomorphic pairs. The direction of 4-fold screw axis along the c-axis in the tetragonal space groups defines the chirality of the material. The Flack parameters are 0.21(3) and 0.16(2), respectively and describes, that the structures contain 21% and 16% of the second enantiomorph. The structure which crystallized in the space group $P4_32_12$ is discussed here.

$[\{Co_2(NCS)_4(\mathbf{5})_4\}\cdot 2CHCl_3\cdot MeOH]_n$ crystallized in the chiral tetragonal space groups $P4_12_12$. Structures $[Co_2(NCS)_4(\mathbf{4})_4]_n$ and $[\{Co_2(NCS)_4(\mathbf{5})_4\}\cdot 2CHCl_3\cdot MeOH]_n$ contain four ligands **4** and **5** and two $Co(NCS)_2$ building blocks in the asymmetric unit, respectively. The packing and assembly of the 3D frameworks is similar and $[\{Co_2(NCS)_4(\mathbf{5})_4\}\cdot 2CHCl_3\cdot MeOH]_n$ will not be discussed in detail. $[Co_2(NCS)_4(\mathbf{4})_4]_n$ showed disorder in the NCS^- ligands, which was removed in the following pictures for a better visualization. The experimental PXRD patterns gave a good match to the patterns predicted from the single crystal data of $[Co_2(NCS)_4(\mathbf{4})_4]_n$ and $[\{Co_2(NCS)_4(\mathbf{5})_4\}\cdot 2CHCl_3\cdot MeOH]_n$.

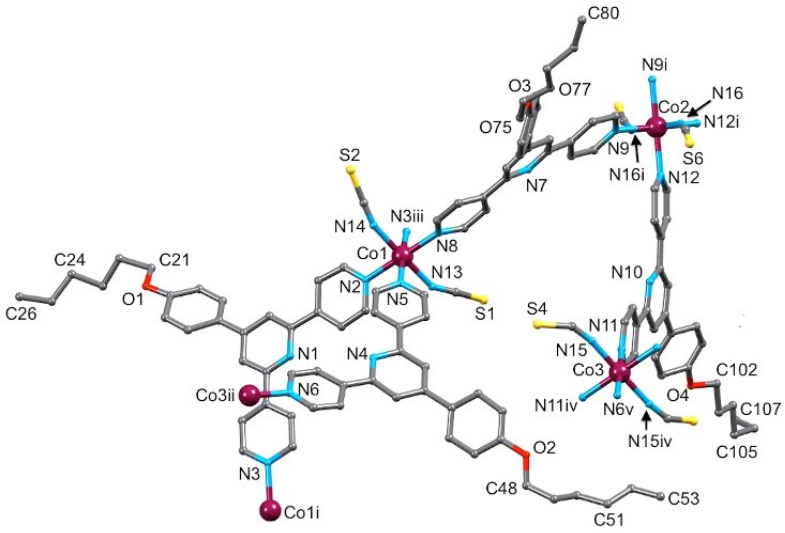

Fig. 106: The asymmetric unit of $[Co_2(NCS)_4(\mathbf{4})_4]_n$ with symmetry-generated atoms (space group $P4_32_12$); H atoms are omitted and only the major sites of the disordered sites are shown. Symmetry codes: i = y, *x*, 1–*z*; ii = $-^1/_2+y$, $^1/_2-x$, $^1/_4+z$; iii = $^1/_2-y$, $-^1/_2+x$, $-^1/_4+z$; iv = 1–*y*, 1–*x*, $^3/_2-z$; v = $^1/_2-x$, $^1/_2+y$, $^7/_4-z$. Selected bond distances: Co1–N2 = 2.166(5), Co1–N3iii = 2.173(5), Co1–N5 = 2.129(5), Co1–N8 = 2.159(5), Co1–N13 = 2.100(6), Co1–N14 = 2.082(6), Co2–N12 = 2.209(5), Co2–N12i = 2.209(5), Co2–N16 = 2.093(7), Co2–N9 = 2.170(3), Co3–N6 = 2.163(5), Co3–N11 = 2.182(5), Co3–N15 = 2.073(7) Å. Reproduced from ref.[98], published by The Royal Society of Chemistry.

The 3D framework has a 6^6 term symbol (obtained with TOPOS[81]) and a **neb** topology. Co atoms are 4-connecting nodes and these nodes are connected by ligands **4**. Six ligands and six $Co(NCS)_2$ units form hexamers with a chair conformation and six hexamers combined form a diamantane motif[119] (Fig. 107).

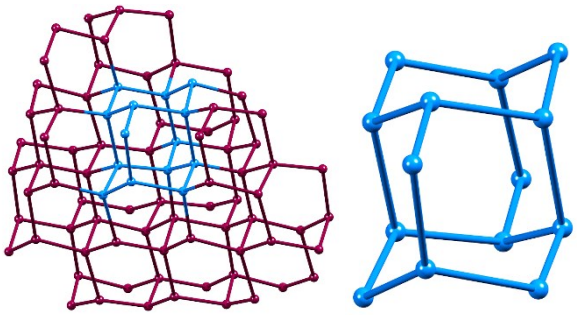

Fig. 107: The TOPOS[81] representation of the scaffold (the Co(II) centres are the nodes) of $[Co_2(NCS)_4(\mathbf{4})_4]_n$ with the diamantane motif highlighted in blue. Reproduced from ref.[98], published by The Royal Society of Chemistry.

A superimposed TOPOS[81] representation for $[Co_2(NCS)_4(\mathbf{4})_4]_n$ is displayed in Fig. 108a and illustrates the orientation of ^{n}hexyloxy chains in the framework. Fig. 108b shows the scaffold of $[\{Co_2(NCS)_4(\mathbf{5})_4\}\cdot 2CHCl_3\cdot MeOH]_n$ forming a similar **neb** net compared to $[Co_2(NCS)_4(\mathbf{4})_4]_n$.

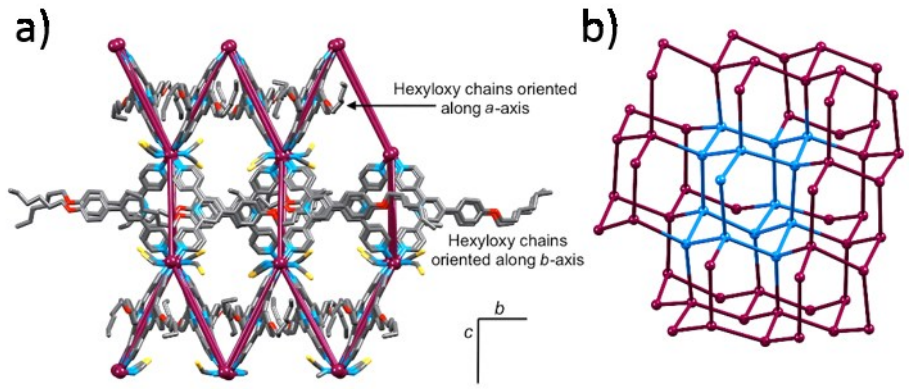

Fig. 108: a) TOPOS[81] overlay structure of $[Co_2(NCS)_4(\mathbf{4})_4]_n$ viewed down the a-axis (the Co(II) centres are the nodes), with hexyloxy chains orientating along the a- and b-axis. b) Similar **neb** topology observed in $[\{Co_2(NCS)_4(\mathbf{5})_4\}\cdot 2CHCl_3\cdot MeOH]_n$; the 6^6 unit is highlighted in blue. Reproduced from ref.[98], published by The Royal Society of Chemistry.

The structures presented here are part of a collection of structures, that combine $Co(NCS)_2$ with ditopic 4,2':6',4"-terpyridines ligands. In section 11.1 four structures were presented, where 4,2':6',4"-terpyridine was substituted in the 4' position by a tert-butyl, ferrocenyl or 4-alkoxyphenyl (alkoxy = methoxy or ethoxy) group. The combination of building blocks lead exclusively to the formation of (4,4) nets. It is noteworthy, that the ligands in these structures were smaller in size compared to ligands **4** and **5** (bearing ^{n}hexyloxy and ^{n}nonyloxy). In a systematic study of 1D polymer chains constructed using ligands **1** (methoxy), **2** (ethoxy), **4** and **5** in combination with $Zn(OAc)_2$ the change in alkyloxy chain length caused a change in the structural motif from 1D coordination chains to discrete complexes. A similar phenomenon is observed when these ligands are combined with $Co(NCS)_2$. For the (4,4) nets the spacing between adjacent layers increased with an increase in alkyloxy chain length. It can be assumed, that the steric demand of ligands **4** and **5** lead to the change from a (4,4) net to a 3D **neb** net.

Additional information can be found in the printed publications (section 18.11).

12.5 Comparison of the structural motifs

The 3D structures obtained in this chapter were not engineered on purpose but can be considered a product of serendipity. In section 11.5 and section 12.3 two very similar ditopic 4,2':6',4"-terpyridines were combined with zinc halides and in one case a 2D sheet and in the other case a 3D **nbo** net was observed. Another important comparison concerns the 3D structures presented in section 12.4 and the 2D structures in section 11.1. In all six cases the same building

blocks were used, namely the four connectivity $Co(NCS)_2$ and two-donor 4,2':6',4''-terpyridines, of varying alkyloxy chain length. Four 2D (4,4) nets and two 3D **neb** nets were obtained. It can be assumed, that the longer *n*hexyloxy and *n*nonyloxy chains might have influenced the packing in the structures in a way, that favours a 3D assembly over a 2D one.

13 GENERAL CONCLUSION

In this PhD thesis ditopic and tetratopic 4,2':6',4"-terpyridines, 3,2':6',3"-terpyridines, bis(4,2':6',4"-terpyridines) and bis(3,2':6',3"-terpyridines) ligands were presented and their ability to form multidimensional structures with various metal salts was presented. Crystal engineering has the aim of controlling the self-assembly process of organic ligands and metal centres and this task has been achieved in several cases. Metal centres, that favour a certain connectivity in the coordination polymer take an important role in the control of the self-assembly process. Many different metal salts were presented throughout the thesis and the most promising one is $Co(NCS)_2$ with the often-observed connectivity of four and its square planar connection geometry, induced by the *trans* positions of NCS^- ligands in the structures. With ditopic 4,2':6',4"-terpyridines, that bear no, or short alkyloxy chains, 2D (4,4) nets are frequently observed. With ditopic 4,2':6',4"-terpyridines, that bear long alkyloxy chains (*n*hexyloxy and *n*nonyloxy) 3D **neb** nets were observed. It can be assumed, that the change in alkyloxy chain length is responsible for this change from 2D network to 3D framework. Important but less controllable metal salts are zinc halides. Zinc halides, incorporated into the coordination polymers presented in this thesis have a connectivity of two and a distorted tetrahedral geometry around the metal centre. It is noteworthy, that Zn(II), can not be a node in 2D and 3D structures, because of its connectivity of two. Zn(II) is a d^{10} metal ion and can react in a flexible manner to stimuli like crystal packing interactions by adapting the coordination geometry around the metal centre.

Several structures of varying dimensionality were obtained with zinc halides and especially the 3D MOF, with the large void space, highlighted that Zn(II) is a very rewarding metal centre in coordination polymers. Other metal centres like Cd(II) and Cu(II) are very flexible in terms of coordination number, geometry, dimerization and anion coordination, what makes the control of the self-assembly processes with these metals very difficult.

The organic ligands play an equally important role in crystal engineering. Rigid ditopic linkers like 4,2':6',4"-terpyridines allow most control over the self-assembly process in this respect. The V-shaped coordination geometry is always retained, what leads to zig-zag like 1D chains with linear two-connecting metal centres and predominantly to (4,4) nets with octahedral metal centres, that have a connectivity of four (Co(II), Cd(II)). Interesting structural motifs were

obtained with flexible 3,2':6',3"-terpyridines, but the flexibility prevents control over self-assembly with this ligand. Tetratopic bis(4,2':6',4"-terpyridines) and bis(3,2':6',3"-terpyridines) were successfully incorporated into coordination polymers and lead to the formation of 2D and 3D frameworks and one MOF. The rotation around the C-C bonds connecting the phenylene ring with the terpyridine units inserts a large degree of flexibility and structural motifs observed with these ligands are based on serendipity, rather than control of the self-assembly. A positive aspect is, that these ligands enhance the possibility, that a 3D framework is observed. A prediction if, how and with which topology the framework forms is not possible. The most promising MOF in terms of possible applications was obtained from the combination of $ZnBr_2$ and the bis(4,2':6',4"-terpyridine) **16**. A honeycomb motif of hexagonal interpenetrating channels with large voids (~ 65% of the total volume) was observed and this material will probably be tested in gas-sorption experiments. Host-guest exchange reactions can also be investigated further.

The essence of crystal engineering with multitopic 4,2':6',4"-terpyridines and 3,2':6',3"-terpyridine is, that construction of 3D motifs can't be controlled and that the assembly of those structures relies on serendipity. 1D and 2D structures however show many similarities and in these cases the outcome of a motif can be assumed, when the right building blocks are used.

Some indications, which building blocks can favour the formation of a certain structure motif were provided by the results presented in this PhD thesis.

14 OUTLOOK

In the last chapters it was demonstrated, that the formation of 3D structures can be controlled by the choice of the right ligand. A prediction for the outcome of a structural motif using ligands, related to the ones presented here (e.g. other bis(4,2':6',4"-terpyridines) and bis(3,2':6',3"-terpyridines)), is not advisable. The results presented in this PhD thesis demonstrated, that small changes in ligand design can have a large impact on the self-assembly processes and the outcome of the structural motif. Combining metal centres with a connectivity of four (or higher) with multitopic organic ligands can increase the probability to obtain 3D frameworks. An application for the presented frameworks was not established, but the structure of compound $[Zn_2Br_4(\mathbf{16})\cdot H_2O]_n$ showing the honeycomb channel motif with ~65% void space is a good example for an unpredicted outcome with an astonishing structure. Gas-sorption, guest exchange, drug-delivery test etc. should be conducted on this material.

A more precise pathway to functional 3D frameworks would be the incorporation of functional groups on the alkoxy chains present in bis(4,2':6',4"-terpyridine) and bis(3,2':6',3"-terpyridine ligands). These functional groups, incorporated into the host material, could be used to interact with specific guests and enhance the host-guest chemistry of these framework. Many possibilities exist for the incorporation of functional groups into bis(4,2':6',4"-terpyridines) and bis(3,2':6',3"-terpyridines) via the alcohol functionality in the precursor compounds.

15 EXPERIMENTAL PART - LIGANDS

Ligands **1**-**5**, **19** and **20** were prepared in my master studies and the synthesis can be found in the according publication[30]. Ligands **6**[76] and **10**[106] were prepared as previously described.

15.1 Ditopic ligands

15.1.1 Ligand 7

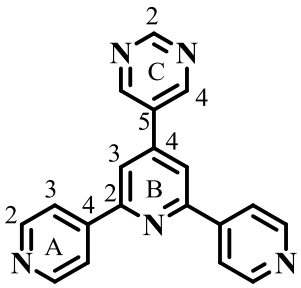

Pyrimidine-5-carbaldehyde (0.28 g, 2.5 mmol) was dissolved in EtOH (40 mL) and 4-acetylpyridine (0.57 mL, 0.62 g, 5 mmol) was added, followed by crushed KOH (0.28 g, 5 mmol). The initially colorless solution changed to yellow and then red. Aqueous NH_3 (25% in water, 12.3 mL, 80 mmol) was added dropwise and the reaction mixture stirred at room temperature overnight. A yellow precipitate formed which was collected by filtration, washed with water (3 × 5 mL) and EtOH (3 × 5 mL) and recrystallized from $CHCl_3$/MeOH. Compound **7** was obtained as a yellow solid (0.34 g, 1.28 mmol, 51%). Decomp. > 260 °C. ^{1}H NMR (500 MHz, $CDCl_3$) ∂ / ppm 9.39 (s, 1H, H^{C2}) 9.13 (s, 2H, H^{C4}), 8.83 (m, 4H, H^{A2}), 8.09 (m, 4H, H^{A3}), 8.04 (s, 2H, H^{B3}). ^{1}H NMR (500 MHz, *d*-TFA) ∂ / ppm 9.97 (s, 2H, H^{C4}) 9.80 (s, 1H, H^{C2}), 9.06–8.90 (m, 8H, H^{A2}/H^{A3}), 8.83 (s, 2H, H^{B3}); ^{13}C{^{1}H} NMR (126 MHz, *d*-TFA) ∂ / ppm 158.4 (C^{C3}), 157.0 (C^{A4}), 155.2 (C^{B2}), 154.5 (C^{C2}), 145.0 (C^{B4}), 144.1 (C^{A2}), 135.8 (C^{C5}), 127.3 (C^{A3}), 125.5 (C^{B3}); IR (solid, ν / cm^{-1}) 4696 (m), 3033 (w), 2925 (w), 1652 (w), 1613 (w), 1596 (s), 1569 (s), 1553 (s), 1544 (m), 1539 (m), 1533 (m), 1506 (w), 1436 (s), 1416 (m), 1393 (s), 1356 (m), 1327 (w), 1318 (w), 1274 (w), 1189 (m), 1133 (w), 1059 (w), 1029 (w), 995 (m), 897 (w), 890 (w), 841 (m), 823 (s), 804 (w), 722 (s), 701 (m), 642 (m), 638 (s), 625 (s), 619 (s), 616 (s), 609 (m), 514 (m), 508 (s), 502 (s). UV-VIS (CH_2Cl_2, 2.5 × 10^{-5} M) λ/nm (ε/ dm^3 mol^{-1} cm^{-1}) 242 (47359), 312 (9184). ESI MS *m/z* 312.2 $[M+H]^+$ (calc. 312.1). Satisfactory elemental analysis could not be obtained.

15.1.2 Ligand 8

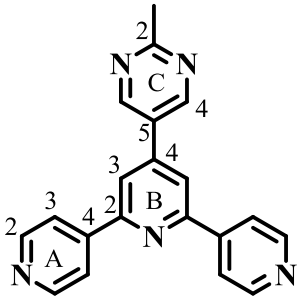

2-Methylpyrimidine-5-carbaldehyde (0.27 g, 2.21 mmol) was dissolved in EtOH (40 mL), and 4-acetylpyridine (0.57 mL, 0.62 g, 5 mmol) was added followed by crushed solid KOH (0.33 g, 5.90 mmol) after which the solution turned red. Aqueous NH_3 (25% in water, 13.9 mL, 90 mmol) was added dropwise and the mixture stirred overnight at ambient temperature. A yellow precipitate formed which was separated by filtration, washed with water (3 × 7 mL) and ethanol (3 × 7 mL) and recrystallized from chloroform/methanol. Compound **8** was obtained as a white solid (0.26 g, 0.78 mmol, 32%). Decomposition > 260 °C. ^{1}H NMR (500 MHz, $CDCl_3$) ∂ / ppm 9.02 (s, 2H, H^{C4}), 8.83 (m, 4H, H^{A2}), 8.09 (m, 4H, H^{A3}), 8.01 (s, 2H, H^{B3}), 2.87 (s, 3H, H^{Me}); ^{13}C{^{1}H} NMR (126 MHz, $CDCl_3$) ∂ / ppm 169.3 (C^{C2}), 155.9 (C^{A4}), 155.14 (C^{C4}), 150.8 (C^{B4}) 150.7 (C^{A2}), 145.3 (C^{B2}), 128.5 (C^{C5}), 121.1 (C^{A3}), 118.3 (C^{B3}), 25.9 (C^{Me}); IR (solid, ν / cm^{-1}) 3077 (w), 3033 (w), 1609 (m), 1594 (s), 1569 (m), 1549 (m), 1544 (m), 1539 (m), 1531 (m), 1464 (s), 1461 (s), 1456 (s), 1447 (m), 1432 (m), 1429 (m), 1423 (m), 1404 (m), 1377 (m), 1373 (m), 1368 (m), 1247 (m), 1064 (m), 1028 (m), 999 (m), 995 (m), 895 (m), 851 (m), 844 (m), 835 (s), 791 (m), 739 (m), 731 (m), 670 (m), 664 (m), 649 (m), 637 (s), 629 (s), 619 (m), 616 (m), 604 (m), 597 (m), 582 (m), 570 (m), 564 (m), 543 (m), 541 (m), 535 (m), 528 (m), 523 (m), 519 (m), 513 (s), 506 (s), 502 (s). UV-VIS (MeCN, 2.5 × 10^{-5} M) λ/nm (ε/ dm^3 mol^{-1} cm^{-1}) 247 (44458), 312 (7856). ESI-MS *m/z* 326.3 $[M+H]^+$ (calc. 326.1). Found C 69.04, H 4.75, N 20.22; required for $C_{20}H_{15}N_5.H_2O$ C 69.96, H 4.99, N 20.40.

15.1.3 Ligand 9

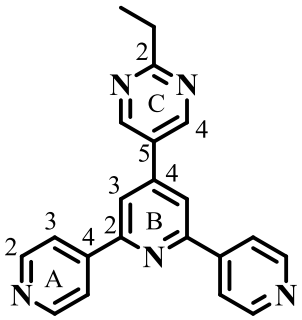

2-Ethylpyrimidine-5-carbaldehyde (0.5 g, 3.67 mmol) was dissolved in EtOH (80 mL), and 4-acetylpyridine (0.92 mL, 0.1 g, 8.07 mmol) was added followed by crushed solid KOH (0.52 g, 9.18 mmol). Aqueous NH_3 (25%, 18.1 mL, 117 mmol) was added dropwise and the mixture was stirred for ~15 h at ambient temperature. A white precipitate formed which was separated by filtration, washed with water (3 × 10 mL), EtOH (3 × 10 mL) and Et_2O (3 × 10 mL). Compound **9** was obtained as a white solid (0.21 g, 3.67 mmol, 16.8 %). M.p. = 275.3 °C. ^{1}H NMR (500 MHz, $CDCl_3$) δ / ppm 9.03 (s, 2H, H^{C4}), 8.82 (m, 4H, H^{A2}), 8.07 (m, 4H, H^{A3}), 8.01 (s, 2H, H^{B3}), 3.13 (q, J = 7.6 Hz, 2H, H^{Et}), 1.45 (t, J = 7.6 Hz, 3H, H^{Et}). ^{13}C{^{1}H} NMR (126 MHz, $CDCl_3$) δ / ppm 173.6 (C^{C2}), 156.1 (C^{A4}), 155.3 (C^{C4}), 150.9 (C^{A2}), 145.5 (C^{B2}), 145.3 (C^{B4}), 128.8 (C^{C5}), 121.3 (C^{A3}), 118.5 (C^{B3}), 32.7 (C^{Et}), 12.8 (C^{Me}). ESI-MS *m/z* 340.23 $[M+H]^+$ (calc. 340.16). High resolution ESI-MS *m/z* 340.1561 $[M+H]^+$ (calc. 340.1557).

15.1.4 Ligand 11

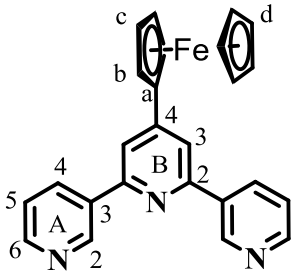

Ferrocenecarboxaldehyde (1.0 g, 4.67 mmol) was dissolved in EtOH (150 mL). 3-Acetylpyridine (1.24 g, 10.3 mmol) and KOH (0.66 g, 11.7 mmol) were added to the solution and a change from red to dark red was observed. Aqueous NH_3 (32%, 18.0 mL) was slowly added to the reaction mixture which was then stirred at room temperature for ~15 h. The solid that formed was collected by filtration, washed with EtOH (3 × 20 mL) and H_2O (3 × 20 mL)

and dried in vacuo. Compound **11** was isolated as a red powder (0.83 g, 1.99 mmol, 43%). Dec. > 210 °C. ^{1}H NMR (500 MHz, CD_3OD) δ / ppm 9.38 (d, J = 2.2 Hz, 2H, H^{A2}), 8.68 (m, 2H, H^{A4}), 8.63 (dd, J = 4.9, 1.6 Hz, 2H, H^{A6}), 8.05 (s, 2H, H^{B3}), 7.62 (dd, J = 8.0, 4.9 Hz, 2H, H^{A5}), 5.15 (m, 2H, H^{b}), 4.55 (m, 2H, H^{c}), 4.11 (s, 4H, H^{d}). ^{13}C{^{1}H} NMR (126 MHz, CD_3OD) δ / ppm 155.7 (C^{B2}), 153.7 (C^{B4}), 150.3 (C^{A6}), 148.8 (C^{A2}), 136.8 (C^{A3}), 136.6 (C^{A4}), 125.4 (C^{A5}), 117.8 (C^{B3}), 81.82 (C^{a}), 71.8 (C^{c}), 71.1 (C^{d}), 68.5 (C^{b}). ESI-MS *m/z* 417.9 $[M+H]^+$ (calc. 418.1). Found C 69.83, H 4.89, N 9.73; required for $C_{25}H_{19}FeN_3 \cdot {}^1/_2H_2O$ C 70.44, H 4.73, N 9.86.

15.2 Tetratopic ligands

15.2.1 Compound 12a

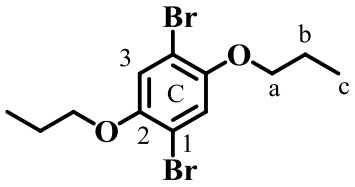

2,5-Dibromohydroquinone (2.0 g, 7.47 mmol), 1-bromopropane (1.72 mL, 2.32 g, 18.7 mmol) and anhydrous K_2CO_3 (3.1 g, 22.4 mmol) were added to dry DMF (100 mL) and the mixture was heated at 100 °C for 16 h. The mixture was cooled to room temperature then poured into a beaker containing ice water (100 mL) and the mixture stirred for 30 min. The precipitate was filtered, washed with water (3 × 30 mL) and dried *in vacuo*. Compound **12a** was isolated as white crystals (2.49 g, 7.07 mmol, 94.6%). ^{1}H NMR (500 MHz, $CDCl_3$) δ / ppm 7.09 (s, 2H, H^{C3}), 3.92 (t, J = 6.5 Hz, 4H, H^{a}), 1.89 – 1.75 (m, 4H, H^{b}), 1.06 (t, J = 7.4 Hz, 6H, H^{c}). This matches the literature data[120].

15.2.2 Compound 12b

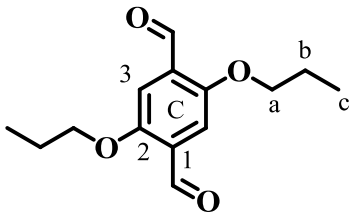

Compound **12a** (1.8 g, 5.11 mmol) and dry Et_2O (100 mL) were added to a dried flask and cooled to 0°C using an ice bath. ^{n}BuLi (1.6 M in hexanes, 9.58 mL, 15.3 mmol) was added

slowly to the solution over a period of 20 min and the temperature maintained at 0°C for 6h. Dry DMF (1.19 mL, 15.3 mmol) was added and the solution stirred for 16 h, while warming up to room temperature. The reaction mixture was neutralized with saturated aqueous NH_4Cl and extracted with CH_2Cl_2 (200 mL). The organic phase was dried over $MgSO_4$ and concentrated *in vacuo*. Compound **12b** was isolated as a yellow solid (0.72 g, 2.88 mmol, 56.3%) and used without further purification. ^{1}H NMR (500 MHz, $CDCl_3$) δ / ppm 10.52 (s, 2H, H^{CHO}), 7.43 (s, 2H, H^{C3}), 4.05 (t, J = 6.5 Hz, 4H, H^a), 1.93 – 1.74 (m, 4H, H^b), 1.06 (m, J = 7.4 Hz, 6H, H^c). This matches the literature data[120].

15.2.3 Ligand 12

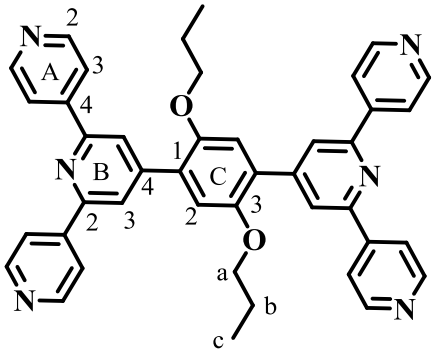

Compound **12b** (0.3 g, 1.2 mmol) was dissolved in EtOH (100 mL), then 4-acetylpyridine (0.54 mL, 0.59 g, 4.8 mmol) and crushed KOH (0.27 g, 4.8 mmol) were added in one portion. Aqueous NH_3 (32%, 3.1 mL) was added dropwise and the reaction mixture was stirred at room temperature for 16 h. The precipitate was collected by filtration and washed with water (3 × 10 mL), EtOH (3 × 10 mL) and Et_2O (3 × 10 mL). Compound **12** was isolated as a white solid (0.17 g, 0.26 mmol, 21.6%). Decomp. > 330°C. ^{1}H NMR (500 MHz, $CDCl_3$) δ / ppm 8.81 (d, J = 6.1 Hz, 8H, H^{A2}), 8.12 (s, 4H, H^{B3}), 8.11 – 8.08 (m, 8H, H^{A3}), 7.16 (s, 2H, H^{C2}), 4.04 (t, J = 6.4 Hz, 4H, H^a), 1.86 – 1.73 (m, 4H, H^b), 0.97 (t, J = 7.4 Hz, 6H, H^c). ^{13}C{^{1}H} NMR (126 MHz, $CDCl_3$) δ / ppm 154.5 (C^{B2}), 150.4 (C^{A2}), 148.0 (C^{B4}), 146.0 (C^{A4}), 128.9 (C^{C1}), 121.3 (C^{B3}), 121.0 (C^{A3}), 115.0 (C^{C2}), 71.1 (C^a), 22.4 (C^b), 10.5 (C^c). C^{C3} was not resolved. ESI-MS *m/z* 657.45 $[M+H]^+$ (calc. 657.30). High resolution ESI-MS *m/z* 657.2983 $[M+H]^+$ (calc. 657.2973).

15.2.4 Compound 13a

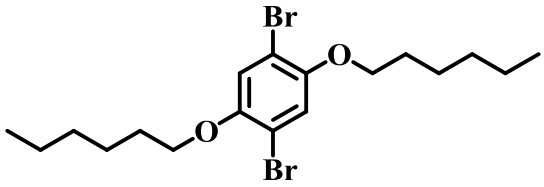

2,5-Dibromohydroquinone (2.00 g, 7.47 mmol), 1-bromohexane (2.64 mL, 3.11 g, 18.7 mmol) and anhydrous K_2CO_3 (3.10 g, 22.4 mmol) were added to dry DMF (100 mL) and the mixture was heated at 100 °C for ~15 h. The reaction mixture was cooled to room temperature, then transferred to a beaker containing 100 mL of ice water and stirred for 30 min. The precipitate was filtered, washed with water (3 × 30 mL) and dried *in vacuo*. The product was recrystallized from a mixture of EtOH and $CHCl_3$ and isolated as white crystals (3.05 g, 6.99 mmol, 93.6%). NMR spectroscopic data agreed with the literature[121]. GC-EI-MS *m/z* 436.1 $[M]^+$ (calc. 436.0). M.p. = 64.4 °C, deviating from the literature value of 51.3-53.1 °C[121].

15.2.5 Compound 13b

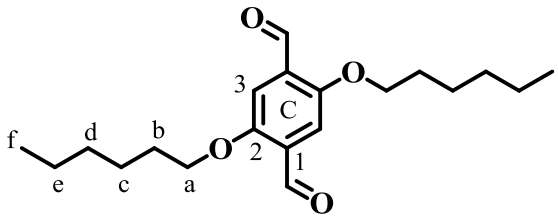

Compound **13a** (1.80 g, 4.13 mmol) and dry Et_2O (150 mL) were added to a dried flask and cooled to 0 °C in an ice bath. ^{n}Butyllithium (1.6 M in hexanes, 7.74 mL, 12.4 mmol) was added slowly to the Et_2O solution over a period of 20 min and the temperature maintained at 0 °C for 6h. Dry DMF (0.96 mL, 12.4 mmol) was added and the solution was stirred for ~15 h, during which time it was allowed to warm to room temperature. The reaction mixture was neutralized with saturated aqueous NH_4Cl and extracted with CH_2Cl_2 (200 mL). The organic phase was dried over $MgSO_4$ and concentrated *in vacuo*. **13b** was isolated as a yellow solid (0.85 g, 2.54 mmol, 61.5%) and used without further purification. M.p. = 68.6 °C. The ^{1}H NMR spectrum agreed with literature data[122]. $^{13}C\{^1H\}$ NMR (126 MHz, $CDCl_3$) δ / ppm 189.6 (C^{CHO}), 155.4 (C^{C2}), 129.4 (C^{C1}), 111.8 (C^{C3}), 69.38 (C^a), 31.6 ($C^{d/e}$), 29.2 (C^b), 25.8 (C^c), 22.7 ($C^{d/e}$), 14.1 (C^f). GC-EI-MS *m/z* 334.2 $[M]^+$ (calc. 334.2).

15.2.6 Ligand 13

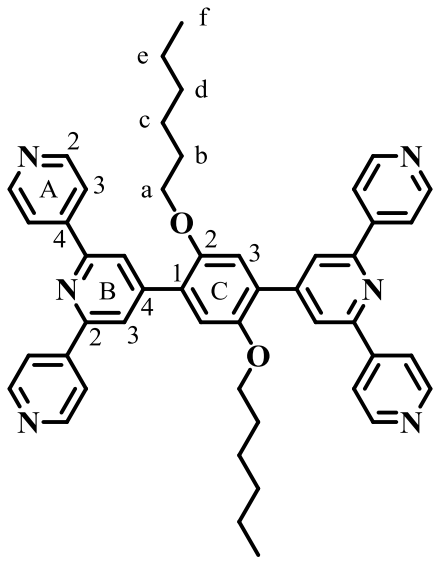

Compound **13b** (0.3 g, 0.9 mmol) was dissolved in EtOH (100 mL), then 4-acetylpyridine (0.41 mL, 0.44 g, 3.59 mmol) and crushed solid KOH (0.20 g, 3.59 mmol) were added. Aqueous NH_3 (32%, 3.0 mL) was added dropwise and the reaction mixture was stirred at room temperature for ~15 h. The precipitate was collected by filtration and washed with water, EtOH and Et_2O (3 × 10 mL, each). Compound **13** was obtained as a white solid (0.15 g, 0.21 mmol, 23.3%). Decomp > 280 °C. ^{1}H NMR (500 MHz, $CDCl_3$) δ / ppm 8.80 (m, 8H, H^{A2}), 8.11 (s, 4H, H^{B3}), 8.09 (m, 8H, H^{A3}), 7.16 (s, 2H, H^{C2}), 4.06 (t, J = 6.3 Hz, 4H, H^{a}), 1.74 (m, 4H, H^{b}), 1.37 (m, 4H, H^{c}), 1.25–1.09 (m, 8H, H^{d+e}), 0.76 (t, J = 7.1 Hz, 6H, H^{f}). ^{13}C{^{1}H} NMR (126 MHz, $CDCl_3$) δ / ppm 154.8 (C^{B2}), 150.7 (C^{A2+C3}), 148.3 (C^{B4}), 146.2 (C^{A4}), 129.3 (C^{C1}), 121.6 (C^{B3}), 121.3 (C^{A3}), 115.3 (C^{C2}), 69.9 (C^{a}), 31.6 ($C^{d/e}$), 29.5 (C^{b}), 26.1 (C^{c}), 22.6 ($C^{d/e}$), 14.1 (C^{f}). ESI-MS *m/z* 741.6 $[M+H]^+$ (calc. 741.4). HR ESI-MS *m/z* 371.1998 $[M+2H]^{2+}$ (calc. 371.1992).

15.2.7 Compound 14a

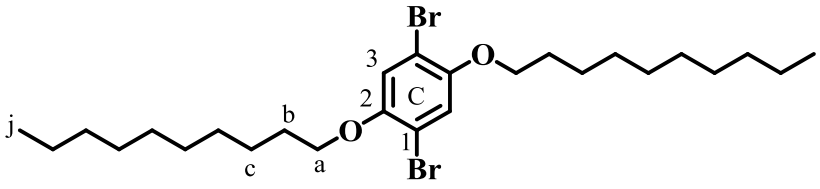

The method was as for **13a** starting with 2,5-dibromohydroquinone (1.00 g, 3.73 mmol), 1-bromodecane (2.33 mL, 2.48 g, 11.2 mmol) and anhydrous K_2CO_3 (1.55 g, 11.2 mmol). **14a** was isolated as white crystals (1.83 g, 3.34 mmol, 89.5%). M.p. = 74.4 °C. ^{1}H NMR

spectroscopic data agreed with the literature[121]. $^{13}C\{^{1}H\}$ NMR (126 MHz, $CDCl_3$) δ / ppm 150.2 (C^{C2}), 118.6 (C^{C3}), 111.3 (C^{C1}), 70.5 (C^{a}), 32.1 (C^{CH2}), 29.7 (C^{CH2}), 29.65 (C^{CH2}), 29.45 (C^{CH2}), 29.5 (C^{CH2}), 29.3 (C^{b}), 26.1 (C^{c}), 22.8 (C^{CH2}), 14.3 (C^{j}). GC-EI-MS *m/z* 548.3 $[M]^+$ (calc. 548.2).

15.2.8 Compound 14b

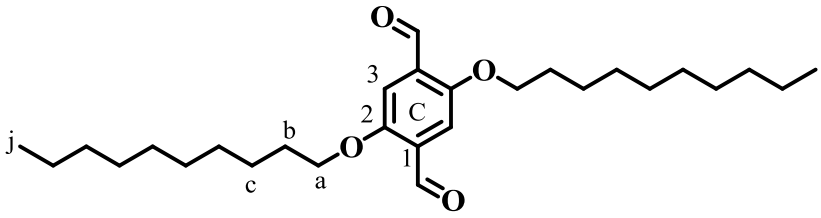

The method and volumes of solvents were as for the synthesis of **13b**, but using **14a** (3.0 g, 5.47 mmol), ^{n}BuLi (1.6 M in hexanes, 10.3 mL, 16.4 mmol), dry DMF (1.27 mL, 16.4 mmol). **14b** was obtained as a yellow solid (2.27 g, 5.08 mmol, 92.9%) and used without further purification. M.p. = 80.3 °C. ^{1}H NMR (500 MHz, $CDCl_3$) δ / ppm 10.52 (s, 2H, H^{CHO}), 7.43 (s, 2H, H^{C3}), 4.08 (t, J = 6.5 Hz, 4H, H^{a}), 1.82 (m, 4H, H^{b}), 1.46 (m, 4H, H^{c}), 1.40–1.18 (m, 24H, H^{d-i}), 0.87 (m, 6H, H^{j}). $^{13}C\{^{1}H\}$ NMR (126 MHz, $CDCl_3$) δ / ppm 189.6 (C^{CHO}), 155.4 (C^{C2}), 129.4 (C^{C1}), 111.8 (C^{C3}), 69.4 (C^{a}), 32.0 (C^{CH2}), 29.7 (C^{CH2}), 29.68 (C^{CH2}), 29.46 (C^{CH2}), 29.45 (C^{CH2}), 29.2 (C^{b}), 26.15 (C^{c}), 22.8 (C^{CH2}), 14.3 (C^{j}). GC-EI-MS *m/z* 446.4 $[M]^+$ (calc. 446.3).

15.2.9 Ligand 14

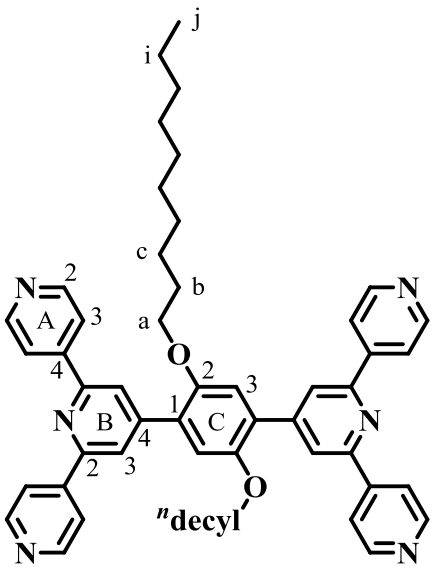

The method and volumes of solvent were as for the synthesis of **13**, but starting with **14b** (0.60 g, 1.34 mmol, 4-acetylpyridine (0.61 mL, 0.66 g, 5.36 mmol), KOH (0.3 g, 5.36 mmol) and aqueous NH_3 (32%, 3.42 mL). Compound **14** was obtained as a white solid (0.25 g, 0.3 mmol, 22.1%). M.p. = 239.8 °C. ^{1}H NMR (500 MHz, $CDCl_3$) δ / ppm 8.81 (m, 8H, H^{A2}), 8.11 (s, 4H, H^{B3}), 8.09 (m, 8H, H^{A3}), 7.16 (s, 2H, H^{C2}), 4.06 (t, J = 6.2 Hz, 4H, H^{a}), 1.74 (m, 4H, H^{b}), 1.37 (m, 4H, H^{c}), 1.23 (m, 8H, H^{i}), 1.19–1.08 (m, 18H, H^{d-h}), 0.84 (t, J = 7.2 Hz, 6H, H^{j}). $^{13}C\{^1H\}$ NMR (126 MHz, $CDCl_3$) δ / ppm 154.8 (C^{B2}), 150.8 (C^{C3}), 150.7 (C^{A2}), 148.3 (C^{B4}), 146.2 (C^{A4}), 129.3 (C^{C1}), 121.5 (C^{B3}), 121.3 (C^{A3}), 115.4 (C^{C2}), 69.9 (C^{a}), 32.0 (C^{CH2}), 29.65 (C^{CH2}), 29.6 (C^{CH2}), 29.5 (C^{CH2}), 29.4 (C^{CH2}), 26.5 (C^{c}), 22.8 (C^{CH2}), 14.2 (C^{j}). ESI-MS *m/z* 853.7 $[M+H]^+$ (calc. 853.5). HR ESI-MS *m/z* 427.2625 $[M+2H]^{2+}$ (calc. 427.2618).

15.2.10 Ligand 15

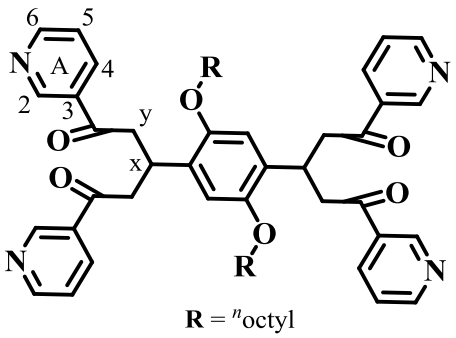

2,5-Bis(octoxy)benzene-1,4-dicarbaldehyde (0.15 g, 0.38 mmol) was dissolved in EtOH (40 mL), then 3-acetylpyridine (0.2 g, 1.61 mmol) and crushed KOH (0.108 g, 1.92 mmol) were added to the solution and the reaction mixture was stirred at room temperature for ~16 h. The colourless solution was concentrated *in vacuo* and left to stand in the freezer at –18°C for 3 days. Compound **15** precipitated and was isolated as an off-white powder (0.1 g, 0.12 mmol, 31.2%). M.p. = 150.5 °C. ^{1}H NMR (500 MHz, $CDCl_3$) δ / ppm 9.13 (dd, *J* = 2.3, 0.9 Hz, 4H, H^{A2}), 8.74 (dd, *J* = 4.8, 1.7 Hz, 4H, H^{A6}), 8.19 (ddd, *J* = 8.0, 2.3, 1.7 Hz, 4H, H^{A4}), 7.38 (ddd, *J* = 7.9, 4.8, 0.9 Hz, 4H, H^{A5}), 6.69 (s, 2H, H^{B3}), 4.17 (p, *J* = 6.8 Hz, 2H, H^{x}), 3.85 (t, *J* = 6.6 Hz, 4H, H^{a}), 3.5 –3.34 (m, 8H, H^{y}), 1.77–1.69 (m, 4H, H^{b}), 1.42 (m, , 4H, H^{c}), 1.36–1.19 (m, 16H, $H^{d/e/f/g}$), 0.91–0.75 (m, 6H, H^{h}). ^{13}C{^{1}H} NMR (126 MHz, $CDCl_3$) δ / ppm 198.2 ($C^{C=O}$), 153.5 (C^{A6}) , 150.4 (C^{B2}), 149.8 (C^{A2}), 135.5 (C^{A4}) , 132.4 (C^{A3}), 129.7 (C^{B1}), 123.7 (C^{A5}) , 113.5 (C^{B3}), 68.7 (C^{a}), 43.2 (C^{y}), 33.5 (C^{x}), 31.9 (C^{f}), 29.7 (C^{b}), 29.5 ($C^{d/e}$), 29.4 ($C^{d/e}$), 26.5 (C^{c}), 22.8 (C^{g}), 14.3 (C^{h}). ESI-MS *m/z* 839.4 $[M+H]^+$ (calc. 839.5). Found C 69.41, H 7.11, N 6.43; required for $C_{52}H_{62}N_4O_6 \cdot 3H_2O$ C 69.93, H 7.67, N 6.27.

15.2.11 Compound 16a

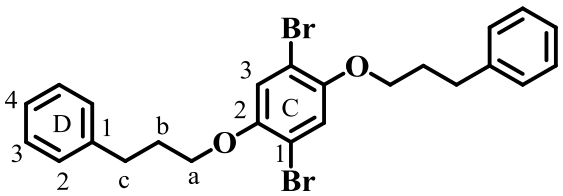

2,5-Dibromohydroquinone (1.00 g, 3.73 mmol), 1-bromo-3-phenylpropane (1.42 mL, 1.86 g, 9.33 mmol) and anhydrous K_2CO_3 (1.55 g, 11.2 mmol) were added to dry DMF (100 mL) and the mixture was heated at 100 °C for ~15 h. The reaction mixture was cooled to room temperature, then transferred to a beaker containing 100 mL of ice water, stirred for 30 min and

extracted with CH_2Cl_2 (200 mL). The organic phase was dried over $MgSO_4$ and concentrated *in vacuo*. The product was recrystallized from a mixture of EtOH and $CHCl_3$ and isolated as white crystals (1.68 g, 3.33 mmol, 89.3 %). M.p. = 88.8 °C. ^{1}H NMR (500 MHz, $CDCl_3$) δ / ppm 7.30 (m, 4H, H^{D3}), 7.24–7.17 (m, 6H, H^{D2+D4}), 7.06 (s, 2H, H^{C3}), 3.95 (t, J = 6.2 Hz, 4H, H^a), 2.86 (m, 4H, H^c), 2.11 (m, 4H, H^b). $^{13}C\{^1H\}$ NMR (126 MHz, $CDCl_3$) δ / ppm 150.1 (C^{C2}), 141.4 (C^{D1}), 128.7 ($C^{D2/D3/D4}$), 128.6 ($C^{D2/D3/D4}$), 126.1 ($C^{D2/D3/D4}$), 118.6 (C^{C3}), 111.3 (C^{C1}), 69.1 (C^a), 32.1 (C^c), 30.9 (C^b). GC-EI-MS *m/z* 503.8 $[M]^+$ (calc. 504.0).

15.2.12 Compound 16b

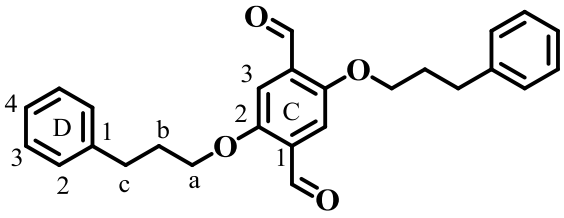

The method and volumes of solvents were as for the synthesis of **14b**, but using **16a** (1.5 g, 2.97 mmol), ^{n}BuLi (1.6 M in hexanes, 5.57 mL, 8.91 mmol) and dry DMF (0.69 mL, 8.91 mmol). **16b** was isolated as a yellow solid (1.08 g, 2.68 mmol, 90.3%) and used without further purification. M.p. = 102.6 °C. ^{1}H NMR (500 MHz, $CDCl_3$) δ / ppm 10.47 (s, 2H, H^{CHO} , 7.41 (s, 2H, H^{C3}), 7.30 (m, 4H, H^{D3}), 7.24–7.19 (m, 6H, H^{D2+D4}), 4.11 (t, J = 6.2 Hz, 4H, H^a), 2.83 (t, J = 7.6 Hz, 4H, H^c), 2.19 (m, 4H, H^b). $^{13}C\{^1H\}$ NMR (126 MHz, $CDCl_3$) δ / ppm 189.4 (C^{CHO}), 155.2 (C^{C2}), 141.10 (C^{D1}), 129.36 (C^{C1}), 128.67 ($C^{D2/D3/D4}$), 128.53 ($C^{D2/D3/D4}$), 126.27 ($C^{D2/D3/D4}$), 111.8 (C^{C3}), 68.3 (C^a), 32.4 (C^c), 30.7 (C^b). GC-EI-MS *m/z* 402.0 (calc. 402.2).

15.2.13 Ligand 16

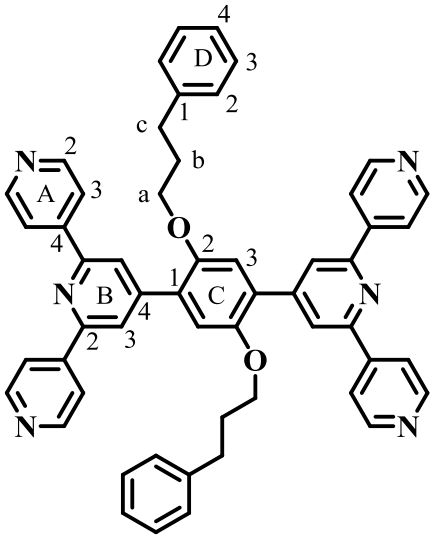

The method and solvent volumes were as for **14** but starting with **16b** (0.89 g, 2.21 mmol), 4-acetylpyridine (1.13 mL, 1.23 g, 9.95 mmol, KOH (0.56 g, 9.95 mmol) and aqueous NH_3 (32%, 17 mL). Compound **16** was obtained as a pale yellow solid (0.74 g, 0.92 mmol, 41.4%). Decomp. > 260°C. ^{1}H NMR (500 MHz, $CDCl_3$) δ / ppm 8.80 (m, 8H, H^{A2}), 8.12 (s, 4H, H^{B3}), 8.09 (m, 8H, H^{A3}), 7.19–7.10 (m, 8H, $H^{C2/D3+D4}$), 6.98 (m, 4H, H^{D2}), 4.09 (t, J = 6.1 Hz, 4H, H^{a}), 2.69 (m, 4H, H^{c}), 2.09 (m, 4H, H^{b}). ^{13}C{^{1}H} NMR (126 MHz, $CDCl_3$) δ / ppm 154.9 (C^{B2}), 150.8 (C^{A2}), 150.6 (C^{C3}), 148.3 (C^{B4}), 146.2 (C^{A4}), 140.9 (C^{D1}), 129.4 (C^{C1}), 128.6 ($C^{C2/D3/D4}$), 128.3 (C^{D2}), 126.3 ($C^{C2/D3/D4}$), 121.5 (C^{B3}), 121.3 (C^{A3}), 115.5 ($C^{C2/D3/D4}$), 68.9 (C^{a}), 32.4 (C^{c}), 31.1 (C^{b}). ESI-MS *m/z* 809.6 $[M+H]^+$ (calc. 809.4). HR ESI-MS *m/z* 809.3587 $[M+H]^+$ (calc. 809.3599).

15.2.14 Ligand 17

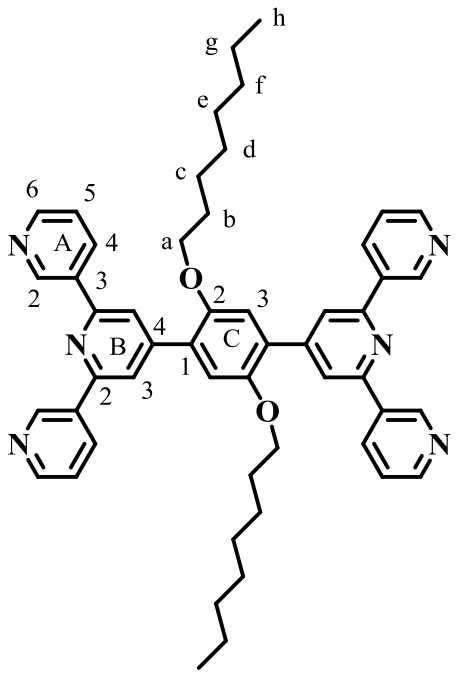

2,5-Bis(octoxy)terephthalaldehyde (0.25 g, 0.64 mmol) was dissolved in EtOH (40 mL), then 3-acetylpyridine (0.36 g, 3.0 mmol) and KOH (0.84 g, 15.0 mmol) were added to the solution and a change from colourless to yellow and then dark red was observed. Aqueous NH_3 (32%, 6.3 mL) was slowly added to the reaction mixture and this was then stirred at room temperature overnight. The solid that formed was collected by filtration, washed with EtOH (3 × 20 mL) and H_2O (3 × 20 mL) and dried *in vacuo*. Compound **17** was isolated as a pale yellow powder (0.21 g, 0.26 mmol, 41%). M.p. = 174.7 °C. ^{1}H NMR (500 MHz, $CDCl_3$) δ / ppm 9.39 (d, J = 1.5 Hz, 4H, H^{A2}), 8.71 (m, 4H, H^{A6}), 8.53 (m, 4H, H^{A4}), 8.03 (s, 4H, H^{B3}), 7.47 (m, 4H, H^{A5}), 7.17 (s, 2H, H^{C3}), 4.06 (t, J = 6.3 Hz, 4H, H^{a}), 1.75 (m, 4H, H^{b}), 1.36 (m, 4H, H^{c}), 1.25 –1.13 overlapping with 1.13–1.01 (m, 16H, $H^{d/e/f/g}$), 0.79 (t, J = 7.1 Hz, 6H, H^{h}). $^{13}C\{^1H\}$ NMR (126 MHz, $CDCl_3$) δ / ppm 154.8 (C^{B2}), 150.7 (C^{C2}), 150.3 (C^{A6}), 148.6 (C^{A2}), 148.1 (C^{C1}), 134.9 (C^{A3}), 134.6 (C^{A4}), 129.4 (C^{B4}), 123.8 (C^{A5}), 120.3 (C^{B3}), 115.4 (C^{C3}), 69.9 (C^{a}), 31.8 (C^{f}), 29.5 (C^{b}), 29.4 ($C^{d/e}$), 29.3 ($C^{d/e}$), 26.4 (C^{c}), 22.7 (C^{g}), 14.2 (Ch). IR (solid, ν / cm^{-1}) 3057 (w), 3037 (w), 2923 (s), 2853 (m), 1904 (w), 1600 (s), 1576(m), 1545 (s), 1515 (m), 1479 (m), 1467 (m), 1439 (m), 1414 (m), 1383 (s), 1339 (m), 1327 (m), 1282 (m), 1264 (m), 1212 (s), 1142 (m), 1129 (m), 1080 (m), 1058 (m), 1031 (m), 1017 (s), 990 (m), 972 (m), 960 (m), 922 (w), 899 (w), 873 (s), 839 (m), 805 (s), 778 (m), 747 (m), 723 (m), 712 (s), 701 (s), 678 (s), 661 (m), 619 (s), 556 (m), 489 (m), 475 (w), 460 (w). UV-VIS (CH_2Cl_2, 1.25 × 10^{-5} M) λ/nm (ε/ dm^3 × mol^{-}

^{1} × cm^{-1}) 241 (51500), 258 sh (47200), 277 sh (42600), 320 (17400), 354 sh (10300). ESI-MS *m/z* 797.8 $[M+H]^+$ (calc. 797.5). Found C 76.75, H 6.98, N 10.52; required for $C_{52}H_{56}N_6O_2 \cdot H_2O$ C 76.63, H 7.17, N 10.31.

15.2.15 Ligand 18

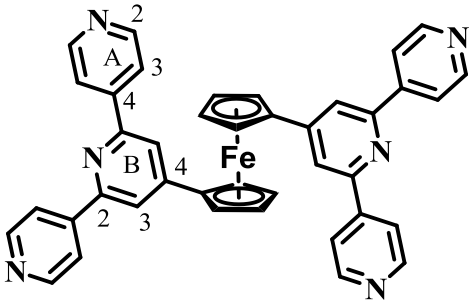

1,1'-Ferrocenedicarboxaldehyde (0.20 g, 0.83 mmol) was dissolved in EtOH (70 mL). 4-Acetylpyridine (0.45 g, 3.63 mmol) and KOH (0.23 g, 4.13 mmol) were added to the solution. Aqueous NH_3 (32%, 6.36 mL) was slowly added to the reaction mixture which was then stirred at room temperature overnight. The solid that formed was collected by filtration, washed with EtOH (3 × 20 mL) and H2O (3 × 20 mL) and dried *in vacuo*. Compound **18** was isolated as a red powder (0.24 g, 0.37 mmol, 44.8%). Decomp >300 °C. ^{1}H NMR (500 MHz, $CDCl_3$, 298 K) δ / ppm 8.60 (m, 4H, H^{A2}), 7.67 (m, 4H, H^{A3}), 7.41 (m, 2H, H^{B3}), 4.85 (m, 2H, H^{Cp}), 4.59 (m, 2H, H^{Cp}). IR (ν/cm^{-1}) 3032 (w), 1612 (m), 1596 (s), 1559 (m), 1541 (m), 1431 (m), 1411 (m), 1398 (m), 1261 (w), 1226 (w), 1067 (w), 1036 (w), 994 (m), 892 (w), 827 (s), 764 (w), 741 (w), 679 (w), 649 (m), 629 (s), 597 (w), 570 (m), 508 (m), 475 (m). MALDI-MS (α-cyano-4-hydroxycinnamic acid matrix) m/z 649.52 $[M + H]^+$ (calc. 649.18). Found C 70.44, H 4.65, N 12.38; calculated for C40H28FeN6·2H2O C 70.18, H 4.71, N 12.28.

16 EXPERIMENTAL PART - COMPLEXES

16.1 Discrete cyclic structures

16.1.1 [{Cu_4Cl_8(**11**)$_4$(MeOH)$_2$}·0.7$CHCl_3$·1.8MeOH]

A MeOH (8 mL) solution of $CuCl_2$ (4.03 mg, 0.03 mmol) was layered over a $CHCl_3$ (5 mL) solution of **11** (12.5 mg, 0.03 mmol) and the crystallization tube left to stand at room temperature. Red crystals of [{Cu_4Cl_8(**11**)$_4$(MeOH)$_2$}·0.7$CHCl_3$·1.8MeOH] (9.8 mg, 0.0041 mmol, 54%) were obtained after 1-2 weeks. The bulk material was characterized by powder diffraction (Fig. 109).

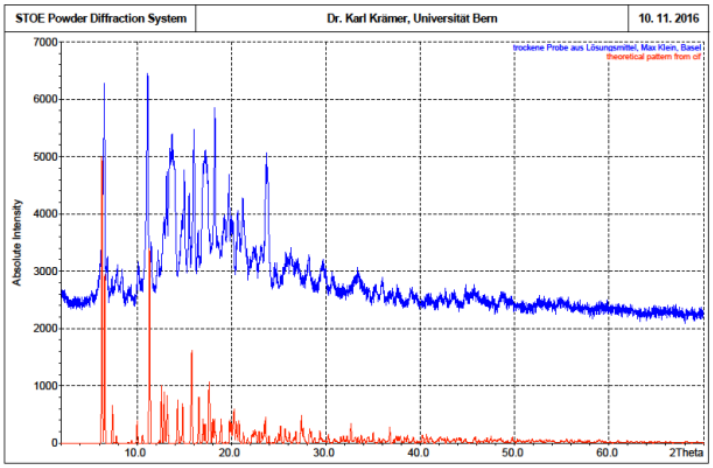

Fig. 109: PXRD pattern of the bulk sample of [{Cu_4Cl_8(**11**)$_4$(MeOH)$_2$}·0.7$CHCl_3$·1.8MeOH] (top, ~295 K) compared to the predicted patter (123K) from the single crystal data. Reproduced from ref.[100], published by Elsevier.

16.1.2 [{ZnI_2(**10**)}$_4$·1.4MeOH·0.8H_2O]

A MeOH (8 mL) solution of ZnI_2 (6.38 mg, 0.02 mmol) was layered over a $CHCl_3$ (5 mL) solution of **10** (8.35 mg, 0.02 mmol) and the crystallization tube was left to stand at room temperature. Red crystals of [{ZnI_2(**10**)}$_4$·1.4MeOH·0.8H_2O] (1.7 mg, 0.0006 mmol, 12% based on Zn) were obtained after 1-2 weeks. The bulk sample was characterized by powder diffraction (Fig. 110).

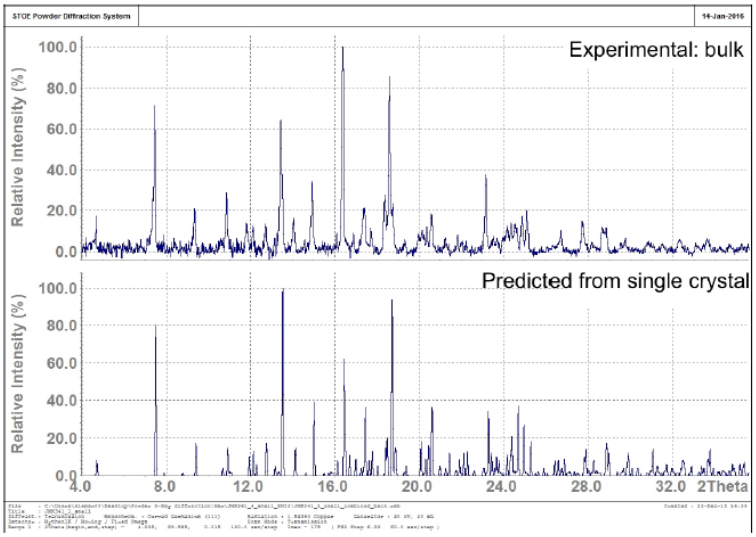

Fig. 110: PXRD pattern of the bulk sample of [{ZnI_2(**10**)}$_4$·1.4MeOH·0.8H_2O] (top, ~295 K) compared to the predicted patter (123K) from the single crystal data. Reproduced from ref.[31], published by CSIRO Publishing.

16.1.3 [{$ZnCl_2$(**11**)}$_4$·3$CHCl_3$·3MeOH]

A MeOH (8 mL) solution of $ZnCl_2$ (2.73 mg, 0.02 mmol) was layered over a $CHCl_3$ (5 mL) solution of **11** (8.35 mg, 0.02 mmol) and the crystallization tube was left at room temperature. A few red crystals of [{$ZnCl_2$(**11**)}$_4$·3$CHCl_3$·3MeOH] were obtained after 1-2 weeks.

16.2 1D coordination chains

16.2.1 [{$Zn(OAc)_2$(**10**)} ·MeOH·H_2O]$_n$

A MeOH (8 mL) solution of $Zn(OAc)_2$·2H_2O (4.39 mg, 0.02 mmol) was layered over a $CHCl_3$ (5 mL) solution of **10** (8.35 mg, 0.02 mmol) and the crystallization tube was left to stand at room temperature. Red crystals of [{$Zn(OAc)_2$(**10**)}$_n$·MeOH·H_2O]$_n$ (2.7 mg, 0.002 mmol, 10% based on Zn) were obtained after 1-2 weeks.

16.2.2 [{$ZnBr_2$(**11**)}·MeOH]$_n$

A MeOH (8 mL) solution of $ZnBr_2$ (4.50 mg, 0.02 mmol) was layered over a $CHCl_3$ (5 mL) solution of **11** (8.35 mg, 0.02 mmol) and the crystallization tube was left to stand at room temperature. Red crystals of [{$ZnBr_2$(**11**)}$_n$·1MeOH]$_n$ (2.8 mg, 0.004 mmol, 20% based on Zn) were obtained after 1-2 weeks.

16.2.3 [{$ZnCl_2$(**7**)}$_n$]

A solution of $ZnCl_2$ (3.41 mg, 0.025 mmol) in MeOH (8 mL) was layered over a $CHCl_3$ solution (5 mL) of **7** (7.78 mg, 0.025 mmol) and the tube was sealed with Parafilm. Colourless crystals of [{$ZnCl_2$(**7**)}$_n$] (7.0 mg, 0.016 mmol, 63%) were obtained after 2 weeks. IR (solid, ν / cm^{-1}) 3062 (m), 1615 (s), 1607 (s), 1572 (m), 1559 (m), 1543 (m), 1506 (m), 1447 (m), 1425 (m), 1396 (s), 1323 (m), 1218 (m), 1195 (m), 1135 (w), 1064 (s), 1029 (s), 990 (w), 891 (w), 874 (m), 836 (s), 744 (w), 714 (s), 666 (w), 648 (s), 629 (s), 514 (m). Found C 49.59, H 3.03, N 14.97; required for $C_{19}H_{13}N_5Cl_2Zn.H_2O$ C 49.01, H 3.25, N 15.04.

16.2.4 [{ZnI_2(**7**)}$_n$]

An MeOH (8 mL) solution of ZnI_2 (8.0 mg, 0.025 mmol) was layered over a $CHCl_3$ (5 mL) solution of **7** (7.78 mg, 0.025 mmol). The tube was sealed with Parafilm and after 2 weeks, yellow crystals of [{ZnI_2(**7**)}$_n$] (3.5 mg, 0.006 mmol, 22%) had grown. IR (solid, ν / cm^{-1}) 3056 (w), 1614 (s), 1606 (s), 1568 (m), 1556 (m), 1506 (w), 1444 (m), 1421 (m), 1396 (s), 1322 (w), 1220 (m), 1192 (w), 1135 (w), 1066 (s), 1025 (s), 991 (w), 886 (w), 873 (w), 851 (m), 836 (s), 746 (w), 717 (m), 668 (w), 648 (s), 634 (s), 626 (s). Found C 35.60, H 2.27, N 10.89; required for $C_{19}H_{13}I_2N_5I_2Zn.H_2O$ C 35.19, H 2.33, N 10.80.

16.2.5 [{ZnI_2(**8**)·MeOH}$_n$]

A solution of ZnI_2 (8.0 mg, 0.025 mmol) in MeOH (8 mL) was layered on top of a solution of **8** (4.07 mg, 0.013 mmol) in $CHCl_3$(5 mL) and the tube was left sealed with Parafilm. Yellow crystals of [{ZnI_2(**8**)·MeOH}$_n$] (8.0 mg, 0.012 mmol, 91%) were obtained after 2 weeks. IR (solid, ν / cm^{-1}) 2922 (m), 1608 (s), 1548 (m), 1460 (s), 1406 (m), 1372 (m), 1221 (w), 1065 (m), 1024 (s), 871 (w), 836 (s), 750 (w), 686 (m), 645 (s), 630 (s), 599 (w), 505 (w). Found C 38.11, H 2.95, N 10.50; required for $C_{20}H_{15}I_2N_5Zn$.MeOH C 37.28, H 2.83, N 10.35.

16.2.6 [{$Co_2(NCS)_4(MeOH)_4$(**8**)$_2$}·2MeOH·$8H_2O$]$_n$

A solution of $Co(NCS)_2$ (1.75 mg, 0.01 mmol) in MeOH (8 mL) was layered over a solution of **8** (9.76 mg, 0.03 mmol) in $CHCl_3$ (5 mL). A few pink crystals of [{$Co_2(NCS)_4(MeOH)_4$(**8**)$_2$}·2MeOH·$8H_2O$]$_n$ were obtained after 2–4 weeks.

16.2.7 $[Cu_2(OAc)_4(9)]_n$

A solution of $Cu(OAc)_2 \cdot H_2O$ (4.11 mg, 0.021 mmol) in MeOH (8 mL) was layered over a solution of **9** (7.0 mg, 0.021 mmol) in $CHCl_3$ (5 mL). Blue crystals of $[Cu_2(OAc)_4(\mathbf{9})]_n$ (0.9 mg, 0.00128 mmol, 12.2 % based on $Cu(OAc)_2$) were obtained after 1–2 weeks. Insufficient amount of material was obtained for bulk sample analysis.

16.3 1D coordination ladders

16.3.1 $[\{Zn_2(18)Cl_4\} \cdot 3CHCl_3]_n$

A solution of $ZnCl_2$ (1.36 mg, 0.01 mmol) in MeOH (8 mL) was layered over a suspension of **18** (6.49 mg, 0.01 mmol) in $CHCl_3$ (5 mL). Red crystals of $[\{Zn_2(\mathbf{18})Cl_4\} \cdot 3CHCl_3]_n$ (0.2 mg, 0. 156 μmol, 1.6% based on 1) were obtained after 2–4 weeks. Insufficient amount of crystalline material was obtained for bulk analysis.

16.3.2 $[\{Cu_2Cl_4(10)_2(MeOH)\} \cdot 2.25MeOH \cdot H_2O \cdot CHCl_3]_n$

A MeOH (8 mL) solution of $CuCl_2$ (4.03 mg, 0.03 mmol) was layered over a $CHCl_3$ (5 mL) solution of **10** (12.5 mg, 0.03 mmol) and the crystallization tube was left to stand at room temperature. Red crystals of $[\{Cu_2Cl_4(\mathbf{10})_2(MeOH)\} \cdot 2.25MeOH \cdot H_2O \cdot CHCl_3]_n$ (3.7 mg, 0.003 mmol, 20% based on Cu) were obtained after 1-2 weeks.

16.3.3 $[Cd_2(NO_3)_4(MeOH)(4)_3]_n$

A MeOH (8 mL) solution of $Cd(NO_3)_2 \cdot 4H_2O$ (9.25 mg, 0.03 mmol) was layered over a $CHCl_3$ (5 mL) solution of **4** (12.4 mg, 0.03 mmol). The crystallization tube was left to stand at room temperature and colourless crystals of $[Cd_2(NO_3)_4(MeOH)(\mathbf{4})_3]_n$ (12.4 mg, 0.007 mmol, 48% based on Cd) were obtained after 2–4 weeks. Found C 56.11, H 5.07, N 10.83; required for $C_{82}H_{85}Cd_2N_{13}O_{16}$. MeOH C 56.47, H 5.08, N 10.31. The bulk sample was characterized by powder diffraction (Fig. 111).

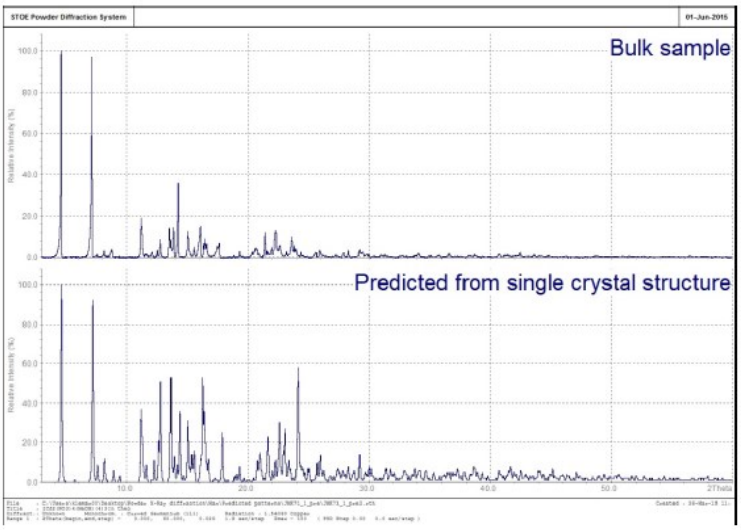

Fig. 111: PXRD pattern of the bulk sample of $[Cd_2(NO_3)_4(MeOH)(\mathbf{4})_3]_n$ (top, ~295 K) compared to the predicted patter (123K) from the single crystal data. Reproduced from ref.[108], published by The Royal Society of Chemistry.

16.4 2D coordination networks

16.4.1 $[\{Cu(9)(OMe)(MeOH)\}\{CF_3SO_3\}\cdot MeOH]_n$

A solution of $Cu_2(CF_3SO_3)_2\cdot C_7H_8$ (10.7 mg, 0.021 mmol) in MeOH (8 mL) was layered over a solution of **9** (7.0 mg, 0.021 mmol) in $CHCl_3$ (5 mL). Blue crystals of $[\{Cu(\mathbf{9})(OMe)(MeOH)\}\{CF_3SO_3\}\cdot MeOH]_n$ (5.4 mg, 0.00834 mmol, 39.7% based on 3) were obtained after 1–2 weeks. The bulk material was characterized by powder diffraction (Fig. 112).

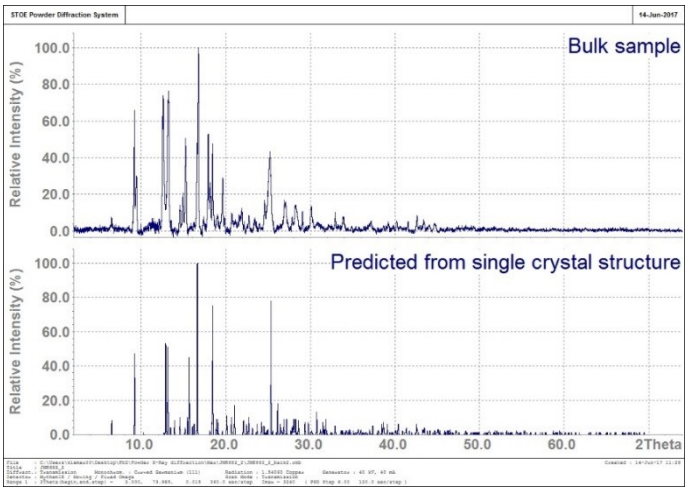

Fig. 112: PXRD pattern of the bulk sample of $[\{Cu(\mathbf{9})(OMe)(MeOH)\}\{CF_3SO_3\}\cdot MeOH]_n$ (top, ~295 K) compared to the predicted patter (123K) from the single crystal data. Reprinted with permission from ref.[99], copyright 2018 American Chemical Society.

16.4.2 $[\{Co(NCS)_2(10)_2\}\cdot 4CHCl_3]_n$

A solution of $Co(NCS)_2$ (1.75 mg, 0.010 mmol) in MeOH (8 mL) was layered over a solution of **10** (4.17 mg, 0.010 mmol) in $CHCl_3$ (5 mL). Orange crystals of $[\{Co(NCS)_2(\mathbf{10})_2\}\cdot 4CHCl_3]_n$ (1.7 mg, 0.0011 mmol, 22% based on **10**) were obtained after 2–4 weeks. The bulk sample was characterized by powder diffraction (Fig. 113).

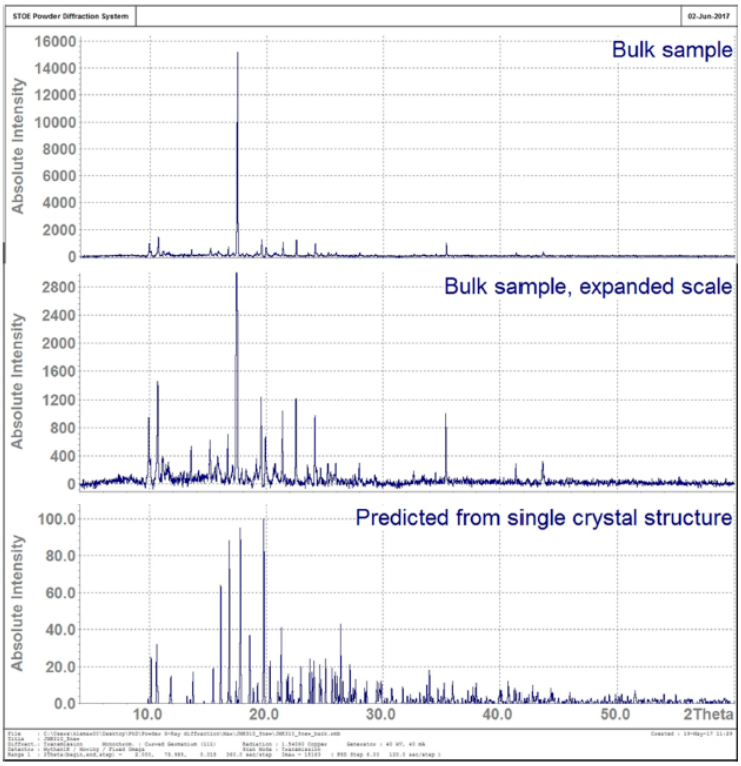

Fig. 113: PXRD pattern of the bulk sample of $[\{Co(NCS)_2(\mathbf{10})_2\}\cdot 4CHCl_3]_n$ (top and middle, ~295 K) compared to the predicted patter (123K) from the single crystal data. Reproduced from ref.[32], published by MDPI.

16.4.3 $[\{Co(NCS)_2(15)\}\cdot 2CHCl_3]_n$

A solution of $Co(NCS)_2$ (0.875 mg, 0.005 mmol) in MeOH (8 mL) was layered over a solution of **15** (12.6 mg, 0.015 mmol) in $CHCl_3$ (5 mL). Pink crystals of $[\{Co(NCS)_2(\mathbf{15})\}\cdot 2CHCl_3]_n$ (0.6 mg, 0.00048 mmol, 9.6%) were obtained after 2–4 weeks. The bulk sample was characterized by powder diffraction (Fig. 114).

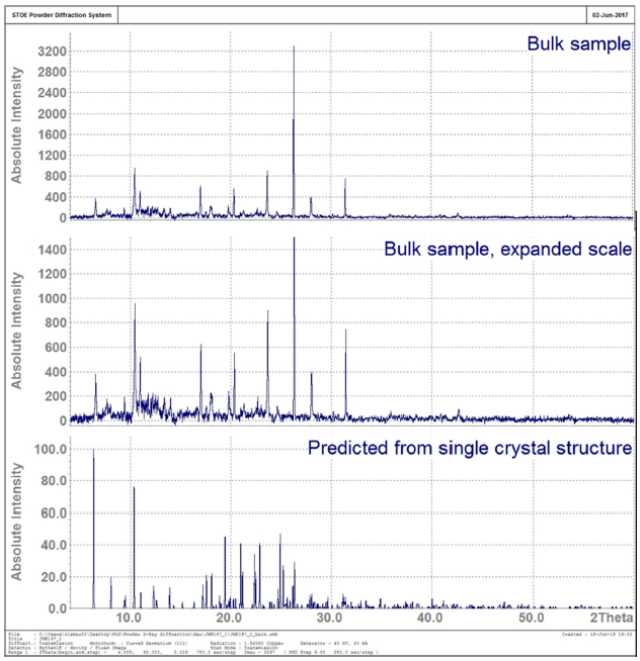

Fig. 114: PXRD pattern of the bulk sample of $[\{Co(NCS)_2(\mathbf{15})\}\cdot 2CHCl_3]_n$ (top and middle, ~295 K) compared to the predicted patter (123K) from the single crystal data. Reproduced from ref.[32], published by MDPI.

16.4.4 $[\{Co_2(NCS)_4(\mathbf{1})_4\}\cdot 2CHCl_3\cdot 1.5MeOH]_n$

A MeOH (8 mL) solution of $Co(NCS)_2$ (5.25 mg, 0.03 mmol) was layered over a $CHCl_3$ (5 mL) solution of **1** (30.5 mg, 0.09 mmol) and left to stand at room temperature. Pink crystals of $[\{Co_2(NCS)_4(\mathbf{1})_4\}\cdot 2CHCl_3\cdot 1.5MeOH]_n$ (14.8 mg, 0.007 mmol, 47% based on Co) were obtained after 1-2 weeks. The bulk sample was characterized by powder diffraction (Fig. 115).

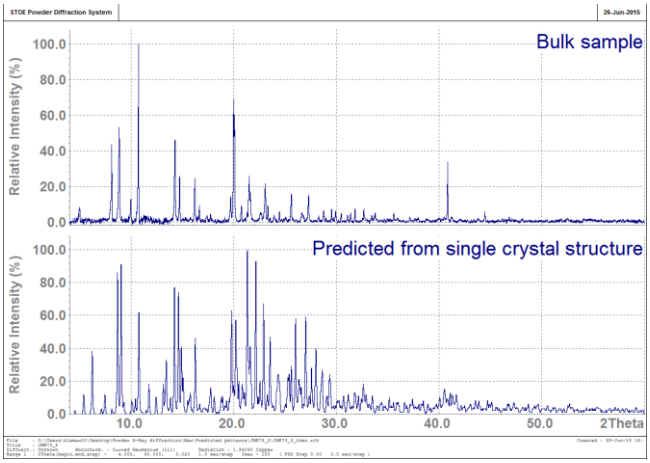

Fig. 115: PXRD pattern of the bulk sample of $[\{Co_2(NCS)_4(\mathbf{1})_4\}\cdot 2CHCl_3\cdot 1.5MeOH]_n$ (top, ~295 K) compared to the predicted patter (123K) from the single crystal data. Reproduced from ref.[110] published by The Royal Society of Chemistry.

16.4.5 $[\{Co(NCS)_2(2)_2\}\cdot 4CHCl_3]_n$

A MeOH (8 mL) solution of $Co(NCS)_2$ (5.25 mg, 0.03 mmol) was layered over a $CHCl_3$ (5 mL) solution of **2** (10.6 mg, 0.03 mmol) and left to stand at room temperature. Pink crystals of $[\{Co(NCS)(\mathbf{2})\}\cdot 2CHCl_3]_n$ (3.0 mg, 0.002 mmol, 7% based on Co) were obtained after 1-2 weeks. The bulk sample was characterized by powder diffraction (Fig. 116).

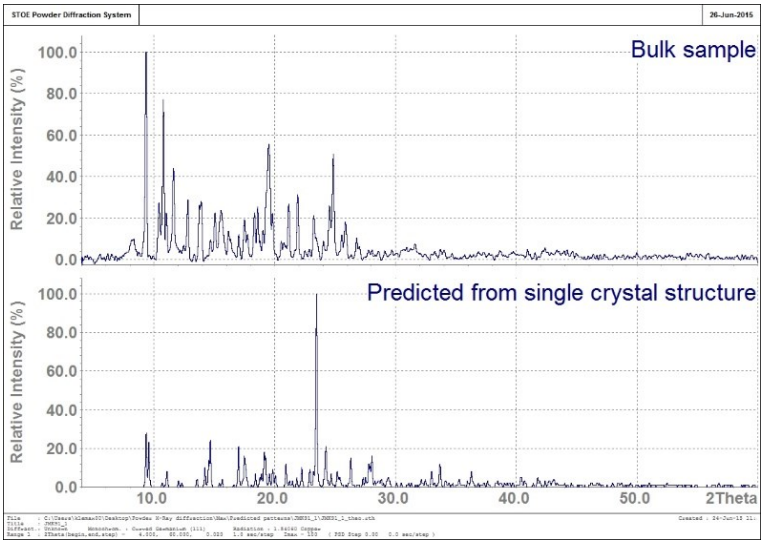

Fig. 116: PXRD pattern of the bulk sample of $[\{Co(NCS)(\mathbf{2})\}\cdot 2CHCl_3]_n$ (top, ~295 K) compared to the predicted patter (123K) from the single crystal data. Reproduced from ref.[110] published by The Royal Society of Chemistry.

16.4.6 $[\{Co(NCS)_2(6)_2\}\cdot 0.5H_2O]_n$

A MeOH (8 mL) solution of $Co(NCS)_2$ (3.50 mg, 0.02 mmol) was layered over a $CHCl_3$ (5 mL) solution of **6** (17.4 mmol, 0.06 mmol) and left to stand at room temperature. Pink crystals of $[\{Co(NCS)_2(\mathbf{6})_2\}\cdot 0.5H_2O]_n$ (5.1 mg, 0.007 mmol, 33% based on Co) were obtained after 1-2 weeks. The bulk sample was characterized by powder diffraction (Fig. 117).

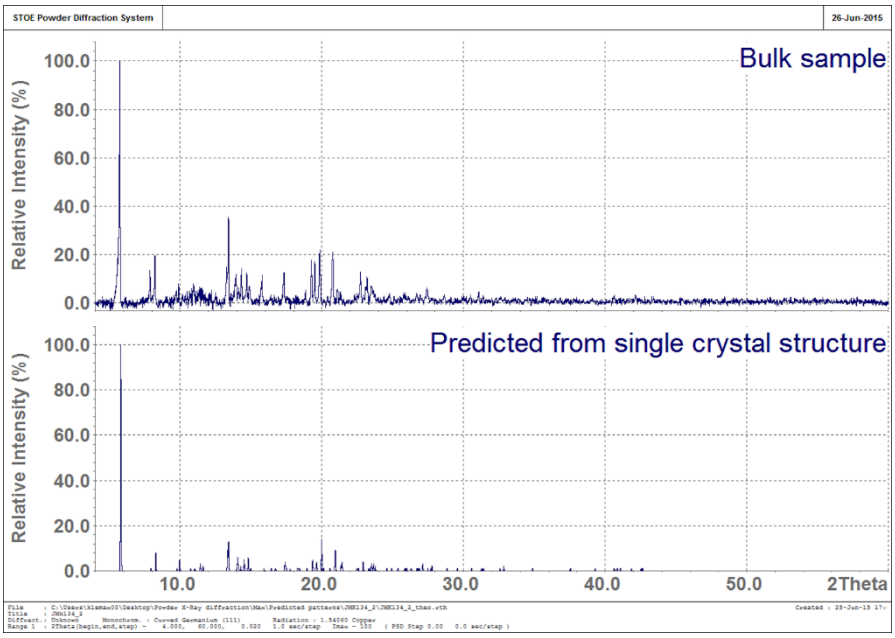

Fig. 117: PXRD pattern of the bulk sample of $[\{Co(NCS)_2(\mathbf{6})_2\}\cdot 0.5H_2O]_n$ (top, ~295 K) compared to the predicted patter (123K) from the single crystal data. Reproduced from ref.[110] published by The Royal Society of Chemistry.

16.4.7 $[Zn_2Cl_4(\mathbf{13})]_n$

A MeOH (8 mL) solution of $ZnCl_2$ (1.36 mg, 0.01 mmol) was layered over a $CHCl_3$ (5 mL) solution of **13** (7.41 mg, 0.01 mmol) and the crystallization tube was left to stand at room temperature. Yellow crystals of $[Zn_2Cl_4(\mathbf{13})]_n$ (7.8 mg) were obtained after 1-2 weeks. Satisfactory elemental analysis of the bulk sample could not be obtained.

16.4.8 $[Zn_2Cl_4(\mathbf{14})\cdot 2MeOH]_n$

A MeOH (8 mL) solution of $ZnCl_2$ (2.04mg, 0.015 mmol) was layered over a $CHCl_3$ (5 mL) solution of **14** (12.8 mg, 0.015 mmol) and the crystallization tube was left to stand at room temperature. Pale yellow crystals of $[Zn_2Cl_4(\mathbf{14})\cdot 2MeOH]_n$ (3.2 mg) were obtained after 1-2 weeks. Satisfactory elemental analysis of the bulk sample could not be obtained. The bulk sample was characterized by powder diffraction (Fig. 118).

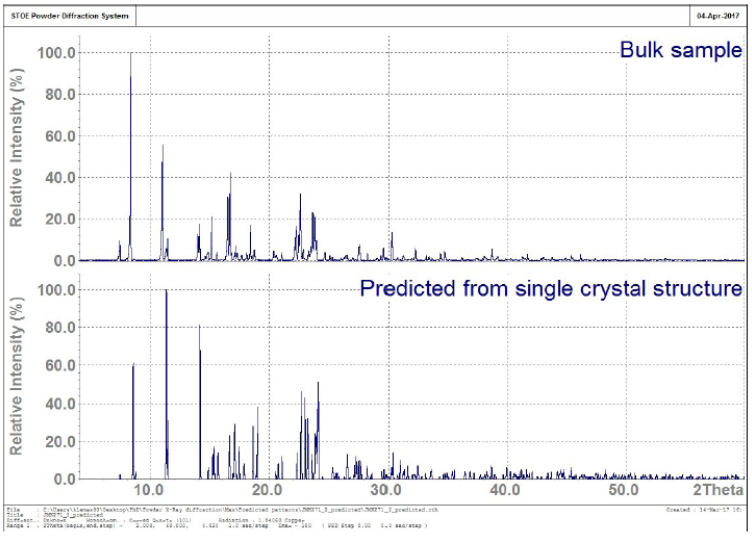

Fig. 118: PXRD pattern of the bulk sample of $[Zn_2Cl_4(\mathbf{14})\cdot 2MeOH]_n$ (top, ~295 K) compared to the predicted patter (123K) from the single crystal data. Reproduced from ref.[111], published by The Royal Society of Chemistry.

16.4.9 $[\{Cd_2(NO_3)_4(3)_3\}\cdot 3CHCl_3]_n$.

A MeOH (8 mL) solution of $Cd(NO_3)_2\cdot 4H_2O$ (9.25 mg, 0.03 mmol) was layered over a $CHCl_3$ (5 mL) solution of **3** (33.1 mg, 0.09 mmol) and the crystallization tube was left to stand at room temperature. Colourless crystals of $[\{Cd_2(NO_3)_4(\mathbf{3})_3\}\cdot 3CHCl_3]_n$ (21.2 mg, 0.011 mmol, 73% based on Cd) were obtained after 2–4 weeks. Satisfactory elemental analysis of the bulk sample could not be obtained. The bulk sample was characterized by powder diffraction (Fig. 119)

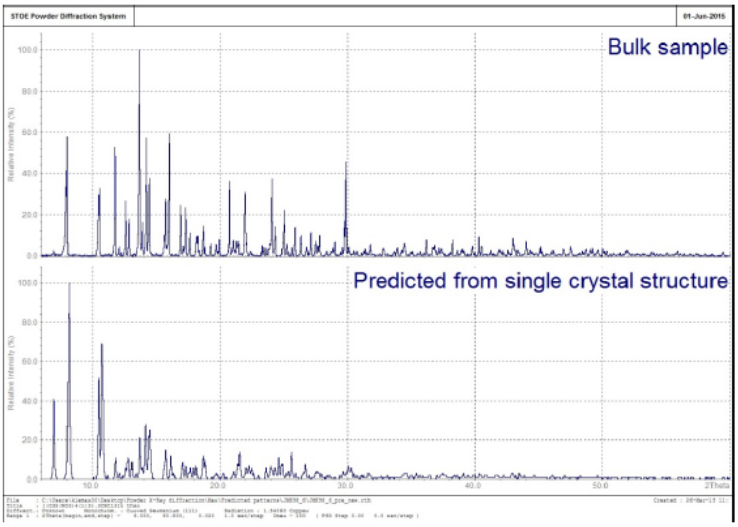

Fig. 119: PXRD pattern of the bulk sample of $[\{Cd_2(NO_3)_4(\mathbf{3})_3\}\cdot 3CHCl_3]_n$ (top, ~295 K) compared to the predicted patter (123K) from the single crystal data. Reproduced from ref.[108], published by The Royal Society of Chemistry.

16.4.10 $[\{Cd_2(NO_3)_4(\mathbf{19})_4\}\cdot 3CHCl_3]_n$

A MeOH (8 mL) solution of $Cd(NO_3)_2\cdot 4H_2O$ (3.08 mg, 0.01 mmol) was layered over a $CHCl_3$ (5 mL) solution of **19** (11.9 mg, 0.03 mmol) and the crystallization tube was left to stand at room temperature. Colourless crystals of $[\{Cd_2(NO_3)_4(\mathbf{19})_4\}\cdot 3CHCl_3]_n$ (8.3 mg, 0.003 mmol, 69% based on Cd) were obtained after 2–4 weeks. Satisfactory elemental analysis of the bulk sample could not be obtained. The bulk sample was characterized by powder diffraction (Fig. 120).

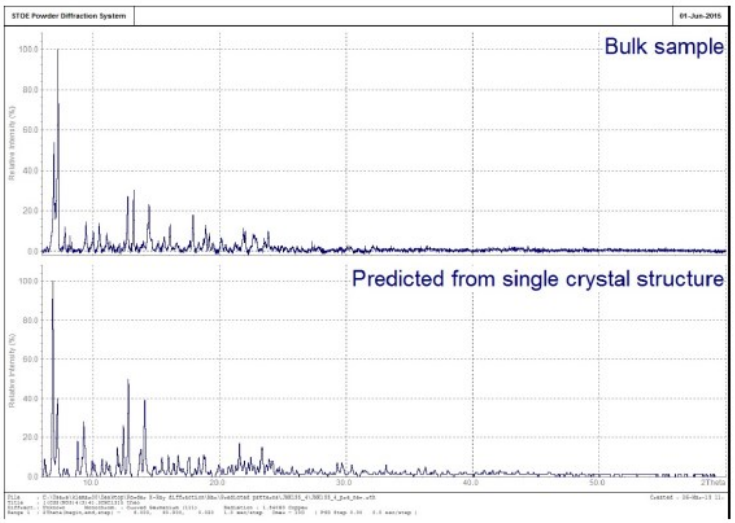

Fig. 120: PXRD pattern of the bulk sample of $[\{Cd_2(NO_3)_4(\mathbf{19})_4\}\cdot 3CHCl_3]_n$ (top, ~295 K) compared to the predicted patter (123K) from the single crystal data. Reproduced from ref.[108], published by The Royal Society of Chemistry.

16.4.11 $[\{Cd_2(NO_3)_4(\mathbf{4})_4\}\cdot CHCl_3\cdot MeOH]_n$

A MeOH (8 mL) solution of $Cd(NO_3)_2\cdot 4H_2O$ (3.08 mg, 0.01 mmol) was layered over a $CHCl_3$ (5 mL) solution of **4** (12.4 mg, 0.03 mmol) and the crystallization was left to stand at room temperature. Colourless crystals of $[\{Cd_2(NO_3)_4(\mathbf{4})_4\}\cdot CHCl_3\cdot MeOH]_n$ (7.6 mg, 0.003 mmol, 67% based on Cd) were obtained after 2–4 weeks. Satisfactory elemental analysis of the bulk sample could not be obtained. The bulk sample was characterized by powder diffraction (Fig. 121).

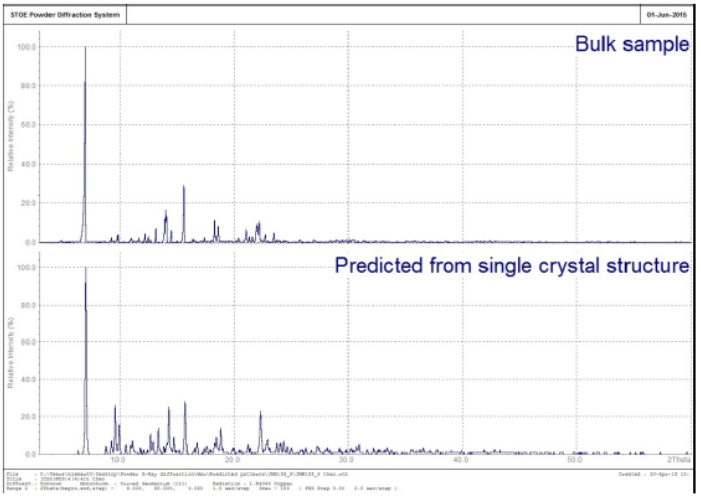

Fig. 121: PXRD pattern of the bulk sample of $[\{Cd_2(NO_3)_4(\mathbf{4})_4\}\cdot CHCl_3\cdot MeOH]_n$ (top, ~295 K) compared to the predicted patter (123K) from the single crystal data. Reproduced from ref.[108], published by The Royal Society of Chemistry.

16.4.12 $[\{Cd(NO_3)_2(\mathbf{20})_2\}\cdot 2MeOH]_n$

A MeOH (8 mL) solution of $Cd(NO_3)_2\cdot 4H_2O$ (3.08 mg, 0.01 mmol) was layered over a $CHCl_3$ (5 mL) solution of **20** (12.7 mg, 0.03 mmol) and the crystallization tube was left standing at room temperature. After 2–4 weeks, colourless crystals of $[\{Cd(NO_3)_2(\mathbf{20})_2\}\cdot 2MeOH]_n$ (5.9 mg, 0.005 mmol, 51% based on Cd) had grown. Satisfactory elemental analysis of the bulk sample could not be obtained. The bulk sample was characterized by powder diffraction (Fig. 122).

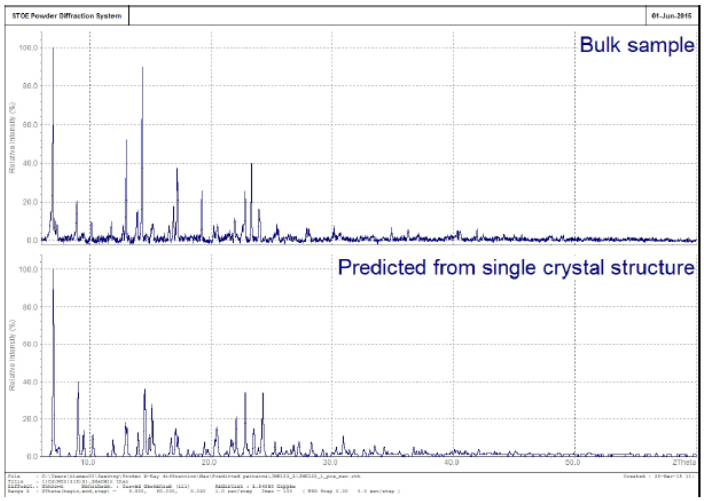

Fig. 122: PXRD pattern of the bulk sample of $[\{Cd(NO_3)_2(\mathbf{20})_2\}\cdot 2MeOH]_n$ (top, ~295 K) compared to the predicted patter (123K) from the single crystal data. Reproduced from ref.[108], published by The Royal Society of Chemistry.

16.5 3D coordination frameworks

16.5.1 $[\{Co(NCS)_2(12)_2\}\cdot 2C_6H_4Cl_2]_n$

A solution of $Co(NCS)_2$ (1.75 mg, 0.010 mmol) in MeOH (8 mL) was layered over a solution of **12** (6.57 mg, 0.010 mmol) in 1,2-$C_6H_4Cl_2$ (5 mL). Pink crystals of $[\{Co(NCS)_2(\mathbf{12})_2\}\cdot 2C_6H_4Cl_2]_n$ (3.9 mg, 0.0035 mmol, 70% based on **12**) were obtained after 2–4 weeks. The bulk sample was characterized by powder diffraction (Fig. 123).

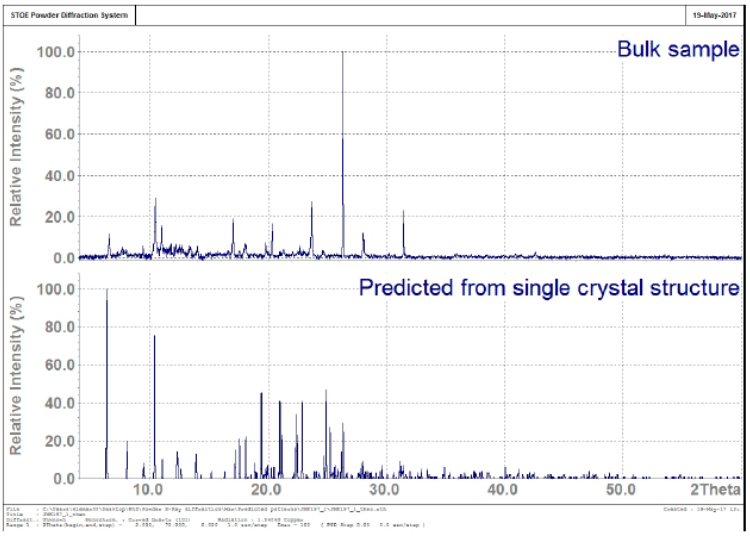

Fig. 123: PXRD pattern of the bulk sample of $[\{Co(NCS)_2(\mathbf{12})_2\}\cdot 2C_6H_4Cl_2]_n$ (top, ~295 K) compared to the predicted patter (123K) from the single crystal data. Reproduced from ref.[32], published by MDPI.

16.5.2 $[Co_2(NCS)_4(4)_4]_n$

A MeOH (8 mL) solution of $Co(NCS)_2$ (5.25 mg, 0.03 mmol) was layered over a $CHCl_3$ (5 mL) solution of **4** (36.9 mg, 0.09 mmol) and left to stand at room temperature. Pink crystals of $[Co_2(NCS)_4(\mathbf{4})_4]_n$ (20.3 mg, 0.01 mmol, 17% based on Co) were obtained after 1-2 weeks. IR (solid): 2929 (w), 2851 (w), 2050 (s), 1598 (s), 1558 (w), 1539 (w), 1516 (s), 1502 (m), 1468 (w), 1431 (w), 1397 (m), 1291 (w), 1238 (s), 1217 (m), 1180 (s), 1063 (w), 1014 (m), 825 (s), 733 (w), 678 (w), 646 (s), 621 (w), 602 (m), 525 (m). UVVIS (solid) 494, 638 (sh) nm. The bulk sample was characterized by powder diffraction (Fig. 124).

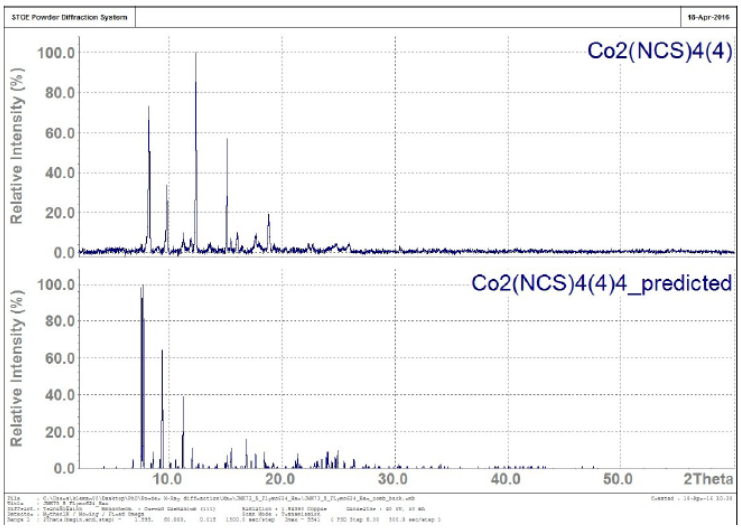

Fig. 124: PXRD pattern of the bulk sample of $[Co_2(NCS)_4(\mathbf{4})_4]_n$ (top, ~295 K) compared to the predicted patter (123K) from the single crystal data. Reproduced from ref.[98], published by The Royal Society of Chemistry.

16.5.3 $[\{Co_2(NCS)_4(\mathbf{5})_4\}\cdot 2CHCl_3\cdot MeOH]_n$

A MeOH (8 mL) solution of $Co(NCS)_2$ (5.25 mg, 0.03 mmol) was layered over a $CHCl_3$ (5 mL) solution of **5** (40.6 mg, 0.09 mmol) and left to stand at room temperature. Pink crystals of $[\{Co_2(NCS)_4(\mathbf{5})_4\}\cdot 2CHCl_3\cdot MeOH]_n$ (26.7 mg, 0.011 mmol, 18% based on Co) were obtained after 1-2 weeks. The bulk sample was characterized by powder diffraction (Fig. 125).

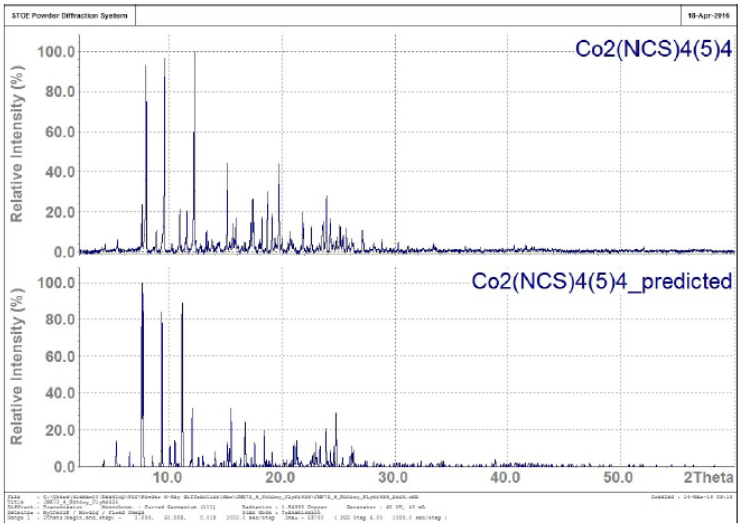

Fig. 125: PXRD pattern of the bulk sample of $[\{Co_2(NCS)_4(\mathbf{5})_4\}\cdot 2CHCl_3\cdot MeOH]_n$ (top, ~295 K) compared to the predicted patter (123K) from the single crystal data. Reproduced from ref.[98], published by The Royal Society of Chemistry.

16.5.4 $[Zn_2Br_4(16)\cdot H_2O]_n$.

A MeOH (8 mL) solution of $ZnBr_2$ (4.5 mg, 0.02 mmol) was layered over a $CHCl_3$ (5 mL) solution of **16** (16.2 mg, 0.02 mmol) and the crystallization tube was left to stand at room temperature. Yellow crystals of $[\{Zn_2Br_4(\mathbf{16})\}\cdot H_2O]_n$ (6.7 mg) were obtained after 1-2 weeks. Satisfactory elemental analysis of the bulk sample could not be obtained.

16.5.5 $[Co(NCS)_2(17)\cdot 4CHCl_3]_n$

A solution of $Co(NCS)_2$ (5.25 mg, 0.03 mmol) in MeOH (8 mL) was layered over a solution of **17** (12.0 mg, 0.015 mmol) in $CHCl_3$ (5 mL). Pink crystals of $[Co(NCS)_2(\mathbf{17})\cdot 4CHCl_3]_n$ were obtained after 2–4 weeks (3.00 mg, 0.002 mmol, 13%). Inadequate material was obtained for bulk elemental analysis.

17 CRYSTALLOGRAPHIC DATA

17.1 Ligand structures

8: $C_{20}H_{15}N_5$, M = 325.37, colourless block, orthorhombic, space group $Pmn2_1$, a = 18.0817(12), b = 4.3834(3), c = 9.7540(6) Å, $\alpha = \beta = \gamma = 90°$, U = 773.10(9) Å^3, Z = 2, D_c = 1.398 Mg m^{-3}, μ(Cu-Kα) = 0.691 mm^{-1}, T = 123 K. Total 9665 reflections, 1449 unique, R_{int} = 0.0295. Refinement of 1429 reflections (121 parameters) with $I > 2\sigma(I)$ converged at final $R1$ =0.0262 ($R1$ all data = 0.0265), $wR2$ = 0.0731 ($wR2$ all data = 0.0736), gof = 1.088.

11: $C_{25}H_{19}FeN_3$, M = 417.29, orange plate, orthorhombic, space group $P2_12_12_1$, a = 9.9004(5), b = 11.3629(6), c = 16.9105(9) Å, $\alpha = \beta = \gamma = 90°$, U = 1902.38(17) Å^3, Z = 4, D_c = 1.457 Mg m^{-3}, μ(Cu-Kα) = 6.472 mm^{-1}, T = 123 K. Total 7433 reflections, 3204 unique, R_{int} = 0.036. Refinement of 2710 reflections (263 parameters) with $I > 2\sigma(I)$ converged at final $R1$ = 0.0313 ($R1$ all data = 0.0389), $wR2$ = 0.0685 ($wR2$ all data = 0.0741), gof = 0.8994. CCDC 1504341.

17.2 Discrete cyclic structures

[{ZnI_2(**10**)}$_4$·1.4MeOH·0.8H_2O]: $C_{101.40}H_{83.20}Fe_4I_8N_{12}O_{2.20}Zn_4$, M = 3005.20, red block, triclinic, space group P–1, a = 11.4704(10), b = 11.7733(10), c = 19.2202(17) Å, α = 90.351(4), β = 102.329(4), γ = 91.929(4)°, U = 2534.1(4) Å^3, Z = 1, D_c = 1.969 Mg m^{-3}, μ(Cu-Kα) = 25.046 mm^{-1}, T = 123 K. Total 33089 reflections, 9131 unique, R_{int} = 0.037. Refinement of 7691 reflections (589 parameters) with $I > 2\sigma(I)$ converged at final $R1$ = 0.0360 ($R1$ all data = 0.0445), $wR2$ = 0.0851 ($wR2$ all data = 0.0899), gof = 0.9080. CCDC 1504338.

[{Cu_4Cl_8(**11**)$_4$($MeOH)_2$}·0.7$CHCl_3$·1.8MeOH]: $C_{104.5}H_{91.9}Cl_{10.1}Cu_4Fe_4N_{12}O_{3.8}$, M = 2412.30, red block, monoclinic, space group $P2_1/c$, a = 14.0480(7), b = 22.6509(14), c = 16.6921(9) Å, β = 90.507(3)°, U = 5311.2(5) Å^3, Z = 2, D_c = 1.508 Mg m^{-3}, μ(Cu-Kα) = 7.892 mm^{-1}, T = 123 K. Total 33091 reflections, 9788 unique, R_{int} = 0.056. Refinement of 6392 reflections (667 parameters) with $I > 2\sigma(I)$ converged at final $R1$ = 0.0874 ($R1$ all data = 0.1195), $wR2$ = 0.2286 ($wR2$ all data = 0.2562), gof = 0.9985.

[{$ZnCl_2$(**11**)}$_4$·3$CHCl_3$·3MeOH]: $C_{102}H_{78}Cl_{14}Fe_4N_{12}Zn_4$, M = 2668.57, red block, orthorhombic, space group *Pccn*, a = 25.0374(9), b = 19.6115(7), c = 23.4639(9) Å, $\alpha = \beta = \gamma$ = 90°, U = 11521.3(7) Å^3, Z = 4, D_c = 1.54 Mg m^{-3}, μ(Cu-Kα) = 8.882 mm^{-1}, T = 123 K. Total 76606 reflections, 10807 unique, R_{int} = 0.182. Refinement of 5214 reflections (613 parameters) with $I > 2\sigma(I)$ converged at final $R1$ = 0.0934 ($R1$ all data = 0.1562), $wR2$ = 0.2478 ($wR2$ all data = 0.3154), gof = 1.0169. CCDC 1504342.

17.3 1D coordination chains

[$Cu_2(OAc)_4$(**9**)]$_n$: $C_{29}H_{29}Cu_2N_5O_8$, M = 702.67, blue plate, monoclinic, space group $C2/c$, a = 26.0869(15), b = 14.8694(9), c = 8.1356(5) Å, β = 108.012(3)°, U = 3001.11(18) Å^3, Z = 4, D_c = 1.555 Mg m^{-3}, μ(Ga-Kα) = 2.248 mm^{-1}, T = 123 K. Total 29718 reflections, 2832 unique, R_{int} = 0.037. Refinement of 2686 reflections (236 parameters) with $I > 2\sigma(I)$ converged at final $R1$ =0.0495 ($R1$ all data = 0.0520), $wR2$ = 0.1250 ($wR2$ all data = 0.1261), gof = 1.0222. CCDC 1585047.

[{$ZnCl_2$(**7**)}$_n$]: $C_{19}H_{13}Cl_2N_5Zn$, M = 447.63, colourless needle, monoclinic, space group $P2_1/n$, a = 8.4559(11), b = 19.194(2), c = 11.2787(13) Å, β = 97.057(9)°, U = 1816.6(4) Å^3, Z = 4, D_c = 1.637 Mg m^{-3}, μ(Cu-Kα) = 4.701 mm^{-1}, T = 123 K. Total 15849 reflections, 3260 unique, R_{int} = 0.0643. Refinement of 2331 reflections (281 parameters) with $I > 2\sigma(I)$ converged at final $R1$ =0.0528 ($R1$ all data = 0.0795), $wR2$ = 0.1330 ($wR2$ all data = 0.1473), gof = 1.015.

[{ZnI_2(**7**)}$_n$]: $C_{19}H_{13}I_2N_5Zn$, M = 630.53, yellow block, monoclinic, space group $P2_1/n$, a = 10.0386(7), b = 11.2543(8), c = 18.3065(13) Å, β = 103.838(3)°, U = 2008.2(2) Å^3, Z = 4, D_c = 2.085 Mg m^{-3}, μ(Cu-Kα) = 25.948 mm^{-1}, T = 123 K. Total 36476 reflections, 3628 unique, R_{int} = 0.0436. Refinement of 3516 reflections (244 parameters) with $I > 2\sigma(I)$ converged at final $R1$ =0.0272 ($R1$ all data = 0.0283), $wR2$ = 0.0710 ($wR2$ all data = 0.0718), gof = 1.104.

[{ZnI_2(**8**)]·MeOH}$_n$]: $C_{21}H_{19}I_2N_5OZn$, M = 676.58, yellow block, monoclinic, space group $P2_1/n$, a = 11.3508(4), b = 11.6668(4), c = 17.6152(6) Å, β = 103.204(2)°, U = 2271.07(14) Å^3, Z = 4, D_c = 1.979 Mg m^{-3}, μ(Cu-Kα) = 23.030 mm^{-1}, T = 123 K. Total 33192 reflections, 4126 unique, R_{int} = 0.0387. Refinement of 4126 reflections (274 parameters) with $I > 2\sigma(I)$ converged at final $R1$ =0.0222 ($R1$ all data = 0.0237), $wR2$ = 0.0578 ($wR2$ all data = 0.0588), gof = 1.035.

[{$Co_2(NCS)_4$(**8**)$_2$$(MeOH)_4$}·2MeOH·8$H_2O$]$_n$: $C_{50}H_{70}Co_2N_{14}O_{14}S_4$, M = 1337.32, pink block, triclinic, space group P–1, a = 10.7199(6), b = 11.3886(7), c = 14.7671(11) Å, α = 86.374(5), β = 85.892(5), γ = 88.031(4)°, U = 1793.80(13) Å^3, Z = 1, D_c = 1.238 Mg m^{-3}, μ(Cu-Kα) = 5.235 mm^{-1}, T = 123 K. Total 24308 reflections, 6218 unique, R_{int} = 0.051. Refinement of 3947 reflections (364 parameters) with I >2σ (I) converged at final R1 = 0.1347 (R1 all data = 0.1693), wR2 = 0.3635 (wR2 all data = 0.3934), gof = 1.0474. CCDC 1550589.

[{Zn$(OAc)_2$(**10**)}·MeOH·H_2O]$_n$: $C_{59}H_{56}Fe_2N_6O_{10}Zn_2$, M = 1251.58, red plate, orthorhombic, space group $Pbca$, a = 24.3420(15), b = 16.0495(10), c = 28.2141(17) Å, $\alpha = \beta = \gamma$ = 90°, U = 11022.6(12) Å^3, Z = 8, D_c = 1.508 Mg m^{-3}, μ(Cu-Kα) = 5.661 mm^{-1}, T = 123 K. Total 73603 reflections, 10050 unique, R_{int} = 0.054. Refinement of 8760 reflections (712 parameters) with I >2σ (I) converged at final R1 = 0.0418 (R1 all data = 0.0507), wR2 = 0.0906 (wR2 all data = 0.0939), gof = 0.9044. CCDC 1504343.

[{$ZnBr_2$(**11**)}·MeOH]$_n$: $C_{26}H_{23}Br_2FeN_3OZn$, M = 674.52, red block, triclinic, space group P–1, a = 8.7879(7), b = 17.1107(14), c = 18.0340(14) Å, α = 73.010(3), β = 80.594(3), γ = 82.192(3)°, U = 2547.3(4) Å^3, Z = 4, D_c = 1.759 Mg m^{-3}, μ(Cu-Kα) = 9.589 mm^{-1}, T = 123 K. Total 33199 reflections, 9306 unique, R_{int} = 0.037. Refinement of 9066 reflections (619 parameters) with I >2σ (I) converged at final R1 = 0.0469 (R1 all data = 0.0477), wR2 = 0 .1123 (wR2 all data = 0.1125), gof = 0.8948. CCDC 1504339.

17.4 1D coordination ladders

[$Cd_2(NO_3)_4$(MeOH)(**4**)$_3$]$_n$: $C_{82}H_{85}Cd_2N_{13}O_{16}$, M = 1733.45, colourless block, triclinic, space group P–1, a = 13.1304(7), b = 16.5224(9), c = 19.2845(10) Å, α = 83.670(3), β = 82.840(3), γ = 70.242(3)°, U = 3896.3(2) Å^3, Z = 2, D_c = 1.477 Mg m^{-3}, μ(Cu-Kα) = 5.007 mm^{-1}, T = 123 K. Total 49 970 reflections, 13 661 unique, R_{int} = 0.039. Refinement of 12 221 reflections (1018 parameters) with $I > 2\sigma(I)$ converged at final R_1 = 0.0540 (R_1 all data = 0.0586), wR_2 = 0.1212 (wR_2 all data = 0.1228), gof = 0.9870. CCDC 1402482.

[{Cu_2Cl_4(**10**)$_2$(MeOH)}·2.25MeOH·H_2O·$CHCl_3$]$_n$: $C_{54.25}H_{54}Cl_7Cu_2Fe_2N_6O_{4.25}$, M = 1345.02, red plate, monoclinic, space group $P2_1/n$, a = 16.1181(12), b = 24.7209(18), c = 16.1565(11) Å, β = 112.267(4)°, U = 5957.5(8) Å^3, Z = 4, D_c = 1.50 Mg m^{-3}, μ(Cu-Kα) = 7.913 mm^{-1}, T = 123 K. Total 38865 reflections, 10865 unique, R_{int} = 0.056. Refinement of 7219 reflections (649

parameters) with $I > 2\sigma(I)$ converged at final $R1 = 0.0565$ ($R1$ all data = 0.0863), $wR2 = 0.1439$ ($wR2$ all data = 0.1750), gof = 0.9640. CCDC 1504340.

[{Zn_2(**18**)Cl_4}·3$CHCl_3$]$_n$: $C_{43}H_{31}Cl_{13}FeN_6Zn_2$, M = 1279.25, red block, monoclinic, space group $P2_1/n$, a = 13.5721(11), b = 23.659(2), c = 15.0438(12) Å, β = 94.479(3)°, U = 4815.8(7) Å^3, Z = 4, Dc = 1.764 Mg m^{-3}, μ(Cu-Kα) = 10.517mm^{-1}, T=123 K. Total 49487 reflections, 8941 unique, R_{int}=0.027. Refinement of 8630 reflections (586 parameters) with $I > 2\sigma$ (I) converged at final $R1$ = 0.0749 ($R1$ all data = 0.0765), $wR2$ = 0.1882 ($wR2$ all data = 0.1890), gof = 0.9829.

17.5 2D coordination networks

[{Cu(**9**)(OMe)(MeOH)}{CF_3SO_3}·MeOH]$_n$. $C_{25}H_{28}CuF_3N_5O_6S$, M = 647.13, blue needle, monoclinic, space group $P2_1/n$, a = 7.3589(2), b = 19.2305(3), c = 19.2279(4) Å, β = 93.221(2)°, U = 2716.74(6) Å^3, Z = 4, D_c = 1.582 Mg m^{-3}, μ(Ga-Kα) = 5.221 mm^{-1}, T = 123 K. Total 50738 reflections, 5511 unique, R_{int} = 0.065. Refinement of 4419 reflections (376 parameters) with $I > 2\sigma$ (I) converged at final $R1$ =0.04705 ($R1$ all data = 0.0577), $wR2$ = 0.0976 ($wR2$ all data = 0.1090), gof = 1.0087. CCDC 1585048.

[{Co(NCS)$_2$(**10**)$_2$}·4$CHCl_3$]$_n$: $C_{56}H_{42}Cl_{12}CoFe_2N_8S_2$, M = 1487.19, orange block, monoclinic, space group $P2_1/n$, a = 10.5796(7), b = 17.4860(12), c = 16.9126(11) Å, β = 99.047(3)°, U = 3089.8(4) Å^3, Z = 2, D_c = 1.598 Mg m^{-3}, μ(Cu-Kα) = 11.565 mm^{-1}, T = 123 K. Total 21236 reflections, 5706 unique, R_{int} = 0.030. Refinement of 5555 reflections (367 parameters) with $I > 2\sigma(I)$ converged at final $R1$ = 0.0473 ($R1$ all data = 0.0483), $wR2$ = 0.0964 ($wR2$ all data = 0.0966), gof = 0.9222. CCDC 1550588.

[{Co(NCS)$_2$(**15**)}·2$CHCl_3$]$_n$: $C_{56}H_{64}Cl_6CoN_6O_6S_2$, M = 1252.94, pink block, triclinic, space group P–1, a = 9.5196(10), b = 11.1662(13), c = 14.4682(16) Å, α = 80.088(6), β = 78.780(5), γ = 86.642(6)°, U = 1485.5(3) Å^3, Z = 1, D_c = 1.400 Mg m^{-3}, μ(Cu-Kα) = 5.838 mm^{-1}, T = 123 K. Total 18364 reflections, 5368 unique, R_{int} = 0.049. Refinement of 4997 reflections (349 parameters) with $I > 2\sigma(I)$ converged at final $R1$ = 0.1210 ($R1$ all data = 0.1256), $wR2$ = 0.2862 ($wR2$ all data = 0.2891), gof = 0.9924. CCDC 1550586.

[{$Co_2(NCS)_4$(**1**)$_4$}·2$CHCl_3$·1.5MeOH]$_n$: $C_{95.50}H_{76}Cl_6Co_2N_{16}O_{5.50}S_4$, M = 1994.60, pink block, triclinic, space group P–1, a = 13.7002(12), b = 18.0092(15), c = 20.4275(17) Å, α = 98.287(4), β = 99.998(3), γ = 110.322(3)°, U = 4539.1(4) Å^3, Z = 2, D_c = 1.459 Mg m^{-3}, μ(Cu-Kα) = 5.869 mm^{-1}, T = 123 K. Total 68836 reflections, 16258 unique, R_{int} = 0.036. Refinement of 15530 reflections (1196 parameters) with I >2σ(I) converged at final R1 = 0.1166 (R1 all data = 0.1191), wR2 = 0.2862 (wR2 all data = 0.2867), gof = 0.9939.

[{$Co(NCS)_2$(**2**)$_2$}·4$CHCl_3$]$_n$: $C_{52}H_{42}Cl_{12}CoN_8O_2S_2$, M = 1359.46, pink block, monoclinic, space group $P2_1/n$, a = 11.3206(10), b = 15.9765(14), c = 16.5480(14) Å, β = 91.496(4)°, U = 2991.9(3) Å^3, Z = 2, D_c = 1.509 Mg m^{-3}, μ(Cu-Kα) = 8.216 mm^{-1}, T = 123 K. Total 18554 reflections, 5365 unique, R_{int} = 0.139. Refinement of 5024 reflections (385 parameters) with I >2σ(I) converged at final R1 = 0.1118 (R1 all data = 0.1134), wR2 = 0.2308 (wR2 all data = 0.2310), gof = 1.0458.

[{$Co(NCS)_2$(**3**)$_2$}·4$CHCl_3$]$_n$: $C_{54}H_{46}Cl_{12}CoN_8O_2S_2$, M = 1387.47, pink block, monoclinic, space group $P2_1/n$, a = 11.7747(11), b = 15.5746(15), c = 16.6739(15) Å, β = 93.870(7)°, U = 3050.8(3) Å^3, Z = 2, D_c = 1.51 Mg m^{-3}, μ(Cu-Kα) = 8.070 mm^{-1}, T = 123 K. Total 5909 reflections, 5248 unique, R_{int} = 0.053. Refinement of 4479 reflections (331 parameters) with I >2σ(I) converged at final R1 = 0.1112 (R1 all data = 0.1236), wR2 = 0.2753 (wR2 all data = 0.2832), gof = 0.9761.

[{$Co(NCS)_2$(**6**)$_2$}·0.5H_2O]$_n$: $C_{40}H_{39}CoN_8O_{0.50}S_2$, M = 762.87, pink block, monoclinic, space group $C2/c$, a = 37.272(4), b = 11.9575(12), c = 23.770(3) Å, β = 125.290(6)°, U = 8647.3(17) Å^3, Z = 8, D_c = 1.172 Mg m^{-3}, μ(Cu-Kα) = 4.302 mm^{-1}, T = 123 K. Total 33334 reflections, 7564 unique, R_{int} = 0.117. Refinement of 2975 reflections (469 parameters) with I >2σ(I) converged at final R1 = 0.1514 (R1 all data = 0.2634), wR2 = 0.3615 (wR2 all data = 0.4950), gof = 1.0612.

[{$Cd_2(NO_3)_4$(**3**)$_3$}·3$CHCl_3$]$_n$: SQUEEZE[123] was used to treat the solvent region. $C_{75}H_{66}Cd_2Cl_9N_{13}O_{15}$, M = 1933.30, colourless block, monoclinic, space group $P2_1/n$, a = 15.0312(9), b = 25.4508(11), c = 21.7048(12) Å, β = 92.051(4)°, U = 8298.0(5) Å^3, Z = 4, D_c = 1.55 Mg m^{-3}, μ(Cu-Kα) = 7.363 mm^{-1}, T = 123 K. Total 55 690 reflections, 14 425 unique, R_{int} = 0.090. Refinement of 14 419 reflections (854 parameters) with I > 2σ(I) converged at final R_1 = 0.0814 (R_1 all data = 0.1228), wR_2 = 0.2242 (wR_2 all data = 0.2753), gof = 0.9871. CCDC 1402483.

[{$Cd_2(NO_3)_4$(**19**)$_4$}·3$CHCl_3$]$_n$: SQUEEZE[123] was used to treat the solvent region. $C_{107}H_{103}Cd_2Cl_9N_{16}O_{16}$, M = 2412.97, colourless block, monoclinic, space group $P2_1/c$, a = 25.945(6), b = 24.578(5), c = 17.527(3) Å, β = 91.069(9)°, U = 11 174.7(17) Å^3, Z = 4, D_c = 1.43 Mg m^{-3}, μ(Cu-Kα) = 5.601 mm^{-1}, T = 123 K. Total 76 477 reflections, 19 048 unique, R_{int} = 0.047. Refinement of 19 027 reflections (1232 parameters) with $I > 2\sigma(I)$ converged at final R_1 = 0.1340 (R_1 all data = 0.1419), wR_2 = 0.3465 (wR_2 all data = 0.3513), gof = 1.0024. CCDC 1402485.

[{$Cd_2(NO_3)_4$(**4**)$_4$}·$CHCl_3$·MeOH]$_n$: SQUEEZE[123] was used to treat the solvent region. $C_{108}H_{112}Cd_2Cl_3N_{16}O_{17}$, M = 2261.35, colourless block, monoclinic, space group $P2_1/c$, a = 25.2624(12), b = 25.0809(11), c = 16.7959(8) Å, β = 92.522(3)°, U = 10 631.6(9) Å^3, Z = 4, D_c = 1.41 Mg m^{-3}, μ(Cu-Kα) = 4.500 mm^{-1}, T = 123 K. Total 44 477 reflections, 18 427 unique, R_{int} = 0.089. Refinement of 11 009 reflections (1191 parameters) with $I > 2\sigma(I)$ converged at final R_1 = 0.1026 (R_1 all data = 0.1279), wR_2 = 0.2838 (wR_2 all data = 0.3071), gof = 1.0024. CCDC 1402486.

[{$Cd(NO_3)_2$(**20**)$_2$}·2MeOH]$_n$: $C_{58}H_{66}CdN_8O_{10}$, M = 1147.61, colourless block, monoclinic, space group $P2_1/n$, a = 17.336(3), b = 17.302(3), c = 18.817(3) Å, β = 97.458(7)°, U = 5596.3(8) Å^3, Z = 4, D_c = 1.362 Mg m^{-3}, μ(Cu-Kα) = 3.658 mm^{-1}, T = 123 K. Total 11 3924 reflections, 9826 unique, R_{int} = 0.087. Refinement of 5855 reflections (659 parameters) with $I > 2\sigma(I)$ converged at final R_1 = 0.0986 (R_1 all data = 0.1359), wR_2 = 0.2752 (wR_2 all data = 0.3369), gof = 0.9707. CCDC 1402484.

[Zn_2Cl_4(**13**)]$_n$: $C_{48}H_{48}Cl_4N_6O_2Zn_2$, M = 1013.52, yellow block, monoclinic, space group $C2/c$, a = 20.4985(9), b = 11.6491(3), c = 23.7457(10) Å, β = 91.737(4)°, U = 5667.6(4) Å^3, Z = 4, D_c = 1.188 Mg m^{-3}, μ(Ga-Kα) = 2.036 mm^{-1}, T = 123 K. Total 95 099 reflections, 5516 unique, R_{int} = 0.057. Refinement of 3189 reflections (280 parameters) with $I > 2\sigma(I)$ converged at final R_1 = 0.0451 (R_1 all data = 0.0676), wR_2 = 0.0510 (wR_2 all data = 0.0578), gof = 0.8726. CCDC 1541160.

$[Zn_2Cl_4(\mathbf{14})\cdot 2MeOH]_n$: $C_{58}H_{72}Cl_4N_6O_4Zn_2$, M = 1189.82, colourless plate, monoclinic, space group $C2/c$, a = 20.777(2), b = 11.6382(9), c = 23.8738(17) Å, β = 90.074(7)°, U = 5772.8(8) Å^3, Z = 4, D_c = 1.369 Mg m^{-3}, μ(Cu-Kα) = 3.122 mm^{-1}, T = 123 K. Total 34 161 reflections, 5360 unique, R_{int} = 0.034. Refinement of 5077 reflections (332 parameters) with $I > 2\sigma(I)$ converged at final R_1 = 0.0726 (R_1 all data = 0.0749), wR_2 = 0.1722 (wR_2 all data = 0.1726), gof = 0.7625. CCDC 1541161.

17.6 3D coordination frameworks

$[\{Co(NCS)_2(\mathbf{12})_2\}\cdot 2C_6H_4Cl_2]_n$: $C_{56}H_{44}Cl_4CoN_8O_2S_2$, M = 1125.89, pink block, monoclinic, space group $P2_1/c$, a = 10.2136(9), b = 19.3452(17), c = 16.2214(15) Å, β = 107.027(3)°, U = 3064.6(5) Å^3, Z = 2, D_c = 1.22 Mg m^{-3}, μ(Cu-Kα) = 4.787 mm^{-1}, T = 123 K. Total 20265 reflections, 5638 unique, R_{int} = 0.029. Refinement of 4472 reflections (298 parameters) with $I > 2\sigma(I)$ converged at final $R1$ = 0.1258 ($R1$ all data = 0.0483), $wR2$ = 0.1287 ($wR2$ all data = 0.1437), gof = 0.9942. CCDC 1550587.

$[Co(NCS)_2(\mathbf{17})\cdot 4CHCl_3]_n$: $C_{58}H_{60}Cl_{12}CoN_8O_2S_2$, M = 1449.6, pink block, orthorhombic, space group $Pna2_1$, a = 17.8916(15), b = 19.6745(17), c = 19.088(2) Å $\alpha = \beta = \gamma$ = 90°, U = 6719.1(8) Å^3, Z = 4, D_c = 1.433 Mg m^{-3}, μ(Cu-Kα) = 7.350 mm^{-1}, T = 123 K. Total 64379 reflections, 11789 unique, R_{int} = 0.090. Refinement of 11763 reflections (704 parameters) with $I > 2\sigma(I)$ converged at final $R1$ = 0.1343 ($R1$ all data = 0.1464), $wR2$ = 0.3170 ($wR2$ all data = 0.3268), gof = 1.0827. CCDC 1035825.

$[Co_2(NCS)_4(\mathbf{4})_4]_n$ (enantiomer I): a = 23.7111(4), Å, b = 23.7111(4) Å, c = 46.9783(7) Å, $\alpha = \beta = \gamma$ = 90°; V = 26412.0(9) Å^3, tetragonal, $P4_12_12$, Z = 8, ρ_{calc} = 1.000 Mg/m^3; μ = 0.362 mm^{-1}**;** T = 100(2) K; θ_{max} = 27.221°, 79766 measured reflections, 26743 unique reflections [R_{int} = 0.0691], 12814 with $F^2 > 2\sigma$, R(F, $F^2>2\sigma$) = 0.0901; Rw(F^2, all data) = 0.2795, GoF = 0.940, CCDC: 1474325.

$[Co_2(NCS)_4(\mathbf{4})_4]_n$ (enantiomer II): a = 23.68444(16) Å, b = 23.68444(16) Å, c = 46.9716(4) Å, $\alpha = \beta = \gamma$ = 90°; V = 26348.8(4) Å^3, tetragonal, $P4_32_12$, Z = 8, ρ_{calc} = 1.002 Mg/m^3; μ = 0.363 mm^{-1}**;** T = 100(2) K; θ_{max} = 26.6550°, 294870 measured reflections, 26290 unique reflections [R_{int} = 0.0748], 17361 with $F^2 > 2\sigma$, R(F, $F^2>2\sigma$) = 0.0894; Rw(F^2, all data) = 0.2836, GoF = 1.032, CCDC: 1474326.

[{$Co_2(NCS)_4$(**5**)$_4$}·2$CHCl_3$·MeOH]$_n$: a = 23.88216(9) Å, b = 23.88216(9) Å, c = 46.8514(3) Å, $\alpha = \beta = \gamma = 90°$; V = 26722.0(3) Å^3, tetragonal, $P4_12_12$, Z = 8, ρ_{calc} = 1.207 Mg/m^3; μ = 0.486 mm^{-1}**;** T = 100(2) K; θ_{max} = 27.5260°, 292603 measured reflections, 30625 unique reflections [R_{int} = 0.0437], 28191 with $F^2 > 2\sigma$, R(F, F^2>2σ) = 0.0913; Rw(F^2, all data) = 0.2615, GoF = 1.029, CCDC: 1474327.

[{Zn_2Br_4(**16**)}·H_2O]$_n$: $C_{54}H_{44}Br_4N_6O_3Zn_2$, M = 1275.36, yellow block, trigonal, space group R-3, $a = b$ = 35.9593(6), c = 25.1227(3) Å, U = 28 133.2(9) Å^3, Z = 9, D_c = 0.677 Mg m^{-3}, μ(Ga-Kα) = 1.410 mm^{-1}, T = 123 K. Total 140 567 reflections, 12 851 unique, R_{int} = 0.073. Refinement of 6571 reflections (316 parameters) with $I > 2\sigma(I)$ converged at final R_1 = 0.0898 (R_1 all data = 0.1242), wR_2 = 0.0719 (wR_2 all data = 0.0924), gof = 0.9393. CCDC 1541159.

18 PRINTED PUBLICATIONS

18.1 Paper 1 (Published by Elsevier)

Polyhedron 81 (2014) 98–104

Contents lists available at ScienceDirect

Polyhedron

journal homepage: www.elsevier.com/locate/poly

4′-(Pyrimidin-5-yl)- and 4′-(2-methylpyrimidin-5-yl)-4,2′:6′,4″-terpyridines: Selective coordination to zinc(II) through the 4,2′:6′,4″-terpyridine domain

Y. Maximilian Klein, Edwin C. Constable, Catherine E. Housecroft *, Jennifer A. Zampese

Department of Chemistry, University of Basel, Spitalstrasse 51, 4056 Basel, Switzerland

ARTICLE INFO

Article history:
Received 25 April 2014
Accepted 23 May 2014
Available online 2 June 2014

Keywords:
4,2′:6′,4″-Terpyridine
Zinc
Structure
Coordination polymer
X-ray diffraction

ABSTRACT

The preparation and characterization of the compounds 4′-(pyrimidin-5-yl)-4,2′:6′,4″-terpyridine (**3**) and 4′-(2-methylpyrimidin-5-yl)-4,2′:6′,4″-terpyridine (**4**) are described. Preferential coordination through the terminal pyridine donors of the tpy domain is observed when **3** and **4** are treated with $ZnCl_2$ or ZnI_2. The 1-dimensional coordination polymers $[\{ZnCl_2(\mathbf{3})\}_n]$, $[\{ZnI_2(\mathbf{3})\}_n]$ and $[\{ZnI_2(\mathbf{4})\cdot MeOH\}_n]$ have been structurally characterized by single crystal X-ray crystallography. $[\{ZnI_2(\mathbf{3})\}_n]$ is helical and crystallizes with both *P*- and *M*-helices in the lattice; the packing of *P*- and *M*-chains involves discrete tetradecker π-stacking domains involving 4,2′:6′,4″-tpy units. The introduction of the 2-methyl substituent on going from **3** to **4** has only a small effect on the structure of $[\{ZnI_2(L)\}_n]$ (L = **3** or **4**). The two coordination polymer chains assemble through face-to-face π-interactions into sheets with the pyrimidin-5-yl units projecting outwards. The presence of the 2-methyl substituents in **4** forces the sheets in $[\{ZnI_2(\mathbf{4})\cdot MeOH\}_n]$ further apart compared to those in $[\{ZnI_2(\mathbf{3})\}_n]$, leading to the accommodation of MeOH molecules in cavities between the sheets.

1. Introduction

The use of 4,2′:6′,4″-terpyridine (4,2′:6′,4″-tpy) ligands as metal-binding domains for the assembly of coordination polymers is highly attractive and topical [1]. Of the three nitrogen donors in 4,2′:6′,4″-tpy, only the outer two typically bind metal ions leading to a divergent, V-shaped building block with well-defined directionality. The reaction of 4,2′:6′,4″-tpy with $ZnCl_2$ leads to a helical coordination polymer $[\{ZnCl_2(4,2′:6′,4″\text{-tpy})_n]$ [2], and this structural motif persists in a range of $[\{ZnX_2(4′\text{-R-}4,2′:6′,4″\text{-tpy})\}_n]$ polymers in which R is a *tert*-butyl [3], aryl [4,5] or 4-alkoxyphenyl [6] substituent. Coordinatively non-innocent 4′-R functionalities have the potential to extend the coordination assembly and examples include a closed metallocapsule when R = 4-pyridyl [7,8] and 2- or 3-dimensional networks when R = CO_2H [9–11]. We have also recently illustrated the assembly of a 2D → 2D parallel interpenetrated array of (4,4) sheets by using a ditopic bis(4,2′:6′,4″-terpyridine) [12].

We have previously demonstrated that the 2,2′:6′,2″-tpy domain in ligand **1** (Scheme 1) preferentially binds iron(II) or ruthenium(II) leaving the 5-pyrimidyl substituent as a pendant moiety in the discrete complex cations $[Fe(\mathbf{1})_2]^{2+}$ and $[Ru(\mathbf{1})_2]^{2+}$ [13]. Post-treatment of $[Ru(\mathbf{1})_2][PF_6]_2$ with $CuCl_2\cdot 2H_2O$ results in the assembly of a 2-dimensional network with copper(II) centres coordinated to the pyrimidinyl N-donors [13]. Recently, Granifo et al. [14] have reported the synthesis of ligand **2** and shown that it reacts with $Zn(acac)_2$ (Hacac = acetylacetone) to give the discrete complex $[Zn(acac)_2(\mathbf{2})_2]$, in addition to the 1-dimensional coordination polymer $[\{Zn(acac)_2(\mathbf{2})\}_n]$. In $[Zn(acac)_2(\mathbf{2})_2]$, each ligand **2** is monodentate and binds through one pyridyl unit, while in $[\{Zn(acac)_2(\mathbf{2})\}_n]$, each molecule of **2** bridges two zinc(II) centres and coordinates through the nitrogen donors of one pyridyl and one pyrimidinyl unit. These results contrast with our own observations on the coordination behaviour of ligands **3** and **4**, described in this work.

2. Experimental

2.1. General

^1H and ^{13}C NMR spectra were recorded on a Bruker Avance III-500 spectrometer with chemical shifts referenced to residual solvent peaks (∂(TMS) = 0 ppm). Solution electronic absorption spectra were recorded on a Cary 5000 spectrophotometer. Electrospray

* Corresponding author. Tel.: +41 612671008; fax: +41 61 267 1018.
E-mail address: catherine.housecroft@unibas.ch (C.E. Housecroft).

http://dx.doi.org/10.1016/j.poly.2014.05.058
0277-5387/

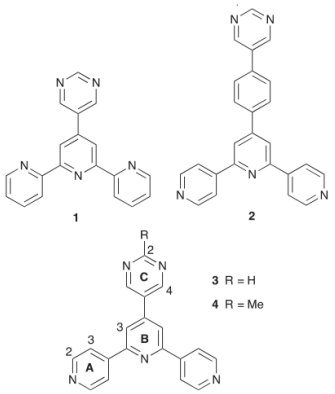

Scheme 1. Ligand structures and atom numbering for NMR spectroscopic assignments.

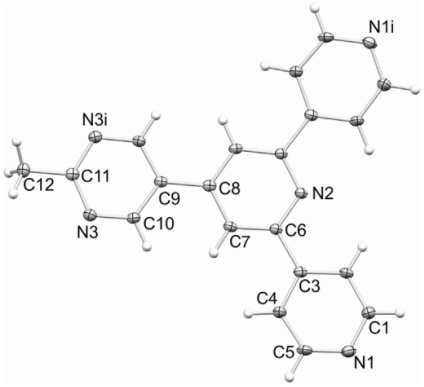

Fig. 1. Structure of molecule **4** with ellipsoids plotted at the 40% probability level. Symmetry code i = 2 − *x*, *y*, *z*. Selected bond parameters: N1–C5 = 1.335(2), N1–C1 = 1.337(2), N2–C6 = 1.3402(19), N3–C10 = 1.336(2), N3–C11 = 1.3395(17) Å; C5–N1–C1 = 116.12(15), C6–N2–C6^{i} = 118.19(19), C10–N3–C11 = 116.69(14)°.

ionization (ESI) mass spectra were recorded on a Bruker esquire 3000^{plus} mass spectrometer.

Pyrimidine-5-carbaldehyde (Alfa Aesar) and 2-methylpyrimidine-5-carbaldehyde (Fluorochem) were used as received.

2.2. Ligand **3**

Pyrimidine-5-carbaldehyde (0.28 g, 2.5 mmol) was dissolved in EtOH (40 mL) and 4-acetylpyridine (0.57 mL, 0.62 g, 5 mmol) was added, followed by crushed KOH (0.28 g, 5 mmol). The initially colourless solution changed to yellow and then red. Aqueous NH_3 (25% in water, 12.3 mL, 80 mmol) was added dropwise and the reaction mixture stirred at room temperature overnight. A yellow precipitate formed which was collected by filtration, washed with water (3 × 5 mL) and EtOH (3 × 5 mL) and recrystallized from $CHCl_3$/MeOH. Compound **3** was obtained as a yellow solid (0.34 g, 1.28 mmol, 51%). Decomp. >260 °C. ^{1}H NMR (500 MHz, $CDCl_3$) ∂/ppm 9.39 (s, 1H, H^{C2}) 9.13 (s, 2H, H^{C4}), 8.83 (m, 4H, H^{A2}), 8.09 (m, 4H, H^{A3}), 8.04 (s, 2H, H^{B3}). ^{1}H NMR (500 MHz, *d*-TFA) ∂/ppm 9.97 (s, 2H, H^{C4}) 9.80 (s, 1H, H^{C2}), 9.06–8.90 (m, 8H, H^{A2}/H^{A3}), 8.83 (s, 2H, H^{B3}); ^{13}C{^{1}H} NMR (126 MHz, *d*-TFA) ∂/ppm 158.4 (C^{C3}), 157.0 (C^{A4}), 155.2 (C^{B2}), 154.5 (C^{C2}), 145.0 (C^{B4}), 144.1 (C^{A2}), 135.8 (C^{C5}), 127.3 (C^{A3}), 125.5 (C^{B3}); IR (solid, *ν*/cm^{-1}) 4696 (m), 3033 (w), 2925 (w), 1652 (w), 1613 (w), 1596 (s), 1569 (s), 1553 (s), 1544 (m), 1539 (m), 1533 (m), 1506 (w), 1436 (s), 1416 (m), 1393 (s), 1356 (m), 1327 (w), 1318 (w), 1274 (w), 1189 (m), 1133 (w), 1059 (w), 1029 (w), 995 (m), 897 (w), 890 (w), 841 (m), 823 (s), 804 (w), 722 (s), 701 (m), 642 (m), 638 (s), 625 (s), 619 (s), 616 (s), 609 (m), 514 (m), 508 (s), 502 (s). UV–Vis (CH_2Cl_2, 2.5 × 10^{-5} M) *λ*/nm (*ε*/dm^3 mol^{-1} cm^{-1}) 242 (47 359), 312 (9184). ESI MS *m*/*z* 312.2 [M+H]$^+$ (calc. 312.1). Satisfactory elemental analysis could not be obtained (see text).

2.3. Ligand **4**

2-Methylpyrimidine-5-carbaldehyde (0.27 g, 2.21 mmol) was dissolved in EtOH (40 mL), and 4-acetylpyridine (0.57 mL, 0.62 g,

Table 1
Crystallographic data for compound **4** and the polymers [{$ZnCl_2$(**3**)}$_n$], [{ZnI_2(**3**)}$_n$] and [{ZnI_2(**4**)}·MeOH}$_n$].

Compound	**4**	[{$ZnCl_2$(**3**)}$_n$]	[{ZnI_2(**3**)}$_n$]	[{ZnI_2(**4**)}·MeOH}$_n$]
Formula	$C_{20}H_{15}N_5$	$C_{19}H_{13}Cl_2N_5Zn$	$C_{19}H_{13}I_2N_5Zn$	$C_{21}H_{19}I_2N_5OZn$
Formula weight	325.37	447.63	630.53	676.58
Crystal colour and habit	colourless block	colourless needle	yellow block	yellow block
Crystal system	orthorhombic	monoclinic	monoclinic	monoclinic
Space group	$Pmn2_1$	$P2_1/n$	$P2_1/n$	$P2_1/n$
a (Å)	18.0817(12)	8.4559(11)	10.0386(7)	11.3508(4)
b (Å)	4.3834(3)	19.194(2)	11.2543(8)	11.6668(4)
c (Å)	9.7540(6)	11.2787(13)	18.3065(13)	17.6152(6)
α (°)	90	90	90	90
β (°)	90	97.057(9)	103.838(3)	103.204(2)
γ (°)	90	90	90	90
U (Å^3)	773.10(9)	1816.6(4)	2008.2(2)	2271.07(14)
D_c (Mg m^{-3})	1.398	1.637	2.085	1.979
T (K)	123	123	123	123
Z	2	4	4	4
μ (Cu Kα) (mm^{-1})	0.691	4.701	25.948	23.030
Reflection collected (R_{int})	9665 (0.0295)	15849 (0.0643)	36476 (0.0436)	33192 (0.0387)
Unique reflection	1449	3260	3628	4126
Reflection for refinement	1429	2331	3516	3891
Parameters	121	281	244	274
Threshold	$I > 2\sigma(I)$	$I > 2\sigma(I)$	$I > 2\sigma(I)$	$I > 2\sigma(I)$
R_1 (R_1 all data)	0.0262 (0.0265)	0.0528 (0.0795)	0.0272 (0.0283)	0.0222 (0.0237)
wR_2 (wR_2 all data)	0.0731 (0.0736)	0.1330 (0.1473)	0.0710 (0.0718)	0.0578 (0.0588)
Goodness of fit (GOF)	1.088	1.015	1.104	1.035

5 mmol) was added followed by crushed solid KOH (0.33 g, 5.90 mmol) after which the solution turned red. Aqueous NH_3 (25% in water, 13.9 mL, 90 mmol) was added dropwise and the mixture stirred overnight at ambient temperature. A yellow precipitate formed which was separated by filtration, washed with water (3 × 7 mL) and ethanol (3 × 7 mL) and recrystallized from chloroform/methanol. Compound **4** was obtained as a white solid (0.26 g, 0.78 mmol, 32%). Decomposition > 260 °C. ^{1}H NMR (500 MHz, $CDCl_3$) ∂/ppm 9.02 (s, 2H, H^{C4}), 8.83 (m, 4H, H^{A2}), 8.09 (m, 4H, H^{A3}), 8.01 (s, 2H, H^{B3}), 2.87 (s, 3H, H^{Me}); $^{13}C\{^1H\}$ NMR (126 MHz, $CDCl_3$) ∂/ppm 169.3 (C^{C2}), 155.9 (C^{A4}), 155.14 (C^{C4}), 150.8 (C^{B4}) 150.7 (C^{A2}), 145.3 (C^{B2}), 128.5 (C^{C5}), 121.1 (C^{A3}), 118.3 (C^{B3}), 25.9 (C^{Me}); IR (solid, ν/cm^{-1}) 3077 (w), 3033 (w), 1609 (m), 1594 (s), 1569 (m), 1549 (m), 1544 (m), 1539 (m), 1531 (m), 1464 (s), 1461 (s), 1456 (s), 1447 (m), 1432 (m), 1429 (m), 1423 (m), 1404 (m), 1377 (m), 1373 (m), 1368 (m), 1247 (m), 1064 (m), 1028 (m), 999 (m), 995 (m), 895 (m), 851 (m), 844 (m), 835 (s), 791 (m), 739 (m), 731 (m), 670 (m), 664 (m), 649 (m), 637 (s), 629 (s), 619 (m), 616 (m), 604 (m), 597 (m), 582 (m), 570 (m), 564 (m), 543 (m), 541 (m), 535 (m), 528 (m), 523 (m), 519 (m), 513 (s), 506 (s), 502 (s). UV–Vis (MeCN, 2.5 × 10^{-5} M) λ/nm (ε/dm^3 mol^{-1} cm^{-1}) 247 (44458), 312 (7856). ESI-MS m/z 326.3 $[M+H]^+$ (calc. 326.1). Found: C, 69.04; H, 4.75; N, 20.22; required for $C_{20}H_{15}N_5.H_2O$ C, 69.96; H, 4.99; N, 20.40.

2.4. *[{$ZnCl_2$(**3**)}$_n$]*

A solution of $ZnCl_2$ (3.41 mg, 0.025 mmol) in MeOH (8 mL) was layered over a $CHCl_3$ solution (5 mL) of **3** (7.78 mg, 0.025 mmol) and the tube was sealed with Parafilm. Colourless crystals of [{$ZnCl_2$(**3**)}$_n$] (7.0 mg, 0.016 mmol, 63%) were obtained after 2 weeks. IR (solid, ν/cm^{-1}) 3062 (m), 1615 (s), 1607 (s), 1572 (m), 1559 (m), 1543 (m), 1506 (m), 1447 (m), 1425 (m), 1396 (s), 1323 (m), 1218 (m), 1195 (m), 1135 (w), 1064 (s), 1029 (s), 990 (w), 891 (w), 874 (m), 836 (s), 744 (w), 714 (s), 666 (w), 648 (s),

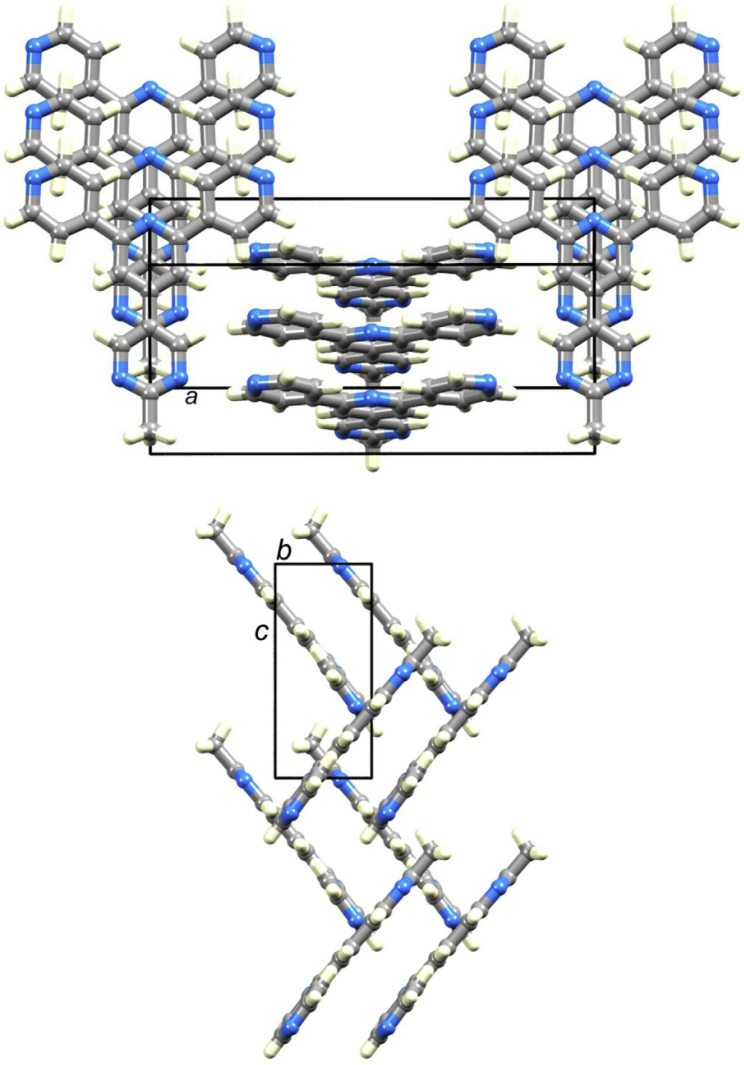

Fig. 2. Packing of molecules of **4** in the crystal lattice showing π-stacking of planar molecules and herring-bone arrangement of the stacks. (Colour online.)

629 (s), 514 (m). Found: C, 49.59; H, 3.03; N, 14.97; required for $C_{19}H_{13}N_5Cl_2Zn{\cdot}H_2O$ C, 49.01; H, 3.25; N, 15.04.

2.5. [{ZnI_2(**3**)}$_n$]

An MeOH (8 mL) solution of ZnI_2 (8.0 mg, 0.025 mmol) was layered over a $CHCl_3$ (5 mL) solution of **3** (7.78 mg, 0.025 mmol). The tube was sealed with Parafilm and after 2 weeks, yellow crystals of [{ZnI_2(**3**)}$_n$] (3.5 mg, 0.006 mmol, 22%) had grown. IR (solid, ν/cm^{-1}) 3056 (w), 1614 (s), 1606 (s), 1568 (m), 1556 (m), 1506 (w), 1444 (m), 1421 (m), 1396 (s), 1322 (w), 1220 (m), 1192 (w), 1135 (w), 1066 (s), 1025 (s), 991 (w), 886 (w), 873 (w), 851 (m), 836 (s), 746 (w), 717 (m), 668 (w), 648 (s), 634 (s), 626 (s). Found: C, 35.60; H, 2.27; N, 10.89; required for $C_{19}H_{13}I_2N_5I_2Zn{\cdot}H_2O$ C, 35.19; H, 2.33; N, 10.80.

2.6. [{ZnI_2(**4**)·MeOH}$_n$]

A solution of ZnI_2 (8.0 mg, 0.025 mmol) in MeOH (8 mL) was layered on top of a solution of **3** (4.07 mg, 0.013 mmol) in $CHCl_3$ (5 mL) and the tube was left sealed with Parafilm. Yellow crystals of [{ZnI_2(**4**).MeOH}$_n$] (8.0 mg, 0.012 mmol, 91%) were obtained after 2 weeks. IR (solid, ν/cm^{-1}) 2922 (m), 1608 (s), 1548 (m), 1460 (s), 1406 (m), 1372 (m), 1221 (w), 1065 (m), 1024 (s), 871 (w), 836 (s), 750 (w), 686 (m), 645 (s), 630 (s), 599 (w), 505 (w). Found: C, 38.11; H, 2.95; N, 10.50; required for $C_{20}H_{15}I_2N_5Zn{\cdot}$MeOH C, 37.28; H, 2.83; N, 10.35.

2.7. Crystallography: general

X-ray quality crystals of the complexes were selected from the bulk samples. Data were collected on a Bruker-Nonius Kappa APEX diffractometer; data reduction, solution and refinement used APEX2 [15] and SHELX13 [16]. The ORTEP plot was produced with Mercury v. 3.2 or 3.3 [17,18] which was also used for structure analysis. Crystallographic data are listed in Table 1.

3. Results and discussion

3.1. Synthesis and characterization of compounds **3** and **4**

Compounds **3** and **4** were synthesized using the one-pot strategy introduced by Hanan [19] and were isolated in 51% and 32% yields, respectively. The electrospray mass spectrum of **3** and **4** showed base peaks at m/z = 312.2 and 326.3, respectively, arising from $[M+H]^+$ ions. Satisfactory elemental analytical data for **3** could not be obtained, despite repeated recrystallizations of the bulk material from MeOH/$CHCl_3$. The ^{1}H NMR spectrum of a $CDCl_3$ solution of **3** was assigned using NOESY with observations of cross peaks between signals for H^{C4}/H^{B3} and H^{A3}/H^{B3}. However, the poor solubility of **3** in $CDCl_3$ (and also in CD_2Cl_2, CD_3CN, CD_3OD and d_6-DMSO) did not permit the ^{13}C NMR spectrum to be resolved, despite the use of HMQC and HMBC methods. Thus, the ^{1}H and ^{13}C NMR spectra of the protonated ligand were recorded in *d*-TFA and were assigned by 2D methods (COSY, HMQC, HMBC and NOESY). The shifting of all ^{1}H NMR signals to higher frequency on going from $CDCl_3$ to *d*-TFA is consistent with multiple protonation of **3** in TFA. Introduction of the 2-methyl-substituent on going from **3** to **4** improves the solubility in $CDCl_3$.

The absorption spectra of CH_2Cl_2 solutions (2.5×10^{-5} mol dm^{-3}) of both **3** and **4** are similar. Intense, high energy bands (λ_{max} = 242 nm for **3** and 247 for **4**) and a lower intensity absorption at 312 nm in both compounds were assigned to $\pi^* \leftarrow \pi$ and $\pi^* \leftarrow$ n transitions.

X-ray quality single crystals of **4** were grown serendipitously during attempts to react **4** with iron(II) perchlorate in MeOH; Fig. 1 depicts the molecular structure of **4**. The compound crystallizes in the orthorhombic $Pmn2_1$ space group with half the molecular in the asymmetric unit; the second half is generated by a mirror plane. Bond distances and angles (caption to Fig. 1) are as expected. The planes containing pyridine rings with N1 and N2 lie at 4.5° with respect to each other, and essentially, the molecule is planar. Molecules of **4** engage in face-to-face π-interactions. Adjacent molecules are slipped with respect to one another leading to the dominant interaction being between central pyridine and pyrimidine rings (Fig. 2a, distance between planes = 3.32 Å; intercentroid separation = 3.63 Å). The stacks assemble in a herringbone arrangement with CH···N hydrogen bonds as the dominant packing interactions (C10H10a···N1^{ii} = 2.52, C4H4a···N1^{ii} = 2.66, C7H7a···N1^{ii} = 2.74, N3···H5a^{iii}C5^{iii} = 2.52 Å, symmetry codes: ii = $^3/_2-x$, $1-y$, $-^1/_2+z$; iii = $^3/_2-x$, $2-y$, $^1/_2+z$).

3.2. Reaction of **3** with $ZnCl_2$

Layering solutions of MeOH/$ZnCl_2$ and $CHCl_3$/**3** resulted in the growth of colourless crystals. Elemental analysis of the bulk sample was consistent with a stoichiometry $ZnCl_2$(**3**) and single crystal X-ray analysis confirmed the formation of the 1-dimensional coordination polymer [{$ZnCl_2$(**3**)}$_n$]. The complex crystallizes in the monoclinic space group $P2_1/n$ with one {$ZnCl_2$(**3**)} unit in the asymmetric unit. The pyrimidin-5-yl substituent is disordered and has been modelled over two sites (0.61 and 0.39 fractional occupancies) both having atoms C17 and C19 in common. Only the major occupancy site is shown in Fig. 3. The rings containing N1, N2 and N3 are essentially coplanar (angles between the planes containing N1/N2 and N2/N3 = 1.8 and 5.3°, respectively); for the major occupancy site, the plane of the pyrimidine ring is twisted 19.8° with respect to the ring containing N3. Atom Zn1 is in a distorted tetrahedral environment and ligand **3** bridges through the outer pyridine rings (N1 and N3) between pairs of $ZnCl_2$units. As is characteristic of 4,2′:6′,4″-tpy ligands [1], the central donor N2 is not coordinated. Atoms N4 and N5 in the pyrimidine ring are also non-coordinating. In this respect, the structure can be compared with that of the 1-dimensional polymer [{$ZnCl_2$(4′-(4-pyridyl)-4,2′:6′,4″-tpy)}$_n$] [20] in which the pendant pyridyl

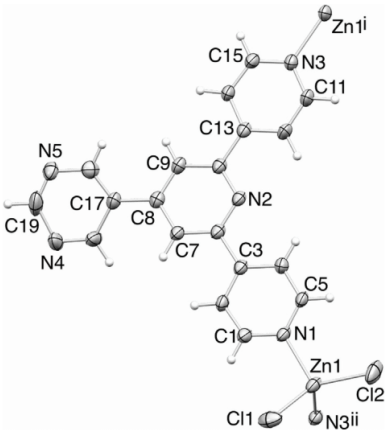

Fig. 3. Repeat unit (showing connectivities to the next units) in [{$ZnCl_2$(**3**)}$_n$]; symmetry codes: i = $^1/_2-x$, $-^1/_2+y$, $^3/_2-z$; ii = $^1/_2-x$, $^1/_2+y$, $^3/_2-z$) and ellipsoids plotted at the 40% probability level. Selected bond parameters: Zn1–N1 = 2.046(3), Zn1–N3^{ii} = 2.054(4), Zn1–Cl2 = 2.1996(15), Zn1–Cl1 = 2.2384(17) Å; N1–Zn1–N3^{ii} = 107.15(15), N1–Zn1–Cl2 = 111.25(12), N3^{ii}–Zn1–Cl2 = 110.22(11), N1–Zn1–Cl1 = 103.37(12), N3^{ii}–Zn1–Cl1 = 101.46(12), Cl2–Zn1–Cl1 = 122.15(8)°.

domain does not coordinate. The structures of $[\{ZnCl_2(\mathbf{3})\}_n]$ and $[\{ZnCl_2(4'\text{-}(4\text{-pyridyl})\text{-}4,2':6',4''\text{-tpy})\}_n]$ are also similar in that the polymer chains are both built up by 2-fold screw axes. That **3** bridges through two pyridyl donors of the 4,2′:6′,4″-tpy domain contrasts with the related ligand **2** (Scheme 1) which has been shown to bridge through one pyridyl donor and one pyrimidinyl unit [14]. The pitch of the helical $[\{ZnCl_2(\mathbf{3})\}_n]$ chain (19.194(2) Å) is related to the N–Zn–N angle [1] and the value of 107.15(15)°) in $[\{ZnCl_2(\mathbf{3})\}_n]$ is similar to that in $[\{ZnCl_2(4'\text{-}(4\text{-pyridyl})\text{-}4,2':6',4''\text{-tpy})\}_n]$ (108.3(1)°) in which the helical pitch is 20.661(3) Å [20].

Both the *P*- and *M*-helices are present in the lattice of $[\{ZnCl_2(\mathbf{3})\}_n]$ and chains of opposite chirality associate through face-to-face π-interactions of 4,2′:6′,4″-tpy units. Fig. 4 shows that this involves discrete tetradecker domains. At the centre of the sandwich, the rings containing N1 and N2 of a centrosymmetric pair of 4,2′:6′,4″-tpy units stack with an interplane separation of 3.35 Å. The outer π-interactions involve stacking of the ring with N3 over the pair of rings with N1/N2. The interactions between *P*- and *M*-chains are closely related to that observed in $[\{ZnCl_2(4'\text{-}(4\text{-pyridyl})\text{-}4,2':6',4''\text{-tpy})\}_n]$ [1,20].

3.3. Reactions of **3** and **4** with ZnI_2

Layering experiments with an MeOH solution of ZnI_2 and $CHCl_3$ solution of **3** or **4** resulted in the formation of yellow crystals of the 1-dimensional coordination polymers $[\{ZnI_2(\mathbf{3})\}_n]$ and $[\{ZnI_2(\mathbf{4})\cdot MeOH\}_n]$, respectively. Despite the presence of solvent molecules in the latter, the two structures are very similar and will be discussed together. Both complexes crystallizes in the monoclinic space group $P2_1/n$ and Fig. 5 depicts the repeat unit in $[\{ZnI_2(\mathbf{4})\cdot MeOH\}_n]$. The same numbering scheme for both compounds has been used and a comparison of important bond parameters is given in Table 2. The tetrahedral coordination environment of Zn1 in each complex is similarly distorted, as indicated by the N–Zn–N and I–Zn–I bond angles (Table 2). Fig. 5 includes the MeOH molecule which forms an O–H···N hydrogen bond with the pyrimidinyl unit (O100H100···N5 = 2.03, O100···N5 = 2.856(3) Å,

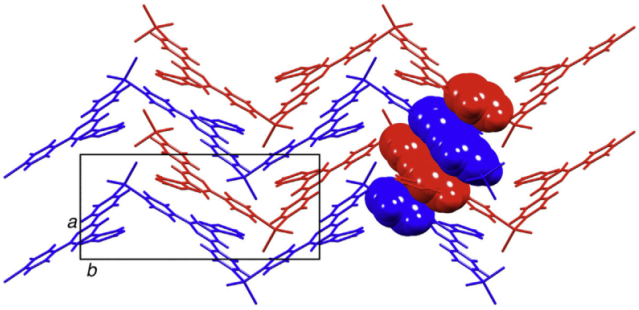

Fig. 4. Packing of *P*- and *M*-chains in $[\{ZnCl_2(\mathbf{3})\}_n]$ involves discrete tetradecker π-stacking domains involving 4,2′:6′,4″-tpy units. Chains of opposite chirality are shown in red and blue, respectively. (Colour online.)

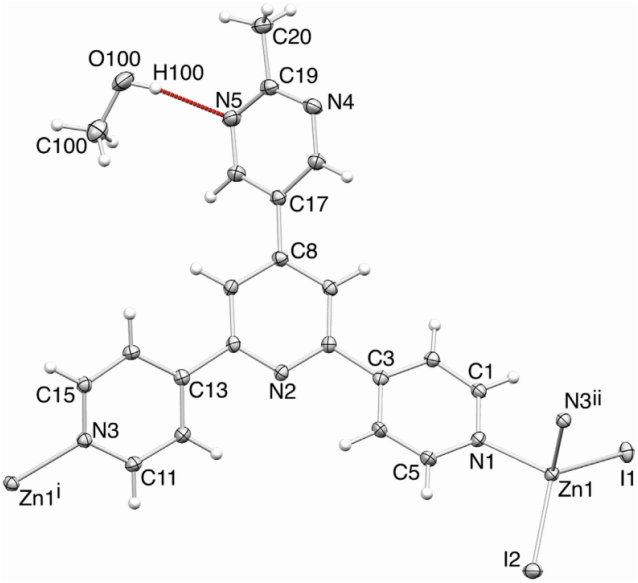

Fig. 5. Repeat unit (showing connectivities to the next units) in $[\{ZnI_2(\mathbf{4})\cdot MeOH\}_n]$; symmetry codes: i = $-{}^1/_2 + x$, ${}^1/_2 - y$, $-{}^1/_2 + z$; ii = ${}^1/_2 + x$, ${}^1/_2 - y$, ${}^1/_2 + z$) and ellipsoids plotted at the 40% probability level.

Table 2
Comparison of selected bond parameters in $[\{ZnI_2(\mathbf{3})\}_n]$ and $[\{ZnI_2(\mathbf{4})\cdot MeOH\}_n]$. The atom numbering for both complexes is as given in Fig. 5.

	$[\{ZnI_2(\mathbf{3})\}_n]$[a]	$[\{ZnI_2(\mathbf{4})\cdot MeOH\}_n]$[b]
Bond distance (Å)		
Zn–N1	2.065(3)	2.076(2)
Zn1–N3^{ii}	2.066(3)	2.066(2)
Zn1–I1	2.5376(5)	2.5530(4)
Zn1–I2	2.5324(5)	2.5426(4)
Bond angle (°)		
N1–Zn1–N3^{ii}	95.54(12)	96.60(9)
I2–Zn1–I1	119.041(19)	123.725(15)

[a] Symmetry code: ii = $^1/_2 + x$, $^1/_2 - y$, $^1/_2 + z$.
[b] Symmetry code: ii = $-^1/_2 + x$, $^1/_2 - y$, $-^1/_2 + z$.

O100–H100···N5 = 169°). Its presence in the lattice is associated with an enlarged cavity which results from the replacement of the hydrogen atom attached to C19 in **3** by the methyl group in **4**. The pyridine and pyrimidine rings are twisted with respect to one another in both $[ZnI_2(\mathbf{3})]_n$ and $[\{ZnI_2(\mathbf{4})\cdot MeOH\}_n]$ with twist angles in the range 17.2–39.7°.

As in $[\{ZnCl_2(\mathbf{3})\}_n]$, only the outer pyridine rings of the 4,2′:6′,4″-tpy domains in $[\{ZnI_2(\mathbf{3})\}_n]$ and $[\{ZnI_2(\mathbf{4})\cdot MeOH\}_n]$ bind to zinc(II). In both compounds, the polymer chain is built up along a glide plane, leading to non-helical polymer chains in contrast to that in $[\{ZnCl_2(\mathbf{3})\}_n]$. The Zn···Zn separations between pairs of adjacent Zn atoms along the chain are 12.9298(9) Å in $[\{ZnI_2(\mathbf{3})\}_n]$ and 13.0295(6) Å in $[\{ZnI_2(\mathbf{4})\cdot MeOH\}_n]$.

Chains in $[\{ZnI_2(\mathbf{3})\}_n]$ interact with one another through π-interactions between 4,2′:6′,4″-tpy domains as shown in Fig. 6a. This results in the assembly of sheets which slice obliquely through the unit cell (Fig. 6b). The pyrimidin-5-yl domains project from each side of the sheet and assist in locking the sheets together in the lattice. Similar packing motifs are present in $[\{ZnI_2(\mathbf{4})\cdot MeOH\}_n]$.

3.4. Solution absorption spectra of the coordination polymers

The absorption spectra of MeCN solutions of dissolved crystalline $[\{ZnCl_2(\mathbf{3})\}_n]$ and $[\{ZnI_2(\mathbf{3})\}_n]$ both showed a broad maximum at 242 nm with a lower energy shoulder at ≈310 nm. The spectra are very similar to that of an MeCN solution of free ligand **3**. The absorption spectra of MeCN solutions of $[\{ZnI_2(\mathbf{4})\}_n]$ and **4** both exhibit the same band maxima at 247 and 312 nm. The data are consistent with dissociation of the complexes in MeCN solution, thus precluding further solution characterization of the materials.

4. Conclusions

We have described the preparation and characterization of two new 4′-functionalized 4,2′:6′,4″-tpy ligands bearing pendant pyrimidin-5-yl or 2-methylpyrimidin-5-yl substituents. In reactions with $ZnCl_2$ and ZnI_2, the ligands bind only through the outer pyridine donors and form 1-dimensional coordination polymers $[\{ZnCl_2(\mathbf{3})\}_n]$, $[\{ZnI_2(\mathbf{3})\}_n]$ and $[\{ZnI_2(\mathbf{4})\cdot MeOH\}_n]$. $[\{ZnCl_2(\mathbf{3})\}_n]$ is

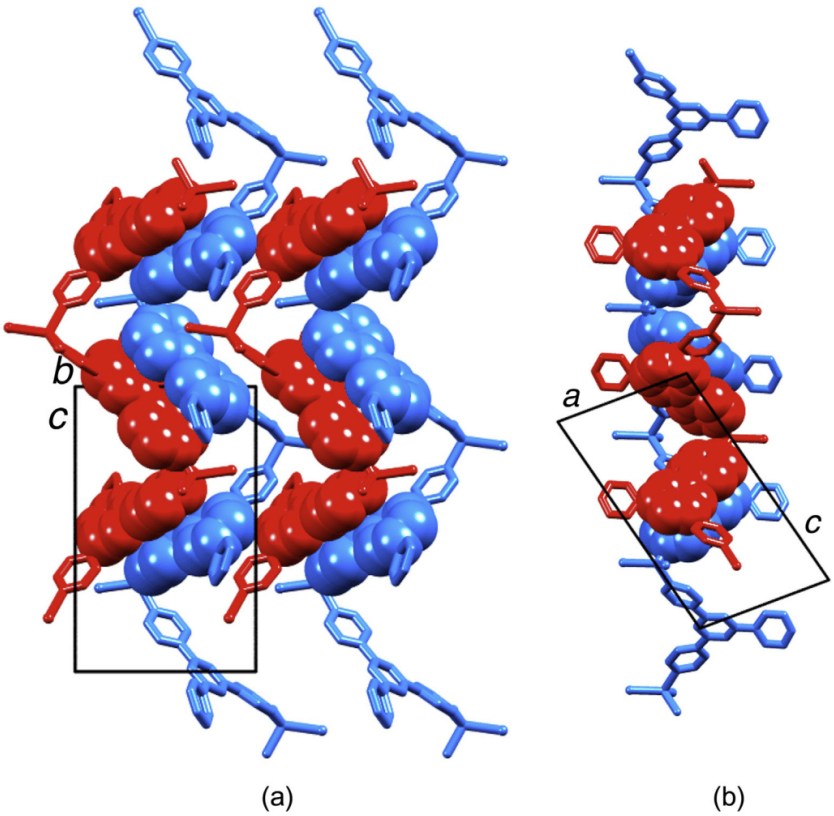

Fig. 6. Assembly of sheets of chains in $[\{ZnI_2(\mathbf{3})\}_n]$. (a) View down the *a*-axis to emphasise the face-to-face π-interactions between chains, and (b) view down the *b*-axis showing the protruding pyrimidin-5-yl domains on each side of the sheet. (Colour online.)

helical and crystallizes as a racemate; it is structurally similar to the previously reported $[\{ZnCl_2(4'\text{-}(4\text{-pyridyl})\text{-}4,2':6',4''\text{-tpy})\}_n]$ [20]. In contrast, the chains in $[\{ZnI_2(\mathbf{3})\}_n]$ and $[\{ZnI_2(\mathbf{4})\cdot MeOH\}_n]$ are built up by glide planes. The two compounds are structurally analogous, and chains pack into sheets through π-interactions between 4,2′:6′,4″-tpy domains; the pyrimidin-5-yl units protrude from the sheets and are involved in interlocking the latter into a 3D assembly. Introducing the 2-methyl substituent on going from **3** to **4** pushes the sheets apart slightly, resulting in MeOH solvent molecules being accommodated in cavities between the layers.

Acknowledgements

We thank the Swiss National Science Foundation and the University of Basel for financial support, and acknowledge additional laboratory support from Srboljub Vujovic.

Appendix A. Supplementary data

Crystallographic data have been deposited with the CCDC (Cambridge Crystallographic Data Centre, 12 Union Road, Cambridge CB2 1EZ, UK; fax +44 1223 336033; e-mail: deposit@ccdc.cam.ac.uk or www: http://www.ccdc.cam.ac.uk) and may be obtained free of charge on quoting the deposition numbers CCDC 996287–996290.

References

[1] C.E. Housecroft, Dalton Trans. 43 (2014) 6594.
[2] M. Barquín, J. Cancela, M.J. González Garmendia, J. Quintanilla, U. Amador, Polyhedron 17 (1998) 2373.
[3] E.C. Constable, C.E. Housecroft, P. Kopecky, M. Neuburger, J.A. Zampese, G. Zhang, CrystEngComm 14 (2012) 446.
[4] L. Hou, D. Li, Inorg. Chem. Commun. 8 (2005) 190.
[5] X.-Z. Li, M. Li, Z. Li, J.-Z. Hou, X.-C. Huang, D. Li, Angew. Chem., Int. Ed. 47 (2008) 6371.
[6] G.W.V. Cave, C.L. Raston, J. Supramol. Chem. 2 (2002) 317.
[7] E.C. Constable, G. Zhang, C.E. Housecroft, J.A. Zampese, CrystEngComm 13 (2011) 6864.
[8] J. Heine, J. Schmedt auf der Günne, S. Dehnen, J. Am. Chem. Soc. 133 (2011) 10018.
[9] F. Yuan, Q.-E. Zhu, H.-M. Hu, J. Xie, B. Xu, C.-M. Yuan, M.-L. Yang, F.-X. Dong, G.-L. Xue, Inorg. Chim. Acta 397 (2013) 117.
[10] H.-N. Zhang, F. Yuan, H.-M. Hu, S.-S. Shen, G.-L. Xue, Inorg. Chem. Commun. 34 (2013) 51.
[11] Y.-L. Gai, F.-L. Jiang, L. Chen, Y. Bu, M.-Y. Wu, K. Zhou, J. Pan, M.-C. Hong, Daltons Trans. 42 (2013) 9954.
[12] E.C. Constable, C.E. Housecroft, S. Vujovic, J.A. Zampese, CrystEngComm 16 (2014) 3494.
[13] J.E. Beves, E.C. Constable, S. Decurtins, E.L. Dunphy, C.E. Housecroft, T.D. Keene, M. Neuburger, S. Schaffner, CrystEngComm 10 (2008) 986.
[14] J. Granifo, R. Gaviño, E. Freire, R. Baggio, J. Mol. Struct. 1063 (2104) 102.
[15] Bruker Analytical X-ray Systems, Inc., APEX2, version 2 User Manual, M86-E01078, Madison, WI, 2006.
[16] G.M. Sheldrick, Acta Crystallogr., Sect. A 64 (2008) 112.
[17] I.J. Bruno, J.C. Cole, P.R. Edgington, M.K. Kessler, C.F. Macrae, P. McCabe, J. Pearson, R. Taylor, Acta Crystallogr., Sect. B 58 (2002) 389.
[18] C.F. Macrae, I.J. Bruno, J.A. Chisholm, P.R. Edgington, P. McCabe, E. Pidcock, L. Rodriguez-Monge, R. Taylor, J. van de Streek, P.A. Wood, J. Appl. Crystallogr. 41 (2008) 466.
[19] J. Wang, G.S. Hanan, Synlett (2005) 1251.
[20] B.-C. Wang, Q.-R. Wu, H.-M. Hu, X.-L. Chen, Z.-H. Yang, Y.-Q. Shangguan, M.-L. Yang, G.-L. Xue, CrystEngComm 12 (2010) 485.

18.2 Paper 2 (Published by CSIRO Publishing)

Coordination behaviour of 1-(4,2':6',4''-terpyridin-4'-yl)ferrocene and 1-(3,2':6',3''-terpyridin-4'-yl)ferrocene: predictable and unpredictable assembly algorithms

*Y. Maximilian Klein,[A] A. Prescimone,[A] E. C. Constable,[A] and C. E. Housecroft[A]**

[A]Department of Chemistry, University of Basel, Spitalstrasse 51, CH4056 Basel, Switzerland

email: catherine.housecroft@unibas.ch

ABSTRACT

The reaction of 1-(4,2':6',4''-terpyridin-4'-yl)ferrocene (**2**) with ZnI_2 leads to $[\{ZnI_2(\mathbf{2})\}_4 \cdot 1.4MeOH \cdot 0.8H_2O]$ which contains a discrete [4+4] metallocycle. Crystal growth experiments demonstrate that reactions of **2** with $Zn(OAc)_2$ or $CuCl_2$ result in the formation of single- or double-stranded 1D-polymer chains, respectively, the latter facilitated by the formation of $\{Cu_2Cl_4\}$ dinuclear nodes. Whilst both **2** and its isomer 1-(3,2':6',3''-terpyridin-4'-yl)ferrocene (**3**) present V-shaped donor sets, rotation about interannular bonds in **3** generates flexible vectorial properties associated with limiting convergent and divergent orientations of the nitrogen donors. The synthesis and characterization of **3** are described as are reactions of **3** with $ZnCl_2$ or $ZnBr_2$ which lead, respectively, to a metallosquare in $[\{ZnCl_2(\mathbf{3})\}_4 \cdot 3CHCl_3 \cdot 3MeOH]$ or a helical polymer in $[\{ZnBr_2(\mathbf{3})\} \cdot MeOH]_n$. The tight pitch of the helix in the latter (8.7879(9) Å) is controlled by a combination of the orientations of the *N*,*N*''-donor sets in **3**, and intra-chain π-stacking interactions involving ferrocenyl and pyridine units.

Dedication: We dedicate this work to our good friend Len Lindoy on the occasion of his 80th birthday – Len, you have been an inspiration and colleague to two of the authors for over 30 years.

Introduction

N-Heterocyclic ligands containing ferrocenyl units can be easily modified to incorporate different functionalities and to imbue tunable properties to their metal complexes.[1] Materials incorporating

ferrocene-building blocks can show interesting magnetic and electrochemical properties, in particular in multimetallic polymers.[2,3] A recent example from Kraatz and coworkers demonstrates that using a ferrocene substituent in an artificial peptide produces a versatile, redox-responsive material.[4] The incorporation of ferrocenyl-units also allows the development of promising properties for applications including photoinduced electron transfer,[5] electrochemical sensing[6] and enhanced stability and reactivity in palladium based catalysts for cross-coupling reactions.[7,8]

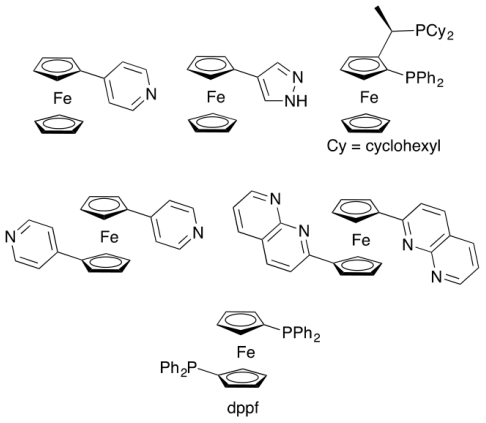

Scheme 1. Examples of mono- and disubstituted ferrocenyl ligands used for the assembly of discrete complexes and coordination polymers.

Some representative ferrocenyl-containing ligands are shown in Scheme 1. Functionalization of one cyclopentadienyl ring typically leads to ligands suited to the formation of discrete complexes,[9,10] and the chiral ligand at the top-right of Scheme 1 is of note for its use in giving enhanced stability and crystallization behaviour in palladium complexes utilized in cross-coupling reactions.[8] Functionalization of both cyclopentadienyl rings with donor groups produces potential linkers in multinuclear assemblies including metallocycles and coordination polymers.[11] On the one hand, the conformational flexibility of the ferrocenyl unit through independent rotation of the Cp rings about the iron atom "ball-bearing" endows 1,1'-substituted ferrocenes with a degree of freedom facilitating the assembly of diverse architectures.[12,13,14] However, this rotational freedom, whilst permitting access to a broad conformational space also reduces the preorganization of the assembly process, making structural engineering design less

predictable. 1,1'-Bis(phosphino)ferrocene ligands such as dppf (Scheme 1) are widely investigated and form both discrete complexes[15] and coordination polymers[16] with a range of metal ions. An alternative approach is the design of *N*-heterocyclic ligands suited to coordination polymer assembly by covalently attaching one or more divergent multinucleating donor sets to the ferrocenyl core. We have demonstrated that 1,1'-(4,2':6',4''-terpyridin-4'-yl)ferrocene (**1**, Scheme 2) reacts with $ZnCl_2$ to give an unusual double-stranded 1D-coordination polymer, the assembly of which is directed by a combination of a *cisoid*-ferrocene moiety and π-π interactions between 4,2':6',4''-terpyridine (4,2':6',4'-tpy) domains.[17] This contrasts with related double-, triple- or quadruple-stranded coordination polymers which have their origins in multinuclear metal nodes[18,19,20] rather than in the ligand-linker. Tian and coworkers recently reported reactions of 1-(4,2':6',4''-terpyridin-4'-yl)ferrocene (**2**, Scheme 2) with zinc(II) salts.[21] Ligand **2** reacts with $ZnCl_2$ and $ZnBr_2$ to give discrete metallohexacycles similar to those obtained with other 4'-substituted 4,2':6',4'-tpy ligands.[22] 1D-coordination polymers result when **2** is treated with ZnI_2, $Zn(NCS)_2$ and $Zn(OAc)_2$. We now report the synthesis and coordination behaviour of 1-(3,2':6',3''-terpyridin-4'-yl)ferrocene (**3**, Scheme 2) with $ZnCl_2$ and $ZnBr_2$, and also demonstrate competitive assembly pathways to different structure types using ligands **2** and **3**.

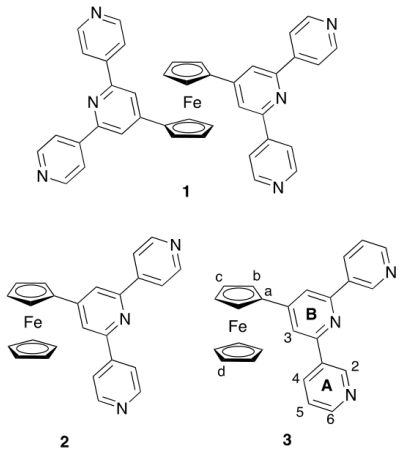

Scheme 2. Structures of ligands **1**–**3**, and numbering scheme of **3** used for NMR spectroscopic assignments.

Experimental Section

General

^{1}H and ^{13}C NMR spectra were recorded on a Bruker Avance III-500 spectrometer with chemical shifts referenced to residual solvent peaks, δ(TMS) = 0 ppm. Electrospray ionization (ESI) mass spectra were recorded on a Bruker esquire 3000^{plus} mass spectrometer. Ligand **2** was prepared as previously reported.[21]

Compound 3

Ferrocenecarboxaldehyde (1.0 g, 4.67 mmol) was dissolved in EtOH (150 mL). 3-Acetylpyridine (1.24 g, 10.3 mmol) and KOH (0.66 g, 11.7 mmol) were added to the solution and a change from red to dark red was observed. Aqueous NH_3 (32%, 18.0 mL) was slowly added to the reaction mixture which was then stirred at room temperature for ~15 h. The solid that formed was collected by filtration, washed with EtOH (3 × 20 mL) and H_2O (3 × 20 mL) and dried in vacuo. Compound **3** was isolated as a red powder (0.83 g, 1.99 mmol, 43%). Dec. > 210 °C. ^{1}H NMR (500 MHz, CD_3OD) δ / ppm 9.38 (d, J = 2.2 Hz, 2H, H^{A2}), 8.68 (m, 2H, H^{A4}), 8.63 (dd, J = 4.9, 1.6 Hz, 2H, H^{A6}), 8.05 (s, 2H, H^{B3}), 7.62 (dd, J = 8.0, 4.9 Hz, 2H, H^{A5}), 5.15 (m, 2H, H^{b}), 4.55 (m, 2H, H^{c}), 4.11 (s, 4H, H^{d}). $^{13}C\{^{1}H\}$ NMR (126 MHz, CD_3OD) δ / ppm 155.7 (C^{B2}), 153.7 (C^{B4}), 150.3 (C^{A6}), 148.8 (C^{A2}), 136.8 (C^{A3}), 136.6 (C^{A4}), 125.4 (C^{A5}), 117.8 (C^{B3}), 81.82 (C^{a}), 71.8 (C^{c}), 71.1 (C^{d}), 68.5 (C^{b}). ESI-MS m/z 417.9 $[M+H]^+$ (calc. 418.1). Found C 69.83, H 4.89, N 9.73; required for $C_{25}H_{19}FeN_3 \cdot {}^{1}/_{2}H_2O$ C 70.44, H 4.73, N 9.86.

[{ZnI_2(2)}$_4$·1.4MeOH·0.8H_2O]

A MeOH (8 mL) solution of ZnI_2 (6.38 mg, 0.02 mmol) was layered over a $CHCl_3$ (5 mL) solution of **2** (8.35 mg, 0.02 mmol) and the crystallization tube was left to stand at room temperature. Red crystals of [{ZnI_2(**2**)}$_4$·1.4MeOH·0.8H_2O] (1.7 mg, 0.0006 mmol, 12% based on Zn) were obtained after 1-2 weeks.

[{Zn(OAc)$_2$(2)}·MeOH·H_2O]$_n$

A MeOH (8 mL) solution of $Zn(OAc)_2 \cdot 2H_2O$ (4.39 mg, 0.02 mmol) was layered over a $CHCl_3$ (5 mL) solution of **2** (8.35 mg, 0.02 mmol) and the crystallization tube was left to stand at room temperature. Red crystals of [{Zn(OAc)$_2$(**2**)}$_n$·MeOH·H_2O]$_n$ (2.7 mg, 0.002 mmol, 10% based on Zn) were obtained after 1-2 weeks.

[{$ZnCl_2$(3)}$_4$·2$CHCl_3$]

A MeOH (8 mL) solution of $ZnCl_2$ (2.73 mg, 0.02 mmol) was layered over a $CHCl_3$ (5 mL) solution of **3** (8.35 mg, 0.02 mmol) and the crystallization tube was left at room temperature. A few red crystals of [{$ZnCl_2$(**3**)}$_4$·2$CHCl_3$] were obtained after 1-2 weeks.

[{$ZnBr_2$(3)}·MeOH]$_n$

A MeOH (8 mL) solution of $ZnBr_2$ (4.50 mg, 0.02 mmol) was layered over a $CHCl_3$ (5 mL) solution of **3** (8.35 mg, 0.02 mmol) and the crystallization tube was left to stand at room temperature. Red crystals of [{$ZnBr_2$(**3**)}$_n$·1MeOH]$_n$ (2.8 mg, 0.004 mmol, 20% based on Zn) were obtained after 1-2 weeks.

[{Cu_2Cl_4(2)$_2$(MeOH)}·2.25MeOH·H_2O·$CHCl_3$]$_n$

A MeOH (8 mL) solution of $CuCl_2$ (4.03 mg, 0.03 mmol) was layered over a $CHCl_3$ (5 mL) solution of **2** (12.5 mg, 0.03 mmol) and the crystallization tube was left to stand at room temperature. Red crystals of [{Cu_2Cl_4(**2**)$_2$(MeOH)}·2.25MeOH·H_2O·$CHCl_3$]$_n$ (3.7 mg, 0.003 mmol, 20% based on Cu) were obtained after 1-2 weeks**.**

Crystallography

Single crystal data were collected on a Bruker APEX-II diffractometer; data reduction, solution and refinement used APEX2, SuperFlip and CRYSTALS respectively.[23,24,25] Structure analysis used Mercury v. 3.6.[26,27] Crystallographic data are given in Table 1. For [{Cu_2Cl_4(**2**)$_2$(MeOH)}·2.25MeOH·H_2O·$CHCl_3$]$_n$, the SQUEEZE[28] procedure had to be used to treat part of the solvent region; the removed electron density equated to an additional H_2O molecule and a $CHCl_3$ molecule. The formulae, molecular mass and density were adjusted accordingly. In [{$ZnCl_2$(**3**)}$_4$·3$CHCl_3$·3MeOH], two $CHCl_3$ molecules were modelled and then SQUEEZE[28] was used to treat the remaining part of the solvent region; the electron density that was removed equated to one extra $CHCl_3$ and three MeOH molecules. All the crystals of this compound were weakly diffracting at high angles; although a sufficient number of reflections were collected, a number did not pass the $I/2\sigma$ cutoff threshold and hence the data-to-parameter ratio is less than 10.

Table 1. Crystallographic data

Compound	**3**	[{ZnI_2(**2**)}$_4$·1.4MeOH ·0.8H_2O]	[{$Zn(OAc)_2$(**2**)} ·MeOH·H_2O]$_n$
Formula	$C_{25}H_{19}FeN_3$	$C_{101.40}H_{83.20}Fe_4I_8N_{12}O_{2.20}Zn_4$	$C_{59}H_{56}Fe_2N_6O_{10}Zn_2$
Formula weight	417.29	3005.20	1251.58
Crystal colour and habit	Orthorhombic	Red block	Red plate
Crystal system	Orthorhombic	Triclinic	Orthorhombic
Space group	$P2_12_12_1$	*P*–1	*Pbca*
a, b, c / Å	9.9004(5), 11.3629(6), 16.9105(9)	11.4704(10), 11.7733(10), 19.2202(17)	24.3420(15), 16.0495(10), 28.2141(17)
α□□*β*□□*γ*□/ °	90 90 90	90.351(4) 102.329(4) 91.929(4)	90 90 90
U / Å^3	1902.38(17)	2534.1(4)	11022.6(12)
D_c / Mg m^{-3}	1.457	1.969	1.508
Z	4	1	8
μ(Mo-*Kα*) / mm^{-1}	6.472	25.046	5.661
□ / K	123	123	123
Refln. collected (R_{int})	7433 (0.036)	33089 (0.037)	73603 (0.054)
Unique refln.	3204	9131	10050
Refln. for refinement	2710	7691	8760
Parameters	263	589	712
Threshold	2*σ*	2*σ*	2*σ*
*R*1 (*R*1 all data)	0.0313 (0.0389)	0.0360 (0.0445)	0.0418 (0.0507)
*wR*2 (*wR*2 all data)	0.0685 (0.0741)	0.0851 (0.0899)	0.0906 (0.0939)
Goodness of fit	0.8994	0.9080	0.9044
CCDC deposition	1504341	1504338	1504343

Compound	[{Cu_2Cl_4(**2**)$_2$(MeOH)} ·2.25MeOH·H_2O·$CHCl_3$]$_n$	[{$ZnCl_2$(**3**)}$_4$·3$CHCl_3$·3MeOH]	[{$ZnBr_2$(**3**)}·MeOH]$_n$
Formula	$C_{54.25}H_{54}Cl_7Cu_2Fe_2N_6O_{4.25}$	$C_{102}H_{78}Cl_{14}Fe_4N_{12}Zn_4$	$C_{26}H_{23}Br_2FeN_3OZn$
Formula weight	1345.02	2668.57	674.52
Crystal colour and habit	Red plate	Red block	Red block
Crystal system	Monoclinic	Orthorhombic	Triclinic
Space group	$P2_1/n$	*Pccn*	*P*–1
a, b, c / Å	16.1181(12), 24.7209(18), 16.1565(11)	25.0374(9), 19.6115(7), 23.4639(9)	8.7879(7), 17.1107(14), 18.0340(14)
α□□*β*□□*γ*□/ °	90 112.267(4) 90	90 90 90	73.010(3) 80.594(3) 82.192(3)
U / Å^3	5957.5(8)	11521.3(7)	2547.3(4)
D_c / Mg m^{-3}	1.50	1.54	1.759
Z	4	4	4
μ(Mo-*Kα*) / mm^{-1}	7.913	8.882	9.589
□ / K	123	123	123
Refln. collected (R_{int})	38865 (0.056)	76606 (0.182)	33199 (0.037)
Unique refln.	10865	10807	9306
Refln. for refinement	7219	5214	9066
Parameters	649	613	619
Threshold	2*σ*	2*σ*	2*σ*
*R*1 (*R*1 all data)	0.0565 (0.0863)	0.0934 (0.1562)	0.0469 (0.0477)
*wR*2 (*wR*2 all data)	0.1439 (0.1750)	0.2478 (0.3154)	0 .1123 (0.1125)
Goodness of fit	0.9640	1.0169	0.8948
CCDC deposition	1504340	1504342	1504339

Results and discussion

Synthesis and characterization of compound 3

The synthesis of compound **2** (Scheme 2) [18] has previously been reported. Although compound **3** (Scheme 2) has previously been prepared in two steps via the isolated 1,5-bis(3-pyridyl)-3-ferrocenyl-pentane-1,5-dione,[29] we find the one-pot method of Wang and Hanan[19] more convenient. Ferrocenecarboxaldehyde was reacted with two equivalents of 3-acetylpyridine under basic conditions followed by treatment with aqueous NH_3; **3** was isolated in 43% yield. The electrospray mass spectrum of **3** shows a base peak at *m/z* 417.9 corresponding to $[M+H]^+$. The ^1H (Fig. 1) and ^{13}C NMR spectra of a CD_3OD solution of **3** were assigned using COSY, NOESY, HMQC and HMBC methods; literature spectroscopic data for a $CDCl_3$ solution of **3** comprise unassigned signals.[29] The signal for H^{B3} (see Scheme 2) appears as a singlet at δ 8.05 ppm. In the NOESY spectrum, cross peaks between the signals for H^{B3} and H^{A2}, H^{A4} and H^{b} were observed. The unsubstituted Cp ring gave rise to a singlet at δ 4.11 ppm, and multiplets at δ 5.15 and 4.55 ppm were assigned to the functionalized Cp ring. The ^{13}C NMR resonance for quaternary C^{B4} could not be confirmed from the HMBC spectrum, but the signal assigned at δ 153.7 ppm is consistent with that in 1-(pyridin-4'-yl)ferrocene.[30]

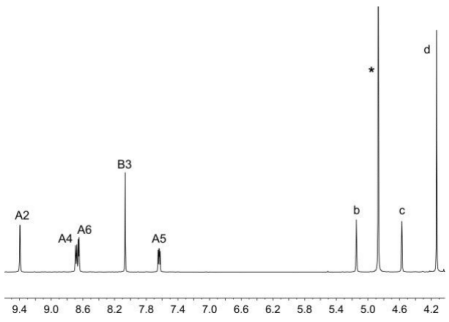

Fig. 1. 500 MHz ^1H NMR spectrum (CD_3OD) of compound **3**. * = Residual CD_3OH. See Scheme 2 for atom labels.

Single crystals of **3** were grown by slow evaporation of a $CHCl_3$ solution. Compound **3** crystallizes in the orthorhombic $P2_12_12_1$ space group, which is one of the 65 Sohnke space groups; the Flack parameter is 0.014. The structure of **3** is shown in Fig. 2a. The view in Fig. 2b reveals the chiral conformation adopted by the molecule in the lattice as a result of the restricted rotation about the C8–C16 bond (an example of

atropisomerism); the torsion angle C7–C8–C16–C17 is –28.8(4)°. The ferrocenyl unit has an eclipsed conformation, as is also observed in the solid-state structure of **2**.[21] In contrast to the adoption of a single atropisomer of **3** in the $P2_12_12_1$ space group, we note that **2** crystallizes in the centrosymmetric space group *P*–1.[21] In **3**, the pyridine rings containing N1 and N2 are approximately coplanar (angle between ring planes = 1.9°), whereas the ring with N3 is twisted through 35.0° with respect to the central pyridine ring. Close CH...N contacts (rather than π-stacking interactions) play an important role in the packing of molecules of **3**.

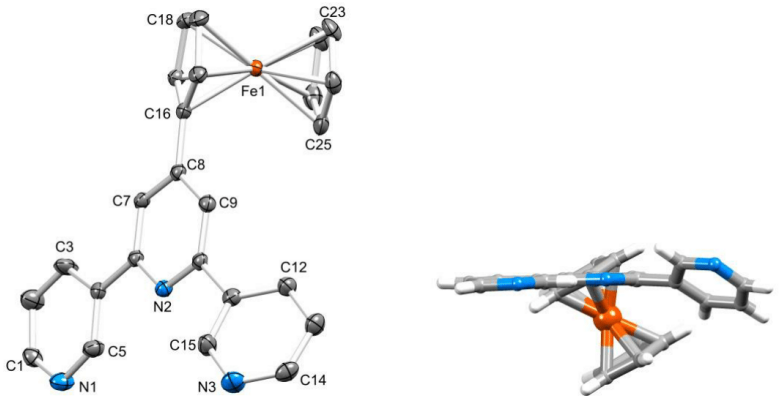

(a) (b)

Fig. 2. (a) Structure of compound **3**; H atoms omitted for clarity and ellipsoids plotted at 40% probability level. Important bond distances: C8 –C16 = 1.468(4), C1–N1 = 1.328(4), C5–N1 = 1.337(4), C6–N2 = 1.349(4), C10–N2 = 1.348(4), C14–N3 = 1.329(4), C15–N3 = 1.342(4) Å. (b) The chiral conformation adopted by **3** in the lattice.

Coordination polymer *versus* metallomacrocycle assembly with ligand 2

Typically, 4,2':6',4''-terpyridines coordinate only through the outer nitrogen atoms and are classed as divergent, V-shaped linkers.[22,31] During the course of our investigations of the coordination chemistry of the ferrocenyl-functionalized 4,2':6',4''- and 3,2':6',3''-terpyridines shown in Scheme 2, Tian and coworkers reported that **2** reacts with $ZnCl_2$ and $ZnBr_2$ to give the discrete metallohexacycles

[{$ZnCl_2$(**2**)}$_6$·6H_2O ·6$CHCl_3$] and [{$ZnBr_2$(**2**)}$_6$·6H_2O ·6$CHCl_3$].[21] Our own observations are consistent with these results.[32] Tian and coworkers also found that the 1D-coordination polymer [{ZnI_2(**2**)}·2$CHCl_3$]$_n$ forms over a period of days when a MeOH/$ZnCl_2$ solution is layered over a $CHCl_3$/**2** solution at room temperature.[21] In contrast, crystal growth under analogous conditions led, in our hands, to the discrete metallomacrocylic coordination compound [{ZnI_2(**2**)}$_4$·1.4MeOH·0.8H_2O]. This crystallizes in the triclinic space group *P*–1 with half of the centrosymmetric [4+4] metallocycle in the asymmetric unit. Fig. 2 shows the structure of the {ZnI_2(**2**)}$_4$ metallosquare. Each of the independent ferrocenyl units adopts an eclipsed conformation. The Cp_2Fe-unit containing Fe1 is twisted with respect to the 4,2':6',4''-tpy to which it is attached (angle between planes of rings containing N2 and C11 = 30.7°), consistent with minimizing close H...H interactions. In contrast, the Cp_2Fe unit with Fe2 exhibits a smaller twist (angle between planes of rings containing N5 and C36 = 8.1°), and this is related to the π-stacking interactions discussed below. Each Zn atom is tetrahedrally coordinated and the bond lengths and angles are unexceptional (Fig. 2 caption, and N–Zn–I bond angles are in the range 106.02(12) to 113.58(11)°). One 4,2':6',4''-tpy domain is slightly twisted with angles between the planes of the rings with N1/N2 and N2/N3 being 10.7 and 19.1°. The 4,2':6',4''-tpy unit containing atoms N4, N5 and N6 is close to planar (angles between planes of adjacent pyridine rings = 6.1 and 6.5°). The planarity is associated with intermolecular face-to-face π-stacking interactions (Fig. 3a) between pyridine rings containing N5/N6 and $N5^{ii}$/$N6^{ii}$ (symmetry code ii = 1–*x*, –*y*, 1–*z*); the stacked heterocyclic rings are in an optimal offset orientation with an interplane separation of 3.37 Å and intercentroid distance of 3.73 Å. The tpy–tpy interaction is augmented by a centrosymmetric embrace of adjacent metallosquares (Fig. 3b) involving π-stacking interactions between the pyridine rings containing N4/N5 and one Cp ring of the ferrocene unit containing $Fe2^{iii}$ (symmetry code iii = –*x*, –*y*, 1–*z*). The distance from the plane through the two pyridine rings to the centroid of the Cp ring with $C45^{iii}$ is 3.30 Å, and $Cp_{centroid}$ to $pyridine_{centroid}$ separations are 3.69 and 4.20 Å.

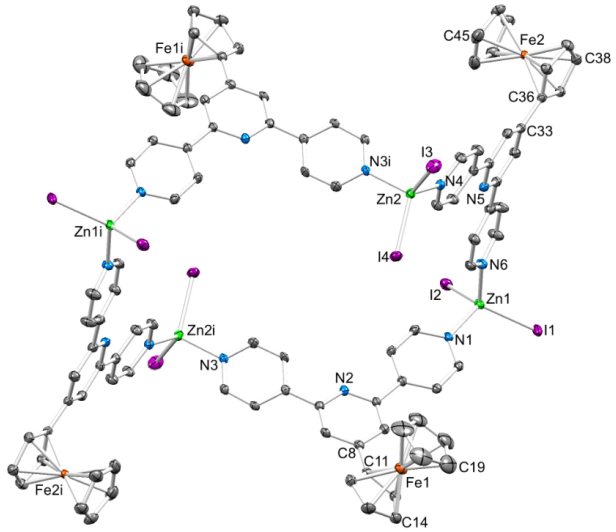

Fig. 2. Structure of the $\{ZnI_2(\mathbf{2})\}_4$ metallosquare in $[\{ZnI_2(\mathbf{2})\}_4 \cdot 1.4MeOH \cdot 0.8H_2O]$; H atoms omitted for clarity and ellipsoids plotted at 40% probability level. Symmetry code i = *–x*, *–y*, *–z*. Selected bond lengths and angles: Zn1–I1 = 2.5318(7), Zn1–I2 = 2.5455(8), Zn1–N1 = 2.043(4), Zn1–N6 = 2.056(4), Zn2–I3 = 2.5456(7), Zn2–I4= 2.5458(7), Zn2–N3i = 2.081(4), Zn2–N4 = 2.039(4) Å; I1–Zn1–I2 = 117.46(3), I3–Zn2–I4 = 115.08(3), N1–Zn1–N6 = 102.00(16), N3–Zn2–N4 = 99.64(15)°.

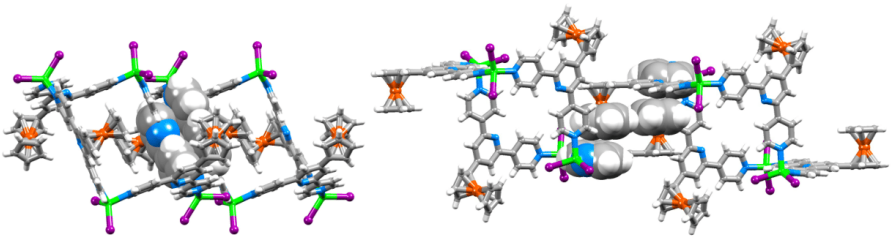

(a) (b)

Fig. 3. (a) Face-to-face π-stacking of 4,2':6',4''-tpy units between $\{ZnI_2(\mathbf{2})\}_4$ molecules; the structure is viewed down the crystallographic *c*-axis. (b) Centrosymmetric intermolecular embrace supported by Cp–pyridine π-stacking.

In an earlier investigation of molecular and polymer assemblies involving 4'-(2',3',4',5',6'-pentafluorobiphenyl-4-yl)-4,2':6',4''-terpyridine and zinc(II) halides, we observed competitive formation of a 1D-coordiantion polymer and a metallosquare in the same crystallization tube.[33] However, in the current investigation, powder diffraction data are consistent with $[\{ZnI_2(\mathbf{2})\}_4 \cdot 1.4MeOH \cdot 0.8H_2O]$ being representative of the bulk material obtained from the reaction of ZnI_2 and **2.** Figures S1 and S2 in the supporting material compare the powder diffraction patterns of the bulk sample obtained from the reaction of ZnI_2 and **2** with those predicted from the single crystal structure of $[\{ZnI_2(\mathbf{2})\}_4 \cdot 1.4MeOH \cdot 0.8H_2O]$ (good agreement) and $[\{ZnI_2(\mathbf{2})\} \cdot 2CHCl_3]_n$ (CSD[34] recode TUNKEU[21], poor agreement). This result once again underlines the non-predictability of assembly processes.[35,36]

Single- *versus* double-stranded 1D-coordination polymer with ligand 2

Red single crystals grown from a MeOH solution of $Zn(OAc)_2 \cdot 2H_2O$ layered over a $CHCl_3$ solution of **2** proved to be the 1D-coordination polymer $[\{Zn(OAc)_2(\mathbf{2})\} \cdot MeOH \cdot H_2O]_n$. The compound crystallizes in the orthorhombic space group *Pbca*, with polymer chains propagating along the crystallographic *a*-axis. Fig. 5 depicts the repeat unit with symmetry-generated atoms. Each of the two crystallographically independent Zn atoms is coordinated by the N atom of two different 4,2':6',4''-tpy units and by two monodentate acetato ligands; the acetate group with O4 shows a weak second contact to Zn1 (Zn1–O4 = 2.751(2) Å). Bond distances in the coordination sphere (caption to Fig. 5) are typical with N–Zn–O, N–Zn–N and O–Zn–O bond angles in the range 98.67(9) to 121.23(9)°. Each ferrocenyl group has an eclipsed conformation, and each C_5H_4-ring is close to coplanar with the pyridine ring to which it is bonded. As in $[\{ZnI_2(\mathbf{2})\}_4 \cdot 1.4MeOH \cdot 0.8H_2O]$, this is attributed to packing effects (see below). The 1D-chain in $[\{Zn(OAc)_2(\mathbf{2})\} \cdot MeOH \cdot H_2O]_n$ is similar to that reported for $[\{Zn(OAc)_2(\mathbf{2})\} \cdot 2H_2O]_n$ (CSD refcode TUNCIQ[21]) and an overlay of the two structures is shown in Fig. 6. In $[\{Zn(OAc)_2(\mathbf{2})\} \cdot MeOH \cdot H_2O]_n$, the chain is built up by translation (space group *Pbca*), whereas in $[\{Zn(OAc)_2(\mathbf{2})\} \cdot 2H_2O]_n$ (space group $P2_1/n$) the chain is built up by a glide plane; these assemblies are similar to those of $[ZnX_2(4'\text{-}(4\text{-}(3\text{-chloropyridyl}))\text{-}4,2':6',4''\text{-tpy})]_n$ (X = Cl, I)[36] and $[ZnI_2(4'\text{-}(4\text{-pyridyl})\text{-}4,2':6',4''\text{-tpy})]_n$[37] and stand apart from the range of helical $[ZnY_2(4'\text{-R-}4,2':6',4''\text{-tpy})]_n$ chains (R and Y = various) built up along screw axes.[22]

Adjacent chains in [{Zn(OAc)$_2$(**2**)}·MeOH·H$_2$O]$_n$ interact through π-stacking of pairs of pyridine and cyclopentadienyl rings (Fig. 7). Both independent Cp$_2$Fe units are involved, and the distances from the centroid of the C$_5$H$_4$ ring containing C11 or C36 (see Fig. 5) to the plane of the pyridine ring containing N4^{iii} or N1^{iv} (symmetry codes iii = $-x$, $-{}^1/_2+y$, ${}^1/_2-z$, iv = $-x$, ${}^1/_2+y$, ${}^1/_2-z$) are 3.35 and 3.29 Å, respectively.

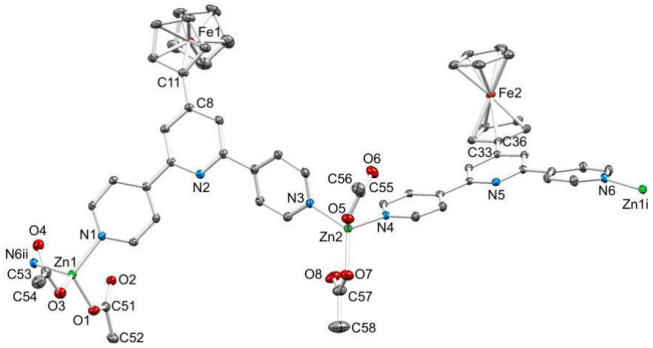

Fig. 5. Structure of the repeat unit in [{Zn(OAc)$_2$(**2**)}·MeOH·H$_2$O]$_n$ with symmetry-generated atoms; H atoms and solvent molecules are omitted and ellipsoids plotted at 30% probability level. Symmetry code i = $-1+x$, y, z, ii = $1+x$, y, z. Selected bond distances: Zn1–N6^{ii} = 2.033(2), Zn1–N1 = 2.030(2), Zn1–O1 = 1.9403(19), Zn1–O3 = 1.955(2), Zn2–N3 = 2.036(2), Zn2–N4 = 2.028(2), Zn2–O5 = 1.936(2), Zn2–O7 = 1.947(2) Å.

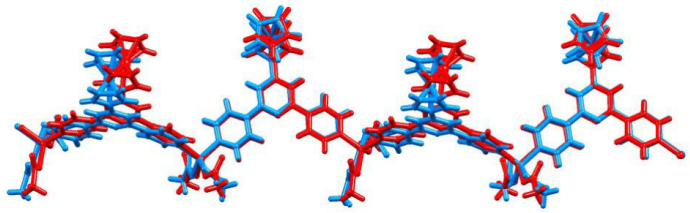

Fig. 6. Overlay of parts of the 1D-coordination polymer chains in [{Zn(OAc)$_2$(**2**)}·MeOH·H$_2$O]$_n$ (red) and [{Zn(OAc)$_2$(**2**)}·2H$_2$O]$_n$ (blue, CSD refcode TUNCIQ).

Fig. 7. Three adjacent chains in [{Zn(OAc)$_2$(**2**)}·MeOH·H$_2$O]$_n$ viewed down the *a*-axis; solvent molecules are omitted. Pyridine...cyclopentadienyl π-stacking interactions are shown in spacefilling representation.

Coordination assemblies formed between zinc(II) salts and 4,2':6',4''-tpy ligands are typified by 2-connecting zinc nodes, compatible with either 1D-coordination polymers or metallomacrocycles. We argued that a change from $ZnCl_2$ to $CuCl_2$ should introduce the potential for increased coordination number at the metal node as well as chlorido-bridge formation. Red plates grew over a period of several days when a MeOH/$CuCl_2$ solution was layered over a $CHCl_3$/**2** solution at room temperature. Single crystal X-ray diffraction revealed the formation of the coordination polymer [{Cu$_2$Cl$_4$(**2**)$_2$(MeOH)}·2.25MeOH·H$_2$O·CHCl$_3$]$_n$; SQUEEZE[28] was used to treat part of the solvent region. The repeat unit of the polymer is shown in Fig. 8, and selected bond lengths are given in the figure caption. The chain is supported by a {Cu$_2$Cl$_2$(μ-Cl)$_2$} unit; this building block is well represented in the Cambridge Structural Database[34] (402 hits found in the CSD v. 5.37 with updates to Feb 2016, using Conquest v. 1.18[26]). Each Cu atom binds two *N*-donor atoms of two different 4,2':6',4''-tpy units in a *trans*-arrangement leading to the assembly of a double-stranded chain (Fig. 9a). This type of assembly has previously been observed with {Cd$_2$(OAc)$_4$} nodes connecting 4'-(4-biphenylyl)-4,2':6',4''-tpy linkers,[18] and related nodes in [Cd(1,4-ndc)(4'-(4-pyridyl)- 4,2':6',4''-tpy)·1.5H$_2$O]$_n$ (H$_2$ndc = 1,4-naphthalene dicarboxylic acid) direct a 3D-'pillar-layer' assembly which incorporates double-stranded chains.[38] A MeOH molecule completes the octahedral coordination sphere of atom Cu1 (Fig. 8), whereas Cu2 is 5-coordinate (square-based pyramidal). There are no short contacts within the lattice to fill the vacant coordination site.[39]

Each of the two crystallographically independent tpy units is close to planar and the C_5H_4 ring of each ferrocene substituent is twisted only 6.2° out of the plane of the pyridine ring to which it is attached. Once again, this is a consequence of π-stacking contacts and Fig. 9b shows how this extends along the length of the chain, and that the pairs of heterocyclic rings adopt an optimal offset arrangement. The separation of stacked pairs of 4,2':6',4''-tpy units (~3.4 Å) is slightly shorter than the Cu...Cu distance in each $\{Cu_2Cl_4\}$ node (Cu...Cu = 3.667(1) Å). Fig. 9b also shows that pairs of Cp_2Fe groups containing Fe1/Fe2^{i} and Fe2/Fe1^{i} (symmetry code i = $^1/_2-x$, $-^1/_2+y$, $^1/_2-z$) also stack across the double-stranded chain (angle between Cp planes = 5.5°; intercentroid distance = 3.81 Å).

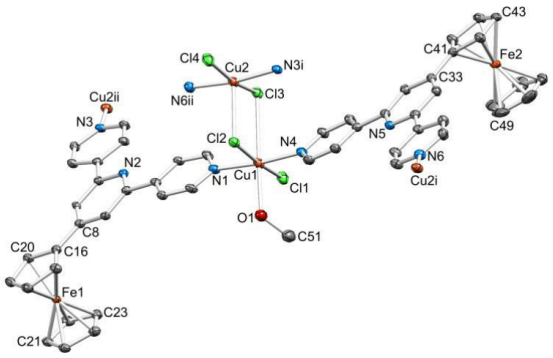

Fig. 8. Structure of the repeat unit in $[\{Cu_2Cl_4(\mathbf{2})_2(MeOH)\}\cdot 2.25MeOH\cdot H_2O\cdot CHCl_3]_n$ with symmetry-generated atoms; H atoms and solvent molecules are omitted and ellipsoids plotted at 30% probability level. Symmetry code i = $^1/_2-x$, $-^1/_2+y$, $^1/_2-z$, ii = $^1/_2-x$, $^1/_2+y$, $^1/_2-z$. Selected bond distances: Cu1–Cl1 = 2.3406(15), Cu1–Cl2 = 2.3688(14), Cu1–Cl3 = 3.0436(14), Cu1–N1 = 1.996(4), Cu1–N4 = 1.992(4), Cu1–O1 = 2.319(4), Cu2–N6^{ii} = 2.001(4), Cu2–N3^{i} = 2.000(4), Cu2–Cl2 = 2.6392(13), Cu2–Cl3 = 2.3008(14), Cu2–Cl4 = 2.3333(16) Å.

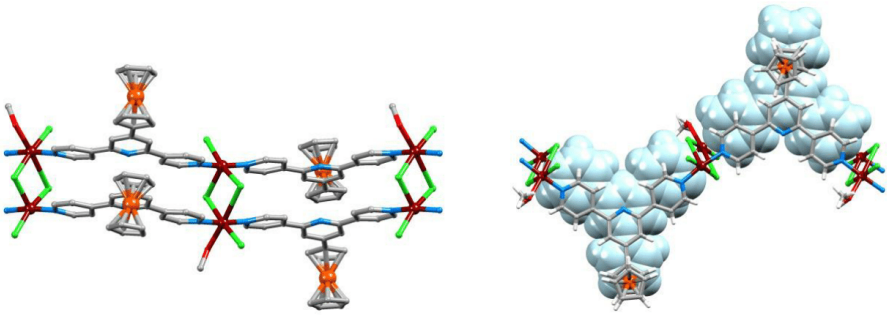

(a) (b)

Fig. 9. (a) Part of one double-stranded chain in [{Cu_2Cl_4(**2**)$_2$(MeOH)}·2.25MeOH·H_2O·$CHCl_3$]$_n$ (viewed down the *a*-axis) and (b) the same chain viewed down the *c*-axis to show the face-to-face π-stacking; the back chain is shown in spacefilling representation.

From a 4,2':6',4''- to 3,2':6',3''-tpy donor set

While the directionality of the *N,N''*–donor set in 4,2':6',4''-tpy is fixed, that in 3,2':6',3''-tpy varies as the interannular C–C bonds rotate.[31] Thus, the change in the vectorial properties of the *N*-donor set on going from **2** to **3** (Scheme 2) reduces (still further) the predictability of the metal-binding mode. Methanol solutions of $ZnCl_2$ or $ZnBr_2$ were layered over chloroform solutions of **3**, and red blocks grew in both crystallization tubes within two weeks. Single crystal X-ray diffraction showed the products to be the discrete molecule [{$ZnCl_2$(**3**)}$_4$·3$CHCl_3$·3MeOH] and the 1D-coordination polymer [{$ZnBr_2$(**3**)}·MeOH]$_n$, respectively.

[{$ZnCl_2$(**3**)}$_4$·3$CHCl_3$·3MeOH] crystallizes in the orthorhombic space group *Pccn* with half of the molecule in the asymmetric unit. The second half is generated by a 2-fold axis, and Fig. 10 depicts the resulting metallosquare. Each Zn atom is tetrahedrally sited with typical Zn–N and Zn–Cl distances (caption to Fig. 10); the bond angles in the coordination spheres of Zn1 and Zn2 range from 98.1(3) to 117.5(2)°. The 3,2':6',3''-tpy unit in each coordinated **3** adopts a *cis,trans*-conformation (Fig. 10), with angles between the planes of the rings containing N1/N2, N2/N3 and N4/N5, N5/N6 being 17.9, 23.2° and 37.7, 17.8°. Each of the two independent ferrocenyl units has an eclipsed conformation and the plane of the C_5H_4 ring is twisted (12.6 and 14.4°, respectively) with respect to the central pyridine ring of each 3,2':6',3''-tpy unit. Although these twist angles are similar, only one is associated with a C_5H_4...pyridine π-

stacking contact. The cyclopentadienyl ring containing C36 lies in an offset orientation over the ring containing N1^{ii} (symmetry code iii = $^{1}/_{2}+x$, $1-y$, $^{1}/_{2}-z$) with centroid...centroid separation of 3.51 Å; the angle between the ring planes is 3.6° and the pyridine(plane)...C_6H_4(centroid) distance is 3.29 Å. When viewed down the crystallographic *a*-axis, the {$ZnCl_2$(**3**)}$_4$ tetramer adopts a V-shaped conformation and molecules pack along the *b*-axis with π-stacking interactions between the pyridine rings[40] containing N2 and N5^{iii} (symmetry code iii = $1-x$, $-^{1}/_{2}+y$, $^{1}/_{2}-z$) as shown in Fig. 11. The interaction between offset (but mutually twisted) rings are characterized by the distances ring N2-centroid...ring N5^{iii}-plane = 3.58 Å, centroid...centroid separation = 3.72 Å, and an angle between the pyridine ring planes of 2.9°. The V-shaped cavity of {$ZnCl_2$(**3**)}$_4$ hosts at least one $CHCl_3$ molecule, but we refrain from a discussion of molecule...solvent interactions because some solvent molecules were removed by SQUEEZE (see experimental section). In contrast to the situation for [{ZnI_2(**2**)}$_4$·1.4MeOH·0.8H_2O] (see earlier), we were unable to confirm if the metallosquare in [{$ZnCl_2$(**3**)}$_4$·3$CHCl_3$·3MeOH] is representative of the bulk sample; only a few single crystals were obtained and the bulk material was an amorphous powder unsuited to powder X-ray diffraction. However, competitive assembly processes are indicated by a report[41] of the 1D-coordination polymer [{$ZnCl_2$(**3**)}·1.5H_2O]$_n$ but no details of synthesis are available.

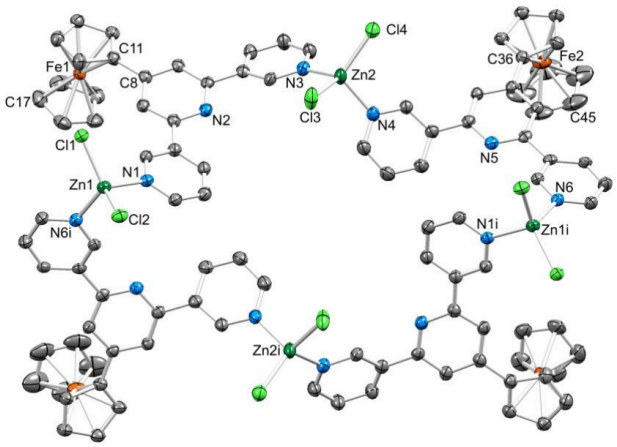

Fig. 10. Structure of the {$ZnCl_2$(**3**)}$_4$ molecule in [{$ZnCl_2$(**3**)}$_4$·3$CHCl_3$·3MeOH]; H atoms and solvent molecules are omitted and ellipsoids plotted at 30% probability level. Symmetry code i = $^{1}/_{2}-x$, $^{1}/_{2}-y$, z. Selected bond distances: Zn1–N6^{i} = 2.063(8), Zn1–Cl1 = 2.202(2), Zn1–Cl2 = 2.235(3), Zn1–N1 = 2.074(8), Zn2–Cl3 = 2.243(3), Zn2–Cl4 = 2.224(3), Zn2–N3 = 2.043(8), Zn2–N4 = 2.038(9) Å.

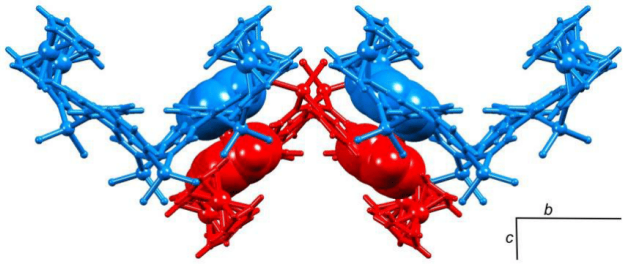

Fig. 11. Adjacent metallosquares in [{$ZnCl_2$(**3**)}$_4$·3$CHCl_3$·3MeOH] interact along the *b*-axis through π-stacking interactions between pairs of pyridine rings.

The repeat unit in the 1D-coordination polymer [{$ZnBr_2$(**3**)}·MeOH]$_n$ (which crystallizes in the triclinic space group *P*–1) is depicted in Fig. 12. Both independent Zn atoms are tetrahedrally coordinated; bond distances are in the caption to Fig. 12, and bond angles lie between 96.54(12)° (N3–Zn2–N4) and 119.17(2)° (Br3–Zn2–Br4). As in the other structures in this work, the ferrocene units are in eclipsed conformations. The functionalized C_5 ring of one unit (with Fe1) lies only 6.4° out of the plane of the pyridine ring to which it is bonded, while the second is significantly twisted (41.3°, see later). The 3,2':6',3''-tpy unit containing N1, N2 and N3 is in a *cis,cis*-conformation, with pairs of rings with N1/N2 and N2/N3 mutually twisted through 7.8 and 35.7°, respectively. In contrast, the ligand with N4, N5 and N6 adopts a *cis,trans*-conformation, and adjacent rings are twisted through 24.8 and 25.0°. These differences in conformation lead to alternating short and long Zn...Zn separations (Zn1...Zn2 = 6.7181(7) Å and Zn2...Zn1^{i} = 11.0715(9) Å). The 1D-chain is built up by translation, but the helical twist within the asymmetric unit (Fig. 12) leads to a chiral polymer; chains of both handednesses are present in the unit cell. The helical chain has a pitch of 8.7879(9) Å (Zn1...Zn1^{i}). This tight turn is related both to the orientations of the *N,N''*-donor sets in the 3,2':6',3''-tpy units, and to the π-stacking interactions within the chain (Fig. 13). The latter occur between the Cp ring containing C16 and the two pyridine rings with N1^{iii} and N2^{iii} (symmetry code iii = 1+*x*, *y*, *z*). The distance from the least squares plane through the two pyridine rings and the centroid of the Cp ring is 3.42 Å, and the angle between the planes through the stacked units is 8.3°. An analogous packing motif is present in [{$ZnCl_2$(**3**)}·1.5H_2O]$_n$, but this structure has not been discussed in detail.[41]

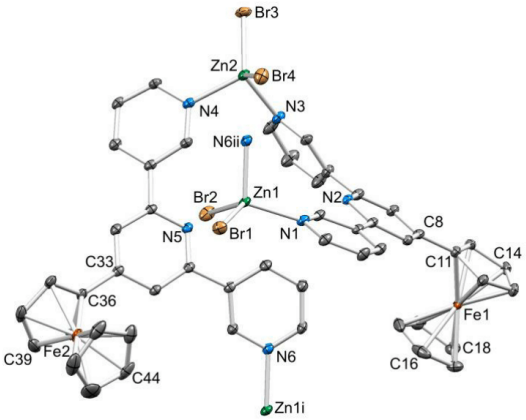

Fig. 12. Structure of the repeat unit in [{$ZnBr_2$(**3**)}·MeOH]$_n$ with symmetry-generated atoms; ellipsoids are plotted at 30% probability level, and H atoms and solvent molecules are omitted. Symmetry code i = 1–*x*, *y*, *z*, ii = –1+*x*, *y*, *z*. Selected bond distances: Zn1–N6^{ii} = 2.038(3), Zn1–Br1 = 2.3504(6), Zn1–Br2 = 2.3587(6), Zn1–N1 = 2.041(3), Zn2–Br3 = 2.3515(6), Zn2–Br4 = 2.3455(6), Zn2–N3 = 2.050(3), Zn2–N4 = 2.059(3) Å.

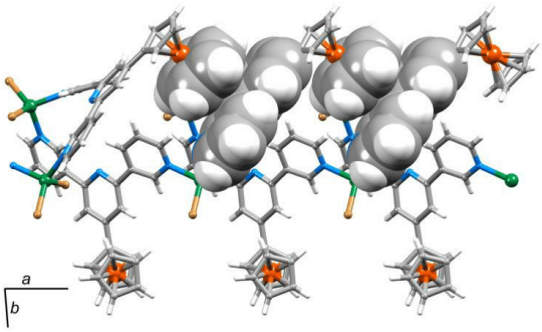

Fig. 13. Part of one helical chain in [{$ZnBr_2$(**3**)}·MeOH]$_n$ (solvent molecules are omitted) which follows the *a*-axis. Intra-chain π-stacking interactions (see text) are shown in space-filling representation.

Conclusions

The synthesis and characterization, including a single crystal structure determination, of ligand **3** have been described. Both **2** and **3** coordinate metal ions through the outer two pyridine rings. Reactions of **2** with $ZnCl_2$ and $ZnBr_2$ lead to discrete metallohexacycles which confirms earlier an report.[21] However,

predictable assembly algorithms cannot be assumed as demonstrated by the formation of either a 1D-polymer[21] or a discrete metallosquare (this work) when ZnI_2 reacts with **2** apparently under the same conditions of crystal growth. A switch from single- to double-stranded 1D-polymer chains is achieved by combining the divergent donor set of **2** with $Zn(OAc)_2$ or $CuCl_2$; the potential for increased coordination number of Cu(II) versus Zn(II) and the propensity for formation of bridging chlorido ligands leads to dinuclear metal nodes which support a double-stranded chain. Whereas **2** exhibits a fixed V-shaped donor set, its isomer **3** offers greater variation in the vectorial properties of the donor set. This has been demonstrated in the reactions of **3** with $ZnCl_2$ or $ZnBr_2$ which lead, respectively, to a metallosquare in $[\{ZnCl_2(\mathbf{3})\}_4 \cdot 3CHCl_3 \cdot 3MeOH]$ but to a helical polymer in $[\{ZnBr_2(\mathbf{3})\} \cdot MeOH]_n$. The tight pitch of the helix in the latter (8.7879(9) Å) is governed by a combination of the orientations of the *N,N''*-donor sets in the 3,2':6',3''-tpy units in **3**, and to intra-chain π-stacking interactions involving ferrocenyl and pyridine units.

Although the 4,2':6',4''-tpy unit in **2** offers a fixed V-shaped donor set, it does not lead to a predictable assembly algorithm; under similar crystal growth conditions, polymer and metalloamacrocycle formation (both 4- and 6-membered rings) may be in competition. Similar competitive behaviour is observed for ligand **3** with zinc(II) halides, but the greater conformational flexibility of **3** versus **2** adds to the non-predictability of the outcome of the assembly process.

Acknowledgements

We thank the Swiss National Science Foundation (Grant number 200020_144500) and the University of Basel for support. The Swiss National Science Foundation through the NCCR Molecular Systems Engineering is acknowledged for partial funding of the powder diffractometer.

References

[1] R. Horikoshi, *Coord. Chem. Rev.* **2013**, *257*, 621. doi:10.1016/j.ccr.2012.09.026

[2] O. Oms, J. Le Bideau, F. Leroux, A. van der Lee, D. Leclercq, A. Vioux, *J. Am. Chem. Soc.* **2004**, *126*, 12090. doi:10.1021/ja049457p

[3] J. G. Eaves, R. Mirrazaei, D. Parker, H. S. Munro, *J. Chem. Soc., Perkin Trans. 2* **1989**, 373. doi:10.1039/P29890000373.

[4] B. Adhikari, C. Singh, A. Shah, A. J. Lough, H.-B. Kraatz, *Chem. Eur. J.* **2015**, *21*, 11560. doi:10.1002/chem.201501395

[5] M. Kubo, Y. Mori, M. Otani, M. Murakami, Y. Ishibashi, M. Yasuda, K. Hosomizu, H. Miyasaka, H. Imahori, S. Nakashima, *J. Phys. Chem. A* **2007**, *111*, 5136. doi: 10.1021/jp071546b

[6] C. Bucher, C. H. Devillers, J.-C. Moutet, G. Royal, E. Saint-Aman, *Chem. Commun*. **2003**, 888. doi:10.1039/B301177A

[7] M. C. Carrión, F. A. Jalón, A. López-Agenjo, B. R. Manzano, W. Weissensteiner, K. Mereiter, *J. Organomet. Chem.* **2006**, *691*, 1369. doi:10.1016/j.jorganchem.2005.12.023

[8] H.-U. Blaser, W. Brieden, B. Pugin, F. Spindler, M. Studer, A. Togni, *Top. Catal.* **2002**, *19*, 3. doi:10.1023/A:1013832630565

[9] O. Carugo, G. De Santis, L. Fabbrizzi, M. Licchelli, A. Monichino, P. Pallavicini, *Inorg. Chem.* **1992**, *31*, 765. doi:10.1021/ic00031a014

[10] T. Mochida, F. Shimizu, H. Shimizu, K. Okazawa, F. Sato, D. Kuwahara, *J. Organomet. Chem.* **2007**, *692*, 1834. doi: 0.1016/j.jorganchem.2006.11.011

[11] R. Horikoshi and T. Mochida, *Eur. J. Inorg. Chem.* **2010**, 5355. DOI: 10.1002/ejic.201000525

[12] D. Braga, M. Polito, M. Bracaccini, D. D'Addario, E. Tagliavini, D. M. Proserpio, F. Grepioni, *Chem. Commun.* **2002**, 1080. doi:10.1039/B200344A

[13] N. Sadhukhan, J. K. Bera, *Inorg. Chem.* **2009**, *48*, 978. doi:10.1021/ic801586d

[14] D. Braga, M. Curzi, S.L. Giaffreda, F. Grepioni, L. Maini, A. Pettersen, M. Polito in 'Ferrocenes: Ligands, materials and biomolecules', ed. P. Stepnicka, **2008**, Wiley, Chichester.

[15] See for example: P. Lai-Tee, T. S. A. Hor, Z. Zhong-Yuan, T. C. W. Mak, *J. Organomet. Chem.* **1994**, *469*, 253. doi:10.1016/0022-328X(94)88080-8

[16] M. Concepcion Gimeno, P. G. Jones, A. Laguna, C. Sarroca, *J. Chem. Soc., Dalton Trans.* **1998**, 1277. doi:10.1039/A708959G

[17] Y. M. Klein, A. Prescimone, E. C. Constable, C. E. Housecroft, *Inorg. Chem. Commun.* **2016**, *70*, 118. doi:10.1016/j.inoche.2016.05.027

[18] E. C. Constable, C. E. Housecroft, M. Neuburger, J. Schönle, S. Vujovic, J. A. Zampese, *Polyhedron* **2013**, *60*, 120. doi:10.1016/j.poly.2013.05.026

[19] E. C. Constable, G. Zhang, E. Coronado, C. E. Housecroft, M. Neuburger, *CrystEngComm* **2010**, *12*, 2139. doi:10.1039/B926597J

[20] E. C. Constable, C. E. Housecroft, S. Vujovic, J. A. Zampese, A. Crochet and S. R. Batten, *CrystEngComm* **2013**, *15*, 10068. DOI: 10.1039/C3CE41384E

[21] L. Xiao, L. Zhu, Q. Zeng, Q. Liu, J. Zhang, S. Li, H. Zhou, S. Zhang, J. Wu, Y. Tian, *J. Organomet. Chem.* **2015**, *789–790*, 22. doi:10.1016/j.jorganchem.2015.05.007

[22] C. E. Housecroft, *Dalton Trans.* **2014**, *43*, 6594. doi: 10.1039/C4DT00074A and references therein.

[23] Bruker Analytical X-ray Systems, Inc., 2006, APEX2, version 2 User Manual, M86-E01078, Madison, WI.

[24] L. Palatinus, G. Chapuis, *J. Appl. Cryst.* **2007**, *40*, 786. doi: 10.1107/S0021889807029238

[25] P. W. Betteridge, J. R. Carruthers, R. I. Cooper, K. Prout, D. J. Watkin, *J. Appl. Cryst.* **2003**, *36*, 1487. doi: 10.1107/S0021889803021800

[26] I. J. Bruno, J. C. Cole, P. R. Edgington, M. K. Kessler, C. F. Macrae, P. McCabe, J. Pearson and R. Taylor, *Acta Cryst. B* **2002**, *58*, 389. doi: 10.1107/S0108768102003324.

[27] C. F. Macrae, I. J. Bruno, J. A. Chisholm, P. R. Edgington, P. McCabe, E. Pidcock, L. Rodriguez-Monge, R. Taylor, J. van de Streek and P. A. Wood, *J. Appl. Cryst.* **2008**, *41*, 466. doi: 10.1107/S0021889807067908

[28] A. L. Spek, *Acta Crystallogr., Sect. C* **2015**, *71*, 9. doi:10.1107/S2053229614024929

[29] I.R. Butler, S.J. McDonald, M.B. Hursthouse and K.M.A. Malik, *Polyhedron*, 1995, **14**, 529. doi: 10.1016/0277-5387(94)00266-H.

[30] T.M. Miller, K.J. Ahmed and M.S. Wrighton, *Inorg. Chem*. **1989**, *28*, 2347. DOI: 10.1021/ic00311a020.

[31] C. E. Housecroft, *CrystEngComm* **2015**, *17*, 7461. doi: 10.1039/C5CE01364J.

[32] Y.M. Klein, A. Prescimone, E. C. Constable, C. E. Housecroft, unpublished results.

[33] E. C. Constable, C. E. Housecroft, A. Prescimone, S.Vujovic and J. A. Zampese *CrystEngComm* **2014**, *16*, 8691. doi: 10.1039/c4ce00783b.

[34] C.R. Groom, I.J. Bruno, M.P. Lightfoot, S. C. Ward, *Acta Cryst.* **2016**, *B72*, 171. doi

10.1107/S2052520616003954.

[35] E.C. Constable, C.E. Housecroft, B.M. Kariuki, N.Kelly, C.B. Smith, *Comptes Rendues* **2002**, *5*, 425. doi.org/10.1016/S1631-0748(02)01401-7

[36] E.C. Constable, G. Zhang, C.E. Housecroft, J. A. Zampese, *CrystEngComm* **2011**, *13*, 6864. DOI: 10.1039/C1CE05884C.

[37] J. Heine, J. S. auf der Gunne, S. Dehnen, *J. Am. Chem. Soc.* **2011**, *133*, 10018. DOI: 10.1021/ja2030273.

[38] D.L. An, Y-Q. Chen, Y. Tian, *Z. Anorg. Allg. Chem.* **2014**, *640*, 1776. DOI: 10.1002/zaac.201400037

[39] E. C. Constable, C. E. Housecroft, J. R. Price, J. A. Zampese, *CrystEngComm* **2010**, *12*, 3163. DOI: 10.1039/C0CE00019A

[40] C. Janiak, *CrystEngComm* **2000**, 3885. doi. 10.1039/B003010O.

[41] L. Xiao, Y. Tian, **2015**, private communication to the CSD, refcode VUKMOF.

18.3 Paper 3 (Published by Elsevier)

Polyhedron 129 (2017) 71–76

Contents lists available at ScienceDirect

Polyhedron

journal homepage: www.elsevier.com/locate/poly

Coordination behavior of 1-(3,2′:6′,3″-terpyridin-4′-yl)ferrocene: Structure and magnetic and electrochemical properties of a tetracopper dimetallomacrocycle

Y. Maximilian Klein [a], Angelo Lanzilotto [a], Alessandro Prescimone [a], Karl W. Krämer [b], Silvio Decurtins [b], Shi-Xia Liu [b], Edwin C. Constable [a], Catherine E. Housecroft [a,*]

[a] Department of Chemistry, University of Basel, Spitalstrasse 51, 4056 Basel, Switzerland
[b] Department of Chemistry and Biochemistry, University of Bern, Freiestrasse 3, 3012 Bern, Switzerland

ARTICLE INFO

Article history:
Received 21 February 2017
Accepted 16 March 2017
Available online 24 March 2017

Keywords:
Copper
Divergent terypyridine
Ferrocene
Structure
Magnetism
Electrochemistry

ABSTRACT

The discrete coordination compound $[Cu_4Cl_8(\mathbf{3})_4(MeOH)_2]$ is obtained from the reaction of a chloroform solution of 1-(3,2′:6′,3″-terpyridin-4′-yl)ferrocene (**3**) with a methanol solution of $CuCl_2$; the single crystal structure of $[\{Cu_4Cl_8(\mathbf{3})_4(MeOH)_2\}\cdot 0.7CHCl_3\cdot 1.8MeOH]$ is described. Two $\{Cu_2Cl_4(\mathbf{3})_2(MeOH)\}$ units are connected by bridging chlorido ligands to generate a centrosymmetric tetranuclear molecule featuring face-to-face π-interactions between ferrocene units and between tpy domains. Intermolecular π-stacking of ferrocene and tpy units lead to quadruple-decker stacking motifs in the solid-state. The tetranuclear compound represents a pair of μ-Cl bridged Cu(II) dimers exhibiting a weak antiferromagnetic coupling *via* the bridging chlorido ligands. The redox behavior of **3** has been investigated by cyclic voltammetry and spectroelectrochemistry; a ferrocenyl oxidation process is observed for $[Cu_4Cl_8(\mathbf{3})_4(MeOH)_2]$.

1. Introduction

The spontaneous self-assembly of coordination polymers using 4,2′:6′,4″- and 3,2′:6′,3″-terpyridines (tpy) as organic linkers has seen significant growth in the last decade [1,2]. However, the coordination behavior of 3,2′:6′,3″-tpy ligands has received less attention than that of 4,2′:6′,4″-tpy analogs. While the latter presents a fixed V-shaped donor set, rotation about interannular bonds in a 3,2′:6′,3″-tpy leads to more flexible coordination modes. Typically, the central pyridine ring of both 4,2′:6′,4″- or 3,2′:6′,3″-tpy ligands is non-coordinating [2]. Functionalization of the tpy unit in the 4′-position with a variety of substituents is synthetically straightforward through use of Kröhnke [3] or Wang and Hanan [4] methodologies. A ferrocenyl substituent introduces a redox-active center as well as a structurally flexible motif. The inherent rotational freedom of the cyclopentadienyl rings about the iron center is of particular significance in a ditopic ligand such as **1** (Scheme 1) [5]. The isomeric ferrocenyl-decorated ligands **2** and **3** differ in the directional properties associated with nitrogen donors of the outer rings. We [6] and Tian and coworkers [7] have demonstrated that combinations of **2** with zinc(II) salts lead to the assembly of metallosquares, metallohexacycles or one-dimensional coordination polymers. This structural diversity mirrors that observed with other 4,2′:6′,4″-tpys [1]. In the case of ligand **2**, cyclopentadienyl-tpy π-stacking interactions play a significant role in the solid state [6]. The reaction of divergent **2** with $CuCl_2$ leads to a double stranded one-dimensional coordination polymer, the double chain being supported by $\{Cu_2Cl_2(\mu\text{-}Cl)_2\}$ units (Fig. 1) [6]. The divergent donor set of **2** is preorganized for this type of architecture, whereas we could envisage limiting convergent or divergent directionalities for **3** (Scheme 2) as well as intermediate vectorial definitions. We report here the assembly of a tetracopper dimetallomacrocycle and describe its structural, magnetic and electrochemical characteristics.

2. Experimental

2.1. Synthesis

A MeOH (8 mL) solution of $CuCl_2$ (4.03 mg, 0.03 mmol) was layered over a $CHCl_3$ (5 mL) solution of **3** (12.5 mg, 0.03 mmol) and the crystallization tube left to stand at room temperature. Red crystals of $[\{Cu_4Cl_8(\mathbf{3})_4(MeOH)_2\}\cdot 0.7CHCl_3\cdot 1.8MeOH]$ (9.8 mg, 0.0041 mmol, 54%) were obtained after 1–2 weeks. See Fig. S1† for powder diffraction data of bulk sample.

* Corresponding author.
E-mail address: catherine.housecroft@unibas.ch (C.E. Housecroft).

http://dx.doi.org/10.1016/j.poly.2017.03.030
0277-5387/

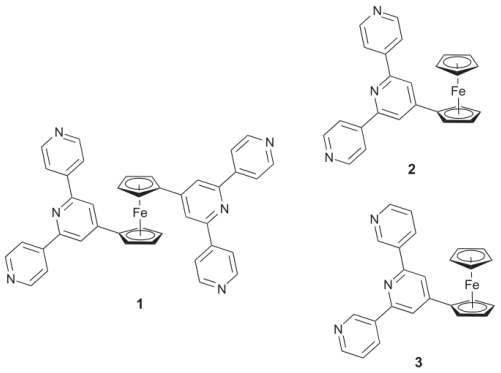

Scheme 1. Structures of ligands **1**–**3**.

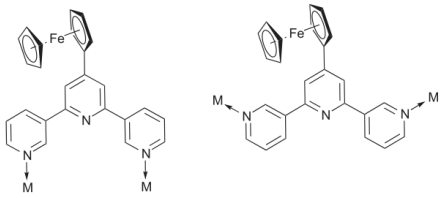

Scheme 2. Limiting convergent (left) or divergent (right) binding modes for **3**.

2.2. Crystallography

Single crystal data were collected on a Bruker APEX-II diffractometer; data reduction, solution and refinement used APEX2, SuperFlip and CRYSTALS respectively [8–10]. Structure analysis used Mercury v. 3.6 [11,12]. In the solvent region, thermal and vibrational restraints were used. Bond distances and angles on the $CHCl_3$ molecule were restrained to chemically reasonable values. The solvent molecules refined to non-integer occupancies that were rounded up to 0.35 $CHCl_3$, 0.40 MeOH and 0.50 MeOH.

[{Cu_4Cl_8(**3**)$_4$(MeOH)$_2$}·0.7$CHCl_3$·1.8MeOH]: $C_{104.5}H_{91.9}Cl_{10.1}Cu_4Fe_4N_{12}O_{3.8}$, M = 2412.30, red block, monoclinic, space group $P2_1/c$, a = 14.0480(7), b = 22.6509(14), c = 16.6921(9) Å, β = 90.507(3)°, U = 5311.2(5) Å^3, Z = 2, D_c = 1.508 Mg m^{-3}, μ(Cu Kα) = 7.892 mm^{-1}, T = 123 K. Total 33091 reflections, 9788 unique, R_{int} = 0.056. Refinement of 6392 reflections (667 parameters) with $I > 2\sigma$ (I) converged at final $R1$ = 0.0874 ($R1$ all data = 0.1195), $wR2$ = 0.2286 ($wR2$ all data = 0.2562), gof = 0.9985.

2.3. Magnetic measurements

The magnetic susceptibility measurement was made on a Quantum Design MPMS SQUID-XL magnetometer under an applied magnetic field of 10^3 Oe between 300 and 1.9 K. The magnetization measurement was conducted at 1.9 K up to a magnetic field of 50 kOe. The sample was prepared in a gelatin capsule. Diamagnetic correction was made for the sample using the approximation – 0.45 × molecular weight × 10^{-6} cm^3 mol^{-1}, and the sample holder was corrected for by measuring directly the susceptibility of the empty capsule.

2.4. Electrochemistry and spectroelectrochemistry

Electrochemical measurements were carried out with a CH Instruments 900B potentiostat using propylene carbonate solutions with [^{n}Bu$_4$N][PF_6] (0.1 M) as supporting electrolyte and at a scan rate of 0.1 V s^{-1}. The working electrode was glassy carbon, the reference electrode was a leakless Ag+/AgCl (eDAQ ET069-1) electrode and the counter-electrode a platinum wire. Quoted potentials were referenced with respect to the Fc/Fc$^+$ couple. Spectroelectrochemical measurements were performed using a propylene carbonate solution of **3** or ferrocene (5 mM) at room temperature with [^{n}Bu$_4$N][PF_6] (0.1 M) as the supporting electrolyte. The solution was added to an optically transparent thin-layer electrochemical (OTTLE) cell with two Pt minigrid electrodes (working and auxiliary), a silver wire as pseudoreference electrode, and a path length of ≈0.2 mm. The potential was controlled using a VersaSTAT 3 potentiostat (Princeton Applied Research). For the study of [{Cu_4Cl_8(**3**)$_4$(MeOH)$_2$}·0.7$CHCl_3$·1.8MeOH], the working electrode (FTO glass, SolaronixTCO22-7, 2.2 mm thickness, sheet resistance ≈7 Ω square^{-1}) and counter-electrode (Solaronix Test Cell Platinum Electrode) were glued together using thermoplast hot-melt sealing foil by heating while pressing together. A suspension of finely ground [{Cu_4Cl_8(**3**)$_4$(MeOH)$_2$}·0.7$CHCl_3$·1.8MeOH] in propylene carbonate containing [^{n}Bu$_4$N][PF_6] was inserted by vacuum backfilling through a hole drilled in the counter electrode. The cell was not sealed. Silver paint was applied to the edges of both electrodes to improve the electrical contact with the potentiostat terminals (two electrode setup).

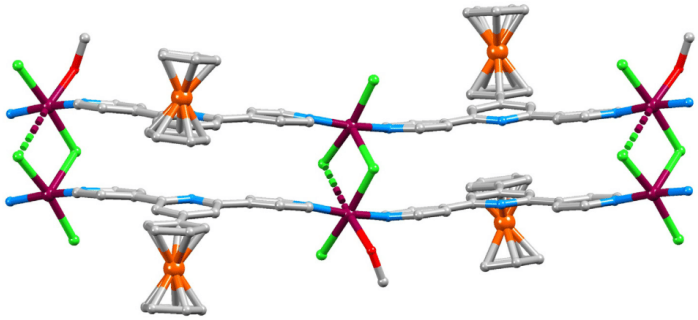

Fig. 1. Part of one double-stranded chain in the coordination polymer [{Cu_2Cl_4(**2**)$_2$(MeOH)}·2.25MeOH·H_2O·$CHCl_3$]$_n$ [6].

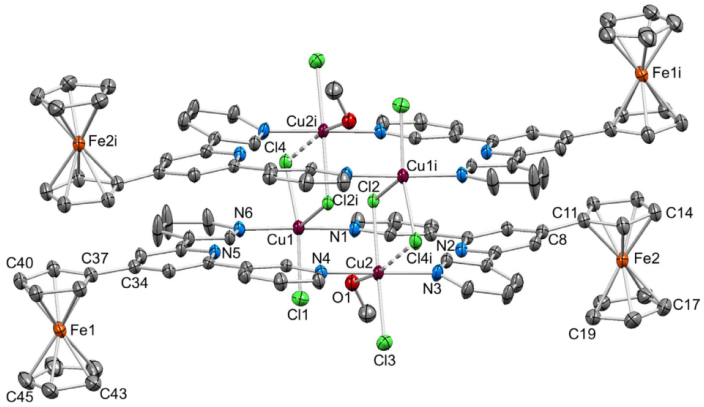

Fig. 2. Structure of the $[Cu_4Cl_8(\mathbf{3})_4(MeOH)_2]$ molecule in $[\{Cu_4Cl_8(\mathbf{3})_4(MeOH)_2\}\cdot 0.7CHCl_3\cdot 1.8MeOH]$. Hydrogen atoms are omitted and ellipsoids are plotted at 30% probability level. Selected bond distances and angles: Cu1–Cl1 = 2.269(2), Cu1–Cl4 = 2.3201(19), Cu1–$Cl2^i$ = 2.5459(19), Cu2–Cl2 = 2.3471(17), Cu2–Cl3 = 2.309(2), Cu1–N1 = 2.018(6), Cu1–N6 = 2.007(5), Cu2–N3 = 2.016(5), Cu2–N4 = 2.024(5), Cu2–O1 = 2.287(5) Å; N1–Cu1–N6 = 173.1(3), N3–Cu2–N4 = 174.2(3), Cl2–Cu2–Cl3 = 177.24(8), $Cl4^i$–Cu1–Cl1 = 157.32(9) $Cu1^i$–Cl2–Cu2 = 97.03(6)°.

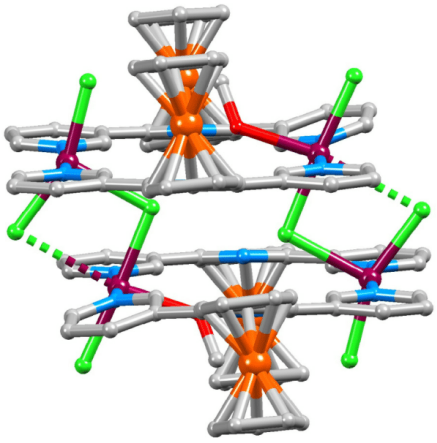

Fig. 3. View of the $[Cu_4Cl_8(\mathbf{3})_4(MeOH)_2]$ molecule in $[\{Cu_4Cl_8(\mathbf{3})_4(MeOH)_2\}\cdot 0.7CHCl_3\cdot 1.8MeOH]$ showing the interconnection of [2 + 2] metallomacrocycles. Hydrogen atoms omitted.

3. Results and discussion

3.1. Structural description

Ligand **3** was prepared as previously reported [6]. Layering of a MeOH solution of copper(II) chloride over a $CHCl_3$ solution of **3** at room temperature resulted after one or two weeks in the formation of red single crystals of $[\{Cu_4Cl_8(\mathbf{3})_4(MeOH)_2\}\cdot 0.7CHCl_3\cdot 1.8MeOH]$. The bulk sample was characterized by X-ray powder diffraction (Fig. S1). The compound crystallizes in the monoclinic space group $P2_1/c$, and structural analysis revealed a discrete, centrosymmetric tetranuclear assembly (Figs. 2 and 3). The asymmetric unit contains one [2 + 2] metallomacrocycle with two, near planar 3,2′:6′,3″-tpy units. Each outer *N*-donor of ligand **3** coordinates to one Cu(II) center, with a trans-arrangement of N-donors from different ligands. The [2 + 2] metallomacrocyclic motif is similar to those in $[Zn_2Cl_2L_2]$ and $[Zn_2Br_2L_2]$ where L is 4′-(5-(N,N-diphenylamino)thien-2-yl)-3,2′:6′,3″-terpyridine [13]. However, in the latter, the 3,2′:6′,3″-tpy units are significantly twisted to accommodate both the tetrahedral geometry at zinc(II) and a centrosymmetric assembly.

Each of atoms Cu1 and Cu2 in the $[Cu_4Cl_8(\mathbf{3})_4(MeOH)_2]$ molecule is 5-coordinate with *trans*-N atoms occupying two basal sites in the square pyramidal coordination sphere (see below). The remaining basal sites are occupied by chlorido ligands (see caption to Fig. 2 for bond lengths). The axial site of Cu2 is occupied by a coordinated methanol molecule (Cu2–O1 = 2.287(5) Å). In contrast, Cu1 is bound to atom Cl2i (symmetry code $i = 1 - x, 1 - y, -z$) and the latter forms a bridge between the first [2 + 2] metallomacrocycle and its symmetry related partner (Cu1–Cl2i = 2.5459(19) Å). The square-pyramidal coordination description is consistent with values of τ (defined by Addison et al. [14]) of 0.051 for atom Cu2 and 0.263 for Cu1. We note, however, that the terminal chlorido ligand Cl4i faces Cu2 (Fig. 2) leading to a weak interaction (Cu2···Cl4i = 3.158(2) Å). In the one-dimensional polymer $[\{Cu_2Cl_4(\mathbf{2})_2(MeOH)\}\cdot 2.25MeOH\cdot H_2O\cdot CHCl_3]_n$ [6], one Cu–Cl contact in the $\{Cu_2(\mu\text{-}Cl)_2\}$ bridging unit is also longer than the other three (2.3688(14), 2.6392(13), 2.3008(14) and 3.0436(14) Å) (Fig. 1). The similarity of the bridging units in $[\{Cu_4Cl_8(\mathbf{3})_4(MeOH)_2\}\cdot 0.7CHCl_3\cdot 1.8MeOH]$ and $[\{Cu_2Cl_4(\mathbf{2})_2(MeOH)\}\cdot$

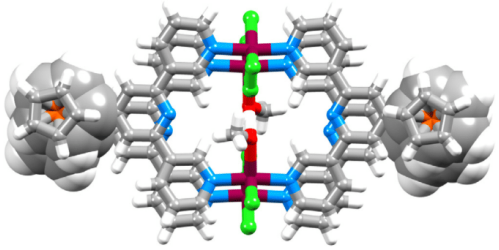

Fig. 4. Face-to-face π-stacking of ferrocenyl units (space-filling representation) and between 3,2′:6′,3″-tpy units.

$2.25MeOH{\cdot}H_2O{\cdot}CHCl_3]_n$ is reflected in the comparable Cu···Cu separations of 3.668(1) versus 3.667(1) Å.

The angles between the planes of the pyridine rings containing N1/N2, N2/N3, N4/N5 and N5/N6 are 11.9, 21.4, 8.9 and 8.5°, respectively. Both independent ferrocenyl units exhibit very little twist with respect to the central pyridine ring of ligand **3** angle to which each is bonded (angles between the pyridine and attached cyclopentadienyl rings = 7.7 and 5.3°). The latter is associated with efficient face-to-face π-interactions between ferrocenyl units of symmetry-related metallomacrocycles (space-filling representation in Fig. 4). The angle between pairs of stacked cyclopentadienyl rings is 1.9°, and the inter-centroid distance is 3.52 Å. The stacking interactions extend to pairs of 3,2′:6′,3″-tpy units (Fig. 4) which exhibit an optimal slipped orientation. For the three independent pairs of stacked pyridine rings, centroid···ring plane distances are 3.69, 3.36 and 3.47 Å, and centroid···centroid separations are 3.90, 3.67 and 3.71 Å.

The $[Cu_4Cl_8(\mathbf{3})_4(MeOH)_2]$ molecules pack into sheets lying in the *bc*-plane (Fig. S2). The space between the layers is filled by $CHCl_3$ and MeOH solvent molecules in partially occupied positions. Within a sheet, centrosymmetric pairs of $[Cu_4Cl_8(\mathbf{3})_4(MeOH)_2]$ molecules engage in face-to-face π-interactions between ferrocene and tpy domains. This extends the intramolecular π-interactions between ferrocenyl units into a quadruple-decker stack. This is shown in Fig. 5 for three adjacent pairs of molecules; for the red molecules, both intra- and intermolecular π-stacking is shown in spacefilling representation. Tightly associated pairs of molecules interlock with one another into the two-dimensional sheet assembly.

3.2. Magnetic measurements

Among studies focusing on magnetism, the structural motif of chlorido-bridged copper(II) compounds is well represented in doubly-bridged dimers [15,16] and in infinite chains [17–21], but there are fewer examples of discrete copper(II) compounds featuring singly-bridged Cu–Cl–Cu units [22–24]. $[\{Cu_4Cl_8(\mathbf{3})_4(MeOH)_2\}\cdot 0.7CHCl_3\cdot 1.8MeOH]$ was investigated by magnetic susceptibility measurements. The $\chi_mT(T)$ plot (Fig. 6) of a polycrystalline sample of $[\{Cu_4Cl_8(\mathbf{3})_4(MeOH)_2\}\cdot 0.7CHCl_3\cdot 1.8MeOH]$ exhibits a value of 1.04 $cm^3\ K\ mol^{-1}$ at 300 K (per two Cu(II) ions) which decreases only slightly with lowering the temperature to around 50 K. At lower temperatures, a pronounced decrease of χ_mT is evident leading to a value of 0.39 $cm^3\ K\ mol^{-1}$ at 1.9 K. The shape of the curve is typical for antiferromagnetic exchange interactions, though with weak coupling between adjacent Cu(II) centers, and the high temperature χ_mT values point to a *g* factor > 2 and two magnetically isolated spin doublets (half of the molecule $[Cu_4Cl_8(\mathbf{3})_4(MeOH)_2]$).

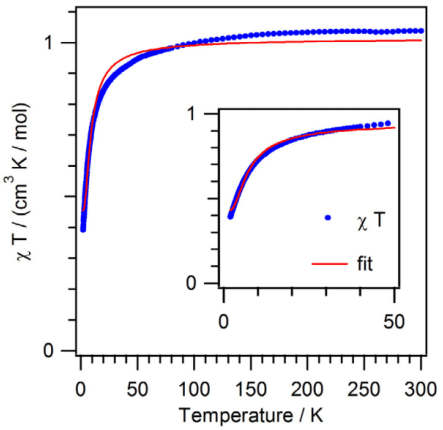

Fig. 6. Thermal variation of χ_mT for **1** (per two Cu(II) ions); inset highlights the 50–1.9 K region. Solid lines represent fitted curves.

In a first approach, the data over the whole temperature range were modeled following the theoretical approach for a dimeric Cu(II) system (twice $S = ½$) assuming isotropic intradimer interactions. In other words, the molecule $[Cu_4Cl_8(\mathbf{3})_4(MeOH)_2]$ is viewed as a magnetically uncoupled pair of μ-Cl bridged Cu(II) dimers where the magnetic superexchange is likely propagated *via* the bridging chlorido ligands. A least-squares fit resulted in the parameters $g = 2.4$ and $J = 16.2(4)$ K (11.2(3) cm^{-1}) based on the Hamiltonian $\mathbf{H} = J(\mathbf{S}_1\cdot\mathbf{S}_2)$. As it is obvious from the fitted curve in Fig. 6, this model does not capture very well the curvature of the experimental χ_mT values below 50 K, and the least-squares fit clearly compensates for it in the high temperature region. Next, a model with two *J* parameters was applied [25], one for the mono μ-Cl bridges and the other one for additional weak coupling pathways through two tpy units connecting the two adjacent Cu(II) ions of each [Cu–Cl(bridge)–Cu] dimer. However, also this model did not improve the fit over the whole temperature range. Therefore, the first model with only one *J* parameter was taken for a fit over the lower temperature regime only, while taking into account that the information about the coupling strength lies predominantly in that temperature range. The inset of Fig. 6 shows now a reasonable fit for the 50–1.9 K range resulting in the parameters $g = 2.3$ and $J = 13.0(2)$ K (9.0(1) cm^{-1}). This *J* value lies within the range of literature values [19] of μ-Cl bridged Cu(II) compounds. Fig. S3 shows the magnetization data for the compound taken at 1.9 K.

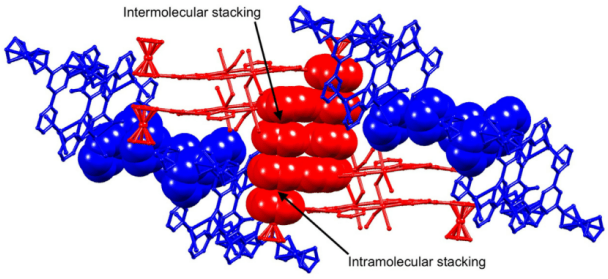

Fig. 5. Adjacent centrosymmetric pairs of $[Cu_4Cl_8(\mathbf{3})_4(MeOH)_2]$ molecules (red or blue). π-Stacking interactions are shown in spacefilling representation, both intra- and intermolecular for the red molecules, and only intermolecular for the blue molecules. (Color online.)

For mono-chlorido bridged Cu(II) complexes, no magneto-structural correlations have been reported so far. In this context it must be recognized that the symmetry of the coordination environment for the Cu(II) ions is very low and consequently, an extensive mixing of the d-orbitals occurs. Thus, besides bond-distances, the angle of the Cu–Cl(bridging)–Cu unit, the symmetry of the coordination environment, and the degree of spin density of the unpaired electron of the Cu(II) ions on the bridge are decisive for the coupling strength.

3.3. Electrochemistry and spectroelectrochemistry

An investigation of the redox activity of $[Cu_4Cl_8(\mathbf{3})_4(MeOH)_2]$ was hindered by the very low solubility of solid $[\{Cu_4Cl_8(\mathbf{3})_4(MeOH)_2\}\cdot 0.7CHCl_3\cdot 1.8MeOH]$ in common solvents. Propylene carbonate was the most suitable solvent of a range investigated. Cyclic voltammograms (two cycles) of an orange solution of **3** are shown in Fig. 7. The ferrocenyl unit undergoes a reversible oxidation at +0.12 V ($E_{pc} - E_{pa}$ = 40 mV) referenced to external Fc/Fc^+. The shift in oxidation potential on going from ferrocene to **3** was confirmed using an internal Fc/Fc^+ reference (Fig. S4). Within the solvent accessible window a quasi-reversible reduction process (−2.44 V, $E_{pc} - E_{pa} \sim 100$ mV) presumably centered on the tpy unit is also observed (Fig. 7). Addition of crystals of $[\{Cu_4Cl_8(\mathbf{3})_4(MeOH)_2\}\cdot 0.7CHCl_3\cdot 1.8MeOH]$ to propylene carbonate resulted in a pale orange solution in contact with crystalline material. The CV of the pale orange solution is compared with that of ligand **3** in Fig. 7 and the close similarity of the two cycles suggests that they both arise from the same redox active motif or the same compound. We cannot state whether the redox activity is from the intact species $[\{Cu_4Cl_8(\mathbf{3})_4(MeOH)_2\}]$ or from free **3** arising from complex dissociation.

To further investigate the compound, we prepared a suspension of finely ground crystals of $[\{Cu_4Cl_8(\mathbf{3})_4(MeOH)_2\}\cdot 0.7CHCl_3\cdot 1.8MeOH]$ in propylene carbonate containing $[^nBu_4N][PF_6]$ to study the pseudo-solid-state electrochemical behavior. This paste was inserted into the cavity between two FTO glass electrodes, one of which was coated with platinum (see Section 2), a fabrication that mimics a dye-sensitized solar cell [26]. Fig. 8 shows a CV with five consecutive cycles obtained from this configuration. The compound undergoes a reversible, iron-centered oxidative process at +0.01 V and in this case we assign the process as arising from $[Cu_4Cl_8(\mathbf{3})_4(MeOH)_2]$. The reductive process seen in Fig. 8 around −0.9 V is reproducible in each cycle.

Spectroelectrochemical data for compound **3** were also recorded. The oxidative cycle for a propylene carbonate solution of **3** was investigated by recording an absorbance spectrum every 0.1 V, from 0 to +1.5 V and back from +1.5 to 0 V (Fig. 9). The absorption maximum at 461 nm responsible for the orange color of **3** diminishes and is replaced by a broad band with $\lambda_{max} \sim 660$ nm, consistent with the typical blue color of ferrocenium (Fc^+) species. The absorption spectra corresponding to **3** and $[\mathbf{3}]^+$ are presented in Fig. S5.

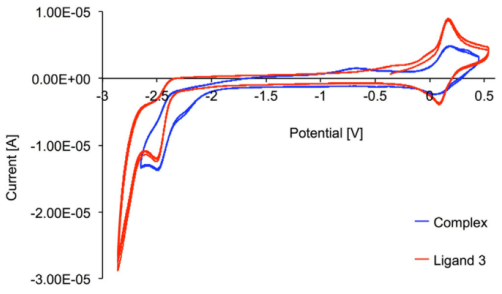

Fig. 7. Cyclic voltammograms (two scans) of propylene carbonate solutions of **3** (red) and $[Cu_4Cl_8(\mathbf{3})_4(MeOH)_2]$ (blue) with $[^nBu_4N][PF_6]$ supporting electrolyte, and scan rate of 0.1 V s^{-1}. Referenced with respect to external Fc/Fc^+. See also Fig. S4. (Color online.)

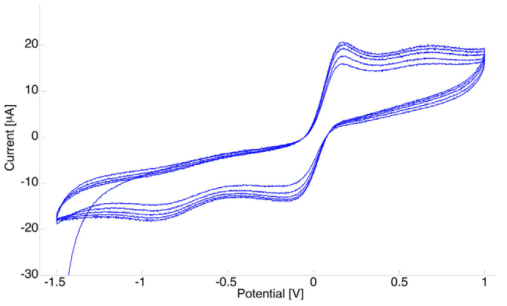

Fig. 8. Cyclic voltammogram (five cycles) of a cell (see text) containing a paste of $[\{Cu_4Cl_8(\mathbf{3})_4(MeOH)_2\}\cdot 0.7CHCl_3\cdot 1.8MeOH]$/propylene carbonate/$[^nBu_4N][PF_6]$ paste. Scan rate 0.1 V s^{-1}.

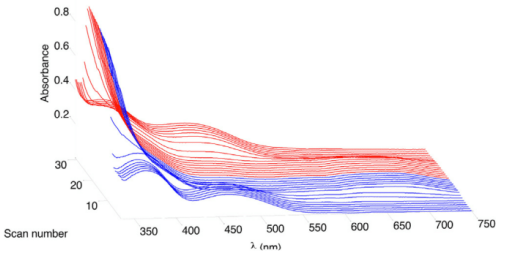

Fig. 9. Spectroelectrochemical data for the oxidative cycle of **3** (propylene carbonate solution, $[^nBu_4N][PF_6]$ as supporting electrolyte) starting from 0 V (first blue line, scan 1) to +1.5 V (last blue line, scan 16) and back from +1.5 V (first red line, scan 17) to 0 V (last red line, scan 31). (Color online.)

4. Conclusion

We have described the formation of the discrete complex $[Cu_4Cl_8(\mathbf{3})_4(MeOH)_2]$ and the single crystal structure of $[\{Cu_4Cl_8(\mathbf{3})_4(MeOH)_2\}\cdot 0.7CHCl_3\cdot 1.8MeOH]$. Two $\{Cu_2Cl_4(\mathbf{3})_2(MeOH)\}$ metallomacrocycles are linked through bridging chlorido ligands to generate a centrosymmetric tetracopper dimetallomacrocycle. The two metallomacrocycles engage in efficient face-to-face π-interactions between ferrocene units and between tpy domains. Intermolecular packing interactions extend the former into quadruple-decker stacking motifs. From the perspective of magnetic exchange interactions, the tetranuclear compound can be viewed as a pair of μ-Cl bridged Cu(II) dimers exhibiting a weak antiferromagnetic coupling *via* the bridging chloride ligands. Compound **3** undergoes a ferrocenyl-centered reversible oxidation at +0.12 V and a tpy-based quasi-reversible reduction process at −2.44 V. Spectroelectrochemistry showed that the oxidation process is accompanied by loss of an absorption at 461 nm and the appearance of an absorption at 660 nm; this process is fully reversible. Electrochemical data for $[Cu_4Cl_8(\mathbf{3})_4(MeOH)_2]$ was obtained

using a suspension of the material in propylene carbonate; the only well-defined process was a ferrocene-based oxidation.

Acknowledgements

We thank the Swiss National Science Foundation (Grant numbers 200020_162631 and 200020-150257, and as part of the NCCR Molecular Systems Engineering) and the University of Basel for support.

Appendix A. Supplementary data

CCDC 1530973 contains the supplementary crystallographic data for [{Cu_4Cl_8(**3**)$_4$(MeOH)$_2$}·0.7$CHCl_3$·1.8MeOH]. These data can be obtained free of charge via http://www.ccdc.cam.ac.uk/conts/retrieving.html, or from the Cambridge Crystallographic Data Centre, 12 Union Road, Cambridge CB2 1EZ, UK; fax: (+44) 1223-336-033; or e-mail: deposit@ccdc.cam.ac.uk. Supplementary data associated with this article can be found, in the online version, at http://dx.doi.org/10.1016/j.poly.2017.03.030.

References

[1] C.E. Housecroft, Dalton Trans. 43 (2014) 6594.
[2] C.E. Housecroft, CrystEngComm 17 (2015) 7461.
[3] F. Kröhnke, Synthesis (1976) 1.
[4] J. Wang, G.S. Hanan, Synlett (2005) 1251.
[5] Y.M. Klein, A. Prescimone, E.C. Constable, C.E. Housecroft, Inorg. Chem. Comm. 70 (2016) 118.
[6] Y.M. Klein, A. Prescimone, E.C. Constable, C.E. Housecroft, Aus. J. Chem. (2017), http://dx.doi.org/10.1071/CH16527 (advance article).
[7] L. Xiao, L. Zhu, Q. Zeng, Q. Liu, J. Zhang, S. Li, H. Zhou, S. Zhang, J. Wu, Y. Tian, J. Organomet. Chem. 22 (2015) 789.
[8] Bruker Analytical X-ray Systems Inc, APEX2, version 2 User Manual, M86–E01078, Madison, WI, 2006.
[9] L. Palatinus, G. Chapuis, J. Appl. Cryst. 40 (2007) 786.
[10] P.W. Betteridge, J.R. Carruthers, R.I. Cooper, K. Prout, D.J. Watkin, J. Appl. Cryst. 36 (2003) 1487.
[11] I.J. Bruno, J.C. Cole, P.R. Edgington, M.K. Kessler, C.F. Macrae, P. McCabe, J. Pearson, R. Taylor, Acta Cryst. B 58 (2002) 389.
[12] C.F. Macrae, I.J. Bruno, J.A. Chisholm, P.R. Edgington, P. McCabe, E. Pidcock, L. Rodriguez-Monge, R. Taylor, J. van de Streek, P.A. Wood, J. Appl. Cryst. 41 (2008) 466.
[13] M. Zhao, J. Tan, J. Su, J. Zhang, S. Zhang, J. Wu, Y. Tian, Dyes Pigments 130 (2016) 216.
[14] A.W. Addison, T.N. Rao, J. Reedijk, J. van Rijn, G.C. Verschoor, J. Chem. Soc., Dalton Trans. (1984) 1349.
[15] W.E. Marsh, K.C. Patel, W.E. Hatfield, D.J. Hodgson, Inorg. Chem. 22 (1983) 511.
[16] W.A. Alves, R.H. de Almeida Santos, A. Paduan-Filho, C.C. Becerra, A.C. Borin, A. M. Da Costa Ferreira, Inorg. Chim. Acta 357 (2004) 2269.
[17] W.E. Estes, W.E. Hatfield, J.A.C. van Ooijen, J. Reedijk, J. Chem. Soc., Dalton Trans. (1980) 2121.
[18] S. Decurtins, H.W. Schmalle, P. Schneuwly, L.-M. Zheng, J. Ensling, A. Hauser, Inorg. Chem. 34 (1995) 5501.
[19] H. Grove, J. Sletten, M. Julve, F. Lloret, J. Chem. Soc., Dalton Trans. (2001) 2487, and references cited therein.
[20] F.J. Barros-Garcia, A. Bernalte-Garcia, F.J. Higes-Rolando, F. Luna-Giles, A.M. Pizarro-Galan, E. Vinuelas-Zahinos, Z. Anorg, Allg. Chem. 631 (2005) 1898.
[21] S. Walha, H. Naili, S. Yahyaoui, B.F. Ali, M.M. Turnbull, T. Mhiri, J. Supercond. Nov. Magn. 26 (2013) 437.
[22] M. Du, Y.M. Guo, X.H. Bu, J. Ribas, M. Monfort, New. J. Chem. 26 (2002) 939.
[23] G. Seeber, B.M. Kariuki, L. Cronin, P. Kögerler, Polyhedron 24 (2005) 1651.
[24] C. Deckert, D. Bittner, L.M. Carrella, D. Schollmeyer, E. Rentschler, Eur. J. Inorg. Chem. (2016) 1738.
[25] J.W. Hall, W.E. Estes, E.D. Estes, R.P. Scaringe, W.E. Hatfield, Inorg. Chem. 16 (1977) 1572.
[26] See for example: Y.M. Klein, M. Willgert, A. Prescimone, E.C. Constable, C.E. Housecroft Dalton Trans. 45 (2016) 465.

18.4 Paper 4 (Published by MDPI)

materials

MDPI

Article

4,2′:6′,4″- and 3,2′:6′,3″-Terpyridines: The Conflict between Well-Defined Vectorial Properties and Serendipity in the Assembly of 1D-, 2D- and 3D-Architectures

Y. Maximilian Klein, Alessandro Prescimone, Edwin C. Constable and Catherine E. Housecroft *

Department of Chemistry, University of Basel, Spitalstrasse 51, 4056 Basel, Switzerland; max.klein@unibas.ch (Y.M.K.); alessandro.prescimone@unibas.ch (A.P.); edwin.constable@unibas.ch (E.C.C.)
* Correspondence: catherine.housecroft@unibas.ch; Tel.: +41-61-207-1008

Received: 12 June 2017; Accepted: 28 June 2017; Published: 30 June 2017

Abstract: A comparative investigation of the coordination assemblies formed between $Co(NCS)_2$ and two monotopic 4,2′:6′,4″-terpyridine (4,2′:6′,4″-tpy) ligands or two related ditopic ligands is reported. Crystals were grown by layering MeOH solutions of $Co(NCS)_2$ over a $CHCl_3$ or 1,2-$C_6H_4Cl_2$ solution of the respective ligand at room temperature. With 4′-(2-methylpyrimidin-5-yl)-4,2′:6′,4″-terpyridine (**6**), the 1D-coordination polymer $\{[Co_2(NCS)_4(MeOH)_4(\mathbf{6})_2]\cdot 2MeOH\cdot 8H_2O\}_n$ assembles with **6** coordinating only through the outer N-donors of the 4,2′:6′,4″-tpy unit; coordination by the MeOH solvent blocks two cobalt coordination sites preventing propagation in a higher-dimensional network. A combination of $Co(NCS)_2$ and 1-(4,2′:6′,4″-terpyridin-4′-yl)ferrocene (**7**) leads to $\{[Co(NCS)_2(\mathbf{7})_2]\cdot 4CHCl_3\}_n$ which contains a (4,4) net; the 2D-sheets associate through π-stacking interactions between ferrocenyl and pyridyl units. A 3D-framework is achieved through use of the ditopic ligand 1,4-bis(^{n}propoxy)-2,5-bis(4,2′:6′,4″-terpyridin-4′-yl)benzene (**8**) which acts as a 4-connecting node in $\{[Co(NCS)_2(\mathbf{8})_2]\cdot 2C_6H_4Cl_2\}_n$; the combination of metal and ligand planar 4-connecting nodes results in a $\{6^5.8\}$ **cds** net. For a comparison with the coordinating abilities of the previously reported 1,4-bis(^{n}octoxy)-2,5-bis(4,2′:6′,4″-terpyridin-4′-yl)benzene (**3**), a more flexible analogue **9** was prepared. $\{[Co(NCS)_2(\mathbf{9})]\cdot 2CHCl_3\}_n$ contains a (4,4) net defined by both metal and ligand planar 4-connecting nodes. The ^{n}octoxy tails of **9** protrude from each side of the (4,4) net and thread through adjacent sheets; the arene-attached ^{n}octoxy chains associate through a combination of van der Waals and C–H...π interactions.

Keywords: coordination polymer; coordination network; 4,2′:6′,4″-terpyridine; cobalt thiocyanate

1. Introduction

The coordination chemistry of divergent 4,2′:6′,4″-terpyridine (4,2′:6′,4″-tpy) and 3,2′:6′,3″-terpyridine ligands is now a mature field, with the former ligand in particular being increasingly employed as a building block for the assembly of coordination polymers and networks [1,2]. There are a few examples of 4,2′:6′,4″-tpy ligands acting in a monodentate mode [3–7] but, typically, 4,2′:6′,4″-tpy coordinates through the two outer nitrogen atoms, with the central nitrogen atom non-coordinated. Therefore, ligands based upon a 4,2′:6′,4″-tpy metal-binding domain present moderately rigid, well-defined V-shaped motifs (Scheme 1a) which are ideal linkers in coordination assemblies.

Starting with the 4,2′:6′,4″-tpy unit as a well-defined V-shaped building block, there are a number of strategies that can be applied to direct an assembly towards 2D- or 3D-architectures in preference to a 1D-chain. Since 4,2′:6′,4″-tpy is easily modified in the 4′-position using Kröhnke [8]

or Hanan [9] syntheses, one approach is the incorporation of a coordinatively non-innocent domain D (Scheme 1b), for example D = pyridyl or carboxylate groups. The use of multitopic ligands [10–12] is an attractive way forward but has, so far, been little exploited. Scheme 1c illustrates a generic bis(4,2′:6′,4″-tpy) acting as a 4-connecting node. Rotation about the C–spacer bonds permits the node to have limiting planar or approximately tetrahedral geometries, and the directionality of the assembly can be modified by switching from 4,2′:6′,4″-tpy to 3,2′:6′,3″-tpy domains. We have recently employed such ditopic ligands in which the spacer (Scheme 1c) is a 1,4-C_6H_4 ring to assemble parallel interpenetrating 2D→2D sheets [13–15] and 3D-metal-organic frameworks (MOFs) [15,16]. Going to a ferrocen-1,1′-yl spacer introduces rotational freedom and, in $[\{Zn_2(\mathbf{1})Cl_4\}\cdot 3CHCl_3]_n$ where **1** = 1,1′-bis(4,2′:6′,4″-terpyridin-4′-yl)ferrocene (Scheme 2), the ligand adopts a cisoid-conformation, leading to a double-stranded 1D-polymer chain [17].

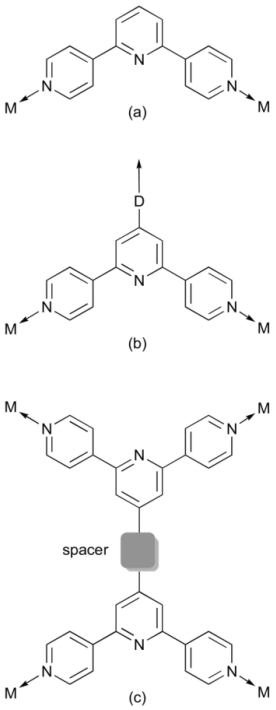

Scheme 1. (**a**) Divergent V-shaped motif of 4,2′:6′,4″-tpy; (**b**) introduction of a donor group, D, in the 4′-position; and (**c**) 4-connecting node presented by ditopic bis(4,2′:6′,4″-tpy).

The discussion above focuses on bis(4,2′:6′,4″-tpy) or bis(3,2′:6′,3″-tpy) as a 4-connecting node. However, the choice of metal is naturally important since its preferred coordination number and geometry dictate whether it will act as a linker or node. When connected through ZnX_2 units (X = halide) as in $[Zn_2Br_4(\mathbf{2})\cdot H_2O]_n$ (**2** is shown in Scheme 2), ligand **2** acts as a 4-connecting node and the zinc(II) atoms are linkers; the assembly is a MOF consisting of 2-fold interpenetrating **nbo** nets [15]. In contrast, when ligand **3** (Scheme 2) is combined with $Co(NCS)_2$, both the metal and ligand function as 4-connecting nodes (planar and approximately tetrahedral, respectively) and assemble into a 3D $\{4^2.8^4\}$ **lvt** net [16]. Limiting the ligand to a single 4,2′:6′,4″-tpy domain as in **4** and **5** (Scheme 2) and reacting with $Co(NCS)_2$ leads to the formation of 3D chiral **neb** nets [18]. This assembly is noteworthy in that a chiral MOF is built from achiral node and linkers. The presence of the long alkyl-tails appears to be important in directing or stabilizing these **neb** nets, since related 4,2′:6′,4″-tpy ligands bearing

in the 4′-position ^{t}Bu, Ph, 4-MeOC$_6$H$_4$, 4-EtOC$_6$H$_4$, 4-^{n}PrOC$_6$H$_4$, 4-HC≡CC$_6$H$_4$, 1*H*-imidazol-4-yl or benzo[*d*][1,3]dioxol-5-yl substituents form 2D-nets with Co(NCS)$_2$ [6,19–22]. With the exception of the work of Mondal et al. [20], crystal growth of the coordination networks described above was by layering under room temperature conditions.

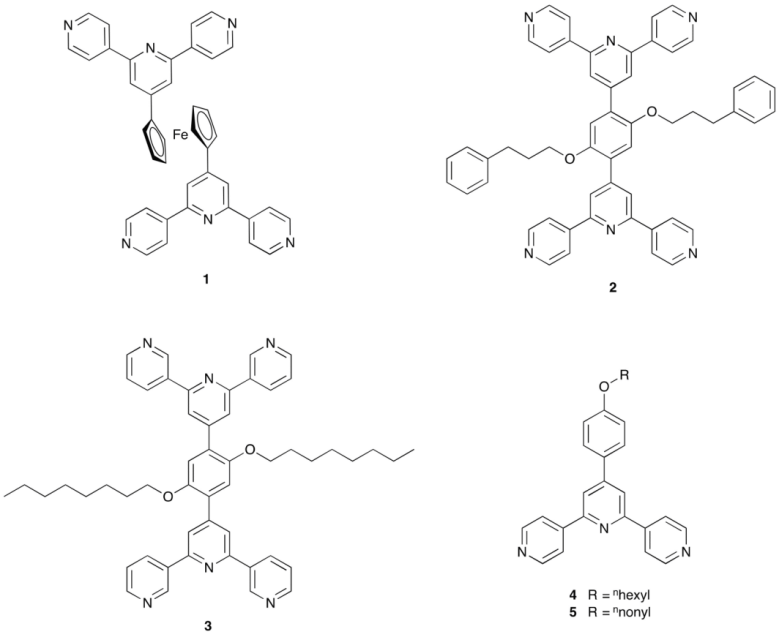

Scheme 2. Structures of ditopic ligands **1** and **2** with 4,2′:6′,4″-tpy domains, and **3** with 3,2′:6′,3″-tpy metal-binding units and of the monotopic ligands **4** and **5**.

We now present a comparative investigation of the coordination assemblies formed between Co(NCS)$_2$ and two monotopic 4,2′:6′,4″-tpy ligands and two ditopic ligands. Ligand **6** (Scheme 3) contains a 2-methylpyrimidin-5-yl substituent and we were interested to see if this would be an additional metal-binding domain to cobalt(II). We have previously reported that the pyrimidinyl units in 4′-(pyrimidin-5-yl)-4,2′:6′,4″-terpyridine or **6** remain uncoordinated in reactions with zinc(II) halides [23], whereas Grafino et al. observe examples of both coordinated and non-coordinated pyrimidinyl *N*-donors in reactions of 4′-(4-(pyrimidin-5-yl)phenyl)- 4,2′:6′,4″-terpyridine with Zn(acac)$_2$ [5]. Ligand **7** (Scheme 3) is related to ditopic ligand **1** (Scheme 2) but offers only one 4,2′:6′,4″-tpy domain. Both 1D-polymer chains and metallomacrocycles have been reported for combinations of **7** with ZnX$_2$ (X = Cl, Br, I, SCN or OAc) [24,25]. The assemblies are competitive for ZnI$_2$ and both the 1D-chain [{ZnI$_2$(**7**)}·2CHCl$_3$]$_n$ [25] and discrete metallosquare [Zn$_4$I$_8$(**7**)$_4$·1.4MeOH] [24] have been crystallographically characterized. A feature that the ferrocenyl unit in **1** or **7** brings to crystal packing is its possibility for face-to-face π-stacking with pyridine rings [24]. Ditopic ligand **8** (Scheme 3) is a member of the 1,4-bis(alkoxy)-2,5-bis(4,2′:6′,4″-terpyridin-4′-yl)benzene family to which **2** (Scheme 2) belongs; while we have investigated assemblies formed between such ligands with zinc(II) halides [15], we have not described reactions with Co(NCS)$_2$. Finally, ligand **9** (Scheme 3) is analogous to **3** in terms of the four *N*-donors. The flexibility of **9** is greater than that of **3**, and we wished to investigate how this would redirect the coordination assembly as compared to the 3D {$4^2.8^4$} **lvt** net in [Co(NCS)$_2$(**3**)·4CHCl$_3$]$_n$ [16].

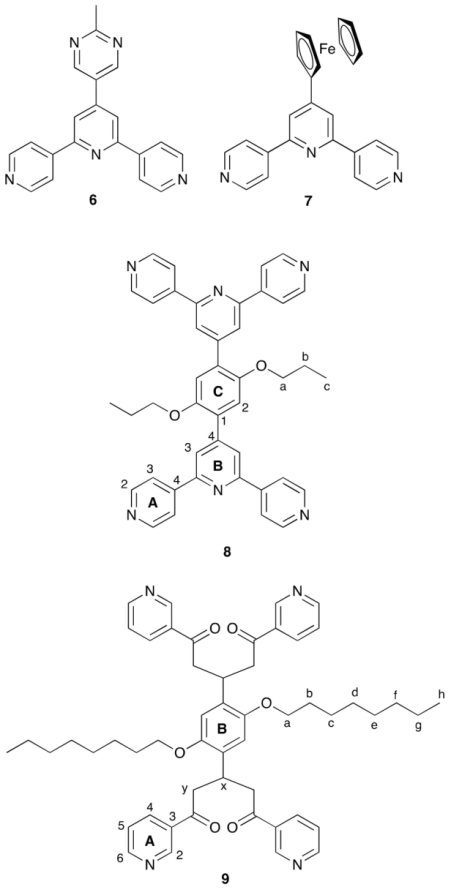

Scheme 3. Structures of ligands **6**–**9** with atom labelling for NMR spectroscopic assignments in **8** and **9**.

2. Results and Discussion

2.1. Ligand Syntheses and Characterization

Ligands **6** and **7** were prepared as previously reported [23,25]. The synthetic route to **8** is summarized in Scheme 3 and is closely related to the synthesis of **2** [15]. Compound **8a** (Scheme 3) was prepared from the commercially available 2,5-dibromohydroquinone and then reacted with ^{n}BuLi followed by DMF to yield the dialdehyde **8b**. The ^{1}H NMR spectrum of **8b** was consistent with previously reported data [26]. The one-pot method of Hanan [9] (Scheme 3) was then used to transform **8b** into compound **8**. The disappearance of the aldehyde signal at δ 10.52 ppm confirmed that derivatization of both aldehyde groups had occurred (Figure 1). The ^{1}H and ^{13}C NMR spectra of compound **8** were assigned using COSY, HMQC, HMBC and NOESY methods and were in accord with the structure shown in Scheme 4.

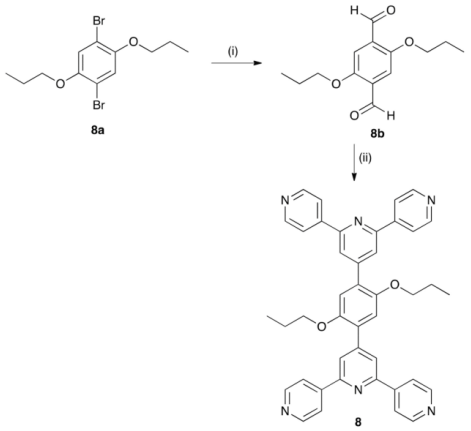

Scheme 4. Synthetic route to compound **8**. Conditions: (**i**) ^{n}BuLi, Et_2O, 0 °C, 6 h; DMF, room temperature, yield 56.3%; and (**ii**) 4-acetylpyridine, KOH, EtOH, aqueous NH_3, room temperature, yield 21.6%.

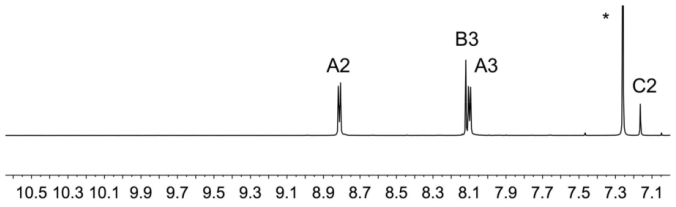

Figure 1. Part of the 500 MHz ^{1}H NMR spectrum of **8** in $CDCl_3$ showing the aromatic region of **8** and confirming the loss of both aldehyde groups of the precursor **8b**. * = residual $CHCl_3$.

Compound **9** was prepared by the reaction of four equivalents of 3-acetylpyridine with 2,5-bis(octoxy)benzene-1,4-dicarbaldehyde under basic conditions (Scheme 5). In the electrospray mass spectrum of **9**, the base peak at m/z 839.4 corresponded to $[M+H]^+$. Figure 2 shows the ^{1}H NMR spectrum of **9**. Both this and the ^{13}C NMR spectrum were assigned using 2D methods (Figure S1 shows the HMQC spectrum) and were consistent with the structure shown in Scheme 5. In the ^{13}C NMR spectrum, a resonance at δ 198.2 ppm characterized the carbonyl groups and a band at 1681 cm^{-1} arising from the C=O stretch was observed in the IR spectrum of **9**.

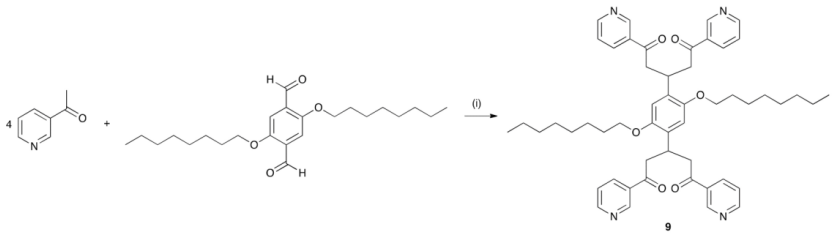

Scheme 5. Synthetic route to compound **9**. Conditions: (**i**) KOH, EtOH, room temperature, yield 31.2%.

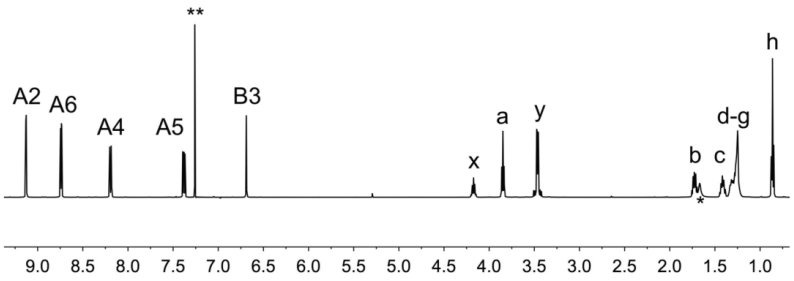

Figure 2. The 500 MHz ^{1}H NMR spectrum of **9** in $CDCl_3$. ** = residual $CHCl_3$; * = water. See Scheme 3 for atom labelling.

2.2. 4′-(2-Methylpyrimidin-5-yl)-Functionalization: Assembly of a 1D-Chain

Layering of a methanol solution of $Co(NCS)_2$ over a chloroform solution of **6** yielded a few X-ray quality pink crystals under ambient conditions over a period of 2–4 weeks. Single-crystal X-ray diffraction confirmed a formulation of $\{[Co_2(NCS)_4(MeOH)_4(\mathbf{6})_2]\cdot 2MeOH\cdot 8H_2O\}_n$, but there was insufficient material for characterization of the bulk sample by powder diffraction. The compound crystallizes in the triclinic *P*–1 space group, and Figure 3 shows the structure of the repeat unit in the coordination polymer. Selected bond distances and angles are given in the figure caption. Ligand **6** binds to cobalt through atoms N1 and N3 of the 4,2′:6′,4″-tpy, leaving the central pyridine N-donor and the two pyrimidinyl N-donors uncoordinated. The two crystallographically independent cobalt atoms are in similar octahedral coordination spheres, and since each of Co1 and Co2 resides on an inversion centre, the pairs of 4,2′:6′,4″-tpy, thiocyanato and MeOH ligands are necessarily *trans* to one another (Figure 3). The MeOH molecule containing C1 is disordered (50:50 site occupancies), each site sharing a common O2 atom. Since each of Co1 and Co2 binds two ligands **6** which are mutually *trans*, each metal centre acts as a linear, 2-connecting node. The structure in Figure 3 propagates into a 1D-zigzag chain and as shown in Figure 4a. Coordination by the MeOH solvent blocks two cobalt coordination sites precluding propagation into a higher-dimensional network. The zigzag chains lie over one another such that one pyridine ring of the 4,2′:6′,4″-tpy unit stacks over a pyrimidine ring in the next chain. However, the stacking is not optimal. Although the $pyridine_{centroid}\cdots pyrimidine_{plane}$ separation is 3.35 Å, the angle between the planes of the ring containing N1 and pyrimidine ring containing $N4^{iv}/N5^{iv}$ (symmetry code iv = $-x$, $1-y$, $2-z$) is 23.8° (Figure 4b). The presence of the methyl substituent on the pyrimidine ring may sterically hinder a more optimal π-stacking arrangement.

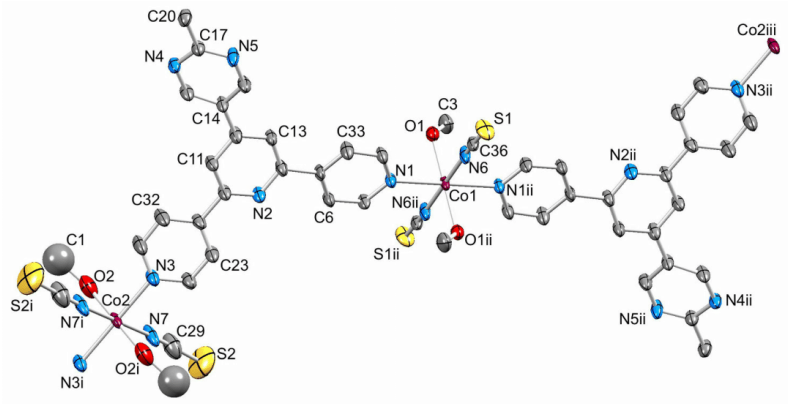

Figure 3. Structure of the repeat unit in $\{[Co_2(NCS)_4(MeOH)_4(\mathbf{6})_2]\cdot 2MeOH\cdot 8H_2O\}_n$ with symmetry generated atoms; H atoms and solvent molecules are omitted. Ellipsoids are plotted at 40% probability; atom C1 was refined isotropically (see text). Symmetry codes: i = 1 − *x*, 2 − *y*, 1 − *z*; ii = 1 − *x*, −*y*, 2 − *z*; iii = *x*, −2 + *y*, 1 + *z*. Selected bond parameters: Co1–N1 = 2.189(6), Co1–N6 = 2.095(7), Co1–O1 = 2.098(6), Co2–N3 = 2.154(6), Co2–N7 = 2.069(7), Co2–O2 = 2.077(9) Å; N1–Co1–N6 = 88.8(2), N1–Co1–O1 = 86.5(2), N3–Co2–N7 = 90.1(2), N3–Co2–O2 = 91.8(3), N7–Co2–O2 = 90.9(4)°.

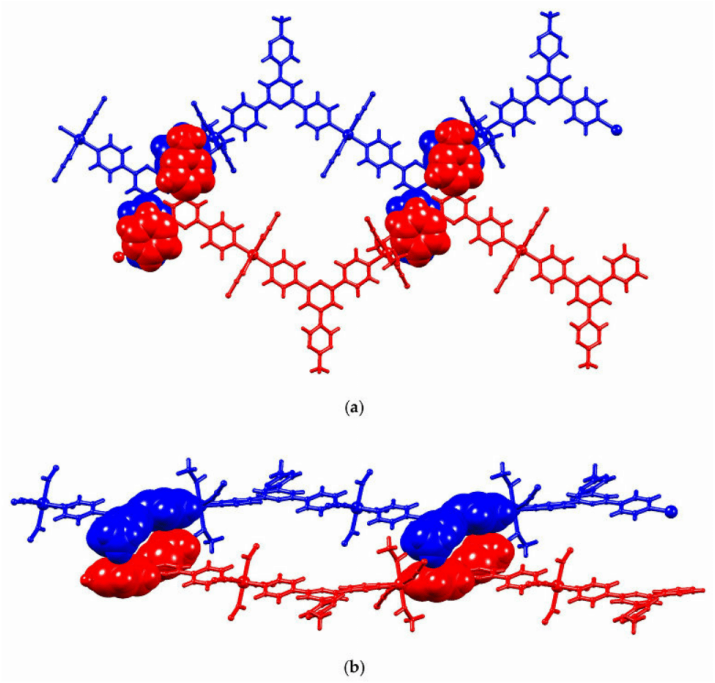

Figure 4. Parts of two adjacent 1D chains in $\{[Co_2(NCS)_4(MeOH)_4(\mathbf{6})_2]\cdot 2MeOH\cdot 8H_2O\}_n$. (**a**) View showing the zigzag profile of the chain and association between pyridine and pyrimidine rings in adjacent chains; (**b**) The same polymer units as in (**a**) viewed down the crystallographic *a*-axis.

Ligands based on 4,2′:6′,4″-tpy feature in a large number of 1D zigzag chains in which the metal nodes are 2-connecting $\{M_2(\mu\text{-}OAc)_4\}$ paddle-wheel units [1]. A common structural motif in these assemblies is the accommodation of the 4′-substituent of the 4,2′:6′,4″-tpy within the V-shaped cleft of a 4,2′:6′,4″-tpy domain in an adjacent chain leading to planar 2D-sheets with a herringbone packing motif. In $\{[Co_2(NCS)_4(MeOH)_4(\mathbf{6})_2]\cdot 2MeOH\cdot 8H_2O\}_n$, rather than being accommodated within the V-shaped pocket of the adjacent chain, the methyl group of the 4′-(2-methylpyrimidin-5-yl) substituent sits over the central N2 atom of the chain beneath it (C_{Me}...N = 3.42(1) Å) as shown in Figure 5. This arrangement of neighbouring chains leads to short S...H contacts [27] as shown in Figure 5. The S...H distances of 2.96 and 2.82 Å (the H atoms are in calculated positions) compare with 3.00 Å for the sum of the H and S van der Waals radii using Bondi values [28], although this value may be an overestimate [29,30]. An analysis by Rowland and Taylor [30] of crystallographic data for intermolecular contacts in organic compounds suggests that the Bondi van der Waals radius for H of 1.2 Å is overestimated by 0.1 Å.

Cavities in the lattice in $\{[Co_2(NCS)_4(MeOH)_4(\mathbf{6})_2]\cdot 2MeOH\cdot 8H_2O\}_n$ are occupied by H_2O and MeOH molecules. There are (in the asymmetric unit) two independent MeOH molecules, each half-occupancy. The lattice water molecules comprise three independent full-occupancy molecules and two independent half-occupancy molecules. Because of the fractional occupancies, discussion of any hydrogen-bonded interactions involving solvent molecules is not warranted.

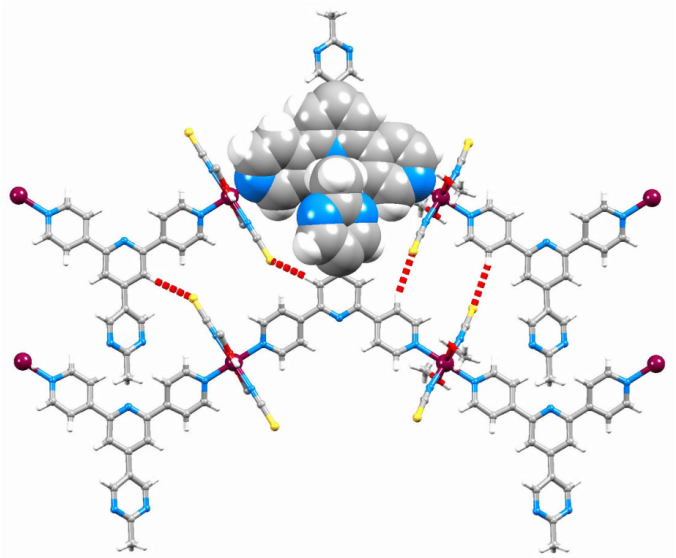

Figure 5. Arrangement of zigzag chains in $\{[Co_2(NCS)_4(MeOH)_4(\mathbf{6})_2]\cdot 2MeOH\cdot 8H_2O\}_n$ showing short S...H contacts (hashed red lines).

2.3. Ferrocenyl-Functionalization: Assembly of a 2D-Network

Layering of a methanol solution of $Co(NCS)_2$ over a chloroform solution of **7** resulted in the growth of orange crystals of $\{[Co(NCS)_2(\mathbf{7})_2]\cdot 4CHCl_3\}_n$. An X-ray quality crystal was chosen for single-crystal structure determination and the bulk sample was characterized by powder diffraction (Figure S2). The compound crystallizes in the monoclinic $P2_1/n$ space group. Figure 6 depicts the octahedral coordination environment of the cobalt(II) centre and selected bond parameters are given in the figure caption. Atom Co1 lies on an inversion centre and is bound by two thiocyanato ligands (necessarily *trans*) and four ligands **7**. The near square-planar arrangement of N1, N1i, N3v and N3iv (Figure 6)

leads to the metal being a planar, 4-connecting node. The structure propagates into a (4,4) net (Figure 7) and belongs to the family of (4,4) nets which have been reported for combinations of $Co(NCS)_2$ and a number of 4′-functionalized 4,2′:6′,4″-tpy ligands (functionality = ^{t}Bu, Ph, 4-$MeOC_6H_4$, 4-$EtOC_6H_4$, 4-^{n}PrOC_6H_4, 4-HC≡CC_6H_4, 1*H*-imidazol-4-yl or benzo[*d*][1,3]dioxol-5-yl [6,19–22]. As Figure 7b shows, the ferrocenyl units protrude above and below the 2D-sheet, and adjacent sheets are interlocked with each ferrocenyl unit of one sheet lying over a 4,2′:6′,4″-tpy unit in the next sheet. The 4,2′:6′,4″-tpy unit deviates slightly from planarity with angles between the planes of the pyridine rings containing N1/N2 and N2/N3 of 11.4 and 13.5°, respectively. The cyclopentadienyl ring containing C16 is twisted 16.0° with respect to the pyridine ring with N2. We have previously described the role of face-to-face π-stacking between ferrocenyl and pyridyl units in crystal packing [24]. Similar effects are observed in $\{[Co(NCS)_2(\mathbf{7})_2]\cdot 4CHCl_3\}_n$ and Figure 8 illustrates that adjacent (4,4) sheets associate through stacking interactions. These involve the pyridine ring containing N1 and cyclopentadienyl ring containing C24^v (symmetry code v = $-1+x, y, z$). The angle between the ring planes is 6.9° and the pyridine$_{centroid}$···C$_5$-ring$_{plane}$ distance is 3.22 Å; the distance of 4.17 Å between the ring centroids is rather long for an optimal interaction. The pyridine ring containing N3 also lies over a ferrocenyl unit (that with C16^{vi}, symmetry code vi = $1-x, -y, 1-z$), but, in this case, the inter-plane angle is 19.2°, leading to an inefficient π-stacking contact.

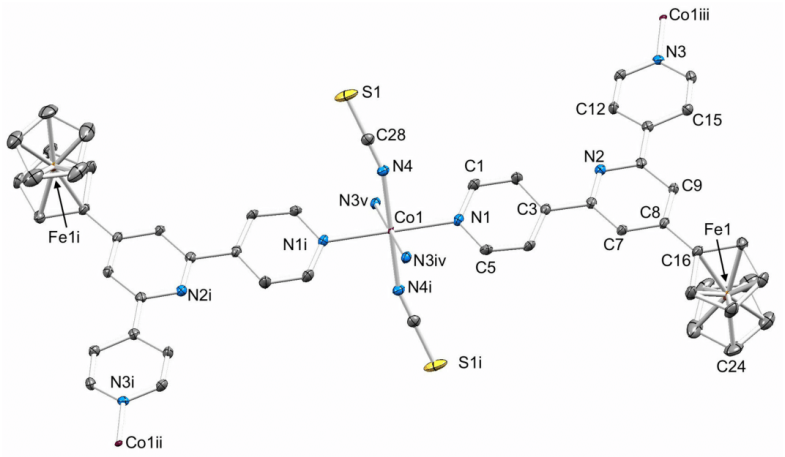

Figure 6. Structure of the repeat unit in $\{[Co(NCS)_2(\mathbf{7})_2]\cdot 4CHCl_3\}_n$ with symmetry generated atoms; H atoms and solvent molecules are omitted. Ellipsoids are plotted at 50% probability. Symmetry codes: i = $-x, 1-y, 1-z$; ii = $-{}^1/_2+x, {}^3/_2-y, -{}^1/_2+z$; iii = ${}^1/_2+x, {}^1/_2-y, {}^1/_2+z$; iv = $-{}^1/_2+x, {}^1/_2-y, -{}^1/_2+z$; v = ${}^1/_2-x, {}^1/_2+y, {}^3/_2+z$. Important bond parameters: Co1–N1 = 2.183(2), Co1–N3^{iv} = 2.183(2), Co1–N4 = 2.083(2), C8–C16 = 1.472(3) Å; N–Co1–N angles are in the range 86.77(8)–93.23(8)°.

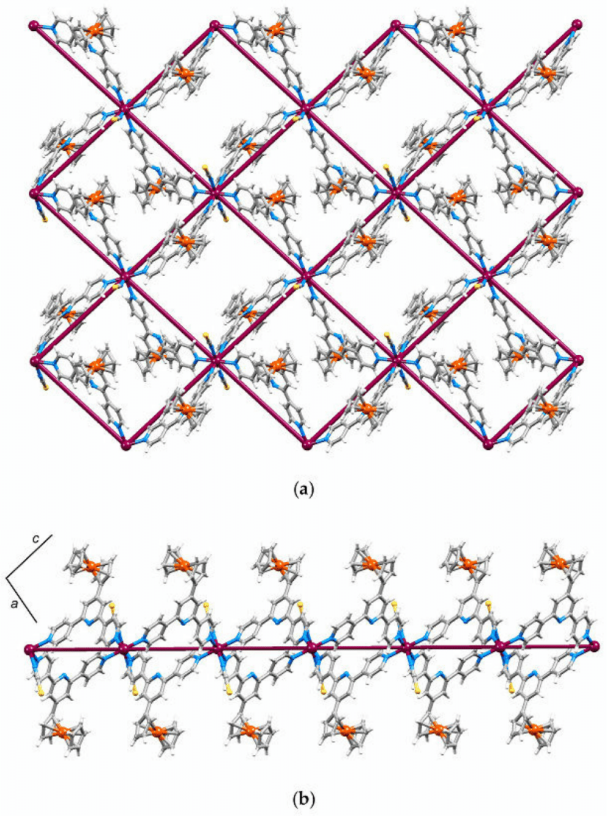

Figure 7. (**a**) TOPOS [31] representation of part of one (4,4) sheet in $\{[Co(NCS)_2(\mathbf{7})_2]\cdot 4CHCl_3\}_n$ overlaid with the structure; and (**b**) the same part of the sheet viewed down the crystallographic *b*-axis.

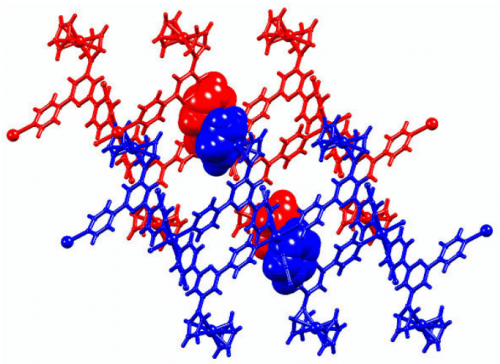

Figure 8. Parts of two adjacent sheets in $\{[Co(NCS)_2(\mathbf{7})_2]\cdot 4CHCl_3\}_n$ showing the π-stacking between a ferrocenyl ring in one sheet and pyridyl ring in the next sheet.

2.4. To a 3D-Network: {[Co(NCS)$_2$(8)$_2$]·2C$_6$H$_4$Cl$_2$}$_n$

Ligand **8** presents two 4,2′:6′,4″-tpy units connected in a "back-to-back" fashion through a spacer which contains two *n*-propoxy tails. We have demonstrated that the length of such tails can have a significant impact on the outcome of assembly processes [13–15]. Single crystals grown by layering a MeOH solution of Co(NCS)$_2$ over a $CHCl_3$ solution of **8** were not of X-ray quality. However, a change to a 1,2-dichlorobenzene solution of **8** led to crystals that were harvested after a few weeks, and single crystal X-ray diffraction showed the formation of a coordination network of formula {[Co(NCS)$_2$(**8**)$_2$]·2C$_6$H$_4$Cl$_2$}$_n$. The compound crystallizes in the monoclinic space group $P2_1/c$ and the repeat unit in the structure is depicted in Figure 9. Atom Co1 is octahedrally sited and since it resides on an inversion centre, the two thiocyanato ligands are necessarily *trans*. Atom Co1 binds to four different ligands **8** (Figure 9) and thereby functions as a planar, 4-connecting node. Selected bond parameters within the coordination sphere are given in the caption to Figure 9, and the N_{tpy}–Co–N_{tpy} bond angles that define the planar node are in the range 84.44(8)–95.56(8)°. The asymmetric unit contains half of a molecule of **8**, and the second half is generated by inversion (Figure 9). Thus, like the cobalt centre, the ditopic ligand also acts as a planar 4-connecting node. The 4,2′:6′,4″-tpy unit deviates from planarity with angles between the rings containing N1/N2 and N2/N3 being 31.3 and 19.5°, respectively. The twist of the pyridine ring with N2 with respect to the central aryl ring is 40.5°, thereby minimizing inter-ring repulsive H...H contacts. The combination of 4-connecting metal and ligand nodes leads to the assembly of a 3D {6^5.8} **cds** [32,33] net, a TOPOS [31] representation of which is shown in Figure 10. In a **cds** net, half of the adjacent nodes are perpendicular to one another and half are coplanar [33]. The preference for the **cds** architecture is in contrast to the assembly of the {4^2.8^4} **lvt** net which forms from Co(NCS)$_2$ and ditopic ligand **3** (Scheme 2) [16]. Ligands **3** and **8** both act as 4-connecting nodes, but differ in having two 3,2′:6′,3″-tpy or 4,2′:6′,4″-tpy domains, respectively. In addition to a change in the vectorial properties of the ligands, ligand **8** possesses shorter alkoxy tails than **3** (*n*-propoxy versus *n*-octoxy). Figure 11 shows an overlay of the structure on the TOPOS representation of the net and this orientation reveals the accommodation of the extended propoxy tails within cavities in the network. Remaining cavities in the **cds** net are occupied by 1,2-dichlorobenzene molecules (see Experimental Section). The bulk sample was characterized by powder diffraction (Figure S3).

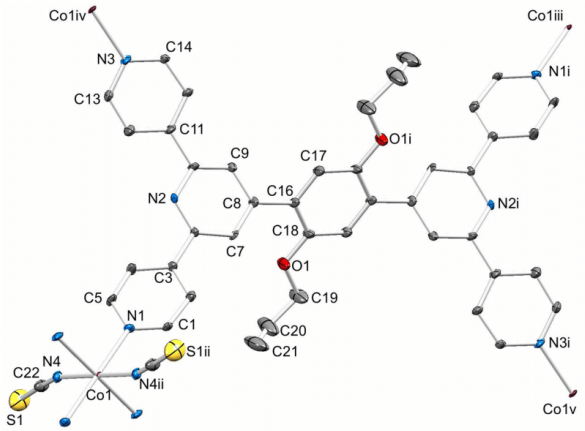

Figure 9. Structure of the repeat unit in {[Co(NCS)$_2$(**8**)$_2$]·2C$_6$H$_4$Cl$_2$}$_n$ with symmetry generated atoms; H atoms and solvent molecules are omitted. Ellipsoids are plotted at 40% probability. Symmetry codes: i = $-x$, $2-y$, $1-z$; ii = $1-x$, $1-y$, $1-z$; iii = $-1+x$, $1+y$, z; iv = x, $^3/_2-y$, $-^1/_2+z$; v = $-1+x$, $^3/_2+y$, $^1/_2+z$. Selected bond parameters: Co1–N1 = 2.173(2), Co1–N4 = 2.047(3), Co1^{iv}–N3 = 2.193(2), O1–C18 = 1.361(4), O1–C19 = 1.431(4) Å; N1–Co1–N4 = 90.47(10)°.

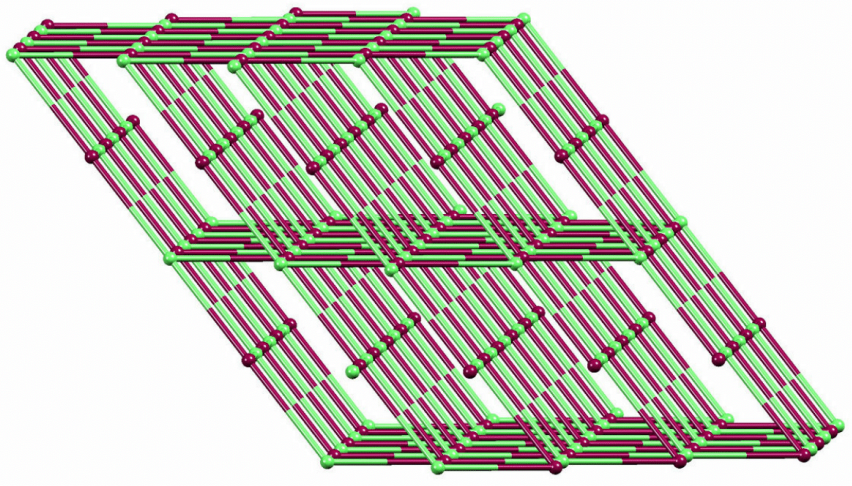

Figure 10. TOPOS [31] representation of part of the **cds** net in $\{[Co(NCS)_2(\mathbf{8})_2]\cdot 2C_6H_4Cl_2\}_n$. Both Co (maroon) and ligand (green) are planar, 4-connecting nodes.

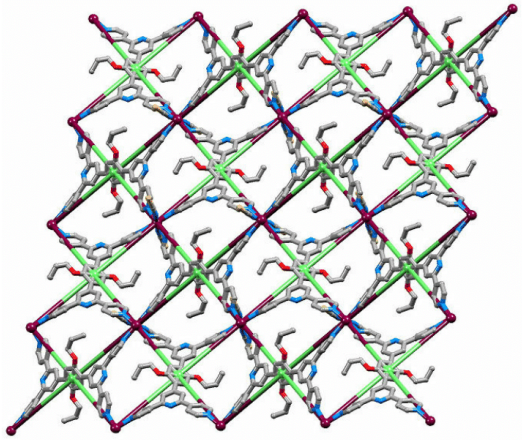

Figure 11. Overlay of the structure of $\{[Co(NCS)_2(\mathbf{8})_2]\cdot 2C_6H_4Cl_2\}_n$ (H atoms and solvent molecules omitted) on a TOPOS [31] representation of part of the **cds** net. The ligand node (green) is defined as the centroid of the arene ring.

*2.5. Relaxing the Backbone: Going from an **lvt** Net to a 2D-Sheet*

As described above, ditopic ligand **3** (Scheme 2) reacts with $Co(NCS)_2$ under conditions of crystal growth by layering to give $\{[Co(NCS)_2(\mathbf{3})]\cdot 4CHCl_3\}_n$ which possesses a $\{4^2.8^4\}$ **lvt** net [16]. This assembly is rather uncommon among MOFs consisting of 4-connected nets [32] and in $\{[Co(NCS)_2(\mathbf{3})]\cdot 4CHCl_3\}_n$, the **lvt** net is produced by a combination of planar Co nodes and approximately tetrahedral ligand nodes. We decided to investigate the effects of modifying the ligand structure so as to retain a 4-connecting domain with similar metrics to **3** but with a more flexible backbone. Ligand **9** (Scheme 3) conforms to these criteria. A methanol solution of $Co(NCS)_2$

was layered over a chloroform solution of **9** and, after 2–4 weeks, X-ray quality crystals had grown. Single-crystal X-ray diffraction analysis confirmed the formation of $\{[Co(NCS)_2(\mathbf{9})]\cdot 2CHCl_3\}_n$ with a Co:ligand ratio equivalent to that in $\{[Co(NCS)_2(\mathbf{3})]\cdot 4CHCl_3\}$n [16]; the bulk sample was characterized by powder diffraction (Figure S4). The compound crystallizes in the triclinic space group *P*–1 with atom Co1 lying on an inversion centre. The repeat unit is shown in Figure 12 and the coordination environment of Co1 resembles that in $\{[Co(NCS)_2(\mathbf{8})_2]\cdot 2C_6H_4Cl_2\}_n$ (Figure 9). Metrical parameters for the coordination sphere (caption to Figure 12) are unexceptional. The closeness of each N_{tpy}–Co1–N_{tpy} angle to 90° leads to a square-planar metal node. The asymmetric unit contains half of a ligand **9**, and the second half is generated by inversion leading to **9** being a planar 4-connecting node (Figure 12), the centre of which is defined by the centroid of the arene ring containing atom C16. The planarity of the ligand **9** node in $\{[Co(NCS)_2(\mathbf{9})]\cdot 2CHCl_3\}_n$ contrasts with the tetrahedral node that **3** presents in $\{[Co(NCS)_2(\mathbf{3})]\cdot 4CHCl_3\}_n$ [16]; recall from the introduction that ditopic ligands of the type exemplified by **2** or **3** (Scheme 2) have limiting planar or approximately tetrahedral geometries. A comparison of the conformations of the coordinated ligands **3** and **9** in $\{[Co(NCS)_2(\mathbf{3})]\cdot 4CHCl_3\}_n$ and $\{[Co(NCS)_2(\mathbf{9})]\cdot 2CHCl_3\}_n$, respectively, is shown in Figure S5.

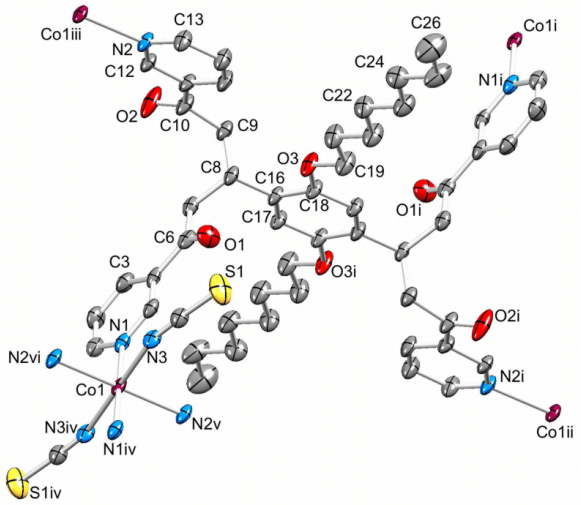

Figure 12. Structure of the repeat unit in $\{[Co(NCS)_2(\mathbf{9})]\cdot 2CHCl_3\}_n$ with symmetry generated atoms; H atoms and solvent molecules are omitted. Ellipsoids are plotted at 40% probability. Symmetry codes: i = $-1+x, 1+y, 1+z$; ii = $-1+x, y, 1+z$; iii = $x, -1+y, z$; iv = $2-x, 3-y, -z$; v = $x, 1+y, z$; vi = $2-x, 2-y, -z$. Selected bond parameters: Co1–N1 = 2.196(4), Co1–N3 = 2.070(4), Co1–$N2^v$ = 2.199(4), O1–C6 = 1.216(6), O2–C10 = 1.193(7), O3–C18 = 1.383(6), O3–C19 = 1.413(6) Å; N1–Co1–N3 = 91.13(17), N_{tpy}–Co1–N_{tpy} range 87.68(16)–92.32(16)°.

Propagation of the unit in Figure 12 leads to a 2D (4,4) net. In contrast to the (4,4) net in $\{[Co(NCS)_2(\mathbf{7})_2]\cdot 4CHCl_3\}_n$, which is defined only by the metal nodes, the net in $\{[Co(NCS)_2(\mathbf{9})]\cdot 2CHCl_3\}_n$ is defined by a combination of metal and ligand 4-connected nodes (Figure 13). The one crystallographically independent octoxy chain in $\{[Co(NCS)_2(\mathbf{9})]\cdot 2CHCl_3\}_n$ is ordered and has a fully extended conformation. These features are associated with the threading of the octoxy tail through an adjacent sheet (Figure 14a) and the alignment of the tails (Figure 14b). Both van der Waals and C–H...π interactions play a role with inter-chain C...C and C...O separations of 4.35 and 4.33 Å and a close C–H...π contact of 3.26 Å (C...π distance = 4.04 Å) [34].

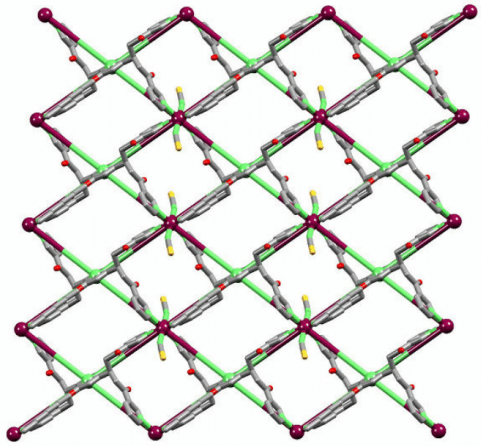

Figure 13. Overlay of the structure of {[Co(NCS)$_2$(**9**)]·2CHCl$_3$}$_n$ (H atoms and solvent molecules omitted) on a TOPOS [31] representation of part of a 2D-sheet. The ligand node (green) is defined as the centroid of the central arene ring in **9**.

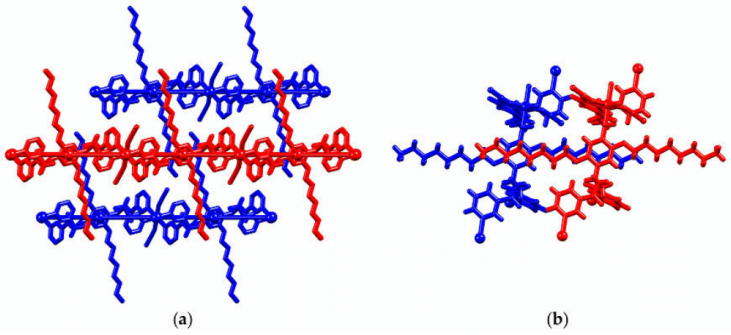

Figure 14. (**a**) Parts of three adjacent 2D-sheets in {[Co(NCS)$_2$(**9**)]·2CHCl$_3$}$_n$ (H atoms and solvent molecules omitted) showing threading of the octoxy tails through neighbouring sheets; and (**b**) alignment of octoxy tails in adjacent sheets.

3. Materials and Methods

3.1. General

^{1}H and ^{13}C NMR spectra were recorded on a Bruker DRX-500 NMR spectrometer with chemical shifts referenced to residual solvent peaks (TMS = δ 0 ppm). Electrospray ionisation (ESI) mass spectra were measured on a Bruker esquire 3000plus spectrometer or Shimadzu LCMS-2020 instrument and high resolution ESI mass spectra on a Bruker maXis 4G QTOF instrument. The IR spectrum of **9** was recorded on a Perkin Elmer Spectrum Two (UATR) FT-IR.

3-Acetylpyridine, 4-acetylpyridine, 1-bromopropane, 2,5-dibromohydroquinone and 2,5-bis(octoxy)benzene-1,4-dicarbaldehyde were purchased from Sigma-Aldrich (Switzerland) and used without further purification. Ligands **6** and **7** were prepared as previously reported [23,25].

3.2. Synthesis of **8a**

2,5-Dibromohydroquinone (2.0 g, 7.47 mmol), 1-bromopropane (1.72 mL, 2.32 g, 18.7 mmol) and anhydrous K_2CO_3 (3.1 g, 22.4 mmol) were added to dry DMF (100 mL) and the mixture was heated at 100 °C for 16 h. The mixture was cooled to room temperature then poured into a beaker containing ice water (100 mL) and the mixture stirred for 30 min. The precipitate was filtered, washed with water (3 × 30 mL) and dried in vacuo. Compound **8a** was isolated as white crystals (2.49 g, 7.07 mmol, 94.6%). ^{1}H NMR (500 MHz, $CDCl_3$) δ/ppm 7.09 (s, 2H, H^{C3}), 3.92 (t, *J* = 6.5 Hz, 4H, H^a), 1.89–1.75 (m, 4H, H^b), 1.06 (t, *J* = 7.4 Hz, 6H, H^c). This matches the literature data [26].

3.3. Synthesis of **8b**

Compound **8a** (1.8 g, 5.11 mmol) and dry Et_2O (100 mL) were added to a dried flask and cooled to 0 °C using an ice bath. ^{n}BuLi (1.6 M in hexanes, 9.58 mL, 15.3 mmol) was added slowly to the solution over a period of 20 min and the temperature maintained at 0 °C for 6 h. Dry DMF (1.19 mL, 15.3 mmol) was added and the solution stirred for 16 h, while warming up to room temperature. The reaction mixture was neutralized with saturated aqueous NH_4Cl and extracted with CH_2Cl_2 (200 mL). The organic phase was dried over $MgSO_4$ and concentrated in vacuo. Compound **8b** was isolated as a yellow solid (0.72 g, 2.88 mmol, 56.3%) and used without further purification. ^{1}H NMR (500 MHz, $CDCl_3$) δ/ppm 10.52 (s, 2H, H^{CHO}), 7.43 (s, 2H, H^{C3}), 4.05 (t, *J* = 6.5 Hz, 4H, H^a), 1.93–1.74 (m, 4H, H^b), 1.06 (m, *J* = 7.4 Hz, 6H, H^c). This matches the literature data [26].

3.4. Synthesis of **8**

Compound **8b** (0.3 g, 1.2 mmol) was dissolved in EtOH (100 mL), then 4-acetylpyridine (0.54 mL, 0.59 g, 4.8 mmol) and crushed KOH (0.27 g, 4.8 mmol) were added in one portion. Aqueous NH_3 (32%, 3.1 mL) was added dropwise and the reaction mixture was stirred at room temperature for 16 h. The precipitate was collected by filtration and washed with water (3 × 10 mL), EtOH (3 × 10 mL) and Et_2O (3 × 10 mL). Compound **8** was isolated as a white solid (0.17 g, 0.26 mmol, 21.6%). Decomp. > 330 °C. ^{1}H NMR (500 MHz, $CDCl_3$) δ/ppm 8.81 (d, *J* = 6.1 Hz, 8H, H^{A2}), 8.12 (s, 4H, H^{B3}), 8.11–8.08 (m, 8H, H^{A3}), 7.16 (s, 2H, H^{C2}), 4.04 (t, *J* = 6.4 Hz, 4H, H^a), 1.86–1.73 (m, 4H, H^b), 0.97 (t, *J* = 7.4 Hz, 6H, H^c). ^{13}C{^{1}H} NMR (126 MHz, $CDCl_3$) δ/ppm 154.5 (C^{B2}), 150.4 (C^{A2}), 148.0 (C^{B4}), 146.0 (C^{A4}), 128.9 (C^{C1}), 121.3 (C^{B3}), 121.0 (C^{A3}), 115.0 (C^{C2}), 71.1 (C^a), 22.4 (C^b), 10.5 (C^c). C^{C3} was not resolved. ESI-MS *m*/*z* 657.45 $[M+H]^+$ (calc. 657.30). High resolution ESI-MS *m*/*z* 657.2983 $[M+H]^+$ (calc. 657.2973).

3.5. Synthesis of **9**

2,5-Bis(octoxy)benzene-1,4-dicarbaldehyde (0.15 g, 0.38 mmol) was dissolved in EtOH (40 mL), then 3-acetylpyridine (0.2 g, 1.61 mmol) and crushed KOH (0.108 g, 1.92 mmol) were added to the solution and the reaction mixture was stirred at room temperature for ~16 h. The colourless solution was concentrated in vacuo and left to stand in the freezer at −18 °C for 3 days. Compound **9** precipitated and was isolated as an off-white powder (0.1 g, 0.12 mmol, 31.2%). M.p. = 150.5 °C. ^{1}H NMR (500 MHz, $CDCl_3$) δ/ppm 9.13 (dd, *J* = 2.3, 0.9 Hz, 4H, H^{A2}), 8.74 (dd, *J* = 4.8, 1.7 Hz, 4H, H^{A6}), 8.19 (ddd, *J* = 8.0, 2.3, 1.7 Hz, 4H, H^{A4}), 7.38 (ddd, *J* = 7.9, 4.8, 0.9 Hz, 4H, H^{A5}), 6.69 (s, 2H, H^{B3}), 4.17 (p, *J* = 6.8 Hz, 2H, H^x), 3.85 (t, *J* = 6.6 Hz, 4H, H^a), 3.5–3.34 (m, 8H, H^y), 1.77–1.69 (m, 4H, H^b), 1.42 (m, 4H, H^c), 1.36–1.19 (m, 16H, $H^{d/e/f/g}$), 0.91–0.75 (m, 6H, H^h). ^{13}C{^{1}H} NMR (126 MHz, $CDCl_3$) δ/ppm 198.2 ($C^{C=0}$), 153.5 (C^{A6}), 150.4 (C^{B2}), 149.8 (C^{A2}), 135.5 (C^{A4}), 132.4 (C^{A3}), 129.7 (C^{B1}), 123.7 (C^{A5}), 113.5 (C^{B3}), 68.7 (C^a), 43.2 (C^y), 33.5 (C^x), 31.9 (C^f), 29.7 (C^b), 29.5 ($C^{d/e}$), 29.4 ($C^{d/e}$), 26.5 (C^c), 22.8 (C^g), 14.3 (C^h). ESI-MS *m*/*z* 839.4 $[M+H]^+$ (calc. 839.5). IR (solid, ν/cm^{-1}) 2953 (w), 2927 (m), 2852 (m), 1681 (s), 1585 (s), 1572 (m), 1511 (m), 1469 (m), 1417 (s), 1379 (m), 1357 (m), 1340 (m), 1285 (m), 1243 (m), 1222 (m), 1200 (s), 1154 (m), 1065 (m), 1040 (w), 1026 (m), 978 (m), 879 (m), 840 (w), 799 (m), 702 (s), 673 (w), 630 (m), 620 (m), 509 (w), 405 (w). Found C 69.41, H 7.11, N 6.43; required for $C_{52}H_{62}N_4O_6 \cdot 3H_2O$ C 69.93, H 7.67, N 6.27.

*3.6. {[Co_2(NCS)$_4$(MeOH)$_4$(**6**)$_2$]·2MeOH·8H_2O}$_n$*

A solution of Co(NCS)$_2$ (1.75 mg, 0.01 mmol) in MeOH (8 mL) was layered over a solution of **6** (9.76 mg, 0.03 mmol) in $CHCl_3$ (5 mL). A few pink crystals of {[Co_2(NCS)$_4$(MeOH)$_4$(**6**)$_2$]·2MeOH·8H_2O}$_n$ were obtained after 2–4 weeks.

*3.7. {[Co(NCS)$_2$(**7**)$_2$]·4$CHCl_3$}$_n$*

A solution of Co(NCS)$_2$ (1.75 mg, 0.010 mmol) in MeOH (8 mL) was layered over a solution of **7** (4.17 mg, 0.010 mmol) in $CHCl_3$ (5 mL). Orange crystals of [Co(NCS)$_2$(**7**)$_2$·4$CHCl_3$]$_n$ (1.7 mg, 0.0011 mmol, 22% based on **7**) were obtained after 2–4 weeks. The bulk sample was characterized by powder diffraction (see Figure S2).

*3.8. {[Co(NCS)$_2$(**8**)$_2$]·2$C_6H_4Cl_2$}$_n$*

A solution of Co(NCS)$_2$ (1.75 mg, 0.010 mmol) in MeOH (8 mL) was layered over a solution of **8** (6.57 mg, 0.010 mmol) in 1,2-dichlorobenzene (5 mL). Pink crystals of {[Co(NCS)$_2$(**8**)$_2$]·2$C_6H_4Cl_2$}$_n$ (3.9 mg, 0.0035 mmol, 70% based on **8**) were obtained after 2–4 weeks. The bulk sample was characterized by powder diffraction (see Figure S3).

*3.9. {[Co(NCS)$_2$(**9**)]·2$CHCl_3$}$_n$*

A solution of Co(NCS)$_2$ (0.875 mg, 0.005 mmol) in MeOH (8 mL) was layered over a solution of **9** (12.6 mg, 0.015 mmol) in $CHCl_3$ (5 mL). Pink crystals of [Co(NCS)$_2$(**9**)·2$CHCl_3$]$_n$ (0.6 mg, 0.00048 mmol, 9.6%) were obtained after 2–4 weeks. The bulk sample was characterized by powder diffraction (see Figure S4).

3.10. Crystallography

Single crystal data were collected on a Bruker APEX-II diffractometer; data reduction, solution and refinement used APEX2, SuperFlip and CRYSTALS, respectively [35–37]. Structure analysis used Mercury v. 3.7 [38,39]. In {[Co(NCS)$_2$(**8**)$_2$]·2$C_6H_4Cl_2$}$_n$, one 1,2-dichlorobenzene molecule was disordered and was refined isotropically, being treated as a rigid body. SQUEEZE [40] was used to treat the remainder of the solvent region in {[Co(NCS)$_2$(**8**)$_2$]·2$C_6H_4Cl_2$}$_n$ and electron density removed equated to one extra molecule of 1,2-dichlorobenzene per formula unit. Powder diffraction data were collected on a Stoe Stadi P powder diffractometer.

{[Co_2(NCS)$_4$(**6**)$_2$(MeOH)$_4$]·2MeOH·8H_2O}$_n$: $C_{50}H_{70}Co_2N_{14}O_{14}S_4$, M = 1337.32, pink block, triclinic, space group P–1, a = 10.7199(6),b = 11.3886(7), c = 14.7671(11) Å, α = 86.374(5), β = 85.892(5), γ = 88.031(4)°, U = 1793.80(13) Å^3, Z = 1, D_c = 1.238 Mg m^{-3}, μ(Cu-Kα) = 5.235 mm^{-1}, T = 123 K. Total 24308 reflections, 6218 unique, R_{int} = 0.051. Refinement of 3947 reflections (364 parameters) with $I > 2\sigma(I)$ converged at final $R1$ = 0.1347 ($R1$ all data = 0.1693), $wR2$ = 0.3635 ($wR2$ all data =0.3934), gof = 1.0474. CCDC 1550589.

{[Co(NCS)$_2$(**7**)$_2$]·4$CHCl_3$}$_n$: $C_{56}H_{42}Cl_{12}CoFe_2N_8S_2$, M = 1487.19, orange block, monoclinic, space group $P2_1/n$, a = 10.5796(7),b = 17.4860(12), c = 16.9126(11) Å, β = 99.047(3)°, U = 3089.8(4) Å^3, Z = 2, D_c = 1.598 Mg m^{-3}, μ(Cu-Kα) = 11.565 mm^{-1}, T = 123 K. Total 21236 reflections, 5706 unique, R_{int} = 0.030. Refinement of 5555 reflections (367 parameters) with $I > 2\sigma(I)$ converged at final $R1$ = 0.0473 ($R1$ all data = 0.0483), $wR2$ = 0.0964 ($wR2$ all data =0.0966), gof = 0.9222. CCDC 1550588.

{[Co(NCS)$_2$(**8**)$_2$]·2$C_6H_4Cl_2$}$_n$: $C_{56}H_{44}Cl_4CoN_8O_2S_2$, M = 1125.89, pink block, monoclinic, space group $P2_1/c$, a = 10.2136(9),b = 19.3452(17), c = 16.2214(15) Å, β = 107.027(3)°, U = 3064.6(5) Å^3, Z = 2, D_c = 1.22 Mg m^{-3}, μ(Cu-Kα) = 4.787 mm^{-1}, T = 123 K. Total 20265 reflections, 5638 unique, R_{int} = 0.029. Refinement of 4472 reflections (298 parameters) with $I > 2\sigma(I)$ converged at final $R1$ = 0.1258 ($R1$ all data = 0.1287), $wR2$ = 0.1436 ($wR2$ all data =0.1437), gof = 0.9942. CCDC 1550587.

{[Co(NCS)$_2$(**9**)]·2$CHCl_3$}$_n$: $C_{56}H_{64}Cl_6CoN_6O_6S_2$, M = 1252.94, pink block, triclinic, space group P–1, a = 9.5196(10),b = 11.1662(13), c = 14.4682(16) Å, α = 80.088(6), β = 78.780(5), γ = 86.642(6)°,

U = 1485.5(3) Å^3, Z = 1, D_c = 1.400 Mg m^{-3}, μ(Cu-Kα) = 5.838 mm^{-1}, T = 123 K. Total 18364 reflections, 5368 unique, R_{int} = 0.049. Refinement of 4997 reflections (349 parameters) with $I > 2\sigma(I)$ converged at final $R1$ = 0.1210 ($R1$ all data = 0.1256), $wR2$ = 0.2862 ($wR2$ all data =0.2891), gof = 0.9924. CCDC 1550586.

4. Conclusions

In conclusion, we have described coordination polymer and network assemblies that result from crystal growth under ambient conditions when $Co(NCS)_2$ is combined with monotopic ligands **6** and **7**, and ditopic ligands **8** and **9**. Although ligand **6** contains both pyrimidine and 4,2′:6′,4″-tpy metal-binding domains, it binds cobalt only through the outer *N*-donors of the 4,2′:6′,4″-tpy unit. In **7**, the ferrocenyl functionality is coordinatively innocent and, like **6**, ligand **7** acts as a V-shaped linker. $\{[Co(NCS)_2(\mathbf{7})_2]\cdot 4CHCl_3\}_n$ contains a (4,4) net defined by 4-connecting cobalt nodes. In contrast, coordinated MeOH (a solvent used in all the experiments reported here) in $\{[Co_2(NCS)_4(MeOH)_4(\mathbf{6})_2]\cdot 2MeOH\cdot 8H_2O\}_n$ blocks two of the octahedral sites and the resulting assembly is a 1D-coordination polymer. This result highlights the role of serendipity in the assembly process. On the other hand, inter-sheet π-stacking interactions between ferrocenyl and pyridyl units in $\{[Co(NCS)_2(\mathbf{7})_2]\cdot 4CHCl_3\}_n$ may assist in directing this assembly.

By moving to the ditopic ligand **8** which may adopt limiting 4-connecting planar or approximately tetrahedral nodal geometries, it is possible to realize a 3D-framework. $\{[Co(NCS)_2(\mathbf{8})_2]\ 2C_6H_4Cl_2\}_n$ consists of a $\{6^5.8\}$ **cds** net which is defined by a combination of metal and ligand planar 4-connecting nodes. This contrasts with the 3D $\{4^2.8^4\}$ **lvt** net present in $[Co(NCS)_2(\mathbf{3})\cdot 4CHCl_3]_n$ where the metal and ligand act as 4-connecting planar and approximately tetrahedral nodes, respectively [16]. On going from **3** to **9**, a more flexible backbone is introduced to the ligand, and reaction of **9** with $Co(NCS)_2$ leads to $\{[Co(NCS)_2(\mathbf{9})]\cdot 2CHCl_3\}_n$ which contains a (4,4) net defined by both metal and ligand planar 4-connecting nodes. The ^{n}octoxy tails of **9** protrude from each side of the (4,4) net and thread through adjacent sheets; the arene-attached ^{n}octoxy chains associate through a combination of van der Waals and C–H...π interactions.

Taking $Co(NCS)_2$ as a common building block with a preference for octahedral coordination, this investigation has once again [24,41] illustrated the difficulties of predicting and understanding coordination assembly algorithms, even when the ligand has well-defined directional properties, in particular in assembly environments containing potentially coordinating solvent molecules.

Supplementary Materials: The following are available online at www.mdpi.com/1996-1944/10/7/728/s1. Supplementary information contains Figure S1: HMQC spectrum of ligand 9. Figures S2–S4: Comparisons of powder diffraction patterns for bulk samples and predicted patterns from single crystal diffraction; Figure S5: Comparison of the conformations of coordinated ligands **3** and **9** in $\{[Co(NCS)_2(\mathbf{3})]\cdot 4CHCl_3\}_n$ and $\{[Co(NCS)_2(\mathbf{9})]\cdot 2CHCl_3\}_n$.

Acknowledgments: We thank the Swiss National Science Foundation (Grant number 200020_162631) and the University of Basel for support. The Swiss National Science Foundation through the NCCR Molecular Systems Engineering is acknowledged for partial funding of the powder diffractometer.

Author Contributions: Y. Maximilian Klein (synthesis, powder diffraction, contribution to writing of manuscript); Alessandro Prescimone (crystallographer); Edwin C. Constable (project concepts); Catherine E. Housecroft (project concepts, writing of manuscript).

Conflicts of Interest: The authors declare no conflict of interest.

References

1. Housecroft, C.E. 4,2′:6′,4′′-Terpyridines: Diverging and diverse building blocks in coordination polymers and metallomacrocycles. *Dalton Trans.* **2014**, *43*, 6594–6604. [CrossRef] [PubMed]
2. Housecroft, C.E. Divergent 4,2′:6′,4′′- and 3,2′:6′,3′′-terpyridines as linkers in 2- and 3-dimensional architectures. *CrystEngComm* **2015**, *17*, 7461–7468. [CrossRef]
3. Granifo, J.; Gaviño, R.; Freire, E.; Baggio, R. Monodentate and bridging behaviour of the sulfur-containing ligand 4′-[4-(methyl-sulfan-yl)phen-yl]-4,2′:6′,4′′-terpyridine in two discrete zinc(II) complexes with acetyl-acetonate. *Acta Crystallogr. Sect. C* **2012**, *68*, m269–m274. [CrossRef] [PubMed]

4. Shen, S.-S.; Bai, C.; Hu, H.-M.; Yuan, F.; Wang, X.; Xue, G. Syntheses, structures, and luminescent properties of two cadmium(II) coordination compounds based on a sulfonate functionalized terpyridine ligand. *Z. Anorg. Allg. Chem.* **2015**, *641*, 1772–1776. [CrossRef]
5. Granifo, J.; Gaviño, R.; Freire, E.; Baggio, R. A novel hybrid terpyridine–pyrimidine ligand and the supramolecular structures of two of its complexes with Zn(II) and acetylacetonato: The underlying role of non-covalent π...π contacts and C–H...X(O, N, π) hydrogen bonds. *J. Mol. Struct.* **2014**, *1063*, 102–108. [CrossRef]
6. Yin, Z.; Zhang, S.; Zheng, S.; Golen, J.A.; Rheingold, A.L.; Zhang, G. Cobalt(II) coordination polymers versus discrete complex with 4,2′:6′,4′′-terpyridine ligands: The role of a pyrenyl substituent. *Polyhedron* **2015**, *101*, 139–145. [CrossRef]
7. Klein, Y.M.; Constable, E.C.; Housecroft, C.E.; Zampese, J.A.; Crochet, A. Greasy tails switch 1D-coordination $[Zn_2(OAc)_4(4'\text{-}(4\text{-}ROC_6H_4)\text{-}4,2':6',4''\text{-tpy})]_n$ polymers to discrete $[Zn_2(OAc)_4(4'\text{-}(4\text{-}ROC_6H_4)\text{-}4,2':6',4''\text{-tpy})_2]$ complexes. *CrystEngComm* **2014**, *16*, 9915–9929. [CrossRef]
8. Kröhnke, F. The specific synthesis of pyridines and oligopyridines. *Synthesis* **1976**, *1975*, 1–24. [CrossRef]
9. Wang, J.; Hanan, G.S. A facile route to sterically hindered and non-hindered 4′-Aryl-2,2′:6′,2″-terpyridines. *Synlett* **2005**, *2005*, 1251–1254. [CrossRef]
10. Cave, G.W.V.; Raston, C.L. Efficient synthesis of pyridines via a sequential solventless aldol condensation and Michael addition. *J. Chem. Soc. Perkin Trans. 1* **2001**, 3258–3264. [CrossRef]
11. Yoshida, J.; Nishikiori, S.-I.; Yuge, H. Bis(3-cyano-pentane-2,4-dionato) Co(II) as a linear building block for coordination polymers: Combinations with two polypyridines. *J. Coord. Chem.* **2013**, *66*, 2191–2200. [CrossRef]
12. Ghozlan, S.A.S.; Hassanien, A.Z.A. β-Amino-β-(pyrid-4-yl)acrylonitrile (I) in heterocyclic synthesis: Synthesis of some new pyridine, pyridone, pyrazole, thiophene, fused pyrimidine and triazine derivatives. *Tetrahedron* **2002**, *58*, 9423–9429. [CrossRef]
13. Constable, E.C.; Housecroft, C.E.; Vujovic, S.; Zampese, J.A. 2D→2D Parallel interpenetration of (4,4) sheets constructed from a ditopic bis(4,2′:6′,4′′-terpyridine). *CrystEngComm* **2014**, *16*, 3494–3497. [CrossRef]
14. Vujovic, S.; Constable, E.C.; Housecroft, C.E.; Morris, C.D.; Neuburger, M.; Prescimone, A. Engineering 2D→2D parallel interpenetration using long alkoxy-chain substituents. *Polyhedron* **2015**, *92*, 77–83. [CrossRef]
15. Klein, Y.M.; Prescimone, A.; Neuburger, M.; Constable, E.C.; Housecroft, C.E. What a difference a tail makes: 2D→2D parallel interpenetration of sheets to interpenetrated nbo networks using ditopic-4,2′:6′,4′′-terpyridine ligands. *CrystEngComm* **2017**, *19*, 2894–2902. [CrossRef]
16. Klein, Y.M.; Constable, E.C.; Housecroft, C.E.; Prescimone, A. A 3-dimensional $\{4^2.8^4\}$ lvt net built from a ditopic bis(3,2′:6′,3″-terpyridine) tecton bearing long alkyl tails. *CrystEngComm* **2015**, *17*, 2070–2073. [CrossRef]
17. Klein, Y.M.; Prescimone, A.; Constable, E.C.; Housecroft, C.E. A double-stranded 1D-coordination polymer assembled using the tetravergent ligand 1,1′-bis(4,2′:6′,4′′-terpyridin-4′-yl)ferrocene. *Inorg. Chem. Commun.* **2016**, *70*, 118–120. [CrossRef]
18. Klein, Y.M.; Prescimone, A.; Pitak, M.B.; Coles, S.J.; Constable, E.C.; Housecroft, C.E. Constructing chiral MOFs by functionalizing 4,2′:6′,4′′-terpyridine with long-chain alkoxy domains: Rare examples of neb nets. *CrystEngComm* **2016**, *18*, 4704–4707. [CrossRef]
19. Klein, Y.M.; Prescimone, A.; Constable, E.C.; Housecroft, C.E. 2-Dimensional networks assembled using 4′-functionalized 4,2′:6′,4′′-terpyridines and $Co(NCS)_2$. *Polyhedron* **2016**, *103*, 58–65. [CrossRef]
20. Mondal, A.K.; Khatua, S.; Tomar, K.; Konar, S. Field-induced single-ion-magnetic behavior of octahedral Co^{II} in a two-dimensional coordination polymer. *Eur. J. Inorg. Chem.* **2016**, *2016*, 3545–3552. [CrossRef]
21. Constable, E.C.; Housecroft, C.E.; Neuburger, M.; Vujovic, S.; Zampese, J.A.; Zhang, G. Cobalt(II) coordination polymers with 4′-substituted 4,2′:6′,4′′- and 3,2′:6′,3″-terpyridines: Engineering a switch from planar to undulating chains and sheets. *CrystEngComm* **2012**, *14*, 3554–3563. [CrossRef]
22. Constable, E.C.; Housecroft, C.E.; Kopecky, P.; Neuburger, M.; Zampese, J.A.; Zhang, G. Coordination polymers with divergent 4′-tert-butyl-4,2′:6′,4′′-terpyridine linkers: From aryl-aryl to ball-and-socket packing. *CrystEngComm* **2012**, *14*, 446–452. [CrossRef]
23. Klein, Y.M.; Constable, E.C.; Housecroft, C.E.; Zampese, J.A. 4′-(Pyrimidin-5-yl)- and 4′-(2-methylpyrimidin-5-yl)-4,2′:6′,4′′-terpyridines: Selective coordination to zinc(II) through the 4,2′:6′,4′′-terpyridine domain. *Polyhedron* **2014**, *81*, 98–104. [CrossRef]

24. Klein, Y.M.; Prescimone, A.; Constable, E.C.; Housecroft, C.E. Coordination behaviour of 1-(4,2′:6′,4′′-terpyridin-4′-yl)ferrocene and 1-(3,2′:6′,3′′-terpyridin-4′-yl)ferrocene: Predictable and unpredictable assembly algorithms. *Aust. J. Chem.* **2017**, *70*, 468–477. [CrossRef]
25. Xiao, L.; Zhu, L.; Zeng, Q.; Liu, Q.; Zhang, J.; Li, S.; Zhou, H.; Zhang, S.; Wu, J.; Tian, Y. Novel metal-organic hybrid materials constructed by ferrocenyl terpyridine derivatives and $Zn^{II}X_2$ (X = Cl^-, Br^-, I^-, SCN^- and CH_3COO^-). *J. Organomet. Chem.* **2015**, *789–790*, 22–28. [CrossRef]
26. Kuhnert, N.; Lopez-Periago, A.; Rossignolo, G.M. The synthesis and conformation of oxygenated trianglimine macrocycles. *Org. Biomol. Chem.* **2005**, *3*, 524–537. [CrossRef] [PubMed]
27. Domagała, M.; Grabowski, S.J. C–H...N and C–H...S hydrogen bonds Influence of hybridization on their strength. *J. Phys. Chem. A* **2005**, *109*, 5683–5688. [CrossRef] [PubMed]
28. Bondi, A. van der Waals volumes and radii. *J. Phys. Chem.* **1964**, *68*, 441–451. [CrossRef]
29. Klein, R.A. Modified van der Waals atomic radii for hydrogen bonding based on electron density topology. *Chem. Phys. Lett.* **2006**, *425*, 128–133. [CrossRef]
30. Rowland, R.S.; Taylor, R. Intermolecular nonbonded contact distances in organic crystal structures: Comparison with distances expected from van der Waals Radii. *J. Phys. Chem.* **1996**, *100*, 7384–7391. [CrossRef]
31. Blatov, V.A.; Shevchenko, A.P. *TOPOS Professional v. 4.0*; Samara State University: Samara, Russia, 2010.
32. Li, D.-S.; Wu, Y.-P.; Zhao, J.; Zhang, J.; Lu, J.Y. Metal-organic frameworks based upon non-zeotype 4-connected topology. *Coord. Chem. Rev.* **2014**, *261*, 1–27. [CrossRef]
33. Batten, S.R.; Neville, S.M.; Turner, D.R. *Coordination Polymers: Design, Analysis and Application*; RSC Publishing: Cambridge, UK, 2009; ISBN 978-0-85404-837-3.
34. Nishio, M. CH/π hydrogen bonds in crystals. *CrystEngComm* **2004**, *6*, 130–158. [CrossRef]
35. Bruker Analytical X-ray Systems, Inc. *APEX2, Version 2 User Manual, M86-E01078*; Bruker Analytical X-ray Systems, Inc.: Madison, WI, USA, 2006.
36. Palatinus, L.; Chapuis, G. SUPERFLIP—A computer program for the solution of crystal structures by charge flipping in arbitrary dimensions. *J. Appl. Cryst.* **2007**, *40*, 786–790. [CrossRef]
37. Betteridge, P.W.; Carruthers, J.R.; Cooper, R.I.; Prout, K.; Watkin, D.J. CRYSTALS version 12: Software for guided crystal structure analysis. *J. Appl. Cryst.* **2003**, *36*, 1487. [CrossRef]
38. Bruno, I.J.; Cole, J.C.; Edgington, P.R.; Kessler, M.K.; Macrae, C.F.; McCabe, P.; Pearson, J.; Taylor, R. New software for searching the Cambridge Structural Database and visualizing crystal structures. *Acta Cryst. B* **2002**, *58*, 389–397. [CrossRef]
39. Macrae, C.F.; Bruno, I.J.; Chisholm, J.A.; Edgington, P.R.; McCabe, P.; Pidcock, E.; Rodriguez-Monge, L.; Taylor, R.; van de Streek, J.; Wood, P.A. Mercury CSD 2.0—New features for the visualization and investigation of crystal structures. *J. Appl. Cryst.* **2008**, *41*, 466–470. [CrossRef]
40. Spek, A.L. PLATON SQUEEZE: A tool for the calculation of the disordered solvent contribution to the calculated structure factors. *Acta Cryst. C* **2015**, *71*, 9–18. [CrossRef] [PubMed]
41. Constable, E.C.; Zhang, G.; Housecroft, C.E.; Zampese, J.A. Zinc(II) coordination polymers, metallohexacycles and metallocapsules—Do we understand self-assembly in metallosupramolecular chemistry: Algorithms or serendipity? *CrystEngComm* **2011**, *13*, 6864–6870. [CrossRef]

18.5 Paper 5 (Reprinted with permission from ref[99] Copyright 2018 American Chemical Society)

JACS JOURNAL OF THE AMERICAN CHEMICAL SOCIETY
Article
Cite This: J. Am. Chem. Soc. 2018, 140, 2933−2939
pubs.acs.org/JACS

The Different Faces of 4′-Pyrimidinyl-Functionalized 4,2′:6′,4′′-Terpyridines: Metal−Organic Assemblies from Solution and on Au(111) and Cu(111) Surface Platforms

Thomas Nijs,[†] Y. Maximilian Klein,[‡] S. Fatemeh Mousavi,[†] Aisha Ahsan,[†] Sylwia Nowakowska,[†] Edwin C. Constable,[‡] Catherine E. Housecroft,*[,‡] and Thomas A. Jung*[,†,§]

[†]Department of Physics, University of Basel, Klingelbergstrasse 82, 4056 Basel, Switzerland
[‡]Department of Chemistry, University of Basel, BPR 1096, Mattenstrasse 24a 4058 Basel, Switzerland
[§]Laboratory for Micro- and Nanotechnology, Paul Scherrer Institut, 5232 Villigen, Switzerland

Supporting Information

ABSTRACT: A comparative investigation of crystal growth from solution and on-surface assembly *in vacuo* between copper and three 4′-(2-R-pyrimidin-5-yl)-4,2′:6′,4′′-terpyridines, with R = H (**1**), Me (**2**), or Et (**3**), is presented. In solution, ligand **3** combines with copper(II) acetate or copper(I) triflate in MeOH solution to give $[Cu_2(OAc)_4(\mathbf{3})]_n$ or $\{[Cu(\mathbf{3})(OMe)(MeOH)][CF_3SO_3]\cdot MeOH\}_n$. In $[Cu_2(OAc)_4(\mathbf{3})]_n$, paddle-wheel $\{Cu_2(\mu\text{-}OAc)_4\}$ nodes direct the assembly of one-dimensional (1D) zigzag chains which pack into two-dimensional (2D) sheets. In $\{[Cu(\mathbf{3})(OMe)(MeOH)][CF_3SO_3]\cdot MeOH\}_n$, the solvent is a ligand and also generates $\{Cu_2(\mu\text{-}OMe)_2\}$ units which function as planar 4-connecting nodes to generate a 2D (4,4) net with ligand **3**. On Au(111) or Cu(111) surfaces *in vacuo*, no additional solvent or anions are involved in the assembly. The different substituents in **1**, **2**, or **3** allow precise molecular resolution imaging in scanning tunneling microscopy. On Au(111), **1** and **2** assemble into close-packed assemblies, while **3** forms a regular porous network. The deposition of Cu adatoms results in reorganization leading to ladder-shaped surface metal−organic motifs. These on-surface coordination assemblies are independent of the 4′-substituent in the 4,2′:6′,4′′-tpy and are reproduced on Cu(111) where Cu adatoms are available during the deposition and relaxation process at room temperature. Upon annealing at elevated temperatures, the original surface assemblies of **1** and **3** are modified and a transition from ladders into rhomboid structures is observed; for **2**, a further quasi-hexagonal nanoporous network is observed.

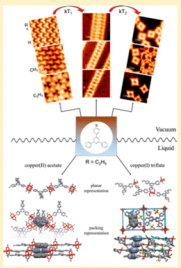

INTRODUCTION

One of the most common strategies for supramolecular assembly is predicated upon the interactions of metal centers with ligands.[1] Metallosupramolecular chemistry[2] is concerned with the matching of commensurate metal centers and metal-binding domains. In contrast to single carbon centers which typically exhibit one of three coordination geometries (two-coordinate linear, three-coordinate planar, and four-coordinate tetrahedral), metal centers can exhibit coordination numbers from one to at least 12 with all possible geometries.[3] Furthermore, the metal−ligand bond may be labile or kinetically inert, allowing access to a dynamic system.[1] These interactions may be used for the assembly of discrete supramolecular systems or extended one-, two-, or three-dimensional (1D, 2D, or 3D) assemblies collectively known as coordination polymers.[4] Metal−organic frameworks (MOFs) are well-established 3D examples with wide-ranging applications in catalysis, electrochemistry, host−guest chemistry, and fuel cells.[5] Two-dimensional networks can be assembled on an atomically flat substrate, allowing templated host−guest interactions in any pockets in the 2D lattice. Nevertheless, 3D and 2D assemblies differ in the elastic response of the host network and in 2D networks interaction with the substrate can mediate cooperative effects[6−8] We are interested in the multi-dimensional structural diversity which can be achieved through variation in molecular structure and processing in bulk materials and in monolayers. We also wish to probe the structural consequences of the constraints of assembly processes on-surfaces as opposed to those in solution.

Of the 48 isomers of terpyridine, the best known is 2,2′:6′,2′′-terpyridine (2,2′:6′,2′′-tpy, Chart 1) which is a chelating ligand typically presenting a convergent *N,N′,N′′*-donor set to a metal center,[9] whereas the less well-investigated 4,2′:6′,4′′-tpy and 3,2′:6′,3′′-tpy (Chart 1) only coordinate to metal centers through the terminal nitrogen donors and present divergent *N,N′*-donor sets ideal for the assembly of extended structures with metal nodes.[10,11] Functionality can readily be introduced at the 4′-position[12,13] allowing the construction of ligands with both innocent and non-innocent substituents. Although 4,2′:6′,4′′-tpy ligands are well-established in 1D and 2D systems,[9,11] few examples of 3D networks in the absence of peripheral coordination units or co-ligands have been described.[14,15]

In networks of 4,2′:6′,4′′-tpy ligands with copper nodes, anions or co-ligands play a critical role in directing the

Received: December 5, 2017
Published: February 9, 2018

DOI: 10.1021/jacs.7b12624
J. Am. Chem. Soc. 2018, 140, 2933−2939

Chart 1. Coordination Modes of Isomeric Terpyridines 2,2′:6′,2″-tpy, 3,2′:6′,3″-tpy, and 4,2′:6′,4″-tpy[a]

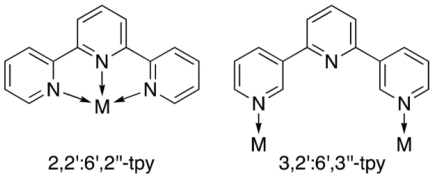

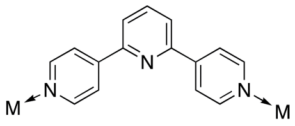

[a]The structural diversity possible with 3,2′:6′,3″-tpy is greater because of rotation about the interannular C−C bonds.

assembly. Reactions of CuCN with 4′-aryl-4,2′:6′,4″-tpy ligands lead to interpenetrated 3D frameworks with bridging 4,2′:6′,4″-tpy and cyanido ligands. Increasing the steric demands of the 4′-functionality suppresses the interpenetration.[16] Bridging cyanido linkers also feature in interpenetrated 3D frameworks found in $[Cu_9(4'\text{-}(NCC_6H_4)\text{-}4,2':6',4''\text{-}tpy)_{4.5}(CN)_9]_n$ (see Chart 2 for the structure of 4′-(NCC_6H_4)-4,2′:6′,4″-tpy).[17] In both of these networks, the copper(I) centers are 3-coordinate. A carboxylic acid group in the 4′-position of the tpy unit is typically non-innocent,[17−20] although Xiao and co-workers suggest that the presence of uncoordinated $-CO_2H$ moieties play a role in the assembly of an unusual 2D → 2D polythreaded network.[21] The ligand 4′-(4-pyridyl)-4,2′:6′,4″-tpy (Chart 2) is well-explored, and coordination to copper(I) through both the 4,2′:6′,4″-tpy and pendant pyridyl units leads to a 3D network with 4-fold interpenetration; in this case nitrate counterions and MeOH solvent molecules are accommodated along channels in the structure.[22] Reactions of copper(II) acetate with 4′-aryl-4,2′:6′,4″-tpy's (aryl = biphenylyl,[23] 2′,3′,4′,5′,6′-pentafluorobiphenyl,[23] phenyl,[24] 4-dimethylaminophenyl[24]) lead to 1D coordination polymers incorporating paddle-wheel $\{Cu_2(\mu\text{-}OAc)_4\}$ nodes connected by bridging 4,2′:6′,4″-tpy domains.

Chart 2. Structures of Selected 4′-Functionalized 4,2′:6′,4″-tpy Ligands

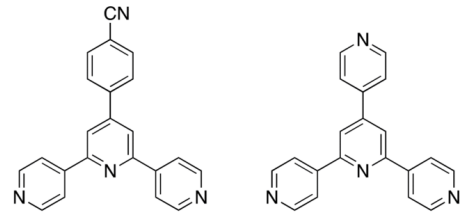

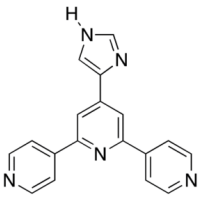

We are interested in 4,2′:6′,4″-tpy building blocks functionalized in the 4′-position with *N*-heterocycles other than pyridine, and focus upon copper as the metal node for the assembly of multi-dimensional networks. The originality of our approach is to combine studies of crystal growth under ambient solution conditions with on-surface deposition on Au(111) and Cu(111) substrates under ultrahigh vacuum (UHV) to investigate the interactions of these ligands with metal centers. This strategy allows us to probe the assembly process with a constant pairing of metal and ligand with and without constraints imposed by a surface architecture. In solution, the oxidation state of the metal-node (Cu^+ or Cu^{2+}) is defined *and* counterions are required for charge neutrality; furthermore, crystallization typically results in incorporation of lattice solvent molecules. In contrast, on-surface assemblies initiated by copper adatoms yield structures free from counterions and solvent molecules. Both 4′-(1*H*-imidazol-4-yl)-4,2′:6′,4″-tpy (Chart 2) and 4′-(pyrimidin-5-yl)-4,2′:6′,4″-tpy (**1**, Chart 3) are attractive building blocks containing both a divergent V-shaped tecton and a functionality with potential for further coordination although their coordination chemistry has been little explored. Each might direct the assembly of 1D chains or 2D networks depending upon the coordinative innocence or non-innocence of the pendant heterocyclic substituent. 4′-(1*H*-Imidazol-4-yl)-4,2′:6′,4″-tpy forms hydrogen-bonded domains on an Au(111) surface, and the addition of copper adatoms results in reorganization into a 2D coordination network; the *N*-donors of both the 4,2′:6′,4″-tpy and imidazolyl units are bonded to copper.[25] In the only example of a coordination assembly involving 4′-(1*H*-imidazol-4-yl)-4,2′:6′,4″-tpy under solution conditions, the imidazolyl unit is uncoordinated.[26] We have also shown that **1** and its 2-methyl-substituted derivative **2** bind zinc(II) selectively through the 4,2′:6′,4″-tpy domain.[27] In contrast, the pendant pyrimidinyl domains in $[Ru(\mathbf{4})_2]^{2+}$ (Chart 3) bind copper(II) to generate a 2D network.[28] In the present work, we report the coordination behavior of pyrimidinyl-functionalized ligands **1**−**3** (Chart 3) with copper with an emphasis on contrasting the coordination behavior in solution with on-surface interactions of these ligands with copper adatoms. The surface-immobilized networks can be tuned by varying the length of any 2-substituent attached to the pyrimidine ring or through external stimulus in the form of annealing.

■ EXPERIMENTAL SECTION

Experimental details and crystallographic data are given in the Supporting Information.

■ RESULTS AND DISCUSSION

Synthesis and Characterization of Compound 3. We have previously reported ligands **1** and **2**,[27] and compound **3**

DOI: 10.1021/jacs.7b12624
J. Am. Chem. Soc. 2018, 140, 2933−2939

Chart 3. Structures of Ligands 1−3 and of the Pyrimidyl-Functionalized Complex $[Ru(4)]^{2+}$

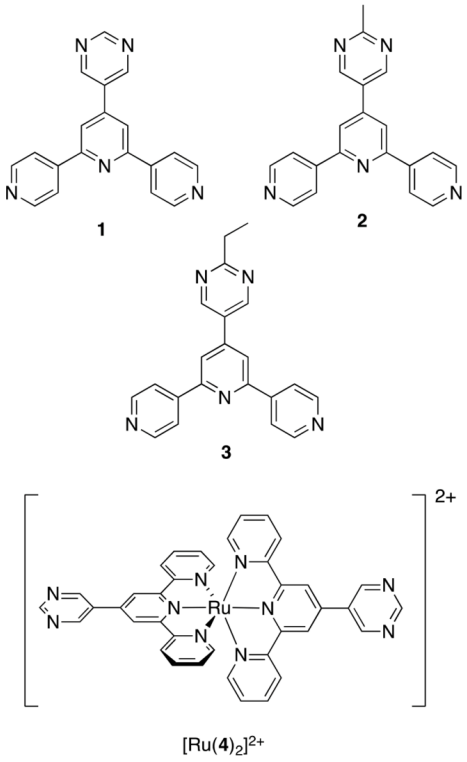

was synthesized in an analogous manner using the one-pot methodology of Hanan.[13] The electrospray mass spectrum of **3** showed a base peak at m/z 340.23 corresponding to $[M+H]^+$. The ^1H and ^{13}C NMR spectra of **3** (Figures S1 and S2) were assigned by COSY, NOESY, HMQC, and HMBC methods and were in accord with the structure shown in Chart 3.

Assembly in Solution of a 1D Coordination Polymer and a 2D Net. Reactions of ligands **1**, **2**, or **3** with copper(II) acetate or copper(I) triflate were investigated by room-temperature crystal growth experiments by layering a MeOH solution of each copper salt over a $CHCl_3$ solution of the ligand. X-ray-quality crystals $[Cu_2(OAc)_4(\mathbf{3})]_n$ and $\{[Cu(\mathbf{3})(OMe)(MeOH)][CF_3SO_3]\cdot MeOH\}_n$ were obtained after 1−2 weeks. Their structures illustrate the roles that the counterion (actetate or triflate) and solvent play in directing the coordination assembly.

$[Cu_2(OAc)_4(\mathbf{3})]_n$ comprises paddle-wheel $\{Cu_2(\mu\text{-}OAc)_4\}$ units linked by molecules of **3** which coordinate through the outer N atoms of the 4,2′:6′,4″-tpy unit (Figure S3). The coordination polymer crystallizes in the monoclinic $C2/c$ space group, and the asymmetric unit contains one $Cu(OAc)_2$ unit and half of one ligand **3**. The second half of the paddle-wheel motif is generated by inversion, and the second half of the 4,2′:6′,4″-tpy unit by 2-fold rotation. The 2-ethylpyrimidinyl unit is disordered with one complete half-occupancy ring and ethyl group in the asymmetric unit (as depicted in Figure S3) and the second half-occupancy ring generated by rotation about a 2-fold axis. Selected bond parameters describing coordination at atom Cu1 are shown in the caption to Figure S3. The structure propagates in a zigzag chain (Figure 1a) and is related

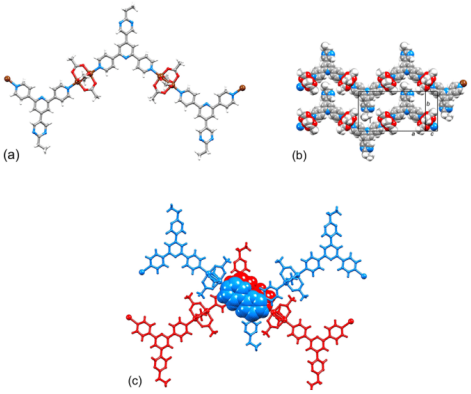

Figure 1. (a) Part of one zigzag chain in $[Cu_2(OAc)_4(\mathbf{3})]_n$. (b) Packing of adjacent chains to form a 2D sheet. (c) π-Stacking interactions between 4,2′:6′,4″-tpy domains in chains in adjacent sheets.

to a series of coordination polymers containing 4′-substituted 4,2′:6′,4″-tpy's and supported by $\{Cu_2(\mu\text{-}OAc)_4\}$ or $\{Zn_2(\mu\text{-}OAc)_4\}$ paddle-wheel nodes.[23,29−34] The zigzag chains pack into 2D sheets with the 2-ethylpyrimidinyl unit nestling into the V-shaped cavity offered by the 4,2′:6′,4″-tpy unit of an adjacent chain (Figure 1b). Finally, 2D sheets are associated through π-stacking interactions between 4,2′:6′,4″-tpy units in different chains (Figure 1c). Pairs of pyridine rings containing $N1^{i}/N2$ in one 4,2′:6′,4″-tpy and $N1^{iii}/N2^{iv}$ in an adjacent 4,2′:6′,4″-tpy (symmetry codes: i = $1-x, y, {}^3/_2-z$; iii = $x, 1-y, {}^1/_2+z$; iv = $1-x, 1-y, 2-z$) are related by inversion and adopt an offset orientation (Figure 1c) typical of an efficient face-to-face π-stack.[35] The distance between the planes of pairs of stacked pyridine rings is 3.32 Å, and the inter-centroid separation is 3.64 Å. The assembly of chains in $[Cu_2(OAc)_4(\mathbf{3})]_n$ is predicated upon paddle-wheel $\{Cu_2(\mu\text{-}OAc)_4\}$ units acting as 2-connecting nodes,[9,36,37] and in $[Cu_2(OAc)_4(\mathbf{3})]_n$ the acetate anions play a crucial role as bridging ligands in the $\{Cu_2(\mu\text{-}OAc)_4\}$ nodes contributing fundamentally to the assembly process.

Layering a MeOH solution of copper(I) triflate over a $CHCl_3$ solution of **3** resulted in X-ray quality blue needles. The color suggested aerial oxidation to copper(II) as confirmed by the single crystal structure of $\{[Cu(\mathbf{3})(OMe)(MeOH)][CF_3SO_3]\cdot MeOH\}_n$. The compound crystallizes in the monoclinic space group $P2_1/n$, and Figure S4 depicts the repeat unit in the extended structure. Ligand **3** coordinates to Cu1 and the symmetry-generated $Cu1^{i}$ (see Figure S4 caption) through the outer two nitrogens N1 and N3. Atoms N2, N4, and N5 in the central pyridine and pyrimidine rings, respectively, are non-coordinated. Atom Cu1 is in a square-based pyramidal environment (τ = 0.20)[38] bound in two,

DOI: 10.1021/jacs.7b12624
J. Am. Chem. Soc. 2018, 140, 2933−2939

mutually *cis*, basal sites to N3 and N3^{iii} of two different ligands **3**. The remaining basal sites are occupied by methoxy ligands which support a $\{Cu_2(\mu\text{-}OMe)_2\}$ unit. A MeOH molecule bound through O2 (Figure S4) occupies the axial site of Cu1. The $\{Cu_2(\mu\text{-}OMe)_2\}$ units act as planar, 4-connecting nodes linked by the 4,2′:6′,4′′-tpy domains of **3** to generate a 2D (4,4) net. A TOPOS[39] representation is shown in Figure 2a

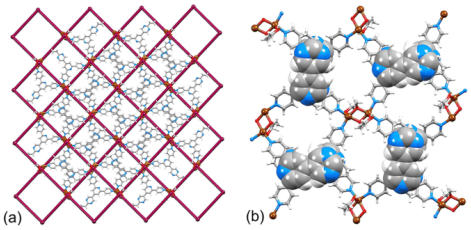

Figure 2. 2D network in $\{[Cu(\mathbf{3})(OMe)(MeOH)][CF_3SO_3]\cdot MeOH\}_n$: (a) TOPOS[39] representation with overlaid structure of part of one (4,4) net, and (b) part of one 2D sheet showing the π-stacking interactions between pyrimidin-5-ylpyridine units in adjacent ligands **3**.

with the molecular network overlaid. Within the 4,2′:6′,4′′-tpy unit, adjacent pyridine rings are twisted 14.9 and 30.7° with respect to one another. The plane of the pyrimidine ring is twisted only 7.0° with respect to the pyridine ring containing N2 (Figure S4). This near planarity is associated with face-to-face π-stacking of pyrimidin-5-ylpyridine units in adjacent ligands (Figure 2b). The stacked units are related by inversion and adopt an optimal offset arrangement.[35] The separation of the least-squares planes through the pyrimidin-5-ylpyridine units containing N2/N4/N5 and N2^{iv}/N4^{iv}/N5^{iv} is 3.48 Å, and the pyridine···pyrimidine centroid-to-centroid distance is 3.60 Å. The interactions lock the ligands into a compact 2D sheet, the cavities in which (Figure 2b) are occupied by triflate anions which exhibit short F···H and O···H contacts within the sheet. There are no π-stacking contacts between 2D sheets. In the assembly of $\{[Cu(\mathbf{3})(OMe)(MeOH)][CF_3SO_3]\cdot MeOH\}_n$, the choice of methanol as solvent plays a critical role, facilitating the formation of $\{Cu_2(\mu\text{-}OMe)_2\}$ units which are the 4-connecting nodes that direct the assembly of the 2D sheet.

■ ON-SURFACE ASSEMBLIES

The solution-based assemblies described above highlight not only the critical roles of solvent and counterions but also emphasizes the expected[27] coordination of **3** through only the outer N atoms of the 4,2′:6′,4′′-tpy domain. Solution-based coordination assemblies using 4′-(1*H*-imidazol-4-yl)-4,2′:6′,4′′-tpy (Chart 2) as the organic linker involve only the outer *N*-donors of the 4,2′:6′,4′′-tpy unit[26] but in contrast, the *N*-donors of the 4,2′:6′,4′′-tpy and imidazolyl units are involved in binding copper adatoms when the latter are added to an assembly of the ligand on an Au(111) surface.[25] We now demonstrate that this switch in coordination behavior is also observed for ligands **1**−**3**. Compounds **1**−**3**, differing only by the presence of an H, Me, or Et 2-substituent on the pyrimidin-5-yl functionality (Chart 3 and Figure 3) were deposited under UHV conditions by thermal sublimation. X-ray photoelectron spectroscopy (XPS) data were used to confirm that the compounds were deposited without chemical change by

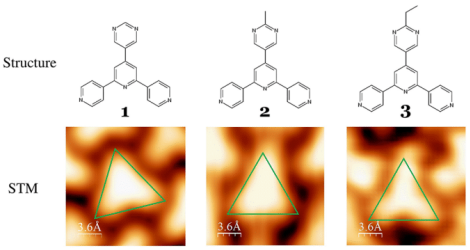

Figure 3. Structures and corresponding STM micrographs of compounds **1**, **2**, and **3** on a Au(111) substrate taken at 5 K with clearly distinguishable alkyl vertices allowing assignment of orientation. An equilateral triangle has been superimposed onto each image to guide the eye toward the different STM contrasts for the molecules. An enlarged version of the figure is given in Figure S7.

analyzing the relative ratios of the (deconvoluted) peaks (see Figure S6). Molecule **1** defines an equilateral triangle, whereas in **2** and **3**, the alkyl substituents act as an "imaging group" in the scanning tunneling microscopy (STM) images shown in Figures 3 and S7. Thus, as the substituent increases in size, it is possible to visualize molecular orientation.

When deposited on the inert surface of Au(111), **1** and **2** arrange in extended close-packed phases (Figures 4 and S8, top) attributed to the symmetry of the molecules, allowing for high packing densities in 2D arrangements. Differently oriented domains are separated by two types of boundaries, depending on the relative orientations of two domains (zipper-like or avoiding). In addition to weak non-classical C−H···N hydrogen-bond interactions,[40] attractive dipole forces are balanced by repulsive H···H interactions. The larger, and less symmetrical, ethyl substituent in **3** increases the "footprint" of the molecule and causes a looser 2D assembly while maintaining the principal assembly motifs. The ethyl groups are located in the so-formed cavity (Figure 4, top right) giving rise to highly

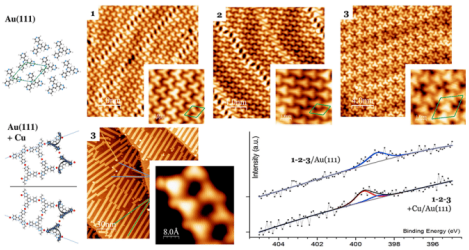

Figure 4. Molecules on Au(111) substrate. Top row: before Cu-coordination, **1** and **2** assemble into a close-packed layer, whereas **3** forms a regular porous vacancy pattern; each 5 × 5 nm inset shows the unit cell in green to emphasize the influence of the substituent on the 2D assembly. Bottom left: after Cu-coordination, 1D ladder-like structures assemble. The expansion shows that the ethyl groups point to the outside of the ladder. Chains are oriented in six directions, five of which are shown and indicated as blue, green, and yellow lines. Bottom right, XPS data showing the chemical change in the N environment, indicating metal coordination of the outer N (red line), while the inner pyridine-ring N of the tpy unit remains unchanged (blue line). An enlarged version of the figure is given in Figure S8.

DOI: 10.1021/jacs.7b12624
J. Am. Chem. Soc. 2018, 140, 2933−2939

structured alternating lines in three principal directions. This space-optimizing is reflected in the unit-cells of the assemblies, marked in green in the insets in Figure 4. The unit cell of **1** is 1 × 1 nm = 1 nm^2, of **2** is 1 × 1.25 nm = 1.25 nm^2, and of **3** is 2.05 × 2.05 nm = 4.20 nm^2 consistent with going from a pyrimidinyl to 2-methylpyrimidinyl to 2-ethylpyrimidinyl substituent. The unit cells of the adlayer exhibit a 60°/120°symmetry (see model Figure 4, as well as the insets) which is broken by the superposition with the Au(111)22×$\sqrt{3}$ reconstruction (*vide infra*).

The *in situ* addition of Cu-adatoms from a thermal evaporation source to the molecular assemblies of **1**, **2**, or **3** on Au(111) at room temperature results, in each case, in the formation of long, straight ladder-like chains. For **3** this is shown in Figure 4, and a comparison of the assemblies for all three ligands is shown in Figure S9, top. To investigate the origin of the re-organization of the on-surface assembly, XPS data were acquired before and after the addition of copper atoms. The peak at 398.9 eV marked in blue in Figures 4 and S8 arises from the uncoordinated N atoms. As we have previously shown,[25] the N atom of the central ring of the 4,2′:6′,4′′-tpy unit does not coordinate, confirmed by the retention of the peak at 398.9 eV after Cu adatoms have been supplied. The XPS spectra are consistent with coordination to copper of both the outer *N*-donors of the 4,2′:6′,4′′-tpy unit and the two pyrimidinyl N atoms, with the ratio of the new peak at 399.6 eV (shown in red in Figure 4 or Figure S10) to the peak at 398.9 eV being 4:1.

The assembly of the ladder-like arrays arises from the rearrangement of the molecules to optimize coordination to the Cu adatoms, and leads to 1D coordination double-chains (see model Figure 5 for more detail). The assemblies appear to be

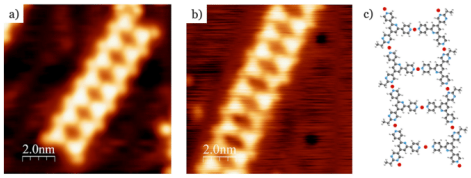

Figure 5. Comparison of ladders of **3** on (a) Au(111)+Cu adatoms and (b) Cu(111). The assemblies are also similar for **1** and **2** (see Figure S7 for full matrix). (c) Model of part of one chain showing the ethyl substituent pointing to the outside of the ladder. An enlarged version of the figure is given in Figure S12.

robust since the ladders remain straight and periodic across the complex domain pattern of the Au(111)22×3 reconstruction. This well-known surface reconstruction occurs due to a reorganization of the top layer of the gold substrate under strain, resulting in herringbone shaped striped domains with different stacking, hcp vs fcc of the top layer Au atoms on the fcc crystal below. The domain walls of the reconstructed Au top layer atoms in between these domains are slightly elevated and visualized in STM as a herringbone pattern.[41,42] The structural models in Figures 4 and S8 reflect what can be seen in the STM data after identification of the substituents of **2** and **3** which point to the outside of the ladders and are most clearly seen in the enlargement of the STM image of **3**. Each unit cell involves three Cu adatoms; in other words, three of the four coordinated N atoms share a Cu adatom with an N atom of a neighboring molecule (marked as red dots). Additionally, due to the orientation of the molecule within the ladder, both left- and right-handed chiralities are present in the three directions related by 120° (see yellow, blue, and green lines in the middle image of the bottom row in Figure 4; only five of the six directions are within the frame shown). The angle between ladders of opposite chiralities formed upon adsorption on the substrate depends on the molecular building block and is 20° for **3** and 38° for **2**. There is no evidence from either XPS or the STM analysis that Au adatoms from the substrate are involved in the formation of similar ladder-like assemblies.[43]

Deposition of ligands **1**−**3** was also carried out on a Cu(111) substrate held at room temperature (see Figure S11 for XPS multilayer result) which provides Cu adatoms for coordination from the surface during preparation.[44−46] Even though the change of substrate from Au(111) to Cu(111) involves a change in lattice constant, we observe a remarkable consistency in the morphology of both assemblies (Figures 5 and S12 versus Figure S9). The appearance of the same ladder-like assemblies testifies to this being a robust motif, and any differences between Cu(111) and Au(111) surfaces are within the error of the measurements. The chain width coincidentally is 2.3 nm (23 Å) on both substrates, which is equivalent to 8 × 2.88 Å (gold lattice constant) or 9 × 2.56 Å (copper lattice constant). The lack of dependence of the core assembly on the substituent is remarkable. As observed on Au(111), the ladders on Cu(111) also reveal their chirality, although in this case, all three functionalities (with **1**, **2**, or **3**) have the same 13 ± 1° chirality angle. All molecules in one strand are oriented in one direction, while all molecules from the other strand point in the opposite direction. No achiral ladders were observed.

As displayed in Figure S13, ladders can reach remarkable lengths of over 125 nm. The discontinuities visible in the chains (e.g., Figures 6 and S14, top left) are attributed to a jump in the

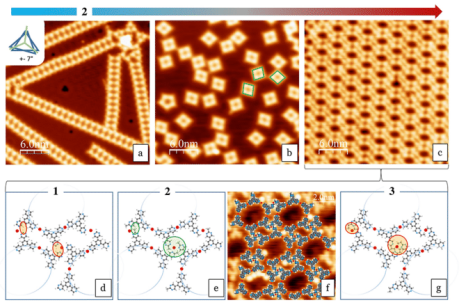

Figure 6. Sequential surface rearrangement. Top: Annealing sequence of **2** (RT, 20 min @ 240 °C, additional 20 min @ 290 °C). Ladders and tetramers are found for all three molecules **1**−**3**, but only **2** forms the porous network. Bottom: Closer examination of quasi-hexagon nanoporous network formation. (d) R = H: high repulsive H···H interactions. (e) R = Me: the ideal case, where in-plane hydrogen is positioned in-between tetrahedral oriented neighbors. (f) Space-filling models of **2** superimposed on a high-quality STM micrograph (base of the models) (recorded with Xe functionalized tip, with single Xe atoms visible as bright protrusions). (g) R = Et: repulsion between the Et groups leads to less efficient packing. For simplicity, non-relevant Cu adatoms have been omitted. An enlarged version of the figure is given in Figure S14.

DOI: 10.1021/jacs.7b12624
J. Am. Chem. Soc. 2018, 140, 2933−2939

registry in a lateral direction of one row on the Cu(111) substrate. The 2D assemblies of ladders are stable up to room temperature, but structural perturbation was achieved by annealing on the Cu(111) substrate. In a first stage, the ladders were transformed to tetramers (20 min at 240 °C, Figure 6b), and after further annealing for 20 min at 290 °C, hexagonal motifs were formed (Figure 6c). These hexagonal assemblies could also be obtained in a single annealing step of 30 min at 240 °C.

The tetramers exhibit three distinct orientations, related by 120° rotations (see the three tetramers highlighted in green in Figures 6b and S14b). For the rhombi, the internal angles are consistently 80/100°, due to the mismatch of square assemblies on a hexagonally oriented substrate. As with the ladder assemblies, the structure is not dependent on the substituents in **1**, **2**, and **3**, which are directed outside the assembly motif (rhombus side length of 2.3 nm ± 0.1 nm; see Figure S15 for a detailed comparison). A similar result is observed when directly depositing **1**, **2**, or **3** on a hot Cu(111) substrate, omitting the ladder assembly. Due to the availability of Cu adatoms at higher temperatures,[47] there is a smaller tendency for the organic molecules to share the Cu adatoms with their neighbors. This results in a preference for discrete tetramers over ladders. Per tetrameric motif, four Cu adatoms are involved in bonding forming a [4+4] metallomacrocyclic unit. This results in two shared adatoms per molecule in comparison to three for the ladders (see Figure S15 for a detailed model).

Unexpectedly, further annealing of the tetramers on Cu(111) with ligand **2** results in a further rearrangement into the nanoporous network seen in Figures 6c and S14c. Within the series of molecules **1**−**3**, the most compact packing is obtained with the methyl substituent (Figures 6 and S14, bottom row); in the analogous assembly formed with **1**, repulsive interactions involving H2 would destabilize this arrangement, whereas with **3** the ethyl has too great a steric demand.[48,49] It is remarkable, how small changes in the alkyl substituent result in such dramatic effects on the surface assembly. The nanoporous assembly of **2** (Figure 6c) is present in both chiral forms (see Figure S16).

Temperature dependent XPS analysis was carried out, revealing neither an annealing dependency of the on-surface assembly (see first column of Figure S17; in line with the result of **1**, **2**, **3** on Au(111) + Cu adatoms where full coordination already takes place at room temperature) nor compound dependency (see right column of Figure S17 for **2** vs **3** comparison; for all compounds N 1s peaks are at ∼398.6 and 399.7 (±0.2) eV). This result shows that the different behavior of **1**, **2**, and **3** is not based on differing chemical reactivity, but rather on the steric demand of the substituents. Tables S1 and S2 give a detailed XPS summary.

■ CONCLUSIONS

In conclusion, we have adopted an unconventional approach to metal−organic architectures by investigating how a common pair of ligand and metal responds to assembly in solution under ambient conditions or on a Au(111) or Cu(111) surface under UHV conditions. In solution, ligand **3** combines with copper(II) acetate or copper(I) triflate in MeOH to yield single crystals of, respectively, $[Cu_2(OAc)_4(\mathbf{3})]_n$ or $\{[Cu(\mathbf{3})(OMe)(MeOH)][CF_3SO_3]\cdot MeOH\}_n$. In the former, the acetate anions are critical to the formation of paddle-wheel $\{Cu_2(\mu\text{-}OAc)_4\}$ units which act as linear nodes and direct the assembly of 1D zigzag chains. In the latter, the methanol solvent is involved in the assembly of $\{Cu_2(\mu\text{-}OMe)_2\}$ units which act as planar, 4-connecting nodes connected by ligands **3** to generate a 2D (4,4) net. The roles of solvent and counteranion are negated by moving from solution to surface assemblies under vacuum. The different R groups in **1**, **2**, or **3** have been used as an imaging tool for STM. The difference in the substitution is visible in the close-packed phase on Au(111). After deposition of Cu adatoms, regular (ladder-shaped) surface metal−organic motifs assemble on the Au(111) surface and in all cases exhibit the same backbone structure, indicating the assembly is not influenced by the substituent. The ladder structure also assembles on Cu(111) where Cu adatoms are available during the deposition and subsequent relaxation process at room temperature. With progressively increasing annealing temperature, the original surface assemblies are modified and undergo a transition from ladders into rhomboid structures, and for ligand **2**, a quasi-hexagonal nanoporous network is observed.

Although both the assembly in solution and the solvent-free coordination assembly in vacuum provide coordination assemblies featuring planar layers, there is an important difference. The Cu coordination center in the case of the solution assembly follows the rules of coordination chemistry while the substrate-supported Cu coordination centers also show other more planar motifs, stabilized by the coordinated metal atom interacting with the underlying substrate. It is also interesting to note that this "surface-supported" Cu coordination does not appear to depend on whether Au(111) or Cu(111) substrates are used. The inclusion of counterions and solvent molecules in the lattice determines that bulk crystalline material and surface assemblies differ in their microstructures, motivating further in depth investigations. It is remarkable, however, that the general principles and algorithms determining the structures of solution-grown crystalline material can be extended to surface assemblies.

■ ASSOCIATED CONTENT

Supporting Information

The Supporting Information is available free of charge on the ACS Publications website at DOI: 10.1021/jacs.7b12624.

Experimental details; NMR spectra; ORTEP-style figures; powder diffraction data; enlarged versions of manuscript figures and additional STM images; XPS analysis (PDF)

X-ray crystallographic data for $[Cu_2(OAc)_4(\mathbf{3})]_n$ (CIF)

X-ray crystallographic data for $\{[Cu(\mathbf{3})(OMe)(MeOH)][CF_3SO_3]\cdot MeOH\}$ CIF)

■ AUTHOR INFORMATION

Corresponding Authors

*catherine.housecroft@unibas.ch

*thomas.jung@psi.ch

ORCID

Sylwia Nowakowska: 0000-0001-9463-7640

Catherine E. Housecroft: 0000-0002-8074-0089

Thomas A. Jung: 0000-0003-0717-9886

Notes

The authors declare no competing financial interest.

DOI: 10.1021/jacs.7b12624
J. Am. Chem. Soc. 2018, 140, 2933−2939

■ ACKNOWLEDGMENTS

We thank the Swiss National Science Foundation (grant numbers 200020-162631, 200020-149713, and 206021-121461), the Swiss Nanoscience Institute P1203, the Swiss Commission for Technology and Innovation (CTI, 16465.1 PFNM-NM), and the Swiss Government Excellence Scholarship Program for Foreign Scholars, as well as the University of Basel for financial support. Dr. Markus Neuburger (University of Basel) is thanked for assistance with single-crystal structure determinations, Aneliia Wäckerlin (University of Basel) for initial assistance and discussions, Mariah O'Doherty (Trinity College, Dublin) for assisting with the STM experiments and for helpful discussions, and Marco Martina and Matthes Senn (University of Basel) for technical support.

■ REFERENCES

(1) Constable, E. C. *Adv. Inorg. Chem.* **2018**, DOI: 10.1016/bs.adioch.2017.11.005.
(2) Constable, E. C. *Chem. Ind.* **1994**, 56.
(3) Housecroft, C. E.; Sharpe, A. G. *Inorganic Chemistry*, 4th ed.; Pearson Education Ltd.: Harlow, UK, 2012.
(4) Batten, S. R.; Neville, S. M.; Turner, D. R. *Coordination Polymers: Design, Analysis and Application*; RSC Publishing, Cambridge, UK, 2009.
(5) See, for example: Kang, Z.; Fan, L.; Sun, S. *J. Mater. Chem. A* **2017**, *5*, 10073. Huang, Y.-B.; Liang, J.; Wang, X.-S.; Cao, R. *Chem. Soc. Rev.* **2017**, *46*, 126. Canivet, J.; Vandichel, M.; Farrusseng, D. *Dalton Trans.* **2016**, *45*, 4090. Liu, J.; Woll, C. *Chem. Soc. Rev.* **2017**, *46*, 5730. Li, B.; Wen, H.-M.; Cui, Y.; Zhou, W.; Qian, G.; Chen, B. *Adv. Mater.* **2016**, *28*, 8819. Furukawa, H.; Cordova, K. E.; O'Keeffe, M.; Yaghi, O. M. *Science* **2013**, *341*, 974. Schoedel, A.; Li, M.; Li, D.; O'Keeffe, M.; Yaghi, O. M. *Chem. Rev.* **2016**, *116*, 12466.
(6) Spillmann, H.; Kiebele, A.; Stöhr, M.; Jung, T. A.; Bonifazi, D.; Cheng, F.; Diederich, F. *Adv. Mater.* **2006**, *18*, 275.
(7) Nowakowska, S.; Wäckerlin, A.; Kawai, S.; Ivas, T.; Nowakowski, J.; Fatayer, S.; Wäckerlin, C.; Nijs, T.; Meyer, E.; Björk, J.; Stöhr, M.; Gade, L. H.; Jung, T. A. *Nat. Commun.* **2015**, *6*, 6071.
(8) Nowakowska, S.; Wäckerlin, A.; Piquero-Zulaica, I.; Nowakowski, J.; Kawai, S.; Wäckerlin, C.; Matena, M.; Nijs, T.; Fatayer, S.; Popova, O.; Ahsan, A.; Mousavi, S. F.; Ivas, T.; Meyer, E.; Stöhr, M.; Ortega, J. E.; Björk, J.; Gade, L. H.; Lobo-Checa, J.; Jung, T. A. *Small* **2016**, *12*, 3757.
(9) Constable, E. C. *Chem. Soc. Rev.* **2007**, *36*, 246.
(10) Housecroft, C. E. *Dalton Trans.* **2014**, *43*, 6594.
(11) Housecroft, C. E. *CrystEngComm* **2015**, *17*, 7461.
(12) Kröhnke, F. *Synthesis* **1976**, *1976*, 1.
(13) Wang, J.; Hanan, G. S. *Synlett* **2005**, *2005*, 1251.
(14) Klein, Y. M.; Prescimone, A.; Pitak, M. B.; Coles, S. J.; Constable, E. C.; Housecroft, C. E. *CrystEngComm* **2016**, *18*, 4704.
(15) Yin, Z.; Zhang, S.; Zheng, S.; Golen, J. A.; Rheingold, A. L.; Zhang, G. *Polyhedron* **2015**, *101*, 139.
(16) Li, X.-Z.; Zhou, X.-P.; Li, D.; Yin, Y.-G. *CrystEngComm* **2011**, *13*, 6759.
(17) Xi, Y.; Wei, W.; Xu, Y.; Huang, X.; Zhang, F.; Hu, C. *Cryst. Growth Des.* **2015**, *15*, 2695.
(18) Yuan, F.; Xie, J.; Hu, H.-M.; Yuan, C.-M.; Xu, B.; Yang, M.-L.; Dong, F.-X.; Xue, G.-L. *CrystEngComm* **2013**, *15*, 1460.
(19) Gong, Y.; Zhang, M. M.; Zhang, P.; Shi, H. F.; Jiang, P. G.; Lin, J. H. *CrystEngComm* **2014**, *16*, 9882.
(20) Yuan, F.; Zhu, Q.; Hu, H.-M.; Xie, J.; Xu, B.; Yuan, C.-M.; Yang, M.-L.; Dong, F.-X.; Xue, G.-L. *Inorg. Chim. Acta* **2013**, *397*, 117.
(21) Yang, J.; Yan, S.-W.; Wang, X.; Xiao, D.-R.; Zhang, H.-Y.; Chi, X.-L.; Zhang, J.-L.; Wang, E. *Inorg. Chem. Commun.* **2013**, *38*, 100.
(22) Chen, Y.-Q.; Li, G.-R.; Chang, Z.; Qu, Y.-K.; Zhang, Y.-H.; Bu, X.-H. *Chem. Sci.* **2013**, *4*, 3678.
(23) Constable, E. C.; Housecroft, C. E.; Neuburger, M.; Schönle, J.; Vujovic, S.; Zampese, J. A. *Polyhedron* **2013**, *60*, 120.
(24) Li, L.; Zhang, Y. Z.; Yang, C.; Liu, E.; Golen, J. A.; Zhang, G. *Polyhedron* **2016**, *105*, 115.
(25) Nijs, T.; Malzner, F. J.; Fatayer, S.; Wäckerlin, A.; Nowakowska, S.; Constable, E. C.; Housecroft, C. E.; Jung, T. A. *Chem. Commun.* **2015**, *51*, 12297.
(26) Constable, E. C.; Housecroft, C. E.; Neuburger, M.; Vujovic, S.; Zampese, J. A.; Zhang, G. *CrystEngComm* **2012**, *14*, 3554.
(27) Klein, Y. M.; Constable, E. C.; Housecroft, C. E.; Zampese, J. A. *Polyhedron* **2014**, *81*, 98.
(28) Beves, J. E.; Constable, E. C.; Decurtins, S.; Dunphy, E. L.; Housecroft, C. E.; Keene, T. D.; Neuburger, M.; Schaffner, S. *CrystEngComm* **2008**, *10*, 986.
(29) Constable, E. C.; Zhang, G.; Coronado, E.; Housecroft, C. E.; Neuburger, M. *CrystEngComm* **2010**, *12*, 2139.
(30) Constable, E. C.; Zhang, G.; Housecroft, C. E.; Neuburger, M.; Zampese, J. A. *CrystEngComm* **2010**, *12*, 2146.
(31) Constable, E. C.; Housecroft, C. E.; Kopecky, P.; Neuburger, M.; Zampese, J. A.; Zhang, G. *CrystEngComm* **2012**, *14*, 446.
(32) Constable, E. C.; Housecroft, C. E.; Vujovic, S.; Zampese, J. A.; Crochet, A.; Batten, S. R. *CrystEngComm* **2013**, *15*, 10068.
(33) Klein, Y. M.; Constable, E. C.; Housecroft, C. E.; Zampese, J. A.; Crochet, A. *CrystEngComm* **2014**, *16*, 9915.
(34) Zhang, G.; Jia, Y.-X.; Chen, W.; Lo, W.-F.; Brathwaite, N.; Golen, J. A.; Rheingold, A. L. *RSC Adv.* **2015**, *5*, 15870.
(35) Janiak, C. *J. Chem. Soc., Dalton Trans.* **2000**, 3885.
(36) Pariyar, A.; Stansbery, J.; Patel, R. L.; Liang, X.; Choudhury, A. *J. Coord. Chem.* **2016**, *69*, 1957.
(37) Köberl, M.; Cokoja, M.; Herrmann, W. A.; Kühn, F. E. *Dalton Trans.* **2011**, *40*, 6834.
(38) Addison, A. W.; Rao, T. N.; Reedijk, J.; van Rijn, J.; Verschoor, G. C. *J. Chem. Soc., Dalton Trans.* **1984**, 1349.
(39) Blatov, V. A.; Shevchenko, A. P. *ToposPro*, v. 4.0; Samara State University, Russia, 2005.
(40) Desiraju, G. R.; Steiner, T. *The Weak Hydrogen Bond in Structural Chemistry and Biology*; Oxford University Press, Oxford, UK, 1999.
(41) Wöll, Ch.; Chiang, S.; Wilson, R. J.; Lippel, P. H. *Phys. Rev. B: Condens. Matter Mater. Phys.* **1989**, *39*, 7988.
(42) Barth, J. V.; Brune, H.; Ertl, G.; Behm, R. J. *Phys. Rev. B: Condens. Matter Mater. Phys.* **1990**, *42*, 9307.
(43) Pham, T. A.; Song, F.; Alberti, M. N.; Nguyen, M.-T.; Trapp, N.; Thilgen, C.; Diederich, F.; Stöhr, M. *Chem. Commun.* **2015**, *51*, 14473.
(44) Lin, N.; Payer, D.; Dmitriev, A.; Strunskus, T.; Wöll, C.; Barth, J. V.; Kern, K. *Angew. Chem., Int. Ed.* **2005**, *44*, 1488.
(45) Pawin, G.; Wong, K. L.; Kim, D.; Sun, D.; Bartels, L.; Hong, S.; Rahman, T. S.; Carp, R.; Marsella, M. *Angew. Chem., Int. Ed.* **2008**, *47*, 8442.
(46) Sirtl, T.; Schlögl, S.; Rastgoo-Lahrood, A.; Jelic, J.; Neogi, S.; Schmittel, M.; Heckl, W. M.; Reuter, K.; Lackinger, M. *J. Am. Chem. Soc.* **2013**, *135*, 691.
(47) Lin, N.; Payer, D.; Dmitriev, A.; Strunskus, T.; Wöll, C.; Barth, J. V.; Kern, K. *Angew. Chem., Int. Ed.* **2005**, *44*, 1488.
(48) Wintjes, N.; Hornung, J.; Lobo-Checa, J.; Voigt, T.; Samuely, T.; Thilgen, C.; Stöhr, M.; Diederich, F.; Jung, T. A. *Chem. - Eur. J.* **2008**, *14*, 5794.
(49) Enache, M.; Maggini, L.; Llanes-Pallas, A.; Jung, T. A.; Bonifazi, D.; Stöhr, M. *J. Phys. Chem. C* **2014**, *118*, 15286.

■ NOTE ADDED IN PROOF

We have become aware that the experimental results presented in this paper further confirm the structural models presented in P. Szabelski, W. Rżysko, and D. Nieckarz, *J. Phys. Chem. C* **2016**, *120*, 13139. We thank Professor Szabelski for making us aware of this publication.

DOI: 10.1021/jacs.7b12624
J. Am. Chem. Soc. 2018, 140, 2933−2939

18.6 Paper 6 (Published by the Royal Society of Chemistry)

Volume 17 | Number 34 | 14 September 2015 | Pages 6459–6608

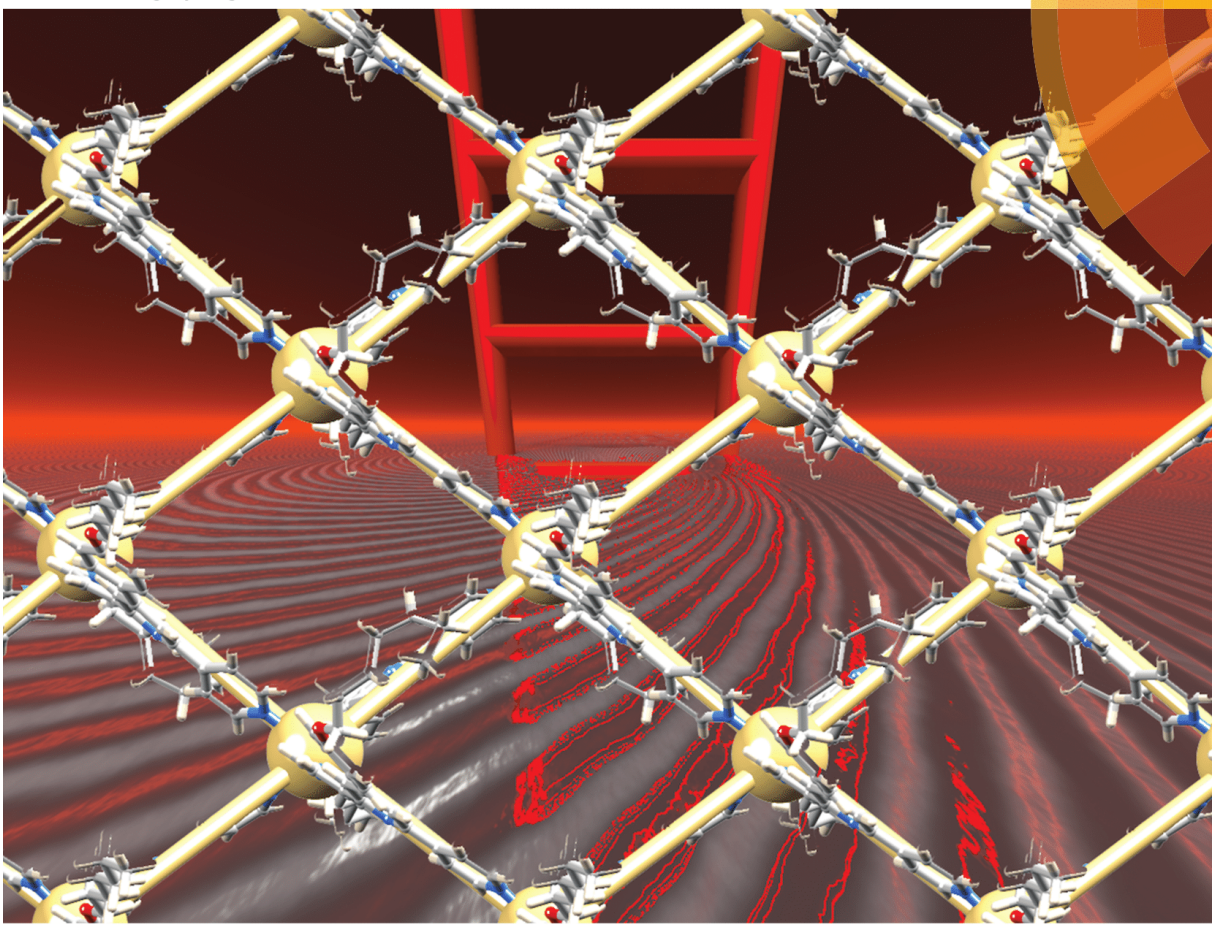

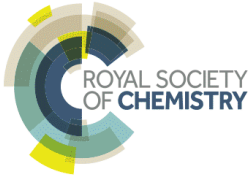

PAPER
Catherine E. Housecroft *et al.*
Manipulating connecting nodes through remote alkoxy chain variation in coordination networks with 4′-alkoxy-4,2′:6′,4″-terpyridine linkers

CrystEngComm

PAPER

View Article Online
View Journal | View Issue

Cite this: *CrystEngComm*, 2015, **17**, 6483

Manipulating connecting nodes through remote alkoxy chain variation in coordination networks with 4′-alkoxy-4,2′:6′,4″-terpyridine linkers†

Y. Maximilian Klein, Alessandro Prescimone, Edwin C. Constable and Catherine E. Housecroft*

Received 8th June 2015,
Accepted 26th June 2015

DOI: 10.1039/c5ce01115a

www.rsc.org/crystengcomm

The effects of increasing the length of the alkoxy substituent in 4′-alkoxy-4,2′:6′,4″-terpyridines when they are combined with cadmium(II) nitrate under conditions of room temperature crystallization and in the same cadmium : ligand (1 : 3) ratio have been investigated. The divergent ligand 4′-*n*-propoxy-4,2′:6′,4″-terpyridine (**2**) reacts with $Cd(NO_3)_2{\cdot}4H_2O$ to give $[\{Cd_2(NO_3)_4(\mathbf{2})_3\}{\cdot}3CHCl_3]_n$ in which the Cd atoms act as 3-connecting nodes and assemble into a (6,3) net with each ligand **2** linking adjacent Cd atoms. One of the three independent *n*-propoxy groups nestles into a cleft in the next 2-dimensional sheet; this 'tail-in-pocket' interaction restricts the length of the alkyl chain that can be accommodated. Replacing the *n*-propoxy by an *n*-pentoxy, *n*-hexoxy or *n*-heptoxy substituent results in a switch from a (6,3) to (4,4) net; in $[\{Cd_2(NO_3)_4(\mathbf{3})_4\}{\cdot}3CHCl_3]_n$ (**3** = 4′-*n*-pentoxy-4,2′:6′,4″-terpyridine) and $[\{Cd_2(NO_3)_4(\mathbf{4})_4\}{\cdot}CHCl_3{\cdot}MeOH]_n$ (**4** = 4′-*n*-hexoxy-4,2′:6′,4″-terpyridine), each Cd atom is a 4-connecting node with *trans*-nitrato ligands, while in $[\{Cd(NO_3)_2(\mathbf{5})_2\}{\cdot}2MeOH]_n$ (**5** = 4′-*n*-heptoxy-4,2′:6′,4″-terpyridine) a *cis*-arrangement of nitrato ligands is observed. The reaction between $Cd(NO_3)_2{\cdot}4H_2O$ and **4** was also investigated using a 1 : 1 ratio of reagents; this leads to the assembly of the 1-dimensional ladder $[Cd_2(NO_3)_4(MeOH)(\mathbf{4})_3]_n$ in which each Cd atom is a 3-connecting node. In each structure, face-to-face π-stacking of the central pyridine rings or of pyridine/phenyl rings of ligands in adjacent sheets or chains is a primary packing interaction; the role of van der Waals interactions as the chain length increases is discussed. Powder diffraction confirmed that each coordination polymer or network characterized by single crystal X-ray crystallography was representative of the bulk sample. The solid-state emission properties of ligands **2**, **3** and **4** and their coordination polymers are reported; the blue emission of the free ligands is red-shifted by up to 59 nm upon formation of the coordination networks, and quantum yields are in the range 11–22%.

Introduction

Diversity in the architectures of 2- and 3-dimensional coordination polymers is engineered through the use of complementary metal nodes and organic (ligand) linkers.[1–7] Oligopyridines remain popular tectons in supramolecular assemblies,[8,9] and over the last 15 years, the divergent 4,2′:6′,4″-terpyridine (4,2′:6′,4″-tpy) domain has proved to be a versatile linker[10] binding metal ions through the outer pyridine rings (Scheme 1). 4,2′:6′,4″-Terpyridines are easily functionalized in the 4′-position to incorporate additional coordination sites[11] or sterically variable substituents (*e.g.* bulky[12] or long chain,[13,14] alkyl groups) that influence packing interactions and assembly motifs.

Although strategies towards 2- and 3-dimensional networks are currently being developed using ditopic 4,2′:6′,4″-tpy and its isomeric 3,2′:6′,3″-tpy linkers,[15,16] the coordination chemistry of 4,2′:6′,4″-tpy remains dominated by 1-dimensional chains. This preference can be modified by turning attention to the metal node. For example, linear $\{Zn_2(OAc)_4\}$ nodes (Scheme 1) combined with 4,2′:6′,4″-tpys

Department of Chemistry, University of Basel, Spitalstrasse 51, CH-4056 Basel, Switzerland. E-mail: catherine.housecroft@unibas.ch

† Electronic supplementary information (ESI) available: Fig. S1–S5: powder diffraction data; Fig. S6: part of the coordination polymer chain in $[Cd_2(NO_3)_4(MeOH)(\mathbf{4})_3]_n$. CCDC 1402482–1402486. For ESI and crystallographic data in CIF or other electronic format see DOI: 10.1039/c2dt12242a

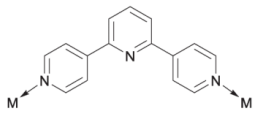

Scheme 1 Typical coordination mode of 4,2′:6′,4″-terpyridine.

result in flat, zig-zag chains, whereas non-linear nodes (often incorporating zinc(II) halides) lead to helical polymers.[10] Single chains can be extended into double-stranded chains[17] by the use of $\{Cd_2(OAc)_4\}$ nodes which are structurally distinct from their zinc(II) counterparts (Scheme 2). This design principle is extended using $\{Mn_3(OAc)_6\}$ nodes for the assembly of triple-stranded chains,[18] but unexpectedly, planar $\{Zn_5(OAc)_{10}\}$ nodes lead to quadruple-stranded, rather than pentuple, chains.[19] Double chains in this family possess a ladder topology, with the rungs of the ladder defined by the $\{Cd_2(OAc)_4\}$-bridges (Scheme 2). The bridging mode of the acetato ligand is key to the formation of $\{M_n(OAc)_{2n}\}$ nodes, and the use of $[AcO]^-$ to assist the formation of multimetal, in particular zinc, cluster building blocks is well established with $[Zn_4(\mu\text{-}OAc)_6(\mu_4\text{-}O)]$[20] derivatives being fundamental to many metal organic frameworks (MOFs).[21]

Within the coordination chemistry of 4,2′:6′,4″-terpyridines, a switch from cadmium(II) acetate to nitrate significantly influences the coordination polymer assembly. For example, 4′-phenyl-4,2′:6′,4″-tpy reacts with $Cd(NO_3)_2{\cdot}4H_2O$ to give a 2-dimensional (4,4) net,[22] while introducing 4-$MeOC_6H_4$,[23] 4-$MeSC_6H_4$ [24] or 4-$HC{\equiv}CC_6H_4$ [24] units into the 4′-position of 4,2′:6′,4-tpy results in ladder assemblies in which each rung is defined by a 4,2′:6′,4″-tpy ligand. However, these ladders with a 2:3 ratio of Cd:ligand have been produced using different ratios of precursors in the crystallization experiments. We present here a systematic investigation of reactions of 4′-(4-alkoxyphenyl)-4,2′:6′,4″-terpyridines (Scheme 3) with cadmium(II) nitrate under room temperature conditions of crystallization. Our focus is to use a constant input ratio of $Cd(NO_3)_2{\cdot}4H_2O$ to ligand (1:3) in order to determine preferred assemblies and their reproducibility. We then demonstrate the effects of reducing the amount of ligand (Cd:ligand = 1:1) on the assembly process.

Experimental

Ligands **1**–**5** were prepared as previously described.[14]

$[\{Cd_2(NO_3)_4(2)_3\}{\cdot}3CHCl_3]_n$. A MeOH (8 mL) solution of $Cd(NO_3)_2{\cdot}4H_2O$ (9.25 mg, 0.03 mmol) was layered over a $CHCl_3$ (5 mL) solution of **2** (33.1 mg, 0.09 mmol) and the crystallization tube was left to stand at room temperature. Colourless crystals of $[\{Cd_2(NO_3)_4(2)_3\}{\cdot}3CHCl_3]_n$ (21.2 mg, 0.011 mmol, 73% based on Cd) were obtained after 2–4 weeks. Satisfactory elemental analysis of the bulk sample could not be obtained; see Fig. S1† for powder diffraction data.

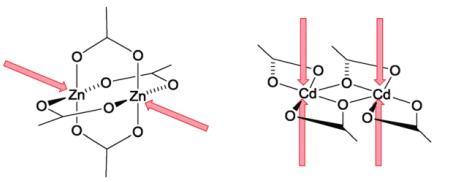

Scheme 2 Structurally different $\{Zn_2(OAc)_4\}$ and $\{Cd_2(OAc)_4\}$ nodes combine with 4,2′:6′,4″-tpy to give single and double-stranded chains, respectively.

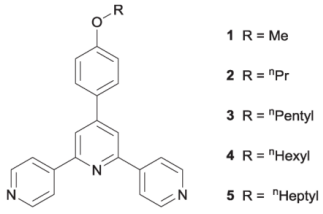

1 R = Me
2 R = ^{n}Pr
3 R = ^{n}Pentyl
4 R = ^{n}Hexyl
5 R = ^{n}Heptyl

Scheme 3 Structures of ligands **1**–**5**.

$[\{Cd_2(NO_3)_4(3)_4\}{\cdot}3CHCl_3]_n$. A MeOH (8 mL) solution of $Cd(NO_3)_2{\cdot}4H_2O$ (3.08 mg, 0.01 mmol) was layered over a $CHCl_3$ (5 mL) solution of **3** (11.9 mg, 0.03 mmol) and the crystallization tube was left to stand at room temperature. Colourless crystals of $[\{Cd_2(NO_3)_4(3)_4\}{\cdot}3CHCl_3]_n$ (8.3 mg, 0.003 mmol, 69% based on Cd) were obtained after 2–4 weeks. Satisfactory elemental analysis of the bulk sample could not be obtained; see Fig. S2† for powder diffraction data.

$[\{Cd_2(NO_3)_4(4)_4\}{\cdot}CHCl_3{\cdot}MeOH]_n$. A MeOH (8 mL) solution of $Cd(NO_3)_2{\cdot}4H_2O$ (3.08 mg, 0.01 mmol) was layered over a $CHCl_3$ (5 mL) solution of **4** (12.4 mg, 0.03 mmol) and the crystallization was left to stand at room temperature. Colourless crystals of $[\{Cd_2(NO_3)_4(4)_4\}{\cdot}CHCl_3{\cdot}MeOH]_n$ (7.6 mg, 0.003 mmol, 67% based on Cd) were obtained after 2–4 weeks. Satisfactory elemental analysis of the bulk sample could not be obtained; see Fig. S3† for powder diffraction data.

$[\{Cd(NO_3)_2(5)_2\}{\cdot}2MeOH]_n$. A MeOH (8 mL) solution of $Cd(NO_3)_2{\cdot}4H_2O$ (3.08 mg, 0.01 mmol) was layered over a $CHCl_3$ (5 mL) solution of **5** (12.7 mg, 0.03 mmol) and the crystallization tube was left standing at room temperature. After 2–4 weeks, colourless crystals of $[\{Cd(NO_3)_2(5)_2\}{\cdot}2MeOH]_n$ (5.9 mg, 0.005 mmol, 51% based on Cd) had grown. Satisfactory elemental analysis of the bulk sample could not be obtained; see Fig. S4† for powder diffraction data.

$[Cd_2(NO_3)_4(MeOH)(4)_3]_n$. A MeOH (8 mL) solution of $Cd(NO_3)_2{\cdot}4H_2O$ (9.25 mg, 0.03 mmol) was layered over a $CHCl_3$ (5 mL) solution of **4** (12.4 mg, 0.03 mmol). The crystallization tube was left to stand at room temperature and colourless crystals of $[Cd_2(NO_3)_4(MeOH)(4)_3]_n$ (12.4 mg, 0.007 mmol, 48% based on Cd) were obtained after 2–4 weeks. Found C 56.11, H 5.07, N 10.83; required for $C_{82}H_{85}Cd_2N_{13}O_{16}$. MeOH C 56.47, H 5.08, N 10.31; see Fig. S5† for powder diffraction data.

Crystallography

Crystallographic data were collected on a Bruker-Nonius Kappa APEX diffractometer; data reduction, solution and refinement used APEX2[25] and CRYSTALS.[26] Powder

diffraction data were collected on a Stoe Stadi P powder diffractometer. Structural diagrams and structural analysis were carried out using Mercury v. 3.5.1,[27,28] and TOPOS.[29] The solvent region of three of the structures treated with the program SQUEEZE,[30] and the electron density removed was equated to appropriate solvent molecules and added to relevant formulae (see below). High thermal motion in some of the alkyl chains meant that some carbon atoms had to be refined isotropically; some bond parameters in these chains were restrained to chemically reasonable values.

$[\{Cd_2(NO_3)_4(2)_3\}\cdot 3CHCl_3]_n$. SQUEEZE[30] was used to treat the solvent region. $C_{75}H_{66}Cd_2Cl_9N_{13}O_{15}$, M = 1933.30, colourless block, monoclinic, space group $P2_1/n$, a = 15.0312(9), b = 25.4508(11), c = 21.7048(12) Å, β = 92.051(4)°, U = 8298.0(5) Å^3, Z = 4, D_c = 1.55 Mg m^{-3}, μ(Cu-Kα) = 7.363 mm^{-1}, T = 123 K. Total 55 690 reflections, 14 425 unique, R_{int} = 0.090. Refinement of 14 419 reflections (854 parameters) with $I > 2\sigma(I)$ converged at final R_1 = 0.0814 (R_1 all data = 0.1228), wR_2 = 0.2242 (wR_2 all data = 0.2753), gof = 0.9871. CCDC 1402483.

$[\{Cd_2(NO_3)_4(3)_4\}\cdot 3CHCl_3]_n$. SQUEEZE[30] was used to treat the solvent region. $C_{107}H_{103}Cd_2Cl_9N_{16}O_{16}$, M = 2412.97, colourless block, monoclinic, space group $P2_1/c$, a = 25.945(6), b = 24.578(5), c = 17.527(3) Å, β = 91.069(9)°, U = 11 174.7(17) Å^3, Z = 4, D_c = 1.43 Mg m^{-3}, μ(Cu-Kα) = 5.601 mm^{-1}, T = 123 K. Total 76 477 reflections, 19 048 unique, R_{int} = 0.047. Refinement of 19 027 reflections (1232 parameters) with $I > 2\sigma(I)$ converged at final R_1 = 0.1340 (R_1 all data = 0.1419), wR_2 = 0.3465 (wR_2 all data = 0.3513), gof = 1.0024. CCDC 1402485.

$[\{Cd_2(NO_3)_4(4)_4\}\cdot CHCl_3\cdot MeOH]_n$. SQUEEZE[30] was used to treat the solvent region. $C_{108}H_{112}Cd_2Cl_3N_{16}O_{17}$, M = 2261.35, colourless block, monoclinic, space group $P2_1/c$, a = 25.2624(12), b = 25.0809(11), c = 16.7959(8) Å, β = 92.522(3)°, U = 10 631.6(9) Å^3, Z = 4, D_c = 1.41 Mg m^{-3}, μ(Cu-Kα) = 4.500 mm^{-1}, T = 123 K. Total 44 477 reflections, 18 427 unique, R_{int} = 0.089. Refinement of 11 009 reflections (1191 parameters) with $I > 2\sigma(I)$ converged at final R_1 = 0.1026 (R_1 all data = 0.1279), wR_2 = 0.2838 (wR_2 all data = 0.3071), gof = 1.0024. CCDC 1402486.

$[\{Cd(NO_3)_2(5)_2\}\cdot 2MeOH]_n$. $C_{58}H_{66}CdN_8O_{10}$, M = 1147.61, colourless block, monoclinic, space group $P2_1/n$, a = 17.336(3), b = 17.302(3), c = 18.817(3) Å, β = 97.458(7)°, U = 5596.3(8) Å^3, Z = 4, D_c = 1.362 Mg m^{-3}, μ(Cu-Kα) = 3.658 mm^{-1}, T = 123 K. Total 11 3924 reflections, 9826 unique, R_{int} = 0.087. Refinement of 5855 reflections (659 parameters) with $I > 2\sigma(I)$ converged at final R_1 = 0.0986 (R_1 all data = 0.1359), wR_2 = 0.2752 (wR_2 all data = 0.3369), gof = 0.9707. CCDC 1402484.

$[Cd_2(NO_3)_4(MeOH)(4)_3]_n$. $C_{82}H_{85}Cd_2N_{13}O_{16}$, M = 1733.45, colourless block, triclinic, space group $P\bar{1}$, a = 13.1304(7), b = 16.5224(9), c = 19.2845(10) Å, α = 83.670(3), β = 82.840(3), γ = 70.242(3)°, U = 3896.3(2) Å^3, Z = 2, D_c = 1.477 Mg m^{-3}, μ(Cu-Kα) = 5.007 mm^{-1}, T = 123 K. Total 49 970 reflections, 13 661 unique, R_{int} = 0.039. Refinement of 12 221 reflections (1018 parameters) with $I > 2\sigma(I)$ converged at final R_1 = 0.0540 (R_1 all data = 0.0586), wR_2 = 0.1212 (wR_2 all data = 0.1228), gof = 0.9870. CCDC 1402482.

Photoluminescence. Solid-state quantum yields were measured using a Hamamatsu absolute PL quantum yield spectrometer C11347 Quantaurus_QY. Lifetimes and emission spectra of solid samples were measured using a Hamamatsu Compact Fluorescence lifetime Spectrometer C11367 Quantaurus-Tau; an LED light source with excitation wavelength of 280 nm was used.

Results and discussion

n-Propoxy-tailed 4,2′:6′,4″-terpyridine

We recently reported that under crystallization conditions in MeOH/$CHCl_3$, ligand **1** (Scheme 3) reacts with $Cd(NO_3)_2\cdot 4H_2O$ to give a 1-dimensional coordination ladder $[\{Cd_2(NO_3)_4(\mathbf{1})_3\}\cdot CHCl_3\cdot MeOH]_n$.[23] The ladder possesses a Cd : ligand ratio of 2 : 3, and both the rungs and rails of the ladder are defined by bridging ligands (Fig. 1). In order to probe the effects of lengthening the alkoxy chain in the linker, crystallization experiments combining $Cd(NO_3)_2\cdot 4H_2O$ with ligands **2**, **3**, **4** or **5** with ratios of Cd : ligand of 1 : 3 in MeOH/$CHCl_3$ were conducted. These resulted in the growth of X-ray quality crystals.

Structural analysis of a crystal selected from the bulk sample of crystals grown from the reaction of **2** (*n*-propoxy-tailed ligand) and $Cd(NO_3)_2\cdot 4H_2O$ confirmed the formation of $[\{Cd_2(NO_3)_4(\mathbf{2})_3\}\cdot 3CHCl_3]_n$. Cell checks on other crystals from the batch revealed consistent cell parameters. A comparison of the powder diffraction pattern for a batch of ground crystals from the bulk sample, with that of predicted from the single crystal structure is shown in Fig. S1.† The data are consistent with the single crystal being representative of the bulk sample.

$[\{Cd_2(NO_3)_4(\mathbf{2})_3\}\cdot 3CHCl_3]_n$ crystallizes in the monoclinic space group $P2_1/n$, and the asymmetric unit contains two independent Cd atoms and three independent ligands (Fig. 2). Although the Cd : ligand ratio of 2 : 3 is the same as in the coordination ladder $[\{Cd_2(NO_3)_4(\mathbf{1})_3\}\cdot CHCl_3\cdot MeOH]_n$, propagation of the structure in $[\{Cd_2(NO_3)_4(\mathbf{2})_3\}\cdot 3CHCl_3]_n$ leads to a 2-dimensional (6,3) net which lies in the *bc*-plane. Each of Cd1 and Cd2 is 7-coordinate, and is bound by the outer pyridine ring of three different ligands **2** and two bidentate nitrato ligands. Bond lengths are unexceptional (see caption to Fig. 2) and the bite angles of the four independent nitrato ligands are in the range 51.1(3)–52.2(3)°. The three N-donors at each Cd centre define a T-shaped environment with N–Cd–

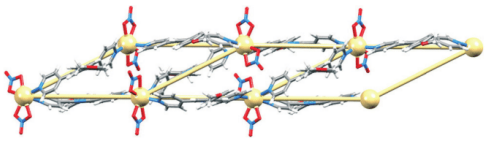

Fig. 1 Superimposition of the structure and TOPOS representation of part of one ladder in $[\{Cd_2(\mathbf{1})_3(NO_3)_4\}\cdot CHCl_3\cdot MeOH]_n$.[23]

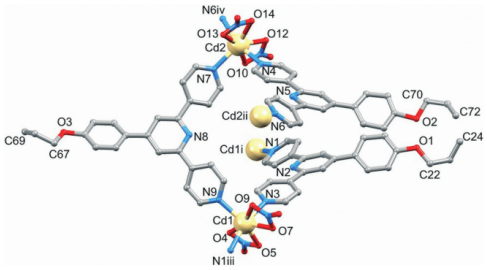

Fig. 2 The asymmetric unit (with symmetry generated atoms) in $[\{Cd_2(NO_3)_4(\mathbf{2})_3\}\cdot 3CHCl_3]_n$; H atoms omitted. Symmetry codes: i = 1/2 − *x*, 1/2 + *y*, 3/2 − *z*; ii = 1/2 − *x*, −1/2 + *y*, 1/2 − *z*; iii = 1/2 − *x*, −1/2 + *y*, 3/2 − *z*; iv = 1/2 − *x*, 1/2 + *y*, 1/2 − *z*. Selected bond distances: Cd1–O4 = 2.400(7), Cd1–O5 = 2.467(7), Cd1–O7 = 2.394(7), Cd1–O9 = 2.489(7), Cd1–$N1^{iii}$ = 2.314(8), Cd1–N3 = 2.338(8), Cd1–N9 = 2.333(8), Cd2–O10 = 2.447(9), Cd2–O12 = 2.408(8), Cd2–O13 = 2.405(7), Cd2–O14 = 2.521(8), Cd2–N4 = 2.325(10), Cd2–N6 = 2.295(9), Cd2–N7 = 2.341(8) Å.

N angles ($N1^{iii}$–Cd1–N9 = 103.5(3) and N3–Cd1–N9 = 91.7(3)°, $N6^{iv}$–Cd2–N7 = 104.7(3) and N4–Cd2–N7 = 91.6(3)°).

Around each 6-membered ring in the (6,3) net, the bridging ligands with extended chains are in an up/up/down/up/up/down sequence, and the nets stack over one another in an ABAB··· arrangement with A and B layers related by inversion (Fig. 3a). The closest Cd···Cd separation between nets is 7.836(1) Å, which is significantly shorter that the separations of 12.3597(9) to 12.9881(9) Å within each hexacycle in the (6,3) net; the latter distances are imposed by the span of bridging ligand **2**. Fig. 3b illustrates the penetration of the 4-propoxyphenyl groups through adjacent sheets. The chain containing atom O3 is neatly accommodated (Fig. 4) within a pocket comprising three ligands **2** containing $N3^{v}$, $N5^{v}$ and $N8^{v}$ (symmetry code v = 1 + *x*, *y*, *z*). The pyridine ring with N8 is sandwiched between two phenyl rings in adjacent chains; angles between the least squares planes of the rings in the triple π-stack (Fig. 4) are 7.9 and 6.2°, and the $phenyl_{centroid}\cdots pyridine_{plane}$ distances are 3.54 and 3.53 Å. The close H···H contacts highlighted in green in Fig. 4 are an important feature of this 'tail-in-pocket' interaction, and limit the length of the alkyl chain that can be accommodated. We were able to obtain preliminary structural data on crystals grown from the reaction of $Cd(NO_3)_2\cdot 4H_2O$ and 4′-(4-*n*-butoxyphenyl)-4,2′:6′,4″-tpy. Significantly, the cell dimensions (*a* = 15.241(9), *b* = 25.2808(13), *c* = 21.913(2) Å, *β* = 90.75(4)°) are similar to those of $[\{Cd_2(NO_3)_4(\mathbf{2})_3\}\cdot 3CHCl_3]_n$ and the preliminary determination confirmed the assembly of a (6,3) with analogous structural features to those shown in Fig. 3 and 4. This implies that no major structural perturbation occurs on going from an *n*-propoxy to *n*-butoxy functionalized ligand.

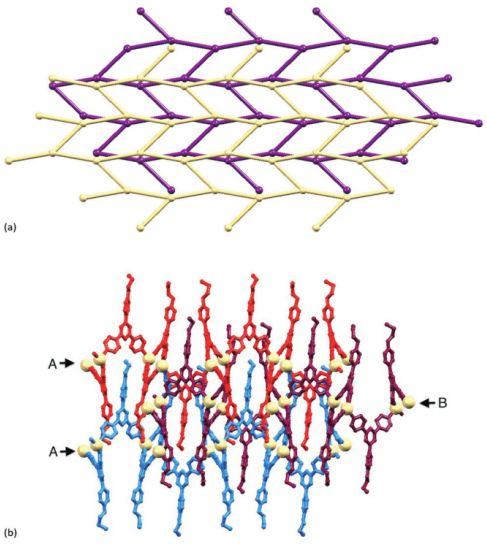

Fig. 3 Structure of $[\{Cd_2(NO_3)_4(\mathbf{2})_3\}\cdot 3CHCl_3]_n$: (a) TOPOS representation of adjacent (6,3) nets (viewed down the *a*-axis); (b) part of three sheets (ABA arrangement) showing the penetration of 4-propoxyphenyl units through adjacent sheets.

From *n*-propoxy to *n*-pentoxy and *n*-hexoxy tails

Reaction of $Cd(NO_3)_2\cdot 4H_2O$ with **3** or **4** (*n*-pentoxy or *n*-hexoxy derivatives, Scheme 3) leads to $[\{Cd_2(NO_3)_4(\mathbf{3})_4\}\cdot 3CHCl_3]_n$ or $[\{Cd_2(NO_3)_4(\mathbf{4})_4\}\cdot CHCl_3\cdot MeOH]_n$, respectively. The compounds are structurally analogous, crystallizing in the space group $P2_1/c$ with similar cell dimensions. Cell parameters consistent with those in the experimental section for $[\{Cd_2(NO_3)_4(\mathbf{3})_4\}\cdot 3CHCl_3]_n$ and $[\{Cd_2(NO_3)_4(\mathbf{4})_4\}\cdot CHCl_3\cdot MeOH]_n$ were obtained for representative crystals chosen from the bulk sample. Fig. S2 and S3† compare the powder diffraction patterns predicted from the single crystal structures of the two coordination polymers with those of ground crystals from the bulk material, and with experimental powder patterns for the precursors. The data confirm that the single crystals chosen were representative of the bulk samples.

In the light of the restricted space associated with the 'tail-in-pocket' interaction in $[\{Cd_2(NO_3)_4(\mathbf{2})_3\}\cdot 3CHCl_3]_n$ and its *n*-butoxy analogue, a change in structure on going to the

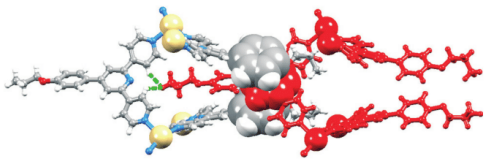

Fig. 4 Accommodation of the 4-propoxyphenyl unit (red) containing atom O3 in a pocket comprising three ligands **2**; short H···H contacts (2.14 and 2.49 Å) are shown in green. See text for details of the π-stacking interaction.

longer *n*-pentoxy or *n*-hexoxy chains is not unexpected. Fig. 5 shows the asymmetric unit (with symmetry generated atoms) in $[\{Cd_2(NO_3)_4(\mathbf{4})_4\}\cdot CHCl_3\cdot MeOH]_n$, with two independent Cd atoms and four independent ligands **4**. Likewise, $[\{Cd_2(NO_3)_4(\mathbf{3})_4\}\cdot 3CHCl_3]_n$ contains two independent Cd atoms and four independent molecules of **3**. The Cd atoms are octahedrally sited, coordinated by four ligands and two, mutually *trans* nitrato ligands. The Cd–N bond lengths are in the range 2.317(9) to 2.362(8) Å in $[\{Cd_2(NO_3)_4(\mathbf{3})_4\}\cdot 3CHCl_3]_n$, and 2.286(8) to 2.407(4) Å in $[\{Cd_2(NO_3)_4(\mathbf{4})_4\}\cdot CHCl_3\cdot MeOH]_n$. The coordination modes of the nitrato ligands in the two compounds are monodentate, bidentate (Fig. 5) or monodentate with an additional long contact; Cd–O distances range from 2.360(7) to 2.879(9) Å in $[\{Cd_2(NO_3)_4(\mathbf{3})_4\}\cdot 3CHCl_3]_n$ and from 2.310(12) to 2.616(8) Å in $[\{Cd_2(NO_3)_4(\mathbf{4})_4\}\cdot CHCl_3\cdot MeOH]_n$. In each structure, one nitrato ligand is disordered and has been modelled over two sites with fractional occupancies of 0.60/0.40 or 0.65/0.35. Each Cd atom in $[\{Cd_2(NO_3)_4(\mathbf{3})_4\}\cdot 3CHCl_3]_n$ and $[\{Cd_2(NO_3)_4(\mathbf{4})_4\}\cdot CHCl_3\cdot MeOH]_n$ acts as a 4-connecting node giving the (4,4) coordination networks shown in Fig. 6 and 7. Each rhombus in the net in $[\{Cd_2(NO_3)_4(\mathbf{3})_4\}\cdot 3CHCl_3]_n$ (Fig. 6a) is characterized by Cd···Cd distances in a range 12.502(3) to 13.063(3) Å and internal angles of 79.02(1), 99.89(1), 79.91(1) and 101.19(1)°. In the net in $[\{Cd_2(NO_3)_4(\mathbf{4})_4\}\cdot CHCl_3\cdot MeOH]_n$ (Fig. 7), each rhombus has Cd···Cd distances between 12.4678(9) and 12.771(1) Å and internal angles of 86.26(1), 92.31(1), 87.61(1) and 93.82(1)°. The bridging ligands **3** or **4** linking the Cd nodes project above and below the net (Fig. 6b), and adopt an up/up/up/down arrangement working around the four sides of the rhombus.

In $[\{Cd_2(NO_3)_4(\mathbf{3})_4\}\cdot 3CHCl_3]_n$ and $[\{Cd_2(NO_3)_4(\mathbf{4})_4\}\cdot CHCl_3\cdot MeOH]_n$, the (4,4) nets lie parallel to the *ab*-plane. The alkoxy chains are in extended or close to extended conformations and are directed approximately along the *c*-axis (Fig. 6b). This has the effect of locking the nets with the 4-membered macrocycles almost directly over one another as shown in Fig. 8 for $[\{Cd_2(NO_3)_4(\mathbf{3})_4\}\cdot 3CHCl_3]_n$. Pairs of pyridine rings (containing N2 and N5^{iv}, symmetry code iv = *x*, 1/2 − *y*, −1/2 + *z*) in ligands from adjacent sheets engage in efficient face-to-face π-stacking interactions; the angle between the least squares planes of the rings is 1.5° and ring-plane to centroid separation = 3.38 Å. (These parameters for the analogous interactions in $[\{Cd_2(NO_3)_4(\mathbf{4})_4\}\cdot CHCl_3\cdot MeOH]_n$ are 0.4° and 3.49 Å.) These interactions (two per macrocycle, Fig. 8b) are central to interlocking the sheets. The shortest Cd···Cd separations between sheets are 8.940(2) and 8.894(2) Å in $[\{Cd_2(NO_3)_4(\mathbf{3})_4\}\cdot 3CHCl_3]_n$, and 8.468(1) and 8.433(1) Å in $[\{Cd_2(NO_3)_4(\mathbf{4})_4\}\cdot CHCl_3\cdot MeOH]_n$; this places the 4′-phenyl substituents of ligands **3** or **4** within the (4,4) net defined by the Cd atoms (central part of Fig. 8a). Additional voids in the lattice are occupied by solvent molecules. SQUEEZE[30] was used to treat the solvent region; the rationalized solvent content in the structurally similar coordination networks in $[\{Cd_2(NO_3)_4(\mathbf{3})_4\}\cdot 3CHCl_3]_n$ and $[\{Cd_2(NO_3)_4(\mathbf{4})_4\}\cdot CHCl_3\cdot MeOH]_n$ is consistent with the greater spatial demands of ligand **4** *versus* **3**.

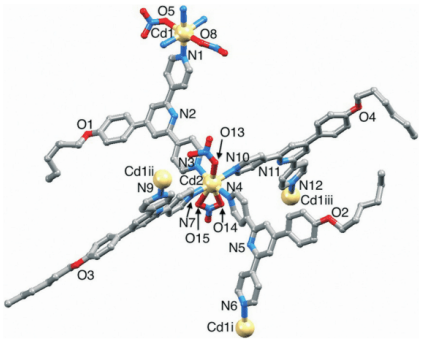

Fig. 5 The asymmetric unit (with symmetry generated atoms) in $[\{Cd_2(NO_3)_4(\mathbf{4})_4\}\cdot CHCl_3\cdot MeOH]_n$; H atoms and solvent molecules omitted. Symmetry codes: i = 1 + *x*, *y*, *z*; ii = 2 − *x*, −1/2 + *y*, 3/2 − *z*; iii = 2 − *x*, 1/2 + *y*, 3/2 − *z*.

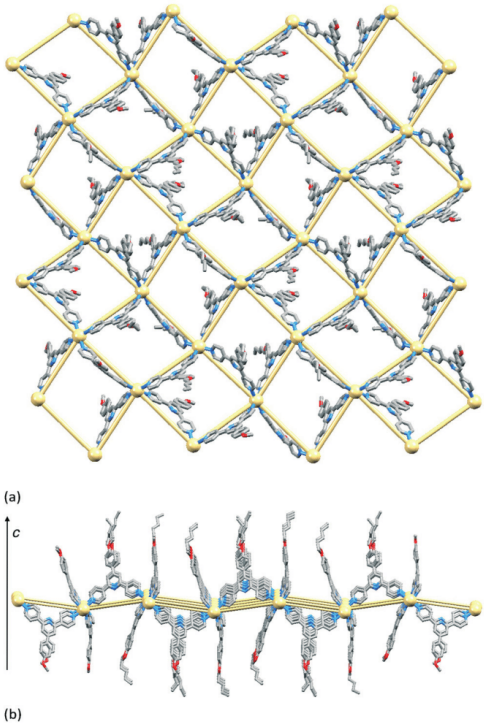

Fig. 6 (a) Superimposition of the structure and TOPOS representation of part of the (4,4) net in $[\{Cd_2(NO_3)_4(\mathbf{3})_4\}\cdot 3CHCl_3]_n$ viewed down the *c*-axis. (b) View down the *a*-axis showing projection of the ligands above and below the sheet. Nitrato ligands, H atoms and solvent molecules omitted.

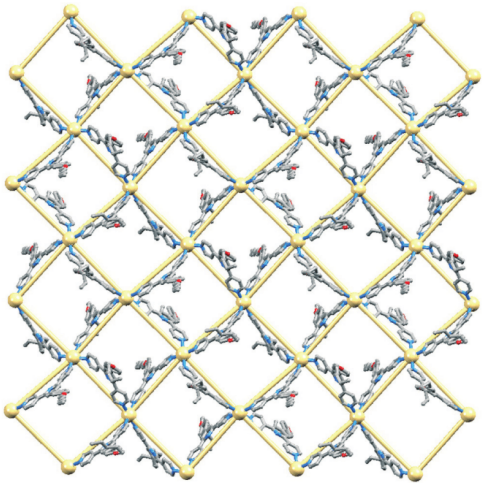

Fig. 7 Superimposition of the structure and TOPOS representation of part of the (4,4) net in $[\{Cd_2(NO_3)_4(\mathbf{4})_4\}\cdot CHCl_3\cdot MeOH]_n$ viewed down the *c*-axis. Nitrato ligands, H atoms and solvent molecules omitted.

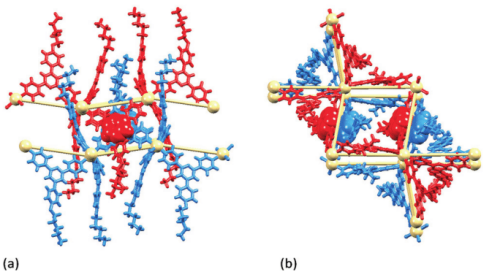

(a) (b)

Fig. 8 $[\{Cd_2(NO_3)_4(\mathbf{3})_4\}\cdot 3CHCl_3]_n$: (a) view down the *a*-axis of part of two sheets (red and blue, Cd atoms and net in TOPOS representation) showing π-stacking between two 4,2′:6′,4″-tpy domains in space filling representation; (b) the same unit viewed down the *c*-axis showing approximate superimposition of 4-membered macrocycles in adjacent nets.

n-Hexoxy to *n*-heptoxy tails and a switch from *trans*- to *cis*-coordination

The effects of further chain lengthening were investigated by treating $Cd(NO_3)_2\cdot 4H_2O$ with ligand **5** which contains an *n*-heptoxy tail (Scheme 3). X-ray quality crystals grown under the same conditions as those with ligands **2**–**4** proved to be $[\{Cd(NO_3)_2(\mathbf{5})_2\}\cdot 2MeOH]_n$. The powder diffraction data shown in Fig. S4† are consistent with the single crystal being representative of the bulk sample.

As in the (4,4) networks with ligands **3** and **4**, the Cd atom in $[\{Cd(NO_3)_2(\mathbf{5})_2\}\cdot 2MeOH]_n$ is octahedrally sited and is coordinated by four 4,2′:6′,4″-tpy and two nitrato ligands. However, the nitrato groups are mutually *cis* (Fig. 9a), in contrast to *trans*-arrangements in $[\{Cd_2(NO_3)_4(\mathbf{3})_4\}\cdot 3CHCl_3]_n$ and $[\{Cd_2(NO_3)_4(\mathbf{4})_4\}\cdot CHCl_3\cdot MeOH]_n$. Bond parameters for the coordination sphere are given in the caption to Fig. 9a. The alkoxy chain with O1 is in a fully extended conformation while that with O2 is folded out of the plane of the phenyl ring to which it is bonded. The Cd atoms act as 4-connecting nodes and assemble into a (4,4) net. Compared to the up/up/up/down arrangement of bridging ligands around each 4-membered metallomacrocycle in $[\{Cd_2(NO_3)_4(\mathbf{3})_4\}\cdot 3CHCl_3]_n$ and $[\{Cd_2(NO_3)_4(\mathbf{4})_4\}\cdot CHCl_3\cdot MeOH]_n$, those in $[\{Cd(NO_3)_2(\mathbf{5})_2\}\cdot 2MeOH]_n$ adopt an up/down/up/down arrangement (Fig. 9b). The two independent Cd···Cd distances within the (4,4) net are 12.938(2) and 12.630(2) Å. The Cd nodes in each net lie in a plane (deviation is ±0.1 Å); the sheets stack over one another (Fig. 10a) and the shortest Cd···Cd separations are 8.566(2) and 8.950(2) Å.

Fig. 10b shows a superimposition of the structure and TOPOS representation of part of one (4,4) net in $[\{Cd(NO_3)_2(\mathbf{5})_2\}\cdot 2MeOH]_n$. A comparison of this with Fig. 6a and 7 illustrates that both *cis* and *trans*-arrangements of nitrato ligands lead to cavities in the network through which long alkoxy chains from the next sheet can penetrate. This is shown for $[\{Cd(NO_3)_2(\mathbf{5})_2\}\cdot 2MeOH]_n$ in Fig. 11a. Just as in $[\{Cd_2(NO_3)_4(\mathbf{3})_4\}\cdot 3CHCl_3]_n$ and $[\{Cd_2(NO_3)_4(\mathbf{4})_4\}\cdot CHCl_3\cdot MeOH]_n$, 4,2′:6′,4″-tpy domains in adjacent sheets interact through π-stacking of the central pyridine rings (Fig. 11b). The angle between the least squares planes of the rings containing N2 ad $N5^{i}$ (symmetry code i = 1 − *x*, 1 − *y*, 1 − *z*) is 5.4° and the ring-plane to centroid separation is 3.57 Å. This type of interaction is found in a range of coordination polymers involving 4,2′:6′,4″-tpy ligands.[10] Fig. 11b also shows that the depth of penetration of one sheet into the next is such that the 4-phenyl substituent in ligand **5** lies within the (4,4) net of Cd atoms. Again this mimics the situation in the networks involving ligands **3**

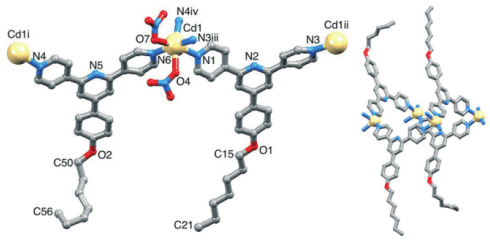

(a) (b)

Fig. 9 (a) The asymmetric unit (with symmetry generated atoms) in $[\{Cd(NO_3)_2(\mathbf{5})_2\}\cdot 2MeOH]_n$; H atoms and solvent molecules omitted. Symmetry codes: i = 1/2 − *x*, −1/2 + *y*, 1/2 − *z*; ii = 1/2 − *x*, 1/2 + *y*, 3/2 − *z*; iii = 1/2 − *x*, −1/2 + *y*, 3/2 − *z*; iv = 1/2 − *x*, 1/2 + *y*, 1/2 − *z*. Selected bond parameters: Cd1–O4 = 2.363(8), Cd1–O6 = 3.030(10), Cd1–O7 = 2.440(8), Cd1–N1 = 2.399(9), Cd1–$N3^{iii}$ = 2.317(8), Cd1–$N4^{iv}$ = 2.359(9), Cd1–N6 = 2.341(8) Å; O4–Cd1–O7 = 86.0(3); N1–Cd1–N6 = 98.7(3), O7–Cd1–N1 = 165.2(3), O4–Cd1–$N4^{iv}$ = 163.2(3)°. (b) One 4-membered metallomacrocyclic unit with up/down/up/down arrangement of ligands **5**.

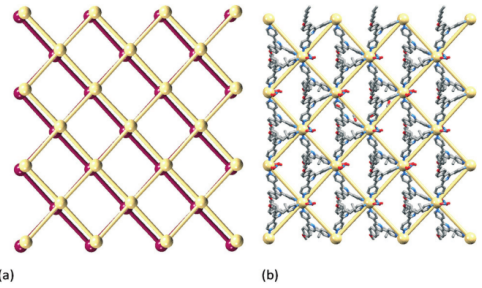

(a) (b)

Fig. 10 Structure of $[\{Cd(NO_3)_2(\mathbf{5})_2\}\cdot 2MeOH]_n$ (viewed down the *a*-axis): (a) TOPOS representation of adjacent (4,4) nets; (b) superimposition of the structure and TOPOS representation of part of one (4,4) net; H atoms and solvent molecules omitted.

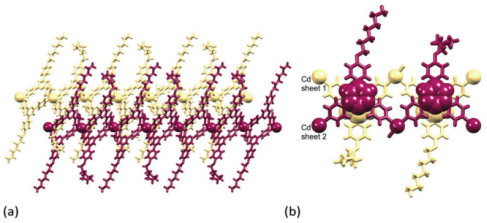

(a) (b)

Fig. 11 (a) Penetration of 4-alkoxyphenyl units of one sheet through the 4-membered metallocycles of an adjacent sheet in $[\{Cd(NO_3)_2(\mathbf{5})_2\}\cdot 2MeOH]_n$. (b) π-stacking between two 4,2′:6′,4″-tpy domains (space filling representation) in adjacent sheets.

and **4**, and leads to a similar inter-sheet separation; shortest Cd···Cd distances between nets are 8.566(2) and 8.950(2) Å with ligand **5** *versus* 8.940(2) and 8.894(2) Å with **3**, and 8.468(1) and 8.433(1) Å with **4**. Thus, despite the change in the local environment at the Cd centre on going from a *trans*- to *cis*-ligand arrangement, the packing interactions between the sheets remain similar.

A change in the ratio of cadmium : ligand

For the coordination networks described above, the ratio of cadmium : ligand in the crystallization experiments was 1 : 3 leading to networks with a 2 : 3 ratio of Cd : ligand **2**, or 1 : 2 for ligands **3**, **4** or **5**. For the hexoxy-tailed ligand **4**, a crystallization experiment was also run with a 1 : 1 ratio of Cd : ligand. Structural analysis (see Fig. S5† for powder diffraction data) revealed the formation of the 1-dimensional coordination polymer $[Cd_2(NO_3)_4(MeOH)(\mathbf{4})_3]_n$ which crystallizes in the triclinic space group $P\bar{1}$, and possesses a ladder structure (Fig. 12 and S6†). The structure is similar to that found for $[\{Cd_2(NO_3)_4(\mathbf{1})_3\}\cdot CHCl_3\cdot MeOH]_n$.[23] The asymmetric unit contains two independent Cd atoms and three independent ligands **4**. Atom Cd1 is 8-coordinate (Fig. 12), binding to three 4,2′:6′,4″-tpys (Cd1–N1 = 2.316(3), Cd1–N4 = 2.359(4),

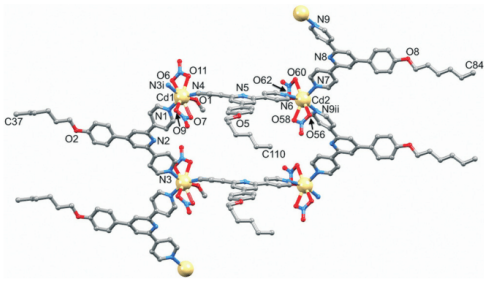

Fig. 12 Building block in the polymer chain in $[Cd_2(NO_3)_4(MeOH)(\mathbf{4})_3]_n$. Atoms in the asymmetric unit are labelled; symmetry codes: i = −1 + *x*, *y*, *z*; ii = 1 + *x*, *y*, *z*. Hydrogen atoms are omitted for clarity.

Cd1–$N3^i$ = 2.340(3) Å), an MeOH molecule (Cd1–O1 = 2.428(3) Å) and two bidentate nitrato ligands, although one Cd–O contact is long (Cd1–O6 = 2.754(4), Cd1–O7 = 2.518(4), Cd1–O9 = 2.541(4), Cd1–O11 = 2.421(3) Å). Atom Cd2 is 7-coordinate (Fig. 12), coordinated by three 4,2′:6′,4″-tpys (Cd2–$N9^{ii}$ = 2.313(4), Cd2–N6 = 2.347(3), Cd2–N7 = 2.302(4) Å) and two bidentate nitrato groups (Cd2–O56 = 2.458(3), Cd2–O58 = 2.455(4), Cd2–O60 = 2.626(4), Cd2–O62 = 2.361(3) Å). The three N-donors at each Cd centre are in a T-shaped arrangement (angles $N3^i$–Cd1–N1 = 104.91(12) and $N3^i$–Cd1–N4 = 93.72(13), $N9^{ii}$–Cd2–N7 = 103.53(13) and N6–Cd2–N7 = 92.16(13)°).

Although topologically the ladders in $[\{Cd_2(NO_3)_4(\mathbf{1})_3\}\cdot CHCl_3\cdot MeOH]_n$ and $[Cd_2(NO_3)_4(MeOH)(\mathbf{4})_3]_n$ are the same, the internal angles of each rhombus in the ladder as defined by the ligand-bridged Cd nodes are 82 and 98° in $[Cd_2(NO_3)_4(MeOH)(\mathbf{4})_3]_n$ (Fig. 13 and S6†), and 27.3 and 152.7° in $[\{Cd_2(NO_3)_4(\mathbf{1})_3\}\cdot CHCl_3\cdot MeOH]_n$ (Fig. 14). The rails (vertical in Fig. 13 and 14) of the ladder are slipped with respect to one another on going from **4** to **1**, and the closest Cd···Cd separation across the ladder decreases from 13.0025(8) Å (ligand-bridged) in

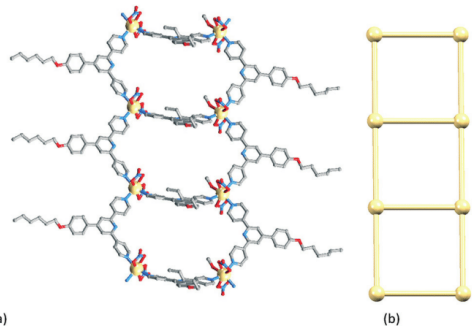

(a) (b)

Fig. 13 (a) Part of the 1-dimensional coordination polymer in $[Cd_2(NO_3)_4(MeOH)(\mathbf{4})_3]_n$ and (b) TOPOS representation of part of the ladder.

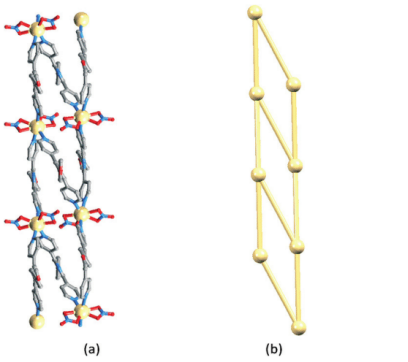

Fig. 14 (a) Part of the 1-dimensional coordination polymer in $[\{Cd_2(NO_3)_4(\mathbf{1})_3\}\cdot CHCl_3\cdot MeOH]_n$ and (b) TOPOS representation of part of a ladder.

$[Cd_2(NO_3)_4(MeOH)(\mathbf{4})_3]_n$ to 6.094(1) Å (unbridged) in $[\{Cd_2(NO_3)_4(\mathbf{1})_3\}\cdot CHCl_3\cdot MeOH]_n$.[23] The ladder conformation shown in Fig. 14b is also seen in $[\{Cd_2(NO_3)_4\ \mathbf{L}_3\}\cdot 4MeOH\cdot 2CHCl_3]_n$ and $[\{Cd_2(NO_3)_4\ \mathbf{L}_3\}\cdot 2MeOH\cdot 3CHCl_3\cdot H_2O]_n$ in which **L** = 4′-(4-MeSC$_6$H$_4$)-4,2′:6′,4″-tpy or 4′-(4-HC≡CC$_6$H$_4$)-4,2′:6′,4″-tpy.[24] A comparison of Fig. 13a and 14a reveals that the ligands defining the rails of the ladder in $[Cd_2(NO_3)_4(MeOH)(\mathbf{4})_3]_n$ (Fig. 13) point outwards from the ladder-framework, in contrast to their orientation in the ladder type found for $[\{Cd_2(NO_3)_4(\mathbf{1})_3\}\cdot CHCl_3\cdot MeOH]_n$ and its analogues.[23,24] Primary packing forces between adjacent coordination polymer chains involve both π-stacking and van der Waals interactions. Adjacent ladders in $[Cd_2(NO_3)_4(MeOH)(\mathbf{4})_3]_n$ interact through a centrosymmetric face-to-face π-stacking of the central pyridine rings of the ligands **4** forming the rungs of the ladder (Fig. 15); the distance between the N5- and N5^{iii}-containing ring planes (symmetry code iii = $-x$, $1-y$, $1-z$) is 3.39 Å and the inter-centroid separation is 3.55 Å. The alkoxy chains containing atoms O2 and O8 are in fully extended conformations and chains from adjacent ladders interdigitate with one another as shown in Fig. 15. The terminal methyl group of each 4-hexoxyphenyl unit lies over the arene ring of the next substituent giving a head-to-tail embrace; both independent $C_{Me}\cdots centroid_{arene}$ distances are 3.78 Å. Extension of the packing motif in Fig. 15 generates sheets which are locked together by penetration of the protruding, folded hexoxy chains into cavities in the next sheet.

Fig. 15 Four ladders in $[Cd_2(NO_3)_4(MeOH)(\mathbf{4})_3]_n$ viewed down the *a*-axis showing π-stacking interactions and interdigitation between 4-hexoxyphenyl substituents between adjacent polymer chains.

Solid-state photoluminescence

Protonation of 2,2′:6′,2″-terpyridine (2,2′:6′,2″-tpy) significantly enhances the photoluminescence (PL) of the ligand in MeCN solution, leading to a red-shift in λ_{max}^{em} from 340 nm to 412 nm, and an increase in quantum yield (QY) from <0.1% to 5.2%.[31] Diprotonation results in a further increase in QY.[32] It has also been observed that in the solid state, amorphous 2,2′:6′,2″-tpy and needle-like crystals (melting point 86–88 °C) are non-emissive, while plate-like crystals (melting point 91–93 °C) are photoluminescent (λ_{max}^{em} = 365 nm) with QY = 20% and an emission lifetime of 4.5 ns.[33] The emission maxima (Fig. 16) and PL quantum yields of crystalline **2**–**4** are given in Table 1. All are blue emitters, with QY values ranging from 15 to 27%; the emission lifetimes are <10 ns. Incorporation of the alkoxy-substituent red-shifts the emission with respect to that of solid 4′-phenyl-4,2′:6′,4″-terpyridine; the latter emits weakly (λ_{max}^{em} = 370 nm) when excited at 345 nm.[34] Note that Hou and Li have reported that solid 4′-phenyl-4,2′:6′,4″-terpyridine exhibits a strong green PL (λ_{max}^{em} = 517 nm, λ_{exc} = 400 nm).[35]

Fig. 16 shows the emission spectra of solid samples of $[\{Cd_2(NO_3)_4(\mathbf{2})_3\}\cdot 3CHCl_3]_n$, $[\{Cd_2(NO_3)_4(\mathbf{3})_4\}\cdot 3CHCl_3]_n$ and $[\{Cd_2(NO_3)_4(\mathbf{4})_4\}\cdot CHCl_3\cdot MeOH]_n$ (all 2-dimensional networks) and of $[Cd_2(NO_3)_4(MeOH)(\mathbf{4})_3]_n$ (a 1-dimensional ladder). With the exception of $[\{Cd_2(NO_3)_4(\mathbf{4})_4\}\cdot CHCl_3\cdot MeOH]_n$, the emission broadens and shifts to lower energy on going from free ligand to complex, but remains in the blue region. Similar red-shifts have been reported when N-donor ligands coordinate to zinc(II) or cadmium(II), and the emissions are assigned to intra-ligand transitions.[34,36] On going from **4** to $[\{Cd_2(NO_3)_4(\mathbf{4})_4\}\cdot CHCl_3\cdot MeOH]_n$, the emission band broadens but λ_{em}^{max} remains at 420 nm. The formation of the coordination polymers incorporating **2**, **3** or **4** has little effect on the QYs compared to those of the free ligands, and for each complex, the emission lifetime is <10 ns.

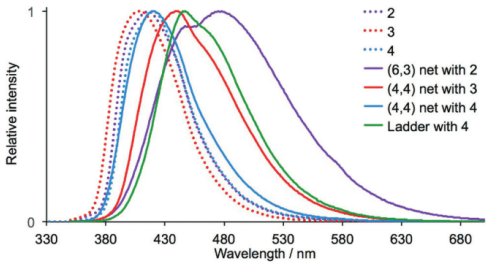

Fig. 16 Solid-state emission spectra of ligands **2**–**4** (dotted lines) and of the 2-dimensional coordination networks $[\{Cd_2(NO_3)_4(\mathbf{2})_3\}\cdot 3CHCl_3]_n$ (solid purple line), $[\{Cd_2(NO_3)_4(\mathbf{3})_4\}\cdot 3CHCl_3]_n$ (solid red line) and $[\{Cd_2(NO_3)_4(\mathbf{4})_4\}\cdot CHCl_3\cdot MeOH]_n$ (solid blue line), and of the 1-dimensional ladder $[Cd_2(NO_3)_4(MeOH)(\mathbf{4})_3]_n$ (green curve). (λ_{exc} = 280 nm).

Table 1 Photoluminescence of **2**–**4** and their coordination networks in the solid state

Compound	λ_{exc}/nm	λ_{em}^{max}/nm	QY/%
2	280	416	15
3	280	408	27
4	280	420	17
$[\{Cd_2(NO_3)_4(\mathbf{2})_3\}\cdot 3CHCl_3]_n$	280	475	11
$[\{Cd_2(NO_3)_4(\mathbf{3})_4\}\cdot 3CHCl_3]_n$	280	440	22
$[\{Cd_2(NO_3)_4(\mathbf{4})_4\}\cdot CHCl_3\cdot MeOH]_n$	280	420	13
$[Cd_2(NO_3)_4(MeOH)(\mathbf{4})_3]_n$	280	447	18

Conclusions

The divergent *N*,*N*-binding mode of 4,2′:6′,4″-terpyridines is readily exploited for the formation of coordination polymers and networks, but determining factors that can encourage the formation of 2- and 3-dimensional networks remains under-developed. In this work, we have demonstrated the structural consequences of increasing the length of the alkoxy substituent in 4′-alkoxy-4,2′:6′,4″-terpyridines when these ligands combine with $Cd(NO_3)_2\cdot 4H_2O$ with a Cd : ligand ratio of 1 : 3. Ligand **2** contains a 4′-*n*-propoxy substituent and forms $[\{Cd_2(NO_3)_4(\mathbf{2})_3\}\cdot 3CHCl_3]_n$ consisting of a (6,3) net. *n*-Propoxy chains protrude from the sheet and are involved in 'tail-in-pocket' interactions which interlock the sheets. Although preliminary data indicate that an *n*-butoxy chain causes no major structural perturbation, introduction of longer chains cause a switch from a (6,3) to (4,4) net. The change is consistent with the pockets in which the smaller chains are accommodated when (6,3) sheets pack together are too small to accommodate longer chains. In $[\{Cd_2(NO_3)_4(\mathbf{3})_4\}\cdot 3CHCl_3]_n$ and $[\{Cd_2(NO_3)_4(\mathbf{4})_4\}\cdot CHCl_3\cdot MeOH]_n$ each 4-connecting Cd atom has a *trans*-arrangement of nitrato ligands, while in $[\{Cd(NO_3)_2(\mathbf{5})_2\}\cdot 2MeOH]_n$, they are *cis*. The reaction between $Cd(NO_3)_2\cdot 4H_2O$ and **4** using a 1 : 1 ratio of Cd : ligand switches the assembly to a 1-dimensional ladder; in $[Cd_2(NO_3)_4(MeOH)(\mathbf{4})_3]_n$ each Cd atom is a 3-connecting node. Face-to-face π-interactions between arene rings (either pyridine/pyridine or pyridine/phenyl) in adjacent sheets or chains are a common feature of the coordination networks, and van der Waals interactions between *n*-hexoxy chains play a dominant role in the packing of ladders in $[Cd_2(NO_3)_4(MeOH)(\mathbf{4})_3]_n$. In the solid state, the coordination polymers are blue emitters; values of λ_{em}^{max} are red-shifted up to 59 nm with respect to the free ligand, and quantum yields are in the range 11–22%.

Acknowledgements

We thank the Swiss National Science Foundation, the European Research Council (Advanced Grant 267816 LiLo) and the University of Basel for financial support. The Swiss National Science Foundation through the NCCR Molecular Systems Engineering is acknowledged for partial funding of the powder diffractometer. Dr Collin D. Morris is thanked for assistance with powder diffraction and photoluminescence measurements.

Notes and references

1 P. J. Stang and B. Olenyuk, *Acc. Chem. Res.*, 1997, **30**, 502.
2 S. Leininger, B. Olenyuk and P. J. Stang, *Chem. Rev.*, 2000, **100**, 853.
3 S. R. Seidel and P. J. Stang, *Acc. Chem. Res.*, 2002, **35**, 972.
4 B. H. Northrop, H. B. Yang and P. J. Stang, *Chem. Commun.*, 2008, 5896.
5 M. Yoshizawa, J. K. Klosterman and M. Fujita, *Angew. Chem., Int. Ed.*, 2009, **48**, 3418.
6 E. C. Constable in *Supramolecular Chemistry: From Molecules to Nanomaterials*, ed. P. A. Gale and J. W. Steed, Wiley, 2012, vol. 6, p. 3073.
7 M. O'Keefe and O. M. Yaghi, *Chem. Rev.*, 2012, **112**, 675.
8 E. C. Constable, *Pure Appl. Chem.*, 1996, **68**, 253.
9 E. C. Constable, *Chem. Soc. Rev.*, 2007, **36**, 246.
10 C. E. Housecroft, *Dalton Trans.*, 2014, **43**, 6594.
11 X. Tan, X. Chen, J. Zhang and C.-Y. Song, *Dalton Trans.*, 2012, **41**, 3616; L. Wen, X. Ke, L. Qiu, Y. Zou, L. Zhou, J. Zhao and D. Li, *Cryst. Growth Des.*, 2012, **12**, 4083; W. Yang, A. J. Davies, X. Lin, M. Suyetin, R. Matsuda, A. J. Blake, C. Wilson, W. Lewis, J. E. Parker, C. C. Tang, M. W. George, P. Hubberstey, S. Kitagawa, H. Sakamoto, E. Bichoutskaia, N. R. Champness, S. Yang and M. Schröder, *Chem. Sci.*, 2012, **3**, 2992; Y.-Q. Chen, S.-J. Liu, Y.-W. Li, G.-R. Li, K.-H. He, Y.-K. Qu, T.-L. Hu and X.-H. Bu, *Cryst. Growth Des.*, 2012, **12**, 5426; P. Yang, M.-S. Wang, J.-J. Shen, M.-X. Li, Z.-X. Wang, M. Shao and X. He, *Dalton Trans.*, 2014, **43**, 1460; Y.-L. Gai, F.-L. Jiang, L. Chen, Y. Bu, M.-Y. Wu, K. Zhou, J. Pan and M.-C. Hong, *Dalton Trans.*, 2013, **42**, 9954; Y.-Q. Chen, G.-R. Li, Y.-K. Qu, Y.-H. Zhang, K.-H. He, Q. Gao and X.-H. Bu, *Cryst. Growth Des.*, 2013, **13**, 901; Y. Li, Z. Ju, B. Wu and D. Yuan, *Cryst. Growth Des.*, 2013, **13**, 4125; F. Yuan, J. Xie, H.-M. Hu, C.-M. Yuan, B. Xu, M.-L. Yang, F.-X. Dong and G.-L. Xue, *CrystEngComm*, 2013, **15**, 1460; F. Yuan, Q. Zhu, H.-M. Hu, J. Xie, B. Xu, C.-M. Yuan, M.-L. Yang, F.-X. Dong and G.-L. Xue, *Inorg. Chim. Acta*, 2013, **397**, 117; H.-N. Zhang, F. Yuan, H.-M. Hu, S.-S. Shen and G.-L. Xue, *Inorg. Chem. Commun.*, 2013, **34**, 51; E. C. Constable, G. Zhang, C. E. Housecroft and J. A. Zampese, *CrystEngComm*, 2011, **13**, 6864; J. Heine, J. Schmedt auf der Günne and S. Dehnen, *J. Am. Chem. Soc.*, 2011, **133**, 10018; V. N. Dorofeeva, S. V. Kolotilov, M. A. Kiskin, R. A. Polunin, Z. V. Dobrokhotova, O. Cador, S. Golhen, L. Ouahab, I. L. Eremenko and V. M. Novotortsev, *Chem. – Eur. J.*, 2012, **18**, 5006; K.-R. Ma, F. Ma, Y.-L. Zhu, L.-J. Yu, X.-M. Zhao, Y. Yang and W.-H. Duan, *Dalton Trans.*, 2011, **40**, 9774.
12 E. C. Constable, C. E. Housecroft, P. Kopecky, M. Neuburger, J. A. Zampese and G. Zhang, *CrystEngComm*, 2012, **14**, 446.
13 E. C. Constable, G. Zhang, C. E. Housecroft and J. A. Zampese, *Inorg. Chem. Commun.*, 2012, **15**, 113.
14 Y. M. Klein, E. C. Constable, C. E. Housecroft, J. A. Zampese and A. Crochet, *CrystEngComm*, 2014, **16**, 9915.

15 E. C. Constable, C. E. Housecroft, S. Vujovic and J. A. Zampese, *CrystEngComm*, 2014, **16**, 3494.
16 Y. M. Klein, E. C. Constable, C. E. Housecroft and A. Prescimone, *CrystEngComm*, 2015, **17**, 2070.
17 E. C. Constable, C. E. Housecroft, M. Neuburger, J. Schönle, S. Vujovic and J. A. Zampese, *Polyhedron*, 2013, **60**, 120.
18 E. C. Constable, G. Zhang, E. Coronado, C. E. Housecroft and M. Neuburger, *CrystEngComm*, 2010, **12**, 2139.
19 E. C. Constable, C. E. Housecroft, S. Vujovic, J. A. Zampese, A. Crochet and S. R. Batten, *CrystEngComm*, 2013, **15**, 10068.
20 V. Auger and I. Robin, *Comptes Rendus*, 1924, **178**, 1546.
21 O. M. Yaghi, M. O'Keeffe, N. W. Ockwig, H. K. Chae, M. Eddaoudi and J. Kim, *Nature*, 2003, **423**, 705.
22 E. C. Constable, G. Zhang, C. E. Housecroft, M. Neuburger and J. A. Zampese, *CrystEngComm*, 2009, **11**, 2279.
23 Y. M. Klein, E. C. Constable, C. E. Housecroft and A. Prescimone, *Inorg. Chem. Commun.*, 2014, **49**, 41.
24 E. C. Constable, G. Zhang, C. E. Housecroft, M. Neuburger and J. A. Zampese, *CrystEngComm*, 2010, **12**, 3733.
25 *APEX2, version 2 User Manual, M86-E01078*, Bruker Analytical X-ray Systems, Inc., Madison, WI, 2006.
26 P. W. Betteridge, J. R. Carruthers, R. I. Cooper, K. Prout and D. J. Watkin, *J. Appl. Crystallogr.*, 2003, **36**, 1487.
27 I. J. Bruno, J. C. Cole, P. R. Edgington, M. K. Kessler, C. F. Macrae, P. McCabe, J. Pearson and R. Taylor, *Acta Crystallogr., Sect. B: Struct. Sci.*, 2002, **58**, 389.
28 C. F. Macrae, I. J. Bruno, J. A. Chisholm, P. R. Edgington, P. McCabe, E. Pidcock, L. Rodriguez-Monge, R. Taylor, J. van de Streek and P. A. Wood, *J. Appl. Crystallogr.*, 2008, **41**, 466.
29 V. A. Blatov and A. P. Shevchenko, *TOPOS Professional v. 4.0*, Samara State University, Russia.
30 A. L. Spek, *Acta Crystallogr., Sect. D: Biol. Crystallogr.*, 2009, **65**, 148.
31 N. Yoshikawa, S. Yamabe, N. Kanehisa, H. Takashima and K. Tsukahara, *J. Phys. Org. Chem.*, 2009, **22**, 410.
32 N. Yoshikawa, S. Yamabe, N. Kanehisa, T. Inoue, H. Takashima and K. Tsukahara, *J. Phys. Org. Chem.*, 2010, **23**, 431.
33 T. Mutai, H. Satou and K. Araki, *Nat. Mater.*, 2005, **4**, 685.
34 E. C. Constable, G. Zhang, C. E. Housecroft, M. Neuburger and J. A. Zampese, *CrystEngComm*, 2010, **12**, 2146.
35 L. Hou and D. Li, *Inorg. Chem. Commun.*, 2005, **8**, 190.
36 See for example: W. Li, H.-P. Jia, Z.-F. Ju and J. Zhang, *Cryst. Growth Des.*, 2006, **6**, 2136; G.-X. Jin, J.-P. Ma and Y.-B. Dong, *J. Mol. Struct.*, 2013, **1052**, 146; C.-M. Che, C.-W. Wan, K.-Y. Ho and Z.-Y. Zhou, *New J. Chem.*, 2001, **25**, 63.

18.7 Paper 7 (Published by Elsevier)

Inorganic Chemistry Communications 70 (2016) 118–120

Contents lists available at ScienceDirect

Inorganic Chemistry Communications

journal homepage: www.elsevier.com/locate/inoche

Short communication

A double-stranded 1D-coordination polymer assembled using the tetravergent ligand 1,1′-*bis*(4,2′:6′,4″-terpyridin-4′-yl)ferrocene

Y. Maximilian Klein, Alessandro Prescimone, Edwin C. Constable, Catherine E. Housecroft *

Department of Chemistry, University of Basel, Spitalstrasse 51, CH 4056, Basel, Switzerland

ARTICLE INFO

Article history:
Received 2 May 2016
Accepted 28 May 2016
Available online 31 May 2016

Keywords:
X-ray
1D-coordination polymer
Zinc
Ferrocene
Double-stranded chain

ABSTRACT

1,1′-Bis(4,2′:6′,4″-terpyridin-4′-yl)ferrocene (**1**) reacts with $ZnCl_2$ to yield a double-stranded 1D-coordination polymer $[\{Zn_2(\mathbf{1})Cl_4\}\cdot 3CHCl_3]_n$. The 1,1′-functionalized ferrocene core adopts a *cisoid*-conformation, giving rise to a folded conformation for **1** and a double-stranded 1D-polymer chain. This contrasts with previously reported multi-stranded chains supported by 4,2′:6′,4″-terpyridine ligands in which the multiple-nature of the chain arises from multinuclear metal nodes.

The use of polytopic ligands is a powerful strategy for directing the assembly of metallomacrocycles and coordination polymers and networks [1]. We have shown that 3,2′:6′,3″- or 4,2′:6′,4″-terpyridines (tpy) are versatile divergent polytopic ligands in which each terminal pyridyl ring can coordinate a different metal centre. The combination of multiple tpy domains generates new tectons [2] for the assembly of 2D-networks, interpenetrating 2D → 2D parallel interpenetrated networks, and 3D-frameworks [3–5]. In these examples to date, the 3,2′:6′,3″- or 4,2′:6′,4″-tpy domains are connected by a phenylene spacer; rotation about the C_{phenyl}–C_{tpy} bonds leads to these polytopic ligands being able to act as planar or $C_2$4-connecting nodes (Scheme 1). Additional rotational freedom can be introduced by using organometallic sandwich units as connectors, the archetype of which is ferrocene [6,7]. Despite the variety of known 1,1′-ferrocenyl-centred polytopic ligands [6,7], few exhibit pyridine or polypyridine metal-binding domains. Braga et al. have investigated the coordination behaviour of 1,1′-bis(pyridin-4-yl)ferrocene, demonstrating that a *cisoid*-conformation is favoured leading to discrete molecular rather than polymeric assemblies [8,9]. 1,1′-Bis(pyridin-2-yl)ferrocene and its permethylated analogue act as *N*,*N*′-chelates to Cu^+ and Pd^{2+} [10–12], or can bind two metal centres in discrete complexes [12]. Here we report the first example of a polytopic bis(4,2′:6′,4″-terpyridine) ligand containing a 1,1′-ferrocenyl spacer and its reaction with $ZnCl_2$ to give an unusual double-chain 1D-coordination polymer.

Compound **1** (Scheme 2) was prepared according to the method reported by Wang and Hanan [13] and is poorly soluble in most organic solvents, although enough material dissolved in $CDCl_3$ to permit a ^1H NMR spectrum to be recorded [14]. The ferrocenyl unit is characterized by two multiplets (δ 4.85 and 4.59 ppm) of equal intensity, consistent with functionalization on each cyclopentadienyl ring. Signals for the tpy domain [14] were also consistent with the structure shown in Scheme 2. In the MALDI mass spectrum, the highest mass peak envelope at *m*/*z* 649.52 was assigned to $[M + H]^+$.

Red crystals of $[\{Zn_2(\mathbf{1})Cl_4\}\cdot 3CHCl_3]_n$ were obtained from reaction of $ZnCl_2$ with **1** under room temperature crystallization conditions [15]. The very poor solubility of **1** resulted in a suspension in $CHCl_3$ rather than a solution of the free ligand being used, and insufficient bulk material of the product for powder diffraction or elemental analysis was obtained. Single-crystal structure determination [16] revealed the

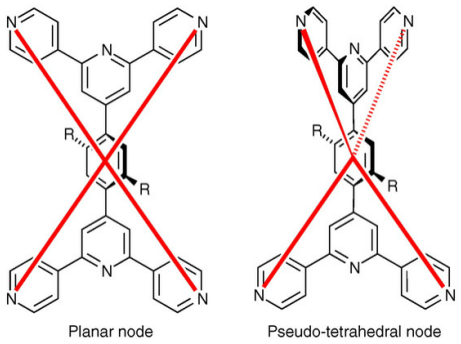

Scheme 1. Limiting topographies of 4-connecting nodes featuring polytopic 4,2′:6′,4″-tpy ligands with phenyl spacers (see references [3–5] for R).

* Corresponding author.
E-mail address: catherine.housecroft@unibas.ch (C.E. Housecroft).

http://dx.doi.org/10.1016/j.inoche.2016.05.027
1387-7003/

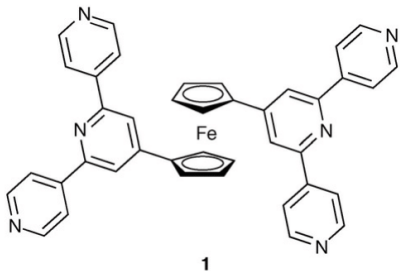

Scheme 2. Structure of ligand **1**.

formation of the coordination polymer $[\{Zn_2(\mathbf{1})Cl_4\}\cdot 3CHCl_3]_n$. The complex crystallizes in the monoclinic space group $P2_1/n$, and Fig. 1 shows the asymmetric unit which contains two independent Zn atoms (each tetrahedrally coordinated) and two halves of two ligands **1**. As expected [17], the 4,2′:6′,4″-tpy unit binds the Zn centres only through the outer pyridine rings. The second half of each ligand is generated by a 2-fold screw axis, with **1** adopting a *cisoid*-conformation. Bond lengths (caption to Fig. 1) and angles in the coordination spheres of Zn1 and Zn2 and in the ferrocene unit are typical.

The *cisoid*-conformation of **1** results in a double-stranded chain, with tpy units in the same ligand lying over the top of each other (Fig. 2). However, each tpy domain is significantly bowed, and only the central pyridine rings of the two tpy units are able to engage in face-to-face π-stacking (centroid...centroid separation = 3.60 Å and centroid...ring-plane distance = 3.35 Å). Double-stranded chains have previously been observed for $[Cd_2(OAc)_4(4'\text{-(biphenyl-4-yl)-4,2':6',4''-tpy})_2]_n$ [18], but in this case, the origin of the double-strands is the presence of dinuclear $\{Cd_2(OAc)_4\}$ nodes, each node binding four separate 4,2′:6′,4″-tpy ligands. Similarly, in $[Mn_3(OAc)_6(4'\text{-(4-Br}C_6H_4)\text{-4,2':6',4''-tpy})_3]_n$, trinuclear $\{Mn_3(OAc)_6\}$ nodes gives rise to a triple-stranded chain [19], and in $[\{Zn_5(OAc)_{10}(4'\text{-(pentafluorobiphenyl-4-yl)-4,2':6',4''-tpy})\}\cdot 11H_2O]_n$, $\{Zn_5(OAc)_{10}\}$ nodes lead to an unusual quadruple-stranded chain [20]. The assembly of $[\{Zn_2(\mathbf{1})Cl_4\}\cdot 3CHCl_3]_n$ is, to the best of our knowledge, the first example of a 1D-coordination polymer with 4,2′:6′,4″-tpy ligand linkers in which a bis(4,2′:6′,4″-tpy) presents a folded conformation to generate a double-stranded chain. The closest Zn...Zn separation across the chain is 4.678(1) Å. Atoms C13 and C14 of one $ZnCl_2$ unit face atom Zn1 across the chain (Fig. 2) but the Zn1...Cl3 and Zn1...Cl4 distances of 4.291(2) and 4.155(2) Å are too long to be considered meaningful interactions.

The double-stranded chains propagate along the *b*-axis, with their zig-zag form (Fig. 3) arising from the V-shape of the 4,2′:6′,4″-tpy domains. Adjacent chains nest together forming sheets, but, in contrast to related structures [17–21], there are no close contacts between neighbouring chains (coloured blue in Fig. 3a). This results in void space which is occupied by $CHCl_3$ molecules.

In conclusion, the ferrocenyl-centred polytopic ligand **1** exhibits a folded conformation in the 1D-coordination polymer $[\{Zn_2(\mathbf{1})Cl_4\}\cdot 3CHCl_3]_n$ leading to a double-stranded zigzag chain. This contrasts with previously reported multiply-stranded chains containing 4,2′:6′,4″-terpyridine ligands in which the nature of the chain arises from di-, tri- or pentanuclear metal nodes.

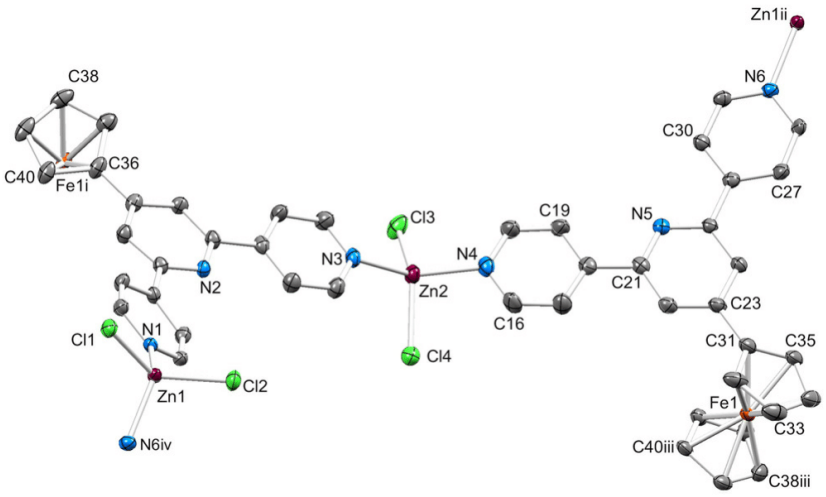

Fig. 1. The asymmetric unit in $[\{Zn_2(\mathbf{1})Cl_4\}\cdot 3CHCl_3]_n$ with symmetry-generated atoms; H atoms and solvent molecules are omitted for clarity. Symmetry codes: *i* = 3/2–x, −1/2 + y, 3/2–z; ii = x, 1 + y, z; iii = 3/2–x, 1/2 + y, 3/2–z; iv = x, −1 + y, z. Selected bond distances: Zn1–N6iv = 2.042(4), Zn1–N1 = 2.035(4), Zn1–Cl1 = 2.2453(13), Zn1–Cl2 = 2.2435(13), Zn2–N3 = 2.076(4), Zn2–N4 = 2.079(4), Zn2–Cl3 = 2.2499(15), Zn2–Cl4 = 2.2708(14) Å. (Colour online.)

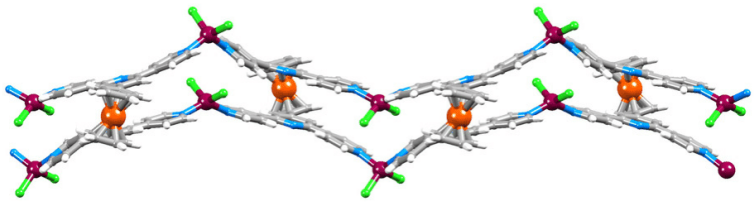

Fig. 2. Part of one chain in $[\{Zn_2(\mathbf{1})Cl_4\}\cdot 3CHCl_3]_n$.

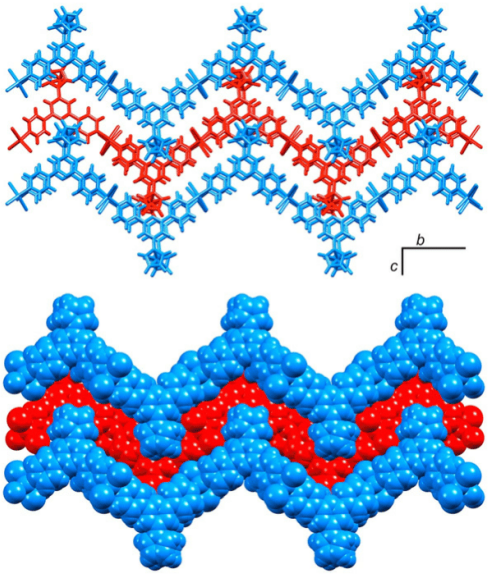

Fig. 3. Stick and space-filling representations of double-stranded chains in $[\{Zn_2(\mathbf{1})Cl_4\}\cdot 3CHCl_3]_n$ to illustrate packing. The structure is viewed down the *a*-axis, and chains coloured blue pack into sheets in the *bc*-plane. Solvent molecules are omitted. (Colour online.)

Acknowledgements

We thank the Swiss National Science Foundation (Grant number 200020_144500) and the University of Basel for support.

Appendix A. Supplementary material

CCDC 1476545 contains the supplementary crystallographic data for this paper. These data can be obtained free of charge via www.ccdc.cam.ac.uk/conts/retrieving.html (or from the Cambridge Crystallographic Data Centre, 12 Union Road, Cambridge CB2 1EZ, UK; fax: (+44) 1223–336-033; or e-mail: deposit@ccdc.cam.ac.uk). Supplementary data to this article can be found online at http://dx.doi.org/10.1016/j.inoche.2016.05.027.

References

[1] E.C. Constable, C.E. Housecroft, in: J. Reedijk, K.R. Poeppelmeier (Eds.), Comprehensive Inorganic Chemistry II, vol. 8, Elsevier, Oxford 2013, p. 1 (Chapter 8.01).
[2] M.W. Hosseini, Acc. Chem. Res. 38 (2005) 313.
[3] E.C. Constable, C.E. Housecroft, S. Vujovic, J.A. Zampese, CrystEngComm 16 (2014) 3494.
[4] S. Vujovic, E.C. Constable, C.E. Housecroft, C.D. Morris, M. Neuburger, A. Prescimone, Polyhedron 92 (2015) 77.
[5] Y.M. Klein, E.C. Constable, C.E. Housecroft, A. Prescimone, CrystEngComm 17 (2015) 2070.
[6] R. Horikoshi, Coord. Chem. Rev. 257 (2013) 621.
[7] R. Horikoshi, T. Mochida, Eur. J. Inorg. Chem. (2010) 5355.
[8] D. Braga, M. Polito, D. D'Addario, E. Tagliavini, D.M. Proserpio, F. Grepioni, J.W. Steed, Organometallics 22 (2003) 4532.
[9] D. Braga, M. Polito, M. Bracaccini, D. D'Addario, E. Tagliavini, D.M. Proserpio, F. Grepioni, Chem.Commun. (2002) 1080.
[10] U. Siemeling, U. Vorfeld, B. Neumann, H.-G. Stammler, Chem. Commun. (1997) 1723.
[11] B. Neumann, U. Siemeling, H.-G. Stammler, U. Vorfeld, J.G.P. Delis, P.W.N.M. van Leeuwen, K. Vrieze, J. Fraanje, K. Goubitz, F. Fabrizi de Bianni, P. Zanello, J. Chem. Soc. Dalton Trans. (1997) 4705.
[12] J.G.P. Delis, P.W.N.M. van Leeuwen, K. Vrieze, N. Veldman, A.L. Spek, J. Fraanje, K. Goubitz, J. Organomet. Chem. 514 (1996) 125.
[13] J. Wang, G.S. Hanan, Synlett (2005) 1251.
[14] 1,1′-Ferrocenedicarboxaldehyde (0.20 g, 0.83 mmol) was dissolved in EtOH (70 mL). 4-Acetylpyridine (0.45 g, 3.63 mmol) and KOH (0.23 g, 4.13 mmol) were added to the solution. Aqueous NH_3 (32%, 6.36 mL) was slowly added to the reaction mixture which was then stirred at room temperature overnight. The solid that formed was collected by filtration, washed with EtOH (3 × 20 mL) and H_2O (3 × 20 mL) and dried in vacuo. Compound **1** was isolated as a red powder (0.24 g, 0.37 mmol, 44.8%). Decomp >300 °C. ^{1}H NMR (500 MHz, $CDCl_3$, 298 K) δ/ppm 8.60 (m, 4H, H^{A2}), 7.67 (m, 4H, H^{A3}), 7.41 (m, 2H, H^{B3}), 4.85 (m, 2H, H^{Cp}), 4.59 (m, 2H, H^{Cp}). IR (ν/cm^{-1}) 3032 (w), 1612 (m), 1596 (s), 1559 (m), 1541 (m), 1431 (m), 1411 (m), 1398 (m), 1261 (w), 1226 (w), 1067 (w), 1036 (w), 994 (m), 892 (w), 827 (s), 764 (w), 741 (w), 679 (w), 649 (m), 629 (s), 597 (w), 570 (m), 508 (m), 475 (m). MALDI-MS (α-cyano-4-hydroxycinnamic acid matrix) *m/z* 649.52 $[M + H]^+$ (calc. 649.18). Found C 70.44, H 4.65, N 12.38; calculated for $C_{40}H_{28}FeN_6\cdot 2H_2O$ C 70.18, H 4.71, N 12.28.
[15] A solution of $ZnCl_2$ (1.36 mg, 0.01 mmol) in MeOH (8 mL) was layered over a suspension of **1** (6.49 mg, 0.01 mmol) in $CHCl_3$ (5 mL). Red crystals of $[\{Zn_2(\mathbf{1})Cl_4\}\cdot 3CHCl_3]_n$ (0.2 mg, 0. 156 μmol, 1.6% based on **1**) were obtained after 2–4 weeks. Insufficient amount of crystalline material was obtained for bulk analysis.
[16] Crystal data for $[\{Zn_2(\mathbf{1})Cl_4\}\cdot 3CHCl_3]_n$: $C_{43}H_{31}Cl_{13}FeN_6Zn_2$, M = 1279.25, red block, monoclinic, space group $P2_1/n$, a = 13.5721(11), b = 23.659(2), c = 15.0438(12) Å, β = 94.479(3)°, U = 4815.8(7) Å^3, Z = 4, D_c = 1.764 Mg m^{-3}, μ(Cu-Kα) = 10.517 mm^{-1}, T = 123 K. Total 49487 reflections, 8941 unique, R_{int} = 0.027. Refinement of 8630 reflections (586 parameters) with $I > 2\sigma(I)$ converged at final $R1$ = 0.0749 ($R1$ all data = 0.0765), $wR2$ = 0.1882 ($wR2$ all data = 0.1890), gof = 0.9829.
[17] C.E. Housecroft, Dalton Trans. 43 (2014) 6594.
[18] E.C. Constable, C.E. Housecroft, M. Neuburger, J. Schönle, S. Vujovic, J.A. Zampese, Polyhedron 62 (2013) 120.
[19] E.C. Constable, G. Zhang, E. Coronado, C.E. Housecroft, M. Neuburger, CrystEngComm 12 (2010) 2139.
[20] E.C. Constable, C.E. Housecroft, S. Vujovic, J.A. Zampese, A. Crochet, S.R. Batten, CrystEngComm 15 (2013) 10068.
[21] L. Li, Y.Z. Zhang, C. Yang, E. Liu, J.A. Golen, G. Zhang, Polyhedron 105 (2016) 115.

18.8 Paper 8 (Published by Elsevier)

Polyhedron 103 (2016) 58–65

Contents lists available at ScienceDirect

Polyhedron

journal homepage: www.elsevier.com/locate/poly

2-Dimensional networks assembled using 4′-functionalized 4,2′:6′,4″-terpyridines and $Co(NCS)_2$☆

Y. Maximilian Klein, Alessandro Prescimone, Edwin C. Constable *, Catherine E. Housecroft *

Department of Chemistry, University of Basel, Spitalstrasse 51, 4056 Basel, Switzerland

ARTICLE INFO

Article history:
Received 4 July 2015
Accepted 7 August 2015
Available online 13 September 2015

Keywords:
Cobalt
4,2′:6′,4″-Terpyridine
Coordination polymer
Coordination network
Substituent effects

ABSTRACT

A series of 2-dimensional (4,4) nets formed in reactions of $Co(NCS)_2$ with divergent 4′-functionalized-4,2′:6′,4″-terpyridine ligands is reported, and the effects of the 4′-substituent R (ligand **1**, R = ^{t}Bu; **5**, R = MeO; **6**, R = EtO; **7**, R = ^{n}PrO) on the packing of the nets are described. The 2D-coordination networks in $[\{Co(NCS)_2(\mathbf{6})_2\}\cdot 4CHCl_3]_n$ and $[\{Co(NCS)_2(\mathbf{7})_2\}\cdot 4CHCl_3]_n$ are essentially isostructural. On going to $[\{Co_2(NCS)_4(\mathbf{5})_4\}\cdot 2CHCl_3\cdot 1.5MeOH]_n$, modification of both the geometry of the rhombuses that comprise the network, and the packing occurs. All three structures feature head-to-tail π-stacking of 4′-(4-alkoxyphenyl) units, but with variation in their relative orientations. In contrast, $[\{Co(NCS)_2(\mathbf{1})_2\}\cdot 0.5H_2O]_n$ comprises double layers of (4,4) nets with hydrophobic coatings of *tert*-butyl groups, leading to alternating wide and close spacings between adjacent nets.

1. Introduction

The coordination chemistry of 4,2′:6′,4″-terpyridines has seen a significant growth since the first coordination polymer of 4,2′:6′,4″-terpyridine (4,2′:6′,4″-tpy) was reported [1]. A 4,2′:6′,4″-tpy binds metal ions through only the two outer nitrogen atoms and therefore possesses a divergent donor set (Scheme 1). 1-Dimensional chains tend to dominate the coordination polymers formed using 4,2′:6′,4″-tpy ligands as linkers [2] but, in part, this has been due to the popularity of zinc as the metal node, either in reactions with zinc(II) halides or zinc acetate; the latter typically results in linear $\{Zn_2(\mu\text{-}OAc)_4\}$ nodes. To encourage the formation of 2- or 3-dimensional architectures, the 4,2′:6′,4″-tpy ligand can be modified by introducing metal-binding domains in the 4′-position. This is readily done using Kröhnke [3] or Wang and Hanan [4] synthetic approaches. Examples of such 4′-donors are pyridinyl [5,6], carboxylato [7–9] or diphenylphosphino [10] groups. Other approaches are to choose metal ions with higher coordination numbers [11] or to design ligands with multiple 4,2′:6′,4″-tpy domains [12–15]. Recently, we extended this latter strategy to a linker bearing two 3,2′:6′,3″-tpy domains and showed that with $Co(NCS)_2$, a $\{4^2.8^4\}$ lvt net is produced [16]. The assembly of this 3-dimensional network was a consequence of using a ligand with two, divergent terpyridine domains (a 4-connecting node) and a metal ion that can also function as a 4-connecting node. Following this success and the results of previous studies in which 2-dimensional nets were obtained from reactions of $Co(NCS)_2$ with ligands **1**–**4** (Scheme 1) [17,18], we have extended our investigations of coordination networks assembled from $Co(NCS)_2$ and 4′-functionalized 4,2′:6′,4″-tpy ligands.

Cobalt(II) thiocyanate combines with a wide range of ditopic ligands containing pyridine metal-binding units. Scheme 2 shows examples of pyridine-donor ligands which form 2- or 3-dimensional architectures with $Co(NCS)_2$. In most cases the cobalt centre acts as a 4-connecting node (octahedral with *trans*-$[NCS]^-$ ligands), although an interesting departure from this is found in $[Co_2(NCS)_4(bpa)_3]_n$ (bpa, Scheme 2) which contains cobalt as both 2- and 4-connecting nodes [19]. The ligands included in Scheme 2 possess rather rigid backbones and, in common with 4,2′:6′,4″-tpy, present divergent sets of *N*-donor atoms. The combination of a divergent *N*,*N*′-linker with a 4-connecting metal node should be preorganized for the formation of a 2-dimensional (4,4) net, and indeed, this is observed for the combinations of $Co(NCS)_2$ with the rod-like ligands 4,4′-bpy, 2,2′-bi(1,6-naphthyridine), bpet, bpo, bpt, bpe, mbpe, mppe and bpaz shown in Scheme 2 [20–29]; inclined interpenetration of (4,4) nets is observed in several cases [22–24]. However, while the reaction of $Co(NCS)_2$ with 4,4′-bpy gives a (4,4) net [30], it has also been shown to give a 1-dimensional chain in $[\{Co(NCS)_2(\mu\text{-}4,4'\text{-}bpy)_2(4,4'\text{-}bpy)_2\}\cdot 2DMF]_n$ in which half of the 4,4′-bpy ligands are

☆ This paper is dedicated to our longstanding friend and colleague Malcolm H. Chisholm on the occasion of his 70th birthday.

* Corresponding authors.
E-mail address: catherine.housecroft@unibas.ch (C.E. Housecroft).

http://dx.doi.org/10.1016/j.poly.2015.08.005
0277-5387/

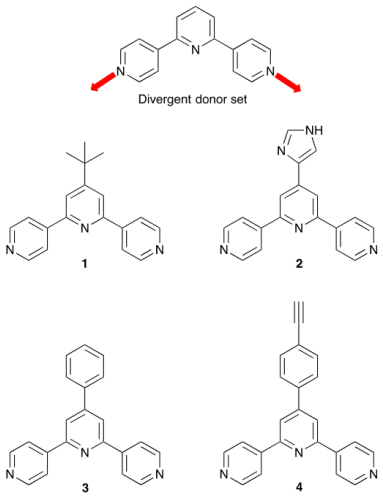

Scheme 1. Definition of 4,2′:6′,4″-tpy as a divergent ligand, and 4,2′:6′,4″-tpys previously shown to form 2-dimensional nets with $Co(NCS)_2$ [17,18].

monodentate and the solvent is implicated in controlling the assembly [31]. An analogous linear chain is seen in $[\{Co(NCS)_2(\mu\text{-}4,4'\text{-bpy})_2(bpaz)_2\}\cdot H_2O]_n$ [32] (see Scheme 2 for bpaz). The advantages of the divergent mode of 4,2′:6′,4″-tpy over the convergent donor

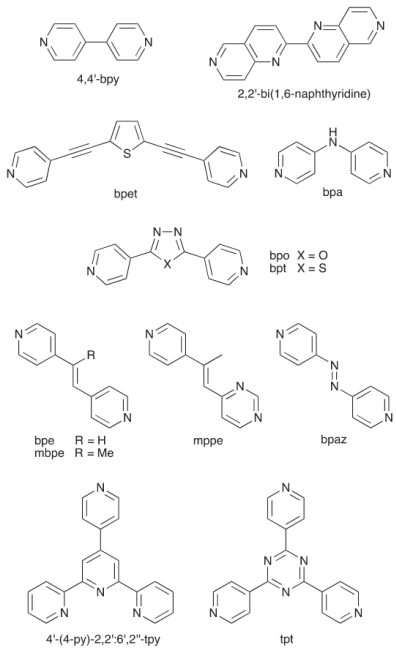

Scheme 2. Representative pyridine-containing ligands which form 2- or 3-dimensional architectures with $Co(NCS)_2$.

set in the more common isomer 2,2′:6′,2″-tpy is seen by comparing the assemblies formed between $Co(NCS)_2$ and either 4′-(4-py)-2,2′:6′,2″-tpy or tpt (Scheme 2); the chelating nature of the 2,2′:6′,2″-tpy domain is restrictive and $[Co(NCS)_2(4'\text{-(4-py)-}2,2':6',2''\text{-tpy})]_n$ forms a linear chain [33] whereas reaction between tpt and $Co(NCS)_2$ gives 3-dimensional networks [34,35].

We now report a series of 2-dimensional nets formed when $Co(NCS)_2$ reacts with the four 4′-functionalized 4,2′:6′,4″-tpy ligands **1** (Scheme 1) and **5–7** (Scheme 3) and discuss variation in packing of the sheets as a function of the 4′-substituent.

2. Experimental

2.1. Ligands

Ligands **1** and **5–7** were prepared as previously described [17,36].

2.2. $[\{Co_2(NCS)_4(\mathbf{5})_4\}\cdot 2CHCl_3\cdot 1.5MeOH]_n$

A MeOH (8 mL) solution of $Co(NCS)_2$ (5.25 mg, 0.03 mmol) was layered over a $CHCl_3$ (5 mL) solution of **5** (30.5 mg, 0.09 mmol) and left to stand at room temperature. Pink crystals of $[\{Co_2(NCS)_4(\mathbf{5})_4\}\cdot 2CHCl_3\cdot 1.5MeOH]_n$ (14.8 mg, 0.007 mmol, 47% based on Co) were obtained after 1–2 weeks. Bulk sample analysis: see text.

2.3. $[\{Co(NCS)_2(\mathbf{6})_2\}\cdot 4CHCl_3]_n$

A MeOH (8 mL) solution of $Co(NCS)_2$ (5.25 mg, 0.03 mmol) was layered over a $CHCl_3$ (5 mL) solution of **6** (10.6 mg, 0.03 mmol) and left to stand at room temperature. Pink crystals of $[\{Co(NCS)(\mathbf{6})\}\cdot 2CHCl_3]_n$ (3.0 mg, 0.002 mmol, 7% based on Co) were obtained after 1–2 weeks. Bulk sample analysis: see text.

2.4. $[\{Co(NCS)_2(\mathbf{7})_2\}\cdot 4CHCl_3]_n$

A MeOH (8 mL) solution of $Co(NCS)_2$ (5.25 mg, 0.03 mmol) was layered over a $CHCl_3$ (5 mL) solution of **7** (22.0 mg, 0.06 mmol) and left to stand at room temperature. Pink crystals of $[\{Co(NCS)_2(\mathbf{7})_2\}\cdot 4CHCl_3]_n$ (12.0 mg, 0.009 mmol, 29% based on Co) were obtained after 1–2 weeks. Bulk sample analysis: see text.

2.5. $[\{Co(NCS)_2(\mathbf{1})_2\}\cdot 0.5H_2O]_n$

A MeOH (8 mL) solution of $Co(NCS)_2$ (3.50 mg, 0.02 mmol) was layered over a $CHCl_3$ (5 mL) solution of **1** (17.4 mmol, 0.06 mmol) and left to stand at room temperature. Pink crystals of $[\{Co(NCS)_2(\mathbf{1})_2\}\cdot 0.5H_2O]_n$ (5.1 mg, 0.007 mmol, 33% based on Co) were obtained after 1–2 weeks. See text for characterization of the bulk sample by powder X-ray diffraction.

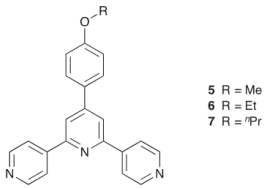

Scheme 3. Structures of ligands **5–7**.

2.6. Crystal structure determinations

Crystallographic data were collected on a Bruker-Nonius Kappa APEX diffractometer, and data reduction, solution and refinement used APEX2 [37] and CRYSTALS [38]. Powder diffraction data were collected on a Stoe Stadi P powder diffractometer. Structural diagrams and structural analysis were carried out using Mercury v. 3.5.1 [39,40] and TOPOS [41]. The solvent region in $[\{Co(NCS)_2(\mathbf{7})_2\}\cdot 4CHCl_3]_n$ was treated using the program SQUEEZE [42], and the electron density removed was equated to two extra molecules of $CHCl_3$ per Co atom which were added to the molecular formula.

2.7. $[\{Co_2(NCS)_4(\mathbf{5})_4\}\cdot 2CHCl_3\cdot 1.5MeOH]_n$

$C_{95.50}H_{76}Cl_6Co_2N_{16}O_{5.50}S_4$, M = 1994.60, pink block, triclinic, space group $P\bar{1}$, a = 13.7002(12), b = 18.0092(15), c = 20.4275(17) Å, α = 98.287(4)°, β = 99.998(3)°, γ = 110.322(3)°, U = 4539.1(4) Å^3, Z = 2, D_c = 1.459 Mg m^{-3}, μ(Cu Kα) = 5.869 mm^{-1}, T = 123 K. Total 68836 reflections, 16258 unique, R_{int} = 0.036. Refinement of 15530 reflections (1196 parameters) with $I > 2\sigma(I)$ converged at final R_1 = 0.1166 (R_1 all data = 0.1191), wR_2 = 0.2862 (wR_2 all data = 0.2867), gof = 0.9939.

2.8. $[\{Co(NCS)_2(\mathbf{6})_2\}\cdot 4CHCl_3]_n$

$C_{52}H_{42}Cl_{12}CoN_8O_2S_2$, M = 1359.46, pink block, monoclinic, space group $P2_1/n$, a = 11.3206(10), b = 15.9765(14), c = 16.5480(14) Å, β = 91.496(4)°, U = 2991.9(3) Å^3, Z = 2, D_c = 1.509 Mg m^{-3}, μ(Cu Kα) = 8.216 mm^{-1}, T = 123 K. Total 18554 reflections, 5365 unique, R_{int} = 0.139. Refinement of 5024 reflections (385 parameters) with $I > 2\sigma(I)$ converged at final R_1 = 0.1118 (R_1 all data = 0.1134), wR_2 = 0.2308 (wR_2 all data = 0.2310), gof = 1.0458.

2.9. $[\{Co(NCS)_2(\mathbf{7})_2\}\cdot 4CHCl_3]_n$

$C_{54}H_{46}Cl_{12}CoN_8O_2S_2$, M = 1387.47, pink block, monoclinic, space group $P2_1/n$, a = 11.7747(11), b = 15.5746(15), c = 16.6739(15) Å, β = 93.870(7)°, U = 3050.8(3) Å^3, Z = 2, D_c = 1.51 Mg m^{-3}, μ(Cu Kα) = 8.070 mm^{-1}, T = 123 K. Total 5909 reflections, 5248 unique, R_{int} = 0.053. Refinement of 4479 reflections (331 parameters) with $I > 2\sigma(I)$ converged at final R_1 = 0.1112 (R_1 all data = 0.1236), wR_2 = 0.2753 (wR_2 all data = 0.2832), gof = 0.9761.

2.10. $[\{Co(NCS)_2(\mathbf{1})_2\}\cdot 0.5H_2O]_n$

$C_{40}H_{39}CoN_8O_{0.50}S_2$, M = 762.87, pink block, monoclinic, space group $C2/c$, a = 37.272(4), b = 11.9575(12), c = 23.770(3) Å, β = 125.290(6)°, U = 8647.3(17) Å^3, Z = 8, D_c = 1.172 Mg m^{-3}, μ(Cu Kα) = 4.302 mm^{-1}, T = 123 K. Total 33334 reflections, 7564 unique, R_{int} = 0.117. Refinement of 2975 reflections (469 parameters) with $I > 2\sigma(I)$ converged at final R_1 = 0.1514 (R_1 all data = 0.2634), wR_2 = 0.3615 (wR_2 all data = 0.4950), gof = 1.0612.

3. Results and discussion

3.1. (4,4)-Nets in $[\{Co_2(NCS)_4(\mathbf{5})_4\}\cdot 2CHCl_3\cdot 1.5MeOH]_n$, $[\{Co(NCS)_2(\mathbf{6})_2\}\cdot 4CHCl_3]_n$ and $[\{Co(NCS)_2(\mathbf{7})_2\}\cdot 4CHCl_3]_n$

The assembly of crystalline coordination polymers with $Co(NCS)_2$ and ligands **5**, **6** and **7** was achieved by crystal growth by solution layering at room temperature. In each crystallization tube, pink crystals grew within 2 weeks. Ligands **5**, **6** or **7** (Scheme 3) differ only in the length of the peripheral alkoxy chain (methyl, ethyl, *n*-propyl). Each combination of **5**, **6** or **7** with $Co(NCS)_2$ leads to a (4,4) net. We first consider the details of the networks, and then evaluate the effects of increasing the length of the 4′-alkoxy tail on the interactions between the sheets in each lattice.

The complex $[\{Co_2(NCS)_4(\mathbf{5})_4\}\cdot 2CHCl_3\cdot 1.5MeOH]_n$ crystallizes in the triclinic space group $P\bar{1}$ with two independent cobalt atoms and four independent ligands in the asymmetric unit (Fig. 1). Each Co atom is octahedral, coordinated by *trans N*-thiocyanato ligands and by one outer pyridine donor of each of four separate **5** ligands. All Co–N bond lengths (caption to Fig. 1) and the angles within the metal coordination sphere are unexceptional. The sulfur atom in the $[NCS]^-$ ligand containing S118 (Fig. 1) is disordered and was modelled over two sites of fractional occupancies 0.60 and 0.40. The pyridine ring containing N67 is also disordered and was modelled over sites of 0.75 and 0.25 occupancies, with atoms N67 and

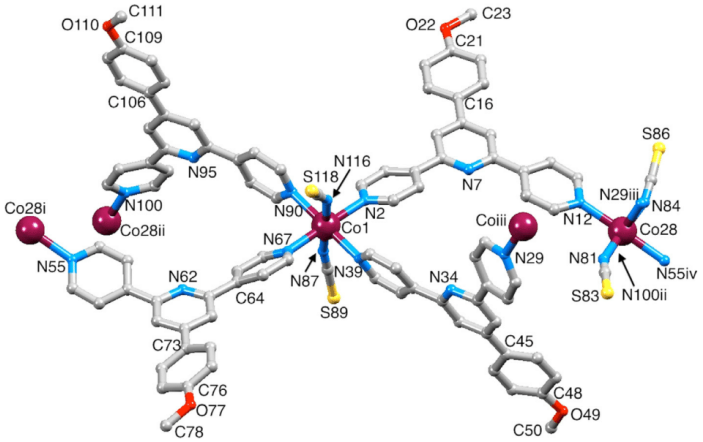

Fig. 1. The asymmetric unit of $[\{Co_2(NCS)_4(\mathbf{5})_4\}\cdot 2CHCl_3\cdot 1.5MeOH]_n$ with symmetry-generated atoms; H atoms and solvent molecules are omitted and only the major sites of the disordered sites (see text) are shown. Symmetry codes: i = 1 + *x*, −1 + *y*, *z*; ii = 1 − *x*, −*y*, −*z*; iii = 1−*x*, 1 − *y*, 1 − *z*; iv = −1 + *x*, 1 + *y*, *z*. Atom N100^{ii} is hidden under Co28. Selected bond distances: Co1–N2 = 2.208(4), Co1–N39 = 2.216(4), Co1–N87 = 2.069(5), Co1–N90 = 2.236(5), Co1–N116 = 2.087(5), Co1–N67 = 2.194(5), Co28–N100^{ii} = 2.172(5), Co28–N29^{iii} = 2.211(5), Co28–N55^{iv} = 2.243(5), Co28–N81 = 2.077(5), Co28–N84 = 2.079(5) Å.

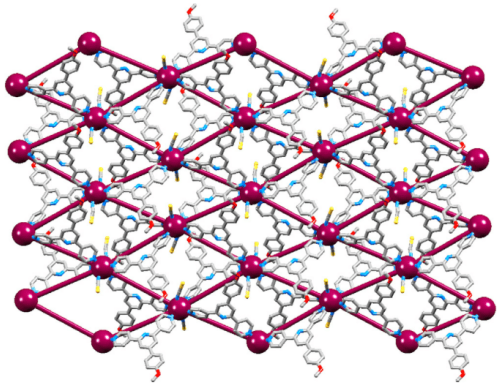

Fig. 2. Overlay of the structure and a TOPOS representation of part of the (4,4) net in $[\{Co_2(NCS)_4(\mathbf{5})_4\}\cdot 2CHCl_3\cdot 1.5MeOH]_n$; H atoms and solvent molecules are omitted.

C64 common to both positions. Each ligand **5** bridges two Co atoms (Fig. 1) and the structure consequently extends to the (4,4) net shown in Fig. 2. Bridged Co–Co distances lie in the range 12.613 (2)–13.193(2) Å, and the internal angles of the two independent rhombuses in the net are 57.75(1)° and 122.25(1)°, and 51.37(1)° and 128.63(1)°.

Crystal growth by layering an MeOH solution of $Co(NCS)_2$ over a $CHCl_3$ solution of **6** or **7** resulted in the formation of $[\{Co(NCS)_2(\mathbf{L})_2\}\cdot 4CHCl_3]_n$ (**L** = **6** or **7**). Both coordination networks crystallize in the monoclinic space group $P2_1/n$ and possess very similar unit cell dimensions (see experimental section). The near-isostructural nature of $[\{Co(NCS)_2(\mathbf{6})_2\}\cdot 4CHCl_3]_n$ and $[\{Co(NCS)_2(\mathbf{7})_2\}\cdot 4CHCl_3]_n$ means that the structures are best considered together. Although the solvent region in $[\{Co(NCS)_2(\mathbf{7})_2\}\cdot 4CHCl_3]_n$ was partially treated using SQUEEZE [42], the consistency between the final solvent content of $[\{Co(NCS)_2(\mathbf{6})_2\}\cdot 4CHCl_3]_n$ and $[\{Co(NCS)_2(\mathbf{7})_2\}\cdot 4CHCl_3]_n$ supports the fitting of the electron density removed from the structure of $[\{Co(NCS)_2(\mathbf{7})_2\}\cdot 4CHCl_3]_n$ to two $CHCl_3$ molecules per Co atom. In each complex, atom Co1 is on an inversion centre; the structure of the repeat unit in $[\{Co(NCS)_2(\mathbf{6})_2\}\cdot 4CHCl_3]_n$ is shown in Fig. 3. The Co–N bond distances (Fig. 3, caption) are similar to analogous bond lengths in $[\{Co(NCS)_2(\mathbf{7})_2\}\cdot 4CHCl_3]_n$ (Co1–N_{tpy} = 2.217(4) and 2.165(4) Å, and Co1–N_{NCS} = 2.084(4) Å). In each structure, the sulfur atom of the $[NCS]^-$ ligand is disordered, and has been modelled over two sites (0.75/0.25 in $[\{Co(NCS)_2(\mathbf{6})_2\}\cdot 4CHCl_3]_n$, and 0.50/0.50 in $[\{Co(NCS)_2(\mathbf{7})_2\}\cdot 4CHCl_3]_n$). The Co–Co separations of 12.913(1) Å in $[\{Co(NCS)_2(\mathbf{6})_2\}\cdot 4CHCl_3]_n$ and 13.093(1) Å in $[\{Co(NCS)_2(\mathbf{7})_2\}\cdot 4CHCl_3]_n$ reflect the comparable spans of the 4,2′:6′,4″-tpy units in **6** and **7**, and lie within the range of bridged Co–Co separations (12.613(2)–13.193(2) Å) in $[\{Co_2(NCS)_4(\mathbf{5})_4\}\cdot 2CHCl_3\cdot 1.5MeOH]_n$. The internal angles of the rhombus in the net in $[\{Co(NCS)_2(\mathbf{6})_2\}\cdot 4CHCl_3]_n$ are 103.57(1)° and 76.43 (1)°, and in $[\{Co(NCS)_2(\mathbf{7})_2\}\cdot 4CHCl_3]_n$ are 107.01(1)° and 72.99(1)°, notably different from those in $[\{Co_2(NCS)_4(\mathbf{5})_4\}\cdot 2CHCl_3\cdot 1.5MeOH]_n$ (see above) (see Fig. 4).

In $[\{Co_2(NCS)_4(\mathbf{5})_4\}\cdot 2CHCl_3\cdot 1.5MeOH]_n$, $[\{Co(NCS)_2(\mathbf{6})_2\}\cdot 4CHCl_3]_n$ and $[\{Co(NCS)_2(\mathbf{7})_2\}\cdot 4CHCl_3]_n$, bridging ligands **5**, **6** or **7** are arranged in an up/up/down/down manner around each rhombus in the (4,4) net. In $[\{Co_2(NCS)_4(\mathbf{5})_4\}\cdot 2CHCl_3\cdot 1.5MeOH]_n$, the ligands **5** are folded over the cavities in the net (Fig. 5a), while this is not the case in $[\{Co(NCS)_2(\mathbf{6})_2\}\cdot 4CHCl_3]_n$ (Fig. 5b) and $[\{Co(NCS)_2(\mathbf{7})_2\}\cdot 4CHCl_3]_n$. This is concomitant with a difference in packing of the (4,4) nets containing ligand **5** and those containing **6** or **7**. Sheets in $[\{Co_2(NCS)_4(\mathbf{5})_4\}\cdot 2CHCl_3\cdot 1.5MeOH]_n$ are interlocked as shown in Fig. 6a, with head-to-tail pairs of 4′-(4-methoxyphenyl)pyridine units from adjacent sheets involved in face-to-face interactions. There are four independent 4′-(4-methoxyphenyl)pyridine units in the asymmetric unit; two form π-stacked interactions with units in the sheet above, and two with 4′-(4-methoxyphenyl)pyridine units in the sheet below. In each head-to-tail pair, the 4′-(4-methoxyphenyl)pyridine units are arranged essentially as shown in Fig. 7a. As Fig. 7a shows, the π-stacking is not optimal due to slippage of the rings, as seen by the $phenyl_{centroid}$...$pyridine_{centroid}$ distance of 4.2 Å. Nonetheless, these interactions are the primary packing contacts between (4,4) nets.

In $[\{Co(NCS)_2(\mathbf{6})_2\}\cdot 4CHCl_3]_n$ and $[\{Co(NCS)_2(\mathbf{7})_2\}\cdot 4CHCl_3]_n$, the 4-ethoxyphenyl (in **6**) or 4-*n*-propoxyphenyl (in **7**) units penetrate the adjacent sheet as shown in Fig. 6b. Head-to-tail π-stacking interactions between 4′-(4-alkoxyphenyl)pyridine units are the dominant packing forces between (4,4) nets in the complexes containing **6** and **7**, but differ from those involving **5** as can be seen by comparing Fig. 7a and b; for **5** the phenyl ring interacts with the middle pyridine ring of the 4,2′:6′,4″-tpy unit, but a slippage in the packing motif on going to the coordination polymers with **6**

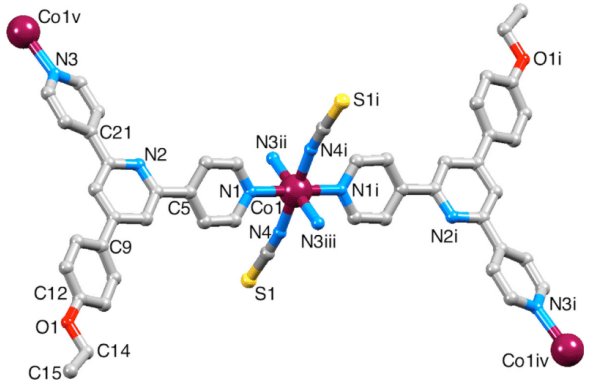

Fig. 3. The repeat unit in $[\{Co(NCS)_2(\mathbf{6})_2\}\cdot 4CHCl_3]_n$ including symmetry-generated atoms; H atoms and solvent molecules are omitted and only the major site of disordered atom S1 is shown. Symmetry codes: i = $-x, 1-y, 1-z$; ii = $^1/_2-x, ^1/_2+y, ^1/_2-z$; iii = $-^1/_2+x, ^1/_2-y, ^1/_2+z$; iv = $-^1/_2-x, ^1/_2+y, ^3/_2-z$; v = $^1/_2-x, -^1/_2+y, ^1/_2-z$. Selected bond distances: Co1–N1 = 2.172(4), Co1–N4 = 2.063(4), Co1–$N3^{ii}$ = 2.200(4) Å.

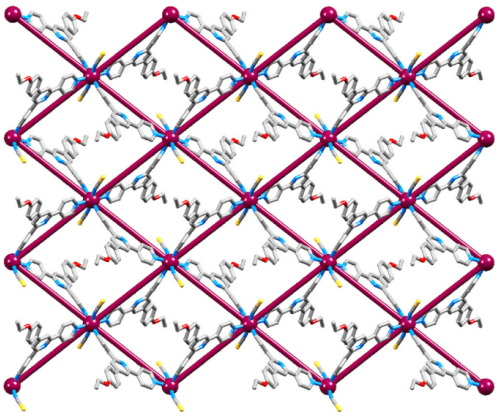

Fig. 4. Overlay of the structure and a TOPOS representation of part of the (4,4) net in $[\{Co(NCS)_2(\mathbf{6})_2\}\cdot 4CHCl_3]_n$; H atoms and solvent molecules are omitted.

or **7** (Fig. 7) results in the phenyl ring lying over the outer pyridine ring of the 4,2′:6′,4″-tpy. As in $[\{Co_2(NCS)_4(\mathbf{5})_4\}\cdot 2CHCl_3\cdot 1.5MeOH]_n$, the orientations of the stacked arene rings are not ideal in $[\{Co(NCS)_2(\mathbf{6})_2\}\cdot 4CHCl_3]_n$, leading to ineffective π-contacts; the angle between the ring planes is 18.7° and the $phenyl_{centroid}\cdots pyridine_{centroid}$ distance is 4.1 Å. These parameters are 25.2° and 4.2 Å in $[\{Co(NCS)_2(\mathbf{7})_2\}\cdot 4CHCl_3]_n$. The translational shift on going from one head-to-tail embrace to the other in Fig. 7 is reminiscent of the variation in π-stacking interactions between 4′-phenyl-2,2′:6′,2″-tpy domains in $[M(4'\text{-phenyl-2,2':6',2''-tpy})_2]^{2+}$ complexes discussed by McMurtrie and Dance [43].

In each of the (4,4) nets described above, the Co atoms are essentially coplanar. The differences in packing of adjacent sheets shown in Fig. 6 lead to only slightly larger inter-plane distances in $[\{Co(NCS)_2(\mathbf{6})_2\}\cdot 4CHCl_3]_n$ (9.228 Å) and $[\{Co(NCS)_2(\mathbf{7})_2\}\cdot 4CHCl_3]_n$ (9.305 Å) compared to $[\{Co_2(NCS)_4(\mathbf{5})_4\}\cdot 2CHCl_3\cdot 1.5MeOH]_n$ (8.936 Å). However, the penetration of the longer alkoxy chains through the holes in the adjacent sheets results in an offset ABAB… arrangement of sheets in $[\{Co(NCS)_2(\mathbf{6})_2\}\cdot 4CHCl_3]_n$ and $[\{Co(NCS)_2(\mathbf{7})_2\}\cdot 4CHCl_3]_n$ with the closest Co…Co inter-net distances of 11.320(1) and 11.775(1) Å, respectively. In $[\{Co_2(NCS)_4(\mathbf{5})_4\}\cdot 2CHCl_3\cdot 1.5MeOH]_n$, the closest Co…Co inter-net distance is 9.414 (1) Å.

After selection of an X-ray quality crystal, the remaining crystalline material for each of $[\{Co_2(NCS)_4(\mathbf{5})_4\}\cdot 2CHCl_3\cdot 1.5MeOH]_n$, $[\{Co(NCS)_2(\mathbf{6})_2\}\cdot 4CHCl_3]_n$ and $[\{Co(NCS)_2(\mathbf{7})_2\}\cdot 4CHCl_3]_n$ was subjected to powder diffraction for bulk sample analysis. However, after removal from the mother liquor, the pink crystals suffer solvent loss, becoming much paler. Figs. S1–S3 compare the powder diffraction patterns for the bulk samples with those predicted from the single crystal structures, and with powder patterns of $Co(NCS)_2$ and the respective free ligand **5**–**7**. For $[\{Co_2(NCS)_4(\mathbf{5})_4\}\cdot 2CHCl_3\cdot 1.5MeOH]_n$ and $[\{Co(NCS)_2(\mathbf{7})_2\}\cdot 4CHCl_3]_n$, characteristic peaks in the predicted patterns are present in the diffraction patterns of the bulk sample, in addition to other peaks. Free ligand is not present, confirming that the change in the crystalline sample occurring on exposure to air is due to simple solvent loss. For $[\{Co(NCS)_2(\mathbf{6})_2\}\cdot 4CHCl_3]_n$, the powder diffraction pattern for the bulk sample (Fig. S2) is ambiguous (taking into account shifts in peaks due to different data collection temperatures) and may contain free ligand **6**.

3.2. $[\{Co(NCS)_2(\mathbf{1})_2\}\cdot 0.5H_2O]_n$

X-ray quality crystals grown from the reaction between $Co(NCS)_2$ and **1** were extremely weakly diffracting. However, we have decided to give a brief description of the structure because of the interesting differences from that previously reported for the methanol solvate $[\{4Co(NCS)_2(\mathbf{1})_2\cdot MeOH\}\cdot H_2O]_n$ [17]. Layering of a MeOH solution of $Co(NCS)_2$ over a $CHCl_3$ solution of **1** led to pink crystals. An X-ray quality crystal was selected and structural determination confirmed the formation of $[\{Co(NCS)_2(\mathbf{1})_2\}\cdot 0.5H_2O]_n$. The X-ray diffraction powder pattern for the bulk sample is in good agreement with that predicted from the single crystal diffraction data (Fig. S4), confirming the homogeneity of the bulk material. The asymmetric unit contains two independent ligands **1** bound to atom Co1; this is octahedrally sited with *trans*-$[NCS]^-$ ligands (Fig. 8). Extension of the structure generates a (4,4) net (Fig. 9a) in which each metallomacrocycle is characterized by bridged Co–Co separations of 13.414(4) and 13.198(4) Å and internal angles of 53.39(2)° and 128.46(2)°. These angles are similar to those in $[\{Co_2(NCS)_4(\mathbf{5})_4\}\cdot 2CHCl_3\cdot 1.5MeOH]_n$ (see above).

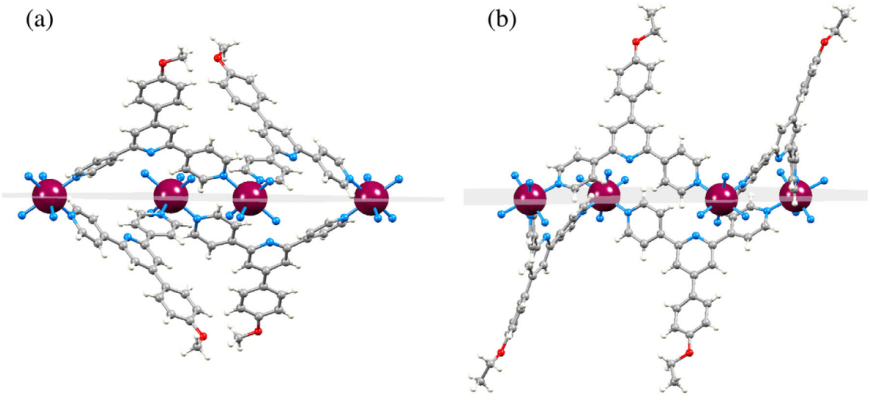

Fig. 5. View through the plane of one metallomacrocycle in (a) $[\{Co_2(NCS)_4(\mathbf{5})_4\}\cdot 2CHCl_3\cdot 1.5MeOH]_n$ and (b) $[\{Co(NCS)_2(\mathbf{6})_2\}\cdot 4CHCl_3]_n$ showing the relative orientations of the bridging ligands with respect to the rhombus.

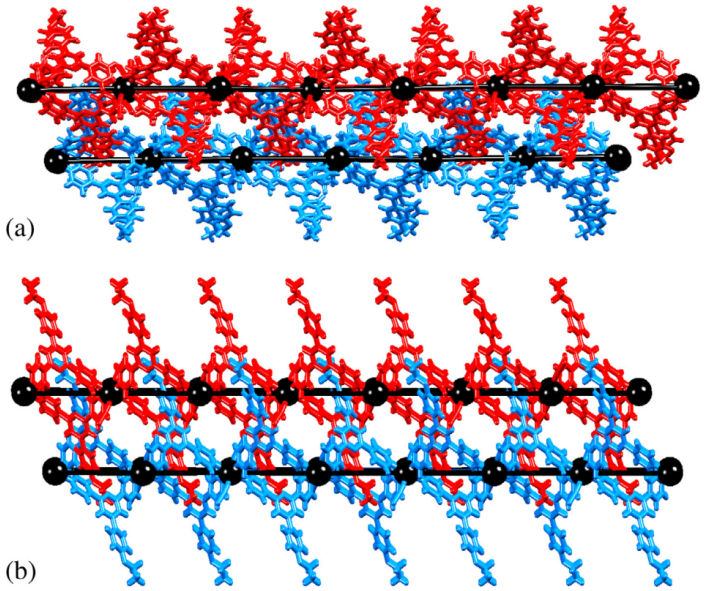

Fig. 6. Overlays of structures and TOPOS (in black) representations to show the packing of adjacent sheets (blue and red) in (a) $[\{Co_2(NCS)_4(\mathbf{5})_4\}\cdot 2CHCl_3\cdot 1.5MeOH]_n$ and (b) $[\{Co(NCS)_2(\mathbf{6})_2\}\cdot 4CHCl_3]_n$. (Color online.)

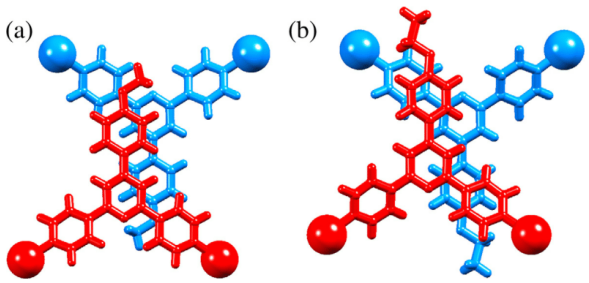

Fig. 7. Face-to-face contacts between 4′-(4-alkoxyphenyl)pyridine units from adjacent sheets in (a) $[\{Co_2(NCS)_4(\mathbf{5})_4\}\cdot 2CHCl_3\cdot 1.5MeOH]_n$ (methoxy tails) and (b) $[\{Co(NCS)_2(\mathbf{6})_2\}\cdot 4CHCl_3]_n$ (ethoxy tails).

A comparison of the structures of $[\{Co(NCS)_2(\mathbf{1})_2\}\cdot 0.5H_2O]_n$ (this work) and $[\{4Co(NCS)_2(\mathbf{1})_2\cdot MeOH\}\cdot H_2O]_n$ [17] shows close similarities within a single (4,4) net, but significant differences in the packing of the nets. $[\{Co(NCS)_2(\mathbf{1})_2\}\cdot 0.5H_2O]_n$ and $[\{4Co(NCS)_2(\mathbf{1})_2\cdot MeOH\}\cdot H_2O]_n$ crystallize in the monoclinic space groups *C*2/*c* and *C*2, respectively. The angles in each rhombus in the net in $[\{Co(NCS)_2(\mathbf{1})_2\}\cdot 0.5H_2O]_n$ (53.39(2)° and 128.46(2)°) are close to those in $[\{4Co(NCS)_2(\mathbf{1})_2\cdot MeOH\}\cdot H_2O]_n$ (49.74(1)° and 130.09(1)°), and in both structures, the bridging ligands are organized in an up/up/down/down arrangement sequentially around a rhombus. In both structures, the Co atoms are coplanar, exactly so in $[\{Co(NCS)_2(\mathbf{1})_2\}\cdot 0.5H_2O]_n$ (a consequence of a translational symmetry operation) and within <0.3 Å in $[\{4Co(NCS)_2(\mathbf{1})_2\cdot MeOH\}\cdot H_2O]_n$. In the latter, the (4,4) nets lie directly over one another with closest Co–Co distances between sheets of 8.327(1) Å. In contrast, in $[\{Co(NCS)_2(\mathbf{1})_2\}\cdot 0.5H_2O]_n$, adjacent sheets are slipped, and have alternating wide and close spacings between adjacent nets as shown in Fig. 9b. For the short inter-net spacing, the Co–Co distances between adjacent nets are 7.715(1) and 9.214(1) Å, while for the longer inter-net spacing, the shortest Co–Co separations are 13.830(1) and 13.981(1) Å. We have previously described the inter-sheet interactions in $[\{4Co(NCS)_2(\mathbf{1})_2\cdot MeOH\}\cdot H_2O]_n$ as 'ball-and-socket packing' [17] with the *tert*-butyl groups accommodated in V-shaped cavities in the next sheet. In the newly reported structure of $[\{Co(NCS)_2(\mathbf{1})_2\}\cdot 0.5H_2O]_n$, the *tert*-butyl groups (shown in red in Fig. 10) face outwards from the pair of closely associated (4,4) nets, and result in hydrophobic layers filling the wider inter-sheet spacings.

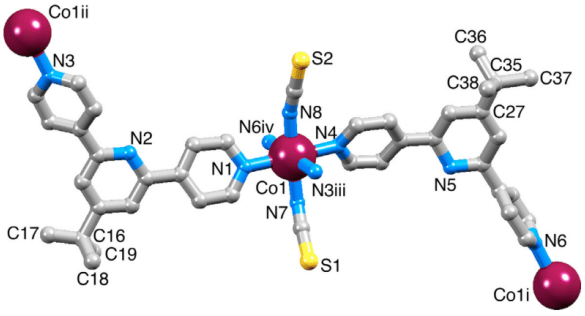

Fig. 8. The repeat unit in $[\{Co(NCS)_2(\mathbf{1})_2\}\cdot 0.5H_2O]_n$ including symmetry-generated atoms; H atoms and water molecules are omitted for clarity. Symmetry codes: i = x, $1-y$, $^1/_2-z$; ii = x, $-y$, $-^1/_2-z$; iii = x, $-y$, $^1/_2-z$; iv = x, $1-y$, $-^1/_2-z$. Selected bond lengths: Co1–N3^{iii} = 2.178(10), Co1–N6^{iv} = 2.165(10), Co1–N1 = 2.211(9), Co1–N4 = 2.181(9), Co1–N7 = 2.106(10), Co1–N8 = 2.078(10) Å.

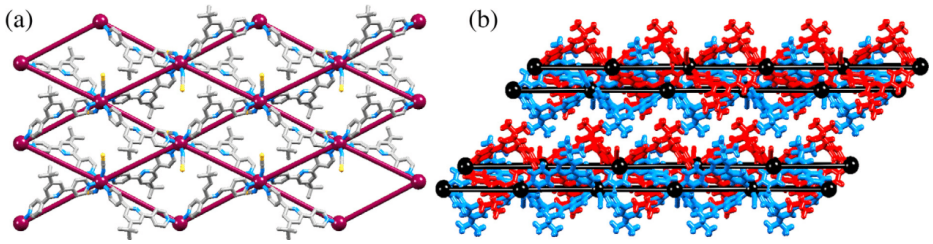

Fig. 9. (a) Overlay of the structure and a TOPOS representation of part of the (4,4) net in $[\{Co(NCS)_2(\mathbf{1})_2\}\cdot 0.5H_2O]_n$; H atoms and solvent molecules are omitted. (b) View through four adjacent sheets (H atoms included) showing their short/long/short alternating separations; Co atoms and the (4,4) nets are shown in black. The (4,4) nets lie parallel to the *bc*-plane.

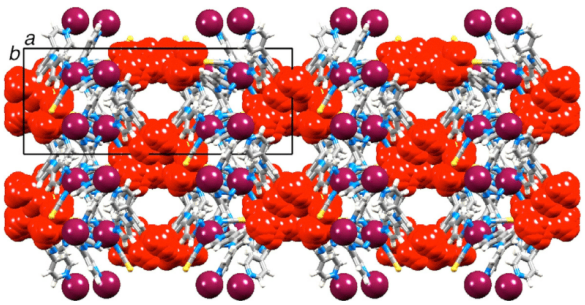

Fig. 10. Packing in $[\{Co(NCS)_2(\mathbf{1})_2\}\cdot 0.5H_2O]_n$ (viewed down the *c*-axis) with (4,4) nets parallel to the *bc*-plane; *tert*-butyl groups are shown in red space-filling representation.

4. Conclusions

We report four 2-dimensional (4,4) nets assembled through room temperature crystal growth experiments from reactions between $Co(NCS)_2$ and divergent 4,2′:6′,4″-terpyridine ligands **1**, **5**, **6** and **7**. The 2D-coordination networks in $[\{Co(NCS)_2(\mathbf{6})_2\}\cdot 4CHCl_3]_n$ and $[\{Co(NCS)_2(\mathbf{7})_2\}\cdot 4CHCl_3]_n$ are near isostructural and the internal angles in the rhombus in each net are 103.57(1)° and 76.43(1)°, and 107.01(1)° and 72.99(1)°, respectively. Although the (4,4) net in $[\{Co_2(NCS)_4(\mathbf{5})_4\}\cdot 2CHCl_3\cdot 1.5MeOH]_n$ is topologically the same as those containing **6** and **7**, the geometries of the rhombuses comprising the net are considerably different. Packing of sheets in all three coordination networks involves head-to-tail π-stacking of 4′-(4-alkoxyphenyl) units, but with variation in their relative orientations. In contrast, $[\{Co(NCS)_2(\mathbf{1})_2\}\cdot 0.5H_2O]_n$ consists of double layers of (4,4) nets with hydrophobic coatings of *tert*-butyl groups, leading to alternating wide and close spacings between adjacent nets. This contrasts with the previously reported structure of $[\{4Co(NCS)_2(\mathbf{1})_2\cdot MeOH\}\cdot H_2O]_n$ in which the (4,4) nets are equally spaced [17].

Acknowledgements

We thank the Swiss National Science Foundation, the University of Basel, and the European Research Council (Advanced Grant 267816 LiLo) for financial support. The Swiss National Science Foundation through the NCCR Molecular Systems Engineering is acknowledged for partial funding of the powder diffractometer.

Appendix A. Supplementary data

CCDC 1407339–1407342 contains the supplementary crystallographic data for all complexes. These data can be obtained free of charge via http://www.ccdc.cam.ac.uk/conts/retrieving.html, or from the Cambridge Crystallographic Data Centre, 12 Union Road, Cambridge CB2 1EZ, UK; fax: (+44) 1223 336 033; or e-mail: deposit@ccdc.cam.ac.uk. Supplementary data associated with this article can be found, in the online version, at http://dx.doi.org/10.1016/j.poly.2015.08.005.

References

[1] M. Barquín, J. Cancela, M.J. González Garmendia, J. Quintanilla, U. Amador, Polyhedron 17 (1998) 2373.
[2] C.E. Housecroft, Dalton Trans. 43 (2014) 6594.
[3] F. Kröhnke, Synthesis (1976) 1.
[4] J. Wang, G.S. Hanan, Synlett (2005) 1251.
[5] Y.-Q. Chen, G.-R. Li, Z. Chang, Y.-K. Qu, Y.-H. Zhang, X.-H. Bu, Chem. Sci. 4 (2013) 3678. and references cited therein.
[6] C. Liu, Y.-B. Ding, X.-H. Shi, D. Zhang, M.-H. Hu, Y.-G. Yin, D. Li, Cryst. Growth Des. 9 (2009) 1275.
[7] P. Yang, M.-S. Wang, J.-J. Shen, M.-X. Li, Z.-X. Wang, M. Shao, X. He, Dalton Trans. 43 (2014) 1460. and references cited therein.
[8] F. Yuan, J. Xie, H.-M. Hu, C.-M. Yuan, B. Xu, M.-L. Yang, F.-X. Dong, G.-L. Xue, CrystEngComm 15 (2013) 1460. and references therein.
[9] Y. Li, Z. Ju, B. Wu, D. Yuan, Cryst. Growth Des. 13 (2013) 4125. and references therein.
[10] X. Tan, X. Chen, J. Zhang, C.-Y. Song, Dalton Trans. 41 (2012) 3616.
[11] Y.M. Klein, A. Prescimone, E.C. Constable, C.E. Housecroft, CrystEngComm 17 (2015) 6483.
[12] G.W.V. Cave, C.L. Raston, J. Chem. Soc., Perkin Trans. 1 (2001) 3258.
[13] J. Yoshida, S.-I. Nishikiori, H. Yuge, J. Coord. Chem. 66 (2013) 2191.
[14] S.A.S. Ghozlan, A.Z.A. Hassanien, Tetrahedron 58 (2002) 9423.
[15] E.C. Constable, C.E. Housecroft, S. Vujovic, J.A. Zampese, CrystEngComm 16 (2014) 3494.
[16] Y.M. Klein, E.C. Constable, C.E. Housecroft, A. Prescimone, CrystEngComm 17 (2015) 2070.
[17] E.C. Constable, C.E. Housecroft, P. Kopecky, M. Neuburger, J.A. Zampese, G. Zhang, CrystEngComm 14 (2012) 446.
[18] E.C. Constable, C.E. Housecroft, M. Neuburger, S. Vujovic, J.A. Zampese, G. Zhang, CrystEngComm 14 (2012) 3554.
[19] W.R. Knapp, D.P. Martin, R.L. LaDuca, Acta Crystallogr., Sect. E 63 (2007) m2745.
[20] D.M. Shin, I.S. Lee, D. Cho, Y.K. Chung, Inorg. Chem. 42 (2003) 7722.
[21] Z. Huang, H.-B. Song, M. Du, S.-T. Chen, X.-H. Bu, J. Ribas, Inorg. Chem. 43 (2004) 931.
[22] S. Wöhlert, I. Jess, C. Näther, Acta Crystallogr., Sect. E 69 (2013) m482.
[23] D.M. Shin, I.S. Lee, Y.K. Chung, M.S. Lah, Chem. Commun. (2003) 1036.
[24] H.-P. Wu, C. Janiak, L. Uehlin, P. Klüfers, P. Mayer, Chem. Commun. (1998) 2637.
[25] D.M. Shin, I.S. Lee, Y.K. Chung, Cryst. Growth Des. 6 (2006) 1059.
[26] M. Kondo, M. Shimamura, S. Noro, S. Minakoshi, A. Asami, K. Seki, S. Kitagawa, Chem. Mater. 12 (2000) 1288.
[27] L.M. Callejo, N. de la Pinta, G. Madariaga, L. Fidalgo, L. Lezama, R. Cortes, Cryst. Growth Des. 10 (2010) 4874.
[28] S. Wöhlert, J. Boeckmann, M. Wriedt, C. Näther, Angew. Chem., Int. Ed. 50 (2011) 6920.
[29] S.U. Son, B.Y. Kim, C.H. Choi, S.W. Lee, Y.S. Kim, Y.K. Chung, Chem. Commun. (2003) 2528.
[30] J. Lu, T. Paliwala, S.C. Lim, C. Yu, T. Niu, A.J. Jacobson, Inorg. Chem. 36 (1997) 923.
[31] L.-N. Zhu, Q.-L. Wang, W.-Z. Wang, D.-Z. Liao, Z.-H. Jiang, S.-P. Yan, J. Mol. Struct. 649 (2003) 111.
[32] B. Li, H. Liu, J. Chen, Z. Xu, Chem. Lett. (2001) 902.
[33] N. Masuhara, S. Hayami, N. Motokawa, A. Shuto, K. Inoue, Y. Maeda, Chem. Lett. 36 (2007) 90.
[34] S.M. Neville, G.J. Halder, K.S. Murray, B. Moubaraki, C.J. Kepert, Aust. J. Chem. 66 (2013) 452.
[35] Y. Inokuma, T. Arai, M. Fujita, Nat. Chem. 2 (2010) 780.
[36] Y.M. Klein, E.C. Constable, C.E. Housecroft, J.A. Zampese, A. Crochet, CrystEngComm 16 (2014) 9915.
[37] Bruker Analytical X-ray Systems, Inc., 2006, APEX2, version 2 User Manual, M86-E01078, Madison, WI.
[38] P.W. Betteridge, J.R. Carruthers, R.I. Cooper, K. Prout, D.J. Watkin, J. Appl. Crystallogr. 36 (2003) 1487.
[39] I.J. Bruno, J.C. Cole, P.R. Edgington, M.K. Kessler, C.F. Macrae, P. McCabe, J. Pearson, R. Taylor, Acta Crystallogr., Sect. B 58 (2002) 389.
[40] C.F. Macrae, I.J. Bruno, J.A. Chisholm, P.R. Edgington, P. McCabe, E. Pidcock, L. Rodriguez-Monge, R. Taylor, J. van de Streek, P.A. Wood, J. Appl. Crystallogr. 41 (2008) 466.
[41] V.A. Blatov, A.P. Shevchenko, TOPOS Professional v. 4.0, Samara State University, Russia.
[42] A.L. Spek, Acta Crystallogr., Sect. D 65 (2009) 148.
[43] J. McMurtire, I. Dance, CrystEngComm 11 (2009) 1141.

18.9 Paper 9 (Published by the Royal Society of Chemistry)

CrystEngComm

PAPER

View Article Online
View Journal | View Issue

Cite this: *CrystEngComm*, 2017, **19**, 2894

What a difference a tail makes: 2D → 2D parallel interpenetration of sheets to interpenetrated nbo networks using ditopic-4,2′:6′,4″-terpyridine ligands†

Y. Maximilian Klein, Alessandro Prescimone, Markus Neuburger, Edwin C. Constable and Catherine E. Housecroft *

Received 11th April 2017,
Accepted 9th May 2017

DOI: 10.1039/c7ce00686a

rsc.li/crystengcomm

Under conditions of crystal growth by layering at room temperature, 1,4-bis(*n*-hexoxy)-2,5-bis(4,2′:6′,4″-terpyridin-4′-yl)benzene (**4**) or 1,4-bis(*n*-decoxy)-2,5-bis(4,2′:6′,4″-terpyridin-4′-yl)benzene (**5**) reacts with $ZnCl_2$ to yield $[Zn_2Cl_4(\mathbf{4})]_n$ or $[Zn_2Cl_4(\mathbf{5})\cdot 2MeOH]_n$. The compounds crystallize in the *C*2/*c* space group with 2-dimensional (4,4) nets which interpenetrate in a 2D → 2D parallel manner. The ligands act as planar 4-connecting nodes linked through the zinc(II) centres. In contrast, 1,4-bis(3-phenylpropoxy)-2,5-bis(4,2′:6′,4″-terpyridin-4′-yl)benzene (**6**) reacts with $ZnBr_2$ to give $[Zn_2Br_4(\mathbf{6})\cdot H_2O]_n$ which crystallizes in the trigonal $R\bar{3}$ space group with a 3D assembly consisting of 2-fold interpenetrating **nbo** nets. Ligand **6** acts as a 4-connecting node and the zinc(II) centres are linkers. The pendant phenyl rings in **6** lie over the 4,2′:6′,4″-tpy domains in an adjacent net and the resulting close association of the interpenetrated nets leads to a highly porous network.

Introduction

The design and assembly of coordination architectures incorporating 4,2′:6′,4″-terpyridine (4,2′:6′,4″-tpy, Scheme 1) ligands is a mature strategy in crystal engineering.[1–3] A 4,2′:6′,4″-tpy ligand presents a V-shaped building block, coordinating only through the outer N-donors.[1,2] Kröhnke[4] or Wang and Hanan[5] synthetic methodologies permit ready functionalization of the 4′-position of the tpy unit. If the functional group is non-coordinating, the common assembly motifs for architectures supported by 4,2′:6′,4″-tpy ligands are 1D-chains and 2D-sheets depending upon the coordination geometry of the metal nodes.[1,2] The introduction of coordinatively non-innocent domains such as pyridyl[6] or carboxylate[7] moieties is a proven approach to increasing the dimensionality of 4,2′:6′,4″-tpy-based coordination assemblies.

Another approach to increasing architectural complexity is the use of ditopic ligands comprising two 4,2′:6′,4″-tpy domains connected by a spacer (Scheme 1). Ligands in this class are also of interest as optoelectronic materials[8] and for the assembly of supramolecular organic frameworks for CO_2 adsorption.[9] The coordination chemistry of ditopic bis(4,2′:6′,4″-tpy) and isomeric bis(3,2′:6′,3″-tpy) ligands remains relatively unexplored. When the spacer (Scheme 1) is a 1,1′-ferrocenyl unit, its preference for a cisoid-conformation leads to the bis(4,2′:6′,4″-tpy) ligand adopting a folded conformation and reaction with $ZnCl_2$ produces a double-stranded 1D-coordination polymer.[10] With the exception of this example, ditopic bis(4,2′:6′,4″-tpy) ligands typically contain a 1,4-C_6H_4 spacer which predisposes the ligand towards functioning as a 4-connecting node, either as a planar or approximately tetrahedral node (Scheme 2). Additional structural

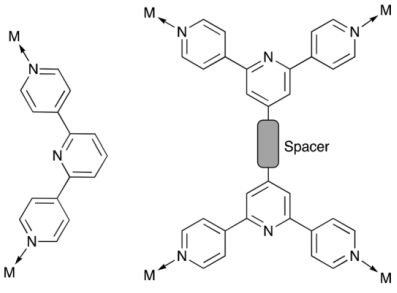

Scheme 1 Typical divergent coordination modes of 4,2′:6′,4″-tpy units in mono- and ditopic ligands.

Department of Chemistry, University of Basel, Spitalstrasse 51, CH-4056 Basel, Switzerland. E-mail: catherine.housecroft@unibas.ch

† Electronic supplementary information (ESI) available: Table S1: Comparison of cell parameters for related compounds; Fig. S1: powder diffraction data; Fig. S2–S5: ^{1}H NMR spectra of compounds 4–6; Fig. S6–S8: additional structural diagrams. CCDC 1541159–1541161. For ESI and crystallographic data in CIF or other electronic format see DOI: 10.1039/c7ce00686a

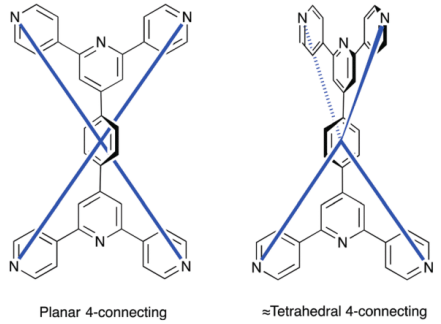

Scheme 2 Ditopic bis(4,2′:6′,4″-tpy) ligands as limiting planar and tetrahedral 4-connecting nodes.

variation may be achieved through a different substitution pattern in the aryl spacer,[11] or by replacing the 4,2′:6′,4″-tpy by 3,2′:6′,3″-tpy metal-binding units.[12] We are currently exploring a series of ditopic bis(4,2′:6′,4″-tpy) and bis(3,2′:6′,3″-tpy) ligands with different alkoxy substituents attached to the central spacer. We have shown that reaction of **1** (Scheme 3) with $Co(NCS)_2$ leads to a 3D $\{4^2{\cdot}8^4\}$ **lvt** net.[12] This assembly depends upon both the metal and ligand acting as 4-connecting nodes (planar and approximately tetrahedral, respectively). In contrast, combining **2** (Scheme 3) with $ZnCl_2$ or $ZnBr_2$ leads to 2D-sheets in which the ligands are the unique nodes.[13,14] While the (4,4) nets in $[\{Zn_2Cl_4(2)\}{\cdot}4H_2O]_n$ and $[\{Zn_2Br_4(2)\}]_n$ interpenetrate in a 2D → 2D parallel fashion, analogous nets present in $[\{Zn_2Br_4(3)\}{\cdot}2C_6H_4Cl_2]_n$ and $[\{Zn_2I_4(3)\}{\cdot}2.3C_6H_4Cl_2]_n$ show no interpenetration.[14] The ^{n}octyl-chains in **2** are in extended conformations in $[\{Zn_2Cl_4(2)\}{\cdot}4H_2O]_n$ and $[\{Zn_2Br_4(2)\}]_n$, and are threaded within the interpenetrated sheets. We have previously suggested that the long chains may assist in directing the assembly process.[13] We have now extended the investigation to ligands **4**–**6**. Ligands **4** and **5** possess shorter and longer alkoxy tails than **3**, while each alkoxy chain in **6** is terminated by a phenyl group.

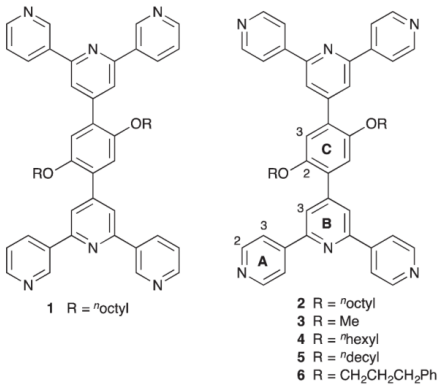

Scheme 3 Structures of ligands **1**–**6**. Ring labelling is used for NMR assignments; in compound **6**, the phenyl ring is ring D. Alkoxy chains are labelled $C/H^{a,b\cdots}$ starting at the OCH_2 group.

Experimental

General

^1H and ^{13}C NMR spectra were recorded on a Bruker DRX-500 NMR spectrometer with chemical shifts referenced to residual solvent peaks (TMS = δ 0 ppm). Electrospray ionisation (ESI) mass spectra were measured on a Bruker esquire 3000plus spectrometer or Shimadzu LCMS-2020 instrument, and high resolution ESI mass spectra on a Bruker maXis 4G QTOF instrument. For GC/MS analysis, a Shimadzu GCMS/QP2010 SE gas chromatograph system with ZB-5HT inferno column (30 m × 0.25 mm × 0.25 mm), at 1 mL min^{-1} He-Flow rate (split = 20 : 1) with a Shimadzu mass detector (EI 70 eV) was used.

1-Bromohexane, 1-bromodecane, 2,5-dibromohydroquinone and 1-bromo-3-phenylpropane were purchased from Sigma-Aldrich. 1,4-Dibromo-2,5-bis(^{n}hexoxy)benzene (**4a**) and 1,4-dibromo-2,5-bis(^{n}decoxy)benzene (**5a**) have previously been reported[15] but we find the following method of synthesis convenient, giving a higher yield of **4a**.

Compound 4a

2,5-Dibromohydroquinone (2.00 g, 7.47 mmol), 1-bromohexane (2.64 mL, 3.11 g, 18.7 mmol) and anhydrous K_2CO_3 (3.10 g, 22.4 mmol) were added to dry DMF (100 mL) and the mixture was heated at 100 °C for ~15 h. The reaction mixture was cooled to room temperature, then transferred to a beaker containing 100 mL of ice water and stirred for 30 min. The precipitate was filtered, washed with water (3 × 30 mL) and dried *in vacuo*. The product was recrystallized from a mixture of EtOH and $CHCl_3$ and isolated as white crystals (3.05 g, 6.99 mmol, 93.6%). NMR spectroscopic data agreed with the literature.[15] GC-EI-MS *m*/*z* 436.1 $[M]^+$ (calc. 436.0). M.p. = 64.4 °C, deviating from the literature value of 51.3–53.1 °C.[15]

Compound 5a

The method was as for **4a** starting with 2,5-dibromohydroquinone (1.00 g, 3.73 mmol), 1-bromodecane (2.33 mL, 2.48 g, 11.2 mmol) and anhydrous K_2CO_3 (1.55 g, 11.2 mmol). **5a** was isolated as white crystals (1.83 g, 3.34 mmol, 89.5%). M.p. = 74.4 °C. ^1H NMR spectroscopic data agreed with the literature.[15] $^{13}C\{^1H\}$ NMR (126 MHz, $CDCl_3$) δ/ppm 150.2 (C^{C2}), 118.6 (C^{C3}), 111.3 (C^{C1}), 70.5 (C^a), 32.1 (C^{CH_2}), 29.7 (C^{CH_2}), 29.65 (C^{CH_2}), 29.45 (C^{CH_2}), 29.5 (C^{CH_2}), 29.3 (C^b), 26.1 (C^c), 22.8 (C^{CH_2}), 14.3 (C^j). GC-EI-MS *m*/*z* 548.3 $[M]^+$ (calc. 548.2).

Compound 6a

2,5-Dibromohydroquinone (1.00 g, 3.73 mmol), 1-bromo-3-phenylpropane (1.42 mL, 1.86 g, 9.33 mmol) and anhydrous

K_2CO_3 (1.55 g, 11.2 mmol) were added to dry DMF (100 mL) and the mixture was heated at 100 °C for ~15 h. The reaction mixture was cooled to room temperature, then transferred to a beaker containing 100 mL of ice water, stirred for 30 min and extracted with CH_2Cl_2 (200 mL). The organic phase was dried over $MgSO_4$ and concentrated *in vacuo*. The product was recrystallized from a mixture of EtOH and $CHCl_3$ and isolated as white crystals (1.68 g, 3.33 mmol, 89.3%). M.p. = 88.8 °C. ^{1}H NMR (500 MHz, $CDCl_3$) δ/ppm 7.30 (m, 4H, H^{D3}), 7.24–7.17 (m, 6H, H^{D2+D4}), 7.06 (s, 2H, H^{C3}), 3.95 (t, J = 6.2 Hz, 4H, H^a), 2.86 (m, 4H, H^c), 2.11 (m, 4H, H^b). $^{13}C\{^1H\}$ NMR (126 MHz, $CDCl_3$) δ/ppm 150.1 (C^{C2}), 141.4 (C^{D1}), 128.7 ($C^{D2/D3/D4}$), 128.6 ($C^{D2/D3/D4}$), 126.1 ($C^{D2/D3/D4}$), 118.6 (C^{C3}), 111.3 (C^{C1}), 69.1 (C^a), 32.1 (C^c), 30.9 (C^b). GC-EI-MS m/z 503.8 $[M]^+$ (calc. 504.0).

Compound 4b

Compound **4a** (1.80 g, 4.13 mmol) and dry Et_2O (150 mL) were added to a dried flask and cooled to 0 °C in an ice bath. ^{n}Butyllithium (1.6 M in hexanes, 7.74 mL, 12.4 mmol) was added slowly to the Et_2O solution over a period of 20 min and the temperature maintained at 0 °C for 6 h. Dry DMF (0.96 mL, 12.4 mmol) was added and the solution was stirred for ~15 h, during which time it was allowed to warm to room temperature. The reaction mixture was neutralized with saturated aqueous NH_4Cl and extracted with CH_2Cl_2 (200 mL). The organic phase was dried over $MgSO_4$ and concentrated *in vacuo*. **4b** was isolated as a yellow solid (0.85 g, 2.54 mmol, 61.5%) and used without further purification. M.p. = 68.6 °C. The ^{1}H NMR spectrum agreed with literature data.[16] $^{13}C\{^1H\}$ NMR (126 MHz, $CDCl_3$) δ/ppm 189.6 (C^{CHO}), 155.4 (C^{C2}), 129.4 (C^{C1}), 111.8 (C^{C3}), 69.38 (C^a), 31.6 ($C^{d/e}$), 29.2 (C^b), 25.8 (C^c), 22.7 ($C^{d/e}$), 14.1 (C^f). GC-EI-MS m/z 334.2 $[M]^+$ (calc. 334.2).

Compound 5b

The method and volumes of solvents were as for the synthesis of **4b**, but using **5a** (3.0 g, 5.47 mmol), ^{n}BuLi (1.6 M in hexanes, 10.3 mL, 16.4 mmol), dry DMF (1.27 mL, 16.4 mmol). **5b** was obtained as a yellow solid (2.27 g, 5.08 mmol, 92.9%) and used without further purification. M.p. = 80.3 °C. ^{1}H NMR (500 MHz, $CDCl_3$) δ/ppm 10.52 (s, 2H, H^{CHO}), 7.43 (s, 2H, H^{C3}), 4.08 (t, J = 6.5 Hz, 4H, H^a), 1.82 (m, 4H, H^b), 1.46 (m, 4H, H^c), 1.40–1.18 (m, 24H, H^{d-i}), 0.87 (m, 6H, H^j). $^{13}C\{^1H\}$ NMR (126 MHz, $CDCl_3$) δ/ppm 189.6 (C^{CHO}), 155.4 (C^{C2}), 129.4 (C^{C1}), 111.8 (C^{C3}), 69.4 (C^a), 32.0 (C^{CH_2}), 29.7 (C^{CH_2}), 29.68 (C^{CH_2}), 29.46 (C^{CH_2}), 29.45 (C^{CH_2}), 29.2 (C^b), 26.15 (C^c), 22.8 (C^{CH_2}), 14.3 (C^j). GC-EI-MS m/z 446.4 $[M]^+$ (calc. 446.3).

Compound 6b

The method and volumes of solvents were as for the synthesis of **4b**, but using **6a** (1.5 g, 2.97 mmol), ^{n}BuLi (1.6 M in hexanes, 5.57 mL, 8.91 mmol) and dry DMF (0.69 mL, 8.91 mmol). **6b** was isolated as a yellow solid (1.08 g, 2.68 mmol, 90.3%) and used without further purification. M.p. = 102.6 °C. ^{1}H NMR (500 MHz, $CDCl_3$) δ/ppm 10.47 (s, 2H, H^{CHO}, 7.41 (s, 2H, H^{C3}), 7.30 (m, 4H, H^{D3}), 7.24–7.19 (m, 6H, H^{D2+D4}), 4.11 (t, J = 6.2 Hz, 4H, H^a), 2.83 (t, J = 7.6 Hz, 4H, H^c), 2.19 (m, 4H, H^b). $^{13}C\{^1H\}$ NMR (126 MHz, $CDCl_3$) δ/ppm 189.4 (C^{CHO}), 155.2 (C^{C2}), 141.10 (C^{D1}), 129.36 (C^{C1}), 128.67 ($C^{D2/D3/D4}$), 128.53 ($C^{D2/D3/D4}$), 126.27 ($C^{D2/D3/D4}$), 111.8 (C^{C3}), 68.3 (C^a), 32.4 (C^c), 30.7 (C^b). GC-EI-MS m/z 402.0 (calc. 402.2).

Compound 4

Compound **4b** (0.3 g, 0.9 mmol) was dissolved in EtOH (100 mL), then 4-acetylpyridine (0.41 mL, 0.44 g, 3.59 mmol) and crushed solid KOH (0.20 g, 3.59 mmol) were added. Aqueous NH_3 (32%, 3.0 mL) was added dropwise and the reaction mixture was stirred at room temperature for ~15 h. The precipitate was collected by filtration and washed with water, EtOH and Et_2O (3 × 10 mL, each). Compound **4** was obtained as a white solid (0.15 g, 0.21 mmol, 23.3%). Decomp. >280 °C. ^{1}H NMR (500 MHz, $CDCl_3$) δ/ppm 8.80 (m, 8H, H^{A2}), 8.11 (s, 4H, H^{B3}), 8.09 (m, 8H, H^{A3}), 7.16 (s, 2H, H^{C2}), 4.06 (t, J = 6.3 Hz, 4H, H^a), 1.74 (m, 4H, H^b), 1.37 (m, 4H, H^c), 1.25–1.09 (m, 8H, H^{d+e}), 0.76 (t, J = 7.1 Hz, 6H, H^f). $^{13}C\{^1H\}$ NMR (126 MHz, $CDCl_3$) δ/ppm 154.8 (C^{B2}), 150.7 (C^{A2+C3}), 148.3 (C^{B4}), 146.2 (C^{A4}), 129.3 (C^{C1}), 121.6 (C^{B3}), 121.3 (C^{A3}), 115.3 (C^{C2}), 69.9 (C^a), 31.6 ($C^{d/e}$), 29.5 (C^b), 26.1 (C^c), 22.6 ($C^{d/e}$), 14.1 (C^f). ESI-MS m/z 741.6 $[M + H]^+$ (calc. 741.4). HR ESI-MS m/z 371.1998 $[M + 2H]^{2+}$ (calc. 371.1992).

Compound 5

The method and volumes of solvent were as for the synthesis of **4**, but starting with **5b** (0.60 g, 1.34 mmol, 4-acetylpyridine (0.61 mL, 0.66 g, 5.36 mmol), KOH (0.3 g, 5.36 mmol) and aqueous NH_3 (32%, 3.42 mL). Compound **5** was obtained as a white solid (0.25 g, 0.3 mmol, 22.1%). M.p. = 239.8 °C. ^{1}H NMR (500 MHz, $CDCl_3$) δ/ppm 8.81 (m, 8H, H^{A2}), 8.11 (s, 4H, H^{B3}), 8.09 (m, 8H, H^{A3}), 7.16 (s, 2H, H^{C2}), 4.06 (t, J = 6.2 Hz, 4H, H^a), 1.74 (m, 4H, H^b), 1.37 (m, 4H, H^c), 1.23 (m, 8H, H^i), 1.19–1.08 (m, 18H, H^{d-h}), 0.84 (t, J = 7.2 Hz, 6H, H^j). $^{13}C\{^1H\}$ NMR (126 MHz, $CDCl_3$) δ/ppm 154.8 (C^{B2}), 150.8 (C^{C3}), 150.7 (C^{A2}), 148.3 (C^{B4}), 146.2 (C^{A4}), 129.3 (C^{C1}), 121.5 (C^{B3}), 121.3 (C^{A3}), 115.4 (C^{C2}), 69.9 (C^a), 32.0 (C^{CH_2}), 29.65 (C^{CH_2}), 29.6 (C^{CH_2}), 29.5 (C^{CH_2}), 29.4 (C^{CH_2}), 26.5 (C^c), 22.8 (C^{CH_2}), 14.2 (C^j). ESI-MS m/z 853.7 $[M + H]^+$ (calc. 853.5). HR ESI-MS m/z 427.2625 $[M + 2H]^{2+}$ (calc. 427.2618).

Compound 6

The method and solvent volumes were as for **4** but starting with **6b** (0.89 g, 2.21 mmol), 4-acetylpyridine (1.13 mL, 1.23 g, 9.95 mmol, KOH (0.56 g, 9.95 mmol) and aqueous NH_3 (32%, 17 mL). Compound **6** was obtained as a pale yellow solid (0.74 g, 0.92 mmol, 41.4%). Decomp. >260 °C. ^{1}H NMR (500 MHz, $CDCl_3$) δ/ppm 8.80 (m, 8H, H^{A2}), 8.12 (s, 4H, H^{B3}), 8.09 (m, 8H, H^{A3}), 7.19–7.10 (m, 8H, $H^{C2/D3+D4}$), 6.98 (m, 4H, H^{D2}), 4.09 (t, J = 6.1 Hz, 4H, H^a), 2.69 (m, 4H, H^c), 2.09 (m, 4H,

H^b). $^{13}C\{^1H\}$ NMR (126 MHz, $CDCl_3$) δ/ppm 154.9 (C^{B2}), 150.8 (C^{A2}), 150.6 (C^{C3}), 148.3 (C^{B4}), 146.2 (C^{A4}), 140.9 (C^{D1}), 129.4 (C^{C1}), 128.6 ($C^{C2/D3/D4}$), 128.3 (C^{D2}), 126.3 ($C^{C2/D3/D4}$), 121.5 (C^{B3}), 121.3 (C^{A3}), 115.5 ($C^{C2/D3/D4}$), 68.9 (C^a), 32.4 (C^c), 31.1 (C^b). ESI-MS m/z 809.6 $[M + H]^+$ (calc. 809.4). HR ESI-MS m/z 809.3587 $[M + H]^+$ (calc. 809.3599).

$[Zn_2Cl_4(4)]_n$

A MeOH (8 mL) solution of $ZnCl_2$ (1.36 mg, 0.01 mmol) was layered over a $CHCl_3$ (5 mL) solution of **4** (7.41 mg, 0.01 mmol) and the crystallization tube was left to stand at room temperature. Yellow crystals of $[Zn_2Cl_4(4)]_n$ (7.8 mg) were obtained after 1–2 weeks. Satisfactory elemental analysis of the bulk sample could not be obtained; see text for discussion of powder diffraction data.

$[Zn_2Cl_4(5)\cdot 2MeOH]_n$

A MeOH (8 mL) solution of $ZnCl_2$ (2.04 mg, 0.015 mmol) was layered over a $CHCl_3$ (5 mL) solution of **5** (12.8 mg, 0.015 mmol) and the crystallization tube was left to stand at room temperature. Pale yellow crystals of $[Zn_2Cl_4(5)]_n$ (3.2 mg) were obtained after 1–2 weeks. Satisfactory elemental analysis of the bulk sample could not be obtained; see Fig. S1† for powder diffraction data.

$[Zn_2Br_4(6)\cdot H_2O]_n$

A MeOH (8 mL) solution of $ZnBr_2$ (4.5 mg, 0.02 mmol) was layered over a $CHCl_3$ (5 mL) solution of **6** (16.2 mg, 0.02 mmol) and the crystallization tube was left to stand at room temperature. Yellow crystals of $[\{Zn_2Br_4(6)\}\cdot H_2O]_n$ (6.7 mg) were obtained after 1–2 weeks. Satisfactory elemental analysis of the bulk sample could not be obtained; see text for discussion of powder diffraction data.

Crystallography

Single crystal data were collected on a STOE StadiVari diffractometer equipped with a Pilatus300K detector and with a Metaljet D2 source or a Bruker APEX-II diffractometer; data reduction, solution and refinement used the programs STOE X-AREA, STOE X-RED, APEX2, SuperFlip and CRYSTALS respectively.[17–19] SQUEEZE[20] was used in $[Zn_2Cl_4(4)]_n$ because solvent molecules could not be identified in the residual electron density. Four cavities of ~350 Å^3 were identified, and in each, contributions corresponding to 68 electrons were removed, equating to 3 to 4 molecules of MeOH per cavity. SQUEEZE was used in the solvent region of $[Zn_2Br_4(6)\cdot H_2O]_n$. There are 20 587 Å^3 out of 28 228 Å^3 accessible to solvent molecules,[20] which, according to SQUEEZE corresponds to 646 electrons or 4 molecules of MeOH per formula unit. Unfortunately the refinement did not improve after applying SQUEEZE, therefore the structure was left at this stage of refinement without unambiguously identifying solvent molecules in the residual electron density; it follows that the calculated density is low. Powder diffraction data were collected on a Stoe Stadi P powder diffractometer. Structure analysis used the program Mercury v. 3.7 (ref. 21 and 22) and TOPOS.[23]

$[Zn_2Cl_4(4)]_n$

$C_{48}H_{48}Cl_4N_6O_2Zn_2$, M = 1013.52, yellow block, monoclinic, space group $C2/c$, a = 20.4985(9), b = 11.6491(3), c = 23.7457(10) Å, β = 91.737(4)°, U = 5667.6(4) Å^3, Z = 4, D_c = 1.188 Mg m^{-3}, μ(Ga-Kα) = 2.036 mm^{-1}, T = 123 K. Total 95 099 reflections, 5516 unique, R_{int} = 0.057. Refinement of 3189 reflections (280 parameters) with $I > 2\sigma(I)$ converged at final R_1 = 0.0451 (R_1 all data = 0.0676), wR_2 = 0.0510 (wR_2 all data = 0.0578), gof = 0.8726. CCDC 1541160.

$[Zn_2Cl_4(5)\cdot 2MeOH]_n$

$C_{58}H_{72}Cl_4N_6O_4Zn_2$, M = 1189.82, colourless plate, monoclinic, space group $C2/c$, a = 20.777(2), b = 11.6382(9), c = 23.8738(17) Å, β = 90.074(7)°, U = 5772.8(8) Å^3, Z = 4, D_c = 1.369 Mg m^{-3}, μ(Cu-Kα) = 3.122 mm^{-1}, T = 123 K. Total 34 161 reflections, 5360 unique, R_{int} = 0.034. Refinement of 5077 reflections (332 parameters) with $I > 2\sigma(I)$ converged at final R_1 = 0.0726 (R_1 all data = 0.0749), wR_2 = 0.1722 (wR_2 all data = 0.1726), gof = 0.7625. CCDC 1541161.

$[Zn_2Br_4(6)\cdot H_2O]_n$

$C_{54}H_{44}Br_4N_6O_3Zn_2$, M = 1275.36, yellow block, trigonal, space group $R\bar{3}$, $a = b$ = 35.9593(6), c = 25.1227(3) Å, U = 28 133.2(9) Å^3, Z = 9, D_c = 0.677 Mg m^{-3}, μ(Ga-Kα) = 1.410 mm^{-1}, T = 123 K. Total 140 567 reflections, 12 851 unique, R_{int} = 0.073. Refinement of 6571 reflections (316 parameters) with $I > 2\sigma(I)$ converged at final R_1 = 0.0898 (R_1 all data = 0.1242), wR_2 = 0.0719 (wR_2 all data = 0.0924), gof = 0.9393. CCDC 1541159.

Results and discussion

Ligand synthesis and characterization

Compounds **4**, **5** and **6** were prepared as summarized in Scheme 4. The dibromo-precursors **4a** and **5a** have been previously prepared by bromination of the respective 1,4-dialkoxybenzenes, the latter first being prepared from hydroquinone.[15] However, we found it more convenient to start with the commercially available 2,5-dibromohydroquinone. Reaction of **4a**, **5a** or **6a** with ^{n}BuLi followed by DMF (see Scheme 4) yielded dialdehydes **4b**, **5b** or **6b**. The intermediates were characterized by NMR spectroscopy (assigned using 2D methods) and GC-EI mass spectrometry, before being converted to the bis(4,2′:6′,4″-tpy) ligands **4**–**6** using a one-pot Hanan-type[5] synthesis. ^{1}H and ^{13}C NMR spectra were assigned using COSY, HMQC, HMBC and NOESY methods. The ^{1}H NMR spectrum of **5** is shown in Fig. S2.† The disappearance of the ^{1}H NMR resonance at ~δ 10.5 ppm on going from **4b** to **4**, **5b** to **5**, or **6b** to **6** was consistent with functionalization of the aryl core at both aldehyde sites. The ^{1}H NMR signature of each 4,2′:6′,4″-tpy unit consisted of a singlet (δ 8.11, 8.11 or 8.12 ppm in **4**, **5** or **6**) for proton H^{B3}

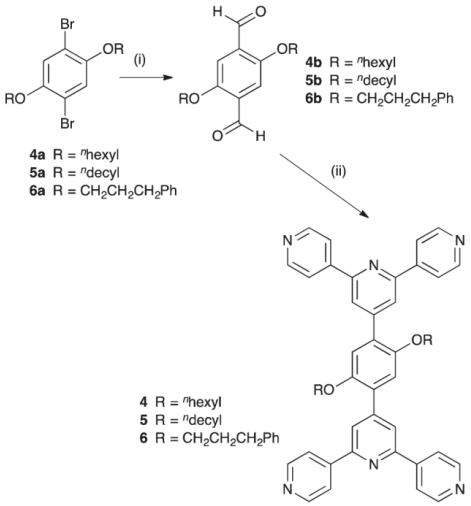

Scheme 4 Synthetic method for preparation of ligands **4**, **5** and **6**. Conditions: (i) ^{n}BuLi, Et_2O, 0 °C, 6 h; DMF, room temperature; (ii) 4-acetylpyridine, KOH, EtOH; aqueous NH_3.

and multiplets for protons H^{A2} and H^{A3} at δ 8.80 or 8.81 and 8.09 ppm, respectively (see Scheme 3 for atom labelling). A comparison of the aromatic regions of the ^{1}H NMR spectra of **4**, **5**, and **6** is shown in Fig. S3–S5.† The parent ions in the electrospray mass spectra (EIS MS) and high resolution EIS MS of **4**–**6** (see Experimental section) were in accordance with expected molecular masses.

Alkoxy chains: 2D → 2D parallel interpenetrated sheets

We initially chose to investigate the reactions of ligands **4** and **5** with zinc(II) chloride as an extension of our previous studies of the 2D networks formed when **2** (^{n}octyl functionality) and **3** (methyl functionality) react with ZnX_2 (X = Cl, Br, I). The difference between **4** and **5** is the length of the alkoxy chain (Scheme 3), the ^{n}hexoxy and ^{n}decoxy chains in **4** and **5** being, respectively, shorter and longer than the ^{n}octyl chains known to give 2D → 2D parallel interpenetrated sheets in $[\{Zn_2Cl_4(2)\}\cdot 4H_2O]_n$ and $[\{Zn_2Br_4(2)\}]_n$.[13,14] Ligand **4** contains alkoxy chains that are longer than the methyl substituents in $[\{Zn_2Br_4(3)\}\cdot 2C_6H_4Cl_2]_n$ and $[\{Zn_2I_4(3)\}\cdot 2.3C_6H_4Cl_2]_n$; these assemble into 2D-networks with no interpenetration.

A MeOH solution of $ZnCl_2$ was layered over a $CHCl_3$ solution of **4** or **5** and after one to two weeks, X-ray quality crystals were harvested. Single crystal X-ray diffraction revealed the formation of $[Zn_2Cl_4(4)]_n$ and $[Zn_2Cl_4(5)\cdot 2MeOH]_n$. The lattice in $[Zn_2Cl_4(4)]_n$ also contains solvent molecules, but these were not unambiguously identified (see Experimental section). Both $[Zn_2Cl_4(4)]_n$ and $[Zn_2Cl_4(5)\cdot 2MeOH]_n$ crystallize in the monoclinic space group $C2/c$, with similar cell dimensions. These parameters are also comparable with those of $[\{Zn_2Cl_4(2)\}\cdot 4H_2O]_n$ and $[\{Zn_2Br_4(2)\}]_n$ (Table S1†),[13,14] consistent with the assembly of similar extended structures. The asymmetric unit in each of $[Zn_2Cl_4(4)]_n$ and $[Zn_2Cl_4(5)\cdot 2MeOH]_n$ contains one $ZnCl_2$ unit and half of ligand **4** or **5**; the second half of the repeat unit is generated by inversion. The repeat units of $[Zn_2Cl_4(4)]_n$ and $[Zn_2Cl_4(5)\cdot 2MeOH]_n$ with symmetry generated atoms are shown in Fig. 1 and S6,† and selected bond lengths and angles are given in the figure captions. As expected,[1] each of ligands **4** and **5** coordinates through only the four outer nitrogen atoms. Atom Zn1 (in both structures) is tetrahedrally sited, bound to two Cl atoms and to two N atoms of different ligands. The angles that define the tetrahedral coordination sphere are in the range 103.35(9) to 123.64(5)° in $[Zn_2Cl_4(4)]_n$, and 104.44(10) to 122.26(5)° in $[Zn_2Cl_4(5)\cdot 2MeOH]_n$. The 4,2′:6′,4″-tpy unit in each compound deviates from planarity to a similar degree; in $[Zn_2Cl_4(4)]_n$, the angles between the planes of adjacent pyridine rings are 0.3 and 15.9°, and the corresponding angles in $[Zn_2Cl_4(5)\cdot 2MeOH]_n$ are 3.5 and 16.4°. The twist of the arene spacer with respect to the pyridine ring to which it is bonded is 51.5° for coordinated **4** and 51.8° for **5**.

Ligand **4** acts as a 4-connecting node, generating a uninodal (4,4) net with the zinc(II) centres functioning only as linkers. Fig. 2a illustrates that each metallomacrocycle in the net is defined by two 4,2′:6′,4″-tpy domains from different ligands (coloured orange in Fig. 2a) and two 'half-ligands' (shown in blue in Fig. 2a). The non-planarity of the macrocyclic units leads to a net with a corrugated topology. The (4,4) nets lie in the *bc*-plane and Fig. 2b views part of one net looking down the *c*-axis. The centroids of the arene rings running across the middle of Fig. 2b correspond to the nodes of the net. The ^{n}hexoxy chains adopt an extended conformation

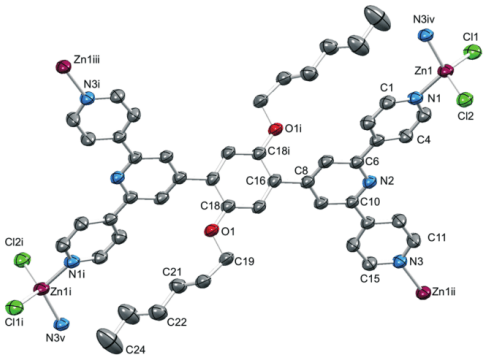

Fig. 1 The repeat unit (with symmetry generated atoms) in $[Zn_2Cl_4(4)]_n$ (H atoms omitted; ellipsoids plotted at 40% probability level). Symmetry codes: i = 1 − *x*, −*y*, −*z*; ii = *x*, 1 − *y*, −1/2 + *z*; iii = 1 − *x*, 1 + *y*, 1/2 − *z*; iv = *x*, 1 − *y*, 1/2 + *z*; v = 1 − *x*, −1 + *y*, −1/2 − *z*. Selected bond parameters: Zn1–N1 = 2.026(3), Zn1–$N3^{iv}$ = 2.034(3), Zn1–Cl1 = 2.2137(11), Zn1–Cl2 = 2.2445(12), O1–C18 = 1.361(4), O1–C19 = 1.439(4) Å; $N3^{iv}$–Zn1–Cl1 = 107.06(9), $N3^{iv}$–Zn1–Cl2 = 106.02(10), Cl1–Zn1–Cl2 = 123.64(5), $N3^{iv}$–Zn1–N1 = 112.07(12), Cl1–Zn1–N1 = 104.68(9), Cl2–Zn1–N1 = 103.35(9), C18–O1–C19 = 118.8(3)°.

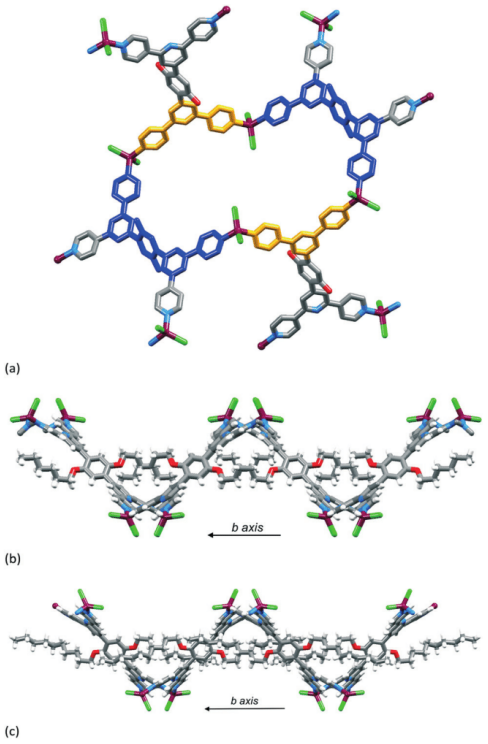

Fig. 2 (a) One macrocyclic unit within one network in $[Zn_2Cl_4(4)]_n$ contains four Zn atoms, two complete 4,2′:6′,4″-tpy domains (orange) and two 'half-ligands' (blue). ^{n}Hexoxy chains and H atoms are omitted for clarity. Part of one net in (b) $[Zn_2Cl_4(4)]_n$ and (c) $[Zn_2Cl_4(5)\cdot 2MeOH]_n$ showing the corrugated topology and the alignment of the ^{n}hexoxy (in (b)) or ^{n}decoxy (in (c)) chains parallel to the *b*-axis.

and are directed within the corrugated sheet. These structural features are replicated in $[Zn_2Cl_4(5)\cdot 2MeOH]_n$ (Fig. 2c). The profile (Fig. 2b and c) of the (4,4) nets in $[Zn_2Cl_4(4)]_n$ and $[Zn_2Cl_4(5)\cdot 2MeOH]_n$ are essentially invariant of the length of the alkoxy tail with the node···node separations being 16.6 and 16.7 Å, respectively; the distance is measured between centroids of the arene rings. The corresponding separations in $[\{Zn_2Cl_4(2)\}\cdot 4H_2O]_n$ and $[\{Zn_2Br_4(2)\}]_n$ which contain ^{n}octyl chains[13,14] are 16.6 and 16.8 Å, respectively. The corrugated topology of the (4,4) nets in $[Zn_2Cl_4(4)]_n$ and $[Zn_2Cl_4(5)\cdot 2MeOH]_n$ allows them to interpenetrate in a 2D → 2D parallel manner, just as we have previously observed in $[\{Zn_2Cl_4(2)\}\cdot 4H_2O]_n$ and $[\{Zn_2Br_4(2)\}]_n$.[13,14] This is shown for $[Zn_2Cl_4(4)]_n$ in Fig. 3. We have previously shown that shortening the tails (*i.e.* going from ^{n}octoxy to methoxy functionalization) causes the profile of the corrugated sheet to change.[14] Although a (4,4) net is retained, the profile flattens, switching off the 2D → 2D parallel interpenetration. The persistence of the same structural motifs in the series of compounds $[Zn_2Cl_4(4)]_n$, $[\{Zn_2Cl_4(2)\}\cdot 4H_2O]_n$, $[\{Zn_2Br_4(2)\}]_n$ and $[Zn_2Cl_4(5)\cdot 2MeOH]_n$ further supports our earlier proposal that the chain contributes to the assembly process. The structures do not feature close alignment of the chains, indicating that inter-chain van der Waals interactions are not a contributing factor. In each of $[Zn_2Cl_4(4)]_n$ and $[Zn_2Cl_4(5)\cdot 2MeOH]_n$, the alkoxy chain lies over two pyridine rings of a 4,2′:6′,4″-tpy unit (Fig. 4), giving rise to short CH···π contacts.[24] The closest CH···π distances are 3.01 in $[Zn_2Cl_4(4)]_n$ and 3.47 Å in $[Zn_2Cl_4(5)\cdot 2MeOH]_n$. We note that a similar arrangement is observed in $[\{Zn_2Cl_4(2)\}\cdot 4H_2O]_n$ (CSD[25] refcode NOTPUJ)[13] with the closest CH···π contact being 2.95 Å (Fig. S7†).

The X-ray powder diffraction pattern of the bulk sample of $[Zn_2Cl_4(5)\cdot 2MeOH]_n$ (Fig. S1†) gave a reasonable fit with that predicted from the single crystal structure data. Shifts between observed and predicted peaks are expected since the powder and single crystal measurements were carried out at room temperature and 123 K, respectively. Crystals of $[Zn_2Cl_4(4)]_n$ readily lost solvent and this, combined with the use of SQUEEZE for $[Zn_2Cl_4(4)]_n$, resulted in a poor fit between the bulk sample powder diffraction pattern and that predicted from the single crystal structure.

Introduction of a terminal phenyl functionality

The consistency of structural architecture obtained for alkoxy tails containing between six and ten carbon atoms led us to

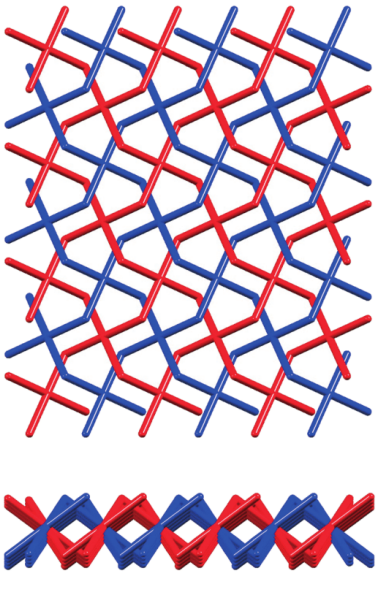

Fig. 3 2D → 2D parallel interpenetrated networks within one sheet (*bc*-plane) in $[Zn_2Cl_4(4)]_n$ viewed (a) down the *a*-axis and (b) down the *c*-axis.

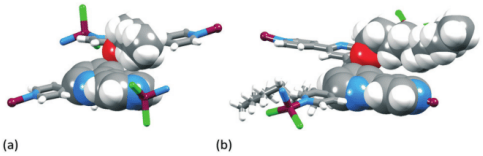

Fig. 4 Orientation of an (a) ^{n}hexoxy and (b) ^{n}decoxy chain over a 4,2′:6′,4″-tpy domain in $[Zn_2Cl_4(4)]_n$ and $[Zn_2Cl_4(5)\cdot 2MeOH]_n$, respectively.

consider the effects of introducing a structural unit to switch the assembly process. We have already shown that loss of long alkoxy functionalities results in retention of a (4,4) network but loss of 2D → 2D parallel interpenetration.[14] We chose to replace the ^{n}alkoxy unit by a 3-phenylpropoxy substituent, retaining a length similar to ^{n}hexoxy but incorporating a terminal phenyl group. This terminal unit has potential for additional π-stacking interactions. Methanol solutions of $ZnCl_2$ or $ZnBr_2$ were each layered over a $CHCl_3$ solution of **6** but X-ray quality crystals grew only from the $ZnBr_2$ containing reaction mixture. Structural analysis revealed the formation of solvated $[Zn_2Br_4(6)\cdot H_2O]_n$. The solvent region in the structure proved problematical during refinement (see Experimental section), and crystals readily lost solvent resulting in a poor fit between the bulk sample powder diffraction pattern and that predicted from the single crystal structure.

$[Zn_2Br_4(6)\cdot H_2O]_n$ crystallizes in the trigonal $R\bar{3}$ space group and the asymmetric unit contains one $ZnBr_2$ unit and half a molecule of **6**. The second half is generated by inversion and the repeat unit in $[Zn_2Br_4(6)\cdot H_2O]_n$ with symmetry generated atoms is shown in Fig. 5. The repeat unit resembles those in $[Zn_2Cl_4(4)]_n$ (Fig. 1) and $[Zn_2Cl_4(5)\cdot 2MeOH]_n$ (Fig. S6†). Bond angles in the coordination sphere of tetrahedral Zn1 are in the range 104.90 to 126.32(4)°, and bond distances (caption to Fig. 5) are unexceptional. The angles between the planes of the pyridine rings containing N1/N2 and N2/N3 are 22.0 and 12.5°, respectively, while the ring containing C16 is twisted through 51.4° with respect to the pyridine ring to which it is bonded.

As in $[Zn_2Cl_4(4)]_n$ and $[Zn_2Cl_4(5)\cdot 2MeOH]_n$, the bis(4,2′:6′,4″-tpy) ligand in $[Zn_2Br_4(6)\cdot H_2O]_n$ acts as a 4-connecting node and the Zn atom is a linker. However, in contrast to the 2D (4,4) nets in $[Zn_2Cl_4(4)]_n$ and $[Zn_2Cl_4(5)\cdot 2MeOH]_n$, the combination of $ZnBr_2$ and **6** leads to a 3D architecture. Fig. 6 shows an overlay of the repeat units of $[Zn_2Cl_4(4)]_n$ and $[Zn_2Br_4(6)\cdot H_2O]_n$. The only significant difference between the two motifs is the direction in which the peripheral N donors (atoms $N3^{iv}$ and $N3^{v}$ in Fig. 1 and 5) point. This change is brought about by rotation about the Zn–N bonds and appears to be associated with the proximity of the terminal phenyl substituent to the $\{ZnX_2N_2\}$ unit. Unfortunately, we were not able to grow X-ray quality crystals of the chlorido-analogue of $[Zn_2Br_4(6)\cdot H_2O]_n$, but we propose that it is the presence of the phenyl group (rather than the bromine atoms) that directs the switch from 2D to 3D assembly. This conjecture is based

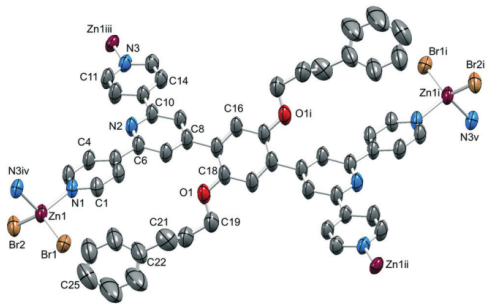

Fig. 5 The repeat unit (with symmetry generated atoms) in $[Zn_2Br_4(6)\cdot H_2O]_n$ (H atoms and water molecule omitted; ellipsoids plotted at 40% probability level). Symmetry codes: i = 1 − *x*, 1 − *y*, 2 − *z*; ii = 1/3 − *x* + *y*, 2/3 − *x*, 2/3 + *z*; iii = 2/3 + *x* + *y*, 1/3 + *x*, 4/3 − *z*; iv = −1/3 + *y*, 1/3 − *x* + *y*, 4/3 − *z*; v = 4/3 − *y*, 2/3 + *x* − *y*, 2/3 + *z*. Selected bond parameters: Zn1–$N3^{iv}$ = 2.052(4), Zn1–Br1 = 2.3635(8), Zn1–Br2 =2.3462(8), Zn1–N1 = 2.058(3), O1–C18 = 1.382(6), O1–C19 = 1.435(8) Å; $N3^{iv}$–Zn1–Br1 = 104.90(11), $N3^{iv}$–Zn1–Br2 = 106.83(10), Br1–Zn1–Br2 = 126.32(4), $N3^{iv}$–Zn1–N1 = 105.99(15), Br1–Zn1–N1 = 105.36(11), Br2–Zn1–N1 = 105.97(11), C18–O1–C19 = 119.4(4)°.

upon the analogous 2D assemblies observed for $[\{Zn_2Cl_4(2)\}\cdot 4H_2O]_n$ and $[\{Zn_2Br_4(2)\}]_n$ (Table S1†).

The structure of $[Zn_2Br_4(6)\cdot H_2O]_n$ propagates into a 3D-framework of 2-fold interpenetrating $\{6^4\cdot 8^2\}$ **nbo** nets.[26,27] Fig. 7 shows a TOPOS[23] representation of part of the lattice. The distortion away from an ideal **nbo** net arises from the difference between an archetype square-planar geometry and the X-shaped 4-connecting node of **6** which has internal angles of 54.3 and 125.7°. The $R\bar{3}$ symmetry leads to hexagonal channels which follow the crystallographic *c*-axis (Fig. 8 and S8†). As Fig. 8a shows, the pendant phenyl rings are directed into the channels and each ring is oriented to face a 4,2′:6′,4″-tpy in the adjacent net. The distance between the centroid of the phenyl ring with C22 and the least squares plane through the two pyridine rings containing $N2^{vi}$ and $N3^{vi}$ (symmetry code vi = 1/3 + *x* − *y*, −1/3 + *x*, 5/3 − *z*) is 3.57 Å, and the angle between the planes through these units is

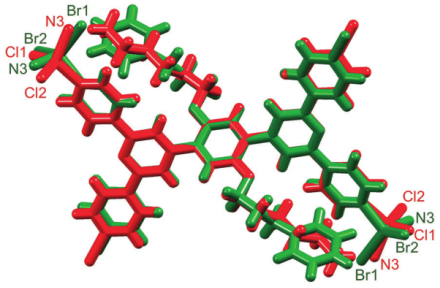

Fig. 6 Overlay of the repeat units with symmetry generated atoms of $[Zn_2Cl_4(4)]_n$ (in red) and $[Zn_2Br_4(6)\cdot H_2O]_n$ (in green).

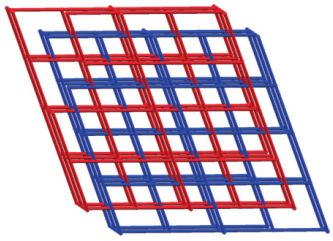

Fig. 7 TOPOS[23] representation of the interpenetrated **nbo** nets in $[Zn_2Br_4(\mathbf{6})\cdot H_2O]_n$.

7.1°. The shortest distance between a C_{phenyl} atom (C27) and the centroid of the unit comprising the two pyridine rings with N2^{vi} and N3^{vi} is 3.77 Å. The relative positions of the two aromatic units are too far offset for the interaction to be classed as a typical face-to-face π-stacking contact.[28,29] Nonetheless, the interactions around the walls of the hexagonal channels serve to lock the interpenetrated nets in close proximity to one another, leaving large voids in the lattice. The solvent accessible void space in the lattice represents ~65% of the total volume[21] (Fig. 8b). The close association of two interpenetrated **nbo** nets leading to large, unobstructed channels has also been described by Hawes *et al.*,[30] and Chun and coworkers[31] in related structures that crystallize in the $R\bar{3}$ space group. Both these assemblies are predicated upon copper(II) 4-connecting nodes and organic linkers. In the first example,[30] the **nbo** nets associate through NH···O hydrogen bonded interactions. In the second,[31] non-coordinated N-donors of pyrimidine-5-carboxylate linkers in one **nbo** net weakly bind to square planar copper(II) nodes in the second net. Interestingly, attempts to produce a corresponding assembly by replacing pyrimidine-5-carboxylate by pyridine-3-carboxylate linkers (thereby removing the additional N-donors) were unsuccessful.[31] This lends support to our premise that the peripheral phenyl groups in **6** play a role in stabilizing the interpenetrated 3D architecture in $[Zn_2Br_4(\mathbf{6})\cdot H_2O]_n$. A number of related assemblies (space group $R\bar{3}$) involving 2-fold interpenetrating **nbo** nets with large-diameter hexagonal channels running parallel to the *c*-axis have been described.[32] In each case, the 4-connecting nodes are metal ions and the linkers are organic ligands. This contrasts with the reverse situation in $[Zn_2Br_4(\mathbf{6})\cdot H_2O]_n$.

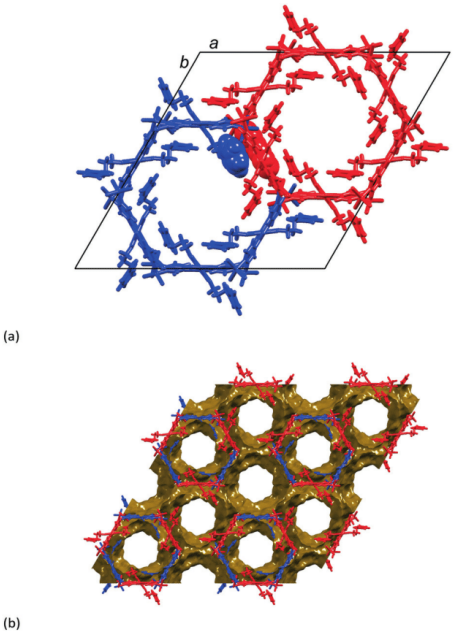

Fig. 8 (a) Parts of interpenetrated nets (red and blue) in $[Zn_2Br_4(\mathbf{6})\cdot H_2O]_n$. View down the *c*-axis showing location of the terminal phenyl groups within the hexagonal channels; one stacking contact is shown in space-filling representation. (b) View down the *c*-axis showing the void space in the hexagonal channels (drawn using Mercury v. 3.7 (ref. 21 and 22)).

Conclusions

We have described the synthesis and characterization of three ditopic bis(4,2′:6′,4″-tpy) ligands, **4**–**6**. Ligands **4** and **5** bear ^{n}hexoxy and ^{n}decoxy tails, respectively, while **6** is functionalized with 3-phenylpropoxy tails. Reactions of **4** or **5** with $ZnCl_2$ lead to $[Zn_2Cl_4(\mathbf{4})]_n$ or $[Zn_2Cl_4(\mathbf{5})\cdot 2MeOH]_n$, respectively. The compounds crystallize in the *C*2/*c* space group with similar 2D → 2D parallel interpenetrating (4,4) nets; the ditopic ligands act as planar 4-connecting nodes. The ^{n}alkoxy tails are in extended conformations and are threaded within the sheets. The close structural similarities between $[Zn_2Cl_4(\mathbf{4})]_n$ and $[Zn_2Cl_4(\mathbf{5})\cdot 2MeOH]_n$ and the previously reported $[\{Zn_2Cl_4(\mathbf{2})\}\cdot 4H_2O]_n$ and $[\{Zn_2Br_4(\mathbf{2})\}]_n$ (ref. 13 and 14) provide strong support for the network being invariant for ^{n}alkoxy tails containing six to ten carbon atoms. However, the presence of ^{n}alkoxy tails is a prerequisite for the 2D → 2D parallel interpenetration. The introduction of a terminal phenyl group in going to ligand **6** switches the 2D assembly to a highly porous 3D architecture. $[Zn_2Br_4(\mathbf{6})\cdot H_2O]_n$ crystallizes in the $R\bar{3}$ space group and the structure comprises 2-fold interpenetrating **nbo** nets. Again, the 4-connecting nodes are the bis(4,2′:6′,4″-tpy) ligands, contrasting with related structures in which the 4-connecting nodes are metal centres.[30–32] The pendant phenyl rings in **6** lie over the 4,2′:6′,4″-tpy domains in an adjacent net and these contacts result in tight interlocking of the interpenetrated nets. As a consequence of this, the lattice contains hexagonal channels which follow the crystallographic *c*-axis. We are now exploring the consequences of adapting the terminal functionality, in an effort to better understand[33,34] the factors that direct the interpenetration of the 3D-nets.

Acknowledgements

We acknowledge the Swiss National Science Foundation (grant number 200020_162631) and the University of Basel for financial support. The Swiss National Science Foundation through the NCCR Molecular Systems Engineering is acknowledged for partial funding of the powder diffractometer. Professor Stuart Batten is acknowledged for his helpful comments.

Notes and references

1 C. E. Housecroft, *Dalton Trans.*, 2014, **43**, 6594.
2 C. E. Housecroft, *CrystEngComm*, 2015, **17**, 7461.
3 See for example: S. Khatua, A. K. Bar and S. Konar, *Chem. – Eur. J.*, 2016, **22**, 16277; S. Khatua, S. Goswani, S. Biswas, K. Tomar, H. S. Jena and S. Konar, *Chem. Mater.*, 2015, **27**, 5349; A. K. Mondal, S. Khatua, K. Tomar and S. Konar, *Eur. J. Inorg. Chem.*, 2016, 3545; Y. M. Klein, A. Prescimone, E. C. Constable and C. E. Housecroft, *Aust. J. Chem.*, 2017, **70**, 468; M. Zhao, J. Tan, J. Su, J. Zhang, S. Zhang, J. Wu and Y. Tian, *Dyes Pigm.*, 2016, **130**, 216; G. Zhang, J. Tan, T. Phoenix, D. R. Manke, J. A. Golen and A. L. Rheingold, *RSC Adv.*, 2016, **6**, 9270; Z. Yin, S. Zhang, S. Zheng, J. A. Golen, A. L. Rheingold and G. Zhang, *Polyhedron*, 2015, **101**, 139; L. Li, Y. Z. Zhang, C. Yang, E. Liu, J. A. Golen and G. Zhang, *Polyhedron*, 2016, **105**, 115; Y. M. Klein, A. Prescimone, E. C. Constable and C. E. Housecroft, *Polyhedron*, 2016, **103A**, 58; Y. M. Klein, A. Prescimone, M. B. Pitak, S. J. Coles, E. C. Constable and C. E. Housecroft, *CrystEngComm*, 2016, **18**, 4704 and references therein.
4 F. Kröhnke, *Synthesis*, 1976, 1.
5 J. Wang and G. S. Hanan, *Synlett*, 2005, 1251.
6 See for example: M. Lusi, P. B. A. Fechine, K.-J. Chen, J. J. Perry IV and M. J. Zaworotko, *Chem. Commun.*, 2016, **525**, 4160; N. Li and R. Huang, *J. Solid State Chem.*, 2016, **233**, 320; W. Sun, J. Liu, H. Liu and Z. Liu, *Polyhedron*, 2016, **109**, 1.
7 See for example: Y. Wu, L. Lu, J. Feng, Y. Li, Y. Sun and A. Ma, *J. Solid State Chem.*, 2017, **245**, 213; Z.-L. Wu, C.-H. Wang, B. Zhao, J. Dong, F. Lu, W.-H. Wang, W.-C. Wang, G.-J. Wu, J.-Z. Cui and P. Cheng, *Angew. Chem., Int. Ed.*, 2016, **55**, 4938; X. Li, X.-L. Chi, Y.-C. Xu, Y. Chen, Q. Yang, X.-S. Zeng, H.-L. Xu and D.-R. Xiao, *Inorg. Chem. Commun.*, 2016, **69**, 52; J. Liu, J. Xiao, D. Wang, W. Sun, X. Guo, H. Yu, H. Liu and Z. Liu, *Cryst. Growth Des.*, 2016, **17**, 1096.
8 Y. Watanabe, R. Yoshioka, H. Sasabe, T. Kamata, H. Katagiri, D. Yokoyama and J. Kido, *J. Mater. Chem. C*, 2016, **4**, 8980.
9 J. Lü, C. Perez-Krap, M. Suyetin, N. H. Alsmail, Y. Yan, S. Yang, W. Lewis, E. Bichoutskaia, C. C. Tang, A. J. Blake, R. Cao and M. Schröder, *J. Am. Chem. Soc.*, 2014, **136**, 12828.
10 Y. M. Klein, A. Prescimone, E. C. Constable and C. E. Housecroft, *Inorg. Chem. Commun.*, 2016, **70**, 118.
11 J. Yoshida, S.-I. Nishikiori and H. Yuge, *J. Coord. Chem.*, 2013, **66**, 2191.
12 Y. M. Klein, E. C. Constable, C. E. Housecroft and A. Prescimone, *CrystEngComm*, 2015, **17**, 2070.
13 E. C. Constable, C. E. Housecroft, S. Vujovic and J. A. Zampese, *CrystEngComm*, 2014, **16**, 3494; E. C. Constable, C. E. Housecroft, S. Vujovic and J. A. Zampese, *CrystEngComm*, 2017, **19**, 2271.
14 S. Vujovic, E. C. Constable, C. E. Housecroft, C. D. Morris, M. Neuburger and A. Prescimone, *Polyhedron*, 2015, **92**, 77.
15 C. L. Moy, R. Kaliappan and A. J. McNeil, *J. Org. Chem.*, 2011, **76**, 8501.
16 M. K. Choi, H. L. Kim and D. H. Suh, *J. Appl. Polym. Sci.*, 2006, **101**, 1228.
17 Stoe & Cie (2011). *X-area Software*, Stoe & Cie (1996). XRED V1.08.
18 L. Palatinus and G. Chapuis, *J. Appl. Crystallogr.*, 2007, **40**, 786.
19 P. W. Betteridge, J. R. Carruthers, R. I. Cooper, K. Prout and D. J. Watkin, *J. Appl. Crystallogr.*, 2003, **36**, 1487.
20 A. L. Spek, *Acta Crystallogr., Sect. C: Struct. Chem.*, 2015, **71**, 9.
21 I. J. Bruno, J. C. Cole, P. R. Edgington, M. K. Kessler, C. F. Macrae, P. McCabe, J. Pearson and R. Taylor, *Acta Crystallogr., Sect. B: Struct. Sci.*, 2002, **58**, 389.
22 C. F. Macrae, I. J. Bruno, J. A. Chisholm, P. R. Edgington, P. McCabe, E. Pidcock, L. Rodriguez-Monge, R. Taylor, J. van de Streek and P. A. Wood, *J. Appl. Crystallogr.*, 2008, **41**, 466.
23 V. A. Blatov and A. P. Shevchenko, *TOPOS Professional v. 4.0*, Samara State University, Russia.
24 M. Nishio, *CrystEngComm*, 2004, **6**, 130.
25 C. R. Groom, I. J. Bruno, M. P. Lightfoot and S. C. Ward, *Acta Crystallogr., Sect. B: Struct. Sci., Cryst. Eng. Mater.*, 2016, **72**, 171.
26 D.-S. Li, Y.-P. Wu, J. Zhao, J. Zhang and J. Y. Lu, *Coord. Chem. Rev.*, 2014, **261**, 1.
27 S. R. Batten, S. M. Neville and D. R. Turner, *Coordination Polymers: Design, Analysis and Application*, RSC Publishing, Cambridge, 2009.
28 C. A. Hunter and J. K. M. Sanders, *J. Am. Chem. Soc.*, 1990, **112**, 5525.
29 C. A. Hunter, K. R. Lawson, J. Perkins and C. J. Urch, *J. Chem. Soc., Perkin Trans. 2*, 2001, 651.
30 C. S. Hawes, R. Babarao, M. R. Hill, K. F. White, B. F. Abrahams and P. E. Kruger, *Chem. Commun.*, 2012, **48**, 11558.
31 J. Seo, N. Jin and H. Chun, *Inorg. Chem.*, 2010, **49**, 10833.
32 See for example: W.-W. Dong, L. Xia, Z. Peng, J. Zhao, Y.-P. Wu, J. Zhang and D.-S. Li, *J. Solid State Chem.*, 2016, **238**, 170; P. Yang, H.-Y. Zhou, K. Zhang and B.-H. Ye, *CrystEngComm*, 2011, **13**, 5658; G.-G. Hou, Y. Liu, Q.-K. Liu, J.-P. Ma and Y.-B. Dong, *Chem. Commun.*, 2011, **47**, 10731; D. Liu, M. Li and D. Li, *Chem. Commun.*, 2009, 6943.
33 S. R. Batten, *J. Solid State Chem.*, 2005, **178**, 2475.
34 D. Zhao, D. J. Timmons, D. Yuan and H.-C. Zhou, *Acc. Chem. Res.*, 2011, **44**, 123.

18.10 Paper 10 (Published by the Royal Society of Chemistry)

Volume 17 | Number 10 | 14 March 2015 | Pages 2053–2214

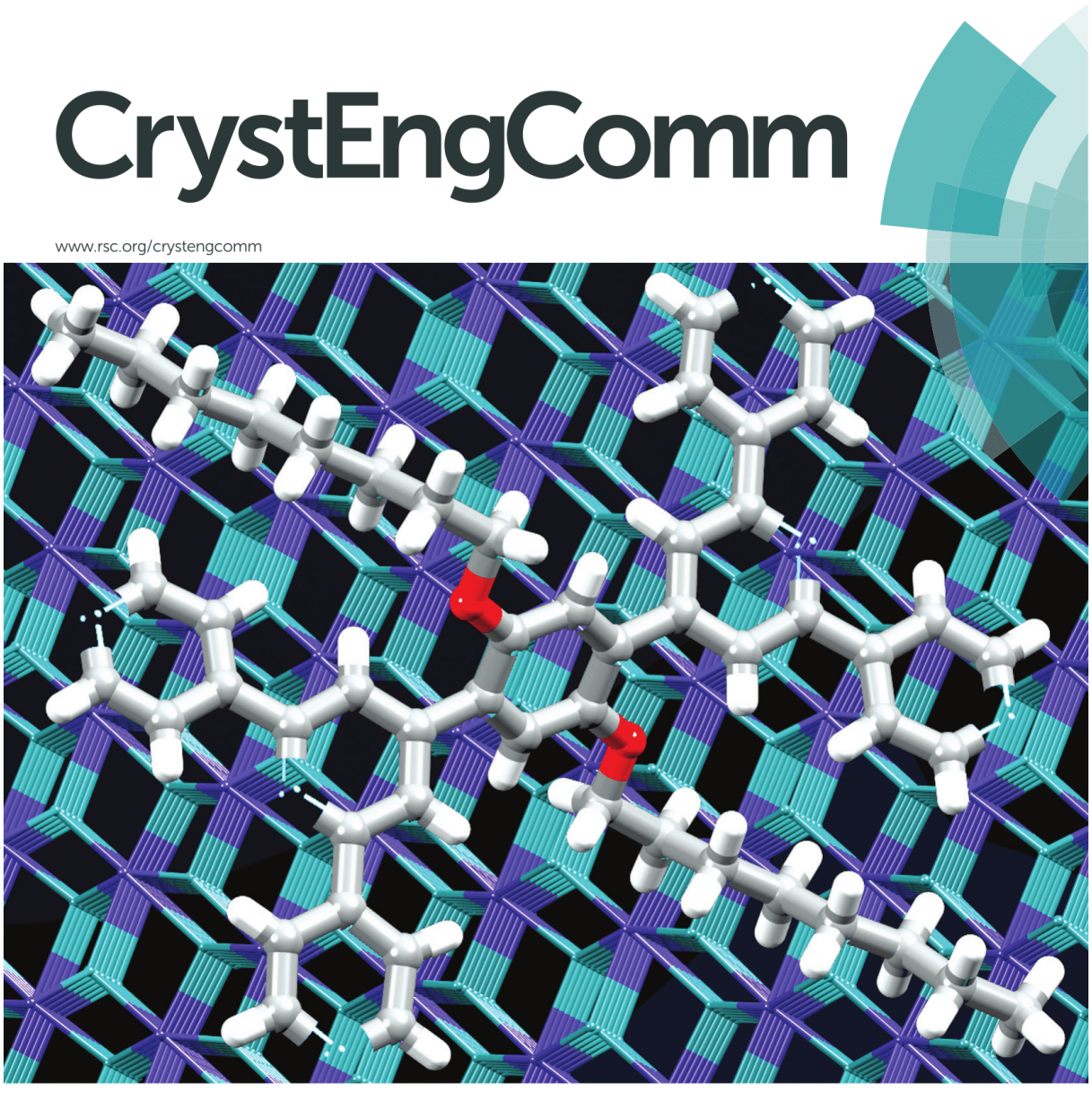

CrystEngComm

COMMUNICATION

View Article Online
View Journal | View Issue

Cite this: *CrystEngComm*, 2015, **17**, 2070

Received 27th November 2014,
Accepted 13th December 2014

DOI: 10.1039/c4ce02347a

www.rsc.org/crystengcomm

A 3-dimensional $\{4^2{\cdot}8^4\}$ lvt net built from a ditopic bis(3,2′:6′,3″-terpyridine) tecton bearing long alkyl tails†

Y. Maximilian Klein, Edwin C. Constable, Catherine E. Housecroft* and Alessandro Prescimone

Divergent bis(terpyridine) tectons are versatile ligands for the assembly of coordination networks; we demonstrate the assembly of a 3-dimensional $\{4^2{\cdot}8^4\}$ **lvt** net (still relatively sparse among 4-connected nets in metal–organic frameworks) from the reaction of 1,4-bis(*n*-octoxy)-2,5-bis(3,2′:6′,3″-terpyridin-4′-yl)benzene and $Co(NCS)_2$.

Oligopyridines[1] remain as one of the most widespread building blocks in the toolbox of a coordination chemist. The bis(chelate) 2,2′:6′,2″-terpyridine (2,2′:6′,2″-tpy) is especially popular and multitopic ligands containing peripheral 2,2′:6′,2″-tpy domains[2] have been used in a wide variety of architectures. 4,2′:6′,4″-Terpyridine (4,2′:6′,4″-tpy, Scheme 1) and 3,2′:6′,3″-terpyridine (3,2′:6′,3″-tpy, Scheme 1) are less familiar isomers of terpyridine, but in the last decade, the use of 4,2′:6′,4″-tpy as a building block of coordination polymers has grown significantly.[3] In metal complexes of 4,2′:6′,4″-tpy, the central pyridine ring is non-coordinated and the remaining *N*,*N*′-donor set presents a divergent domain, with vectorial properties that are unaffected by inter-ring bond rotation (red bonds in Scheme 1). In contrast, rotation about the interannular bonds in 3,2′:6′,3″-tpy alters its divergent coordination mode.[4]

The beauty of terpyridine metal-binding domains is the ease with which substituents can be introduced into the 4′-position, for example by using Kröhnke's[5] or Wang and Hanan's[6] strategies. With coordinatively innocent 4′-substituents, reactions between 4,2′:6′,4″-terpyridines and metal ions yield metallomacrocycles, 1-dimensional chains or 2-dimensional nets.[3] Extension to 3-dimensions is achieved by introducing non-innocent domains such as diphenylphosphino,[7] carboxylato,[8] or pyridyl[9] functionalities, or by using co-ligands.[10] An alternative approach to increase dimensionality is through the coordination capacity of multitopic 4,2′:6′,4″-tpy ligands, although such compounds have received scant attention.[11–14] We have demonstrated that 1,4-bis(*n*-octoxy)-2,5-bis(4,2′:6′,4″-terpyridin-4′-yl)benzene reacts with $ZnCl_2$ to give a network consisting of (4,4)-sheets engaging in 2D → 2D parallel interpenetration,[14] and a report on a triply interpenetrating network formed between cobalt(II) and 1,3-di((4,2′:6′,4″-terpyridin)-4′-yl)benzene has appeared.[12] We now describe the synthesis of the bis(3,2′:6′,3″-tpy) ligand **1** (Scheme 1) and its reaction with $Co(NCS)_2$ to give a 3-dimensional $\{4^2{\cdot}8^4\}$ **lvt** net.[15] The inclusion of the long alkoxy chains in **1** enhances the solubility of the ligand with respect to analogues with simple phenylene spacers,[14] and also has a stabilizing influence on an infinite architecture.

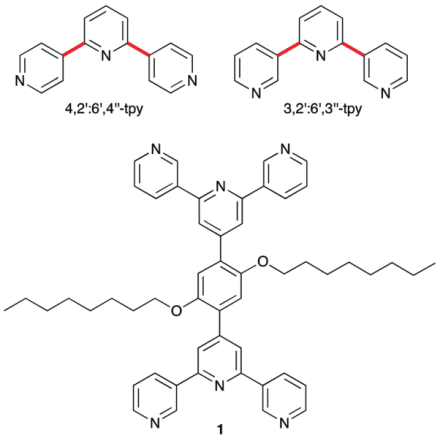

Scheme 1 Structures of divergent isomers of terpyridine and the ditopic ligand **1**. See text for significance of the bonds marked in red.

Department of Chemistry, University of Basel, Spitalstrasse 51, CH4056 Basel, Switzerland. E-mail: catherine.housecroft@unibas.ch; Fax: +41 61 267 1018; Tel: +41 61 267 1008

† Electronic supplementary information (ESI) available: Synthetic and crystallographic details; Fig. S1–S2 solution ^{1}H NMR and absorption spectra of **1**. CCDC 1035825. See DOI: 10.1039/c4ce02347a

Ligand **1** was synthesized† using the one-pot method of Wang and Hanan[6] starting from 2,5-bis(octoxy)benzene-1,4-dicarbaldehyde and 4.7 equivalents of 3-acetylpyridine in EtOH in the presence of NH_3. Compound **1** was isolated in 41% yield. The electrospray mass spectrum exhibited a base peak at *m*/*z* 797.8 arising from $[M+H]^+$, and ^1H (Fig. S1†) and ^{13}C NMR spectra (assigned using COSY, DEPT, HMQC and HMBC techniques) were consistent with the symmetrical structure shown in Scheme 1. The absorption spectrum of **1** has broad and intense, high energy bands arising from $\pi^* \leftarrow n$ and $\pi^* \leftarrow \pi$ transitions which extend into the visible region (Fig. S2†).

Layering of MeOH and $CHCl_3$ solutions of $Co(NCS)_2$ and **1**, respectively, resulted in the formation of pink crystals of $[Co(NCS)_2(\mathbf{1})\cdot 4CHCl_3]_n$ within 2–4 weeks in 14% yield. The crystal selected for single crystal X-ray diffraction was solved and refined in the non-centrosymmetric space group $Pna2_1$. The Flack parameter of 0.480(10) suggested that it was a twin by inversion[16] as every attempt to either solve or refine the structure in *Pnma* failed and ADDSYMM[17] could not identify an alternative space group. The asymmetric unit contains one molecule of **1** and a $Co(NCS)_2$ unit; the octoxy chain containing atom C19 was refined isotropically and three of the C–C distances were restrained to chemically reasonable values. The cobalt ion is octahedrally coordinated, and **1** binds through the outer *N*-donors to four cobalt centres (Fig. 1), leaving the central nitrogen atoms N2 and N6 uncoordinated. Atom Co1 coordinates to two $[NCS]^-$ ligands in a *trans*-arrangement and to four different **1** ligands in the equatorial plane. The two independent octoxy chains are in non-extended conformation, and each is folded over a 3,2′:6′,3″-tpy unit with close C–H···π contacts (H···centroid = 3.19 and 3.23 Å for the pyridine rings containing N1 and N4).

Pairs of cobalt atoms are either bridged by a single 4,2′:6′,4″-tpy (*e.g.* Co1 and Co1^{v} in Fig. 1) or by two *N*-donors from each of the two 4,2′:6′,4″-tpy domains of **1** (*e.g.* Co1 and Co1^{iv} in Fig. 1). The latter coordination mode extends to the formation of [2 + 2] metallomacrocycles (Fig. 2a) which are interlinked through the cobalt centres, as shown in Fig. 2b. The structure propagates into a 2-nodal $\{4^2\cdot 8^4\}$ **lvt** net.[14] The two 4-connected nodes are Co1 and the centroid of the arene spacer in **1**, which are planar and approximately tetrahedral, respectively. Although the local $\{Co(N_{tpy})_4\}$ domain in $[Co(NCS)_2(\mathbf{1})\cdot 4CHCl_3]_n$ is square planar (N_{tpy}–Co–N_{tpy} angles = 90.9(3), 89.1(3), 92.9(3) and 87.1(3)°), the cobalt node is distorted in the topological description of the net (centroid–Co–centroid angles = 96.6, 64.6, 132.2 and 67.4°) while remaining planar. Topological representations of the framework in $[Co(NCS)_2(\mathbf{1})\cdot 4CHCl_3]_n$ are shown in Fig. 3. The view down the *a*-axis in Fig. 3a is directly comparable with the structure in Fig. 2b.

The voids in the net are occupied by the octoxy chains and $CHCl_3$ molecules. Fig. 4 illustrates that the chains lie in the *ac*-plane, a consequence of the close CH···π contacts between the terminal CH_2CH_3 units of each chain and pyridine rings (see above).

In conclusion, we have shown that, by adopting a conformation in which the two 3,2′:6′,3″-tpy metal-binding domains

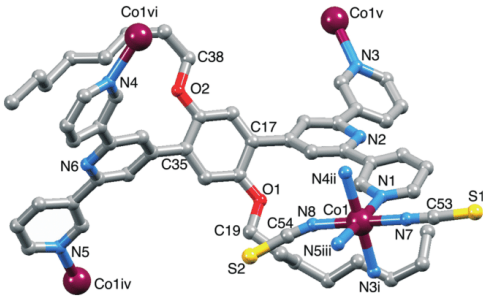

Fig. 1 The repeat unit (with symmetry generated Co atoms) in $[Co(NCS)_2(\mathbf{1})\cdot 4CHCl_3]_n$ (H atoms and solvent molecules are omitted). Symmetry codes: i = 1/2 + *x*, 1/2 − *y*, *z*; ii = −*x*, 1 − *y*, −1/2 + *z*; iii = 1/2 − *x*, 1/2 + *y*, 1/2 − *z*; iv = 1/2 − *x*, −1/2 + *y*, 1/2 + *z*; v = −1/2 + *x*, 1/2 − *y*, *z*; vi = −*x*, 1 − *y*, 1/2 + *z*. Selected bond parameters: Co1–N1 = 2.185(8), Co1–N3i = 2.212(7), Co1–N4ii = 2.204(8), Co1–N5iii = 2.181(8), Co1–N7 = 2.096(8), Co1–N8 = 2.079(8) Å; Co1–N7–C53 = 161.0(8), Co1–N8–C54 = 151.2(8), N1–Co1–N5iii = 176.2(3), N3i–Co1–N4ii = 178.6(3)°.

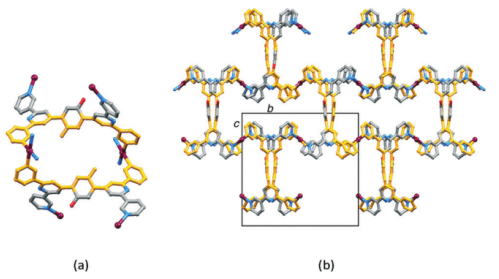

Fig. 2 (a) A [2 + 2] metallomacrocycle formed from two Co1 atoms and two half-ligands (in orange). (b) Interconnection of metallomacrocycles with the unit cell viewed down the *a*-axis.

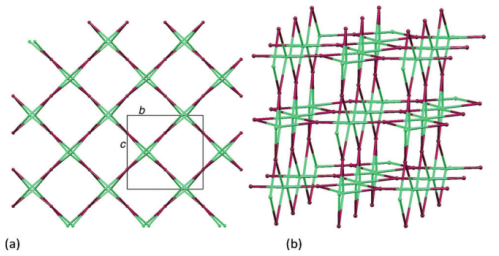

Fig. 3 TOPOS[18] representations of the $\{4^2\cdot 8^4\}$ **lvt** net in $[Co(NCS)_2(\mathbf{1})\cdot 4CHCl_3]_n$: (a) view down the *a*-axis for comparison with Fig. 2b, and (b) showing the 4- and 8-membered metallomacrocycles. Metal nodes, purple; ligand–centroid nodes, green.

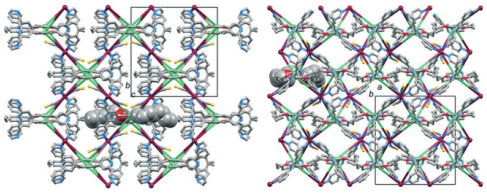

Fig. 4 Superimposition of the topological representation of the **lvt** net in $[Co(NCS)_2(\mathbf{1})\cdot 4CHCl_3]_n$ and the structure (H atoms and $CHCl_3$ molecules are omitted); the octoxy chains of one ligand are shown in the space-filling representation: views down the (a) *a*-axis and (b) *c*-axis.

are orthogonal, ligand **1** can combine with a planar 4-connecting metal node to produce a $\{4^2{\cdot}8^4\}$ **lvt** net. Among metal–organic frameworks, the **lvt** topology is scarce in comparison with other 4-connected nets.[19] The conformational flexibility of ditopic bis(4,2′:6′,4″-tpy) and bis(3,2′:6′,3″-tpy) ligands allows the two tpy units to lie on a path between coplanar[13] and orthogonal (as in the current work), making these isomeric ligands attractive tectons. We are currently developing the coordination chemistry of multitopic 4,2′:6′,4″-tpy and 3,2′:6′,3″-tpy ligands to investigate which building blocks favour the assembly of 2- *versus* 3-dimensional networks.

Acknowledgements

We thank the Swiss National Science Foundation (grant 200020_149067), the European Research Council (Advanced grant 267816 LiLo) and the University of Basel for financial support.

Notes and references

1 R. P. Thummel, *Comprehensive Coordination Chemistry II*, ed. J. A. McCleverty and T. J. Meyer, Elsevier, Oxford, 2003, vol. 1, p. 41.
2 See for example: E. C. Constable, *Chem. Soc. Rev.*, 2007, **36**, 246; E. C. Constable, *Coord. Chem. Rev.*, 2008, **252**, 842; E. C. Constable, A. M. W. Cargill Thompson, P. Harveson, L. Macko and M. Zehnder, *Chem. – Eur. J.*, 1995, **1**, 360; A. Wild, A. Winter, F. Schluetter and U. S. Schubert, *Chem. Soc. Rev.*, 2011, **40**, 1459; Y. Yan and J. Huang, *Coord. Chem. Rev.*, 2010, **254**, 1072; E. C. Constable, *Chimia*, 2013, **67**, 388, and references therein and references therein.
3 C. E. Housecroft, *Dalton Trans.*, 2014, **43**, 6594.
4 E. C. Constable, C. E. Housecroft, M. Neuburger, S. Vujovic, J. A. Zampese and G. Zhang, *CrystEngComm*, 2012, **14**, 3554.
5 F. Kröhnke, *Synthesis*, 1976, 1.
6 J. Wang and G. S. Hanan, *Synlett*, 2005, 1251.
7 X. Tan, X. Chen, J. Zhang and C.-Y. Song, *Dalton Trans.*, 2012, **41**, 3616.
8 See for example: L. Wen, X. Ke, L. Qiu, Y. Zou, L. Zhou, J. Zhao and D. Li, *Cryst. Growth Des.*, 2012, **12**, 4083; C. Niu, A. Ning, C. Feng, X. Wan and C. Kou, *J. Inorg. Organomet. Polym.*, 2012, **22**, 519; P. Yang, M.-S. Wang, J.-J. Shen, M.-X. Li, Z.-X. Wang, M. Shao and X. He, *Dalton Trans.*, 2014, **43**, 1460; Y.-L. Gai, F.-L. Jiang, L. Chen, Y. Bu, M.-Y. Wu, K. Zhou, J. Pan and M.-C. Hong, *Dalton Trans.*, 2013, **42**, 9954; Y. Li, Z. Ju, B. Wu and D. Yuan, *Cryst. Growth Des.*, 2013, **13**, 4125; F. Yuan, J. Xie, H.-M. Hu, C.-M. Yuan, B. Xu, M.-L. Yang, F.-X. Dong and G.-L. Xue, *CrystEngComm*, 2013, **15**, 1460; F. Yuan, Q. Zhu, H.-M. Hu, J. Xie, B. Xu, C.-M. Yuan, M.-L. Yang, F.-X. Dong and G.-L. Xue, *Inorg. Chim. Acta*, 2013, **397**, 117; H.-N. Zhang, F. Yuan, H.-M. Hu, S.-S. Shen and G.-L. Xue, *Inorg. Chem. Commun.*, 2013, **34**, 51; W. Yang, A. J. Davies, X. Lin, M. Suyetin, R. Matsuda, A. J. Blake, C. Wilson, W. Lewis, J. E. Parker, C. C. Tang, M. W. George, P. Hubberstey, S. Kitagawa, H. Sakamoto, E. Bichoutskaia, N. R. Champness, S. Yang and M. Schröder, *Chem. Sci.*, 2012, **3**, 2992; Y.-Q. Chen, S.-J. Liu, Y.-W. Li, G.-R. Li, K.-H. He, Y.-K. Qu, T.-L. Hu and X.-H. Bu, *Cryst. Growth Des.*, 2012, **12**, 5426; F. Yuan, J. Xie, H.-M. Hu, C.-M. Yuan, B. Xu, M.-L. Yang, F.-X. Dong and G.-L. Xue, *CrystEngComm*, 2013, **15**, 1460.
9 J. Heine, J. Schmedt auf der Günne and S. Dehnen, *J. Am. Chem. Soc.*, 2011, **133**, 10018; E. C. Constable, G. Zhang, C. E. Housecroft and J. A. Zampese, *CrystEngComm*, 2011, **13**, 6864; V. N. Dorofeeva, S. V. Kolotilov, M. A. Kiskin, R. A. Polunin, Z. V. Dobrokhotova, O. Cador, S. Golhen, L. Ouahab, I. L. Eremenko and V. M. Novotortsev, *Chem. – Eur. J.*, 2012, **18**, 5006; Y.-Q. Chen, G.-R. Li, Y.-K. Qu, Y.-H. Zhang, K.-H. He, Q. Gao and X.-H. Bu, *Cryst. Growth Des.*, 2013, **13**, 901; C. Liu, Y.-B. Ding, X.-H. Shi, D. Zhang, M.-H. Hu, Y.-G. Yin and D. Li, *Cryst. Growth Des.*, 2009, **9**, 1275; J. Song, B.-C. Wang, H.-M. Hu, L. Gou, Q.-R. Wu, X.-L. Yang, Y.-Q. Shangguan, F.-X. Dong and G.-L. Xue, *Inorg. Chim. Acta*, 2011, **366**, 134; K.-R. Ma, F. Ma, Y.-L. Zhu, L.-J. Yu, X.-M. Zhao, Y. Yang and W.-H. Duan, *Dalton Trans.*, 2011, **40**, 9774; Y.-Q. Chen, G.-R. Li, Z. Chang, Y.-K. Qu, Y.-H. Zhang and X.-H. Bu, *Chem. Sci.*, 2013, **4**, 3678.
10 See for example: N. Li, Q.-E. Zhu, H.-M. Hu, H.-L. Guo, J. Xie, F. Wang, F.-X. Dong, M.-L. Yang and G.-L. Xue, *Polyhedron*, 2013, **49**, 207; B.-C. Wang, X.-L. Chen, H.-M. Hu, H.-L. Yao and G.-L. Xue, *Inorg. Chem. Commun.*, 2009, **12**, 856; N. Li, H.-L. Guo, H.-M. Hu, J. Song, B. Xu, M.-L. Yang, F.-X. Dong and G.-L. Xue, *J. Solid State Chem.*, 2013, **198**, 416; B.-C. Wang, Q.-R. Wu, H.-M. Hu, X.-L. Chen, Z.-H. Yang, Y.-Q. Shangguan, M.-L. Yang and G.-L. Xue, *CrystEngComm*, 2010, **12**, 485.
11 G. W. V. Cave and C. L. Raston, *J. Chem. Soc., Perkin Trans. 1*, 2001, 3258.
12 J. Yoshida, S.-I. Nishikiori and H. Yuge, *J. Coord. Chem.*, 2013, **66**, 2191.
13 S. A. S. Ghozlan and A. Z. A. Hassanien, *Tetrahedron*, 2002, **58**, 9423.
14 E. C. Constable, C. E. Housecroft, S. Vujovic and J. A. Zampese, *CrystEngComm*, 2014, **16**, 3494.

15 S. R. Batten, S. M. Neville and D. R. Turner, *Coordination Polymers: Design, Analysis and Application*, RSC Publishing, Cambridge, 2009.
16 H. D. Flack, *Helv. Chim. Acta*, 2003, **86**, 905.
17 A. L. Spek, *J. Appl. Crystallogr.*, 2003, **36**, 7.
18 V. A. Blatov and A. P. Shevchenko, *TOPOS Professional v. 4.0*, Samara State University, Russia.
19 D.-S. Li, Y.-P. Wu, J. Zhao, J. Zhang and J. Y. Lu, *Coord. Chem. Rev.*, 2014, **261**, 1.

18.11 Paper 11 (Published by the Royal Society of Chemistry)

CrystEngComm

COMMUNICATION

View Article Online
View Journal | View Issue

Cite this: *CrystEngComm*, 2016, **18**, 4704

Received 22nd April 2016,
Accepted 16th May 2016

DOI: 10.1039/c6ce00939e

www.rsc.org/crystengcomm

Constructing chiral MOFs by functionalizing 4,2′:6′,4″-terpyridine with long-chain alkoxy domains: rare examples of *neb* nets†

Y. Maximilian Klein,[a] Alessandro Prescimone,[a] Mateusz B. Pitak,[b] Simon J.Coles,[b] Edwin C. Constable[a] and Catherine E. Housecroft*[a]

Reactions of 4′-(4-^{n}alkyloxyphenyl)-4,2′:6′,4″-terpyridines (alkyl = hexyl or nonyl) with $Co(NCS)_2$ lead to three structurally characterized chiral 3D assemblies which adopt rare *neb* topologies. For the ^{n}hexyl-functionalized ligands, both enantiomorphic lattices of the *neb* nets (crystallizing in the tetragonal space groups $P4_12_12$ and $P4_32_12$, respectively) are presented.

The coordination chemistry of the divergent ligands 4,2′:6′,4″- and 3,2′:6′,3″-terpyridine is dominated by the assembly of extended 1D chain or 2D sheet structures or discrete metallomacrocycles.[1–4] 4,2′:6′,4″-Terpyridines (4,2′:6′,4″-tpy) coordinate only through the outer two pyridine donors, providing the V-shaped tecton shown in Scheme 1. This coordination motif is well-established and entry into higher-dimensionality architectures is typically accomplished by introducing donor groups in the 4′-position. In addition to the widespread use of pyridinyl[5–7] and carboxylate[8–13] functionalities, sulfonate donors have also been used to access 3D frameworks.[14] 3D-networks utilizing only the two pendant donors of the 4,2′:6′,4″-tpy domain are relatively rare, although the reaction of 4′-(pyridin-2-yl)-4,2′:6′,4″-tpy and $Co(NCS)_2$ gives a 3D structure in which the pyridinyl substituent is not coordinated.[15] This is an unusual case where combination of a simple 4,2′:6′,4″-tpy ligand and $Co(NCS)_2$ leads to a 3D framework; more usually, 2D (4,4) or (6,3) nets result.[16–18] A (4,4) net also forms when $CoCl_2{\cdot}6H_2O$ reacts with 4′-(3,4-dimethoxyphenyl)-4,2′:6′,4″-tpy.[19]

Although coordination polymers and networks containing a wide variety of 4,2′:6′,4″-tpy or 3,2′:6′,3″-tpy ligands are known, it remains a challenge to code for 3D frameworks rather than 1D-chains or 2D-nets in the absence of additional coordination domains or of co-ligands. To direct the assembly of 3D architectures predicated upon 4,2′:6′,4″- and 3,2′:6′,3″-tpy motifs, we have adopted two strategies. In the first, we have used ditopic ligands[20] containing 'back-to-back' 4,2′:6′,4″-tpy or 3,2′:6′,3″-tpy domains.[21–23] In the second, we have selected metal-nodes which prefer 6-(or higher) coordination numbers, *e.g.* reaction between the tpy ligands and $Co(NCS)_2$ (ref. 16–18) or $Cd(NO_3)_2{\cdot}4H_2O$.[24–26]

One way to modify assembly algorithms is with 4′-(4-alkyloxyphenyl)-4,2′:6′,4″-terpyridines (Scheme 2) in which the steric demands of the 4′-substituent are altered. We have shown that 1D $[Zn_2(OAc)_4(4'\text{-}(4\text{-}ROC_6H_4)\text{-}4,2':6',4''\text{-tpy})]_n$ coordination polymers in which the main packing interactions are π-stacking between arene domains are favoured for small R groups, whereas with longer-chain alkoxy units in which van der Waals interactions are important, discrete complexes $[Zn_2(OAc)_4(4'\text{-}(4\text{-}ROC_6H_4)\text{-}4,2':6',4''\text{-tpy})_2]$ form.[27] In a second example, functionalization of the spacer in ditopic 4,2′:6′,4″-tpy ligands with ^{n}octyloxy chains directs the formation of 2D → 2D parallel interpenetrated nets, whereas single nets result with methoxy-substituents.[21,22] We recently reported the assembly of 2D (4,4) nets in the reactions of $Co(NCS)_2$ with ligands **1**–**3** (Scheme 2).[17] In each net, the Co atom acts as a 4-connecting, planar node; subtle differences in packing resulted in inter-sheet separations increasing from 8.936 Å (R = Me, Scheme 2) to 9.228 Å (R = Et) to 9.305 Å (R = ^{n}Pr). The

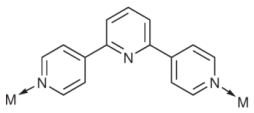

Scheme 1 Divergent coordination mode of the archetype 4,2′:6′,4″-tpy ligand.

[a] *Department of Chemistry, University of Basel, Spitalstrasse 51, CH-4056 Basel, Switzerland. E-mail: catherine.housecroft@unibas.ch*
[b] *Chemistry, Faculty of Natural & Environmental Sciences, University of Southampton, Highfield, Southampton, SO17 1BJ, UK*

† Electronic supplementary information (ESI) available: Experimental and crystallographic details. Fig. S1 and S3: powder diffraction data and additional figures of lattices in $[Co_2(NCS)_4(4)_4]_n$; Fig. S4. interpenetrating *nbo* nets in $[Co(NCS)_2(4'\text{-(pyridin-2-yl)-4,2':6',4''-tpy})]_n$ (refcode XUVPAH). CCDC 1474325–1474327. For ESI and crystallographic data in CIF or other electronic format see DOI: 10.1039/c6ce00939e

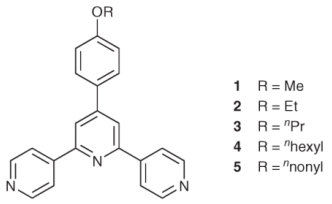

1 R = Me
2 R = Et
3 R = ^{n}Pr
4 R = ^{n}hexyl
5 R = ^{n}nonyl

Scheme 2 The structures of the 4′-(4-alkyloxyphenyl)-4,2′:6′,4″-terpyridine ligands **1**–**5**.

most significant differences in packing arose from the intrusion of the longer alkoxy chains through the cavities in adjacent sheets.[17] These results prompted us to investigate the effects of further increasing the length of the alkyl chains, and we report here the assembly of infrequently observed *neb* nets with 6^6 cage units.[28]

Ligands **4** and **5** were prepared as previously reported.[27] Single crystals of $[Co_2(NCS)_4(\mathbf{4})_4]_n$ were grown at room temperature by layering an MeOH solution of anhydrous $Co(NCS)_2$ over a $CHCl_3$ solution of **4** (36.9 mg, 0.09 mmol). Two different crystals were selected from the bulk material for single-crystal structure determination. These crystallized in the tetragonal space groups $P4_12_12$ and $P4_32_12$, respectively. Since $P4_12_12$ and $P4_32_12$ constitute an enantiomorphic pair, the structure of $[Co_2(NCS)_4(\mathbf{4})_4]_n$ is inherently chiral. However, since the Flack parameters are 0.21(3) and 0.16(2), respectively, each structure contains 21% or 16% of the second enantiomorph. We discuss the local details of the structure for only one structure (that in space group $P4_32_12$). The bulk sample was characterized by powder diffraction (see Fig. S1†).

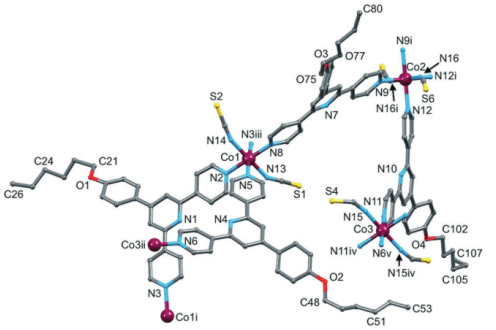

Fig. 1 The asymmetric unit of $[Co_2(NCS)_4(\mathbf{4})_4]_n$ with symmetry-generated atoms (space group $P4_32_12$); H atoms are omitted and only the major sites of the disordered sites (see text) are shown. Symmetry codes: i = $y, x, 1-z$; ii = $-\frac{1}{2}+y, \frac{1}{2}-x, \frac{1}{4}+z$; iii = $\frac{1}{2}-y, -\frac{1}{2}+x, -\frac{1}{4}+z$; iv = $1-y, 1-x, \frac{3}{2}-z$; v = $\frac{1}{2}-x, \frac{1}{2}+y, \frac{7}{4}-z$. Selected bond distances: Co1–N2 = 2.166(5), Co1–N3iii = 2.173(5), Co1–N5 = 2.129(5), Co1–N8 = 2.159(5), Co1–N13 = 2.100(6), Co1–N14 = 2.082(6), Co2–N12 = 2.209(5), Co2–N12i = 2.209(5), Co2–N16 = 2.093(7), Co2–N9 = 2.170(3), Co3–N6 = 2.163(5), Co3–N11 = 2.182(5), Co3–N15 = 2.073(7) Å.

Fig. 1 shows the asymmetric unit of $[Co_2(NCS)_4(\mathbf{4})_4]_n$ with symmetry-generated atoms. Each of the three independent Co atoms is octahedrally sited with a *trans* arrangement of N-bonded thiocyanato ligands. The thiocyanates containing S2, S4 and S6 are disordered and each has been modelled over two sites of 60.3/39.7, 62.1/37.9 and 56.4/43.6% occupancies, respectively. Each of the four independent ligands **4** coordinates through the outer two pyridine rings, consistent with previously reported coordination modes.[1,2] The Co–N bond distances (see caption to Fig. 1) and bond angles within the coordination spheres are unexceptional. No significant deviations from planarity are noted for the tpy units; twist angles between pairs of bonded pyridine rings range from 6.5 to 16.3°. Each phenyl ring is, as expected on steric grounds, twisted with respect to the pyridine ring to which it is attached (range of angles = 36.1 to 37.6°).

The structure shown in Fig. 1 propagates into a 3D framework. The differences in coordination environments about Co1, Co2 and Co3 in $[Co_2(NCS)_4(\mathbf{4})_4]_n$ are structurally insignificant and the framework is uninodal. Fig. 2 shows views down the crystallographic *c* and *b*-axes, generated using a combination of TOPOS[29] and Mercury (v. 3.7).[30,31] The 4-fold screw axes that define the chirality (*i.e.* opposite handednesses in each of space groups $P4_12_12$ and $P4_32_12$, Fig. S2†) of the lattice run along the *c*-axis. Views down either the *a* or *b*-axes (Fig. 2, right) reveal the 6-membered rings present in the 4-connected net. The combination of 4-coordinate nodes and 6-membered rings is reminiscent of diamond. However, whereas a diamond net consists of interconnected 6^4 cage units, Fig. 3 illustrates that the 4-connected framework in $[Co_2(NCS)_4(\mathbf{4})_4]_n$ is constructed from 6^6 cage units.[28] Each Co···Co edge of the 3D framework is spanned by one ligand **4** and the hexyloxy-chains are in close to extended conformations, directed along the *a* and *b*-axes (Fig. 4).

The reaction of **5** with $Co(NCS)_2$ led to single crystals of $[\{Co_2(NCS)_4(\mathbf{5})_4\}\cdot 2CHCl_3\cdot MeOH]_n$. The compound crystallizes in the tetragonal space group $P4_12_12$, once again signifying a chiral network. The asymmetric unit contains three independent Co atoms and four independent ligands **5**, and structural details within the coordination sphere of each Co atom are analogous to those shown in Fig. 1 for $[Co_2(NCS)_4(\mathbf{4})_4]_n$. As in the latter, the Co–N(NCS) bond distances (range 2.065(5) to 2.107(5) Å) in $[\{Co_2(NCS)_4(\mathbf{5})_4\}\cdot 2CHCl_3\cdot MeOH]_n$ are shorter than the C–N(tpy) bond lengths (range 2.153(5) to

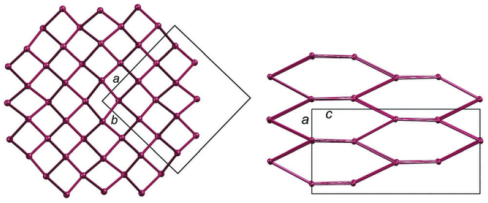

Fig. 2 $[Co_2(NCS)_4(\mathbf{4})_4]_n$ (space group $P4_32_12$): views down the crystallographic *c* and *b* axes, generated using TOPOS and Mercury.

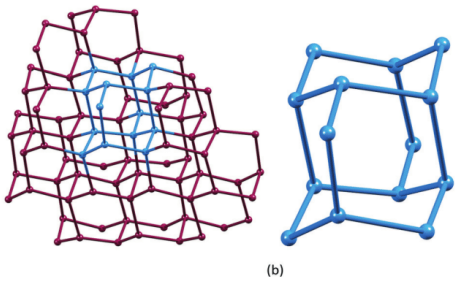

(a) (b)

Fig. 3 (a) TOPOS/Mercury representation of the structure of $[Co_2(NCS)_4(\mathbf{4})_4]_n$ showing Co nodes. (b) The fundamental 6^6 unit of the *neb* topology excised from the framework shown in (a).

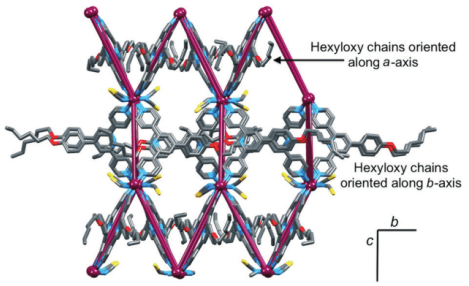

Fig. 4 TOPOS/Mercury representation of $[Co_2(NCS)_4(\mathbf{4})_4]_n$ with superimposed ligand structures (H atoms omitted) viewed down the *a*-axis.

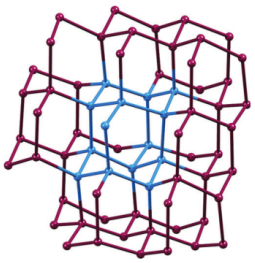

Fig. 5 TOPOS representation of part of the *neb* net in $[\{Co_2(NCS)_4(\mathbf{5})_4\}\cdot 2CHCl_3\cdot MeOH]_n$ showing Co nodes; one 6^6 cage that characterizes the *neb* net is shown in blue.

2.175(4) Å). All thiocyanate ligands and solvent molecules are ordered. The bulk material for $[\{Co_2(NCS)_4(\mathbf{5})_4\}\cdot 2CHCl_3\cdot MeOH]_n$ was characterized by powder diffraction (see Fig. S3†).

Replacing ligand **4** (^{n}hexyloxy chains) by **5** (^{n}nonyloxy chains) has little effect on the overall structure, although the unit cell expands slightly along the *a* and *b* axes in response to the accommodation of the longer alkyl chains which are oriented along these axes (Fig. 4). In the two enantiomorphs of $[Co_2(NCS)_4(\mathbf{4})_4]_n$, $a = b = 23.7111(4)$ and $c = 46.9783(7)$ Å ($V = 26412.0(9)$ Å^3), and $a = b = 23.68444(16)$ and $c = 46.9716(4)$ Å ($V = 26348.8(4)$ Å^3), respectively, while in $[\{Co_2(NCS)_4(\mathbf{5})_4\}\cdot 2CHCl_3\cdot MeOH]_n$, $a = b = 23.88216(9)$ and c = 46.8514(3) Å ($V = 26722.0(3)$ Å^3). This expansion also leads to inclusion of solvate of crystallization. Fig. 5 reveals the assembly of the chiral *neb* net in $[\{Co_2(NCS)_4(\mathbf{5})_4\}\cdot 2CHCl_3\cdot MeOH]_n$, confirming that a change from ^{n}hexyloxy to ^{n}nonyloxy functionality has no effect on the overall architecture.

In addition to the scarcity of the *neb* net among coordination polymers and hydrogen-bonded networks,[32] we note that the space groups $P4_12_12$ and $P4_32_12$ are relatively rare. A search of the Cambridge Structural Database[33,34] (CSD which contains ~800 000 entries) using Conquest[35] v. 5.37 (with November 2015 update) revealed 1563 and 1346 hits for $P4_12_12$ and $P4_32_12$, respectively.

To assess the impact of the long alkoxy chains, we have four benchmark structures. In $[Co(NCS)_2(4'\text{-(pyridin-2-yl)-4,2':6',4''-tpy})]_n$, the pyridin-2-yl substituent is non-coordinating[15] and spatially analogous to the phenyl spacer in ligands **4** and **5**. Although the 3D network was not defined in the original work,[15] inspection of the structure (CSD refcode XUVPAH) reveals interpenetrating *nbo* frameworks (Fig. S4†). Modification with small alkoxy domains leads to 2D (4,4) nets in $[\{Co(NCS)_2(\mathbf{1})_2\}\cdot 4CHCl_3]_n$ and $[\{Co(NCS)_2(\mathbf{2})_2\}\cdot 4CHCl_3]_n$ and $[\{Co_2(NCS)_4(\mathbf{3})_4\}\cdot 2CHCl_3\cdot 1.5MeOH]_n$; these structures all exhibit head-to-tail π-stacking of 4′-(4-alkoxyphenyl) units with the alkyl units protruding into the holes in adjacent sheets. In the current work, we have demonstrated that longer tails switch the structure to an unusual 3D *neb* network in which the extended alkyl chains thread through the lattice. We also note that the chiral MOFs described in this work assemble from achiral nodes and linkers.[36]

Acknowledgements

We acknowledge the Swiss National Science Foundation (Grant number 200020_144500) and the University of Basel for financial support. The Swiss National Science Foundation through the NCCR Molecular Systems Engineering is acknowledged for partial funding of the powder diffractometer. We thank the EPSRC UK National Crystallography Service at the University of Southampton for the collection of the crystallographic data.[37]

Notes and references

1 C. E. Housecroft, *Dalton Trans.*, 2014, **43**, 6594.
2 C. E. Housecroft, *CrystEngComm*, 2015, **17**, 7461.
3 G. Zhang, J. Tan, T. Phoenix, D. R. Manke, J. A. Golen and A. L. Rheingold, *RSC Adv.*, 2016, **6**, 9270 and references therein.
4 L. Li, Y. Z. Zhang, C. Yang, E. Liu, J. A. Golen and G. Zhang, *Polyhedron*, 2016, **105**, 115 and references therein.
5 Y.-Q. Chen, G.-R. Li, Z. Chang, Y.-K. Qu, Y.-H. Zhang and X.-H. Bu, *Chem. Sci.*, 2013, **4**, 3678 and references therein.

6 C. Liu, Y.-B. Ding, X.-H. Shi, D. Zhang, M.-H. Hu, Y.-G. Yin and D. Li, *Cryst. Growth Des.*, 2009, **9**, 1275.
7 X. Li, X.-L. Chi, Y.-C. Xu, Y. Chen, Q. Yang, X.-S. Zeng, H.-L. Xu and D.-R. Xiao, *Inorg. Chim. Acta*, 2016, **445**, 160.
8 P. Yang, M.-S. Wang, J.-J. Shen, M.-X. Li, Z.-X. Wang, M. Shao and X. He, *Dalton Trans.*, 2014, **43**, 1460 and references therein.
9 F. Yuan, J. Xie, H.-M. Hu, C.-M. Yuan, B. Xu, M.-L. Yang, F.-X. Dong and G.-L. Xue, *CrystEngComm*, 2013, **15**, 1460 and references therein.
10 Y. Li, Z. Ju, B. Wu and D. Yuan, *Cryst. Growth Des.*, 2013, **13**, 4125 and references therein.
11 Y. Xi, W. Wei, Y. Xu, X. Huang, F. Zhang and C. Hu, *Cryst. Growth Des.*, 2015, **15**, 2695.
12 B. Xu, B. Liu, H.-M. Hu, Y. Cheng, Z. Chang and G. Xue, *Polyhedron*, 2015, **96**, 88.
13 F. Yuan, R. An, H.-M. Hu, S.-S. Shen, X. Wang, M.-L. Yang and G. Xue, *Inorg. Chem. Commun.*, 2015, **56**, 1.
14 L. Zhang, J.-D. Zheng, Y.-T. Chen, S.-R. Zheng, J. Fan and W.-G. Zhang, *CrystEngComm*, 2015, **17**, 5538.
15 Z. Yin, S. Zhang, S. Zheng, J. A. Golen, A. L. Rheingold and G. Zhang, *Polyhedron*, 2015, **10**, 139.
16 Y. M. Klein, A. Prescimone, E. C. Constable and C. E. Housecroft, *CrystEngComm*, 2015, **17**, 6483.
17 Y. M. Klein, A. Prescimone, E. C. Constable and C. E. Housecroft, *Polyhedron*, 2016, **103**, 58.
18 E. C. Constable, C. E. Housecroft, M. Neuburger, S. Vujovic, J. A. Zampese and G. Zhang, *CrystEngComm*, 2012, **14**, 3554.
19 U. P. Singh, S. Narang, P. Pachfule and R. Banerjee, *CrystEngComm*, 2014, **16**, 5012.
20 J. Yoshida, S.-I. Nishikiori and H. Yuge, *J. Coord. Chem.*, 2013, **66**, 2191.
21 E. C. Constable, C. E. Housecroft, S. Vujovic and J. A. Zampese, *CrystEngComm*, 2014, **16**, 3494.
22 S. Vujovic, E. C. Constable, C. E. Housecroft, C. D. Morris, M. Neuburger and A. Prescimone, *Polyhedron*, 2015, **92**, 77.
23 Y. M. Klein, E. C. Constable, C. E. Housecroft and A. Prescimone, *CrystEngComm*, 2015, **17**, 2070.
24 E. C. Constable, G. Zhang, C. E. Housecroft, M. Neuburger and J. A. Zampese, *CrystEngComm*, 2009, **11**, 2279.
25 E. C. Constable, G. Zhang, C. E. Housecroft, M. Neuburger and J. A. Zampese, *CrystEngComm*, 2010, **12**, 3733.
26 Y. M. Klein, A. Prescimone, E. C. Constable and C. E. Housecroft, *CrystEngComm*, 2015, **17**, 6483.
27 Y. M. Klein, E. C. Constable, C. E. Housecroft, J. A. Zampese and A. Crochet, *CrystEngComm*, 2014, **16**, 9915.
28 D.-S. Li, Y.-P. Wu, J. Zhao, J. Zhang and J. Y. Lu, *Coord. Chem. Rev.*, 2014, **261**, 1.
29 V. A. Blatov and A. P. Shevchenko, *TOPOS Professional v. 4.0*, Samara State University, Russia.
30 C. F. Macrae, P. R. Edgington, P. McCabe, E. Pidcock, G. P. Shields, R. Taylor, M. Towler and J. van de Streek, *J. Appl. Crystallogr.*, 2006, **39**, 453.
31 C. F. Macrae, I. J. Bruno, J. A. Chisholm, P. R. Edgington, P. McCabe, E. Pidcock, L. Rodriguez-Monge, R. Taylor, J. van de Streek and P. A. Wood, *J. Appl. Crystallogr.*, 2008, **41**, 466.
32 See for example: O. Ermer and A. Eling, *J. Chem. Soc., Perkin Trans. 2*, 1994, 925.
33 F. H. Allen, *Acta Crystallogr., Sect. B: Struct. Sci.*, 2002, **58**, 380.
34 C. R. Groom, I. J. Bruno, M. P. Lightfoot and S. C. Ward, *Acta Crystallogr., Sect. B: Struct. Sci., Cryst. Eng. Mater.*, 2016, **72**, 171.
35 I. J. Bruno, J. C. Cole, P. R. Edgington, M. Kessler, C. F. Macrae, P. McCabe, J. Pearson and R. Taylor, *Acta Crystallogr., Sect. B: Struct. Sci.*, 2002, **58**, 389.
36 See for example: N. Chen, M.-X. Li, P. Yang, X. He, M. Shao and S.-R. Zhu, *Cryst. Growth Des.*, 2013, **13**, 2650 and references therein.
37 S. J. Coles and P. A. Gale, *Chem. Sci.*, 2012, **3**, 683.

19 REFERENCES

[1] S. L. James, *Chem. Soc. Rev.* **2003**, *32*, 276-288.

[2] C. E. Housecroft, A. G. Sharpe, in *Inorganic Chemistry, 3rd edn*, Pearson, **2008**, pp. 198-199.

[3] R. Martin, S. L. Buchwald, *Acc. Chem. Res.* **2008**, *41*, 1461-1473.

[4] J. C. Bailar, *Inorganic Chemicals and Reactions* **1964**, *1*, 1.

[5] S. Kitagawa, R. Kitaura, S.-i. Noro, *Angew. Chem., Int. Ed.* **2004**, *43*, 2334-2375.

[6] C. Janiak, *Dalton Trans.* **2003**, 2781-2804.

[7] K. Biradha, A. Ramanan, J. J. Vittal, *Cryst. Growth Des.* **2009**, *9*, 2969-2970.

[8] C. E. Housecroft, E. C. Constable, *J. Inorg. Organomet. Polym. Mater.* **2017**.

[9] H.-C. Zhou, S. Kitagawa, *Chem. Soc. Rev.* **2014**, *43*, 5415-5418.

[10] D. J. Tranchemontagne, J. L. Mendoza-Cortes, M. O'Keeffe, O. M. Yaghi, *Chem. Soc. Rev.* **2009**, *38*, 1257-1283.

[11] C. E. Housecroft, *Dalton Trans.* **2014**, *43*, 6594-6604.

[12] S. R. Batten, S. M. Neville, D. R. Turner, in *Coordination Polymers*, The Royal Society of Chemistry, **2009**, pp. 001-424.

[13] G. R. Desiraju, in *The Crystal as a Supramolecular Entity*, Wiley, **1996**, pp. 1-326.

[14] X. Lin, A. J. Blake, C. Wilson, X. Z. Sun, N. R. Champness, M. W. George, P. Hubberstey, R. Mokaya, M. Schröder, *J. Am. Chem. Soc.* **2006**, *128*, 10745-10753.

[15] J.-R. Li, R. J. Kuppler, H.-C. Zhou, *Chem. Soc. Rev.* **2009**, *38*, 1477-1504.

[16] H. Zheng, Q. Wang, Y. Long, H. Zhang, X. Huang, R. Zhu, *Chem. Commun.* **2011**, *47*, 10650-10652.

[17] Z.-Y. Liu, J. Chu, B. Ding, X.-J. Zhao, E.-C. Yang, *Inorg. Chem. Commun.* **2011**, *14*, 925-928.

[18] Y. Liu, G. Li, X. Li, Y. Cui, *Angew. Chem., Int. Ed.* **2007**, *46*, 6301-6304.

[19] M.-H. Zeng, Q.-X. Wang, Y.-X. Tan, S. Hu, H.-X. Zhao, L.-S. Long, M. Kurmoo, *J. Am. Chem. Soc.* **2010**, *132*, 2561-2563.

[20] B. Kesanli, W. Lin, *Coord. Chem. Rev.* **2003**, *246*, 305-326.

[21] A. U. Czaja, N. Trukhan, U. Müller, *Chem. Soc. Rev.* **2009**, *38*, 1284-1293.

[22] A. L. Goodwin, C. J. Kepert, *Phys. Rev. B* **2005**, *71*, 140301.

[23] C. J. Kepert, *Chem. Commun.* **2006**, 695-700.

[24] L. Carlucci, G. Ciani, D. M. Proserpio, *Coord. Chem. Rev.* **2003**, *246*, 247-289.

[25] M. Eddaoudi, J. Kim, D. Vodak, A. Sudik, J. Wachter, M. O'Keeffe, O. M. Yaghi, *Proc. Natl. Acad. Sci.* **2002**, *99*, 4900-4904.

[26] A. Y. Robin, K. M. Fromm, *Coord. Chem. Rev.* **2006**, *250*, 2127-2157.

[27] J. J. Perry Iv, J. A. Perman, M. J. Zaworotko, *Chem. Soc. Rev.* **2009**, *38*, 1400-1417.

[28] R. Robson, *J. Chem. Soc., Dalton Trans.* **2000**, 3735-3744.

[29] C. E. Housecroft, A. G. Sharpe, in *Inorganic Chemistry, 3rd edn*, Pearson, **2008**, pp. 621-627.

[30] Y. M. Klein, E. C. Constable, C. E. Housecroft, J. A. Zampese, A. Crochet, *CrystEngComm* **2014**, *16*, 9915-9929.

[31] Y. M. Klein, A. Prescimone, E. C. Constable, C. E. Housecroft, *Aust. J. Chem.* **2017**, *70*, 468-477.

[32] Y. M. Klein, A. Prescimone, E. C. Constable, C. E. Housecroft, *Mater.* **2017**, *10*, 728.

[33] D. F. Schrempp, E. Schneider, E. Kaifer, H. Wadepohl, H.-J. Himmel, *Chem. - Eur. J.* **2017**, *23*, 11636-11648.

[34] C. R. Groom, I. J. Bruno, M. P. Lightfoot, S. C. Ward, *Acta Crystallogr., Sect. B* **2016**, *72*, 171-179.

[35] I. J. Bruno, J. C. Cole, P. R. Edgington, M. Kessler, C. F. Macrae, P. McCabe, J. Pearson, R. Taylor, *Acta Crystallogr., Sect. B* **2002**, *58*, 389-397.

[36] R. Rajak, M. Saraf, A. Mohammad, S. M. Mobin, *J. Mater. Chem. A* **2017**, *5*, 17998-18011.

[37] L. Li, R.-B. Lin, R. Krishna, X. Wang, B. Li, H. Wu, J. Li, W. Zhou, B. Chen, *J. Mater. Chem. A* **2017**, *5*, 18984-18988.

[38] S.-Y. Zhang, C.-X. Yang, W. Shi, X.-P. Yan, P. Cheng, L. Wojtas, M. J. Zaworotko, *Chem* **2017**, *3*, 281-289.

[39] X. Wang, J. Feng, J. Huang, J. Zhang, M. Pan, C.-Y. Su, *CrystEngComm* **2010**, *12*, 725-729.

[40] S.-L. Kuang, H.-Y. Li, D.-B. Dang, X.-J. Pan, *Synth. React. Inorg., Met.-Org., Nano-Met. Chem.* **2012**, *42*, 59-64.

[41] H. Konaka, L. P. Wu, M. Munakata, T. Kuroda-Sowa, M. Maekawa, Y. Suenaga, *Inorg. Chem.* **2003**, *42*, 1928-1934.

[42] J. Barnes, *Acta Crystallogr., Sect. E* **2004**, *60*, m971-m972.

[43] B. Nohra, Y. Yao, C. Lescop, R. Réau, *Angew. Chem., Int. Ed.* **2007**, *46*, 8242-8245.

[44] N. Sinha, F. Roelfes, A. Hepp, F. E. Hahn, *Chem. - Eur. J.* **2017**, *23*, 5939-5942.

[45] R. J. Hill, D.-L. Long, M. S. Turvey, A. J. Blake, N. R. Champness, P. Hubberstey, C. Wilson, M. Schroder, *Chem. Commun.* **2004**, 1792-1793.

[46] D. W. Agnew, M. Gembicky, C. E. Moore, A. L. Rheingold, J. S. Figueroa, *J. Am. Chem. Soc.* **2016**, *138*, 15138-15141.

[47] M. S. Shimazu, X. Zhao, D. M. Huynh, X. Bu, *Cryst. Growth Des.* **2015**, *15*, 2550-2554.

[48] K. H. Stone, D. L. Turner, M. P. Singh, T. P. Vaid, P. W. Stephens, *Acta Crystallogr., Sect. B* **2011**, *67*, 409-415.

[49] S. Finoto, A. Machulek, A. R. L. Caires, E. J. de Arruda, G. A. Casagrande, C. Raminelli, L. H. C. Andrade, S. M. Lima, *Polyhedron* **2015**, *99*, 96-102.

[50] G. Férey, C. Mellot-Draznieks, C. Serre, F. Millange, J. Dutour, S. Surblé, I. Margiolaki, *Science* **2005**, *309*, 2040-2042.

[51] Y. Inokuma, T. Arai, M. Fujita, *Nat. Chem.* **2010**, *2*, 780.

[52] M. Fujita, D. Oguro, M. Miyazawa, H. Oka, K. Yamaguchi, K. Ogura, *Nature* **1995**, *378*, 469.

[53] Y. Inokuma, S. Yoshioka, J. Ariyoshi, T. Arai, Y. Hitora, K. Takada, S. Matsunaga, K. Rissanen, M. Fujita, *Nature* **2013**, *495*, 461.

[54] Y. Inokuma, S. Yoshioka, J. Ariyoshi, T. Arai, M. Fujita, *Nat. Protoc.* **2014**, *9*, 246.

[55] E. C. Constable, G. Zhang, C. E. Housecroft, J. A. Zampese, *CrystEngComm* **2011**, *13*, 6864-6870.

[56] B.-C. Wang, Q.-R. Wu, H.-M. Hu, X.-L. Chen, Z.-H. Yang, Y.-Q. Shangguan, M.-L. Yang, G.-L. Xue, *CrystEngComm* **2010**, *12*, 485-492.

[57] C. Liu, Y.-B. Ding, X.-H. Shi, D. Zhang, M.-H. Hu, Y.-G. Yin, D. Li, *Cryst. Growth Des.* **2009**, *9*, 1275-1277.

[58] J. Song, B.-C. Wang, H.-M. Hu, L. Gou, Q.-R. Wu, X.-L. Yang, Y.-Q. Shangguan, F.-X. Dong, G.-L. Xue, *Inorg. Chim. Acta* **2011**, *366*, 134-140.

[59] D.-Y. Ma, D.-E. Sun, G.-Q. Li, *Acta Crystallogr., Sect. E* **2011**, *67*, m913.

[60] G. Zhang, J. Tan, T. Phoenix, D. R. Manke, J. A. Golen, A. L. Rheingold, *RSC Adv.* **2016**, *6*, 9270-9277.

[61] J. Heine, J. Schmedt auf der Günne, S. Dehnen, *J. Am. Chem. Soc.* **2011**, *133*, 10018-10021.

[62] Y.-Q. Chen, G.-R. Li, Y.-K. Qu, Y.-H. Zhang, K.-H. He, Q. Gao, X.-H. Bu, *Cryst. Growth Des.* **2013**, *13*, 901-907.

[63] W. Sun, J. Liu, H. Liu, Z. Liu, *Polyhedron* **2016**, *109*, 1-6.

[64] G. Zhang, Y.-X. Jia, W. Chen, W.-F. Lo, N. Brathwaite, J. A. Golen, A. L. Rheingold, *RSC Adv.* **2015**, *5*, 15870-15879.

[65] J. Granifo, R. Gaviño, E. Freire, R. Baggio, *Acta Crystallogr., Sect. C* **2012**, *68*, m269-m274.

[66] E. C. Constable, C. E. Housecroft, S. Vujovic, J. A. Zampese, *CrystEngComm* **2014**, *16*, 328-338.

[67] J. Granifo, R. Gavino, E. Freire, R. Baggio, *Acta Crystallogr., Sect. C* **2012**, *68*, m269-m274.

[68] E. C. Constable, C. E. Housecroft, S. Vujovic, J. A. Zampese, A. Crochet, S. R. Batten, *CrystEngComm* **2013**, *15*, 10068-10078.

[69] V. N. Dorofeeva, S. V. Kolotilov, M. A. Kiskin, R. A. Polunin, Z. V. Dobrokhotova, O. Cador, S. Golhen, L. Ouahab, I. L. Eremenko, V. M. Novotortsev, *Chem. - Eur. J.* **2012**, *18*, 5006-5012.

[70] G. W. V. Cave, C. L. Raston, *J. Supramol. Chem.* **2002**, *2*, 317-319.

[71] H. Kanno, S. Yamauchi, *J. Solution Chem.* **1991**, *20*, 589-594.

[72] X.-L. Yang, Y.-Q. Shangguan, H.-M. Hu, B. Xu, B.-C. Wang, J. Xie, F. Yuan, M.-L. Yang, F.-X. Dong, G.-L. Xue, *J. Solid State Chem.* **2014**, *216*, 13-22.

[73] E. C. Constable, G. Zhang, E. Coronado, C. E. Housecroft, M. Neuburger, *CrystEngComm* **2010**, *12*, 2139-2145.

[74] Y. Gong, M. M. Zhang, P. Zhang, H. F. Shi, P. G. Jiang, J. H. Lin, *CrystEngComm* **2014**, *16*, 9882-9890.

[75] U. P. Singh, S. Narang, P. Pachfule, R. Banerjee, *CrystEngComm* **2014**, *16*, 5012-5020.

[76] E. C. Constable, C. E. Housecroft, P. Kopecky, M. Neuburger, J. A. Zampese, G. Zhang, *CrystEngComm* **2012**, *14*, 446-452.

[77] S.-S. Shen, X. Wang, H.-M. Hu, F. Yuan, F.-X. Dong, G. Xue, *Polyhedron* **2015**, *91*, 52-58.

[78] W. Yang, X. Lin, J. Jia, A. J. Blake, C. Wilson, P. Hubberstey, N. R. Champness, M. Schroder, *Chem. Commun.* **2008**, 359-361.

[79] J. Wang, G. S. Hanan, *Synlett* **2005**, *2005*, 1251-1254.

[80] J. Yoshida, S.-i. Nishikiori, H. Yuge, *J. Coord. Chem.* **2013**, *66*, 2191-2200.

[81] V. A. Blatov and A. P. Shevchenko, TOPOS Professional v. 4.0, Samara State University, Russia.

[82] E. C. Constable, C. E. Housecroft, S. Vujovic, J. A. Zampese, *CrystEngComm* **2014**, *16*, 3494-3497.

[83] C. F. Macrae, I. J. Bruno, J. A. Chisholm, P. R. Edgington, P. McCabe, E. Pidcock, L. Rodriguez-Monge, R. Taylor, J. van de Streek, P. A. Wood, *J. Appl. Crystallogr.* **2008**, *41*, 466-470.

[84] J. Granifo, M. Vargas, M. T. Garland, A. Ibáñez, R. Gaviño, R. Baggio, *Inorg. Chem. Commun.* **2008**, *11*, 1388-1391.

[85] M. Zhao, J. Tan, J. Su, J. Zhang, S. Zhang, J. Wu, Y. Tian, *Dyes Pigm.* **2016**, *130*, 216-225.

[86] L. Zhang, C.-J. Li, J.-E. He, Y.-Y. Chen, S.-R. Zheng, J. Fan, W.-G. Zhang, *J. Solid State Chem.* **2016**, *233*, 444-454.

[87] J.-Y. Cheng, F.-W. Ding, P. Wang, C.-W. Zhao, Y.-B. Dong, *ChemPlusChem* **2016**, *81*, 743-751.

[88] L. Li, Y. Z. Zhang, C. Yang, E. Liu, J. A. Golen, G. Zhang, *Polyhedron* **2016**, *105*, 115-122.

[89] D. Toledo, A. Vega, N. Pizarro, R. Baggio, O. Peña, T. Roisnel, J.-Y. Pivan, Y. Moreno, *J. Solid State Chem.* **2017**, *253*, 78-88.

[90] P. Yang, M.-S. Wang, J.-J. Shen, M.-X. Li, Z.-X. Wang, M. Shao, X. He, *Dalton Trans.* **2014**, *43*, 1460-1470.

[91] N. Li, H.-L. Guo, H.-M. Hu, J. Song, B. Xu, M.-L. Yang, F.-X. Dong, G.-L. Xue, *J. Solid State Chem.* **2013**, *198*, 416-423.

[92] S.-Q. Guo, D. Tian, X. Zheng, H. Zhang, *CrystEngComm* **2012**, *14*, 3177-3182.

[93] Bruker Analytical X-ray Systems, Inc., APEX2, version 2 User Manual, M86-E01078, Madison, WI, 2006.

[94] Stoe & Cie (2011). X-area Software, Stoe & Cie (1996). XRED V1.08.

[95] L. Palatinus, G. Chapuis, *J. Appl. Crystallogr.* **2007**, *40*, 786-790.

[96] P. W. Betteridge, J. R. Carruthers, R. I. Cooper, K. Prout, D. J. Watkin, *J. Appl. Crystallogr.* **2003**, *36*, 1487.

[97] A. Spek, *Acta Crystallogr., Sect. C* **2015**, *71*, 9-18.

[98] Y. M. Klein, A. Prescimone, M. B. Pitak, S. J.Coles, E. C. Constable, C. E. Housecroft, *CrystEngComm* **2016**, *18*, 4704-4707.

[99] T. Nijs, Y. M. Klein, S. F. Mousavi, A. Ahsan, S. Nowakowska, E. C. Constable, C. E. Housecroft, T. A. Jung, *J. Am. Chem. Soc.* **2018**.

[100] Y. M. Klein, A. Lanzilotto, A. Prescimone, K. W. Krämer, S. Decurtins, S.-X. Liu, E. C. Constable, C. E. Housecroft, *Polyhedron* **2017**, *129*, 71-76.

[101] Y. Maximilian Klein, E. C. Constable, C. E. Housecroft, J. A. Zampese, *Polyhedron* **2014**, *81*, 98-104.

[102] W. A. Alves, R. H. d. A. Santos, A. Paduan-Filho, C. C. Becerra, A. C. Borin, A. M. D. C. Ferreira, *Inorg. Chim. Acta* **2004**, *357*, 2269-2278.

[103] W. E. Marsh, K. C. Patel, W. E. Hatfield, D. J. Hodgson, *Inorg. Chem.* **1983**, *22*, 511-515.

[104] S. Decurtins, H. W. Schmalle, P. Schneuwly, L.-M. Zheng, J. Ensling, A. Hauser, *Inorg. Chem.* **1995**, *34*, 5501-5506.

[105] H. Grove, J. Sletten, M. Julve, F. Lloret, *J. Chem. Soc., Dalton Trans.* **2001**, 1029-1034.

[106] L. Xiao, L. Zhu, Q. Zeng, Q. Liu, J. Zhang, S. Li, H. Zhou, S. Zhang, J. Wu, Y. Tian, *J. Organomet. Chem.* **2015**, *789-790*, 22-28.

[107] E. C. Constable, G. Zhang, C. E. Housecroft, M. Neuburger, J. A. Zampese, *CrystEngComm* **2010**, *12*, 2146-2152.

[108] Y. M. Klein, A. Prescimone, E. C. Constable, C. E. Housecroft, *CrystEngComm* **2015**, *17*, 6483-6492.

[109] Y. M. Klein, A. Prescimone, E. C. Constable, C. E. Housecroft, *Inorg. Chem. Commun.* **2016**, *70*, 118-120.

[110] Y. M. Klein, A. Prescimone, E. C. Constable, C. E. Housecroft, *Polyhedron* **2016**, *103*, 58-65.

[111] Y. M. Klein, A. Prescimone, M. Neuburger, E. C. Constable, C. E. Housecroft, *CrystEngComm* **2017**, *19*, 2894-2902.

[112] Y. Maximilian Klein, E. C. Constable, C. E. Housecroft, A. Prescimone, *CrystEngComm* **2015**, *17*, 2070-2073.

[113] S. R. Batten, R. Robson, *Angew. Chem., Int. Ed.* **1998**, *37*.

[114] S. R. Batten, *CrystEngComm* **2001**, *3*, 67-72.

[115] S. R. Batten, *Curr. Opin. Solid State Mater. Sci.* **2001**, *5*, 107-114.

[116] T. M. Reineke, M. Eddaoudi, D. Moler, M. O'Keeffe, O. M. Yaghi, *J. Am. Chem. Soc.* **2000**, *122*, 4843-4844.

[117] M. Kondo, M. Shimamura, S.-i. Noro, S. Minakoshi, A. Asami, K. Seki, S. Kitagawa, *Chem. Mater.* **2000**, *12*, 1288-1299.

[118] R. Kitaura, K. Seki, G. Akiyama, S. Kitagawa, *Angew. Chem., Int. Ed.* **2003**, *42*, 428-431.

[119] H. Schwertfeger, A. A. Fokin, P. R. Schreiner, *Angew. Chem., Int. Ed.* **2008**, *47*, 1022-1036.

[120] N. Kuhnert, A. Lopez-Periago, G. M. Rossignolo, *Org. Biomol. Chem.* **2005**, *3*, 524-537.

[121] C. L. Moy, R. Kaliappan, A. J. McNeil, *J. Org. Chem.* **2011**, *76*, 8501-8507.

[122] A. A. Buelt, C. A. Conrad, W. D. Mackay, M. F. Shehata, V. D. Smith, R. C. Smith, *Polym. Int.* **2015**, *64*, 730-739.

[123] A. Spek, *Acta Crystallogr., Sect. D* **2009**, *65*, 148-155.